Transactions of the ASME®

Transactions of the ASME, Journal of Engineering for Gas Turbines and Power (ISSN 0742-4795) is published quarterly (Jan., Apr., July, Oct.,) for $150.00 per year by The American Society of Mechanical Engineers, 345 East 47th Street, New York, NY 10017. Second class postage paid at New York, NY and additional mailing offices. POSTMASTER: Send address changes to Transactions of the ASME, Journal of Engineering for Gas Turbines and Power, c/o THE AMERICAN SOCIETY OF MECHANICAL ENGINEERS, 22 Law Drive, Box 2300, Fairfield, NJ 07007-2300.
CHANGES OF ADDRESS must be received at Society headquarters seven weeks before they are to be effective. Please send old label and new address.
PRICES: To members, $40.00, annually; to nonmembers, $150.00.
Add $30.00 for postage to countries outside the United States and Canada.
STATEMENT from By-Laws. The Society shall not be responsible for statements or opinions advanced in papers or . . . printed in its publications (B 7.1, para. 3).

INDEXED by Applied Mechanics Reviews and Engineering Information, Inc.
Canadian Goods & Services Tax Registration #126148048

Journal of Engineering for Gas Turbines and Power

Published Quarterly by The American Society of Mechanical Engineers
VOLUME 116 • NUMBER 3 • JULY 1994

TECHNICAL PAPERS

(Contents Continued on Inside Back Cover)

ANNOUNCEMENTS

Second-Law Analysis of Vapor Compression Heat Pumps With Solution Circuit

K. Amrane
ICF Inc.,
Global Change Division,
1850 K Street NW Suite 1000,
Washington, DC 20006

R. Radermacher
Mechanical Engineering Department,
Center for Environmental
Energy Engineering,
The University of Maryland,
College Park, MD 20742

A second-law analysis is conducted on both the single-stage vapor compression heat pump with solution circuit (VCHSC) and its modified version, the cycle with a preheater and additional desorber. The results are compared to a conventional heat pump cycle operating with pure ammonia. The location and magnitude of the irreversibilities of the individual components constituting the cycles are determined. The entropic average temperature is used in computing the irreversibilities. The total work input to the heat pumps is then conveniently decomposed into two parts: the minimum work input or the work of a reversible cycle operating between the desorber and absorber entropic average temperatures, plus an additional input of work caused by the irreversibilities of the different processes of the cycles. The analysis reveals that the compressor is the most inefficient component of the heat pumps with losses accounting for about one fourth of the work input. The irreversibilities in the desorber and absorber are found to be minimum when there is a good match in both the solution and heat transfer fluid temperature glides. By adding a preheater and an additional desorber, the irreversibilities in the single-stage VCHSC are considerably reduced. However, it is shown that it is the preheater and not the additional desorber that has by far the most significant impact on the heat pump's efficiency improvements. Compared to a conventional ammonia vapor compression cycle, the modified VCHSC, which has twice as many sources of irreversibility, shows nevertheless a maximum improvement of 56.1 percent in second-law efficiency.

Introduction

The second-law analysis, when performed on a system, helps to understand and locate the irreversibilities associated with inefficient processes. Then, the development of new techniques such as better component designs and operating conditions that minimize the irreversible production of entropy and improve the system's performance becomes possible.

The importance of the second-law analysis comes from the fact that it combines the first and second laws of thermodynamics to show the direct relationship that exists between the entropy generated (irreversibilities) by inefficient processes and the inadequate use of energy (loss of work for a power system, or additional work requirements for a refrigeration system) resulting from that.

Studies applying the second-law analysis to various energy systems and components are numerous, as reflected by the large number of scientific publications and textbooks printed (Ahern, 1980; Bejan, 1982; Kotas, 1985; Liu and Wepfer, 1983; Moran, 1989; Sussman, 1981). Of particular interest is the work done on heat pumps, vapor compression refrigeration, and absorption cooling systems (Anand et al., 1984; Bosnjakovic et al., 1986; Briggs, 1971; Cheng and Shih, 1988; Egrican, 1988; Egrican and Karakas, 1986; Knoche and Stehmeier, 1982; Koehler et al., 1988; Kumar et al., 1989; Le Goff et al., 1988; Liang and Kuehn, 1991; Protsenko and Safanov, 1989; Tripp, 1966; Tyagi, 1986). In most of these studies, the second-law analysis is presented as an exergy or availability analysis and is based on a reference state (usually the environment), the characterization of which has been ambiguous and difficult to establish and still need to be standardized (Ahrendts, 1980; Gallo and Milanez, 1990; Sussman, 1979; Wepfer and Gaggioli, 1980). The choice of an appropriate reference state becomes essential when comparing different processes since the exergetic efficiency (usually used for such comparisons) is dependent upon such a reference state.

Alefeld has shown in his work on heat pumps and refrigerators (Alefeld, 1987) and absorption cycles (Alefeld, 1988a, b, 1989) that by applying a rigorous second-law analysis, it is possible to compute the individual irreversibilities without the confusion of having to select a reference state. In his studies, he pointed out that the additional work (for heat pumps and refrigerators) needed to overcome the irreversibilities associated with real processes is a direct function of a temperature that can widely differ from the surroundings or reference temperature. As will be seen later, the choice of this temperature,

Contributed by the Advanced Energy Systems Division for publication in the JOURNAL OF ENGINEERING FOR GAS TURBINES AND POWER. Manuscript received by the Advanced Energy Systems Division January 15, 1992; revision received October 13, 1992. Associate Technical Editor: M. J. Moran.

which is either the condensing or evaporating entropic average temperature of the heat transfer fluid for a refrigerator (cooling mode) or a heat pump (heating mode), respectively, turns out to be the most convenient when analyzing vapor compression heat pumps with solution circuits (VCHSC).

Based on Alefeld's scheme, a second-law analysis is conducted on a single-stage VCHSC and on one of its modified versions; i.e., the cycle with a preheater and additional desorber. The result is then compared to that of a conventional heat pump cycle operating with pure ammonia. The irreversibilities associated with the different processes in the cycles are determined for different operating conditions. Possible systems improvements are then indentified.

Thermodynamic Principles

The formulation of the second law of thermodynamics applied to an arbitrary process $1 \rightarrow 2$ in a closed system, takes the form of an inequality such as:

$$S_2 - S_1 \geq \int_1^2 \frac{\delta Q}{T} \tag{1}$$

where δQ and T represent the variation in the heat transfer interaction and temperature during such a process, respectively. The inequality of Eq. (1) can be transformed to a more useful equality sign by introducing the concept of the entropy generation, S_{gen}:

$$S_{\text{gen}} = S_2 - S_1 - \int_1^2 \frac{\delta Q}{T} \tag{2}$$

S_{gen} is positive for real processes and zero for reversible ones, but is never negative. If the heat transfer during the process $1 \rightarrow 2$ occurs at constant temperature T, then Eq. (2) becomes:

$$S_{\text{gen}} = S_2 - S_1 - \frac{Q_{1\rightarrow 2}}{T} \tag{3}$$

Equation (3), although very useful and simple, is of no practical use for nonisothermal heat transfer processes such as those occurring in cooling units like absorption cycles or VCHSC. These systems use mixtures as their working fluids and as a consequence the evaporation and condensation processes are associated with a change in temperature of both the working and heat transfer fluids. These changes in temperature will be referred throughout the text as temperature glides. By defining an average temperature that represents the transport of entropy associated with a nonisothermal heat transfer process, it is possible to express Eq. (2) in the same manner as Eq. (3). This temperature, called entropic average temperature, is defined as:

$$T_{\text{avg}} = \frac{Q_{1-2}}{\int_1^2 \frac{\delta Q}{T}} \tag{4}$$

A complete derivation of Eq. (4) can be found from Herold (1989). With this definition for T_{avg}, Eq. (2) becomes for nonisothermal heat transfer processes:

$$S_{\text{gen}} = S_2 - S_1 - \frac{Q_{1\rightarrow 2}}{T_{\text{avg}}} \tag{5}$$

A generalization of the second law, i.e., Eq. (5), can be written for a control volume (open system) as:

$$S_{\text{gen}} = \frac{dS}{dt} + \Sigma m_e s_e - \Sigma m_i s_i - \sum_i \frac{Q_i}{T_i} \geq 0 \tag{6}$$

In Eq. (6), the temperature T_i of the heat reservoir at the portion i of the control volume is either uniform for isothermal heat transfer processes or is the entropic average as defined in Eq. (4) for variable temperature ones.

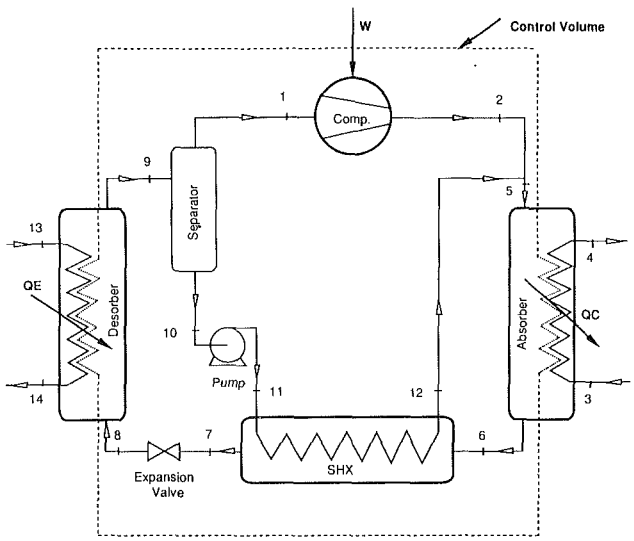

Fig. 1 Single-stage VCHSC

Application to the Single-Stage VCHSC

Figure 1 represents a single-stage vapor compression heat pump with solution circuit. This cycle, which can be seen in many respects as a hybrid system between conventional vapor compression and absorption heat pumps, is made up of six main components: a desorber and an absorber where the refrigerant is desorbed and absorbed out to and into an absorbent, respectively, a pump used to circulate the weak solution (weak in refrigerant) coming out of the desorber, a solution heat exchanger (SHX) where the weak solution is heated by the strong solution, an expansion device used to expand the high-pressure strong solution back to the low pressure and the compressor where the refrigerant vapor coming out of the desorber is compressed to the high-pressure level. The single-stage VCHSC has been studied repeatedly in the literature (Ahlby, 1987; Mucic, 1984; Rane et al., 1989; Stokar and Trepp, 1987) but exclusively from the first law of thermodynamics perspective.

Applying the first and second law of thermodynamics to the control volume shown in Fig. 1 for the single-stage VCHSC gives:

First law

$$Q_c = Q_E + W_T \tag{7}$$

Second law

$$S_{\text{gen}} = \frac{Q_c}{T_{f\ \text{avg},C}} - \frac{Q_E}{T_{f\ \text{avg},E}} \tag{8}$$

where Q_c and Q_E are respectively the heating and cooling loads, W_T the sum of the compressor and pump work and $T_{f\ \text{avg},C}$ and $T_{f\ \text{avg},E}$ the heat transfer fluid entropic average temperature of the absorber (sink) and desorber (source).

The entropy generation as written in Eq. 8 is the sum over all entropy-producing processes constituting the cycle, including the heat transfer to and from the sink and source, respectively. If $S_{\text{gen},i}$ represents the entropy generation of process i in the cycle, then noting that there are seven such processes in the single-stage VCHSC shown in Fig. 1 (other contributions such as those caused by pressure drops and heat losses are neglected), Eq. 8 can be written as:

$$S_{\text{gen}} = \frac{Q_c}{T_{f\ \text{avg},C}} - \frac{Q_E}{T_{f\ \text{avg},E}} = \sum_{i=1}^{7} S_{\text{gen},i} \tag{9}$$

where $\Sigma S_{\text{gen},i}$ represents the following irreversible processes:

•Compression between 1 and 2

$$S_{\text{gen},1} = S_2 - S_1 \tag{10}$$

•Pumping between 10 and 11

$$S_{\text{gen},2} = S_{11} - S_{10} \tag{11}$$

•Mixing of streams 2 and 12

$$S_{\text{gen},3} = S_5 - S_2 - S_{12} \tag{12}$$

•Heat transfer in the solution heat exchanger

$$S_{\text{gen},4} = S_7 - S_6 + S_{12} - S_{11} \tag{13}$$

•Throttling between 7 and 8

$$S_{\text{gen},5} = S_8 - S_7 \tag{14}$$

•Heat transfer in the desorber

$$S_{\text{gen},6} = S_9 - S_8 - \frac{Q_E}{T_{f\ \text{avg},E}} \tag{15}$$

•Heat transfer in the absorber

$$S_{\text{gen},7} = S_6 - S_5 + \frac{Q_c}{T_{f\ \text{avg},C}} \tag{16}$$

It is clear that by summing Eqs. (10)–(16) and by noting that $S_9 = S_{10} + S_1$, Eq. (9) is then obtained.

By substituting Q_c in Eq. (7) into Eq. (9), the following expression is obtained for the work:

$$W_T = Q_E \left[\frac{T_{f\ \text{avg},C} - T_{f\ \text{avg},E}}{T_{f\ \text{avg},E}} \right] + T_{f\ \text{avg},C} \sum_{i=1}^{7} S_{\text{gen},i} \tag{17}$$

The term in brackets in Eq. (17) is the inverse of the cooling COP obtained when the cycle is reversible ($S_{\text{gen}} = 0$):

$$\text{COP}_{\text{rev},C} = \frac{T_{f\ \text{avg},E}}{T_{f\ \text{avg},C} - T_{f\ \text{avg},E}} \tag{18}$$

Equation (17) could be rewritten in a more useful way as:

$$W_T = W_{\text{rev},C} + \sum_{i=1}^{7} W_{i,C} \tag{19}$$

where

$$W_{\text{rev},C} = Q_E \left[\frac{T_{f\ \text{avg},C} - T_{f\ \text{avg},E}}{T_{f\ \text{avg},E}} \right] \tag{20}$$

and

$$\sum_{i=1}^{7} W_{i,C} = T_{f\ \text{avg},C} \sum_{i=1}^{7} S_{\text{gen},i} \tag{21}$$

According to Eq. (19), the work required to produce a cooling load Q_E is made up of a minimum amount, i.e., the work of a reversible cycle working between the heat transfer fluid entropic average temperatures $T_{f,\ \text{avg},C}$ and $T_{f\ \text{avg},E}$, plus an additional work caused by the irreversibilities of the seven processes mentioned above. The additional work of Eq. (21) is frequently referred to in the literature as the "lost available work" (Kestin, 1980; Bejan, 1988) or simply "lost work" (De Nevers and Seader, 1980; Sonntag and Van Wylen, 1982). It is important to realize that the temperature by which the entropy generation is multiplied in Eq. (21), i.e., $T_{f\ \text{avg},C}$, can widely differ from the surroundings temperature T_o usually used in an exergy or availability analysis. The necessity to use a temperature different from that of the surroundings in such analysis has been advocated by other researchers as well (Akau and Schoenhals, 1980; Bejan, 1988; De Nevers and Seader, 1980; London, 1982).

One way of measuring the effectiveness of the heat pump to utilize energy is to evaluate the second-law efficiency. Although different kinds of second-law efficiencies exist in the literature, the one most frequently used is defined as the ratio of the minimum work input (obtained for a reversible cycle) to the actual work input. If we denote by $\eta_{\text{II},C}$ this efficiency in the cooling mode, we have:

$$\eta_{\text{II},C} = \frac{W_{\text{rev},C}}{W_T} \tag{22}$$

By noting that the work W_T can be expressed as the ratio of the cooling load Q_E to the cooling COP and by using Eq. (20), Eq. (22) becomes:

$$\eta_{\text{II},C} = \frac{\text{COP}_C}{\text{COP}_{\text{rev},C}} \tag{23}$$

A look at Eqs. (22) and (23) shows that the value $\eta_{\text{II},C}$ increases from 0 to 1 as the heat pump approaches its reversible limit. For real systems, the value of $\eta_{\text{II},C}$ will always be less than unity, the difference (between 1 and $\eta_{\text{II},C}$) representing the potential for the system's energy utilization improvements.

It should be noted that the second-law efficiency as defined in Eqs. (22) and (23) is identical to the definition of Akau and Schoenhals (1980), as well as to the utilization factor or relative efficiency defined by Kestin (1980) or Bejan (1988) or the quality factor defined by Alefeld (1987, 1988a, b, 1989).

A similar expression for the work as given in Eq. (17) can be obtained for heat pumps (heating mode) if the cooling load Q_E in Eq. (7) is substituted into Eq. (9):

$$W_T = Q_C \left[\frac{T_{f\ \text{avg},C} - T_{f\ \text{avg},E}}{T_{f\ \text{avg},C}} \right] + T_{f\ \text{avg},E} \sum_{i=1}^{7} S_{\text{gen},i} \tag{24}$$

Equation (24) can be rewritten as:

$$W_T = W_{\text{rev},H} + \sum_{i=1}^{7} W_{i,H} \tag{25}$$

where

$$W_{\text{rev},H} = Q_C \left[\frac{T_{f\ \text{avg},C} - T_{f\ \text{avg},E}}{T_{f\ \text{avg},C}} \right] \tag{26}$$

and

$$\sum_{i=1}^{7} W_{i,H} = T_{f\ \text{avg},E} \sum_{i=1}^{7} S_{\text{gen},i} \tag{27}$$

When the VCHSC works in a heating mode, the work required to produce a heating load Q_C is the sum of the minimum work required $W_{\text{rev},H}$ (reversible work) and the additional work due to the irreversibilities $\Sigma W_{i,H}$. It is worth noting here that when the system works in a heating mode, the entropy generation is multiplied by the entropic average temperature of the desorber heat transfer fluid.

Similarly, the second-law efficiency in the heating mode is defined as:

$$\eta_{\text{II},H} = \frac{W_{\text{rev},H}}{W_T} \tag{28}$$

or

$$\eta_{\text{II},H} = \frac{\text{COP}_H}{\text{COP}_{\text{rev},H}} \tag{29}$$

where

$$\text{COP}_H = \frac{Q_c}{W_T} \tag{30}$$

and

$$\text{COP}_{\text{rev},H} = \frac{T_{f\ \text{avg},C}}{T_{f\ \text{avg},C} - T_{f\ \text{avg},E}} \tag{31}$$

Results and Discussions

Operating Conditions. The cycles are simulated using a

computer model based on mass and energy conservation equations along with heat transfer relations. The heat exchangers are described by their UA values. The model's description and logic have been discussed in details by Amrane et al. (1991). Here, only the assumptions made will be reviewed:

1 Negligible pressure drops in the system (except the expansion valve).
2 Heat losses to the surroundings are negligible.
3 The state of the solution leaving the absorber is saturated.
4 Isentropic compressor efficiency and pump efficiency of both 70 percent.
5 Compressor volumetric efficiency of 100 percent.

The thermodynamic properties of the ammonia-water mixture used in this study, including entropy, are evaluated from computer subroutines described by Ziegler and Trepp (1984). The operating conditions at which the cycles are simulated are summarized in Table 1.

Results and Discussion. Figure 2 shows a typical irreversibilities distribution in the single-stage VCHSC. The main contributor to the losses is the compressor, which accounts for about 24 percent of the total work input. Also important are the irreversibilities associated with the mixing of streams 2 and 12, which are in this case even higher than those associated with the heat tranferred in the absorber and desorber. The throttling process makes a considerable contribution to the total system loss with 8 percent, while those of the pump and solution heat exchanger are relatively small. The minimum work, i.e., the work of a reversible (ideal) cycle operating between the same low and high entropic average temperatures required to achieve the desired cooling capacity, represents about 38.5 percent of the total work input. The remaining 61.5 percent is the additional work needed to overcome the irreversibilities associated with the above-mentioned processes.

Table 1 Operating conditions for the basic and modified single-stage VCHSC

Heat Exchangers	H.T. Fluid Inlet Temp. °C	H.T. Fluid Outlet Temp. °C	UA Values Basic VCHSC kW/°C	UA Values Modified VCHSC kW/°C
Desorber	25	10	4.5	4.25
Add.Desorber	-	-	-	0.2
SHX	-	-	0.6	0.3
Preheater	-	-	-	0.75
Absorber	25	45	5.9	5.5
			Total=11.0	Total=11.0
Pump Volumetric Flow Rate: 5.0 E-5 m^3/s Compressor Volumetric Flow Rate: 0.01 m^3/s				

The second-law efficiency in the cooling mode $\eta_{II,C}$ for the single-stage VCHSC is plotted as a function of the weak solution concentration in Fig. 3. As expected, the efficiency is always less than unity with a maximum value of 0.385 at a concentration of 40 wt% ammonia. Also plotted on the figure is the cooling COP. As can be seen, the COP and second-law efficiency curves have exactly the same trend. This is not surprising, since according to the definition, $\eta_{II,C}$ is the ratio of the COP to that of a reversible cycle operating between the low and high heat transfer fluid entropic average temperatures. The reversible COP being constant (because the entropic average temperatures are kept the same) implies that the second-law efficiency is directly proportional to the cooling COP.

The various irreversibility contributions in the single-stage VCHSC are shown in Fig. 4. The largest irreversibilities occur in the compressor and represent about 24 percent of the total work input to the system. Interestingly, these losses are relatively constant and seem to be independent of other irreversibility changes and solution concentrations. This result is understandable since the compressor irreversibility is directly proportional to the compressor volumetric and isentropic efficiencies and changes in these efficiencies affect the entropy production. In this particular example, the volumetric efficiency was assumed to be 100 percent while the isentropic efficiency was taken as constant at 70 percent. As the compressor irreversibilities account for about one fourth of the total work input, one can easily imagine that a more efficient compressor will improve the system's performance significantly. One way of achieving that is to inject the weak solution from the desorber directly into the compressor. By using such an arrangement, isothermal compression can be approached, which drastically reduces the superheat and therefore the ir-

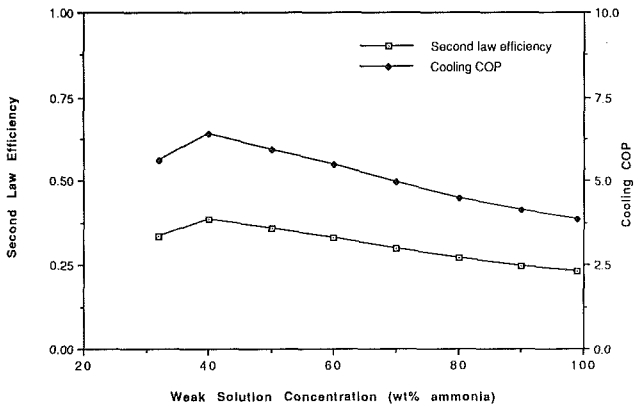

Fig. 3 Variations in second-law efficiency and cooling COP in the single-stage VCHSC with concentration at a pump flow rate of 5 E-5 m^3/s

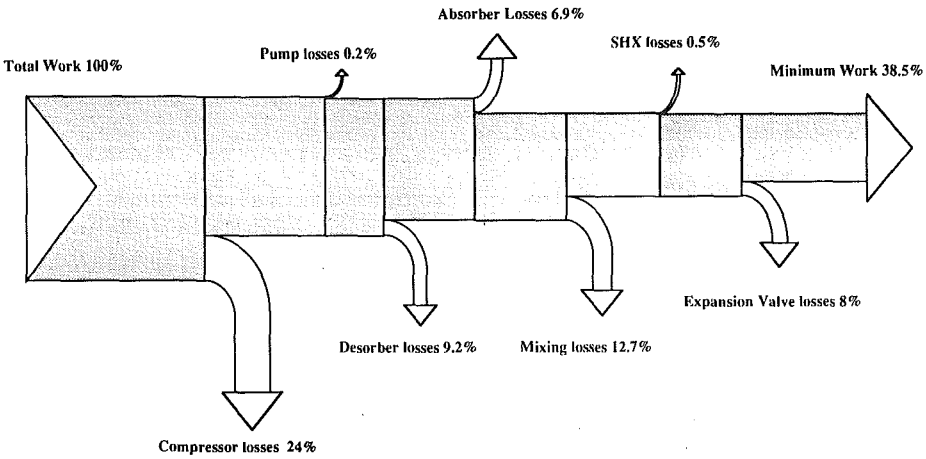

Fig. 2 Irreversibility distribution in the single-stage VCHSC

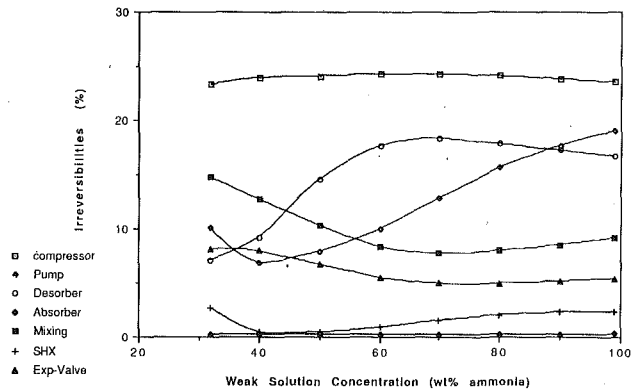

Fig. 4 Irreversibility variations in the single-stage VCHSC with concentration at a pump flow rate of 5 E-5 m^3/s

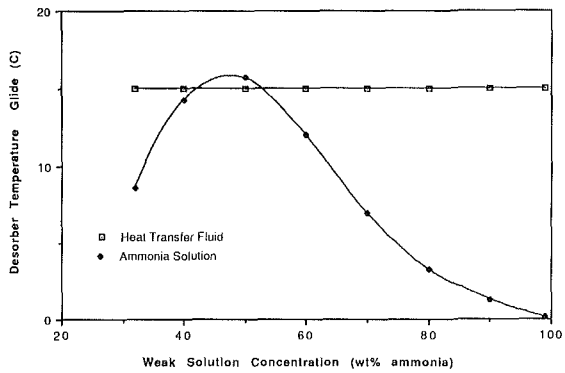

Fig. 5 Desorber temperature glide in the single-stage VCHSC

reversibilities. The screw compressor is one compressor of that kind that can handle both vapor and liquid streams.

The irreversibilities caused by mixing streams 2 and 12 are quite important. They are decreasing with increases in concentration from a maximum of 14.8 percent of the total work at a concentration of 32 percent to a minimum of 7.7 percent at a concentration of 70 percent. This behavior is explained by noting that the mixing losses are due to two different reasons: the difference in temperature of the two streams and the difference in their concentrations. The larger these differences, the larger are the losses. As the weak solution concentration increases, i.e., the concentration of stream 12, the difference in concentration of the two streams (2 and 12) decreases since the vapor concentration (state 1 or 2), which is very close to pure ammonia, remains virtually constant. The temperature difference between streams 2 and 12 also decreases with increases in concentration but only up to the 70 wt% ammonia mark, and then starts to increase. The fact that both the concentration and temperature differences decrease with increasing concentration explains the sharp decline in mixing irreversibilities in the first part of the concentration range. At concentrations higher than 70 percent, and because of competing effects, i.e., the concentration and temperature differences varying in opposite direction, the losses level off. The variation in temperature difference is mainly dictated by the vapor temperature at the compressor outlet and therefore the compressor pressure ratio, which happens to decrease in the lower concentration range and increase at higher concentrations.

The irreversibilities in the desorber are substantial as they are changing from a minimum of 7 percent at a concentration of 32 wt% ammonia to a maximum of 18.4 percent of the work input at a concentration of 70 percent. These losses are caused by the heat transfer through finite temperature differences. One way of explaining these irreversibilities is by looking at Fig. 5, which represents the temperature glide variations in both the solution and heat transfer fluid streams. The minimum entropy generation corresponds to the concentration where there is a good match in the temperature glides. At higher concentrations, the match in temperature glides deteriorates, which explains the increase in irreversibilities.

Similarly, the absorber irreversibilities are also important and vary from a minimum of 7 percent to a maximum of 19 percent of the total work input. The causes and reasons of these losses are identical to those stated above for the desorber. However, it is important to note that the COP and the second-law efficiency are maximum when the absorber irreversibilities are minimum. This tends to suggest that the absorber heat transfer has the greatest impact on the system's performance.

The irreversibilities in the expansion valve are not negligible as they vary from a maximum of 8 percent of the total work at a concentration of 32 percent to a minimum of 4.1 percent at a concentration of 70 percent. The irreversibilities in the expansion valve are caused by two main reasons: the pressure drop across the valve and the degree of subcooling of the solution at the inlet of the throttling device. The lower the pressure drop and the larger the degree of subcooling, the lower the irreversibilities will be. As the concentration increases, the degree of subcooling of the solution at the valve inlet is increasing, explaining the reduction in irreversibilities (the pressure drop across the valve being relatively constant). The increase in the degree of subcooling which is only the temperature drop of the strong solution in the solution heat exchanger (SHX), is due to the increase in the SHX effectiveness as the concentration increases. This is what is happening when the weak solution concentration varies from 32 to 70 wt% ammonia. At higher concentrations, the irreversibilities level off as the degree of subcooling of the solution stabilizes because of relatively constant SHX effectiveness.

The solution heat exchanger irreversibilities are the lowest in the system (next to those of the solution pump, which are negligible). They are from a maximum of 2.7 percent of the input work at 32 wt% ammonia to a minimum of 0.4 percent around 42 percent concentration. These irreversibilities are caused by the heat transferred through finite temperature differences between the weak and strong ammonia solution. As in any heat exchanger, the heat transfer losses are minimum when there is a good match in the temperature change (or glide) of the cold and hot fluid streams. For the SHX, the match in temperature glide can never be perfect since the change in temperature of the weak solution is always greater than that of the strong solution. Nevertheless, the minimum in entropy generation occurs when the difference in the solution temperatures at the cold and hot ends of the exchanger is minimum. This happens when the SHX effectiveness increases significantly at low concentrations. At higher concentrations, the irreversibilities increase as the SHX effectiveness remains relatively constant and the difference in temperatures gets larger.

The variations in the second law efficiency and cooling COP with temperature lift are shown in Fig. 6. The analysis is conducted for a constant pump flow rate of 5.0 E-5 m^3/s and a fixed weak solution concentration of 50 wt% ammonia. Also, when varying the temperature lift, the source temperature and the UA values were kept identical to those selected previously. As expected, the COP continuously decreases with increase in temperature lift since the pressure ratio and consequently the compressor work are increasing while the cooling load remains unchanged. The second-law efficiency curve has a totally different trend. The efficiency first increases until it reaches a maximum of 0.424 at a temperature lift of 50°C and then decreases. The increase in $\eta_{II,C}$ when the temperature lift varies from 20 to 50°C is around 19 percent while for the same changes in temperature lift the COP decreases by as much as 56 percent. This time, the second-law efficiency and the COP

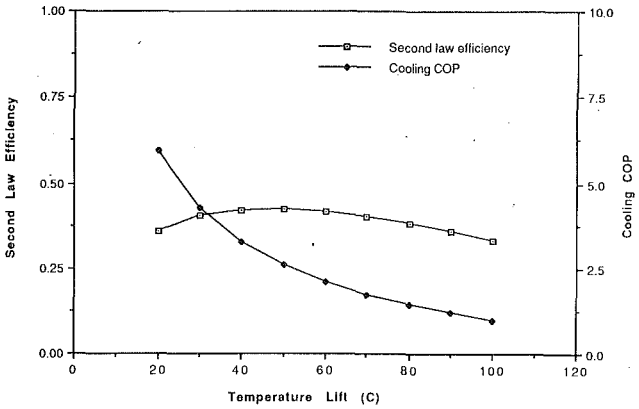

Fig. 6 Variations of second-law efficiency and COP in the single-stage VCHSC with temperature lift

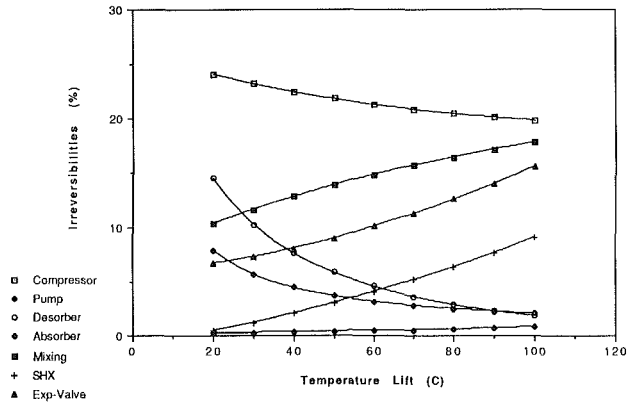

Fig. 7 Irreversibility variations in the single-stage VCHSC with temperature lift

curves have different shapes because the heat transfer fluid entropic average temperature in the absorber is constantly changing. Quite different and opposite conclusions can be drawn from Fig. 6. According to the first-law efficiency the heat pump should be operated at the lowest possible temperature lift. But according to the second-law efficiency, the system uses energy more efficiently at a temperature lift of 50°C. In other words, it is at that temperature lift that the entropy production is minimum. These results seem to indicate that the single-stage VCHSC is more suited for midrange temperature lifts.

The irreversibility variations in the various components of the heat pump are shown in Fig. 7. The irreversibilities in the expansion valve, SHX and those due to mixing are sharply increasing with increase in temperature lift while the irreversibilities in the desorber, absorber, and compressor are decreasing. The irreversibilities in the pump are constant and almost negligible. The maximum in the second-law efficiency curve corresponds to the temperature lift where the sum of all irreversibilities is minimum (or when the minimum work is maximum).

The increase in irreversibilities due to mixing is solely caused here by the difference in temperature of streams 2 and 12, which is continuously increasing with the temperature lift. The difference in concentration remains constant in this case since the weak solution concentration was kept unchanged.

The expansion valve losses are this time very important. They increase rapidly with the temperature lift because of large increases in pressure drop across the valve, which keep getting larger at higher temperature lifts.

The solution heat exchanger irreversibilities are substantial in this particular case. They increase monotonically with the temperature lift because of increasing temperature difference at the cold and hot ends of the heat exchanger.

Interestingly, both irreversibilities in the absorber and desorber are decreasing as the temperature lift increases. A look at the temperature glides shows that they are relatively constant (because of constant pump flow rate and concentration) and that they match quite well their respective heat transfer fluid temperature changes for the entire range in temperature lift investigated. A closer look at the temperature difference in the cold and hot ends of the heat exchangers reveals that the irreversibilities are minimum when the temperature differences are minimum, principally the one in the cold end. This finding is quite important because it reveals that in order to generate the minimum possible entropy in the absorber and desorber, not only should there be a good match in the temperature glides, but the difference in temperature at the cold end of the heat exchanger should be as small as possible.

The compressor irreversibilities are slightly decreasing with higher temperature lifts, although the compressor isentropic efficiency remains constant. This slight decline in irreversibilities is due to a decrease in the rate of entropy generation during the compression process as the high side pressure gets larger and larger (the low side pressure being relatively constant) as can be seen by the diverging entropy lines of ammonia on P–h diagram (ASHRAE, 1989).

The irreversibilities in the single-stage VCHSC can be reduced by adding a preheater and an additional desorber, as shown in Fig. 8. The preheater does not need to be an independent unit as it is assumed here but can be integrated in the absorber by using a triple pass heat exchanger.

Figure 9 shows the variations in the second-law efficiency for both the basic and the modified VCHSC with concentrations at a pump flow rate of 5.0 E-5 m^3/s. At low concentrations, the modified VCHSC performs much better with improvements in efficiency by as much as 15.5 percent. At high concentrations, the improvement reduces to be almost negligible at concentrations above 70 wt% ammonia. The reasons for a better efficiency can be explained by looking at Fig. 10 where the irreversibility contributions of the various components of the modified VCHSC are plotted with respect to concentration. In addition to the irreversibilities of the component already present in the basic VCHSC, are those due to the additional desorber and the preheater. The irreversibilities due to the mixing of streams 2 and 12 are replaced here by those due to the mixing of streams 19 and 25, 22 and 24 (see Fig. 8). At first glance, it seems that the irreversibilities in the major components, i.e., the compressor, the desorber, the absorber, SHX, and the expansion valve are not very much altered by the two new additional heat exchangers except for the irreversibilities due to mixing. Indeed, by comparing Figs. 10 and 4 we can conclude that by preheating the solution after the solution heat exchanger, the irreversibilities due to mixing can be reduced by as much as 50 percent in the low concentration range. At higher concentrations, the reduction in irreversibilities is less important since the heat exchanged in the preheater is much less (because of decreasing mass flow rates) and therefore the solution temperature rise is less significant. It should be noted that although streams 19 and 22, and similarly 24 and 25 are at the same temperatures and concentrations, the losses due to the mixing of streams 22 and 24 are much more important (than that of streams 19 and 25) because their respective mass flow rates are much higher.

With a closer look at Fig. 10, one can see that the irreversibilities in the absorber get reduced at low concentrations because of better match in temperature glides, which results from preheating the solution. At higher concentrations the irreversibilities are almost identical to that in the basic cycle since the preheater's role is reduced. The reduction of the absorber irreversibilities is compensated by the losses in the preheater such that their sum (losses in absorber plus losses in

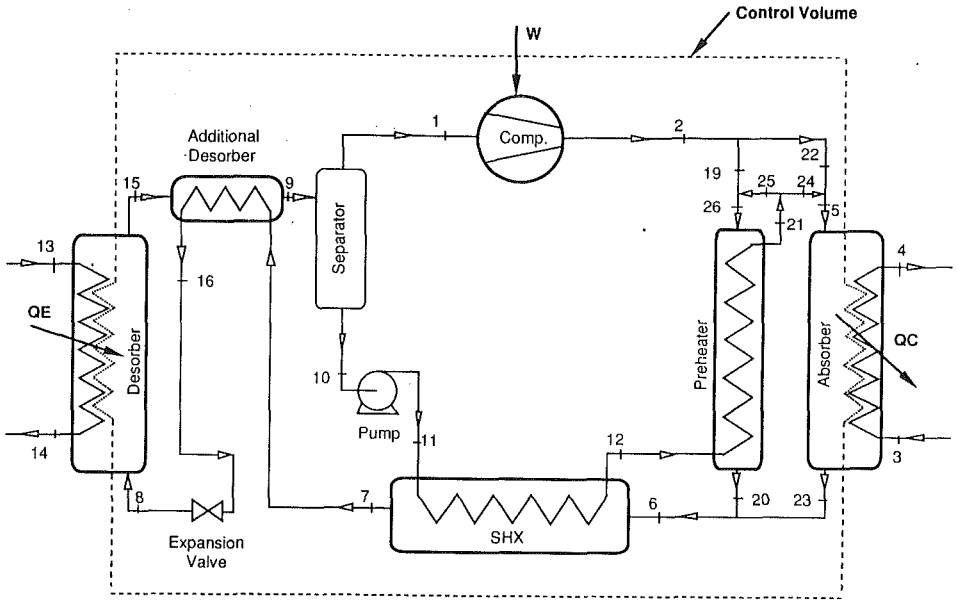

Fig. 8 Single-stage VCHSC with preheater and additional desorber

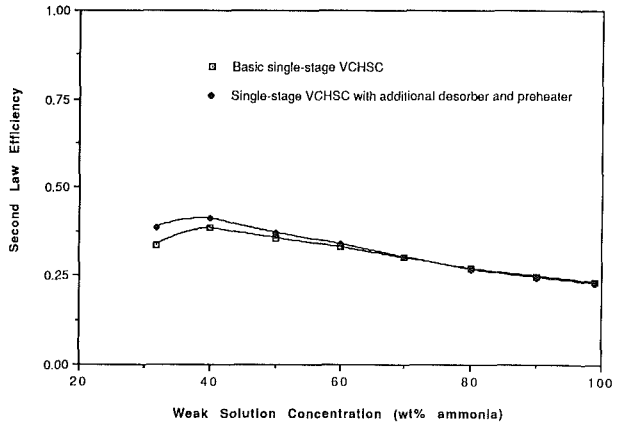

Fig. 9 Second-law efficiency comparison in the basic and modified VCHSC at a pump flow rate of 5 E-5 m^3/s

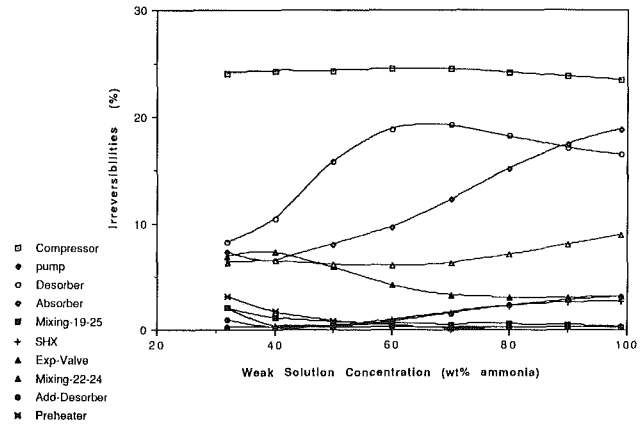

Fig. 10 Irreversibility variations in the modified VCHSC with concentration at a pump flow rate of 5 E-5 m^3/s

preheater) is very close to that of the absorber in the basic VCHSC.

The solution heat exchanger sees its irreversibilities reduced for most of the concentration range mainly because the temperature of the strong solution at the SHX inlet is lowered in the preheater. Again much of the improvement in entropy generation disappears at higher concentration because of less heat exchanged in the preheater.

The irreversibilities in the expansion valve are significantly less in the modified VCHSC. The reason for that reduction in irreversibilities is attributed to the substantial subcooling that the strong solution undergoes inside the additional desorber.

The decrease in the expansion valve losses is offset by an increase in the desorber irreversibilities and those resulting from the heat transfer inside the additional desorber. The somewhat larger desorber losses are due to the decrease in the solution temperature at the heat exchanger, inlet, which results in a larger temperature difference between the solution and the heat transfer fluid.

The compressor irreversibilities remain unchanged, although the pressure ratio and the compressor work are reduced. This result, which does not fully demonstrate the benefit of the additional desorber to the compression process from the second-law point of view, is due to the isentropic efficiency assumed constant. In a more realistic approach, the reduction in pressure ratio would have been translated in an increase in the isentropic efficiency and a reduction in irreversibilities.

From the preceding discussion, it is clear that the addition of a preheater and an extra desorber has a beneficial impact on the performance of the system. Nevertheless, the analysis above demonstrates with certainty that it is the preheater and not the additional desorber that has the greatest repercussions on the heat pump efficiency.

Comparison With Conventional Ammonia Cycle. A conventional ammonia vapor compression cycle is then simulated and the irreversibilities of the different processes compared to those of the basic and modified VCHSC as shown in Table 2. The comparison is made for the operating conditions outlined in Table 1 and at a concentration of 40 wt% ammonia for both VCHSCs. The results clearly indicate that vapor compression heat pumps with solution circuit utilize energy more efficiently than the conventional ammonia cycle as can be seen by looking at the second-law efficiency. In this example, a maximum increase of 56.1 percent in $\eta_{II,C}$ is obtained when comparing the conventional ammonia cycle to the modified VCHSC. The reasons for improved performances for the VCHSCs can be readily understood by further examining Table

Table 2 Irreversibility distribution in the cycle components

Components	Irreversibilities kW, (percentage of input work)		
	Conventional NH3	Basic VCHSC	Modified VCHSC
Compressor	2.53 (24.4)	0.59 (24.0)	0.56 (24.4)
Desorber	1.86 (17.8)	0.225 (9.2)	0.24 (10.5)
Absorber	2.60 (24.9)	0.17 (6.9)	0.15 (6.5)
Expansion Valve	0.675 (6.5)	0.195 (8.0)	0.17 (7.3)
SHX	-	0.012 (0.5)	0.009 (0.4)
Solution Pump	-	0.006 (0.25)	0.005 (0.23)
Mixing 2-12	-	0.31 (12.7)	-
Mixing 22-24	-	-	0.15 (6.5)
Mixing 19-25	-	-	0.03 (1.1)
Additional Desorber	-	-	0.005 (0.21)
Preheater	-	-	0.04 (1.7)
$\Sigma W_{i,C}$	7.66 (73.6)	1.51 (61.5)	1.36 (58.8)
$\eta_{II,C}$	0.264	0.385	0.412

2. The most important difference in irreversibilities comes from the two main heat exchangers, namely the desorber and absorber (or evaporator and condenser for the conventional cycle). For the conventional NH3 refrigeration cycle, the desorber and absorber irreversibilities account for about 18 and 25 percent of the input work, respectively, while for both VCHSCs, the losses are around only 10 percent for the desorber and as little as 7 percent for the absorber. This shows how important heat transfer through temperature glides is in helping to achieve higher efficiencies. This is further reflected by noting that although the modified VCHSC has twice as many sources of irreversibility as the pure ammonia cycle, its "lost work" ($\Sigma W_{i,C}$) represents 58.8 percent of the input work as compared to 73.6 percent for the pure ammonia refrigeration cycle.

Conclusions

A second-law analysis was conducted on the single-stage VCHSC and its modified version. The irreversibilities associated with the different processes in the cycles were determined for a variety of operating conditions. The irreversibilities were computed with an average temperature representing the flow of entropy associated with a nonisothermal heat transfer process. This temperature, called entropic average temperature, is evaluated either in the absorber when the heat pump works in the cooling mode or in the desorber when it works in the heating mode. The total work input can then be expressed as the sum of the minimum work, i.e., the work of a reversible cycle operating between the low and high heat transfer fluid entropic average temperatures, plus additional work caused by the different irreversibilities.

Based on this analysis, the following conclusions can be drawn:

1 The largest sources of irreversibility is in the compressor and accounts for about 24 percent of the total work input. These losses remain constant for the entire range of concentration investigated because of constant compressor isentropic and volumetric efficiencies.

2 The irreversibilities resulting from mixing different streams are important and are caused by the difference in temperatures and concentrations of the streams. The entropy production is found to decrease at low concentrations because of lower temperature and concentration differences. At higher weak solution concentrations the losses increase as the superheated vapor temperature keeps increasing.

3 The irreversibilities in the absorber and desorber are caused by the heat transfer through finite temperature differences. The losses are found to depend on the match in both the solution and heat transfer fluid temperature glides; the better the match, the lower the irreversibilities. Of all the components, the absorber heat transfer has the greatest impact on the system's performance.

4 The entropy production in the expansion valve averages a value of 6 percent of the input work. The irreversibilities are found to depend strongly on the degree of subcooling of the solution at the valve.inlet; the larger it is, the lower the losses.

5 The solution heat exchanger irreversibilities are the lowest in the system and are caused by the heat transfer through finite temperature differences and mismatch of heat capacities. The losses depend on the temperature difference at the cold and hot ends of the heat exchanger, the lower the temperature difference, the lower the entropy production.

6 The second-law efficiency and the COP curves have different trends when the temperature lift is varied. According to the second law the heat pump uses energy more efficiently at a temperature lift of 50°C, suggesting that the single-stage VCHSC is more suited for midrange temperature applications.

7 The addition of a preheater and a desorber reduces the system's irreversibilities. Losses due to mixing are reduced by as much as 50 percent in the low concentration range. The entropy generation in the absorber is reduced, but this reduction is compensated by losses in the preheater. The analysis shows clearly that of the two additional heat exchangers, it is the preheater that has the most significant impact on the system's improvement.

8 The irreversibilities in the expansion valve are noticeably less than what they are in the basic VCHSC because of significant subcooling of the solution inside the additional desorber. But again, this reduction in losses is offset by larger desorber irreversibilities and new losses inside the additional desorber.

9 Finally, when compared to a conventional ammonia cycle, the modified VCHSC shows a maximum improvement of 56.1 percent in second law efficiency, although it has twice as many sources of irreversibility.

Acknowledgments

The support of this study by the National Science Foundation, the US Department of Energy, and the University of Maryland, Engineering Research Center is gratefully acknowledged.

References

Ahern, J. E., 1980, *The Exergy Method of Energy System Analysis*, Wiley, New York.

Ahlby, L., 1987, "Compression/Absorption Cycles for Large Heat Pumps—System Simulation," Licentiate thesis, Department of Heat and Power Technology, Chalmers University, Gothenburg, Sweden.

Ahrendts, J., 1980, "Reference States," *Energy*, Vol. 5, pp. 667-677.

Akau, R. L., and Schoenhals, R. J., 1980, "The Second Law Efficiency of a Heat Pump System," *Energy*, Vol. 5, pp. 853-863.

Alefeld, G., 1987, "Efficiency of Compressor Heat Pumps and Refrigerators Derived From the Second Law of Thermodynamics," *International Journal of Refrigeration*, Vol. 10, pp. 331-341.

Alefeld, G., 1988a, "Second Law Analysis of Absorption Heat Pumps and Heat Transformers," presented at CEC British Gas International Workshop on Absorption Heat Pumps, London, United Kingdom, April 12-14.

Alefeld, G., 1988b, "Problems With the Exergy Concept (or the Missing Second Law)," *Newsletter to the IEA Heat Pump Center*, Vol. 6, No. 3.

Alefeld, G., 1989, "Second Law Analysis of an Absorption Chiller," *Newsletter to the IEA Heat Pump Center*, Vol. 7, No. 2.

Amrane, K., Rane, M. V., and Radermacher, R., 1991, "Performance Curves for Single-Stage Vapor Compression Cycles With Solution Circuit," ASME JOURNAL OF ENGINEERING FOR GAS TURBINES AND POWER, Vol. 113, pp. 221-227.

Anand, D. K., Lindler, K. W., Schweitzer, S., and Kennish, W. J., 1984, "Second Law Analysis of Solar Powered Absorption Cooling Cycles and Systems," ASME *Journal of Solar Energy Engineering*, Vol. 106, pp. 291-298.

ASHRAE, 1989, *Handbook of Fundamentals*, Atlanta, GA.

Bejan, A., 1982, *Entropy Generation Through Heat and Fluid Flow*, Wiley, New York.

Bejan, A., 1988, *Advanced Engineering Thermodynamics*, Wiley, New York.

Bosnjakovic, F., Knoche, K. F., and Stehmeier, D., 1986, "Exergetic Analysis of Ammonia/Water Absorption Heat Pumps," presented at the ASME Winter Annual Meeting Anaheim, CA, Dec. 7-12.

Briggs, S. W., 1971, "Second Law Analysis of Absorption Refrigeration," *Proceedings of AGA and ISF Conference on Natural Gas Research and Technology*, Chicago, IL.

Cheng, C. S., and Shih, Y. S., 1988, "Exergy and Energy Analysis of Absorption Heat Pumps," *International Journal of Energy Research*, Vol. 12, pp. 189-203.

De Nevers, N., and Seader, J. D., 1980, "Lost Work: A Measure of Thermodynamics Efficiency," *Energy*, Vol. 5, pp. 757-769.

Egrican, A. N., and Karakas, A., 1986, "Second Law Analysis of a Solar Powered Rankine Cycle/Vapor Compression Cycle," *Journal of Heat Recovery Systems*, Vol. 6, pp. 135-141.

Egrican, N., 1988, "The Second Law Analysis of Absorption Cooling Cycles," *Heat Recovery Systems & CHP*, Vol. 8, No. 6, pp. 549-558.

Gallo, W. L. R., and Milanez, L. F., 1990, "Choice of a Reference State for Exergetic Analysis," *Energy*, Vol. 15, No. 2, pp. 113-121.

Herold, K. E., 1989, "Performance Limits for Thermodynamic Cycles," presented at the ASME Winter Annual Meeting, San Francisco, CA.

Kestin, J., 1980, "Availability: The Concept and Associated Terminology," *Energy*, Vol. 5, pp. 679-692.

Knoche, K. F., and Stehmeier, D., 1982, "Exergetic Criterion for the Development of Absorption Heat Pumps," *Chem. Eng. Commun.*, Vol. 17, pp. 183-194.

Koehler, W. J., Warren, I. E., Soltes, J., and Winter, E. R., 1988, "Availability Simulations of a Lithium Bromide Absorption Heat Pump," *Heat Recovery Systems & CHP*, Vol. No. 2, pp. 157-171.

Kotas, T. J., 1985, *The Exergy Method of Thermal Plant Analysis*, Butterworth, London.

Kumar, S., Prevost, M., and Bugarel, R., 1989, "Exergy Analysis of a Compression Refrigeration System," *Heat Recovery System & CHP*, Vol. 9, No. 2, pp. 151-157.

Le Goff, P., Louis, G., and Ramadane, A., 1988, "Multi-stage Absorption Heat Pumps, Exergy Analysis and New Design," presented at the Absorption Expert Meeting, Dallas, TX, Feb. 4-6.

Liang, H., and Kuehn, T. H., 1991, "Irreversibility Analysis of a Water to Water Mechanical-Compression Heat Pump," *Energy*, Vol. 6, pp. 883-896.

Liu, Y. A., and Wepfer, W. J., 1983, "Theory and Applications of Second Analysis: a Bibliography," in: R. Gaggioli, ed., *Thermodynamics: Second Law Analysis*, Vol. II, ACS Symposium Series, Washington, DC.

London, A. L., 1982, "Economics and the Second Law: An Engineering View Point and Methodology," *International Journal of Heat and Mass Transfer*, Vol. 25, No. 6, pp. 743-751.

Moran, M. J., 1989, *Availability Analysis: A Guide to Efficient Energy Use*, ASME Press, New York.

Mucic, V., 1984, "Two Media Resorption Compression Heat Pump With Solution Circuit," presented at the 2nd International Symposium on the Large Scale Application of Heat Pumps, Sept. 25-27, York, United Kingdom.

Protsenko, V. P., and Safanov, V. K., 1989, "Exergetic Efficiency of Heat Pump Units," *Power Engineering*, Vol. 27, No. 1, pp. 110-117.

Rane, M. V., Radermacher, R., and Herold, K. E., 1989, "Experimental Investigation of a Single-Stage Vapor Compression Heat Pump With Solution Circuit," presented at the ASME Winter Annual Meeting, San Francisco, CA.

Sonntag, R. E., and Van Wylen, G., 1982, *Introduction to Thermodynamics Classical and Statistical*, Wiley, New York.

Stokar, M., and Trepp, Ch., 1987, Compression Heat Pump With Solution Circuit. Part 1: Design and Experimental Results," *International Journal of Refrigeration*, Vol. 10, pp. 87-96.

Sussman, M. V., 1979, "Choosing a Reference Environment State for Available Energy Computations," presented at the 72nd Annual Meeting of the Institute of Chemical Engineers, San Francisco, CA, Nov. 25-29.

Sussman, M. V., 1981, *Available (Exergy) Analysis*, Mulliken House, Lexington, MA.

Tripp, W., 1966, "Second Law Analysis of Compression Refrigeration Systems," *ASHRAE Journal*, Vol. 8, No. 1, pp. 49-57.

Tyagi, K. P., 1986, "Second Law Analysis of NH3-NaSCN Absorption Refrigeration Cycle," *Journal of Heat Recovery Systems*, Vol. 6, pp. 73-82.

Wepfer, R. A., and Gaggioli, R. A., 1980, "Reference Datum for Available Energy," *ASC Symposium Series*, Vol. 122, pp. 77-92.

Ziegler, B., and Trepp, C., 1984, "Equation of State for Ammonia-Water Mixtures," *International Journal of Refrigeration*, Vol. 7, pp. 101-107.

Application of an Expert System to the Design of Furnace of a Circulating Fluidized Bed Boiler

P. Basu

S. Mitra

Department of Mechanical Engineering,
Technical University of Nova Scotia,
Halifax, Canada B3J 2X4

The design of a boiler using a new technology, i.e., circulating fluidized bed combustion, requires a considerable amount of expertise, which is a combination of experience, knowledge of the subject, and intuition. Boiler vendors, who are required to prepare a large number of proposals, rely heavily on the the skill and judgment of their senior (expert) designers. An artificial intelligence based expert system can greatly simplify this task. This system can assist expert designers to store their experience and decision-making skill through the code of a computer program, which remains intact and ready to apply their skill uniformly and rapidly to all designs when required. This may allow novice designers to carry out routine proposal designs, freeing the experts to improve current designs. The present paper gives an illustration of the use of expert systems to the design of only one aspect of the furnace, which is furnace cross section. It shows that in addition to the standard method of determining the furnace area from the fluidization, the design can take advantage of previous experience, which lists grate heat release rate and other relevant parameters. The expert system also modifies the calculated value to meet different concerns of the boiler purchaser and/or his consultants. Finally the expert develops a compromise of different considerations and requirements with importance attached to them. The paper also shows how the design will change when the importance attached to a particular constraint is relaxed.

1 Introduction

Design of the furnace of a Circulating Fluidized Bed (CFB) boiler requires a large amount of compromise. Ironically, information needed for this design is speculative at best. This throws a formidable challenge to the designers. The design of even the most basic item requires numerous considerations. These considerations may be generally classified under the following groups.

1 Mandatory conditions.
2 Preferred conditions amenable to compromise.
3 Additional conditions/considerations imposed by the client and/or his consultant.
4 Manufacturer's design philosophy or experience base.

For the furnace design the mandatory conditions may include:

(*a*) Coal of a given specification must complete combustion within the CFB furnace loop with an acceptable efficiency.
(*b*) The stipulated level of sulfur dioxide emission must be met at the specified calcium to sulfur ratio.
(*c*) Specified level of nitrogen oxide emission must not be exceeded.
(*d*) Steam quality and output must meet the specification.

Preferred conditions include:

(*a*) The furnace should operate under "fast-fluidized" conditions (some designers may consider this mandatory).
(*b*) Erosion of furnace wall tubes is minimum.
(*c*) Capital cost of the furnace is minimum.
(*d*) The furnace is well fluidized during start-up and part-load.

Additional considerations stipulated by the client or his consultants may vary widely. Some of the considerations may be as follows:

(*a*) The boiler may have to work under part-load conditions for a substantial part of the time.
(*b*) The consultant may require very conservative feed point spacing.
(*c*) The plant owner may want full-load with half the sorbent feeders in operation.

In addition to the above, there may be some auxiliary stipulations from the consideration of fabrication, serviceability, and/or instrumentation.

Each manufacturer has its own distinct design preference. For example, some may use a furnace superficial velocity slightly higher than that used by others. The other major distinguishing features of the design of different manufacturers are:

(*a*) Use of in-bed heat transfer surfaces like platen or cross-tube bundles.

Contributed by the Fuels and Combustion Technologies Division for publication in the JOURNAL OF ENGINEERING FOR GAS TURBINES AND POWER. Manuscript received by the Fuels and Combustion Technologies Division November 2, 1992. Associate Technical Editor: D. W. Pacer.

(*b*) Use of external bubbling fluidized bed heat exchangers.
(*c*) Use of bubbling fluidized bed heat exchangers integral to the furnace.
(*d*) Use of tapered lower furnace.
(*e*) Use of impact separator instead of hot cyclones.

Each of the features or considerations above has some bearing on the size and height of the furnace. So, a rational design finds the best compromise of the above factors. The present paper will demonstrate the use of an expert system in meeting some of the design considerations through a rational compromise while determining the cross-sectional area of the furnace of a CFB boiler.

2 Design Procedure

If the designs were unconstrained, the designer would be guided by one of the mandatory conditions, steam ouput for example. So, one can follow a simple procedure as below:

For a given steam output, one can calculate the required heat input into the furnace by using the heat balance (Basu and Fraser, 1991). Stoichiometric calculations are carried out for the design fuel giving the amount of flue gas (G) generate at normal temperature (273 K). A furnace temperature (T_b) of 1123 K is chosen as being the most favorable temperature for sulfur retention using limestone. The width of this favored temperature zone may, however, depend on the sorbent particle size. Once the bed temperature is known, the flue gas volume can be calculated at this temperature.

Now, the designer must choose an "appropriate" superficial furnace gas velocity (U_f). For the chosen velocity the furnace cross section (A) can be calculated as

$$A = \frac{G}{U_f} \cdot \frac{T_b}{273 \times 1.3} \tag{1}$$

The next question is how to choose the fluidizing velocity U_f. By definition U_f should be within the "fast fluidization" regime. This stipulation is important because the best features of a CFB boiler result directly from the special hydrodynamic condition of the "fast fluidization" regime. Unlike other gas-solid contacting processes (bubbling fluidization or pneumatic transport for example), the velocity limits are not known very precisely in fast-fluidized beds at the moment. From their experience, the CFB manufacturers found a velocity range of 4–6 m/s to be adequate for fast fluidization under normal operating conditions in a CFB boiler. Some empirical relations defining the limits of fast fluidization are available in the literature, but they have to be used with caution because of the restricted range of data on which they are based. One such relation is given below (Guilin and Junke, 1991):

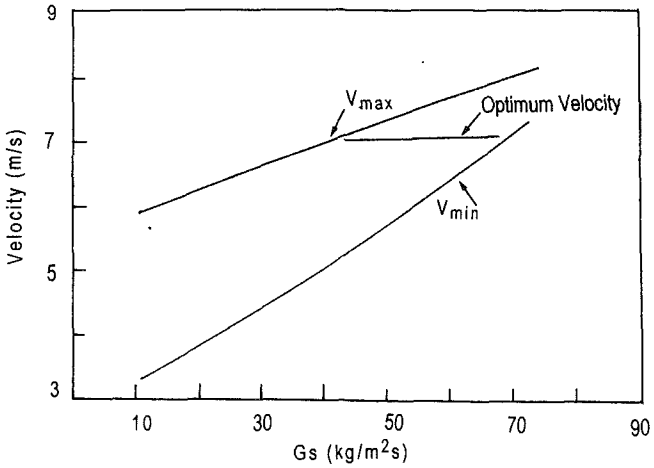

Fig. 1 Limits of velocity for fast fluidization

Lower limit of fast fluidization

$$V_{\min} = 1.172 \left(\frac{G_s}{\rho_p \sqrt{g d_p}} + 1 \right)^{1.968} (\mathrm{Ar})^{0.356} \frac{\mu_f}{d_p \rho r} \tag{2}$$

Upper limit of fast fluidization

$$V_{\max} = 2.050 \left(\frac{G_s}{\rho_p \sqrt{g d_p}} + 1 \right)^{0.793} (\mathrm{Ar})^{0.393} \frac{\mu_f}{d_p \rho_f} \tag{3}$$

where G_s is the circulation rate (kg/m^{2}s). It is assumed from experience as 10.0.

This limit is plotted in Fig. 1. Equations (2) and (3) may be modified when better correlations are available. However, from Fig. 1 we see that for a given circulation rate a range of velocities can be obtained from which a design velocity should be chosen to maintain the bed in the fast bed condition under most operating conditions. Designers often rely on the experience of previously designed units to choose a value of this velocity. They look for plants operating on fuels similar to the designed fuel, and use a grate heat release rate (hence the velocity) close to that of the operating plant. Such a practice greatly removes the uncertainty from the design.

Nomenclature

A = furnace bed cross-sectional area, m^2
Ar = Archimedes number = $gdp^3Pg(P_p - P_g)/u^2$
d_p = average diameter of particles, m
g = acceleration due to gravity, dm/s^2
G = flue gas mass velocity, kg/m^{2}s
G_s = solid circulation rate, kg/m^{2}s
H = steam enthalpy, kJ/kg
HHV = high heating value, kJ/kg
L = length of the furnace bed, m
M_s = steam flow rate, kg/s
m = mass of flue gas of combustion heat at full load, kg/kJ
m_f = mass of flue gas per second, kg/s
P = pressure, bar
Q = heat absorption rate of steam, kW
Q_i = furnace heat input, kW
Q_F = amount of heat absorbed by heat transfer surface, kW
Q_W = amount of heat absorbed by furnace water wall tubes, kW
q = grate heat release rate, MW/m^2
T_b = furnace temperature, K
U_f = optimum fluidizing velocity chosen form experience table, m/s
u_{choice} = velocity suggested by the expert system for the given constraint, m/s
$V_{\max}$ = maximum limit of superficial gas velocity for fast fluidization, m/s
$V_{\min}$ = minimum limit of superficial gas velocity for fast fluidization, m/s
V_f = volume of flue gas per second at furnace temperature, m^3/s
W = breadth of the furnace bed, m
x = weightage, fraction
β = fractional load at which the boiler may operate most of the time
η = thermal efficiency
μ_f = gas viscosity, kg/m·s
ρ_p = particle density, kg/m^3
ρ_f = gas density, kg/m^3

Subscripts

f, b = furnace or bed
1, 2 = values at discrete conditions at which data are available in the steam table
i = designation of design consideration or constraint

Table 1 Design of CFB furnace using conventional approach

step	CALCULATIONS	VALUE	UNIT
1.#	Find steam enthalpy from steam table	H	kJ/kg
2.	Find steam flow rate from boiler specification	M_s	kg/s
3.	Heat absorption ratio by = H x M_s	Q	kW
4.*	Carry out heat balance to give thermal efficiency	η	
5.	Furnace heat input = Q/η	Q_i	kW
6.	Carry out stoichiometric calculation giving mass of flue gas per kJ combustion heat release at full load	m	kg/KJ
7.	Mass of flue gas per sec. at full load = Q_i x m	m_f	kg/s
8.*	Choose a furnace temperature at full load	T_b	K
9.	Volume of flue gas at furnace temperature = $(m_f \times T_b)/273$	V_f	m^3/s
10.*#	Choose a grate heat release rate in line with those proven in plants operating successfully on similar fuels using experience table	q	MW/m^2
11.*	Calculate a superficial gas velocity corresponding to this heat release rate = q x m x T_b x 1000/(273 x 1.3)	U_f	m/s
12.	Furnace cross section area = V_f/U_f	A	m^2
13.*	Check against limiting velocities (Eq (2), (3)) and other considerations. Then recalculate the furnace grate heat release rate if necessary.		

2.1 Algorithm Design. A conventional algorithm-type computer program will carry out a step-by-step arithmetic operation following this procedure to determine the velocity and thereby the bed or furnace cross-sectional area. It is difficult for conventional algorithm software to take any decision and to carry out a compromise. The designer is required to intervene by stopping the program at intermediate steps to assess the intermediate results. Then in light of overall design and current results, the designer feeds further decisions for subsequent calculations. An example of such an algorithmic design is shown in Table 1.

In the example of algorithmic design the steps marked with an asterisk (*) i.e., steps (4), (8), (10), (11), and (13) involve assessment of intermediate results and decision making. The steps marked with (#) such as step (1) require reading data from tables. This can be implemented by algorithms. But those marked with * involve rules of thumb, and some design tables that require finding a closest match of relevant parameters of a plant and interpretation of data. Step (10) involves both table reading and decision making. It requires reading the table using the experience of an expert designer. Table 2 is an example of an experience table. It lists a selected number of fuel-fired plants and the year of commissioning the plant. The year of commissioning is listed because this may have some bearing on the design of the plants, which are based on a still developing technology like the circulating fluidized bed. Therefore, recent plants are likely to be more optimally designed than those designed at an early stage of development of CFB technology. Thus grate heat release rates of more recently designed plants are more credible than those of earlier years. Also, among different constituents of coal, some have more important influence on the design than others. For example, the moisture content of fuel influences the furnace cross section more than its fixed carbon content. Thus when the designer matches his/her design fuel with those of other operating plants he/she needs to give greater importance to some parameters than others. These decisions depend on the expert's knowledge level, so it is extremely difficult to achieve this in conventional algorithmic programs. Use of expert system techniques helps take such design decisions. The next section of the paper demonstrates this.

Table 2 Experience table of design features of commercially operating CFB boiler plants

F	FC (%)	M (%)	Ash (%)	VM (%)	HHV (kJ/kg)	Long m	Wide m	High m	Q MW	GHR MW/m^2	Yr
BIT	34.0	27.0	12.3	39.1	21013	7.6	33.0	40.0	943.0	3.76	95
BIT	47.0	11.0	18.8	33.0	26820	7.52	18.0	32.6	394.0	2.91	91
BIT	47.0	11.0	28.8	33.0	26820	7.9	14.5	22.0	464.0	2.88	91
LIG	36.6	30.7	15.5	27.0	15658	12.45	10.25	30.0	422.0	3.3	91
BIT	63.3	6.5	5.6	32.0	26440	5.45	10.9	30.0	211.0	3.55	90
BIT	43.5	9.5	26.3	28.4	22460	13.8	7.37	31.0	327.0	3.21	87
Ant	47.2	20.1	27.6	7.0	17453	5.84	9.42	27.4	230.0	4.18	86
BIT	67.3	10.0	10	31.0	26046	5.12	5.12	24.4	123.0	4.69	85

BIT = Bituminous FC = Fixed Carbon F = Type of Fuel
LIG = lignite M = Moisture GHR = Grate heat release rate
ANT = Anthracite Coal VM = Volatile

2.2 Expert System Approach. An example of the application of expert systems to the design of CFB boilers is presented here by performing the design above using an expert system. To restrict the length of the paper, the design is limited to the determination of the cross-sectional area of the upper furnace. Here, the program has been written using INSIGHT-II Plus Expert System shell. The Expert System shell can carry out both intelligent and conventional algorithm type calculations. Here we use a Quick Basic program for algorithmic type calculations. One may also use FORTRAN or similar programming languages for straight calculations.

2.2.1 Design Considerations. We consider a case where a client specified the following:

Mandatory conditions:

Steam conditions	Feed-stock
Main flow	Coal composition
Drum pressure	Fuel analysis
Economizer inlet temperature	(C, H, S, O, N, Ash, HHV)
Superheater outlet temperature	

Bed particle size

Preferred condition: The consultant is worried about erosion of the furnace wall tubes, so he suggests use of a lower fluidization velocity.

Additional conditions: The plant owner expressed the desirability of a good and stable performance under low load because his boiler would be required to operate at full load only during the brief period of evenings and early mornings. The rest of the time it will operate at part-load.

Other Stipulations: The consultant also suggests that in view of the high ash content of the coal, the designer should avoid in-bed or external heat exchanger tubes as far as possible. It is also desired by the designer to reduce the capital cost.

The client and consultant also realized that some of their design preferences are in conflict with each other. For example, erosion would favor a reduced design velocity, while good operation at part-load would call for a higher velocity, while good operation at part-load would call for a higher velocity at the full load. So they would like to see the effect of the importance they attach to these criteria on the design so that they can relax some of them as needed. It may be noted that the conditions above generally fall under the four types of design consideration described earlier.

2.2.2 Table Reading. Designs often involve reading data from tables. Values from the tables can be read by matching

either one parameter or two parameters. In the current design, the enthalpy of steam is to be read against both pressure and temperature from a steam table. A steam table gives experimental values of the enthalpy at discrete values of temperature and pressure. Design steam conditions do not necessarily coincide with the discrete values given in the table. So it is necessary to interpolate the steam properties between given values of temperature and pressure. This is done as follows:

1 Read enthalpy $H_{1,1}$ for a temperature and pressure (T_1, P_1) just higher than the required values (T, P)
2 Now for the same pressure (P_1) but temperature (T_2) just lower than the required value (T), read the enthalpy $H_{2,1}$.
3 Interpolate the enthalpy (H_1) between the two values, $H_{2,1}$ and $H_{1,1}$.
4 Similarly find the enthalpy (H_2) at pressure P_2 and required temperature T.
5 Finally an interpolation between H_1 and H_2 gives the value of enthalpy H at the required temperature and pressure (T, P).

2.2.3 Intelligent Reading of Existing Data Base. Table 2 lists grate heat release rates of a number of successfully operating commercial CFB plants. The grate heat release rates may be influenced by a number of factors. Some of these are:

- Moisture in fuel
- Volatile matters in fuel
- Ash in fuel
- Capacity of the unit
- Maturity of the design

Boilers designed during early stages of CFB development are less optimized than those designed more recently. Therefore, the parameter currentness of the design (present year-year of commissioning) may have some influence. The influences of this parameter and other parameters like the plant capacity and fuel constituents are not necessarily same. So, we attach different importance on a scale of 0 to 1.0 to these factors to find the best match of grate heat release rate. A special program has been developed to find the best match by attaching appropriate importance to the influencing parameters.

Based on the calculation of the grate heat release rate, we find the superficial gas velocity. This value is taken as the most desirable or optimum value of superficial gas velocity for this design.

In step (8), the furnace temperature is to be selected. The selection may involve a compromise between a number of other parameters. For example, combustion efficiency is greater at higher temperature, but sulfur capture requires it to be around 1123 K. For the sake of simplicity, we avoid this compromise by taking a furnace temperature of 1123 K. The selection of superficial gas velocity involves a compromise between a number of parameters. So, the expert system approach is applied to make the right choice.

The parameter for this selection is given, as mentioned earlier:

I Minimize erosion (consultant's worry)
II Maximize furnace wall heat absorption (designer's choice supported by the consultant)
III Good performance under part load (plant owner's preference)

Now, we first examine how the above design goals are related to the choice of furnace gas velocity.

2.2.4 Design Parameter Dependence

I Erosion. Figure 2 plots specific weight loss of tube materials against the fluidization velocity (Makansi, 1992) for CFB boilers using different bed materials. The graph of specific weight loss suggests a square relationship with the fluidization velocity in excess of 3 m/s. The quartz content of the bed material significantly influences the erosion. Higher quartz bearing bed solids result in higher erosion at the same fluidization velocity. Thus the type of fuel and sorbent fired has an important bearing on the erosion rate.

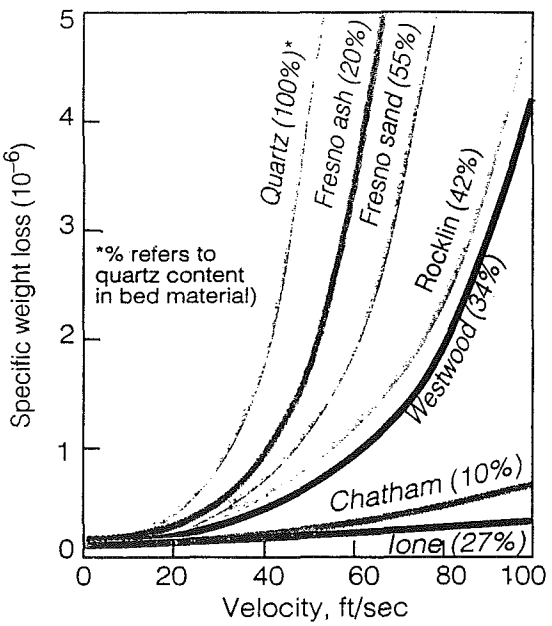

Fig. 2 Specific weight loss versus fluidization velocity

To quantify this effect we assume that the financial loss due to plant outage is proportional to erosion rate. This assumption is justified because a faster erosion rate requires more frequent tube replacement. So we assign a certain financial loss to the specific weight loss and assume that the importance or weightage of this factor is directly proportional to the financial loss. Thus one can write an equation linking the choice of design velocity with this parameter as

$$u_{\text{choice}} = V_{\max} - (V_{\max} - 3.0)x^{1/2} \tag{4}$$

where x is the weightage varying between 0 and 1. The equation is based on another consideration that if erosion is not an issue (situation similar to the bottom curve of Fig. 2) one can choose any velocity up to the absolute limiting value $V_{\max}$ restricted by fast-fluidization conditions.

II Maximimization of furnace heat absorption. Ordinarily the heat absorption in the furnace has no bearing on the superficial furnace gas velocity except through the wall heat transfer coefficient. However, to maintain the furnace temperature at the chosen value (step 8), a certain amount (Q_F) of the combustion heat must be absorbed by the heat transferring surface somewhere in the CFB loop. This amount (Q_F) depends on the fuel type and the chosen (step 9) furnace temperature (Basu and Fraser, 1991, p. 187). The heat absorbed by the furnace water wall tubes is given by

$$Q_W = (L + W)H(T_b - T_w) \tag{5}$$

If $Q_W < Q_F$ the remaining heat, $(Q_F - Q_W)$ may have to be absorbed either

(*a*) by heat transferring surface suspended inside the furnace, or
(*b*) by a bubbling fluidized bed heat exchanger outside the furnace through which a part of the hot solids circulating around the CFB loop is passed.

In the latter two alternatives, additional cost and perhaps additional erosion potential is involved. Thus, if the designer can minimize the amount $(Q_F - Q_W)$, he/she can reduce the impact of additional capital cost and erosion.

For a given boiler,

$Q_F \propto$ furnace cross section, $(L \times W)$

$\propto u_{\text{choice}}$

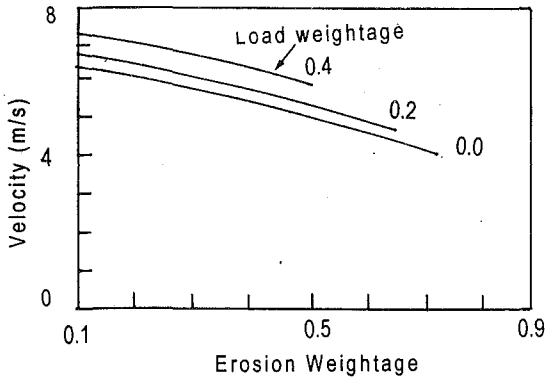

Fig. 3 Variation of fluidization velocity with erosion weightage

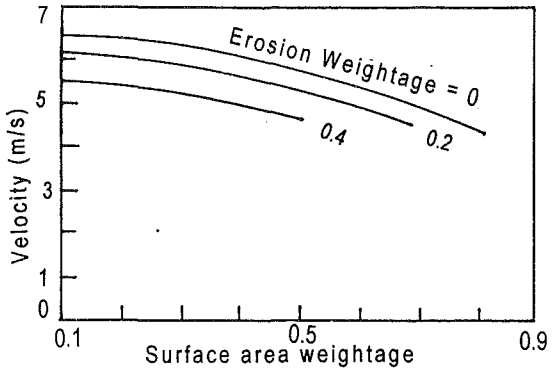

Fig. 4 Variation of fluidization velocity with surface area weightage

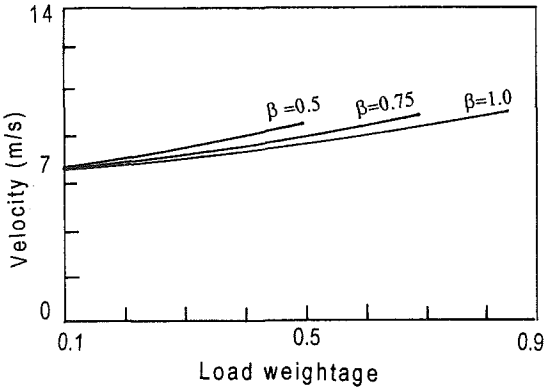

Fig. 5 Variation of fluidization velocity with load weightage

Therefore, Q_F = fractional furnace heat input

$$\propto (L \times W) \times u_{\text{choice}} \tag{6}$$

but $Q_F \propto$ wall area, $(L + W)H$

Thus for a given furnace heat input the required heat absorption in the furnace (Q_F) can be minimized by reducing the velocity, u_{choice}. If one has to maximize the utilization of the wall surface area (or the fraction of input heat absorbed in the furnace) one should choose the minimum velocity $V_{\min}$. Conversely, if the maximization of wall surface area is not concern, the designer can shoot for the optimum velocity U_f. From the nature of interdependence of factors this choice can be written as

$$u_{\text{choice}} = U_f - (U_f - V_{\min})x \tag{7}$$

where x is the weightage of this criterion (0–1.0).

III Part load. To cope with the reduced load on the boiler the furnace velocity is decreased though not at the same rate as that of the load. So, the heat input is proportional to u_{choice}.

Additional constraints demand that the selection of velocity should be such that the bed remains in fast fluidization under both part and full load conditions. Some design values were available from commercial CFB boilers under part and full load conditions. A dependence function can be derived as:

$$u_{\text{choice}} = U_F + (U_f/\sqrt{\beta} - U_f)\sqrt{x} \tag{8}$$

where β is the fractional load at which the boiler is operated and x is the weight age of this factor (0–1.0).

IV Other parameters. The optimum design velocity determined from the experience table is assumed to represent all other parameters influencing the choice of the design velocity. This will naturally carry the balance of all other weightages.

Overall Choice

Now each criterion is given a weightage. Their combined or added normalized value is:

$$u_{\text{choice}} = \sum_{j=1}^{n} V_i x_i$$

and

$$\sum_{i=1} x_i = 1.0 \tag{9}$$

where V_i is the velocity of choice using criterion i and x_i is the the weightage factor associated with criterion i. As we can see from Eqs. (4), (6), and (7), some parameters favor higher velocity while some favor lower. These opposing tendencies on the design parameter variation will try to balance each other in the summation function depending on the weightage factor. The weightage factors are either obtained from the user (an experienced design, client, consultant, etc.) or default values are used. In the present case, we have tried to change these to evaluate their impact on the design.

The value so obtained is checked against two boundaries:

- upper limit of fast fluidization (Eq. (2))
- lower limit of fast fluidization (Eq. (3))

It is noted here that view of the uncertainty of the equations of limiting velocities (Eqs. (2) and (3)), the designer may take the liberty to exceed these limits under severe operating conditions. Part-load operation is one such example. Under such situations, the designer must assess the magnitude of risk and take necessary precautions due to possible departure from the fast-fluidized condition.

3.0 Results and Discussion

Figures 3, 4, and 5 plot results of the above design compromises. Here three design scenarios have been considered. In the first case the maximization of in-furnace heat transfer has been ignored as being a non-issue. The choice of velocity was guided by the option for part-load operation and erosion potential. The importance of the erosion potential was varied from 0 to 1.0 for three discrete weightages of the part-load operation. Figure 3 presents choice velocities for the conditions above. We note that if the part-load operation is 40 percent important, the chosen velocity will decrease from 7.7 m/s to 6.7 m/s if the importance of erosion is increased from 0 to 60 percent. Also when the part-load operation is only 20 percent important, the velocity of choice decreases from a lower value of 6.9 to 5.0 m/s while the weightage of erosion is increased from 0 to 80 percent. It may be noted that the weightage of erosion can be increased to a greater value for a lower weightage of the other parameter because the summation of all weightages including that of the optimum velocity is 1.0.

Figure 4 shows a compromise between the erosion potential

and the in-furnace heating surface utilization criteria. Here the part-load operation is neglected as a non-issue. As expected, the choice velocity decreases with increasing importance of the furnace surface utilization.

Figure 5 shows the effect of increasing the importance of part-load operation alone. The other two considerations used earlier are neglected here. Here we note that the design needs to use higher velocity at full load when the importance of this criterion increases. The desired level of art load operation (75 or 50 percent for example) also affects this choice.The choice velocity for 50 percent load operation will force the full-load velocity to be pegged at a higher value than 75 percent load operation will.

4.0 Conclusion

The step-by-step algorithm type design cannot automate the compromise or decision-making process in a design. The boiler designer has to do that manually. A simple expert system has been shown to perform that task of design compromise effectively. In the present example, the expert system chose the design velocity at full load by striking a compromise among three conflicting requirements and one optimum value determined by intelligent reading of experience table.

Acknowledgments

The authors acknowledge the financial support of the Natural Sciences and Engineering Research Council of Canada. The assistance of Professor T. K. Ghoshal of Jadavpur University and Dr. J. Greenblatt is also acknowledged.

References

Basu, P., and Fraser, S., 1991, *Circulating Fluidized Bed Boiler—Design and Operation*, Butterworths Heinemann, Stoneham, USA.

Guilin, Y., and Junke, S., 1991, "Transition of Flow Regime From Turbulent to Fast Fluidization and From Fast to Dilute Phase Transport," *Fluidization '91 Science and Technology*, M. Kwauk and M. Hasatani, eds., Science Press, Beijing, pp. 37–45.

Makansi, J., 1992, "Factor Field Experience Into Design of Fluidized Bed Boilers," *Power*, McGraw-Hill, Aug. pp. 41–44.

Accuracy and Efficiency Assessments for a Weak Statement CFD Algorithm for High-Speed Aerodynamics

G. S. Iannelli

A. J. Baker

Department of Engineering Science and Mechanics, University of Tennessee, Knoxville, TN 37996

A bilinear finite element, implicit Runge–Kutta space–time discretization has been established for an aerodynamics weak statement CFD algorithm. The algorithm admits real-gas effect simulation, for reliable hypersonic flow characterization, via an equilibrium reacting air model. The terminal algebraic system is solved using an efficient block-tridiagonal quasi-Newton linear algebra procedure that employs tensor matrix product factorizations within a lexicographic mesh-sweeping protocol. A block solution-adaptive remeshing, for totally arbitrary convex elements, is also utilized to facilitate accurate shock and/or boundary layer flow resolution. Numerical validations are presented for representative benchmark supersonic-hypersonic aerodynamics problem statements.

Introduction

Computational aerodynamics is a "Grand Challenge" for the 1990s. The critical need persists for accurate, efficient and stable simulation of transonic, supersonic, and hypersonic reacting flows about aerospace vehicles, ranging from the F-16 in high g maneuver to the NASP (DoD, 1990). This motivates continuing research seeking more reliable computational fluid dynamics (CFD) algorithms/codes for approximately solving the associated governing aerodynamic conservation law systems.

This paper details a Galerkin weak statement formulation for generating approximate solutions to high-speed aerodynamics conservation law forms including equilibrium real-gas thermochemistry. The weak statement theoretical construction permits utilization of general solution approximations, hence spatial semi-discretizations, and serves as a common theoretical platform for interpretation of diverse forms for aerodynamics CFD algorithms, e.g., dissipative finite volume, upwind methods, dissipative or discontinuous finite elements, etc. The weak statement admits block-tridiagonal compact implementation by selection of fundamental, as well as more complex, approximation trial and test function spaces. Its computational framework spans discretizations to spectral global methods and all selections in between.

A fundamental finite element semi-discretization of a dissipative Galerkin weak statement is derived herein for the compressible Euler and laminar Navier–Stokes equations for ideal and equilibrium air. The dissipative construction occurs for these conservation law systems via an appended curvilinear coordinate parabolic-perturbation yielding "companion" systems appropriate for both semi-discrete solution boundedness and essentially nonoscillatory shock-capturing with fully *arbitrary* discretizations. The admissible surface momentum flux and deviatoric traction boundary conditions are naturally enforced within the contour integrals generated in a Green–Gauss transformation of the weak statement for these companion conservation law systems. The resultant finite element (FE) spatial semi-discretization is thereby well posed in fully generalized curvilinear coordinates.

An implicit Runga–Kutta (IRK) time integration algorithm is selected to complement the finite element spatial semi-discretization, yielding the terminal, fully discrete algebraic equation system. The FE-IRK algorithm is nonlinearly stable, in either the time accurate-unsteady, or steady-state relaxation mode, on *absolutely arbitrary* solution-adapted meshes constructed of Lagrange bilinear basis convex elements. The resulting nonlinear algebraic matrix statement is solved, iteratively or noniteratively for large time step (Courant number), using a tensor matrix product factorization quasi-Newton algorithm, which constitutes an efficient alternative to sparse matrix solution methods.

The FE-IRK CFD algorithm is validated for a selection of inviscid and viscous, supersonic–hypersonic benchmark problems in axisymmetric and two-dimensional geometries by comparing predicted shock strength, inclination angles, and standoff distances with available analytical solutions and correlations. Solutions are generated for viscous laminar as well as inviscid flow simulations, and real gas effects are included via a five-species reacting-air equilibrium model. For all simulations, the predicted shocks are crisp, across the entire Mach number range, through use of block solution-adaptive remeshings. Efficiency accrues in the sense that, for a fixed

Contributed by the International Gas Turbine Institute and presented at the 37th International Gas Turbine and Aeroengine Congress and Exposition, Cologne, Germany, June 1–4, 1992. Manuscript received by the International Gas Turbine Institute February 28, 1992. Paper No. 92-GT-433. Associate Technical Editor: L. S. Langston.

number of nodes, solution accuracy is enhanced by clustering discretization elements in high solution-gradient regions. The discretized state-variable distributions are thus both accurately and efficiently computed, and uniformly exhibit an essentially monotone character.

Conservation Law Statement

A Reynolds averaging applied to the compressible Navier–Stokes equations, describing flow of a viscous/turbulent, non-thermally perfect gas yields the nondimensional conservation law form

$$\mathcal{L}(q)=\frac{\partial q}{\partial t}+\frac{\partial}{\partial x_j}(f_j-f_j^v)-s=0 \tag{1}$$

In Eq. (1), $q=q(\mathbf{x}, t)=\{\rho, m_j, E, \ldots\}^T$ is the state variable distributed on $\Omega\cup\partial\Omega\times t\subset\mathcal{R}^n\times\mathcal{R}^1$, where ρ is the density, $m_j=\rho u_j$ is the linear momentum, and E is the volume-specific total internal energy of the statistical mean flow (Baker, 1983).

The companion kinematic and dissipative flux vector definitions, assuming an algebraic Reynolds stress closure modeling, are

$$f_j=\begin{Bmatrix} m_j \\ m_j m_i/\rho+p\delta_{ij} \\ m_j(E+p)/\rho \end{Bmatrix},\quad f_j^v=\begin{Bmatrix} 0 \\ \sigma_{ij}^T \\ m_j\sigma_{ij}^T\rho-q_j^T \end{Bmatrix} \tag{2}$$

where the superscript T denotes the sum of laminar and turbulent contributions for dissipative fluxes, e.g.,

$$\sigma_{ij}^T=\bar{\sigma}_{ij}-\overline{\rho u_i u_j}\approx\frac{1}{\mathrm{Re}}(\mu+\mathrm{Re}^t)\left(E_{ij}-\frac{2}{3}E_{kk}\delta_{ij}\right) \tag{3}$$

Re is Reynolds number, $\mu=\mu(T)$ is nondimensional viscosity, $\mathrm{Re}^t=(\mu^t/\mu)_{\mathrm{dim}}$ is turbulent Reynolds number, and E_{ij} is the mean flow deviatoric strain rate tensor.

Equations (1) and (2) defining q, f_j, and f_j^v may be extended using additional differential equations in the turbulence closure model. These are not included, since computations have been completed for a laminar flow model (only). Therefore, s in Eq. (1) is a null array in the absence of reaction sources in the energy equation.

The general form for the equation of state is $p=p(\rho, \epsilon)$ where ϵ denotes the mass specific internal energy. For a reacting mixture obeying Dalton's Law, the form is

$$p=R\rho T\sum_{i=1}\frac{Y_i}{M_i} \tag{4}$$

where R is the universal gas constant, M_i is the molecular mass of the ith species, and Y_i is the associated mass fraction.

A five species model containing $\{\mathrm{O}, \mathrm{N}, \mathrm{NO}, \mathrm{O}_2, \mathrm{N}_2\}$ requires solution of Eq. (4) with the internal energy equation

$$\epsilon+RT\sum_{i=1}^{5}\frac{Y_i}{M_i}-\sum_{i=1}^{5}Y_i c_{pi}T-\sum_{i=3}^{5}\frac{R\theta_i^v/M_i}{\exp(\theta_i^v/T)-1}-\sum_{i=1}^{3}Y_i h_i^0=0 \tag{5}$$

where $c_{pi}=5/2(R/M_i)$, $i=1, 2$, and $c_{pi}=7/2(R/M_i)$, $i=3, 4, 5$. Further, h_i^0 is the formation enthalpy and θ_i^v is the characteristic vibrational temperature. This equation relies upon the rigid rotor harmonic oscillator model (Desideri et al., 1990; Anderson, 1989), which implies the ideal gas equation of state for each species, which in turn is consistent with Dalton's law. The internal energy thus comprises the species formation chemical energy, the molecular translational and rotational kinetic energies, and the molecular vibrational potential energy with equilibrium magnitude characterized by the static temperature T. Expressions for independent dissociation and exchange reactions among the five species then close the system (Desideri et al., 1990).

Finally, the conservation law system is cast in curvilinear coordinates via a generalized coordinate transformation $\eta_i=\eta_i(x_j)$ that admits full geometric generality for implementation within the intrinsic coordinate systems spanning finite element domains. Hence, Eq. (1) becomes

$$\mathcal{L}(q)=\frac{\partial(q\ \det J)}{\partial t}+e_{jk}\frac{\partial}{\partial\eta_k}(f_j-f_j^v)-s\ \det J=0 \tag{6}$$

assuming the transformation jacobian determinant (det J) is time-invariant, while e_{jk} denotes entries in the matrix J^{-1} det J. Equation (6) can also be written in "*weak*" or divergence form, since $\partial(e_{jk})/\partial\eta_k=0$ by definition of e_{jk} (Iannelli and Baker, 1990, 1992).

Parabolic Perturbation System

The parabolic perturbation companion conservation law system augments Eq. (6) with a higher order kinematic dissipation (Iannelli and Baker, 1990, 1992), modifying Eq. (6) to the form

$$\mathcal{L}_p(q)=\frac{\partial(q\bullet\det J)}{\partial t}+e_{jk}\frac{\partial}{\partial\eta_k}(f_j-f_j^v)-s\ \det J-\frac{\partial}{\partial\eta_k}\left(\beta_k|\mathbf{u}|\frac{\partial q}{\partial\eta_k}\right)=0 \tag{7}$$

where $|\mathbf{u}|$ is the contravariant velocity magnitude

$$|\mathbf{u}|\equiv\left(\sum_{k=1}^{n}\left(e_{jk}\frac{m_j}{\rho}\right)^2\right)^{1/2} \tag{8}$$

In Eq. (7), $\beta_k\le 0.5$ can be a constant or a function of Mach number, and depends upon the tensor index k. The subscript boldface restricts the index to be an indicator only not eligible for summation.

It can be shown, for the scalar one-dimensional case with constant $|\mathbf{u}|$, that the solution of Eq. (7) converges for $\beta_k\to 0$ to a generalized solution of the original equation (Oleinik, 1957, 1959a, 1959b; Kreiss and Lorentz, 1989). Thereafter, a classical Galerkin weak statement on Eq. (7) yields a curvilinear-coordinate directional semidiscretization without fundamental restriction to either the test or trial function spaces.

Weak Statement Finite Element Algorithm

The construction of approximate solutions to the conservation law statement can be achieved via a weak statement for Eq. (7). *Any* solution approximation can be expressed as

$$q(\mathbf{x}, t)\approx q^N(\mathbf{x}, t)\equiv\sum_{j=1}^{N}\Psi_j(\eta(\mathbf{x}))Q_j(t) \tag{9}$$

where $\Psi(\mathbf{x})$ are the members of the user-selected *trial space* and $Q_j(t)$ is the set of unknown time-dependent approximation expansion coefficients. The *error* in the approximation is $e^N(\mathbf{x}, t)\equiv q(\mathbf{x}, t)-q^N(\mathbf{x}, t)$, which any approximation procedure should *extremize* (minimize). This can be mathematically achieved via the weak statement.

$$\int_{\bar{\Omega}} w\mathcal{L}_p(q^N)\,d\tau=0 \tag{10}$$

being identically satisfied on any $\bar{\Omega}\subseteq\Omega$. The test function $w(x, t)$ is totally arbitrary; hence it may coincide with convenient forms for efficient implementations. The selected procedure identifies $w(\mathbf{x}, t)$ as a member of the vector space S of polynomials $\Phi_j(\eta(\mathbf{x}))$ with compact support in $\bar{\Omega}$, which introduces the corresponding interpolation coefficient set $W_j(t)$. Therefore, the computable *extremum* for Eq. (10) is established as the stationary point with respect to these W_j, i.e.,

$$WS^N \equiv \int_\Omega \Phi_j(\eta)\mathcal{L}_p(q^N)d\tau$$

$$\equiv 0, \text{ for all } \Phi_j \tag{11}$$

Equation (11), which is valid for *any* approximation $q^N(\bullet)$ and *any* test function $w(\mathbf{x}, t) \in S$, forms the theoretical platform for formulating a range of approximate solution strategies. These procedures accrue from user-selection of the Φ_j and the Ψ_j, the function sets required for supporting a specific approximation q^N and its error constraint (Baker, 1983; Pironneau, 1989). Certain differentiability and integrability requirements must be met, hence each member belongs to the eligible Banach space (Hutson and Pym, 1980).

Equations (9)–(11) identify some possible choices to implement an approximate finite element CFD solution strategy for Eqs. (1)–(8). For the results presented, the weak statement stationary point is constructed for the optimal *Galerkin* choice of test space identical to the trial space. Hence, Eq. (11) becomes

$$WS^N \equiv \int_\Omega \Psi_j \mathcal{L}_p(q^N)d\tau \equiv 0, \ \forall j \tag{12}$$

The required numerical dissipation for both approximate-solution boundedness and essentially nonoscillatory shock capturing is induced via the choice of $\mathcal{L}_p(\bullet)$ rather than $\mathcal{L}(\bullet)$ in Eq. (12). Further, this also requires that $\beta_k \to 0$ in flow regions containing significant physical diffusion/conduction phenomena, such as boundary layers, to preclude numerical dissipation contamination of local physical diffusion processes.

The trial space is constructed as the union of bilinear Lagrange polynomials, with local compact support on the (FE) spatial semi-discretization $\Omega^h \cup \partial\Omega^h$ of $\Omega \cup \partial\Omega$. Hence, the corresponding FE basis set $\{N_k(\eta)\}$ constitutes the selection for Ψ_j spanning each finite element domain Ω_e. Further, since Ψ_j is differentiable almost everywhere (Hutson and Pym, 1980), the semi-discretization of Eq. (12), using a Green–Gauss theorem, is

$$WS^h = \cup_e \left(\int_{\Omega_e} \{N\} \left(\frac{\partial q_e}{\partial t} - s_e \right) d\tau - \int_{\Omega_e} \frac{\partial \{N\}}{\partial \eta_k} \left(e_{jk}(f_j - f_j^v) - (\beta_k |\mathbf{u}|) \frac{\partial q_e}{\partial \eta_k} \right) d\tau + \int_{\partial\Omega_e} \{N\} \left(e_{jk}(f_j - f_j^v) - (\beta_k |\mathbf{u}|) \frac{\partial q_e}{\partial \eta_k} \right) n_k \bullet d\sigma \right) \equiv \{0\} \tag{13}$$

In Eq. (13), the superscript h emphasizes use of the spatial discretization Ω^h to construct q^N, and subscript e signifies an evaluation restricted to a finite element domain Ω_e. The last term in Eq. (13) admits natural implementation of all admissible surface momentum flux and deviatoric traction boundary conditions for Eq. (1) (cf. Iannelli and Baker, 1992), and n_k denotes the outward-pointing unit normal vector to $\partial\Omega$.

Time Integration

Upon any selection for ϕ_j and ψ_j, be it spectral, pseudo-spectral, finite volume, finite element, etc., Eq. (11), hence Eq. (13), always produces an ordinary differential equation (ODE) system of the form

$$WS^N = [M] \frac{d\{Q\}}{dt} + \{R(t, Q)\} \equiv \{0\} \tag{14}$$

where $[\bullet]$ and $\{\bullet\}$ denote a square and column matrix of order N, and $[M]$ is the mass matrix, which may be diagonal for some choice Φ_j not identical to ψ_j in Eq. (11). Inclusion of real gas physics, in addition to local solution-adapted mesh refinements, markedly increases the intrinsic stiffness of Eq. (14), thus a stiffly stable and second-order accurate ODE solver is desired for efficient time-accurate predictions.

Hence, the weak statement ODE system Eq. (14) is numerically integrated in time using a second-order-accurate, two-stage diagonally implicit Runge–Kutta (IRK) temporal scheme, proven nonlinearly stable for the stiff, semi-discrete Navier–Stokes equations on arbitrary meshes (Iannelli and Baker, 1992; Dekker and Verwer, 1984; Karakashian, 1986). This IRK family consists of the computational sequence

$$Q_{n+1} - Q_n = b_1 K_1 + b_2 K_2 \tag{15}$$

$$MK_1 = -\Delta t R(t_n + c_1 \Delta t, \ Q_n + \alpha_1 K_1) \tag{16}$$

$$MK_2 = -\Delta t R(t_n + c_2 \Delta t, \ Q_n + \beta_{21} K_1 + \alpha_2 K_2) \tag{17}$$

where the subscript n is the time step index. The IRK algorithm coefficients in Eq. (15)–(17) satisfy the constraints

$$b_1 + b_2 = 1, \ b_1 \alpha_1 + b_2(\beta_{21} + \alpha_2) = \frac{1}{2} \tag{18}$$

$$c_1 = \alpha_1, \ b_2 = \beta_{21} + \alpha_2 \tag{19}$$

With these specifications, the IRK scheme Eqs. (15)–(17) can be both second-order accurate and nonlinearly absolutely stable (Iannelli and Baker, 1992; Dekker and Verwer, 1984). Significantly, setting $\alpha_1 = \theta$, $\alpha_2 = 0$, $\beta_{21} = 0$, $b_1 = 1$, and $b_2 = 0$ yields the familiar, single-stage "θ" implicit Euler time integration family as a suboptimal class.

Newton Iteration Solution

Finally, the solution of Eqs. (16)–(17) is expressed via the Newton iteration algorithm

$$[J]\delta K_i^{p+1} = -\Delta t R\{t_n + c_i \Delta t, \ Q_n + \beta_{21} K_1 \delta_i^2 + \alpha_1 K_i^p) - MK_i^p, \ K_i^0 = 0 \tag{20}$$

where

$$[J(Q)] \equiv M + \alpha_i \Delta t \frac{\partial R}{\partial Q} \tag{21}$$

is the Newton jacobian, p is the iteration index, and the solution variable is $k_i = \Sigma_p \delta k_i^{p+1}$ at convergence. The numerical linear algebra method used to solve Eq. (20) approximately employs a tensor matrix product factorization of Eq. (21), as facilitated by the FE-generated nondiagonal matrix $[M]$ appearing in Eq. (14). The resultant grid sweeping jacobians are block tridiagonal, with an $O(\Delta t^2)$ factorization error analagous to that of an approximate factorization (AF) procedure.

Discussion and Results

The FE-IRK CFD algorithm has produced uniformly nonoscillatory, accurate, and efficient shock-capturing solutions for a wide range of supersonic-hypersonic benchmarks; cf. Iannelli (1991). Utilization of the block solution-adaptive remeshing strategy, for accuracy and efficiency, is illustrated in Fig. 1. For an $M_\infty = 3.0$ onset to a wedge at angle $\theta = 20$ deg, each Euler solution sequence utilized only 20 integration time steps of variable size, starting from the previous-mesh solution as the initial condition, to converge R in Eq. (20) to order 10^{-4} in each computational stage. The algebraically constructed, block-solution-adapted mesh becomes highly skewed, Fig. 1(*b*, *d*, *f*); hence the FE semi-discrete ODE system becomes extremely stiff. Nevertheless, each solution stage utilized a terminal CFL > 100, and each solution remains essentially nonoscillatory (ENO) with visually verifiable crisp shock structure.

The weak statement construction allows the shock to propagate undisturbed through the top boundary segment, without spurious reflection or local oscillation. Furthermore, the computed shock strength and inclination angle are essentially iden-

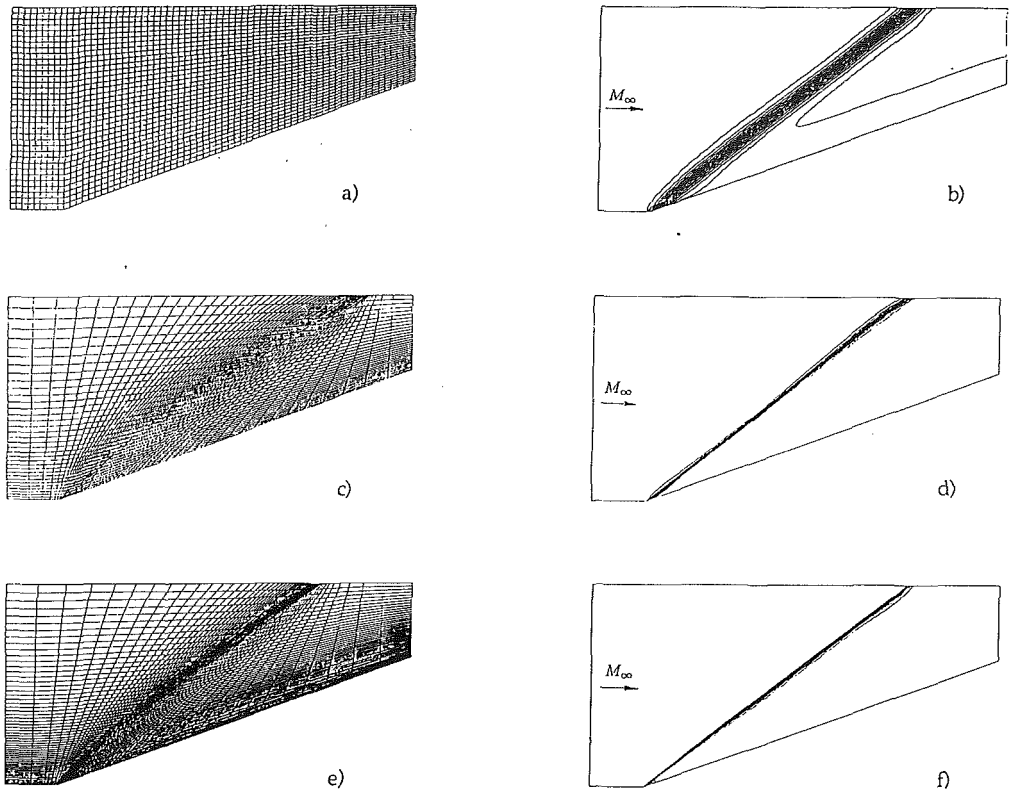

Fig. 1 Steady-state FE-IRK Euler solutions, supersonic compression ramp, $M_\infty = 3.0$, $\theta = 20$ deg, (*a*) original uniform Cartesian mesh, (*b*) corresponding density distribution, 20 contour levels, $n\Delta t = 20$, (*c*) first solution-adapted mesh, (*d*) associated density distribution, 20 contour levels, $n\Delta t = 40$, (*e*) second solution-adapted mesh, (*f*) associated density distribution, 20 contour levels, $n\Delta t = 60$

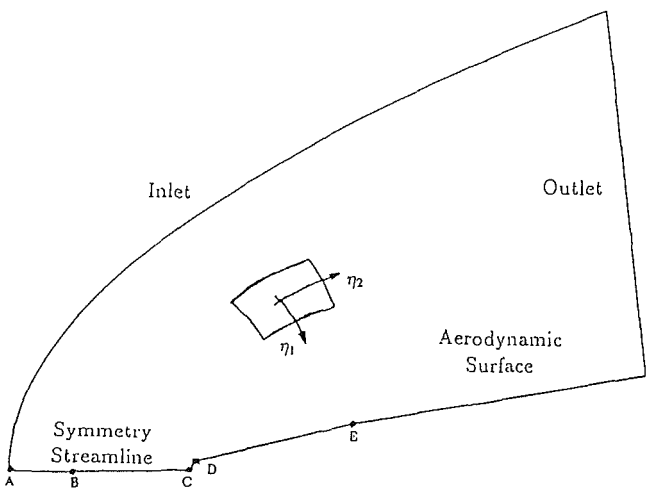

Fig. 2 Sphere-bicone axisymmetric body computational domain, with symmetry streamline inlet point (*A*), shock point (*B*), stagnation point (*C*), sphere-cone juncture (*D*), and bicone juncture (*E*)

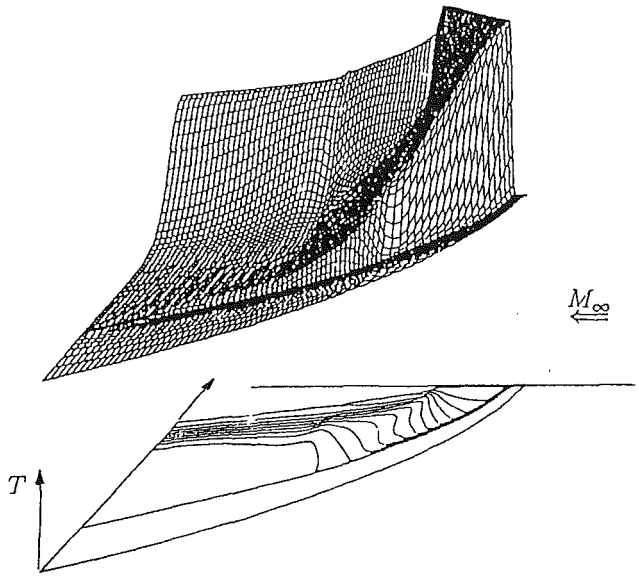

Fig. 3 Hypersonic viscous flow, axisymmetric sphere-bicone, $M_\infty = 8$, $Re_\infty = 500{,}000$, perspective surface and isotherm distribution for terminal mesh steady-state solution

tical with the known solution (Anderson, 1989) for each grid. This result validates the theory and code, at least for inviscid supersonic flows.

A hypersonic benchmark corresponds to $M_\infty = 8$ onset flow about an axisymmetric sphere-bicone, see Fig. 2. For a laminar simulation at $Re_\infty = 500{,}000$, the terminal adapted body-fitted 64×74 element mesh refinement achieved wall resolution to $\Delta y_{min} = O(10^{-5})$, the order of Re^{-1} in the forebody flow region. For free-stream stagnation state $p_\infty = 600$ N/m^2 and $T_\infty = 54$ K, the ideal-gas, viscous steady-state solution convergence occurred in 800 time steps, with final mesh maximum iterative convergence at CFL ~ 200. Figure 3 summarizes, in perspective view, the computed steady temperature distribution confirming an ENO sharpshock compression and subsequent sphere-cone expansion. The entire FE-IRK solution is virtually monotone, and the resultant normalized bow shock computed stand-off distance $\delta/R \cong 0.15$ agrees to within 1.5 percent with the available correlation (Anderson, 1989). This result partially validates the theory and code for viscous, high supersonic flows.

The comparison inviscid flow solution was stable at a max-

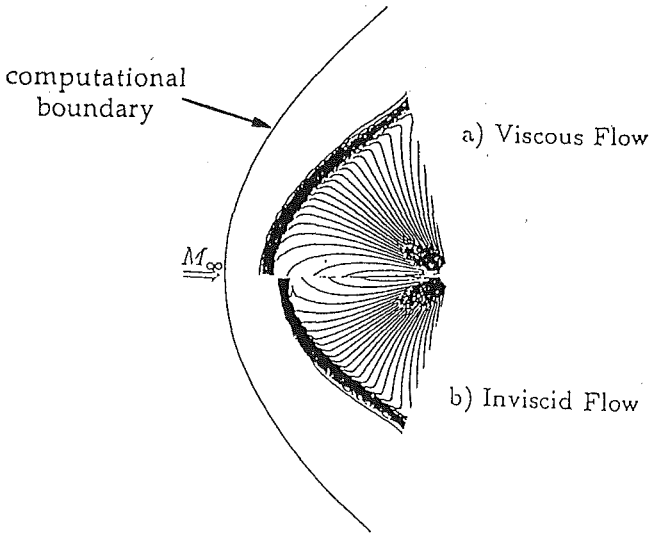

Fig. 4 Hypersonic flow, axisymmetric sphere-bicone, $M_\infty = 8$, steady-state solution isobar distributions for (*a*) viscous simulation, $Re_\infty = 500{,}000$, (*b*) inviscid simulation

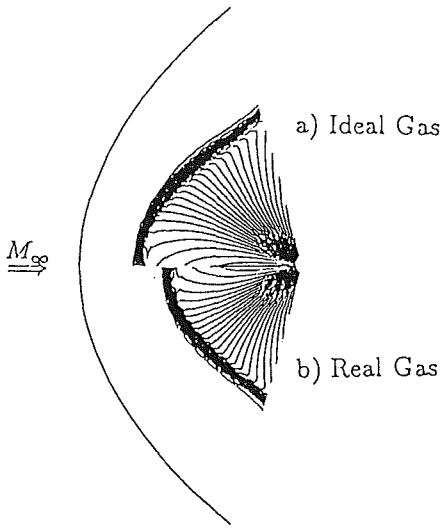

Fig. 5 Hypersonic inviscid flow, axisymmetric sphere-bicone, $M_\infty = 8$, steady-state isobar distributions for (*a*) ideal-gas simulation, (*b*) real-gas simulation

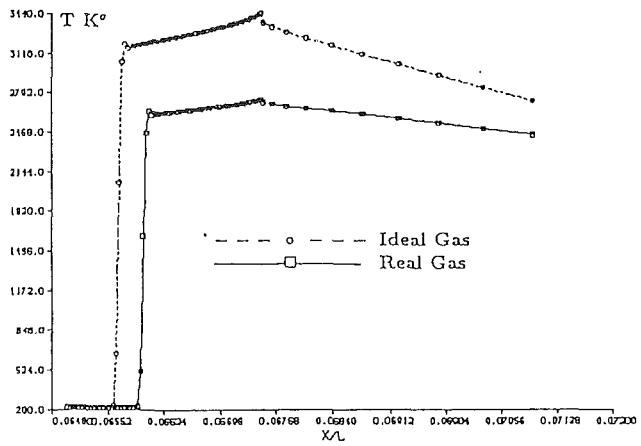

Fig. 6 Hypersonic inviscid flow, axisymmetric sphere-bicone, $M_\infty = 8$, FE-IRK steady-state stagnation-streamline temperature distributions for ideal- and real-gas simulations

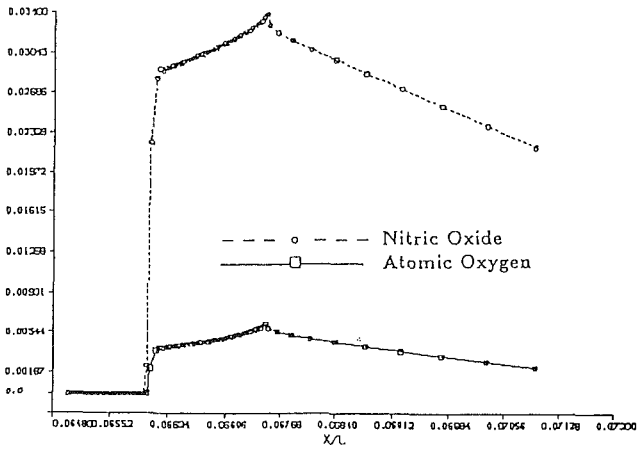

Fig. 7 Hypersonic inviscid flow, axisymmetric sphere-bicone, $M_\infty = 8$, FE-IRK steady-state stagnation-streamline distributions for nitric oxide and atomic oxygen mass fractions, real-gas simulation

imum CFL exceeding 500, with maximum convergence rate occurring at CFL ~ 200. This solution is also virtually monotone, and the computed bow shock stand-off of $\delta/R \cong 0.135$ agrees to within 4 percent with data (Anderson, 1989). Neglecting viscous effects thus increased the error in the computed shock stand-off distance by 2.5 percent. Figure 4 compares the associated nose region static pressure distributions on an axially expanded scale. Therefore, in Figs. 4 and 5, the shock stand-off distance appears 15 times larger. Consequentially, the bow shock thickness appears of the same order as the nose radius.

For a typical wind tunnel stagnation state, no appreciable real-gas effects are generated within the blunt body bow shock layer. Conversely, for a representative at-altitude condition of $p_\infty = 2.7 \times 10^{-2}$ atm and $T_\infty = 221$ K, the bow shock temperature rise will induce substantial real gas effects. The associated inviscid real- and/or ideal-gas FE-IRK steady flow simulation was achieved for maximum CFL ~ 200. As confirmed in Fig. 5, real gas effects lead to a decrease in the bow shock stand-off distance to $\delta/R \cong 0.112$, which is 18 percent less than the associated ideal-gas valued. This reduction is expected, since in the real-gas comparison to the ideal-gas situation, the temperature increase across the bow shock is substantially smaller. Therefore, the real-gas local density is considerably higher than the ideal-gas prediction; hence the free-stream mass flux can be negotiated within a thinner shock layer.

Figure 6 summarizes the flowfield stagnation streamline temperature distributions for the real- and ideal-gas simulations. The ideal-gas shock temperature is $T_S = 3150$ K, whereas the equilibrium-air value is $T_S = 2595$ K. This decrease of 18 percent is accounted for by the energy absorbed during excitation of thermodynamic vibrational modes, and eventual formation of nitric oxide and atomic oxygen. As confirmed in Fig. 7, these species are formed immediately behind the bow shock, with peak production at the sphere stagnation point. The mass fraction of nitric oxide is six times larger than that for elemental oxygen, while only negligible traces of atomic nitrogen are present. No experimental data are available for these distributions. Therefore, these results serve to indicate the relative difference between ideal and real gas predictions, and correctly show the expected reduction in peak static temperature.

The FE-IRK CFD algorithm has thus produced essentially monotone solutions on a quality mesh for a significant Mach number range. This accrues to both the ideal- and real-gas hypersonic flow simulations, and for both inviscid and viscous flow models, the latter with adequate all region mesh resolution.

Summary and Conclusions

A dissipative curvilinear coordinate Galerkin weak statement CFD algorithm has been derived and implemented using a bilinear basis finite element spatial semi-discretization in concert with an implicit Runge–Kutta time discretization. The resultant algebraic statement is solved via a quasi-Newton tensor product factorization yielding block-tridiagonal matrix structures.

Benchmark numerical validations confirm efficient attainment of realistic solutions for supersonic-hypersonic aerodynamics applications, utilizing a block solution-adaptive remeshing strategy for efficiency and accuracy. However, these results constitute (only) a first phase in the ongoing research project. Specifically, the number of nodes for each benchmark simulation remained constant, while the validations focused on solution quality, shock strength, inclination angle, and stand-off distance.

In the near future, solution accuracy will be assessed against successive mesh-node doublings, while critical validations will extend to comparisons of wall heat transfer and shear stress with available data. Finally, the algorithm will be extended to chemical and thermochemical nonequilibrium formulations, both with and without turbulence models.

Acknowledgments

The authors thankfully acknowledge the University of Tennessee Computing Center, and the invaluable support by the Boeing Corporation of the UT CFD Laboratory.

References

Anderson, J. D., 1989, *Hypersonic and High Temperature Gas Dynamics*, Mc-Graw Hill, New York.

Baker, A. J., 1983, *Finite Element Computational Fluid Mechanics*, Hemisphere Publishers, Washington, DC.

Dekker, K., and Verwer, J. G., 1984, *Stability of Runge–Kutta Methods for Stiff Nonlinear Differential Equations*, North Holland, New York.

Department of Defense, 1990, "Critical Technologies Plan," report for the Committees on Armed Services of the United States Congress, DTIC, AD-A219 300.

Desideri, J. A., Glinsky, N., and Hettena, E., 1990, "Hypersonic Reacting Flow Computations," *Computers and Fluids*, Vol. 18, pp. 151–182.

Hutson, V., and Pym, J. S., 1980, *Applications of Functional Analysis and Operator Theory*, Academic Press, New York.

Iannelli, G. S., 1991, "A Globally Well-Posed Accurate and Efficient Finite Element CFD Algorithm for Compressible Aerodynamics," Ph.D. dissertation, University of Tennessee, Knoxville, TN.

Iannelli, G. S., and Baker, A. J., 1990, "An Efficient Solution-Adaptive Implicit Finite Element CFD Navier–Stokes Algorithm," Paper No. AIAA-90-0400.

Iannelli, G. S., and Baker, A. J., 1992, "A Non-linearly Stable Implicit Finite Element Algorithm for Hypersonic Aerodynamics," *Int. J. Num. Meth. Engr.*, Vol. 33, in press.

Karakashian, O. A., 1986, "On Runge–Kutta Methods for Parabolic Problems With Time-Dependent Coefficients," *Math. of Comp.*, Vol. 47, No. 175, pp. 77–101.

Kreiss, H. O., and Lorentz, J., 1989, *Initial-Boundary Value Problems and the Navier–Stokes Equations*, Academic Press, New York.

Oleinik, O., 1957, "Discontinuous Solutions of Nonlinear Differential Equations" [English translation], *Amer. Math. Soc. Trans.*, Vol. 2, No. 26, pp. 95–172.

Oleinik, O., 1959a, "Construction of Generalized Solution of the Cauchy Problem for a Quasi-linear Equation of First Order by the Introduction of *Vanishing Viscosity*" [English translation], *Amer. Math. Soc. Trans.*, Vol. 2, No. 33, pp. 277–283.

Oleinik, O., 1959b, "Uniqueness and Stability of the Generalized Solution of the Cauchy Problem for a Quasi-linear Equation" [English translation], *Amer. Math. Soc. Trans.*, Vol. 2, No. 33, pp. 285–290.

Pironneau, O., 1989, *Finite Element Methods for Fluids*, Wiley, New York.

Aircraft Gas Turbine Emissions Challenge

B. L. Koff
Pratt & Whitney,
West Palm Beach, FL 33410

The new generation of jet powered aircraft faces a significant challenge to reduce pollutant emissions while increasing fuel efficiency. Carbon monoxide (CO) and unburned hydrocarbon (HC) emissions are already very low and continued control of these pollutants is expected as engine temperatures and pressure ratios are increased. In contrast, significant system design improvements are needed to reduce oxides of nitrogen (NO_x) emissions because of their harmful effect on the earth's ozone layer. This paper discusses the prospects and technical approaches for significant NO_x reductions in current and future subsonic and supersonic aircraft.

Current Status

Protecting and improving the global environment is the key international issue of the 21st century. To leave the earth in a habitable environment for the generations to come, we must create and apply technology advances to reduce harmful atmospheric gaseous and particulate emissions in addition to liquid and solid pollutant waste materials. Since jet aircraft pollutant emissions are injected directly into the upper atmosphere, they have the potential to affect the upper atmosphere more directly than other sources of combustion products. However as Fig. 1 shows, jet aircraft are responsible for less than 1 percent of all pollutant emissions from fossil-fuel combustion (GAO/RCED, 1992). Every industry must develop aggressive counter-measures if we are to be successful in protecting the global environment in the years to come.

Aircraft engines release particulate carbon (smoke), carbon monoxide (CO), unburned hydrocarbons (HC) and oxides of nitrogen (NO_x). Figure 2 represents 30 years of progress in aircraft engine emission reduction. This progress has been brought about by a combination of improved combustion designs and continually improved higher efficiency engines that burn less fuel and therefore also release less total emissions. Since gas turbine combustion efficiencies are already well above 99 percent, further efficiency improvement will not produce significant reductions in current atmospheric concentrations of CO and HC. Smoke emission is also under control. Although overall reduction in pollutants is a continuous goal, we must now focus on developing combustion technologies and engine system designs to reduce NO_x emissions because of the ozone affecting implications.

Figure 3 shows the various emissions produced by a gas turbine as a function of engine power. At idle where the combustion efficiency is 99+ percent, the HC and CO are maximum. At high power, takeoff, climb and cruise, the combustion efficiency is 99.9+ percent and the HC and CO are very low.

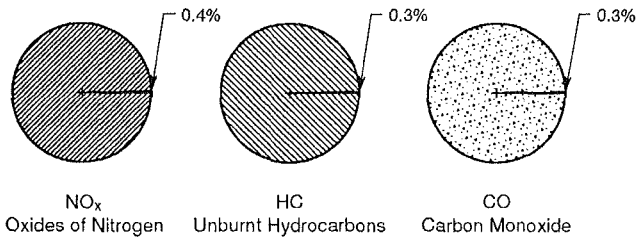

Fig. 1 Jet aircraft emissions (USA, 1989)

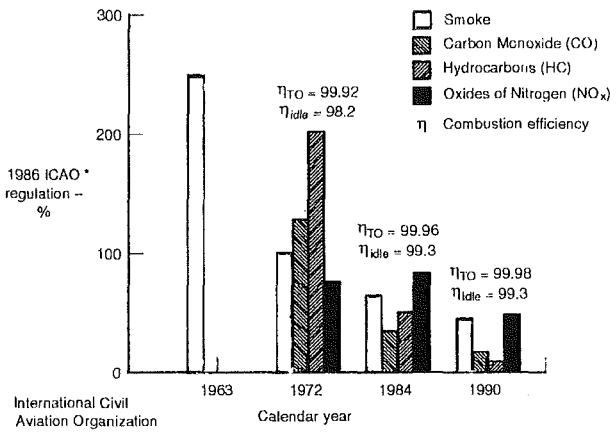

Fig. 2 Emissions reduction progress

NO_x and smoke particulates are the reverse, peaking at maximum power. Obviously, the technology for NO_x and smoke reduction is different than for CO and HC emissions.

NO_x emissions have now become the heavy focus for the 21st century because of its contribution to ground level ozone and smog, acid rain, and stratospheric ozone depletion. Chemical reactivity in the troposphere (below 37,000 feet) is primarily driven by the presence of hydroxyl radicals (OH). OH is formed

Contributed by the International Gas Turbine Institute and presented at the 38th International Gas Turbine and Aeroengine Congress and Exposition, Cincinnati, Ohio, May 24–27, 1993. Manuscript received at ASME Headquarters March 1993. Paper No. 93-GT-422. Associate Technical Editor: H. Lukas.

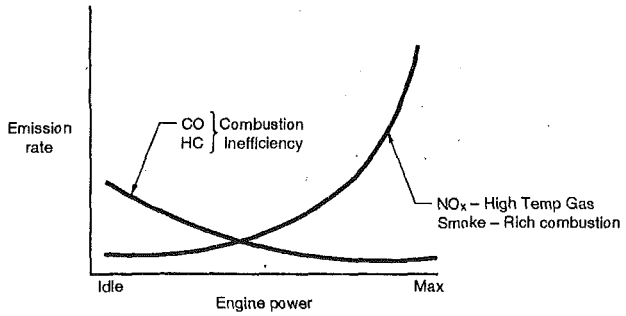

Fig. 3 Gas turbine emission characteristics

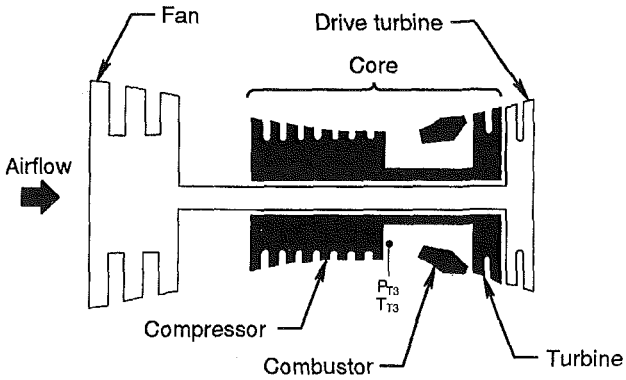

Fig. 4 Jet engine component schematic

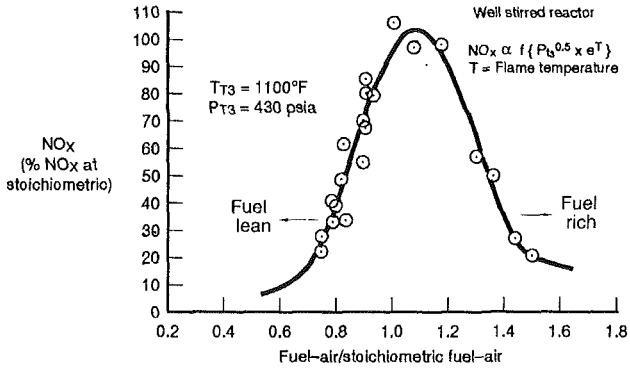

Fig. 5 NO_x generation

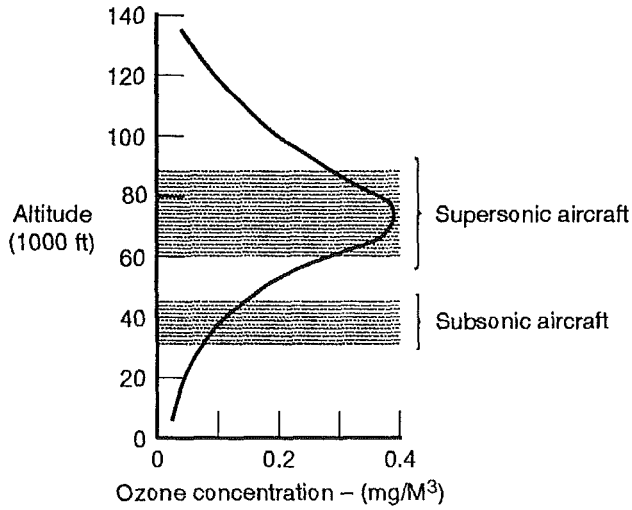

Fig. 6 Oxides of nitrogen deplete stratospheric ozone

from ozone and hydrogen molecules (via photolysis). NO_x released near ground level tends to get rapidly dispersed due to the intense weather process that occurs in the troposphere. NO_x will react with OH radicals to produce HNO_3 (nitric acid), which will be dissipated in the form of acid rain. Tropospheric NO_x and hydrocarbons in the presence of light will react to produce toxic ozone and aldehydes (partially reacted hydrocarbons), which are known as photochemical smog. Ozone in the troposphere is therefore "bad" ozone.

The "good" ozone exists in the stratospheric ozone layer (above 37,000 feet), which protects the Earth from harmful ultraviolet radiation. NO_x and other radicals catalytically convert this desirable ozone to oxygen. NO_x that enters the stratosphere has long stay times (years) due to poor circulation so that one molecule of NO_x can react many times to destroy many molecules of ozone.

NO_x Formation in the Atmosphere

Within a gas turbine engine, NO_x formation is heavily dependent on local gas temperatures within the combustor and the time spent at these elevated temperatures. Higher gas temperatures, and resultant higher NO_x formation rates are produced from combustion near stoichiometric fuel–air ratio (0.068) and at high combustor inlet air (compressor discharge) temperatures. Figure 4 shows the jet engine component schematic for reference. Figure 5 shows that burning either fuel rich or fuel lean can significantly reduce combustion temperature and NO_x production rates.

Today's subsonic aircraft fleet flies at 30–45,000 feet altitude in the high troposphere/low stratosphere region of the atmosphere. Figure 6 illustrates the region of ozone concentration as a function of altitude. Because of the low ambient temperature (−70°F) and pressure (15–30 percent of sea level) at these cruise altitudes, the compressor discharge temperature (T_{T3}) and pressure (P_{T3}) are relatively low, which results in lower NO_x formation. However, higher temperatures exist at high power flight conditions such as take-off, and this produces increased NO_x. The contribution of overall NO_x emissions has led Sweden to impose an in-country tax on NO_x production over the entire flight path including takeoff, climb, cruise, approach, and landing. This tax may not be limited to Sweden alone as world focus on the environment increases. Fortunately, proactive pioneering work has continued on gas turbine combustor concepts for subsonic aircraft engines that will produce significantly lower levels of NO_x. This will improve the local airport environment and also substantially reduce NO_x emissions in the upper atmosphere.

Supersonic aircraft, such as the High Speed Civil Transport (HSCT), will cruise at 60–90,000 feet altitude at Mach 2–3 for best fuel economy. The engines will have higher compressor discharge temperatures so conventional combustors would release high levels of NO_x emission directly into the heart of the stratospheric ozone layer where the most damage can be done. A fleet of civilian supersonic aircraft with high NO_x emissions is not acceptable. Lowering the NO_x emissions starts with an understanding and application of the bell-shaped curve in Fig. 5.

Figure 7 illustrates the challenge to be addressed in reducing NO_x with a conventional combustor. Production engines today operate with rich primary zone fuel–air ratios. Local reacting fuel–air ratios near stoichiometric (0.068) will result in high flame temperatures (near 4000°F) and produce large quantities of NO_x. Since NO_x generation is primarily a function of the maximum gas temperatures in the combustor, the objective is to reduce the local reacting gas temperatures at high engine power levels. However, the combustor must also operate be-

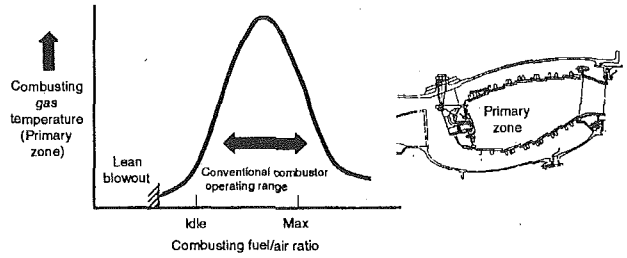

Fig. 7 Single zone combustor design

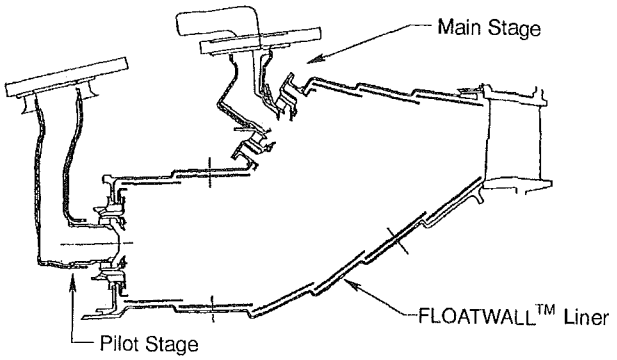

Fig. 8 Pratt & Whitney's axially staged combustor

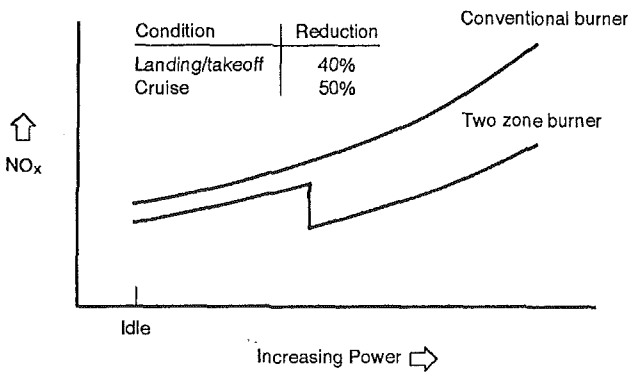

Fig. 9 NO_x emissions reduction

tween idle and maximum power, which is over a three to one (3/1) fuel-air ratio range. The maximum fuel-air ratio in the primary zone, where the reactions take place, is limited by smoke production, whereas the minimum operating fuel-air ratio is limited by lean blowout. Obviously, it isn't easy to significantly reduce NO_x generation from conventional combustors.

P&W's New Low NO_x Combustor

One way to control combusting fuel-air ratios and reduce NO_x is to use a staged combustion concept. Sharing the fuel loading among several fuel and air stages controls the local fuel-air ratio to minimize NO_x formation rates as power is increased. Figure 8 shows an axially staged combustor. The pilot zone is located toward the centerline of the engine and the main zone is outboard and downstream of the pilot zone. One significant advantage of this inboard location of the pilot is that it eliminates the combustor susceptibility to blowout in heavy rain since the compressor centrifuges the water to the outer portion of the flowpath. The design also incorporates the state-of-the-art FLOATWALL™ construction using panels

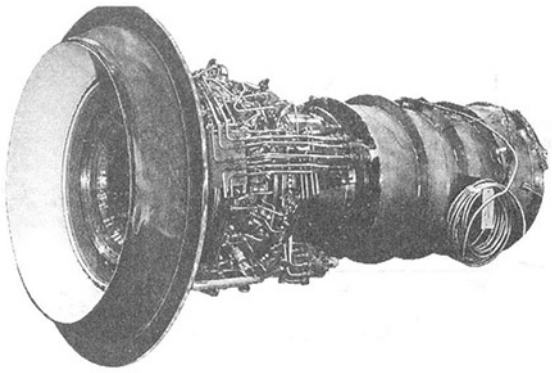

Fig. 10 Pratt & Whitney's full annular combustor rig

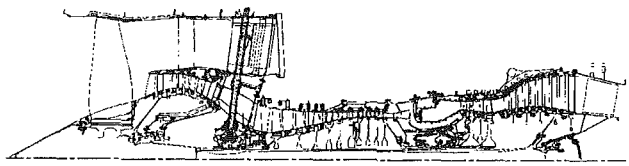

Fig. 11 V2500 engine cross section

with backside convection and slot film cooling to isolate the structural shells from the hot gases. The pilot is designed to be very stable and efficient at low power. It is used for starting the engine and providing energy up through idle power. As the engine power is advanced, the combustor is "staged" by initiating combustion in the main zone. The main combustion zone is located downstream of the pilot zone and is not isolated from the hot pilot gases. Therefore, any fuel introduced into the main zone reacts immediately because of the favorable combustion environment established by the pilot zone. There is no thrust lag introduced, which could result from having isolated pilot and main zones. Another advantage of having the main fuel source outboard of the pilot is that the radial temperature profile peak is toward the outer radius of the turbine flowpath. This provides cooler gases from the blade midspan inward to the root section where the centrifugal stresses are higher. Combined, the pilot and main zones maintain a lean local fuel-air ratio, which controls NO_x emission at higher power levels, including cruise.

Figure 9 shows the characteristic NO_x emission as a function of engine power level for a conventional combustor and a staged combustor. The P&W axially staged combustor operates by fueling only the pilot up through idle, providing excellent operability and low CO and HC emission. As power is advanced above idle, the main zone is fueled and efficient combustion takes place even at low levels of main zone fuel-air ratio. The fuel flow split between the pilot and main stages can be adjusted to provide optimum fuel-air ratios in both stages at high power, achieving lower NO_x emission. Testing in the annular combustor rig (Fig. 10) has demonstrated excellent performance of this concept.

NO_x emitted during the International Civil Aviation Organization (ICAO) defined landing/takeoff cycle is reduced 40 percent and emission during cruise is reduced by 50 percent. This combustor concept is now being developed for qualification, with the first application being the International Aero Engines (IAE) V2500 engine (Fig. 11).

The use of a two-stage combustor requires additional control functions since there are two fuel delivery schedules to satisfy. Fortunately, the introduction of the electronic engine control capable of "threading a needle" makes the combustion staging

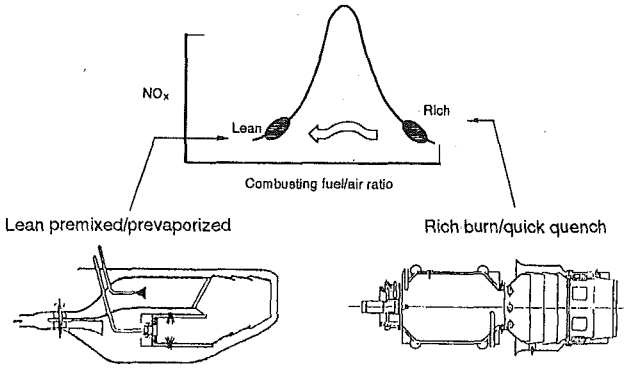

Fig. 12 Ultra-low NO_x combustor concepts

concept practical. However, complexity of the engine external fuel system is significantly increased with fuel zone staging. This requires a system trade-off to provide a balanced design that is reliable, maintainable, affordable, and satisfies emission goals.

Ultra-Low NO_x

For the HSCT aircraft, altitude NO_x emission is a barrier problem due to its impact on the protective ozone layer. Because of the importance of this issue and other barrier issues, Pratt & Whitney, General Electric, and the National Aeronautics and Space Administration (NASA) have formed a team and set extremely aggressive NO_x goals. The goal is 5 g NO_x per kg of fuel burned at cruise, equivalent to over 70 percent less NO_x than today's best conventional subsonic commercial engines. The principals of this team have worked individually for twenty years and have an excellent technical understanding of what must be done. As illustrated by the bell-shaped NO_x emissions characteristics in Figs. 5 and 7, we must burn fuel-lean or fuel-rich in the combustor primary zone. Figure 12 illustrates the two primary approaches being investigated by the team.

The lean premixed/prevaporized concept differs from the staged combustor of Fig. 8 in that the fuel and some of the air is premixed and prevaporized prior to injection, rather than injecting liquid fuel directly into the combustion chamber. This premixing and prevaporizing causes the mixture to be leaner than the staged combustor of Fig. 8 because mixing of fuel vapors is much more uniform and dispersed than the mixing of fine liquid fuel droplets. The flame temperatures, and therefore the NO_x, will be lower as shown in Fig. 5 for lean mixtures. This very lean concept is a challenge requiring extreme care in the design to avoid auto-ignition in the premix chamber and subsequent combustor durability problems. Here, the technology challenges primarily relate go the durability of the premix/vaporizer components.

There are successful premix type combustors in service, such as in the Rolls Royce Concorde Supersonic Transport (SST) engine. However, sufficiently lean and uniform mixtures of fuel–air with adequate vaporization levels needed to satisfy NO_x emission goals have not yet been achieved. Leaner and more uniform fuel–air mixtures are required for minimum NO_x. This must be accomplished while maintaining adequate lean blowout margin. Should the mixture ignite prior to injection into the combustor primary zone, the combustor could be damaged.

The rich burn/quick quench combustor (Fig. 12) operates relatively rich in the primary zone at high power. The lower temperature of the primary zone combustion results in a significantly lower NO_x emission characteristic. The uniqueness of this approach is that the reacted products are rapidly "quenched" to much lower temperatures in a highly effective mixing section. The residence time of the gases in the quenching section is very low, preventing the formation of more NO_x as the gases rapidly increase and then decrease in temperature. Although the primary zone operates fuel-rich, its temperature is low enough to avoid significant smoke production. The technology challenges with this approach are achieving a reasonably uniform mixture of reacting fuel–air in the primary zone, without introduction of cooling air in the primary zone, achieving a fast quench of these gases and controlling smoke emission. The primary zone is the part of the combustor subjected to the highest heat loads, which imposes a major challenge for the designer. Only convection/regenerative cooling can be used, limiting the cooling, structural, and material options. The mechanical design of this internally uncooled primary section may require high temperature ceramics, as an example, to protect the structural shell from the reacting gases.

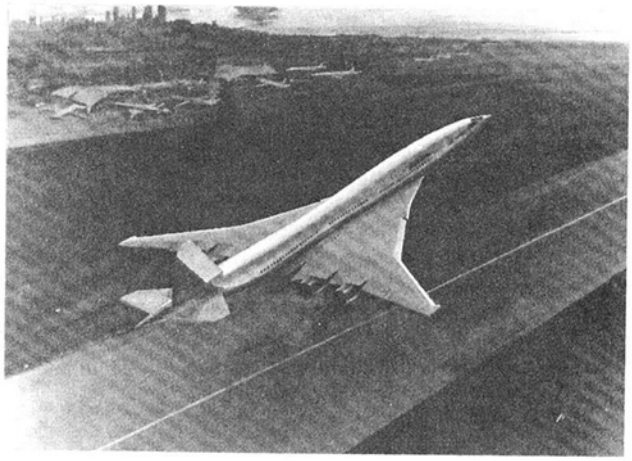

Fig. 13 High Speed Civil Transport

The premixed/prevaporized and rich burn/quick quench approaches may also require variable geometry. Currently, the technical problems including auto-ignition, flashback, durable ceramics, variable geometry, and rapid quenching without freezing the CO reaction, are enormous. However, from a combustion aerothermodynamics viewpoint only, laboratory tests indicate that both concepts have excellent potential to achieve low NO_x objectives. I have confidence that the innovative combustion design engineers at NASA, General Electric, and Pratt & Whitney will be successful.

Figure 13 represents a candidate second-generation HSCT aircraft. One success of this program depends on the progress in the design of ultra-low NO_x emission combustion systems for aircraft flying in the stratosphere.

Conclusions

This paper has presented a perspective focusing on the NO_x emissions barrier for gas turbine engines operating at medium and high altitudes. Technology is close at hand to reduce NO_x levels by a significant 40–50 percent for operational subsonic aircraft engines. Progress has been and concept approaches identified to attack the significant NO_x emissions barrier for supersonic transport aircraft engines. Persistence in working the emissions challenge will develop the technology needed to provide an environmentally responsible supersonic transport aircraft early in the 21st Century.

References

GAO/RCED, 1992, "92-72 Global Pollution From Jet Aircraft Could Increase in the Future," United States General Accounting Office, Jan.

Nitrogen Oxide Emissions Characteristics of Augmented Turbofan Engines

S. P. Seto

T. F. Lyon

GE Aircraft Engines,
Cincinnati, OH 45215

The exhaust plumes of modern military engines can be rendered visible at low augmentor power operation by the presence of nitrogen dioxide (NO_2). Visible plumes have also been observed from some industrial gas turbines that have duct burners downstream of the power turbines. In 1986, gaseous emissions measurements were taken behind two F101 turbofan engines to determine the effect of reheat level on the degree of conversion of nitric oxide (NO) to nitrogen dioxide and to relate the plume visibility to nitrogen dioxide concentration.

Introduction

The introduction of high pressure ratio augmented engines into military aircraft and large turbojet engines into commercial supersonic transports has resulted in a new plume observability problem that is not associated with black (carbonaceous) smoke. Due to their internal operating conditions of high pressure and high temperature, the main combustors of these turbofan engines can produce significant levels of oxides of nitrogen (NO_x). At low augmentor power levels, portions of these oxides of nitrogen (NO_x) can be converted to nitrogen dioxide (NO_2). which is visible as a yellow-brown color in the exhaust plume.

The cases of aircraft engines observed emitting yellow smoke include the F101 engine in the B-1 bomber, the TF30 in the F111, F404 engine in the F18 fighter, the F100 engine in the F-15 fighter, the F110 engine in the F-16, and the Olympus 593 engine in the Concorde supersonic transport. The degree to which this plume color is visible is a function of augmentor power setting, background, observer angle to the plume, and the amount of black smoke produced by the core engine.

Yellow smoke has also been observed in the exhaust of some stationary power gas turbines under combustion conditions similar to the afterburning situation in aircraft engines. This can occur in combined cycle or cogeneration power plants where additional fuel is injected and burned in a duct burner type system behind the power turbine. In these "afterburning" processes, little increase in total NO_x (NO plus NO_2) occurs and, in some cases, a reduction in NO_x has been reported. The mechanism by which the NO is converted to NO_2 has been the subject of some speculation.

In nonaugmented engines, NO_x is emitted mainly as NO that is slowly (over a period of hours to days) oxidized to NO_2 in the atmosphere. The exhaust plume from nonafterburning engines is thus usually well dispersed (over many miles) before complete conversion to NO_2 occurs. The existence of visible yellow smoke does not, then, imply an increase in overall NO_x emitted to the atmosphere, but rather a significant local increase in NO_2 levels.

In 1975, a series of US Air Force sponsored tests of a General Electric (GE J79-15 and a GE J85-5 engine were conducted at Edwards Flight Test Center (EFTC) to measure augmentor emissions for the purpose of developing measuring techniques for afterburning engines [1]. As a result of these measurements, it was noted that for both engines the overall level of oxides of nitrogen (NO_x) remained relatively constant between intermediate power (maximum dry) settings and low augmentor (such as minimum afterburner) power settings, but that the levels of NO decreased significantly, while the levels of NO_2 concentrations approximately doubled.

In 1985, the USAF requested that GE Aircraft Engines examine this plume phenomena using the F101 engine model. GE responded with a program to measure and observe the plume generated from two F101 engines, a new production engine (F101-GE-102) model and an older deteriorated engine. Data were taken at the augmentor discharge of the engine, the exhaust nozzle discharge, and downstream for the purposes of determining the plume constituents.

The tests were conducted at the GE main base test site at EFTC, California, on August 13–17, 1986. Data were obtained with both JP-4 and JP-5 fuels. The NO_x and plume observability data were similar for both engines, so only data for the production engine are presented in this paper.

Engine Description

The F101 augmented mixed flow turbofan engine is a dual rotor aerodynamically coupled machine consisting of a high-pressure gas generator, a mechanically independent low-pressure fan system, and a variable area exhaust nozzle. Engine operation is maintained by regulating the gas generator rotor

Contributed by the International Gas Turbine Institute and presented at the 38th International Gas Turbine and Aeroengine Congress and Exposition, Cincinnati, Ohio, May 24–27, 1993. Manuscript received at ASME Headquarters March 1, 1993. Paper No. 93-GT-120. Associate Technical Editor: H. Lukas.

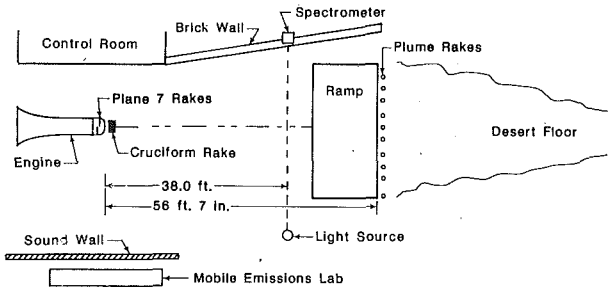

Fig. 1 Edwards test site instrumentation setup

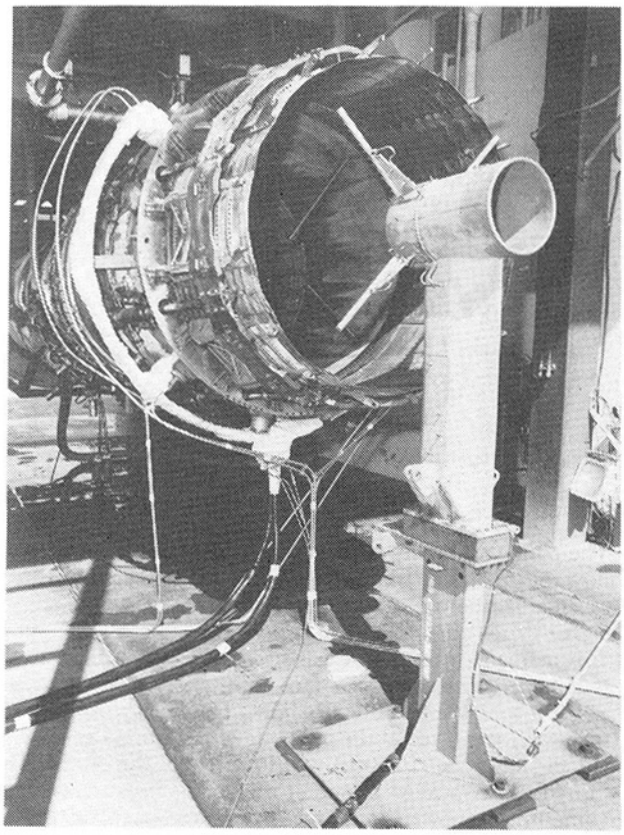

Fig. 2 Aft view of engine-mounted plane 7 rakes and cruciform

speed to obtain the desired fan speed. Modulation of the variable area nozzle and augmentor fuel flow are then used to obtain desired engine thrust level.

The high-pressure gas generator is composed of a nine-stage compressor, an annular combustion chamber, and a single-stage high-pressure turbine. The compressor utilizes variable-geometry inlet guide vanes and stator vanes. The annular combustion chamber is a compact air atomizing, throughflow design with two spark ignitors. The low-pressure fan system consists of a two-stage fan driven by a two-stage low-pressure turbine. The augmentor incorporates a daisy chute mixer and a sequenced fuel injection system coupled to a variable area nozzle. Fuel for augmentor operation is injected from spraybars, located at the inlet to the daisy chute mixer, into both the fan and core airstreams.

Instrumentation

The engine exhaust emissions were measured in four planes aft of the augmentor discharge. At the plane of discharge of the normal engine mounted converging-diverging exhaust nozzle were four individual ten-element gas sample rakes, which were inserted into the slave spool attached to each engine. These four rakes were designated the "Plane 7" rakes. A Pylon-mounted cruciform gas sample rake was located about 4 in. (0.10 m) aft of the actual engine exhaust and used to maximum dry (intermediate) power. It was then removed because it is not internally cooled. A spectrographic (wavelength preferential absorption of light) detector lens and companion light source were located 38.0 ft (11.6 m) aft of the plane of engine exhaust and scanned across the exhaust plume and through the engine centerline. A set of single orifice gas sample rakes was mounted off the backside of the facility blast ramp at a distance of 56 ft 7 in. (17.25 m) aft of the engine exhaust plane. Figure 1 shows the relative positions of these sensors.

A view of the Plane 7 rakes and the cruciform rake is shown in Fig. 2.

The plume rakes were mounted to the backside of the facility blast ramp. Vibration from the engine exhaust eventually destroyed eight of these rakes. Individual rakes were located at the engine centerline and at 1.5 ft (0.46 m), 3.5 ft (1.07 m), 5.0 ft (1.52 m), and 6.5 ft (1.98 m) on either side of the centerline. One rake was mounted at 10 ft (3.05 m) on the left side of the centerline, aft looking forward to account for the plume centerline skewness measured during earlier tests.

The gas samples were transported to gas analysis system consisting of a:

- Beckman Model 402 Flame Ionization Analyzer for hydrocarbons;
- Beckman Model 864 Nondispersive Infrared Analyzer for carbon dioxide and a Beckman Model 865 NDIR analyzer for carbon monoxide;
- Beckman Model 951 chemiluminescent (with thermal converter) analyzer for nitric oxide and nitrogen dioxide; and an
- Inficon Model 020 infrared analyzer for nitrogen dioxide.

The spectrometer system consisted of:

- EG & G/PARC Model 1451 optical multichannel analyzer (OMA)
- Tungsten filament light source (6014 automotive headlamp)
- Belden #226411 fiber optic cable
- Roscolux #69 (brilliant blue) color filter
- Imaging lens [5-7/8 in. (0.15 m) diameter, 13 in. (0.33 m) focal length]

The nitrogen cooled light source was mounted inside an acoustic enclosure to minimize the effects of vibration. The imaging system was mounted in a look-down fashion on top of the cell wall, at an angle of 15 deg. This single pass configuration was chosen to minimize background illumination from the sun.

Results

Gas Analysis. At intermediate power, the main combustor level of NO_x produced was 140 ppm. This level appears to be independent of fuel type. Comparison of the levels measured by the Plane 7 rakes to those of the cruciform rake indicate the level measured at the engine exhaust discharge is 10–12 percent higher; this difference is, however, directly in proportion to the rake measured fuel-air ratio, Table 1. The calculated NO_x emission indices (pounds/1000 pounds fuel) between the two positions varied by less than 2.5 percent, which is excellent agreement. The levels of NO_2 measured at intermediate power are typically 10 percent of the NO_x measured. The very low values obtained with JP-4 fuel are most probably the result of data scatter.

The levels of NO_2 produced during augmentation are limited by the levels of NO_x at each of the test conditions. Figure 3 shows the Plane 7 rake measured average concentrations of NO_x (ppm) at intermediate power and above. Over the range of power levels set, the NO_x concentrations tend to be more or less constant at about 120 ppm. It would normally be ex-

Table 1 Measured average concentration levels of oxides of nitrogen and nitrogen dioxide

Operating Condition	JP-4 Plane 7 Cruciform		JP-5 Plane 7 Cruciform		Visible? Both Fuels
	ppm	ppm	ppm	ppm	
Maximum Dry Power (NO_x)	129.7	141.6	123.6	139.3	No
Maximum Dry Power (NO_2)	5.9	2.9	13.0	13.4	No
Min. Core Augmentor (NO_2)	48.8	--	50.5	--	Yes
80% Max. Core Aug. (NO_2)	64.1	--	66.3	--	Yes
Maximum Core Aug. (NO_2)	70.3	--	66.0	--	Yes
Minimum Fan Aug. (NO_2)	61.3	--	61.9	--	Yes
Low Fan Aug. (NO_2)	53.2	--	--	--	Yes
Mid Fan Aug. (NO_2)	--	--	39.7	--	No
Maximum Aug. (NO_2)	43.8	--	--	--	No

Operating Condition	Description
Minimum Core	Lowest operable fuel flow.
80% Maximum Core	80% allowable fuel to core engine airflow.
Maximum Core	Highest operable fuel flow to core airflow.
Minimum Fan	Lowest operable fuel flow for fan air combustion.
Low Fan	Higher than minimum fan fuel flow.
Mid Fan	Halfway between minimum fan and maximum fan fuel flow.
Max. Attained	Highest power setting reached, less than maximum by about 12%. Limit set by exhaust flap skin temperature.

Table 2 Comparison of measured average NO_2 concentration levels at three axial locations downstream of augmentor exit plane

Sample Type		Gas Analysis	Optical	Gas Analysis	
Location From Eng. Exit		Plane 7	11.6m Aft	17.2m Aft	
Measurement Type		Rakes	Spectrometer	Plume Rakes	
Power Setting	Fuel				Visible?
Maximum Dry	JP-4	5.7 ppm	~0 ppm*	0 ppm	No
Min. Core Aug.	JP-4	48.8 ppm	39.3 ppm	4.0 ppm	Yes
80% Max. Core Aug.	JP-4	64.1 ppm	46.0 ppm	7.6 ppm	Yes
Max. Core Aug.	JP-4	70.3 ppm	41.8 ppm	9.1 ppm	Yes
Min. Fan Aug.	JP-4	61.3 ppm	35.3 ppm	--	Yes
Max. Power Set	JP-4	43.8 ppm	~0 ppm*	--	No
Maximum Dry	JP-5	13.0 ppm	~0 ppm*	--	No
Min. Core Aug.	JP-5	50.5 ppm	(Lost Reading)	--	Yes
80% Max. Core Aug.	JP-5	66.3 ppm	43.2 ppm	--	Yes
Max. Core Aug.	JP-5	66.0 ppm	31.1 ppm	--	Yes
Min. Fan Aug.	JP-5	61.9 ppm	29.0 ppm	--	Yes
Mid Fan Aug.	JP-5	39.7 ppm	~0 ppm	--	No

*Spectrometer measured value not at a significant level.

pected that the levels of NO_x would remain constant at low augmentor power settings and increase slightly as augmentor power level increased toward maximum because of the high temperature levels obtained in the augmentor. Although the concentration levels of JP-5 are not always greater than those of JP-4, the emission index of JP-5 is always greater than that of JP-4 except for one reading at the maximum core power setting.

Once the augmentor is fired, the NO_2 levels increase significantly. As augmentor power is increased, the measured levels of NO_2 increase to a maximum somewhere between 80 percent and maximum core power, and then begin to decrease. This trend is evident for both types of fuel. The change in NO_2 level with power setting corresponds to the observed plume visibility level, which further reinforces the link between these two aspects of the test. Above the low fan power setting the plume was not detectable. This suggests that when Plane 7 concentration levels are below a value of about 45 ppm the plume is not visible. Certainly, at minimum core power, 49-50 ppm, the plume is definitely visible.

The NO_2 data obtained from the spectrometer system and the plume rake system are summarized and compared to the Plane 7 measurement in Table 2.

On a relative basis, agreement (trend) is very good between the measurements taken at the Plane 7 location and the spectrometer location. It should also be noted that at those power settings where the plume was not visible, the spectrometer measured levels of NO_2 were essentially zero (intermediate, maximum aumentor power, midfan power).

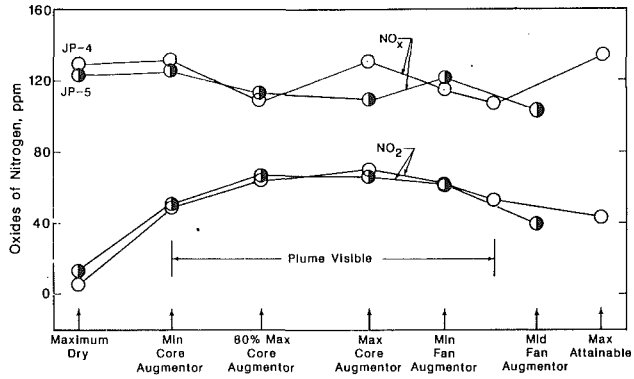

Fig. 3 Engine measured oxides of nitrogen (ppm) and nitrogen dioxide (ppm)

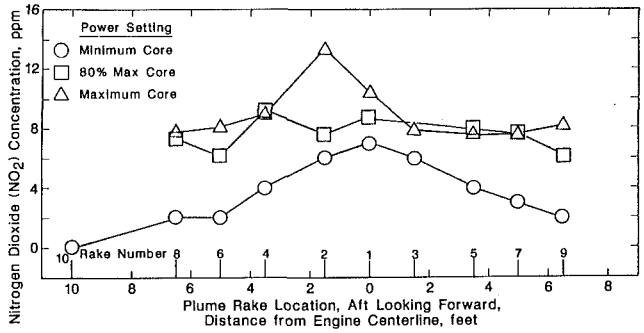

Fig. 4 Nitrogen dioxide at the plume rake position, JP-4 fuel

The plume rake data reflects a 6-9 dilution ratio, but does follow the increasing trend of Plane 7 level for the three readings obtained before rake failures rendered this data source useless.

Downstream of the engine exhaust, one set of measurements was obtained for each of the three most visible plume points during the initial testing on the engine. Figure 4 shows the NO_2 distribution measured at the plume rake position. The level of the data shows the effects of dilution flow in the plume. The expected center-peaked plume profile shape is evident in the minimum core power data and to a lesser extent in the 80 percent maximum core and maximum core data.

Spectrometer Measurements. The engine test data were compared to laboratory test data from known NO_2 calibration gases to confirm that the characteristic absorption shape of the measured data corresponded to NO_2, Fig. 5.

To identify the band structure, the published data [3] for the NO_2 absorption coefficient were transposed from absorption to transmission and then scaled to both the path length used for the before engine laboratory calibration, and a selected concentration level. This aided in indentifying structure by providing prominence to the distribution.

Engine test point data (absorption) were normalized to transmission, then compared to the modified published data. An example is shown in Fig. 6. The structure of the engine measurement matches the published data at numerous wavelengths.

Discussion

Plume Reaction. One method for assessing the presence of NO_x conversion reactions in the plume is to plot the ratio of NO_2 concentration to NO_x present in the samples. If reaction of the available NO continues in the plume, downstream of the augmentor discharge, then the levels of NO_2, as a fraction of the NO_x, will be higher at these locations.

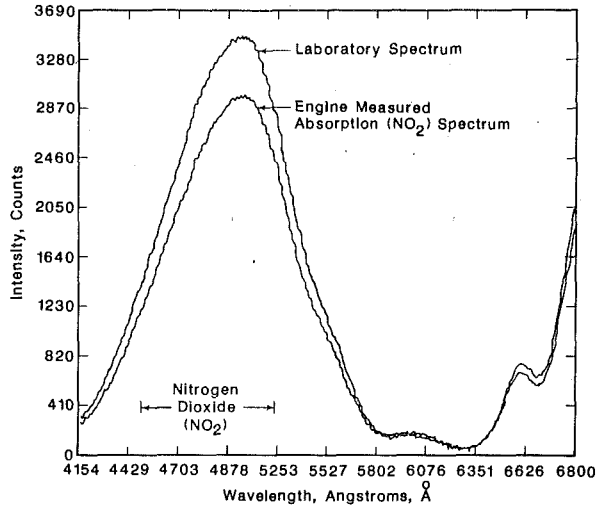

Fig. 5 Engine measured intensity levels compared to laboratory (100 percent nitrogen gas; engine running at minimum core augmentor)

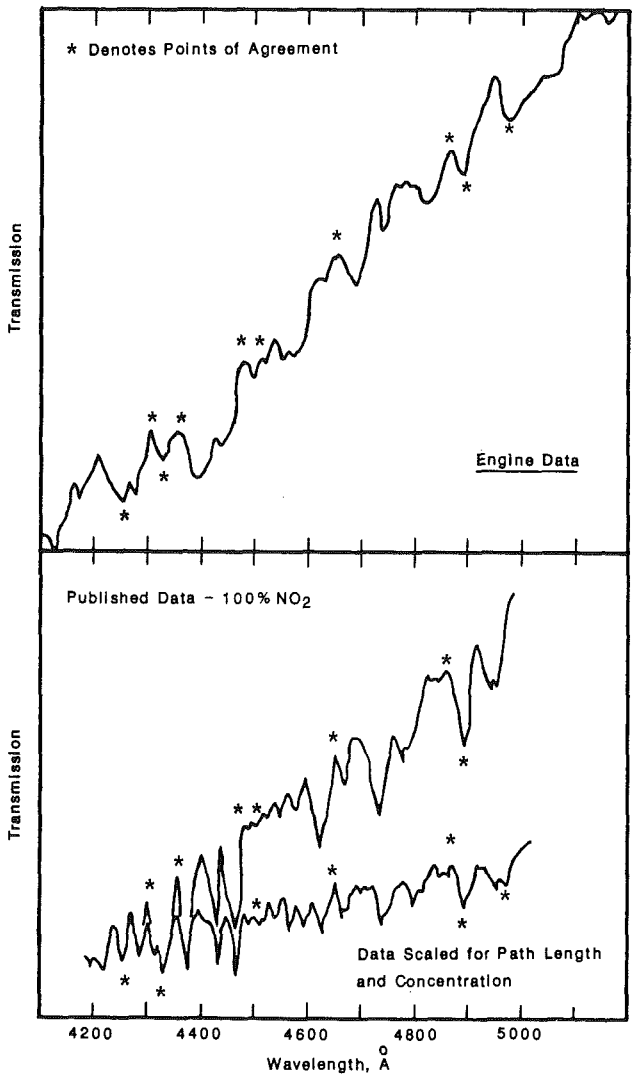

Fig. 6 Comparison of engine measured NO_2 band structure with published data

Figure 7 shows plots of the ratio of NO_2 to NO_x at the plume rake position and for the three augmentor power settings for which data were obtained. Included on this figure are the

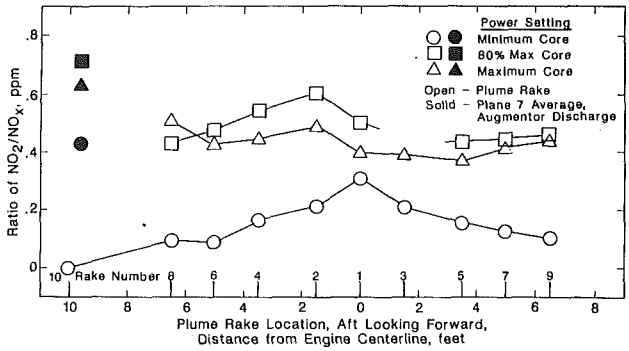

Fig. 7 Comparison of NO_2/NO_x and power setting, JP-4 fuel

Table 3 Comparison of calculated EI (far plume analysis) to gas analysis (GA) measured average EI'S, JP-4 fuel (emission index—pounds per 1000 pounds of fuel)

Operating Condition and Location	CO	HC	NO_x	NO_2	NO
Minimum Core					
Plane 7 (GA)	27.8	142.8	18.2	8.02	10.20
Plume (GA)	23.0	81.3	17.7	2.78	14.31
Plume Calculated	21.6	64.7	16.4	3.03	13.50
80% Max. Core					
Plane 7 (GA)*	73.7	231.8	10.4	7.32	3.09
Plume (GA)	79.8	99.2	9.0	4.46	4.6
Plume Calculated	75.2	77.6	8.4	3.67	3.78
Maximum Core					
Plane 7 (GA)	87.8	99.6	8.0	5.50	3.30
Plume (GA)	90.6	146.0*	6.8	3.10	3.70
Plume Calculated	88.3	130.8*	6.3	2.66	3.52

*Increases downstream of engine exhaust plane caused by a minor hydraulic oil leak from one of the nozzle actuators.

average values of this ratio obtained from the Plane 7 rakes for each power setting.

At the minimum core power the fractional values of NO_2 at the plume rake position are approximately 40 percent of the average Plane 7 value. Similarly, the plume rake measured fraction of NO_2 is about 65 percent of the Plane 7 rake measured value for the two other power settings. The implication of the data is that at these low augmentor power settings, the plume reactions result in decreases in the amounts of NO_2. Further support is provided in the following paragraph, which discusses a study of the emissions indices measured at Plane 7 and the plume rake positions.

Far Plume Analysis. In an effort to examine reactions in the plume further, a "far plume analysis" was done using the methodology outlined in Appendix B of [1]. The procedure involves plotting wet concentration (ppm) values of CO, HC, NO, NO_2, and NO_x versus wet percent CO_2, and calculating the emission index from the slope of a line through the data. Over a range of percent CO_2 from zero to the maximum level measured, a linear (constant) relationship should exist from each of the constituent gases, and the intercept should pass through the value of percent CO_2 in the ambient air if both the mixing and reaction in the plume are completed. This results from the fact that if an arbitrarily unreacting gas is mixed with pure air, the emission index is not changed. The results of this analysis are shown in Table 3. The comparison shows that the values for carbon monoxide (CO) are fairly constant as expected and that levels of hydrocarbons (HC) decrease, a trend seen before in data from other engines [2] because of the continued consumption of HC emissions in the plume. At the maximum core condition, a small leak developed in the hydraulic oil connectors of one exhaust nozzle actuator causing the significant increases of HC emissions at the plume rake position. The measured levels of NO_x at the plume rake position are slightly lower than at the Plane 7 location; however, the

concentrations of NO_x at the plume rake position are very low (approximately 20 ppm compared to 140 ppm at the engine exit), so these differences are not unrealistic. The far plume analysis (calculated) levels of NO_x are fractionally lower than the measured levels, which is true also for CO and HC: a consistent trend. What is of interest is that, both measured and calculated, the levels of NO_2 are lower at the plume rake position, relative to Plane 7, and the corresponding levels of NO are higher. The minor differences in level of EI are attributed to the very low levels of concentrations of NO and NO_2 that were measured. The inference from this analysis is that NO_2 is being converted to NO in the plume.

Augmentor Reactions

The purpose of these tests was to verify that the visible species in the F101 engine exhaust is NO_2, and to estimate the NO_2 concentration at the visibility threshold. This goal was accomplished.

The exact mechanism leading to the excessive NO_2 concentrations is not completely understood. The most likely explanation is contained in the following discussion. At high temperatures such as those found in the augmentor, the equilibrium state for the oxides of nitrogen is essentially 100 percent NO. However, these are nonequilibrium processes that can result in the formation of significant quantities of NO_2 in the augmentor where relatively large quantities of NO are present as a result of combustion in the mainburner.

It has been found in laboratory experiments [4] on both premixed and diffusion flames that the ratio of NO_2 to NO may greatly exceed the value appropriate to the equilibrium:

$$NO + 1/2\ O_2 \rightleftharpoons NO_2$$

It is suggested [4] that the larger ratio is a result of the transient superequilibrium concentrations of O, OH, HO_2, and other species because it is also observed that the ratio NO_2/NO decreased in the burned gases above the flames when the concentrations of O, OH, HO_2, etc., also decreased.

It has also been proposed [4] that NO_2 is rapidly formed by the reaction:

$$HO_2 + NO \rightleftharpoons OH + NO_2$$

The reactions above provide a mechanism for the formation of NO_2 at concentrations much higher than equilibrium. As the combustion reactions are completed, the radical reactions that convert NO_2 back to NO are slowed because of the low concentration of radicals at this point. Final quenching of radicals due to combustion completion or due to mixing with colder gases leaves the NO_2 at conditions above equilibrium. These high NO_2 concentrations may persist into the plume, in the case of the augmented turbine engine, due to quenching of the reactions. At low augmentor power settings, this quenching of the reactions may be aggravated by the cold fan air that is introduced into the reaction zone by mechanical mixers.

While this rather simplified discussion of the formation of high concentration of NO_2 in the augmentor is quite plausible, it does not immediately suggest a method by which the visible plume can be eliminated, except by reducing the NO_x emissions from the mainburner.

Summary

Gas analysis and spectrometer measurements taken at the exhaust of a modern turbofan engine and further downstream indicate that:

- The visible gas constituent in the plume is NO_2.
- The exhaust plume was visible at the low (core fuel flows to initiation of fan fuel flow) augmentor power settings. The plume was not visible at any dry power setting or at any near maximum augmentor power setting.
- The concentration levels (ppm) necessary for visibility are 45 ppm and higher at the engine exhaust plane.
- The plume reactions appear to favor consumption of NO_2, not additional formation.
- The NO_x levels and the NO conversion to NO_2 were essentially the same with both JP-4 or JP-5 fuel.

References

1 Amer, A. A., Jubran, B. A., and Hamdan, M. A., 1992, "Comparison of Different Two-Equation Turbulence Models for Prediction of Film Cooling From Two Rows of Holes," *Numerical Heat Transfer*, Part A, Vol. 21, pp. 143–162.

2 Lyon, T. F., et al., "Development of Emissions Measurement Techniques for Afterburning Turbine Engines," AFAPL-TR-75-52 Oct. 1975.

3 Hall and Blacet, *Journal of Chemistry and Physics*, Vol. 20, 1952, p. 1745.

4 Fenimore, C. P., "The Ratio NO_2/NO in Fuel-Lean Flames," *Combustion and Flame*, Vol. 25, 1975, p. 85.

5 Merryman, E. L., and Levy, A., "Nitrogen Oxide Formation in Flames: The Roles of NO_2 and Fuel Nitrogen," *Fifteenth Symposium (International) on Combustion*, The Combustion Institute, Pittsburgh, PA 1974.

GETRAN: A Generic, Modularly Structured Computer Code for Simulation of Dynamic Behavior of Aero- and Power Generation Gas Turbine Engines

M. T. Schobeiri
Professor.
Mem. ASME

M. Attia
Research Assistant.

C. Lippke
Research Assistant.

Department of Mechanical Engineering,
Texas A&M University,
College Station, TX 77843

The design concept, the theoretical background essential for the development of the modularly structured simulation code GETRAN, and several critical simulation cases are presented in this paper. The code being developed under contract with NASA Lewis Research Center is capable of simulating the nonlinear dynamic behavior of single- and multispool core engines, turbofan engines, and power generation gas turbine engines under adverse dynamic operating conditions. The modules implemented into GETRAN correspond to components of existing and new-generation aero- and stationary gas turbine engines with arbitrary configuration and arrangement. For precise simulation of turbine and compressor components, row-by-row diabatic and adiabatic calculation procedures are implemented that account for the specific turbine and compressor cascade, blade geometry, and characteristics. The nonlinear, dynamic behavior of the subject engine is calculated solving a number of systems of partial differential equations, which describe the unsteady behavior of each component individually. To identify each differential equation system unambiguously, special attention is paid to the addressing of each component. The code is capable of executing the simulation procedure at four levels, which increase with the degree of complexity of the system and dynamic event. As representative simulations, four different transient cases with single- and multispool thrust and power generation engines were simulated. These transient cases vary from throttling the exit nozzle area, operation with fuel schedule, rotor speed control, to rotating stall and surge.

1 Introduction

The continuous efforts of the aircraft and power generation gas turbine industry to design engines that meet increasingly high efficiency and performance requirements have significantly contributed to the current state of the development of the engine design tools utilizing sophisticated three-dimensional CFD methods. These methods, though capable of accurately predicting engine performance at the design point, are not appropriate tools for calculating engine behavior during dynamic operation. In the course of adverse dynamic operation, extreme aerodynamic, thermal, and consequent mechanical stresses are developed that may affect the safety, reliability, and, thus, the operability of the engine. The realistic estimation of these stresses is crucial in the early stages of the design process. One method for estimating this stress situation is to utilize a database, which is built on comprehensive tests of the existing engines with components similar to the ones being designed. This method, however, requires continuous updating of the database, which necessitates a series of comprehensive and critical performance, safety, and reliability tests. Furthermore, it is not viable for estimating the dynamic behavior of a new generation of engines that incorporate components developed under a completely new design strategy. An alternative method for providing comprehensive information about the dynamic behavior of the engine under development is the use of a computational method capable of accurately predicting engine behavior under various dynamic conditions. A computational method with this capability with the corresponding modularly structured simulation code, called GETRAN, has been developed. In this paper, the design concept, the theoretical background for the development of GETRAN, and several simulation cases are presented.

Contributed by the International Gas Turbine Institute and presented at the 38th International Gas Turbine and Aeroengine Congress and Exposition, Cincinnati, Ohio, May 24–27, 1993. Manuscript received at ASME Headquarters March 17, 1994. Paper No. 93-GT-388. Associate Technical Editor: H. Lukas.

2 Engine Representations

Studies of the dynamic behavior of aircraft engines were conducted earlier by NASA Lewis Research Center using the component performance map representation for simulating engines. Koenig and Fishbach (1972) and Seldner et al. (1972) utilized overall component performance maps in their simulation program GENENG, which performs purely steady-state computations. In order to account for the system dynamics, Seller and Daniele (1975) extended the code by introducing simplified dynamic equations. A similar technique was also applied by Fawke and Saravanamuttoo (1972). In a report about a hybrid simulation of single- and twin-spool turbofan engines, Szuch (1974) also described the representation of the engine components by overall performance maps. To estimate gas turbine starting characteristics, Agrawal and Yunis (1982) generated a set of steady component characteristics, where the turbine and compressor components are represented by overall steady performance maps. The engine representation by performance maps, as briefly addressed above and comprehensively discussed by Schobeiri (1985a), exhibits a useful tool for approximating engine behavior within the operation range defined by the component maps. However, the detailed information that is crucial for engine development and design cannot be provided at this simulation level. Furthermore, this representation is not viable for providing the control system designer with the necessary input parameters, such as those describing the aero-thermodynamic and structural conditions of the compressor and turbine blade rows. Consequently, the response of the real system to the intervention of the controller cannot be verified. These and other parameters are required inputs to the controller for triggering precautionary actions such as active surge control, achieved by adjusting variable compressor stator blades.

In order to address these issues, Schobeiri (1985a,b,c, 1986, 1987a) and Schobeiri and Haselbacher (1985) developed the modularly structured computer code COTRAN for simulating the nonlinear dynamic behavior of single-shaft power generation gas turbine engines. To account for the heat exchange between the material and the working fluid during a transient event, diabatic processes are employed in COTRAN. The dynamic expansion process through the turbine component is accomplished by a row-by-row calculation using the stage characteristics. COTRAN reflects real engine configurations and components, and is routinely used at the early stages of design and development of new gas turbine engines. It is also utilized for developing robust control systems and the verification of routine engine tests. Dynamic simulations of different single-shaft engines performed with COTRAN were reported by Schobeiri and Haselbacher (1985) and Schobeiri (1986, 1987b). Although COTRAN represents an advanced, nonlinear dynamic code, its simulation capability is restricted to single-shaft power generation gas turbine engines and, thus, cannot be used for simulating multispool aircraft engines. This circumstance motivated development of a new, generic, modularly structured computer code, GETRAN, for simulating the nonlinear dynamic behavior of single- and multispool high pressure core engines, turbofan engines, and power generation gas turbine engines. The code is capable of simulating aircraft engines having up to five spools with variable geometry, with or without additional power generation shafts. A precise prediction of the dynamic behavior of the engine and the identification of critical parameters by the code enables the engine designer to take appropriate steps using sophisticated control systems. The code may also be used to proof the design concept of the new generation of high performance engines. The modular structure of the code enables the user to develop new components independently and integrate them into GETRAN.

3 Brief Survey of Existing Engines and Their Components

In order to generate a design concept for development of the modularly structured code, the configurations of existing aero-gas turbine engines and their power generation derivatives are briefly surveyed. As shown in Fig. 1, the configurations of single- and multispool base engines incorporate the following main components:

- Inlet diffuser
- Compressors
- Combustion chamber
- Turbines
- Shafts
- Exit diffusers from compressors
- Exit nozzle

Starting from the base engines as shown, various derivatives can easily be created by introducing additional components such as a fan, a propeller, a duct, or a power-generating shaft. Thus, the configurations of the derivatives exhibit different component arrangements. This procedure can be extended to single- or multispool engines without any restrictions. Aside from the components listed above, there are a number of other components such as control systems, speed sensors, and pipes that are encountered in any type of engine.

Nomenclature

C_f = friction coefficient
C_p, C_v = specific heat capacities
D_h = hydraulic diameter
h, H = static, total enthalpy
I = moment of inertia
K = kinetic energy per unit mass
L = stage mechanical energy, length
l = specific mechanical energy
$\dot{m}$ = mass flow
n = number of stations
Nu = Nusselt number
p, P = static, total pressure
$\dot{\mathbf{q}}$ = heat flux vector
Q = rate of heat flow
R = gas constant
S = cross-sectional area
t = time
T, T^* = absolute static temperature
$\mathbf{T} = e_i e_j \tau_{ij}$ = shear stress tensor
V = volume
$\mathbf{V}$ = absolute velocity vector
$\mathbf{X}$ = state vector
α = heat transfer coefficient
ϵ = convergence tolerance
κ = ratio of specific heats
μ = mass flow ratio, kinematic viscosity
$\Pi = e_i e_j \pi_{ij}$ = stress tensor
ρ = density
$\overline{\omega}$ = angular velocity

Subscripts

A = air
c = cold
C = convection
CA = air-side convection
CG = gas-side convection
F = fuel
Fi = film
G = combustion gas
h = hot
i = shaft number
m = mechanical
M, P, S = mixing, primary, segment
R = radiation
W = wall

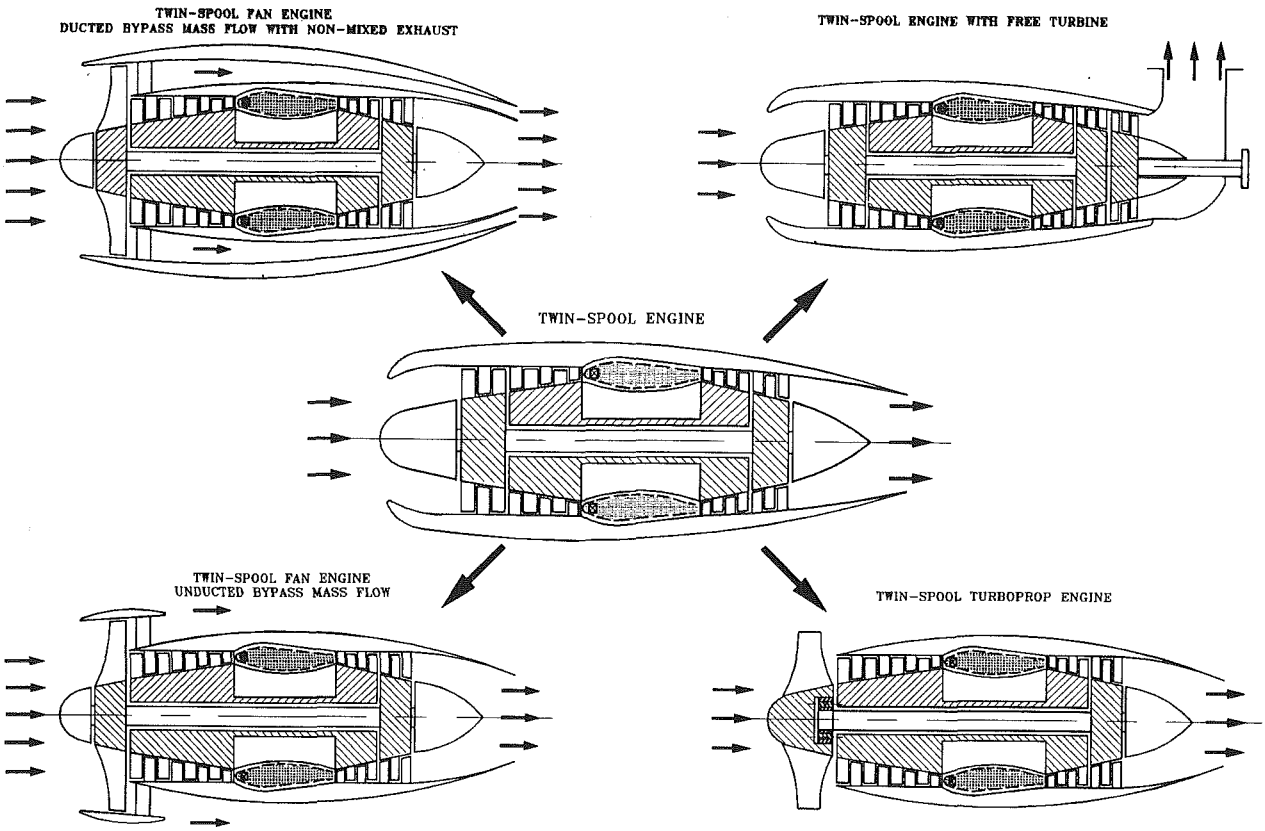

Fig. 1 Survey of twin-spool base engines

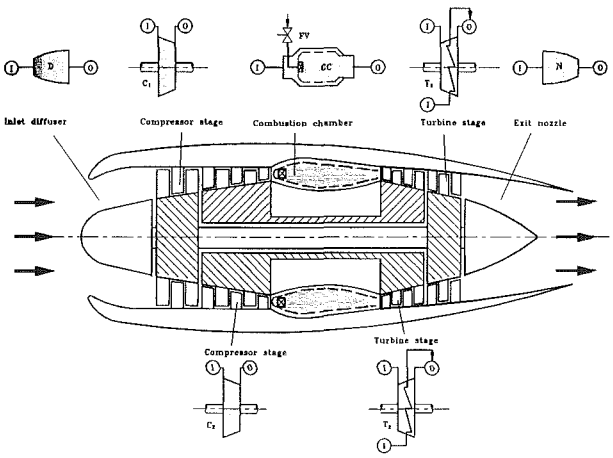

Fig. 2 Twin-spool base engine module allocation

4 Engine Components, Module Addressing and Categories

As a representative example, Fig. 2 shows the schematic component arrangement and modeling of a two-spool base engine. Some of the modules implemented in GETRAN are shown in Fig. 3. According to their individual functions, the modules are classified into four categories that require special physical modeling derived from a generic modeling concept. A brief functional description of these modules followed by physical modeling is given below. Before discussing the modules related to the above-mentioned categories, the plenum, which is the coupling component between two or more successive components, is discussed. The primary function of the plenum is to couple the dynamic information of entering and exiting components. The volume of the plenum reflects the partial volumes of the components that enter and exit the plenum. The inlet components transfer information about mass flow, total pressure, total temperature, fuel/air ratio, and water/air ratio to the plenum. After entering the plenum a mixing process takes place, where the aforementioned quantities reach their equilibrium values. These values are the same for all outlet components exiting the plenum.

Modules belonging to the first category of components exchange no thermal or mechanical energy with surroundings. The function of the diffuser (*D*), nozzle (*N*), and subsonic-supersonic nozzle or diffuser (SSN) modules is the transfer of the mass flow associated with the partial conversion of kinetic energy into potential energy and vice versa. The function of the pipe (*P*) module is to transfer mass flow from one point to another. The cooling air supply for the rotor and turbine blade cooling purposes is a simple example for the application of the component pipe. Each module is identified by its name and the number of its inlet and outlet plena *I* and *O* that serve as component addresses. This module addressing convention is applied to all modules within GETRAN.

The second category of modules includes those components with thermal energy conversion and exchange processes, such as combustion chambers, afterburners, recuperators, and coolers. The recuperators and coolers are frequently used in connection with power generation to increase the thermal efficiency. However, the new generation of high-pressure core engines may also require these components for cooling high-pressure compressor stages.

The third category of modules consists of those components within which conversion and exchange of mechanical and thermal energy take place, such as uncooled and cooled compressor and turbine stages. The modules for cooled compressor and turbine stages represent the last stage of a high-pressure com-

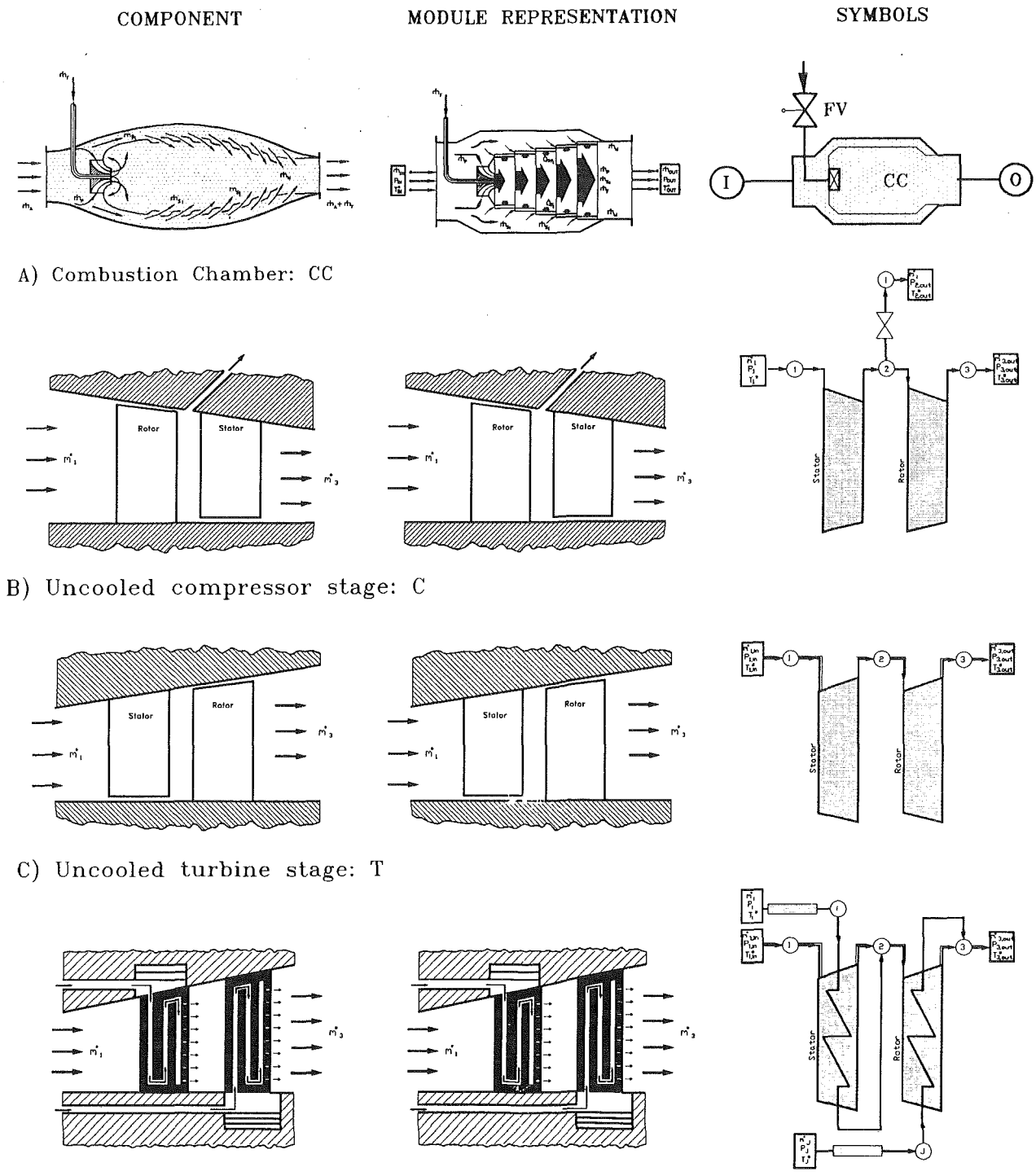

Fig. 3 Component representations

pressor and the first stage of a high-pressure turbine, respectively, Fig. 3. For a multistage compressor or turbine the simulation is provided by a serial arrangement of these components. Unlike the cooled compressor stage where the cooling mass flow enters the cooler and does not participate in the compression process, the turbine cooling mass flow enters the plenum downstream of the turbine stage and is mixed with the turbine main stream combustion gas. The mixing process changes the fuel–air ratio, which is calculated precisely.

The fourth category of modules consists of valves, sensors, control systems, fuel and load schedule generators, etc. The control system is a major module that controls the entire engine. Input information may contain rotor speed transferred by the speed sensors, turbine inlet temperature, pressure, and compressor inlet and exit pressures and temperatures. This information may trigger closing or opening of the fuel valves, several bypass valves, and perform other control functions, such as the adjustment of compressor stator blades to perform active surge protection. Finally, the shaft module represents the rotor speed behavior. The modules listed above, except the control system, are preliminary resident modules; new modules may be developed and added to the system.

5 Design Concept for a Modularly Structured Code

From the conceptual design point of view, the previous survey has led to the practical conclusion that any arbitrary aircraft or power generation gas turbine engine and its derivatives, regardless of configuration, i.e., number of spools and components, can be generically simulated by arranging the components according to the engine of interest. The present nonlinear dynamic code GETRAN is based on this design concept, and is a generic, modularly structured computer program that simulates the transient behavior of existing and new engines and their derivatives. The modules are identified by their names, spool numbers, and the inlet and outlet plena. This information is vital for automatically generating the system of differential equations representing individual modules. Modules are then combined into a complete system that corresponds to the engine configuration. Each module is physically described by the conservation laws of thermofluid mechanics, which result in a system of nonlinear partial differential or algebraic equations. Since an engine consists of a number of components, its modular arrangement leads to a system containing a number of sets of equations. This concept can be systematically applied to any aircraft or power generation gas turbine engine.

6 Levels of Simulation, Component Modeling

The degree of accuracy of a dynamic engine simulation is primarily determined by the level of component modeling and consequently the engine simulation complexity. Thus, the degree of accuracy increases with increasing the level of simulation complexity. Four simulation levels are introduced. The first level uses the steady-state component performance maps without dynamic coupling. The system simulation is described by a set of algebraic equations only. Examples of this level were presented in the first paragraph of section 2. Using the compressor and turbine performance maps, and considering the component dynamics by introducing the plenum as the coupling component, characterizes the second level of simulation, in which algebraic and ordinary differential equations describe the system. A third level of simulation is defined utilizing the conservation laws of thermofluid-dynamics in differential and integral forms to model the engine components. At this level, compressor and turbine components are adiabatically modeled in a row-by-row manner. The compression and expansion calculation processes through compressor and turbine rows are performed using the row characteristics, which include losses and efficiencies. Finally, the fourth level of simulation calculates the compressor and turbine blade temperatures. In this case diabatic processes are used that result in doubling the number of governing differential equations.

7 Physical Description of Components, One-Dimensional Approximation

The components are mathematically modeled by sets of partial differential equations and/or algebraic equations. The dynamic behavior of the components pertaining to categories 1 to 3 discussed previously are described by the conservation laws of thermofluid dynamics. These are the equation of continuity:

$$\frac{\partial \rho}{\partial t} = -\nabla \cdot (\rho \mathbf{V}); \tag{1}$$

the equation of motion:

$$\frac{\partial (\rho \mathbf{V})}{\partial t} + \nabla \cdot (\rho \mathbf{V}\mathbf{V}) = -\nabla p + \nabla \cdot \mathbf{T} \tag{2}$$

the equation of total energy:

$$\frac{\partial H}{\partial t} = -k\mathbf{V} \cdot \nabla H - (\kappa - 1)\left[\frac{1}{\rho}\nabla \cdot (\rho \mathbf{V})(H + K) + \frac{\mathbf{V} \cdot \partial(\rho \mathbf{V})}{\rho \partial t}\right] + \left[-\frac{\kappa \nabla \cdot \dot{\mathbf{q}}}{\rho} + \frac{\kappa}{\rho}\nabla \cdot (\mathbf{V} \cdot \mathbf{T})\right] \tag{3}$$

with $\mathbf{T}$ as the shear stress tensor, $H = h + V^2/2$, the total enthalpy, and $K = V^2/2$ the kinetic energy. The total enthalpy can be expressed in terms of total temperature T^*:

$$c_p \frac{\partial T^*}{\partial t} = -k\mathbf{V} \cdot \nabla (c_p T^*) - (\kappa - 1)\left[\frac{1}{\rho}\nabla \cdot (\rho \mathbf{V})(c_p T^* + K) + \frac{\mathbf{V} \cdot \partial(\rho \mathbf{V})}{\rho \partial t}\right] + \frac{\kappa}{\rho}[-\nabla \cdot \dot{\mathbf{q}} + \nabla \cdot (\mathbf{V} \cdot \mathbf{T})] \tag{4}$$

Finally, the total energy equation in terms of total pressure may be written as:

$$\frac{\partial P}{\partial t} = -k\nabla \cdot (\mathbf{V}P) - (\kappa - 1)[-\nabla \cdot (\dot{\mathbf{q}}) - \nabla \cdot (\mathbf{V} \cdot \mathbf{T})] - (\kappa - 2)\frac{\partial (\rho K)}{\partial t} \tag{5}$$

This equation was obtained by inserting Eqs. (1) and (2) into Eq. (3), where $P = p + \rho V^2/2$ is the total pressure. A three-dimensional solution for the entire engine simulation requires considerable computational efforts using massive parallel processing and probably will not be available in the near future. Two-dimensional treatment likewise requires a great computational effort. For integral engine simulation purposes, a one-dimensional approximation gives sufficiently accurate results. For this purpose, the basic equations must first be made accessible for the one-dimensional treatment of a numerical computation. The partial differential equations can be approximated as ordinary differential equations by means of conversion into difference equations. These ordinary differential equations can then be solved numerically with the prescribed initial and boundary conditions. For this purpose, the flow field is divided into a number of prescribed discrete zones.

Without discussing in detail the various schematics for discretization, a simple schematic is presented below. The equation of continuity is approximated as:

$$\frac{\partial \rho}{\partial t} = -\frac{1}{\Delta x}\left[\frac{\dot{m}_{i+1}}{S_{i+1}} - \frac{\dot{m}_i}{S_i}\right] \tag{6}$$

In Eq. (2), the divergence of the shear stress tensor represents the shear forces acting on the surface. For a one-dimensional flow, the only nonzero term is $\partial \tau_{21}/\partial x_2$, which can be related to the wall shear stress τ_w. The wall shear stress in turn is a function of the friction coefficient c_f, which is directly related to the loss coefficient of the pertinent component under consideration. The momentum equation becomes:

$$\frac{\partial \dot{m}_{i+1}}{\partial t} = -\frac{1}{\Delta x}[\dot{m}_{i+1} V_{i+1} - \dot{m}_i V_i + p_{i+1} S_{i+1} - p_i S_i] + \left[\left(\frac{\dot{m}_k V_k + p_k S_k}{S_k}\right)\left(\frac{S_{i+1} - S_i}{\Delta x}\right)\right] - c_f \frac{\dot{m}_{i+1} V_{i+1}}{2D_h} \tag{7}$$

where S_i is the cross-sectional area. The energy equation in terms of total temperature is approximated as:

$$\frac{\partial T^*_{i+1}}{\partial t} = -\kappa_k \frac{\dot{m}_k}{\rho_k S_k}\left[\frac{c_{p_{i+1}} T^*_{i+1} - c_{p_i} T^*_i}{\Delta x\, c_{p_{i+1}}}\right] - \frac{\kappa_k - 1}{\rho_k c_{p_{i+1}}}\left[\left(\frac{c_{p_k} T^*_k + K_k}{\Delta x}\right) * \left(\frac{\dot{m}_{i+1}}{S_{i+1}} - \frac{\dot{m}_i}{S_i}\right) + \frac{\dot{m}_k}{\rho_k S_k^2}\frac{\partial \dot{m}_{i+1}}{\partial t}\right] - \frac{\kappa_k}{\rho_k c_{p_{i+1}}}\Delta \dot{Q} \tag{8}$$

The energy equation in terms of total pressure:

$$\frac{\partial P_{i+1}}{\partial t} = -\frac{\kappa_k}{\Delta x}\left[\frac{\dot m_{i+1} p_{i+1}}{\rho_{i+1} S_{i+1}} - \frac{\dot m_i p_i}{\rho_i S_i}\right] - (\kappa_k - 1)\left[\Delta\dot Q + c_{f_k}\frac{\dot m_{i+1} V^2_{i+1}}{2 D_{h_{i+1}} S_{i+1}}\right] - (\kappa_k - 2)\frac{\dot m_k}{\rho_k S_k^2}\left[\frac{1}{2}\frac{\dot m_k}{\rho_k}\frac{1}{\Delta x}\left(\frac{\dot m_{i+1}}{S_{i+1}} - \frac{\dot m_i}{S_i}\right) - \frac{\partial \dot m_{i+1}}{\partial t}\right] \quad (9)$$

with:

$$\rho_k = \frac{1}{R}\frac{p_{i+1}+p_i}{T_{i+1}+T_i},\quad c_{p_k} = \frac{H_{i+1}-H_i}{T^*_{i+1}-T^*_i},\quad \kappa_k = \frac{c_{p_k}}{c_{p_k}-R}$$

where the quantities with the subscript k represent the averaged values between the stations i and $i+1$.

8 Modeling of Components

Equations (6)–(9) enable dynamic simulation of the engine components in which fluid and thermodynamic processes take place. The nonlinear dynamic behavior of these components is described by the conservation laws of thermofluid dynamics, resulting in a system of ordinary differential and algebraic equations. The components are modeled mathematically as modules for configurating a complete system of any thrust or power generating gas turbine engine. As pointed out in section 4, these components are classified into three categories according to their functions. The representatives of each of these groups are briefly described below.

8.1 Modeling of Components Pertaining to Category 1: Inlet, Exit, Pipes. The components pertaining to this category are the connecting pipes, inlet and exit diffusers, and nozzles with subsonic or supersonic flows. Their function consists, among other things, of the transportation of mass flow, and, partially, of converting the kinetic energy into potential energy and vice versa. For the application of the conservation laws to a duct with a variable cross section, the equations of continuity and motion, given in a previous section, remain unchanged, whereas the energy equation is modified as follows:

$$\frac{\partial P_{i+1}}{\partial t} = -\frac{\kappa_K}{\Delta x}\left(\frac{\dot m_{i+1} p_{i+1}}{\rho_{i+1} S_{i+1}} - \frac{\dot m_i p_i}{\rho_i S_i}\right) - (\kappa_K - 1)\, c_{f_k}\frac{\dot m^3_{i+1}}{2\rho^2_{i+1} S^3_{i+1} D_{h_{i+1}}} - (\kappa_k - 2)\frac{\dot m_k}{\rho_k S_k^2}\left[\frac{1}{2}\frac{\dot m_k}{\rho_k}\frac{1}{\Delta x}\left(\frac{\dot m_{i+1}}{S_{i+1}} - \frac{\dot m_i}{S_i}\right) - \frac{\partial \dot m_{i+1}}{\partial t}\right] \quad (10)$$

For a constant cross section, the equations of continuity and motion are written, respectively, as:

$$\frac{\partial \rho_{i+1}}{\partial t} = -\frac{1}{\Delta x S}\left[\dot m_{i+1} - \dot m_i\right] \quad (11)$$

$$\frac{\partial \dot m_{i+1}}{\partial t} = -\frac{1}{\Delta x}\left[\frac{\dot m^2_{i+1}}{\rho_{i+1} S} - \frac{\dot m^2_i}{\rho_i S} + S(p_{i+1} - p_i)\right] - c_f\frac{\dot m^2_{i+1}}{2\rho_{i+1} S D_h} \quad (12)$$

Similarly, the equation of energy is simplified to:

$$\frac{\partial P_{i+1}}{\partial t} = -\frac{\kappa_K}{\Delta x S}\left(\frac{\dot m_{i+1} p_{i+1}}{\rho_{i+1}} - \frac{\dot m_i p_i}{\rho_i}\right) - (\kappa_K - 1) c_f\frac{\dot m^3_{i+1}}{2\rho^2_{i+1} S^2 D_h} - (\kappa_k - 2)\frac{\dot m}{\rho_k S^2}\left[\frac{1}{2}\frac{\dot m_k}{\rho_k}\frac{1}{\Delta x S}(\dot m_{i+1} - \dot m_i) - \frac{\partial \dot m_{i+1}}{\partial t}\right] \quad (13)$$

Equations (11), (12), and (13) describe the transient process of a compressible flow within a tube with a constant cross section. For an incompressible flow, this system can be reduced to a single differential equation:

$$\frac{\partial \dot m}{\partial t} = \frac{R\dot m^2}{LS}\left(\frac{T_1}{p_1} - \frac{T_n}{p_n}\right) + \frac{S}{L}(p_1 - p_n) - c_f\frac{\dot m^2}{2\rho S D_h} \quad (14)$$

The friction coefficient c_f can be determined from the known steady-state conditions.

8.2 Modeling of Components Pertaining to Category 2. As mentioned earlier, this category encompasses the combustion chamber, the afterburner, and the heat exchanger. A brief description of the combustion chamber as the representative example is given below. A combustor generally consists of a combustion zone, or primary zone, surrounded by n rows of segments, the cooling zone, and the mixing zone, Fig. 3(*a*). The actual process of combustion occurs in the primary zone. The mixing in of cold air flowing through mixing nozzles, arranged radially, reduces the gas temperature in the mixing zone to a level acceptable for the gas turbine that follows. The rows of segments in the combustion zone are subjected to a severe thermal loading due to direct flame radiation. Film and/or convection cooling on both the air and the gas sides cools these segments. The air required to cool these hot segments flows through finned cooling channels, thereby contributing to the convection cooling of the segments on the air side. The cooling air flow exiting from the jth segment row effects the film cooling process on the gas side within the boundary layer in the next row of segments. At the end of that process, the cooling air mass flow should be mixed completely with the primary air mass flow. The mass flow relationships prevailing in the primary, the cooling, and the mixing zones, are substituted into the energy equation, already formulated. Their effect is significant, particularly in the case of the energy balance, because they determine the temperature distribution in the individual combustion chamber stations. For that reason, we first determine mass flow relationships and then deal with the energy balance.

Mass Flow Balance. The combustion chamber mass flow is divided into primary mass flow, secondary (cooling) mass flow, and mixing mass flow:

$$\dot m_P = \mu_P\,\dot m,\quad \dot m_S = \mu_S\,\dot m,\quad \dot m_M = \mu_M\,\dot m \quad (15)$$

If the primary zone consists of n rows of segments, the cooling mass flow for the jth row of segments is:

$$\dot m_{s_j} = \mu_j \dot m_S = \mu_j\,\mu_S\,\dot m \quad (16)$$

If the fuel component $\mu_F = m_F/m$ is also taken into consideration, the mass flow within the jth row of segments is:

$$\dot m_j = \sigma_j \dot m,\ \sigma_j = \mu_F + \mu_P + \mu_S\sum_{\upsilon=1}^{j}\mu_\upsilon \quad (17)$$

To determine the transient behavior of a combustion chamber that has already been designed, it is necessary to start from the given ratios μ_P, μ_S, μ_M, and σ_j. For a new design, it is possible to vary these ratios until the desired solution is attained. The mass flow in the combustion chamber is obtained as the solution to the modified version of Eq. (7):

$$\frac{\partial \dot m}{\partial t} = \frac{R\dot m^2(1+\mu_F)}{\Delta x S}\left[\left(\frac{T}{p}\right)_I - \left(\frac{T}{P}\right)_O\right] + \frac{S}{\Delta x}\left[\frac{P_I - P_o}{1+\mu_F}\right] - c_f\frac{\dot m^2(1+\mu_F)}{2\rho S D_h} \quad (18)$$

The volume of the combustion chamber is replaced here with an equivalent volume, with a constant cross section S and length Δx. The pressures and temperatures in Eq. (18) thus represent inlet and outlet parameters, which must be known at the design point.

Temperature Transients. To determine the temperature transients for the fluid media within individual parts of the combustion chamber, we start from Eq. (8). Considering the air, fuel, and eventually, water as the main combustion components, the rearrangement of Eq. (8) reads:

$$\frac{\partial T^*_{i+1}}{\partial t}=\frac{1}{V\rho_{i+1}c_{p_{i+1}}}\left(\sum_{k=1}^{K}\dot{m}_{ik}[\kappa_{i+1}(c_{p_i}T^*_i)_k-c_{p_{i+1}}T^*_{i+1}]\right)$$
$$+\frac{1}{V\rho_{i+1}c_{p_{i+1}}}((1-\kappa_{i+1})\dot{m}_{i+1}c_{p_{i+1}}T^*_{i+1}-\kappa_{i+1}\dot{Q}_G)$$
$$-\left(\frac{1-\kappa_{i+1}}{c_{p_{i+1}}}\right)\left(\frac{\dot{m}}{\rho^2S^2}\right)_{i+1}\frac{\partial\dot{m}_{i+1}}{\partial t} \quad (19)$$

with $\dot{Q}_G=V\Delta\dot{Q}$. The index i refers to the computation station in question. The mixing components are identified with the sequential index k, the upper summation limit for which, K, represents the number of components involved in a mixing process. The mixing components at the inlet station are the cooling air, the combustion air, and the fuel. For the cooling zone, Eq. (8) yields:

$$\frac{\partial T^*_{i+1}}{\partial t}=\frac{\kappa}{V\rho c_p}(\dot{m}c_p(T^*_i-T^*_{i+1})-\dot{Q}_A)$$
$$+\frac{1-\kappa}{c_p}\left(\frac{\dot{m}}{\rho^2S^2}\right)\frac{\partial\dot{m}}{\partial t} \quad (20)$$

with $\dot{Q}_A=V\Delta\dot{Q}$.

The temperature distribution within the segment material can be determined as follows using the heat conductance equation:

$$\frac{d\overline{T}_w}{\partial t}=\frac{1}{\rho_w c_w v_w}[\dot{Q}_h+\dot{Q}_c] \quad (21)$$

The heat flows $\dot{Q}_G$, $\dot{Q}_A$, $\dot{Q}_h$, and $\dot{Q}_c$, are those supplied to or carried off from the part of the system. For the primary zone surrounded by a row of segments, $\dot{Q}_G$ is made up of the fuel heat, $\dot{Q}_F$, the flame radiation heat, $\dot{Q}_{RF}$, and the convection heat, $\dot{Q}_{CG}$, on the gas (or hot) side. The increased temperature level produced in the segments from the direct flame radiation is reduced to an acceptable level by an intensive film cooling on the gas side and convective heat removal on the air side. The segments are therefore subjected to the following thermal loading on the gas side (or hot side):

$$\dot{Q}_h=\dot{Q}_{RF}+\dot{Q}_{Fi} \quad (22)$$

with $\dot{Q}_{Fi}$ standing for the amount of heat carried off by the film cooling. The heat flow carried off on the air side, $\dot{Q}_c$, consists of a convection and a radiation component. The latter is due to the difference in temperature between the cold air enclosure liner and the warm surface of the fins. As a result:

$$\dot{Q}_c=\dot{Q}_{CA}+\dot{Q}_{Ra} \quad (23)$$

For the film cooling:

$$\dot{Q}_{Fi}=\overline{\alpha}_{Fi}S_G(\overline{T}_{F_i}-\overline{T}_W) \quad (24)$$

in which $\overline{\alpha}_{F_i}$ is the average heat transfer coefficient and $\overline{T}_{Fi}$ the average film temperature, from Schobeiri (1987a, b). The convection heat removal on the air side is obtained from:

$$\dot{Q}_{CA}=\overline{\alpha}_A S_A(\overline{T}_W-\overline{T}_A) \quad (25)$$

The radiation heat flows $\dot{Q}_{RA}$, $\dot{Q}_{RF}$ have been determined from Schobeiri (1987b):

$$\dot{Q}_G=\dot{Q}_F=\dot{Q}_{RF}+\dot{Q}_{CG} \quad (26)$$

8.3 Modeling of Components Pertaining to Category 3. During a dynamic operation, the uncool turbine and compressor blades undergo a heat transfer process between the materials subjected to the flow, e.g., the blading and the fluid medium. A similar process occurs for cooled turbine and compressor blades during steady-state and dynamic operation. In order to take this heat transfer into consideration, the components must be divided into their individual rows or stages. For the turbine component, the row-by-row expansion calculation method by Schobeiri (1992) and Schobeiri and Abouelkheir (1992) is used, where the row efficiency at off-design points is determined for the given turbine blade geometry and the flow angles calculated from row-velocity diagrams. For the compressor component, a row-by-row compression calculation method may be applied. For subsonic and transonic compressors, the off-design efficiencies are calculated from the total loss correlations as a function of the modified diffusion factor. The nonlinear dynamic behavior of these components is described by the conservation laws in conjunction with the known row characteristics. For the special case in which there are no discontinuities, and no changes in the mass flow or mixing processes within the row, Eq. (8) is reduced to:

$$\frac{\partial T^*_{i+1}}{\partial t}=-\frac{k}{\rho Vc_{p_{i+1}}}[\dot{m}_{i+1}c_{p_{i+1}}T^*_{i+1}-\dot{m}_i c_{p_i}T^*_i+\dot{Q}_R+L_R] \quad (27)$$

with $\dot{Q}_R$ and L_R as the row thermal and mechanical energy flow contributions supplied or carried off. The thermal energy flow on the row hot side is simply obtained by the heat transfer balance:

$$\dot{Q}_h=\overline{\alpha}S_G(\overline{T}^*-\overline{T}_W) \quad (28)$$

where $\overline{\alpha}$ is the average heat transfer coefficient, S_G the surface area exposed to the gas with $\overline{T}^*=(T^*_{i+1}+T^*_i)/2$ as the average gas temperature, and $\overline{T}_w$ as the average temperature of the material. The heat transfer coefficient is obtained as a correlation of the Nusselt number, the Reynolds number, and the blade geometry and cooling method (film cooling, blade surface cooling mass flow ejection). The mechanical energy output L_R can be determined from the specific polytropic stage output as comprehensively discussed by Schobeiri (1992) and Schobeiri and Abouelkheir (1992).

8.4 Modeling of Dynamic Behavior of Shafts. The rotational speed of the ith shaft is determined by:

$$\frac{d\omega_i}{dt}=\frac{1}{I_i\omega_i}(P_T-P_c-P_F-P_G)_i \quad (29)$$

where P_T, P_c, P_F and P_G are the power of the turbine, the compressor, bearing friction and the generator pertaining to the shaft number i.

8.5 Modeling of Plenum: Coupling Module. Two successive components are coupled by the coupling module plenum, whose volume is made up of partial volumes of each of the two components. The temperature and pressure transients are obtained from Eqs. (4) and (5), neglecting, however, the contribution of the kinetic energy and time change in mass flow relative to other terms. This yields the following simplified relationships:

$$\frac{\partial H}{\partial t}=-\frac{\kappa}{\rho}\nabla\cdot(\rho\mathbf{V}H)+\frac{H}{\rho}\nabla\cdot(\rho\mathbf{V}) \quad (30)$$

$$\frac{\partial P}{\partial t}=-(k-1)\nabla\cdot(\rho\mathbf{V}H) \quad (31)$$

Coupling of m outlet (index O) and n inlet (index I) components and assuming one-dimensional flow results in the following two equations:

$$\frac{\partial T^*}{\partial t}=\frac{1}{\rho V}\left[\sum_{i=1}^{n}\dot{m}_{I_i}\left(\frac{c_{pI_i}}{c_p}T^*_{I_i}-T^*\right)\right]$$
$$-\frac{1}{\rho V}\left[(\kappa-1)\sum_{j=1}^{m}\dot{m}_{o_j}T^*\right] \quad (32)$$

where the nonindexed variables describe the plenum.

$$\frac{\partial P}{\partial t}=\frac{\kappa R}{V}\left[\sum_{i=1}^{n}\dot{m}_{I_i}\frac{c_{pI_i}}{c_p}T^*_{I_i}-\sum_{j=1}^{m}\dot{m}_{o_j}T^*\right] \quad (33)$$

9 Numerical Treatment

The partial differential equations given above can be reduced to a system of ordinary differential equations by a one-dimensional approximation. The simulation of a complete gas turbine system is accomplished by combining individual components that have been modeled mathematically. The result is a system of ordinary differential equations that can be dealt with numerically. For weak transients, Runge-Kutta or Predictor-Corrector procedures may be used for the solution. When strong transient processes are simulated, the time constants of the differential equation system can differ significantly so that difficulties must be expected with stability and convergence with the integration methods. An implicit method avoids this problem. The system of ordinary differential equations generated in a mathematical simulation can be represented by:

$$\frac{d\mathbf{X}}{dt}=G(\mathbf{X},\,t) \quad (34)$$

with $\mathbf{X}$ as the state vector sought. If the state vector $\mathbf{X}$ is known at the time t, it can be approximated as follows for the time $t+dt$ by the trapezoidal rule:

$$\mathbf{X}_{t+\Delta t}=\mathbf{X}_t+\frac{1}{2}\Delta t(G_{t+\Delta t}+G_t) \quad (35)$$

Because the vector $\mathbf{X}$ and the function G are known at the time t, i.e., $\mathbf{X}_t$ and G_t are known, Eq. (35) can be expressed as:

$$\mathbf{X}_{t+\Delta t}-\mathbf{X}_t-\frac{1}{2}\Delta t(G_{t+\Delta t}+G_t)=F(\mathbf{X}_{t+\Delta t}) \quad (36)$$

As a rule, the function F is nonlinear. It can be used to determine $\mathbf{X}_{t+dt}$ by iteration when $\mathbf{X}_t$ is known. The iteration process is concluded for the time $t+dt$ when the convergence criterion

$$\frac{\mathbf{X}_i^{(k+1)}-\mathbf{X}_i^{(k)}}{\mathbf{X}_i^{(k+1)}}<\epsilon \quad (37)$$

is fulfilled. If the maximum number of iterations, $k=k_{\max}$, is reached without fulfilling the convergence criterion, the time interval Δt is halved, and the process of iteration is repeated until the criterion of convergence is met. This integration process, based on the implicit one-step method described by Liniger and Willoughby (1970), is reliable for the solution of stiff differential equations. The computer time required by GETRAN depends, first, on the number of components in the system and, second, on the nature of the transient processes. If the transients are very strong, the computer time can be 10 times greater than the real time because of the halving of the time interval. For weak transients, this ratio is less than 1.

10 GETRAN Simulation Tests, Cases

To ensure the capability, accuracy, robustness, and reliability of GETRAN, comprehensive critical performance assessment and validation tests were performed. Table 1 shows the matrix of test cases where the engine types, the simulation objectives, and transient types are listed. The simulations served as the code assessment and validation using different engine configurations ranging from single-spool, single-shaft thrust generation engines to three-spool, four-shaft thrust and power generation engines.

Table 1 Matrix of simulation cases

Simulation Cases With GETRAN			
Test Case	**Engine Type**	**Test Objective**	**Transient Type**
1	Thrust generation, single spool, single shaft	Code performance assessment	Variation of exit nozzle area
2	Thrust and power generation single spool, two shafts	Code performance assessment and test	Operation under compressor surge
3	Thrust and power generation core engine, three spool, four shafts	Code performance assessment and test	Operation with control system
4	Power generation gas turbine engine, single spool, single shaft, BBC GT-9.	Code validation and performance test and assessment	Adverse load changes

For the code validation, the geometry of two existing power generation gas turbine engines was employed. For code assessment purposes, different engine configurations were created and distinctive transient events were simulated. The components utilized for the different engine configurations have geometries similar to real ones. Simulation of the transient behavior of several other existing engines for further code validation is currently under planning. This will be performed in cooperation with the NASA Lewis Research Center.

For each engine configuration the simulation provides comprehensive information about the dynamic behavior of each component and its interaction with the other components. This information includes detailed data such as rotational speed, power match/mismatch between turbine and compressor components, and beginning of rotating stall and surge of individual compressor stages. It also contains details about pressure distribution, combustion gas, air, and material temperature distribution as well as mass flow distribution within components such as compressor and turbine blade rows, combustion chamber, afterburner, etc. For each engine component, these data are plotted in a number of plots ranging from 35 for a single-spool engine to 150 for a three-spool core engine. Since the presentation of the complete simulation results of the four cases listed in Table 1 would exceed the frame of this paper, only a few selected plots will be displayed and discussed for each case.

Case 1: Variation of Exit Nozzle Area of a Single Spool Engine. The engine under consideration, shown in Fig. 4, consists mainly of a compressor divided into three stage groups C_1-C_3: low pressure (LPC), intermediate pressure (IPC), and

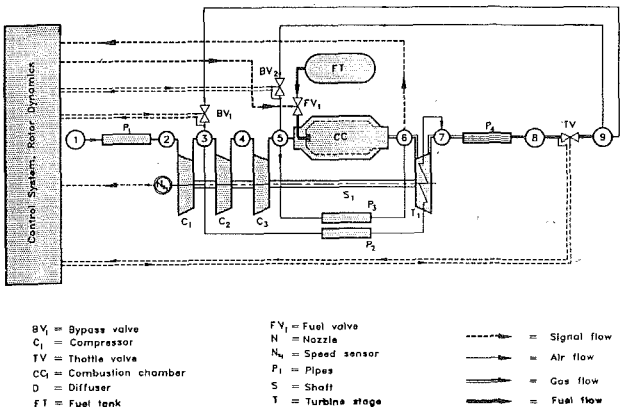

Fig. 4 Simulation schematic for a single-spool, single-shaft engine, case 1

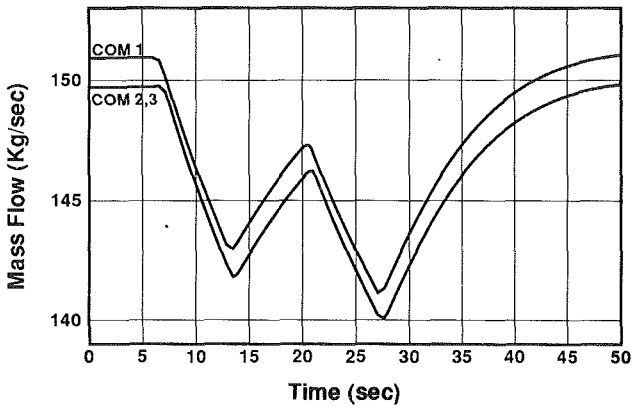

Fig. 6 Compressor mass flows as a function of time, case 1

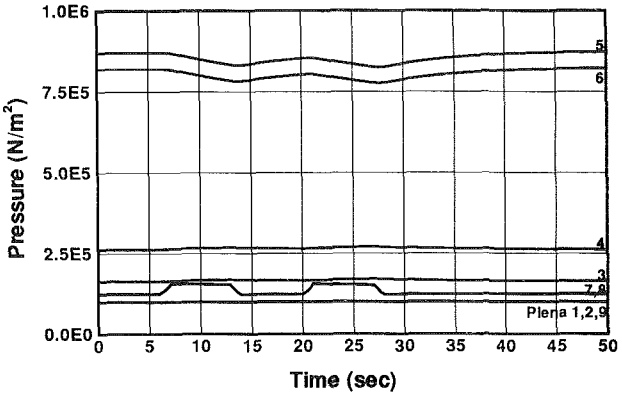

Fig. 5 Plena pressures as a function of time, case 1

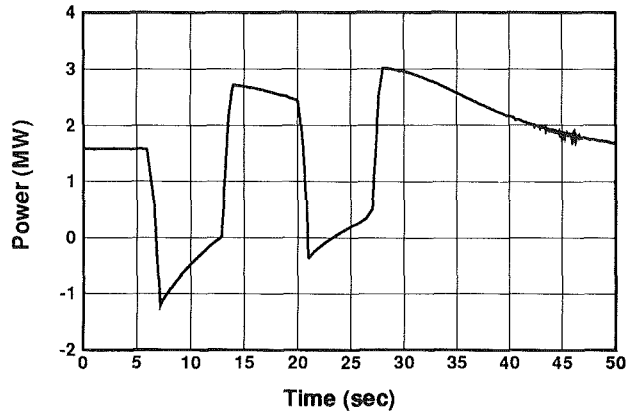

Fig. 7 Gas turbine power output as a function of time, case 1

high pressure (HPC); a combustion chamber (*CC*), a turbine (T_1), a control system (*CS*), which is out of operation for this particular simulation, and the exit nozzle, whose area change is simulated by the throttle (*TR*). The rotor speed and the turbine inlet temperature are the input parameters for the controller; its output parameters are the fuel mass flow and the mass flows of the bypass valves *BV*1 and *BV*2. Elements *P*1 and *P*4 represent the inlet and the exhaust systems. The duct flows from *P*2 and *P*3 are used for sealing air and cooling. This engine was especially designed for the following simulation and test purposes, and does not reflect a particular, existing engine. However, the components utilized for this configuration have geometries similar to real ones.

Starting from a steady-state operating point, the nonlinear dynamic behavior of this engine is simulated for a transient case, where the exit nozzle area changes according to a given ramp with the schedule $\Delta t_{\text{Ramp}} = 1.0$ s, and $t_{\text{Ramp}} = 6.0$ s. During the operation, the fuel mass flow remains constant at the design point value.

Starting from steady operation, the exit nozzle area is reduced to 65 percent. Following the schedule, a reduction in the nozzle exit area would be expected to increase the pressure at the turbine exit, Fig. 5, curve 7. This increase in pressure causes a reduction in the mass flow through the turbine, and consequently through all the other engine components such as the combustor, and the compressor, Fig. 6. The reduction of turbine mass flow, however, results in a decrease of turbine power, as shown in Fig. 7. As a consequence, the rotational speed decreases resulting in a reduction of compressor exit pressure, Fig. 5, curve 5. Since the fuel mass flow was kept constant, the fuel/air ratio has been increased, leading to a temperature increase within the combustor structure, and the

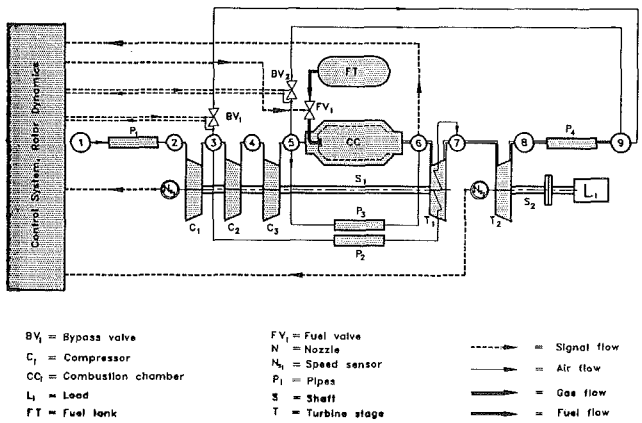

Fig. 8 Simulation schematic for a single-spool, two-shaft engine, case 2

turbine. The result of this transient operation, as expected, is a strong mismatch between the turbine and compressor power, resulting in extreme changes in total power output, Fig. 7, and rotational speed.

After the completion of the transient operation, the exit nozzle is completely opened and the turbine resumes matching the compressor power, and the entire engine approaches the steady-state excess power required to cover the auxiliary devices and the bearing friction.

Case 2: Compressor Rotating Stall and Surge, Single-Spool, Two-Shaft Engine. The purpose of this simulation is to assess the compressor and engine dynamic behavior in a

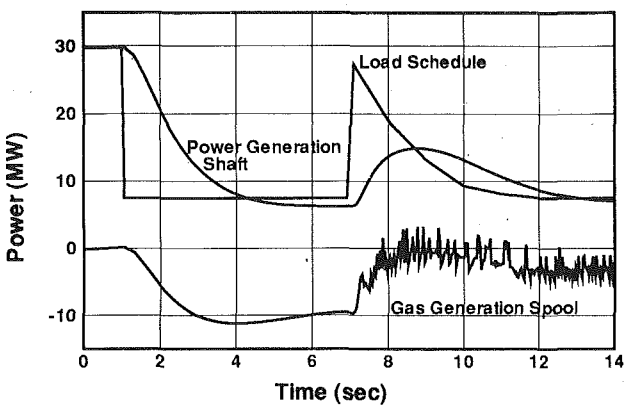

Fig. 9 Gas turbine power output as a function of time, case 2

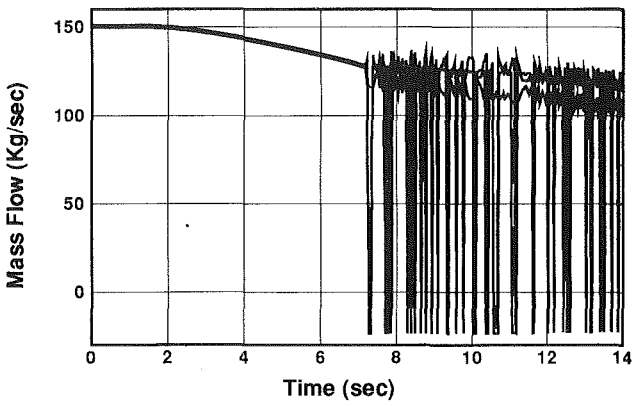

Fig. 12 Compressor mass flows as a function of time, case 2

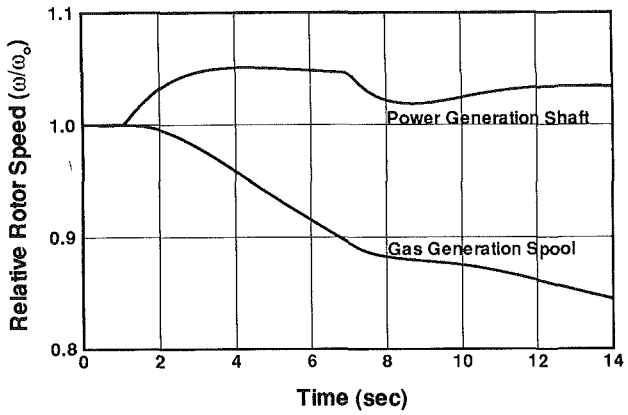

Fig. 10 Relative rotor speed as a function of time, case 2

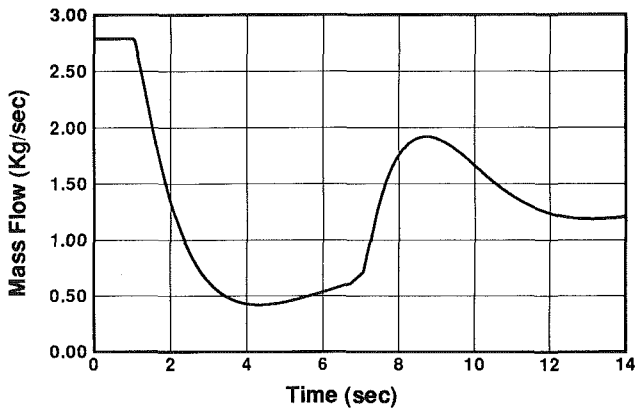

Fig. 11 Fuel mass flow as a function of time, case 2

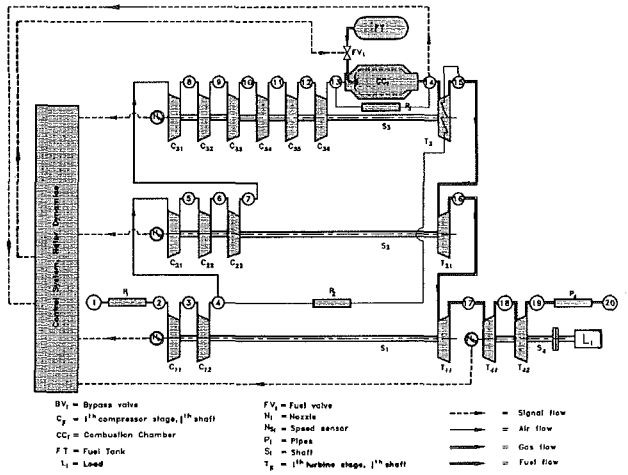

Fig. 13 Simulation schematic for a three-spool, four-shaft engine, case 3

rotating stall and surge environment. The engine configuration consists of a single spool with a single-stage power generation turbine T_2, Fig. 8. To force the compressor component into stall operation, the power shaft is connected with a closed-loop control system. The input parameter for the control system is the rotor speed which is directly determined by the load schedule. Its response is the fuel mass flow.

Starting from a steady-state operating point, the dynamic behavior of this engine is simulated for a transient operation, which is controlled by the prescribed load schedule that acts on the power shaft as shown in Fig. 9. Following this schedule, we first simulate an abrupt loss of load. The power generation shaft reacts to this event with a corresponding increase in rotational speed, Fig. 10. This increase in rotational speed triggers a rapid throttling of the fuel mass flow as shown in Fig. 11. The throttling process lasts until a constant idling speed of the power shaft is attained, Fig. 10. After about seven seconds, load is added suddenly, such that after the completion of load addition, the gas turbine is supplying 25 percent of its rated load, Fig. 9.

At the start, the rotor reacts to this addition of load with a sharp decrease in rotational speed. That, in turn, causes a quick opening of the fuel valve. During this process, the power generation capability of the gas generation turbine deteriorates significantly, causing a major power imbalance between the turbine and compressor components, Fig. 9. This imbalance results in a continuous decrease of the compressor rotor speed, Fig. 10, causing the compressor to operate partially in rotating stall and surge regime. A shown in Fig. 12, reducing the rotor speed below 90 percent forces the first compressor stage group into rotating stall and a short-duration surge process with a reversal in the mass flow direction. Since the magnitude of the reversed mass flow is relatively small and of short duration, a total engine mass flow reversal does not occur.

Case 3: Adverse Transient, Three-Spool, Four-Shaft Engine. After simulation of these single-spool engines with and without power-generating shafts was successfully completed, a decision was made to simulate a more complex engine. For this purpose a three-spool thrust generating engine was designed. To increase the level of engine complexity, a fourth shaft, S_4, with the power generating turbine T_4 was attached to the exit of the three-spool gas generating unit as shown in

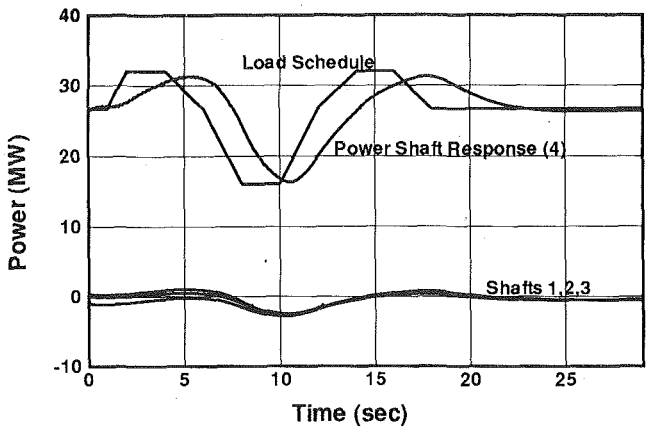

Fig. 14 Gas turbine power output as a function of time, case 3

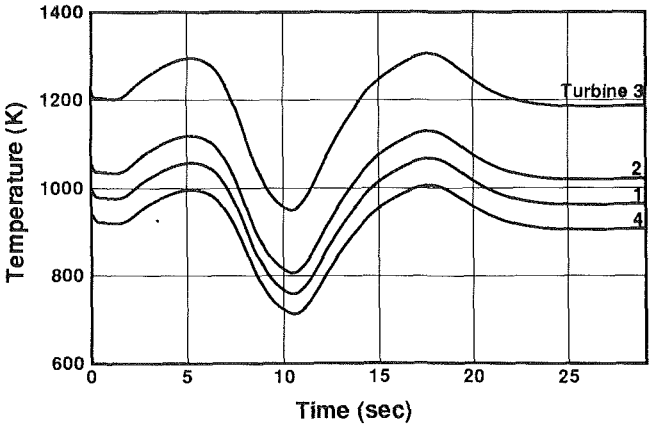

Fig. 16 Turbine inlet temperatures as a function of time, case 3

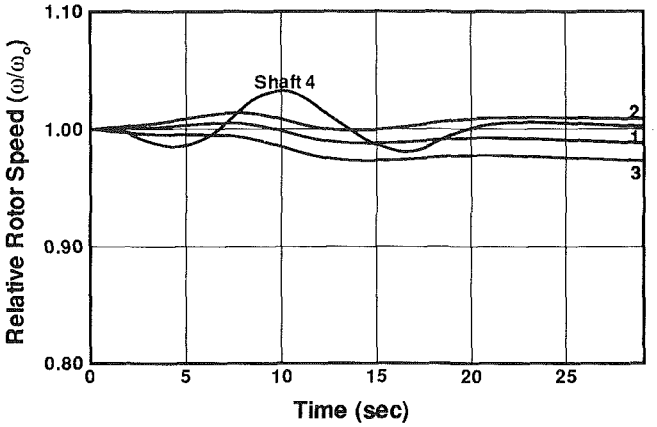

Fig. 15 Relative rotor speed as a function of time, case 3

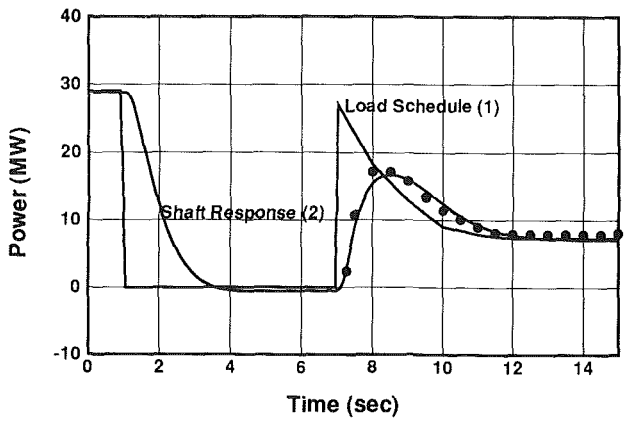

Fig. 17 Gas turbine power output as a function of time, case 4

Fig. 13. The power load L_4 acting on the shaft S_4 is controlled by a given load schedule. The component nomenclature for this configuration is the same as for the previous cases.

Starting from a steady-state operating point, the dynamic behavior of this engine is simulated for a transient operation that is controlled by the load schedule shown in Fig. 14. Following the load schedule, we first simulate a continuous load addition. The power generation rotor, Fig. 15, curve 4, reacts to this event with a corresponding decrease in rotational speed that triggers the opening of the fuel valve and results in increasing the fuel mass flow above the design point. This event triggers an increase in temperature and pressure in different plena. As a consequence of this fuel addition, the inlet temperatures of the four turbines are increased significantly above the design point, Fig. 16, augmenting the power of all turbines, and increasing the compressor mass flow of the gas-generating spool. Following the load schedule further, the subsequent reduction and addition of load causes strong changes in temperature, pressure, and mass flow in all components. The transient operation is completed when the load schedule approaches the generator design point of 29 MW, Fig. 14. As shown in Fig. 15, steady rotational speed is reached after approximately 25 seconds of transient operation. While the rotational speeds of the power shaft S_4 and the second spool S_2 approach their design speed of 100 percent, the rotational speeds of the first and third spools S_1 and S_3 exhibit a deviation. This deviation reflects the slight inconsistency of the input data for this configuration. This inconsistency is considered by GETRAN to be a transient event.

Case 4: Validation, Adverse Transient, Single-Spool, Single-Shaft Power Generation. The purpose of this simulation is to validate the generic and versatile simulation capability of GETRAN by performing an adverse transient operation and comparing the calculation results with experimental measurements. For this purpose the BBC-GT 9 gas turbine is simulated, whose dynamic behavior was experimentally determined for a transient test with extreme load changes. The engine and its transient data were accurately documented by Schobeiri (1986, 1987). Starting from a given network load schedule, the dynamic behavior of the gas turbine is predicted and the results compared with experimental measurements.

The engine under consideration consists mainly of three compressor stage groups, a combustion chamber, a turbine, a control system, and a generator. The simulation schematic of this engine is similar to that of Fig. 4, where a power generation turbine and a generator are added in place of the nozzle. The rotor speed and the turbine inlet temperature are the input parameters for the controller; its output parameters are the fuel mass flow (fuel valve opening), and the mass flows of the bypass valves (bypass valve opening).

Starting from steady state, in accordance with the load schedule indicated in Fig. 17, curve 1, first a generator loss of load is simulated. The rotor at first reacts with a corresponding increase in rotational speed, Fig. 18, which results in a rapid opening of the fuel value. The rotational speed is then brought to an idling point and held approximately constant. The process of control intervention lasts until a constant idling speed is attained. After that, there is an addition of load in sudden increases, such that the gas turbine is supplying approximately 25 percent of its rated load, Fig. 17. The rotor first reacts to this addition of load with a sharp decrease in rotational speed, as demonstrated by Fig. 18, causing a quick opening of the

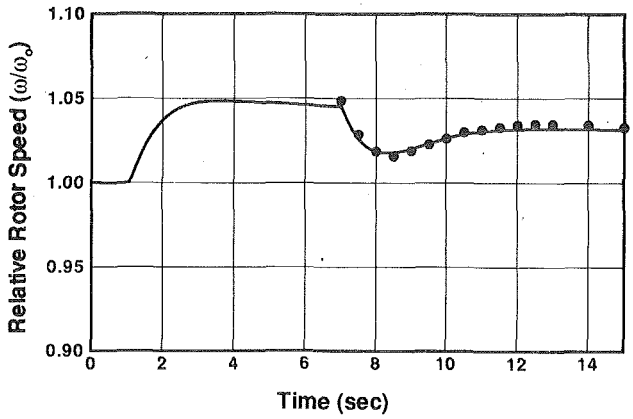

Fig. 18 Relative rotor speed as a function of time, case 4

valve. After completion of the transient process, the steady off-design state is reached.

Comparison Between Measurements and Calculations. The results of this computation were compared with the results of the experiments documented by Schobeiri (1986, 1987). Although the measurements of pressure, and particularly those of temperature, are subject to a certain amount of inaccuracy, the power output can be measured directly, without any major error. This is shown clearly in Fig. 17, in the prescribed load schedule, curve 1, and in the measured gas turbine output, curve 2, where a close agreement can be seen between the experimental measurements and the computation. This is also true of the rotational speed, Fig. 18.

11 Conclusion

The design concept and the theoretical background essential for the development of modularly structured simulation code, GETRAN, were presented. To ensure the capability, accuracy, robustness, and reliability of GETRAN, four critical performance assessment and validation tests were performed by simulating adverse transients for single-spool single-shaft, single-spool two-shaft, and three-spool four-shaft thrust generation, power generation, and thrust/power generation engines. For the code validation, the geometries of an existing single-spool power generation gas turbine engines were employed. For code assessment purposes, different engine configurations were created and distinctive transient events were simulated. The computational results have shown that GETRAN is capable of simulating complex engine configurations regardless of the type of the engine, number of components, spools, or shafts. Adverse transients were simulated, and the high degree of agreement between these results and the experimental data is the first indication of the high prediction accuracy of GETRAN. For exhaustive validation and assessment purposes, a comprehensive engine simulation program is planned in cooperation with NASA Lewis Research Center.

Acknowledgments

The principal investigator and his assistants would like to express their sincere thanks and appreciations to Mr. Carl Lorenzo, Chief Systems Dynamics Branch and Dr. Dan Paxson and the administration of the NASA Lewis Research Center for their continuous cooperation and support of this project.

References

Agrawal, R. K., and Yunis, M., 1982, "A Generalized Mathematical Model to Estimate Gas Turbine Starting Characteristics," ASME JOURNAL OF ENGINEERING FOR POWER, Vol. 104, pp. 194–201.

Fawke, A. J., Saravanamutto, H. I. H., and, Holmes, M., 1972, "Experimental Verification of a Digital Computer Simulation Method for Predicting Gas Turbine Dynamic Behavior," *The Institution of Mechanical Engineers—Combustion Engines Group*, Vol. 186, pp. 32.

Koenig, R. W., and Fishbach, L. H., 1972, "GENENG—A Program for Calculating Design and Off-Design Performance for Turbojet and Turbofan Engines," NASA TN D-6552.

Liniger, W., and Willoughby, R., 1970, "Efficient Integration Methods for Stiff Systems of Ordinary Differential Equations," *SIAM Numerical Analysis*, Vol. 7, No. 1.

Schobeiri, T., 1985a, "Aero-thermodynamics of Unsteady Flows in Gas Turbine Systems," Brown Boveri Company, Gas Turbine Division, Baden, Switzerland, Paper No. BBC-TCG-51.

Schobeiri, T., 1985b, "COTRAN, the Computer Code for Simulation of Unsteady Behavior of Gas Turbines," Brown Boveri Company, Gas Turbine Division Baden Switzerland, Paper No. BBC-TCG-53.

Schobeiri, T., 1985c, "Digital Computer Simulation of the Dynamic Response of Gas Turbines," *VDI Annual Journal of Turbomachinery*, pp. 381–400.

Schobeiri, H., and Haselbacher, H., 1985, "Transient Analysis of Gas Turbine Power Plants Using the Huntorf Compressed Air Storage Plant as an Example," ASME Paper No. 85-GT-197.

Schobeiri, T., 1986, "A General Computational Method for Simulation and Prediction of Transient Behavior of Gas Turbines," ASME Paper No. 86-GT-180.

Schobeiri, T., 1987a, "Digital Computer Simulation of the Dynamic Operating Behavior of Gas Turbines," *Journal Brown Boveri Review*, Vol. 3–87.

Schobeiri, T., 1987b, "Ein einfaches Näherungsverfahren zur Berechnung des Betriebs-verhaltens von Turbinen," *VDI-Forsch. Ing.-Wes*, Vol. 53, No. 1.

Schobeiri, T., 1990a, "Thermo-fluid Dynamic Design Study of Single and Double Inflow Radial and Single-Stage Axial Stream Turbines for Open-Cycle Ocean Thermal Energy Conversion, Net Power Producing Experiment Facility," ASME *Journal of Energy Resources Technology*, Vol. 112, pp. 41–50.

Schobeiri, T., 1990b, "Advanced Code Architecture for the Simulation of Multi-Spool Core Engines," NASA Lewis Research Center.

Schobeiri, T., 1991, "Turbine Component Development for the Integration Into GETRAN," NASA Contract Report NAG-1144.

Schobeiri, T., and Abouelkheir, M., 1992, "Row-by-Row Off-Design Performance Calculation Method for Turbines," *AIAA Journal of Propulsion and Power*, Vol. 8, No. 4, pp. 823–828.

Schobeiri, T., 1992, "One-Dimensional Method for Accurate Prediction of Off-Design Performance Behavior of Axial Turbines," ASME Paper No. 92-GT-54.

Seldner, K., Mihailowe, J. R., and Blaha, R. J., 1972, "Generalized Simulation Technique for Turbojet Engine Systems Analysis," NASA TN D-6610.

Seller, J., and Daniele, C. J., 1975, "DYGEN—A Program for Calculating Steady-State and Transient Performance of Turbojet and Turbofan Engines," NASA TND-7901.

Szuch, J. R., 1974, "HYDES—A Generalized Hybrid Computer Program for Studying Turbojet or Turbofan Engine Dynamics," NASA TM X-3014.

William R. Hawthorne
Gas Turbine Laboratory,
Massachusetts Institute of Technology,
Cambridge, MA 02139

Reflections on United Kingdom Aircraft Gas Turbine History

Robert Thomas Sawyer (1901–1986), Fig. 1, after graduating from the Electrical Engineering Department at Ohio State University, joined the General Electric Company, where he worked on the first successful Diesel Locomotive in the U.S., which went into service in 1927. That summer he built an automobile with electric transmission, which he took with him to Australia, where he sold 10 G.E. Electro-Motive railcars, each with a gasoline engine, generator, and two motors. On his way home in 1929, he visited Dr. Buchi in Switzerland and saw his first gas turbine in Berlin. He then joined the American Locomotive Company, where, from 1930 to 1956, his growing responsibilities included Diesel and Gas Turbines, their applications to locomotives, and nuclear power plants.

He was a member and Fellow of many professional societies. In the ASME, on joining the Executive Committee of its Oil and Power Division, he formed and became Chairman of the Division's Gas Turbine Coordinating Committee, which by 1947 had attracted 250 members. It was then decided to set up the Gas Turbine Division and to make him Chairman of its Executive Committee. He played a major role in the Division's activities. He was Exhibit Director from its first Conference in 1955 until 1972 when he became the first recipient of the Award that honors his name and work.

R. Tom Sawyer was the author of many papers and books, one of which, *The Modern Gas Turbine*, was published in 1945. It contains a well-informed historical account of many gas turbines and turbochargers and their applications to date.

On November 7th, 1945, he presented a paper to the Mohawk-Hudson group of the S.A.E. [15] on "The Diesel and the Gas Turbine." In its introductory paragraph he writes:

> "I have frequently been asked the question, 'Will the gas turbine supersede the Diesel engine?' My answer to that is that the wrong word has been used. The gas turbine will 'supplement' the Diesel engine. The two will go hand in hand. The gas turbine is here to stay and because the gas turbine is here, it means that the Diesel engine will have a greater future than it ever had without the gas turbine."

As time went on he became such an enthusiastic proponent of the gas turbine that he became known as "Mr. Gas Turbine." He was always looking ahead. Amongst the last of his many published works was a paper entitled "The Open Cycle Gas Turbine; The Most Efficient Turbine Burning Any Fuel." In it he highlighted the Combined Cycle and the helium-cooled nuclear reactor.

Fig. 1 Robert Thomas Sawyer (1901–1986)

To do justice in this lecture to the Award and the man it memorializes is quite a task. I propose to use an historical account of the early development of the gas turbine and turbojet in Britain as a background for my reflections on how understanding the past may help us to cope with the future.

The history of the aircraft gas turbine in Britain starts in 1926, when Tom Sawyer was just beginning his career. There are two strands to the history. One strand belongs to Frank Whittle [1], the inventor of the turbojet engine; the other, less well known, was started by Alan Arnold Griffith [2], Fig. 2, of the Royal Aircraft Establishment (RAE). Both strands led to prototype turbojet engines, Fig. 3. The Whittle engine with a centrifugal compressor was first flown in May 1941 and the RAE engine, built by Metropolitan-Vickers Ltd. with an axial compressor, flew first in November 1943.

Contributed by the International Gas Turbine Institute and presented at the 37th International Gas Turbine and Aeroengine Congress and Exposition, Cologne, Germany, June 1–4, 1992. Manuscript received by the International Gas Turbine Institute April 27, 1993. Associate Technical Editor: L. S. Langston.

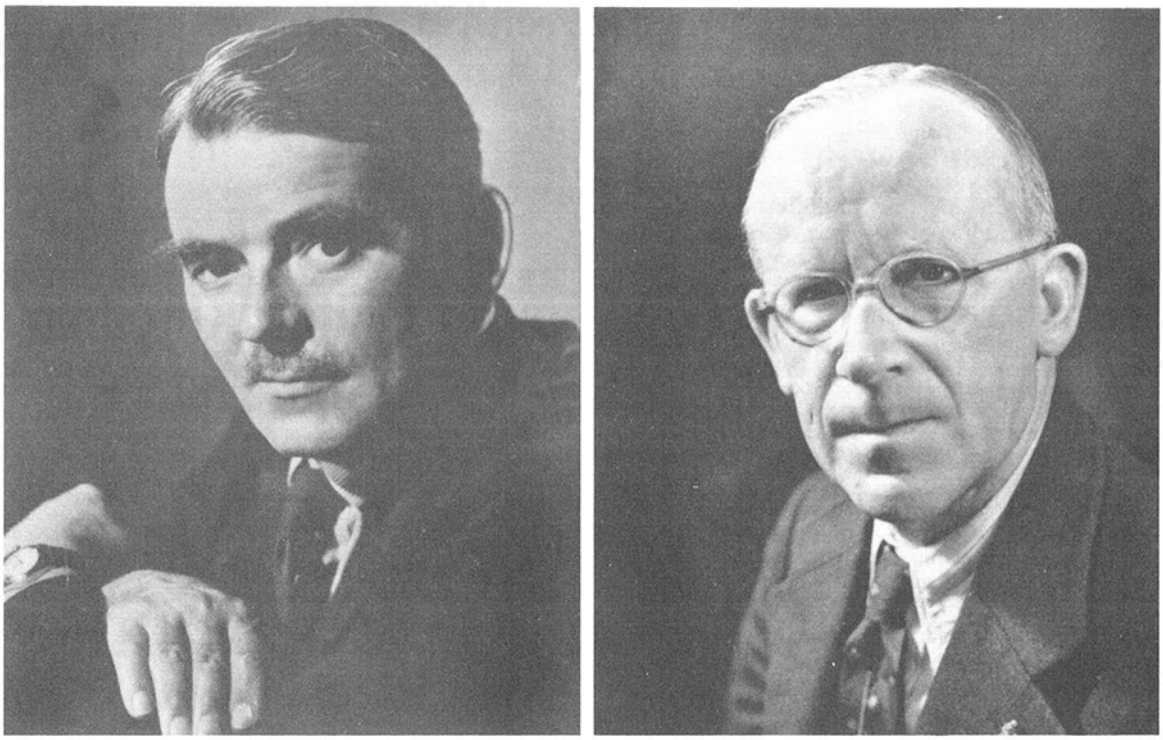

Fig. 2 Sir Frank Whittle and Alan Arnold Griffith (reprinted with permission from Godfrey Argent Studio and *Biographical Memoirs of the Royal Society*, Vol. 10, 1964)

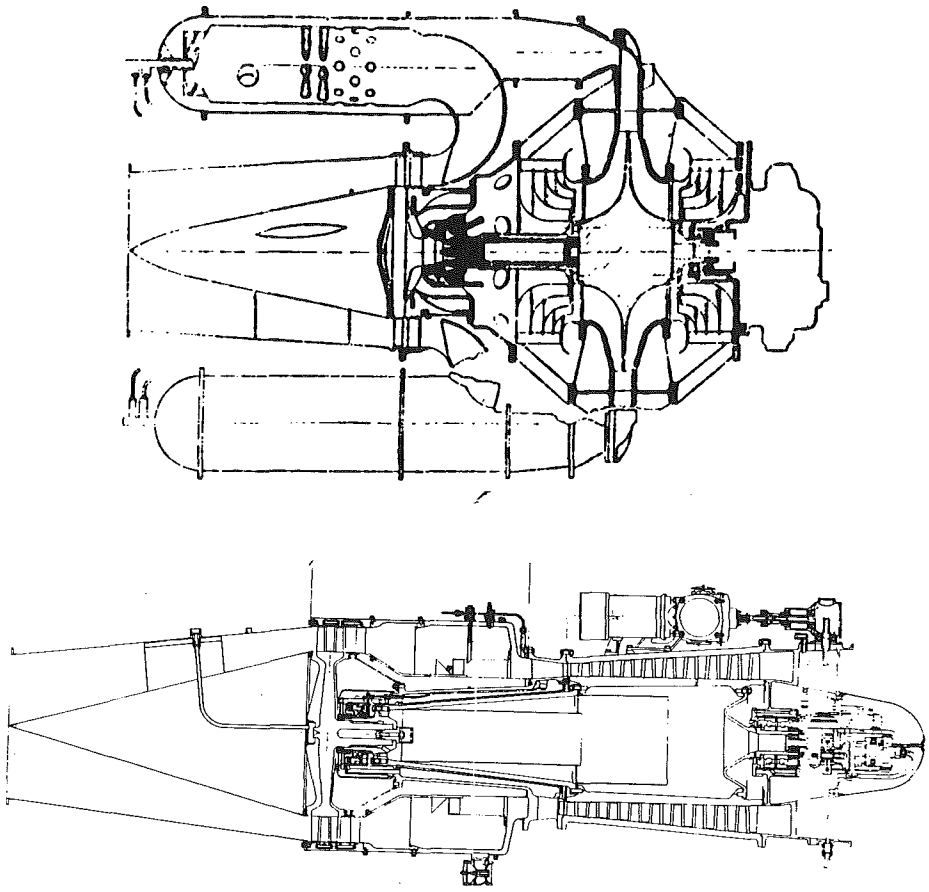

Fig. 3 Prototype turbojet engines: power jets W1 and Royal Aircraft Establishment Metropolitan Vickers F2 ([14], reprinted with permission of *Proc. IMechE*)

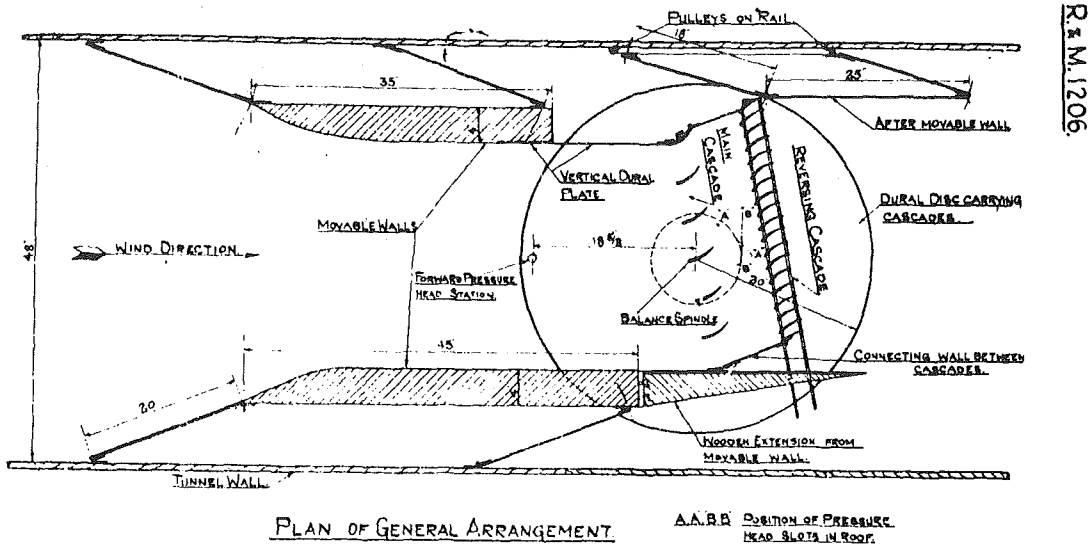

Fig. 4 RAE cascade wind tunnel, 1928 ([4], reprinted with permission of ARM and RAE)

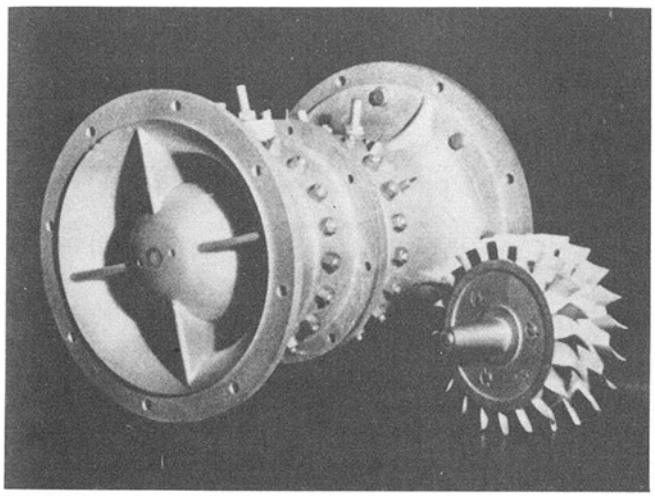

Fig. 5 Griffith's model rotor (reprinted with permission of RAE Crown Copyright)

In 1926 in a report entitled "An Aerodynamic Theory of Turbine Design" [3], Griffith proposed the use of a gas turbine as an aircraft power plant. It was agreed by the Air Ministry that a cascade wind tunnel for experiments on compressor blade profiles should be built, Fig. 4. Results were reported in September 1928 [4]. A model rotor consisting of a row of compressor blades followed by a row of turbine blades of 10 cm tip diameter was also built and tested by sucking air through the blading, Fig. 5. A maximum compression efficiency of 90 percent was obtained [5] and an efficiency of 88.3 percent was obtained at a pressure ratio of 1.16. The design was based on the theories of aerofoils in cascade presented in Griffith's report [6] and data from the cascade tunnel. The model is now in the Science Museum in London.

In a second report entitled "The Present Position of the Internal Combustion Turbine as a Power Plant for Aircraft" in November 1929, Griffith argued the case for the gas turbine. This was not the first time a report had been written on the subject. In September 1920, W. J. Stern [7] had written a report on "The Internal Combustion Turbine" concluding that, with a specific weight of 10 lb/hp, and a specific fuel consumption of 1.5 lb/hp-hr, the turbine was far inferior to the internal combustion engine. But Stern had assumed that cast iron and bronze would be used in the combustion chamber and turbine respectively. Griffith's report came to a very different conclusion:

> "The turbine is superior to existing service engines and to projected compression ignition engines in every respect examined. Efficiency is higher and the weight and bulk less. No external cooling is required. At high altitudes, there is an inherent supercharging effect, coupled with a substantial decrease in the specific consumption. The use of a variable pitch airscrew is unnecessary. Starting presents no difficulty and control is simpler than in the case of existing engines. Any liquid fuel of suitable chemical composition may be used, without reference to anti-knock value or volatility."

One of the features of the report was the discussion of the problem of stalling in the multistage axial compressor of a gas turbine. Griffith calculated that at starting and low rpm the velocity in the front stages of the compressor would be so low that they would stall. If it did occur to him that the compressor might run satisfactorily with several stages stalled, with the rear stages pulling the front stages through stall, he found it difficult to believe. He proposed to avoid the difficulty by mechanical subdivision of the compressor or compounding, as in a two or three-spool engine. But he carried it to extremes and patented the "contraflow" gas turbine, which consisted of rotating disks each carrying a row of turbine blades mounted above a row of compressor blades, Fig. 6. The disks with their blades were mounted in a common casing, so that each could rotate freely and independently of the others in its own bearings. During discussion of his paper with the authorities, Griffith suggested the use of blow-off for unstalling multistage axial compressors and the use of Stellite as a turbine blade material. He also described some combustion experiments, and the laws for dynamic similarity of flames were suggested. The existence of two different types of flow having different aerodynamic efficiencies at the same rotational speed was reported during the discussion of the 10-cm-dia model compressor and turbine tests. One of the types of flow was set up by increasing the suction and hence the speed from a sufficiently low value and the other by coming down from a sufficiently high value.

After some discussion, the Air Ministry decided not to invest any significant effort in the gas turbine. Although Griffith became Head of the Engine Department at RAE in 1931, he did little himself on the gas turbine until he went to Rolls

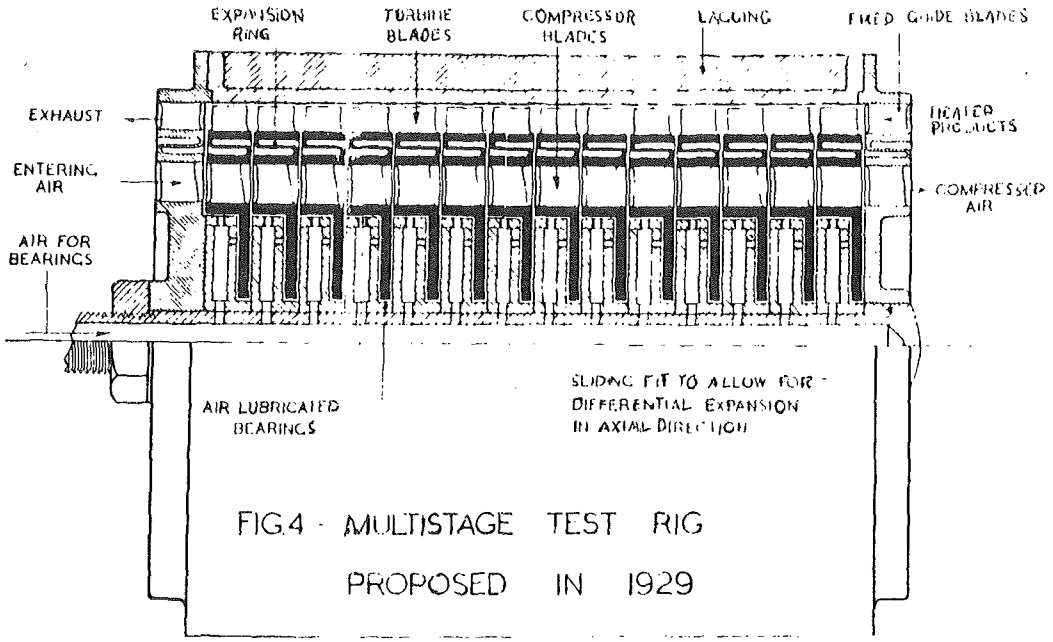

Fig. 6 Drawing of Griffith's contraflow contrarotating gas turbine (reprinted with permission of RAE Crown Copyright)

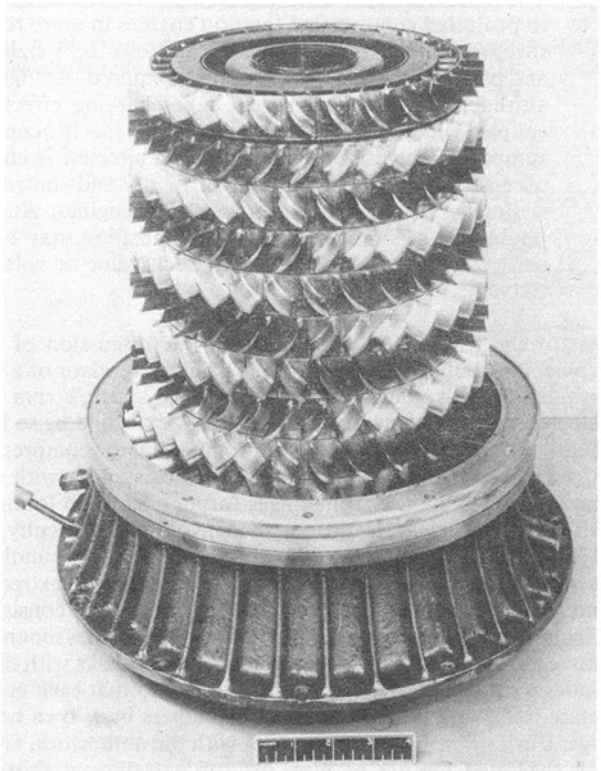

Fig. 7 RAE contraflow gas turbine tested in 1940 (reprinted with permission of RAE Crown Copyright)

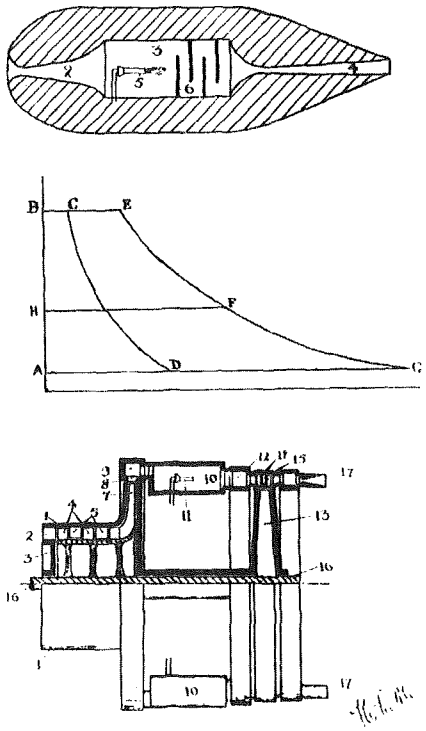

Fig. 8 Drawings from Whittle's patent application, 1930 ([14], reprinted with permission of *Proc. IMechE*)

Royce in 1939. So this strand of the British work on the gas turbine for aircraft was discontinued for nearly six years.

Griffith's contraflow scheme was eventually designed by the RAE in 1938, built by Armstrong Siddeley in 1939 and tested at RAE in 1940, Fig. 7. It has nine independent contrarotating disks, each carrying a row of turbine and compressor blades. Leakage between the disks was a severe handicap and the performance was made worse by the insufficient data on which the blade design had been based. A further extensive experimental program was conducted by Rolls Royce. However, the need for such perfect methods for overcoming stalling eventually disappeared, and the contraflow's other disadvantages led to its abandonment.

The other strand of the British story can also be traced to 1926 when a young Royal Air Force apprentice won a cadetship at the RAF College at Cranwell. Frank Whittle was 19 when he entered the College and he did very well both in flying and in his class work. In 1928 he wrote a thesis on "The Future Developments in Aircraft Design," in which he described aircraft flying at high speed in the stratosphere and the possi-

bilities of rocket propulsion and of gas turbines driving propellers. Between September and December 1929, he had the idea of the turbojet, a gas turbine producing a propelling jet instead of driving a propeller, and he filed a provisional specification on 16 January 1930, thus becoming the recorded inventor of the turbojet engine, Fig. 8.

At about this time, Whittle had described his ideas to the Air Ministry and met Griffith. Whittle's biographer [8] records his disappointment at Griffith's negative attitude and his dismissal of the turbojet in favor of the turboprop, which had been the target for the RAE work. Whittle recorded the Air Ministry response:

> "In due course, I received a letter from the Air Ministry to the effect that the scheme I proposed was a form of gas turbine, and that as such its successful development was considered to be impracticable, because materials did not then exist which were capable of withstanding the combination of high stresses and high temperatures which would be necessary if a gas turbine were to have an acceptable efficiency. In fairness to the Air Ministry, I should add that I think that what they said was true. Nevertheless I feel that they should have foreseen the possibility of big improvements in materials and kept the proposal 'on ice' for a later period. I agree that at the end of 1929 it was before its time, but only by a few years."

Fig. 9 Hayne Constant (1904–1968) (reprinted with permission from *Biographical Memoirs of the Royal Society*, Vol. 19, 1973 and Godfrey Argent Studio)

Although both initiatives on gas turbines failed by 1930, fortunately this was not the end. Whittle, while pursuing his career as a flying officer, practicing aerobatics, and spending a year or so as a catapult test pilot, spent many hours working on his turbojet proposal. He visited several firms and individuals in a vain attempt to interest them. There was no secrecy enforced at that time.

At the RAE, work on related components such as centrifugal compressors driven by exhaust turbines (turbochargers) continued between 1930 and 1936 [9], but of greatest importance, perhaps, was the recruitment in 1928 of a young engineer from the University of Cambridge, Hayne Constant [10], Fig. 9, who was influenced by Griffith and his ideas. After six years at the RAE, Constant joined the teaching staff at Imperial College in 1934, but rejoined the RAE two years later.

Meanwhile, Whittle was sent to the University of Cambridge in October 1934 to do Engineering. He took a First Class degree in 1936. But in January 1935 his 1930 turbojet patent came due for renewal at a fee of five pounds. Reminding him of this, the Air Ministry said that there was no intention of paying for it out of government funds. Whittle noted:

> "By then I had virtually given up hope of ever seeing the engine take practical shape. I had become convinced that it was 'before its time.' I also had a fuller

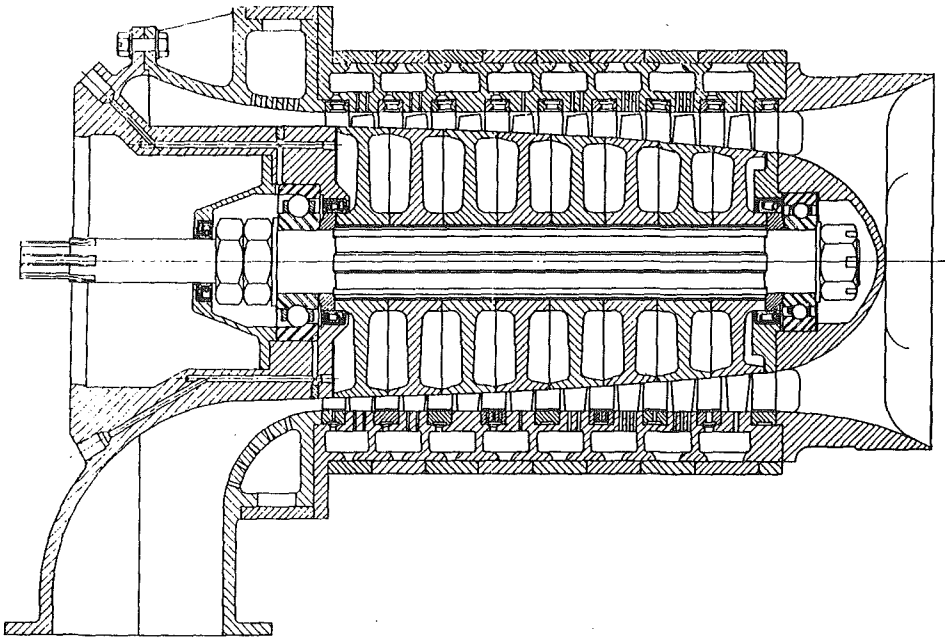

Fig. 10 Drawing of supercharger Anne, first RAE axial compressor with adjustable blow-off on each stage and diffuser bleed (reprinted with permission of RAE Crown Copyright)

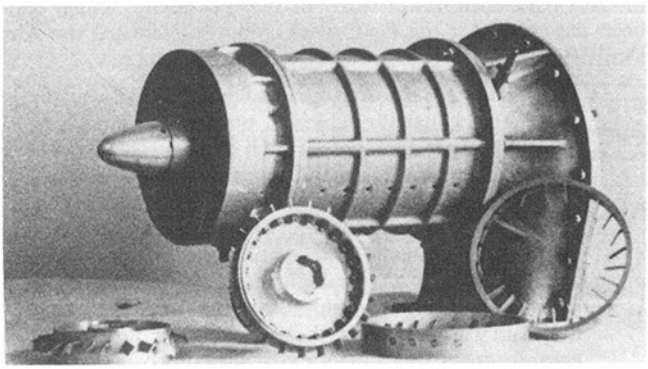

Fig. 11 Reconstructed supercharger Anne without blow-off valves: maximum pressure ratio 2.5, efficiency 80 percent at 1 kg/s mass flow (reprinted with permission of RAE Crown Copyright)

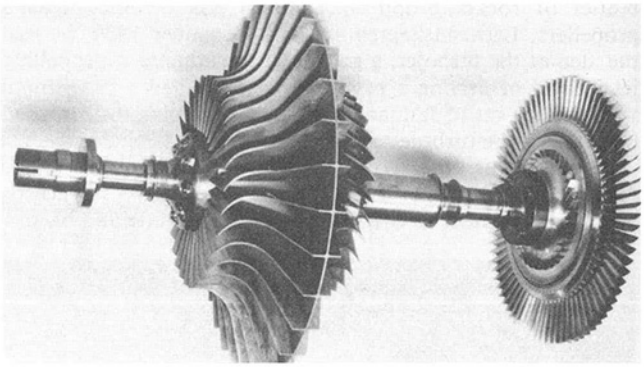

Fig. 12 Whittle's rotor assembly consisting of a double-sided centrifugal compressor and single-stage axial flow turbine ([14], reprinted with permission of *Proc. IMechE*)

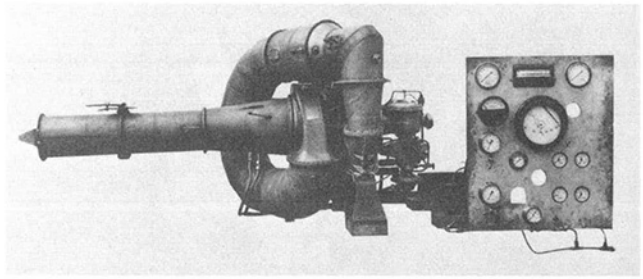

Fig. 13 First assembly of Whittle's experimental turbojet engine ([14], reprinted with permission of *Proc. IMechE*)

> realisation of the cost of the effort which would be required for its development... Moreover, I could ill afford five pounds... I therefore... allowed the patent to lapse."

But in May 1935 a contemporary of Whittle's in the RAF, then retired, and another ex-RAF Officer persuaded him to start trying to develop his engine again. He applied for three more patents, and a company, Power Jets, was formed in March 1936 with sufficient funds to start on development. The detailing of the first design of engine began in April 1936 at the British Thomson Houston Company, Rugby (BTH). After graduating in 1936, Whittle was allowed by the Air Ministry to spend another year at Cambridge working on his turbojet.

Hayne Constant rejoined the RAE in July 1936 and was made head of the Supercharger Division under Griffith, who was still Head of the Engine Department. He immediately obtained authority to design and build an axial flow supercharger. This, the first axial flow compressor to be designed at RAE, had eight stages of free vortex blading. It was originally built with adjustable blow-off on each stage and on the delivery diffuser, Fig. 10. The stage blow-off was to avoid stalling during starting and the diffuser bleed was for boundary layer control. The unit was completed in 1939, but it stripped its blading 30 seconds after starting owing to a faulty design of oil seal, which caused one of the disks to overheat. The compressor was reconstructed, Fig. 11, without blow-off and with larger clearances between the blade rows. The blading used was based on the profiles tested in 1928. A maximum pressure ratio of about 2.5 was obtained at a mass flow of about 1 kg/s. The maximum efficiency was just over 80 percent.

In the spring of 1937 momentous decisions were made. Whittle's engine, which was being manufactured, and a report by Constant [11] were discussed by the authorities. Constant wrote:

> "Possible developments in materials and air compressor design, foreshadowed by recent research, suggest the possibility of constructing in the near future an internal combustion turbine with specific weight which would be less than that of any internal combustion engine at present in production under all conditions of flight and with a specific fuel consumption which would be less than that of any compression ignition engine, under all conditions of flight."

It is of interest that Griffith, reporting on the Whittle engine said:

> "In its present form the proposed jet propulsion system cannot compete with a conventional power plant in any case where economical flight is demanded (e.g., the transport of the maximum percentage of useful load over given distance). It is of value only for special purposes such as the attainment of high speed or high altitude for a short time in cases where take-off requirements are not stringent."

Whittle's biographer has made much of the differences between Griffith and Whittle, but Griffith was genuinely concerned about the take-off thrust of the turbojet. Most airfields were grass and, as the early taxiing trials on the first jet aircraft showed, jet aircraft did have problems when operating without hard runways. Griffith's arguments on fuel consumption also have not lost their force. High bypass ratio fans are now used in the civil air fleet and experiments with propellers are under way. Most pure jets now use afterburners for take off.

As a result of these discussions the Air Ministry decided to start work on the gas turbine at the RAE—who would use turbine manufacturers as subcontractors—and to support the Whittle project. Accordingly RAE and Metropolitan Vickers Ltd forged ahead designing gas turbines with axial compressors for propeller drive. Constant [12] organized a program of research on axial compressors, which included high and low-speed cascade tunnels and nine different compressors.

Looking back it seems strange that the choice of engine layout was a stumbling block. In Whittle's case it was partly related to the difficulties with combustion that dominated the first three and a half years of development.

In order to keep the critical whirling speed of the shaft higher than the maximum speed the rotor of Whittle's engine was almost as short, Fig. 12, as that of a turbocharger, so that in the first build, Fig. 13, the combustion chamber was wrapped around the engine. In the second build, Fig. 14, to improve compressor efficiency, ten diffuser channels were used, delivering into ten curved pipes connected to the front of a long cylindrical casing, concentric with but aft of the turbine. The casing contained a liner in which the flame was located, flame

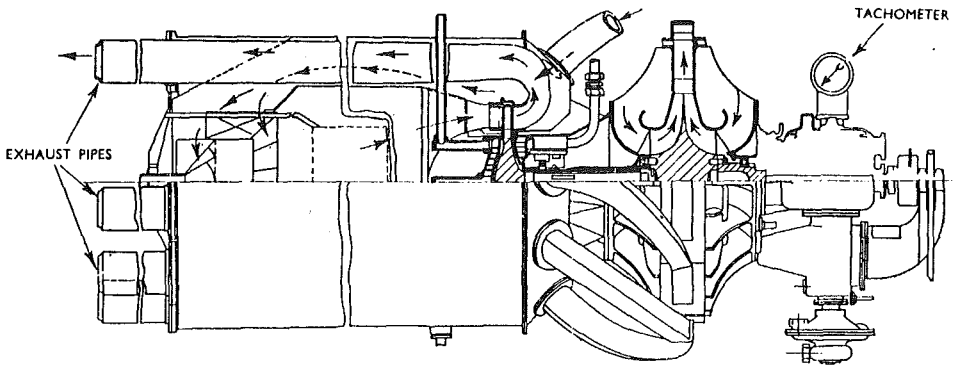

Fig. 14 Second assembly of Whittle's experimental turbojet engine ([14], reprinted with permission of *Proc. IMechE*)

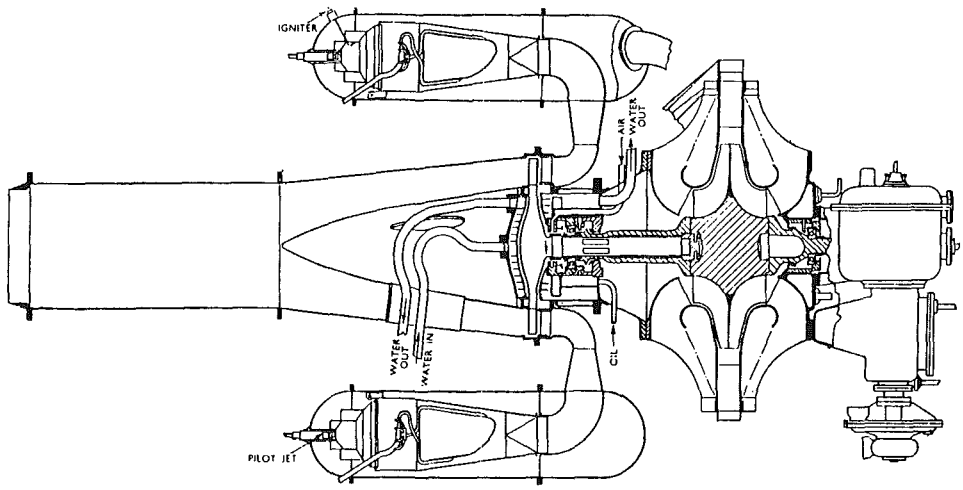

Fig. 15 Third assembly of Whittle's experimental turbojet engine ([14], reprinted with permission of *Proc. IMechE*)

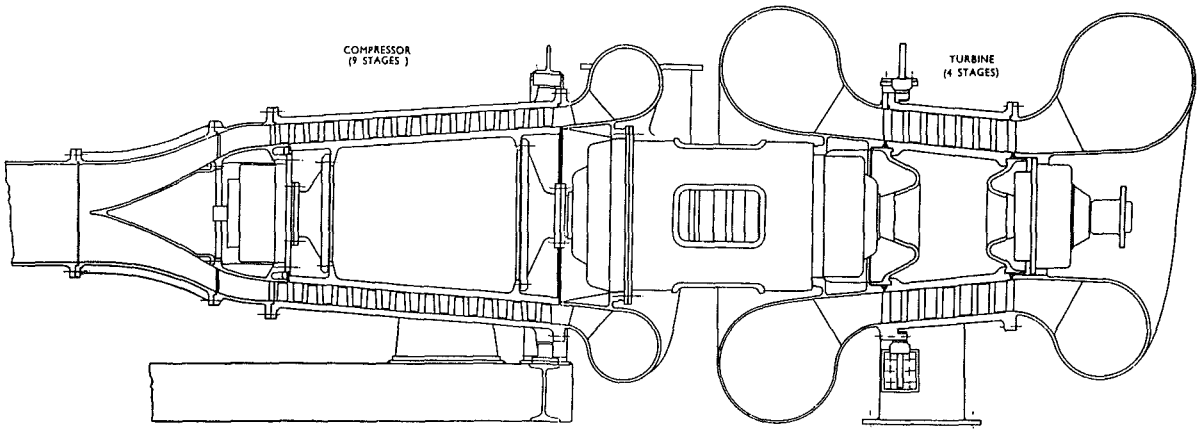

Fig. 16 RAE gas generator B10 with nine-stage axial compressor Betty and five-stage turbine ([16], reprinted with permission of *Proc. IMechE*)

and hot gas passing forward into a turbine nozzle ring and turbine rotor, after which it was split into ten, turned outward through 180 deg and passed aft through ten jet pipes. The working fluid actually turned a total of 630 deg in this build. In the third build the final layout of the ten combustion chambers was adopted, Fig. 15, and although the turning was the same, most of it occurred at high pressure. Note that the use of tubes interconnecting the ten combustion chamber liners had to be invented at this point!

The layouts studied by the RAE also comprised volutes, ducting, and bends carrying air and gas all over the aircraft! The notion of a gas generator feeding a power turbine separately located to give the optimum propeller installation was so tempting that one scheme went ahead. The gas generator consisted of a nine-stage compressor driven by a four-stage turbine, Fig. 16. The compressor gave a peak efficiency above 85 percent over the range up to a pressure ratio of 2.0, Fig. 17. Meanwhile, experimental measurements of the losses in

volutes and ducts showed that they could not be tolerated and that the straighter the flow from force to aft the better.

This conclusion led to the design of the D11, Fig. 18, in which the air flowed without bends through the seventeen-stage compressor, an annular combustion chamber, an eight-stage turbine driving the compressor, and a five-stage independent power turbine. Note the drum construction for the rotors, which will be discussed later. The decision to develop a compressor of large pressure ratio on a single shaft was taken when news from Brown Boveri suggested that 5:1 pressure ratio on a single shaft would be practicable. The D11 compressor, built and tested in 1941, was the first RAE compressor to show compressibility effects, Fig. 19.

Combustion problems gravely hampered the development of the Whittle engine [14]. Specters raised by conventional wisdom seem to have been a handicap. The heat release rate (watts/cubic meter of combustion chamber volume) was at least an order of magnitude grater than that in industrial furnaces, even allowing for the increased density of the gases in the chamber. The residence time in the flame was so short that reaction and evaporation rates might be too slow to allow complete vaporization and combustion of the fuel. It was thought necessary to vaporize the fuel before injecting it into the combustion chamber, and this was attempted first with a kerosene boiler in the turbine exhaust, and then with evaporator tubes in the flame itself, Fig. 20. It was difficult to make and assemble the cluster of vaporizing tubes and injectors with any great precision. Each engine run had to be terminated after red and orange patches on the combustion chamber walls threatened to burn holes in them, and vaporizer tubes would be found blocked with carbon and burned.

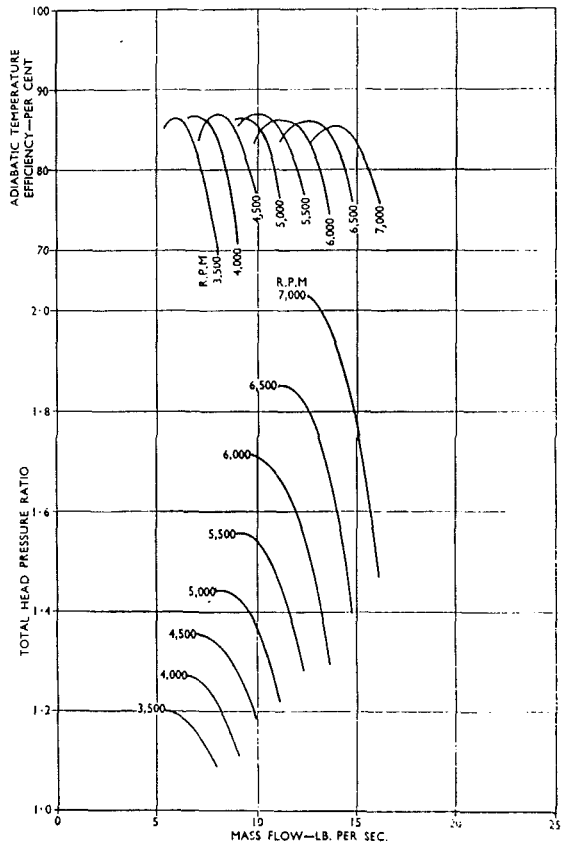

Fig. 17 Characteristics of B10 axial compressor Betty ([16], reprinted with permission of *Proc. IMechE*)

In 1939, in spite of such problems, Whittle's progress was sufficiently promising for the Air Ministry to place contracts for a flight engine, W1, and an experimental aircraft, Gloster E28/39, of which two were built. At the outbreak of war contracts for other development work and for a more powerful engine (W2) enabled Whittle's company, Power Jets, to increase its staff and facilities.

In August 1940 I was sent from RAE (which I had joined in January) on loan to Whittle to lead a group on combustion chamber development. When I arrived, engine runs had been limited to 45 minutes by problems with the vaporizing combustion chambers already described; but I. Lubbock of Shell had just developed a variable geometry swirl-type atomizer, which gave a good spray over a substantial range of fuel flow, around which he had built a combustion chamber somewhat similar in design to a domestic oil burner, Fig. 21. Although the required heat release rate was enormously greater than in its domestic application, it seemed the right approach. I had studied laminar and turbulent diffusion flames for my thesis at MIT, and had found that the length of a turbulent diffusion flame was dependent only on the geometry and not at all the heat release rate over an enormous range. This implied that aerodynamics (i.e., mixing) and not the reaction rate dominated the flame length. It was only a small extrapolation to assume that, if flame stability were ensured, the domestic oil burner could be made to operate at very high heat release rates, particularly at an air–fuel ratio of at least three times stoichiometric.

We used swirl vanes to produce recirculation and flame stability in the primary zone, and holes and pipes to mix the diluent air with the products of combustion from the primary zone, Figs. 22 and 23. Later the RAE sponsored a series of experiments on devices for mixing two streams of air. Some of them are shown in Fig. 24. The lobe mixer is at least fifty years old!

A major lesson was that as much care was required in determining and assuring the aerodynamic features of the com-

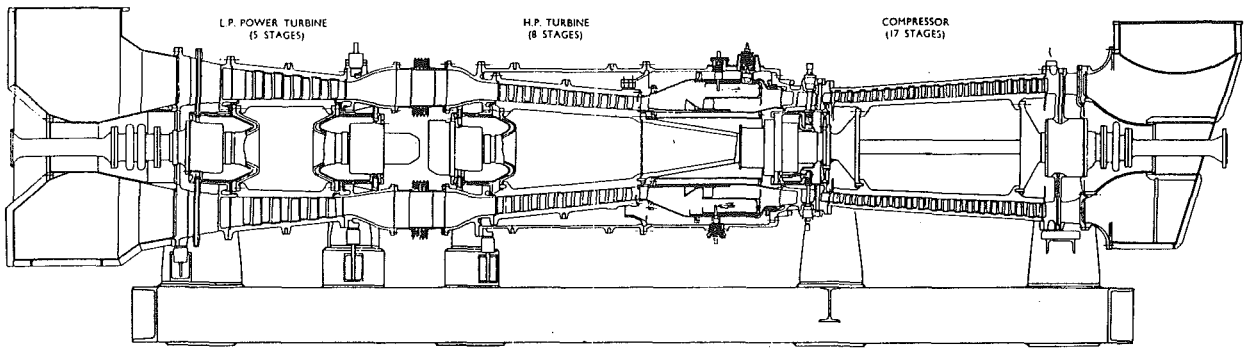

Fig. 18 RAE turboprop engine D11 with straight-through flow and a 17-stage axial compressor Doris ([16], reprinted with permission of *Proc. IMechE*)

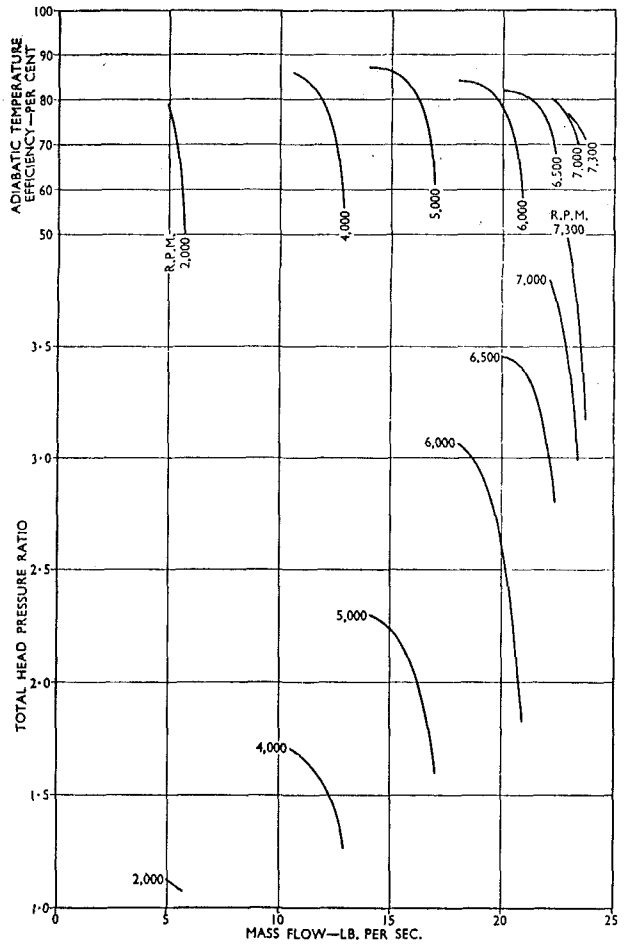

Characteristics of "Doris"

Values plotted are for standard entry conditions: 14·7 lb. per sq. in. at 288 deg. C. (550·4 deg. F.) abs.

Fig. 19 Characteristics of D11 axial compressor Doris: tested in 1941 and showing compressibility effects ([16], reprinted with permission of *Proc. IMechE*)

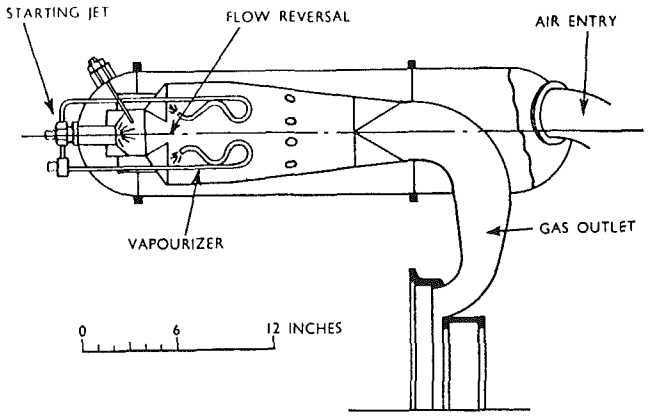

Fig. 20 Power jets vaporizing combustion chamber, 1940 ([17], reprinted with permission of *Proc. IMechE*)

bustion chamber and its fuel injectors as in the design of a blade for a compressor.

The RAE favored an annular combustion chamber with upstream injection from simple nozzles. Their program was aimed toward prototypes for bench testing of gas turbines driving propellers, and as we have seen concentrated heavily on developing the axial compressor. In September 1939 Con-

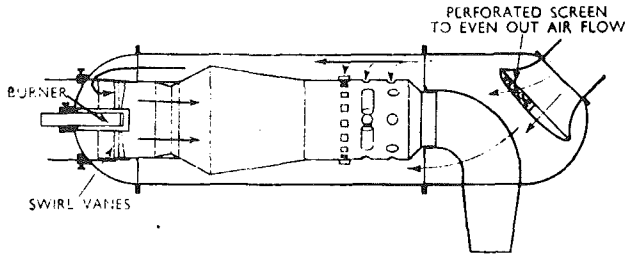

Fig. 21 Lubbock's prototype combustion chamber with variable geometry fuel injector giving good atomization over a wide range of fuel flow ([14], reprinted with permission of *Proc. IMechE*)

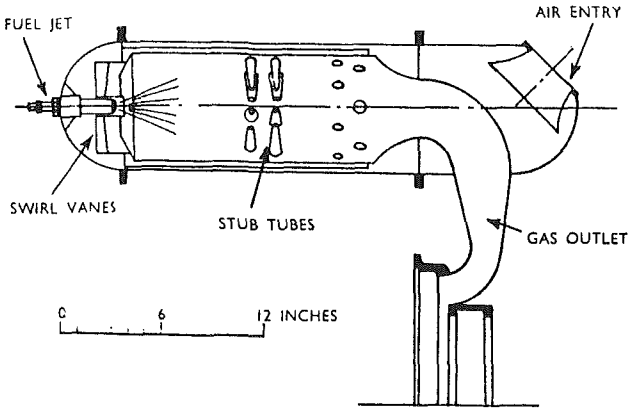

Fig. 22 Power jet combustion chamber type 75: swirler vanes were set at 75 deg by R. F. Darling ([17], reprinted with permission of *Proc. IMechE*)

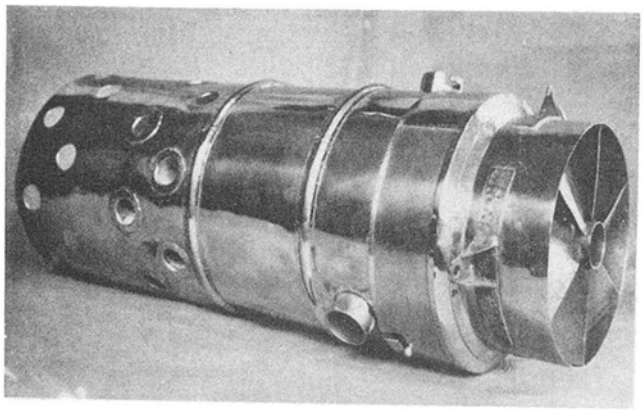

Fig. 23 Photograph of flame tube (liner) of combustion chamber type 75: used in first flight, 1941 ([14], reprinted with permission of *Proc. IMechE*)

stant suggested to Whittle that Power Jets should consider an axial compressor for a turbojet. In December he produced a design, Fig. 25, with the suggestion that the compressor should be designed and built at RAE and the combustion chamber and turbine at Power Jets. In July 1940 Power Jets abandoned the idea—it had too much other work—and Metropolitan Vickers took it on. It was the first gas turbine that RAE designed with Metropolitan Vickers to aircraft engine standards. It became known as the F2 engine; it had a nine-stage compressor, annular combustion chamber, and two-stage turbine, Fig. 26.

Two of the factors that dominated the layout of these early gas turbines were the whirling speed of and the stresses in the rotors. At that time there was only the elastic theory from which to calculate the maximum stresses around a hole drilled in a turbine disk, and it predicted they would be double those in a solid disk. The turbine disks were therefore forged like the valves of piston engines, with a small shaft integral with

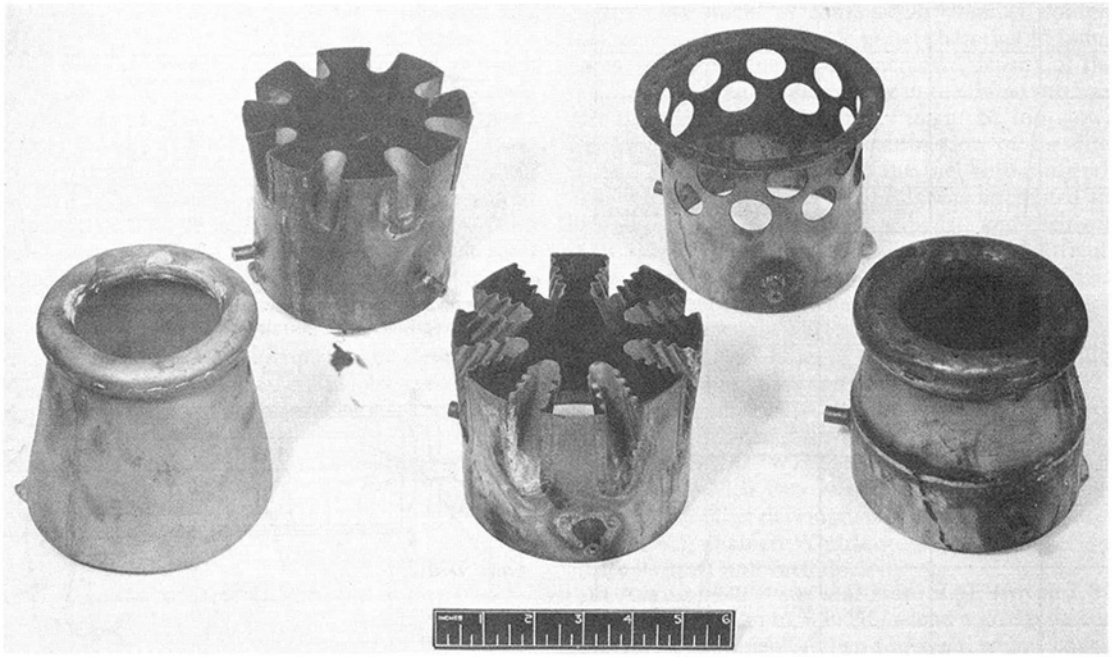

Fig. 24 Experimental mixing devices including lobe mixers, 1942 (reprinted with permission of RAE Crown Copyright)

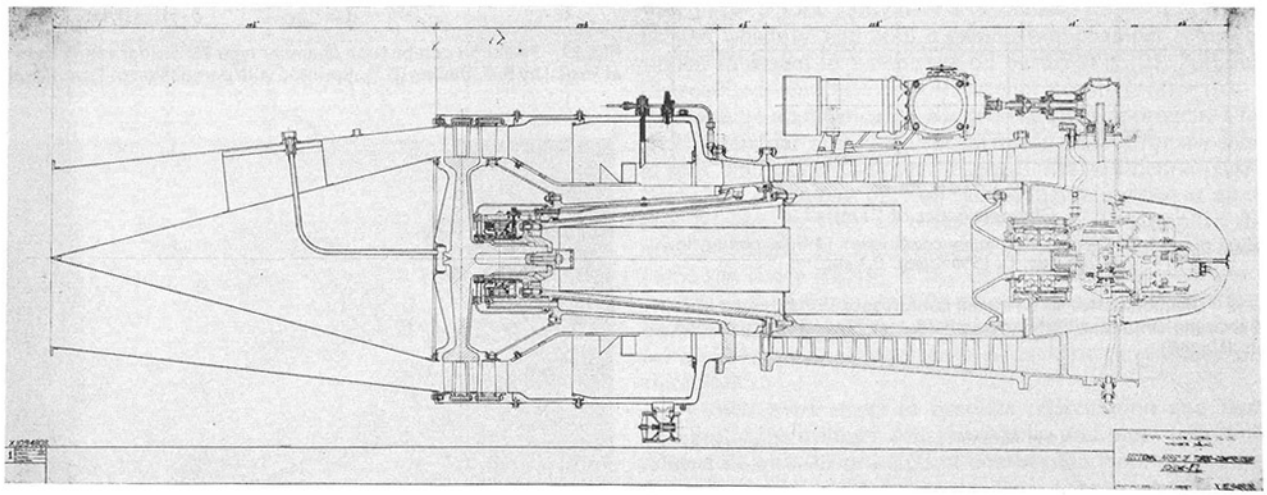

Fig. 25 General arrangement of RAE axial compressor turbojet engine F2, 1939 (reprinted with permission of RAE Crown Copyright)

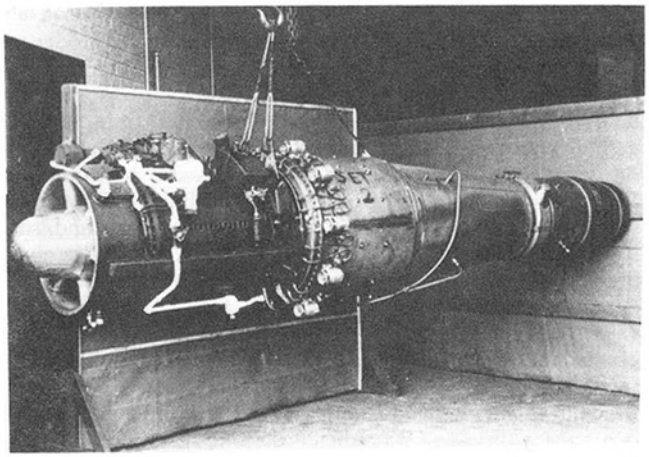

Fig. 26 RAE Metropolitan Vickers F2 turbojet engine (reprinted with permission of RAE Crown Copyright)

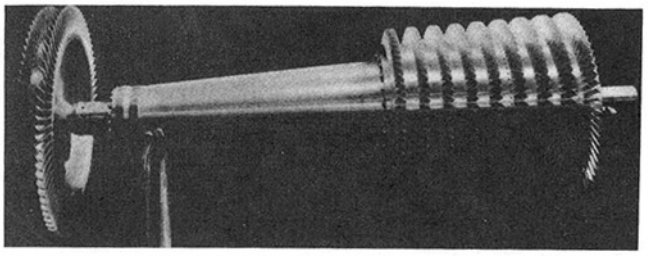

Fig. 27 Rotor of RAE Metropolitan Vickers F2 turbojet engine ([14], reprinted with permission of *Proc. IMechE*)

the disk projecting at one side. The small diameter of this shaft led to various solutions to the rotor critical speed problem. In the Whittle engine the rotor shaft was kept short, leading to the combustion chamber arrangement already discussed. The RAE's axial compressors used drums, because multiple disks without holes would be heavier. The conical portion of the rotor between the compressor and turbine of the F2 engine

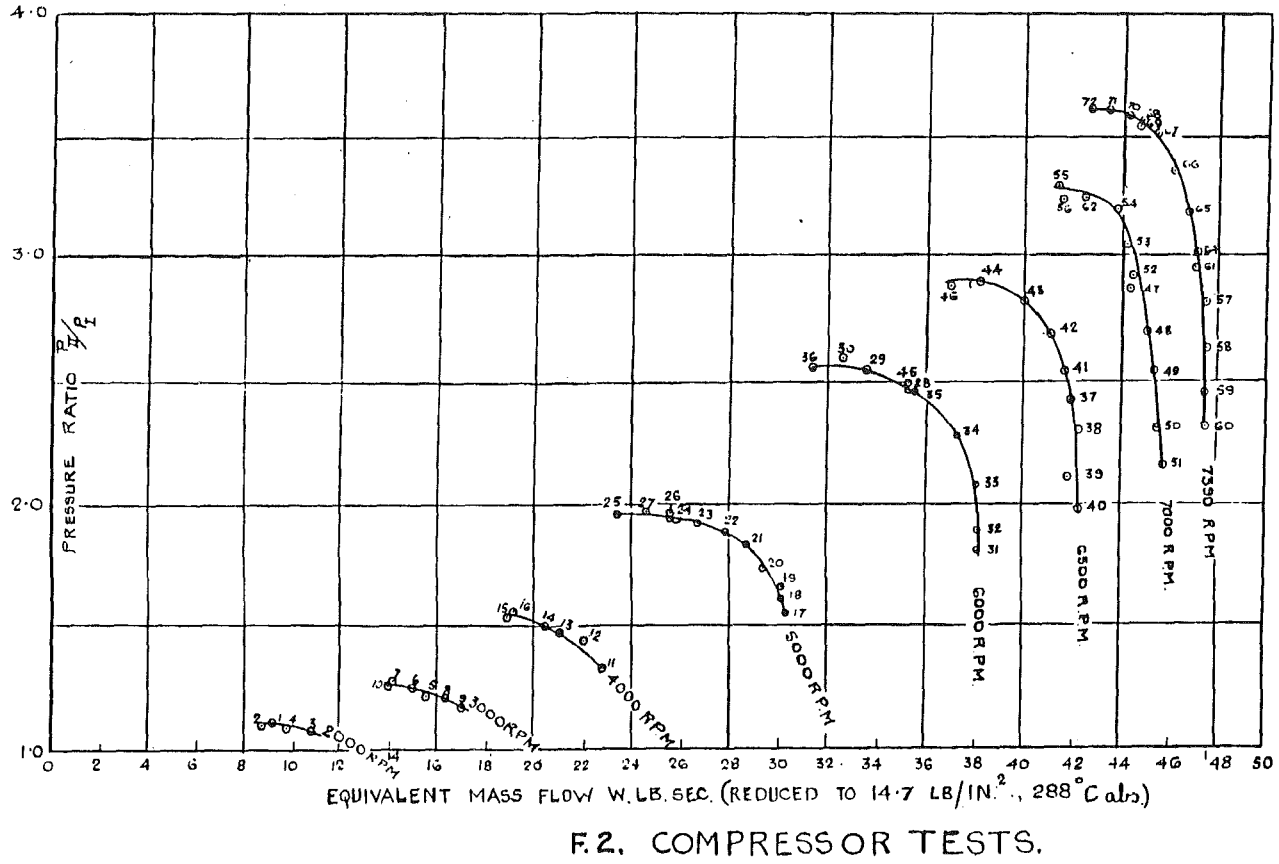

Fig. 28 Characteristics of F2 axial flow compressor (reprinted with permission of RAE Crown Copyright)

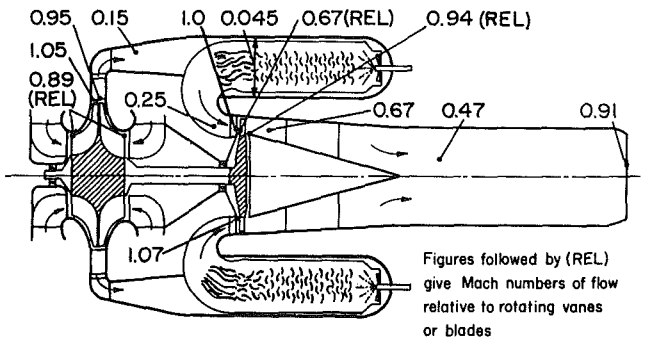

Fig. 29 Mach numbers of the flow at various points in a typical Whittle engine ([20], reprinted with permission of AIAA)

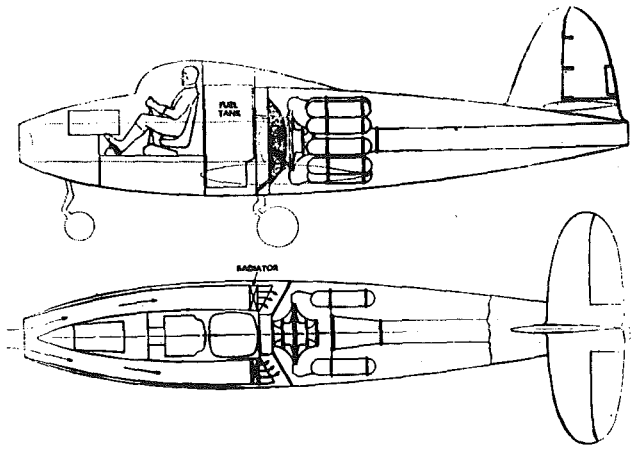

Fig. 30 Layout of Gloster E28/39 experimental jet aircraft showing long jet-pipe passing down the fuselage ([14], reprinted with permission of *Proc. IMechE*)

kept the rotor critical speed high enough and gave enough room for a straight-through combustion chamber, Fig. 27. The damaging effect of the elastic theory extended into compressor aerodynamics. The rim speed of a drum is far less than that of a disk for the same stress. It was in fact limited to 500 ft/sec for the F2 engine. To get enough work per stage the flow coefficient had to be increased from 0.5 (its textbook value for optimum efficiency) to 1.0. Fortunately, this had no great effect on efficiency, for the F2 compressor performance was the best of all the nine RAE compressors, Fig. 28 (it was still first built with blow-off valves), but these high flow coefficients directed cascade tests, analysis, and design to low stagger blading.

When in 1942 theory and experiment showed that plastic yielding reduced the increase of the stresses around holes to a few percent, De Havillands drilled holes in the turbine disk in order to bolt on a long, large-diameter hollow shaft. In this way they could accommodate straight-through combustion chambers on the Goblin without whirling speed problems.

To keep frontal area and weight low, flow velocities in the engine had to be high. Figure 29 shows the Mach number of the flow at various points in a typical Whittle engine. The double entry compressor reduced the Mach number at the inducers and flow velocity in the impeller at the expense of higher Mach numbers in the turbine. The value leaving the turbine was 0.8 in one design. This figure reminds me how little we knew about gas dynamics and how much the engine had to teach us. In the E28/39 aircraft the engine was installed behind the pilot. A long jet pipe extended down the fuselage with the jet nozzle projecting under the tail, Fig. 30. The cross-sectional area of the turbine exhaust annulus and the pipe were kept constant along its length and there was a small contraction in the nozzle. An engine of higher rating than the first was

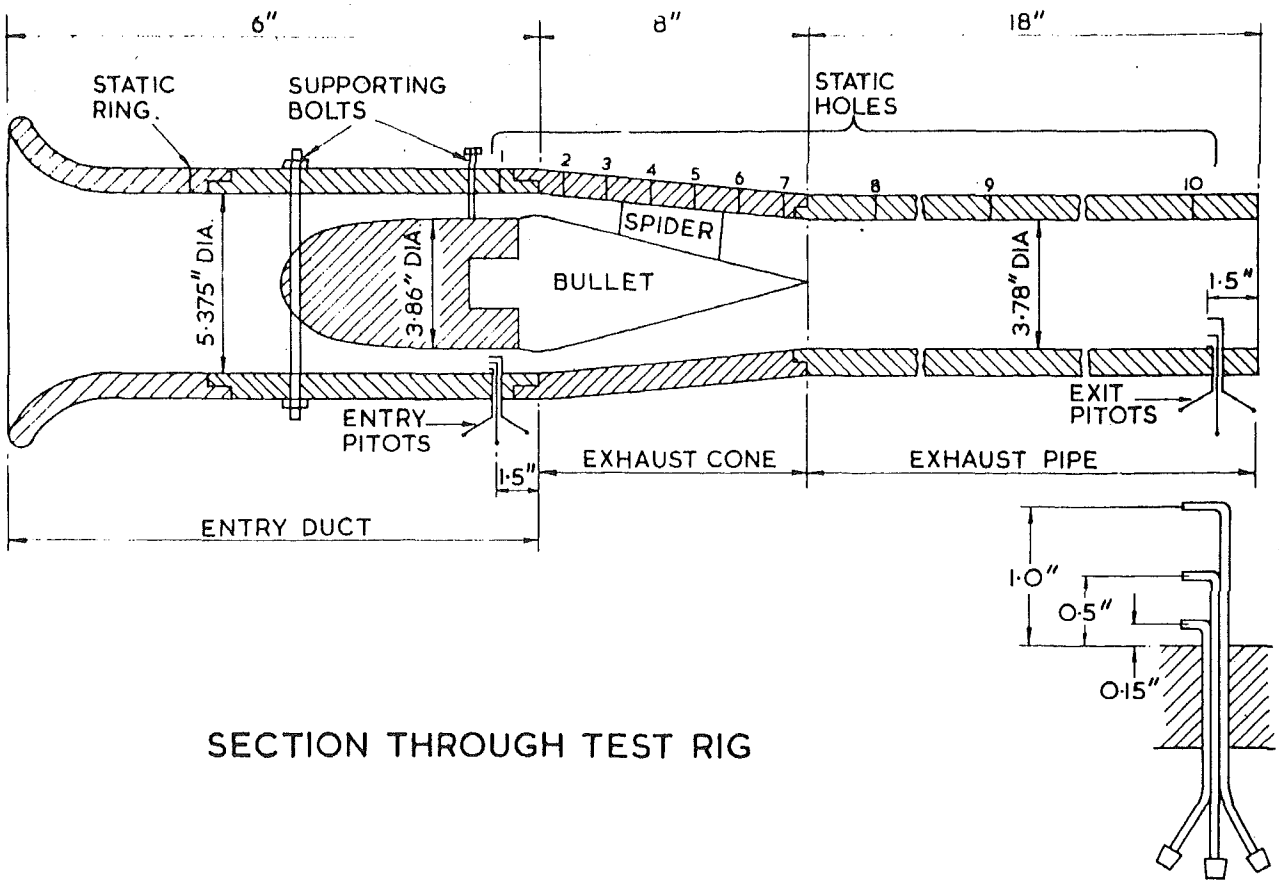

Fig. 31 J. Reeman's (RAE) model of E28/39 jet-pipe in which choking due to friction was demonstrated ([18], reprinted with permission of RAE Crown Copyright)

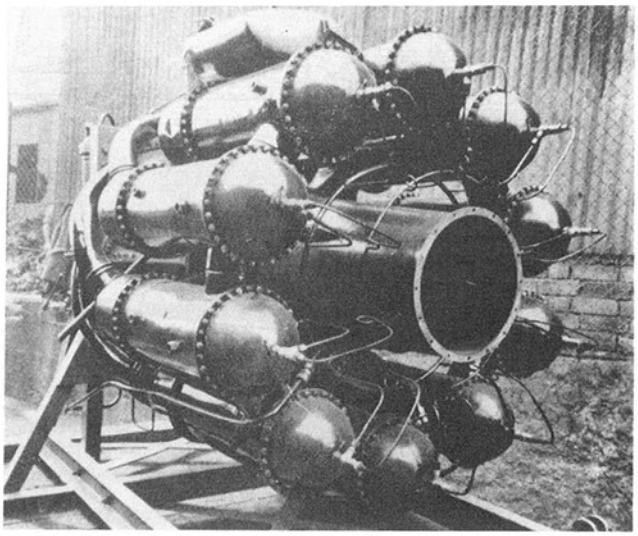

Fig. 32 The Whittle W1 engine used in the first flight 15 May 1941 ([14], reprinted with permission of *Proc. IMechE*)

being proposed for flight trials and the engine, jet pipe and nozzle were assembled on the test stand. As the engine speed was raised the jet pipe temperature went up more rapidly than usual, and rev/min and thrust were limited to avoid overheating the engine. Without the jet pipe full thrust could be obtained, but with the jet pipe thrust was quite inadequate. Taking the jet nozzle off hardly helped. The strange thing was that there seemed to be no loss of efficiency in any of the components, least of all the jet pipe, to account for the high temperature rise.

Fig. 33 Gloster F9/40 (Meteor) with W2B engines (reprinted with permission of RAE Crown Copyright)

Fig. 34 Modified Gloster F9/40 with F2 engines (reprinted with permission of RAE Crown Copyright)

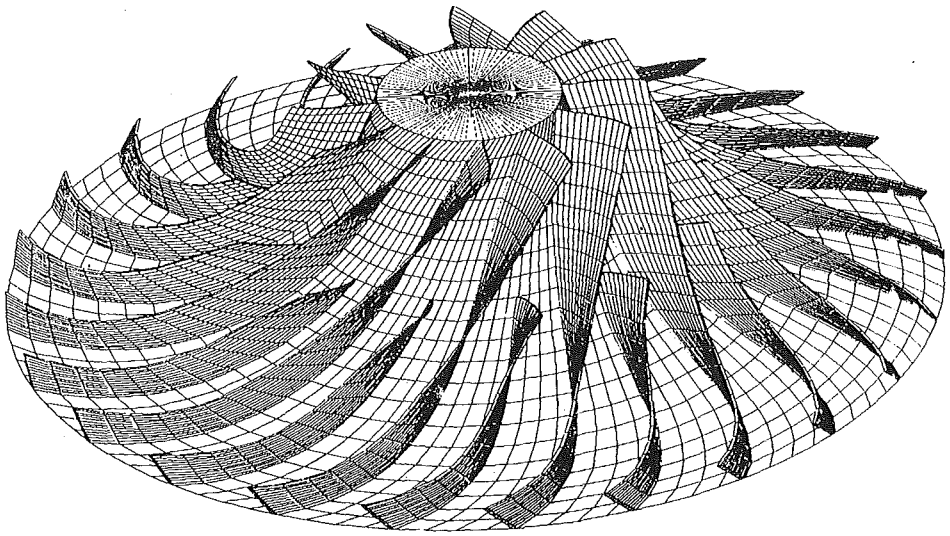

Fig. 35 Outline of centrifugal compressor vanes designed by the inverse method: note the double curvature of the vanes

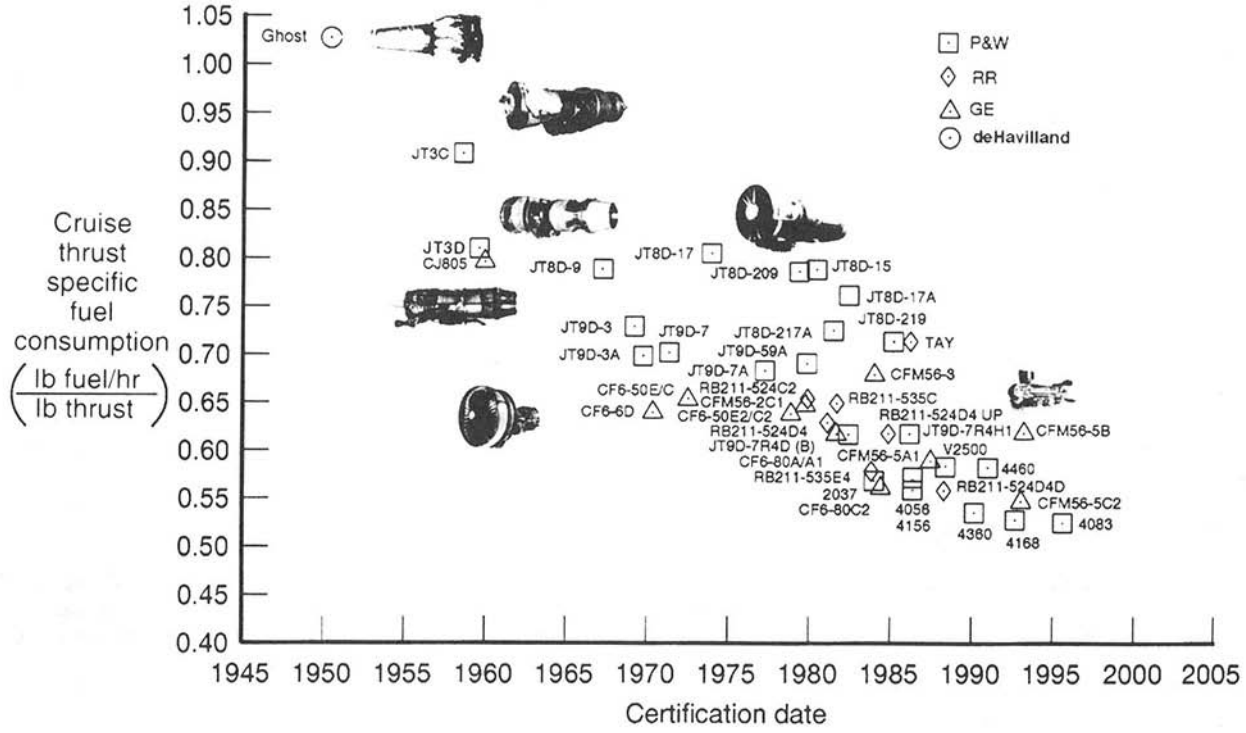

Fig. 36 The cruising specific fuel consumption versus year of certification for engines developed in the last fifty years ([21], reprinted with permission of AIAA)

At RAE J. Reeman built and tested a model of the turbine exhaust and jet pipe assembly, Fig. 31. With it he discovered choking due to friction. The jet pipe length was far too long to allow an inlet Mach number of 0.8, and the engine knew it! The problem was solved by allowing some diffusion in the exhaust assembly that converted the annular to the circular duct.

Another problem that Whittle understood, but Constant and others had difficulty with, was the stagnation pressure "loss" due to combustion or density change. Aerodynamicists use the Pitot tube for measuring losses, and the fact that, however much you streamlined the combustion chamber, there would still be a loss measured by the Pitot tube puzzled them. Where did the loss come from? It was even more puzzling when one noted that if the combustion chamber cooled rather than heated the air there would be a gain. These Rayleigh line effects and choking due to heat addition were also elucidated at that time, and we enjoyed the paradox that it was theoretically possible to add heat to a moving stream of gas and have its temperature drop.

The first flight of the E28/39 took place at RAF Cranwell at 7:45 p.m. on 15 May 1941. The W1 engine, Fig. 32, had its first run on 12 April, and over the next 46 days it was run up to full design speed, cleared for flight in a 25 hour special category test at 850 lb thrust and 16,500 rpm with a fuel consumption of about 1.4 lb/hr/lb thrust; it was installed in

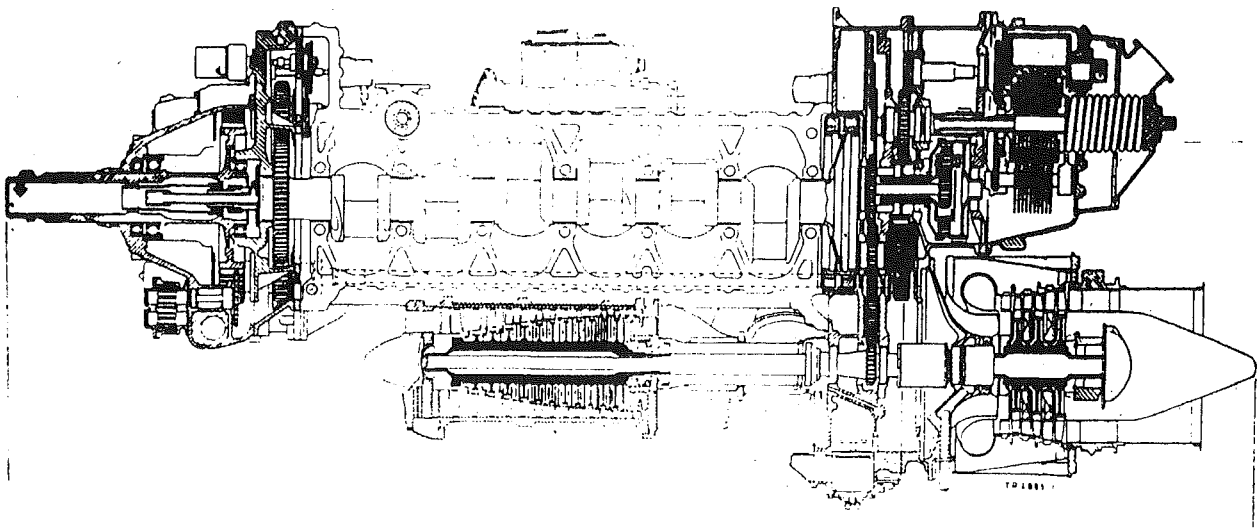

Fig. 37 The Napier Nomad two-stroke Diesel aero-engine with axial flow turbocharger variably geared to the crankshaft [(19), reprinted with permission of RAE)

the aircraft and completed ten hours flying in 17 flights. At about 25,000 ft altitude a top speed of 325 knots was reached, higher than the then top speed of Spitfire.

Early in 1940 the Air Ministry authorized the design and prototype manufacture of a twin-engined interceptor fighter, the Gloster F9/40, which became the RAF Meteor, Fig. 33, and of a Whittle engine of 1600 lb thrust, the W2B. They invited the Rover Co. and later Rolls Royce to develop and produce the engine. The struggles and strains of the period before the Meteor entered service had been noted elsewhere [8, 14], and it was not until May 1944 that the first Meteors powered by Rolls Royce Welland (W2B) engines went into RAF service. In the meantime Rovers and then Rolls Royce extended the distance between turbine and compressor by developing coupling and bearing designs to permit the use of straight through combustion chambers. The Rolls Royce Derwent engine incorporating this feature followed on the Welland in the Meteor.

Although no aircraft had been built for the axial compressor jet engine (F2), it was flown in the tail of a Lancaster bomber until a Meteor was modified, Fig. 34—note the underslung nacelles, to take the long engines—and flown in November 1943. The flight engine produced on the test bed 2000 lb of thrust at a specific fuel consumption of 1.07 lb/hr/lb thrust and a specific weight of about 0.7 lb/lb thrust [12]. Sadly during later trials of the aircraft a flaw in the compressor rotor drum of one of the engines started a fatigue crack, which caused the drum to blow up. The aircraft crashed and the pilot was killed by the high tailplane as he bailed out. The compressor of the F2 engine was used in later engines, but the F2 itself never went into production. It was several years before a British jet with an axial compressor went into service.

When in 1941 Constant became Head of the Engine Department at RAE I was made Head of its Gas Turbine Division, which set out to become the government's main research center for the new aero-engine. It did experimental research, performance calculations, project studies, and flight trials. It prepared designs as well as information for design. A prime example of its work was the correlation of the results of cascade and axial compressor tests and the provision of a guide for axial compressor design written by A. R. Howell in 1942 [13]. Until that time all RAE and Whittle designs were based on free vortex and radial equilibrium between the blade rows. The first departure from free vortex was in the RAE design for the turbine of the De Havilland Goblin, which was a constant specific mass flow design, which required that the product of density and axial velocity was constant at all radii and that radial equilibrium was satisfied between the nozzles and rotor blades. Later, Howell added five stages of non-free vortex blading to the F2 compressor to give a design for the compressor of the Armstrong Siddeley Python propeller turbine. Both these departures from free vortex were not accompanied by identifiable increases in the losses.

Howell allowed for the growth of boundary layer on the walls of the compressor annulus by a "work done factor." Work on end wall flow and three-dimensional flow in turbines and compressors has been continuing steadily for the last fifty years and was responsible for my interest in secondary flow at MIT and Cambridge University.

My reflections on these 66 years of jet propulsion history must largely be confined to the first 33 years, dominated by the slide rule and desk calculators. But we can recognize the climacteric effect of the computer, first in enabling through-flow computations of the flow through multistage compressors, then for inviscid fully three-dimensional flow in rows of blades, and finally for such flows with the effects of viscosity and shock waves. As a result our understanding of the real flows in turbomachines has grown enormously.

Of course these tools only allow us to investigate the flow in a given geometry and iteration aimed at optimizing a design still takes a long time even with a fast computer. To speed this up we look for techniques in which we specify the flow, velocity, pressure or whatever, and compute the blade shape. Such "inverse" design techniques are now used to obtain the blade profile for a given pressure distribution in two-dimensional flow. To do this for three-dimensional flow is more difficult, although a technique for designing marine propellers based on the "panel" method has proved very effective.

An inverse design technique for fully three-dimensional transonic flow in which the mean tangential velocity is specified with the blade shape computed has been used to design radial flow turbines and centrifugal compressors. Figure 35 shows a centrifugal compressor with splitter vanes designed by this technique. This design has constant circulation, i.e., there is no trailing vortex sheet leaving blade or splitter. The design has to be calculated using an inviscid fluid, since the iterative adjustment of the blade shape requires a nonzero velocity on the blade surface. It is now possible to "check" the design with a Navier-Stokes solver to find the behavior of the impeller with a real fluid. Computing the design on a fast work station takes a few minutes, running the Navier–Stokes solver several hours! So far all turbomachines designed by this technique,

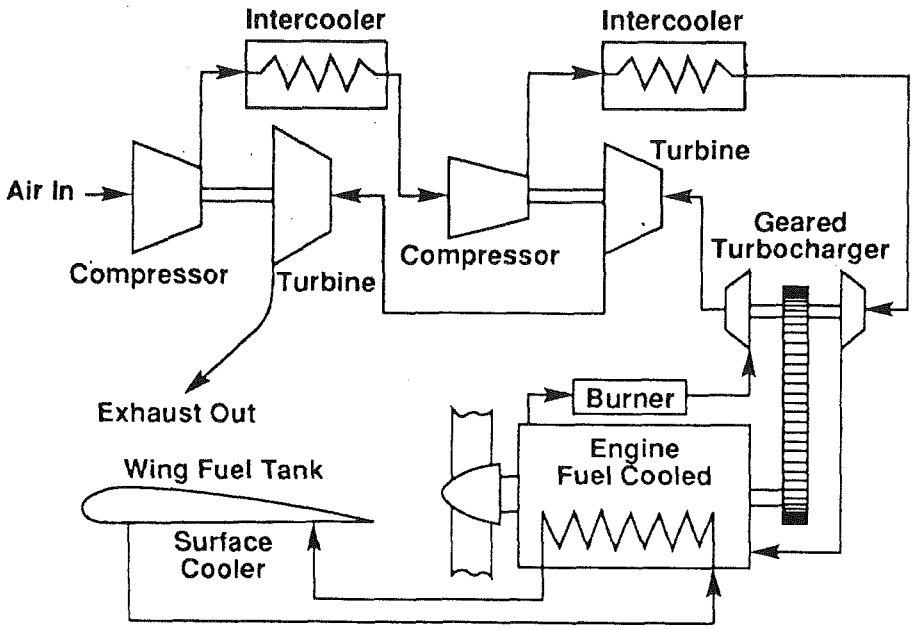

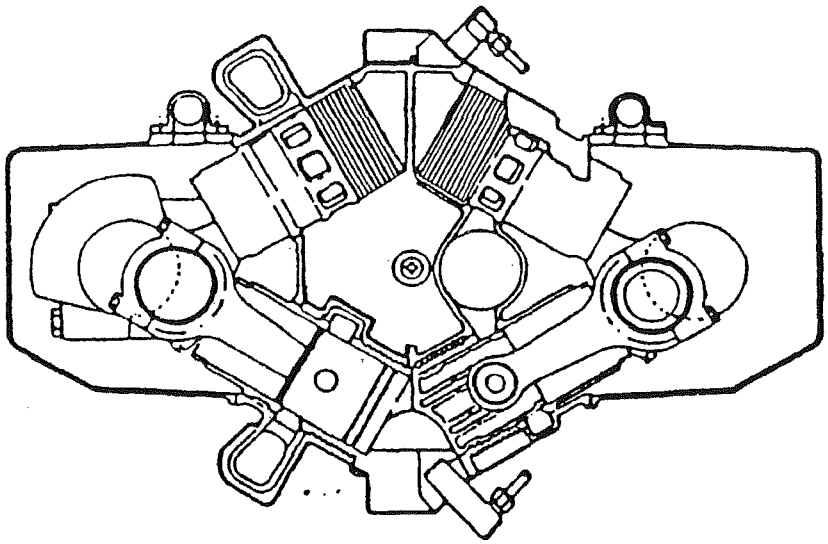

Fig. 38 Layout of a highly turbocharged two-stroke Diesel for a high-altitude long-endurance aircraft

built, and tested have shown an improvement in efficiency.

Although the basic layout and the thermodynamic cycle of the engine have not changed, the years have seen a vast improvement in engine performance and output. Figure 36 shows the performance history of many of the engines developed in the last fifty years as a plot of their cruise specific fuel consumption versus their year of certification. The specific fuel consumption has decreased from over 1.0 to nearly 0.5 lb-hr/lb thrust. How has this been done?

The propulsive efficiency has been improved. Both Whittle and RAE-Metropolitan Vickers group built ducted fan or bypass engines with fans mounted on turbines at the rear. At first the limited aircraft speed range over which the bypass engine would give better fuel economy than the turboprop or turbojet seemed too narrow to be of interest. But it just happens to be the favored cruise range of our commercial aircraft! The lead was taken by Rolls Royce who developed the Conway with the fan in front. The bypass engine eased the takeoff and range problems noted by Griffith. One highlights the continued success in solving the structural problems of the fan shrouds of ever-increasing diameter, which was one of the alleged disadvantages of the bypass engine. We are now envisaging much higher bypass ratios, geared fans, and variable pitch, and have toyed with swept-back contrarotating propellers.

Cycle efficiency has been improved by increasing turbine inlet temperatures and pressures and component efficiencies. To achieve higher temperatures we need to find better materials and to use 20 percent of the air for cooling. Cruising thrust specific fuel consumptions of less than 0.4 kg/hr/kg are targeted for the next century.

So far there has been no change in thermodynamic cycle. Heat exchangers have not yet found favor in aircraft gas turbines. The largest loss of thermodynamic availability occurs in the combustion chamber. What we need is a work-producing combustion chamber.

One of the engines that achieved this work production was

swept away 35 years ago by young people like me who saw the future only in terms of the gas turbine. The engine worked on the thermodynamically more efficient constant volume cycle. It was the Napier Nomad, a turbocharged turbo-compound Diesel two-stroke with a swept volume of 41.1 liters, Fig. 37. The engine output at take-off was 3135 hp or 76 bhp/liter; the specific fuel consumption and specific weight at take-off were 0.345 lb/hp-hr (210 g/kW-h) and 1.17 lb/hp (0.4 kg/kW), respectively. Under cruising conditions (300 knots and 25,000 ft–7,600 m) a specific fuel consumption of 0.326 lb/e.h.p.-hr (198 g/kW-h) was obtained at an output of 2000 e.h.p. (1500 kW). The turbocharger had a twelve-stage axial compressor with a mass flow of 13 lb/sec (5.9 kg/s) at a maximum pressure ratio of 8.25 and was coupled to the crankshaft through a variable gear.

Although the Diesel engine has had little spent on its R&D compared to the aircraft gas turbine, it has made good progress. It is still the most efficient of the prime movers. It achieves this efficiency without the use of exotic materials. A comparatively inexpensive heavy duty truck engine (350 hp) can be tuned to develop about 50 percent thermal efficiency.

Figure 38 shows the layout of a Diesel power plant proposed for a high altitude long endurance (HALE) aircraft. Such a plant if designed for cruising at $M = 0.8$ and 35,000 ft (11,000 m) would offer a thermodynamic efficiency of 53 percent or, if used to drive a ducted fan, about 0.45 kg/h/kg thrust. This performance should be obtainable with little development. The performance would be improved if the maximum cylinder pressure and thermal loading in the cylinder could be raised by using better materials available at extra cost. By increasing the boost and rpm the output per liter could be raised to double that of the Nomad so that with lighter material the specific weight could be more than halved.

Some of the examples I have discussed in this Lecture suggest that it may be a good idea to question conventional wisdom from time to time. R. Tom Sawyer said in 1945 that the gas turbine would supplement the Diesel engine. In the air it supplanted it. Would R. Tom Sawyer now be saying "Has the time come to ask whether in the next century the Diesel engine will be used to supplement the aircraft gas turbine?"

References

Note: Abbreviations:

RAE Royal Aircraft Establishment
ARC Aeronautical Research Committee (later Council)
R&M Reports and Memoranda (of ARC)
AML Air Ministry Laboratory

1 Whittle, F., *Jet—The Story of a Pioneer*, Frederick Muller Ltd., London, 1953.

2 Rubbra, A. A., "A. A. Griffith—Biographical Memoirs of Fellows of the Royal Society," *Proc. R. Soc. London*, Vol. 10, 1964, pp. 117–136.

3 Griffith, A. A., "An Aerodynamic Theory of Turbine Design," RAE Report H1111, ARC T 2317, July 1926.

4 Harris, R. G., and Fairthorne, R. A., "Wind Tunnel Experiments With Infinite Cascades of Aerofoils," ARC R&M 1206, Sept. 1928 (published in 1929).

5 Clothier, W. C., "Test of Aerofoil Section Turbine Blading," RAE Report E2868, Dec. 1929.

6 Griffith, A. A., "The Present Position of the Internal Combustion Turbine as a Powerplant for Aircraft," A.M.L. Report 1050A, Nov. 1929.

7 Stern, W. J., "The Internal Combustion Turbine," ARC Engine Sub-Committee Report No. 54, Sept. 1920.

8 Golley, J., *Whittle—The True Story*, Airlife Publishing Ltd., Shrewsbury, United Kingdom, 1987.

9 Capon, R. S., and Brooke, G. B., "Application of Dimensional Relationship to Air Compressors With Special Reference to Their Variation of Performance With Inlet Conditions," ARC R&M 1336, 1930.

10 Hawthorne, W. R., Cohen, H., and Howell, A. R., "Hayne Constant—Biographical Memoirs of Fellows of the Royal Society," *Proc. R. Soc. London*, Vol. 19, 1973, pp. 269–279.

11 Constant H., "The Internal Combustion Turbine as a Power Plant for Aircraft," RAE Note E3546, Mar. 1937.

12 Constant, H., et al., "Lectures on the Development of the Internal Combustion Turbine," *Proc. IMechE*, Vol. 153, 1945, pp. 409–512.

13 Howell, A. R., (a) "Fluid Dynamics of Axial Compressors," (b) "Design of Axial Compressors," *Proc. IMechE*, Vol. 153, 1945, pp. 441–462.

14 Whittle, F., "Early History of the Whittle Jet Propulsion Turbine," *Proc. IMechE*, Vol. 152, 1945, pp. 419–435.

15 Sawyer, R. T., "The Diesel and the Gas Turbine," lecture given to Mohawk-Hudson Group of SAE, Nov. 7, 1945, SAE Prepint.

16 Constant, H., "The Early History of the Axial Type of Gas Turbine Engine," *Proc. IMechE*, Vol. 153, 1945, pp. 411–426.

17 Lloyd, P., "Combustion in the Gas Turbine," *Proc. IMechE*, Vol. 153, 1945, pp. 462–472.

18 Hawthorne, W. R., "Aircraft Propulsion From the Back Room," *Aeronautical Journal*, Vol. 82, No. 807, 1978.

19 Chatterton, E. E., "Compound Diesel Engines for Aircraft," *J. Roy. Aero. Soc.*, Vol. 58, Sept. 1954, pp. 613–633.

20 Hawthorne, W. R., "Some Aerodynamic Problems of Aircraft Engines," AIAA *Journal of the Aeronautical Sciences*, Vol. 24, No. 24, 1957.

21 Koff, B. L., "William Littlewood Memorial Lecture: Spanning the Globe With Jet Propulsion," AIAA Paper No. 2987, 1991.

Y. Ozawa

J. Hirano

M. Sato

Central Research
Institute of Electric Power Industry,
Yokosuka, Kanagawa, Japan

M. Saiga

S. Watanabe

Kansai Electric Power Co., Inc.,
Amagasaki, Hyogo, Japan

Test Results of Low NO_x Catalytic Combustors for Gas Turbines

Catalytic combustion is an ultralow NO_x combustion method, so it is expected that this method will be applied to a gas turbine combustor. However, it is difficult to develop a catalytic combustor because catalytic reliability at high temperature is still insufficient. To overcome this difficulty, we designed a catalytic combustor in which premixed combustion was combined. By this device, it is possible to obtain combustion gas at a combustion temperature of 1300°C while keeping the catalytic temperature below 1000°C. After performing preliminary tests using LPG, we designed two types of combustor for natural gas with a capacity equivalent to one combustor used in a 20 MW class multican-type gas turbine. Combustion tests were conducted at atmospheric pressure using natural gas. As a result, it was confirmed that a combustor in which catalytic combustor segments were arranged alternately with premixing nozzles could achieve low NO_x and high combustion efficiency in the range from 1000°C to 1300°C of the combustor exit gas temperature.

Introduction

Owing to increasing demand for combined cycle power plants and repowering of existing power plants, the use of gas turbines has gradually expanded in recent years. However, since nitrogen oxides (NO_x) are generated in a high-temperature gas turbine combustor, it is necessary to reduce NO_x emissions. Although NO_x is currently being controlled by selective catalytic reduction system, considering the capital, operating, and maintenance costs it is hoped that a more economical and efficient technology will be developed.

In the 1970s, research was initiated on the application of catalytic combustion to gas turbine combustors as an alternative NO_x control technology [1–5]. This research is being actively promoted [6, 7].

In 1988, CRIEPI and The Kansai Electric Power Co., Inc. (KEPCO) started joint research on the development of a catalytic combustor for gas turbines with the aim of achieving the combustion performance indicated in Table 1. This research is being pursued in accordance with the schedule indicated in Table 2. In the case of the method where most of the combustion occurs within the catalytic bed, catalytic temperature rises considerably, so it is necessary to develop heat-resistant catalysts. But development of such catalysts is extremely difficult. Thus we designed a combustor capable of reducing the catalyst deterioration caused by heat by adding a premixing combustion tap. Then, after conducting preliminary tests using LPG, we designed two combustors for natural gas and evaluated these performances by performing combustion tests at atmospheric pressure. We will present these results in this paper.

Contributed by the International Gas Turbine Institute and presented at the 38th International Gas Turbine and Aeroengine Congress and Exposition, Cincinnati, Ohio, May 24–27, 1993. Manuscript received at ASME Headquarters March 17, 1993. Paper No. 93-GT-344. Associate Technical Editor: H. Lukas.

Table 1 Performance goal of catalytic combustor

Combustor exit gas temperature	1300°C
NO_x emission	<10 ppm
Combustion efficiency	>99.9 percent (at rated load)
Differential pressure	5 percent
Pattern factor	<15 percent

Table 2 Schedule of catalytic combustor development program

	'88	'89	'90	'91	'92	'93~
Feasibility study	▬					
Preliminary test (LPG)		▬	▬			
CCT combustor test (natural gas)			▬	▬		
ACC combustor test (natural gas)						
•Atmospheric pressure test				▬	▬	
•High-pressure test (over 10 atm)						▬

Concept of the Combustor

We designed the process indicated in Fig. 1 to relax the operational conditions of catalysts.

The combustor is composed of a burner system and a premixed combustion section. The burner system is composed of premixing nozzles and catalytic combustor segments in which small catalysts are mounted without cementing. Catalytic combustion is carried out below 1000°C, fuel/air mixture is injected from the premixing nozzles into the catalytic combustion gas, and lean premixed combustion is realized. As a result, the following effects can be expected:

1 As the catalysts become larger and larger, their mechanical and thermal reliability is reduced. Thus, by increasing the number of catalytic segments while keeping the catalysts small, it will be possible to apply catalysts to large combustors without losing their structural reliability.

2 By combining with lean premixed combustion, which emits relatively small amounts of NO_x, it is possible not only to

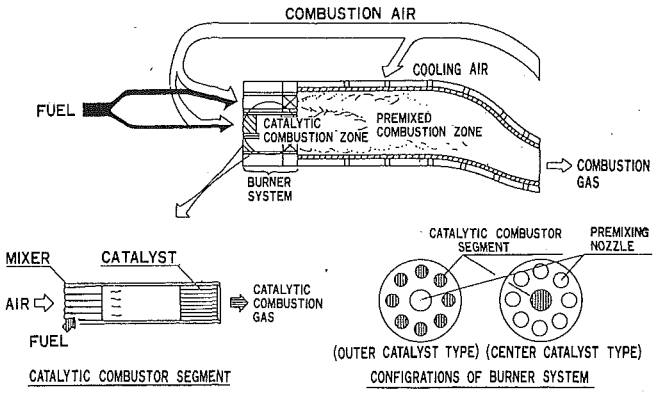

Fig. 1 Concept of catalytic combustor

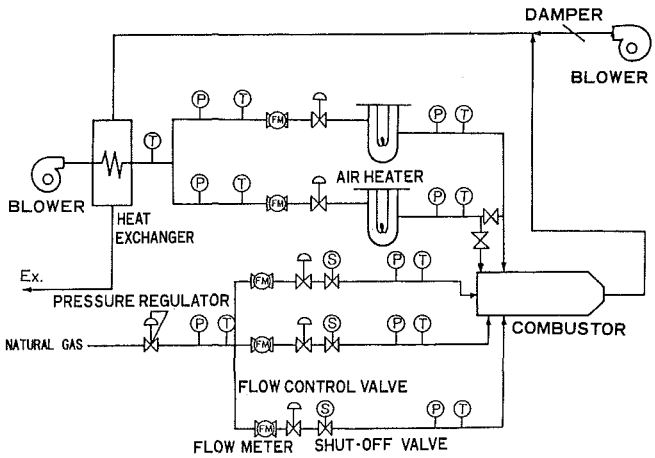

Fig. 2 Schematic diagram of test facility

prevent the catalyst deterioration caused by heat but also to control NO_x. Moreover, by keeping the catalyst temperature low, a certain degree of lack of uniformity in the fuel/air mixture is permitted. Furthermore, since the combustion load is partially distributed in the premixed combustion zone, it will be possible to reduce the load on the catalysts [the space velocity (s.v.)], the pressure losses, and the volume of catalysts.

On the basis of the above mentioned concept, we designed two types of combustors—dubbed CCT (Center Catalyst Type combustor) and ACC (Advanced Catalytic Combustor)—for natural gas with a capacity equivalent to one combustor used

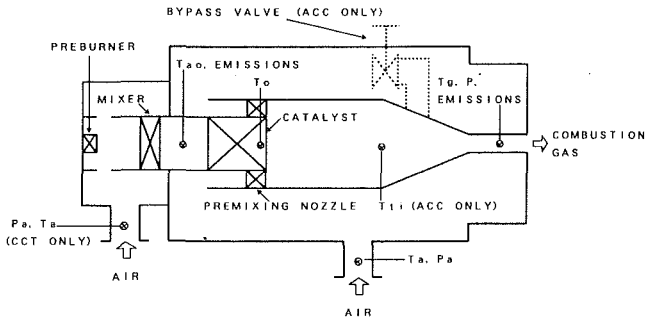

Fig. 3 Location of major instrumentation

Table 3 Measurement instruments

Items	Measurement Instruments
Temperature	Type-K or Type-R Thermocouples (JIS)
Pressure	Bourdon Gages (JIS)
Flow rate	Orifice flow meters (JIS)
Emissions	Gas analyzer
•NO_x, NO	Chemiluminescence
•CO	Nondispersive infrared
•CO_2	Nondispersive infrared
•O_2	Paramagnetic
•UHC	Flame ionization

in a 20MW-class multican-type gas turbine. Combustion tests were conducted at atmospheric pressure and the performance of the combustor was evaluated using natural gas.

Test Facility and Test Conditions

Figure 2 is a schematic diagram of the test facility for a gas turbine combustor. After supplying the combustor with air preheated to the prescribed temperature, catalytic combustion was started by supplying fuel to the catalysts, and the outlet temperature of the catalyst bed was kept below 1000°C. Then, the fuel was supplied to the premixing nozzles, and hybrid premixed combustion was triggered with the igniter.

The location of the instrumentation is shown in Fig. 3, and the measuring method we adopted is given in Table 3. Here, the outlet temperature of the catalyst bed was measured with five sheathed thermocouples for CCT or 24 sheathed thermocouples for ACC inserted in the cells near the exit end of the bed; the combustor exit gas temperature was measured with a traversing array of five thermocouple rakes installed at the transition piece exit, the liner metal wall temperature with a sheathed thermocouple welded to the liner wall, and the liner

Nomenclature

CO = carbon monoxide emission, ppm
Lb = combustion loading rate, kcal/(m^3•h•atm) = (lower calorific value of the fuel × fuel flow rate)/(volume of combustion chamber × combustion pressure)
LPG = liquefied petroleum gas
NO_x = nitrogen oxide emission, ppm
O_2 = oxygen concentration, percent
P = combustion pressure, atm
Pa = inlet pressure of catalytic combustor segment or premixing nozzle (for CCT combustor), inlet pressure of combustor (for ACC combustor), atm
ΔP = (differential pressure/*Pa*) × 100, percent
ΔPd = ΔP from combustor inlet to catalyst inlet, percent
ΔPo = ΔP from catalyst inlet to combustor exit, percent
ΔPp = ΔP from premixing nozzle inlet to combustor exit, percent
ΔPt = total ΔP of combustor, percent
P.F. = pattern factor = $\dfrac{Tg\text{•peak} - Tg}{Tg - Ta} \times 100$, percent
Rao = air flow distribution = (*Vao*/*Vat*) × 100, percent
Ta = inlet air mean temperature of combustor, °C
Tao = catalyst inlet mean temperature, °C
To = catalyst outlet mean temperature, °C
Tti = inlet gas mean temperature of transition piece, °C
Tg = combustor exit gas mean temperature, °C
Tg•peak = combustor exit gas peak temperature, °C
UHC = unburned hydrocarbon emission, ppm
Vao = air flow rate to catalytic combustor segment, m^3/h at 0°C 1 atm
Vat = total air flow rate, m^3/h at 0°C 1 atm
η = combustion efficiency, percent
λt = total excess air ratio

Table 4 Standard conditions

Pressure	P = atmospheric pressure
Inlet air temperature	$Ta = 350°C$
Catalyst inlet temperature	$Tao = 450°C$
Catalyst outlet temperature	$To < 1000°C$
Combustor loading rate	$Lb = 2.3 \times 10^7$ kcal/(m•h•atm) ($Tg = 1300°C$)
Total air flow rate	$Vat = 1017$ m^3_N/h
Fuel	Natural gas

Table 5 Typical properties of fuel (natural gas)

Composition (mole percent)	$CH_4 = 99.2$, $CO_2 = 0.7$, $N_2 = 0.1$
Specific gravity (kg/m^3_N)	0.71767
Viscosity (P (at 44°C, 1 atm))	1060×10^{-7}
Lower heating value ($kcal/m^3_N$)	8485
Higher heating value ($kcal/m^3_N$)	9414

ceramic fiber temperature with the sheathed thermocouples inserted in the fibrous layer. Also, the temperature at the transition piece inlet was measured at five points in the ACC combustor. Moreover, gas samples were taken continuously through a water-cooled stainless steel probe with five suction holes installed at the transition piece exit.

With the conditions listed in Table 4 as the standard, a combustion test was carried out under atmospheric pressure by using the natural gas given in Table 5. In the study of the CCT combustor, air was supplied independently to the catalytic combustor segment and the premixing nozzles, respectively, to be able to examine the hydrid combustion performance more easily. Also, a part of the air supplied to the premixing nozzles was used to cool the liner.

CCT Combustor Design

Figure 4 shows the combustor called CCT. Also, the outlook of the combustor is shown in Photo 1. Based on the results of the preliminary combustor tests using LPG [8], the catalytic segment is arranged at the center of the burner system, and along its periphery, the premixing nozzles are arranged. The catalyst tested has the capacity to start catalytic combustion at 350°C, but the reaction is not stable enough. So, in order to promote catalytic activity, a preburner is installed in the catalyst upstream, and the catalyst is preheated to 450°C. Moreover, to stabilize premixed combustion, the ceramic baffle plate shown in Fig. 5 is installed at the catalytic segment exit, the swirler at the premixing nozzle exit. The cross section of the baffle plate is about 40 percent that of the catalyst, the inward angle of the swirler 90 deg, and the revolving angle 20 deg. Ceramic fiber type liner is used from the combustion chamber and the transition piece [9]. Ceramic fibrous texture is attached to the metal outer liner wall with ceramic bolts.

The catalyst specifications are as follows: The major active ingredient is palladium, which is supported on stabilized alumina washcoat on a honeycomb-type monolith made of cordierite. This was developed by H. Fukuzawa of CRIEPI. Three stages of the catalyst, which is 150 mm in diameter, 25 mm in length, and 3.3 mm in cell pitch, are mounted in a ceramic tube with ceramic fiber layer between the catalysts and the tube. Also, the tube is mounted in the combustor with ceramic fiber layer.

Test Results

Effects of Combustor Exit Gas Temperature. Figure 6 shows the effects of the combustor exit gas temperature (Tg) on emission properties, combustion efficiency (η), and pressure losses (ΔP). This result was obtained when the reaction conditions of the catalytic bed were kept constant while combustor exit gas temperature (Tg) was changed by adjusting the fuel flow rate to the premixing nozzles. The air flow distribution to catalytic combustor segment (Rao) was set at 60 percent.

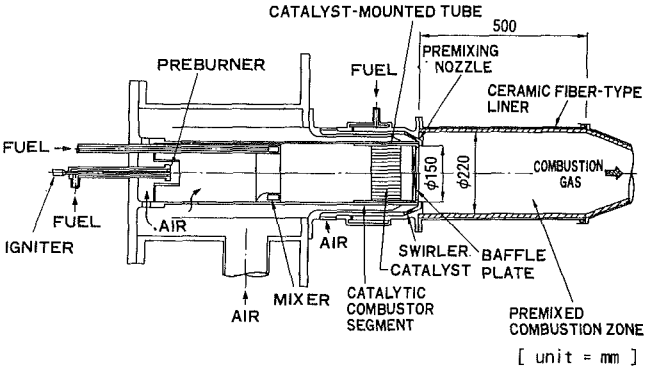

Fig. 4 CCT combustor

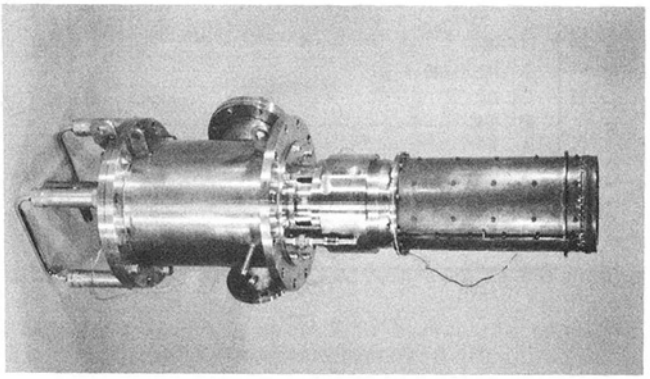

Photo 1 CCT combustor

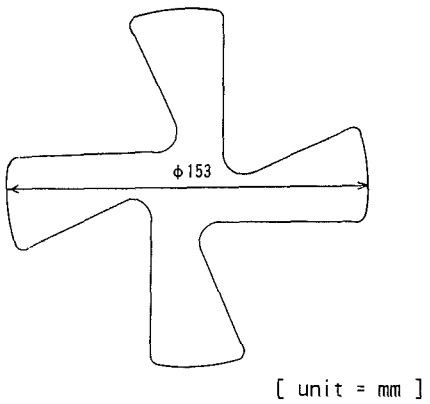

Fig. 5 Baffle plate

Here, actual values measured by thermocouples were used for Tg.

Although NO_x emissions rose with an increase in Tg, low-NO_x combustion of 6 ppm (3 ppm at 16 percent O_2) was achieved by setting Tg at 1300°C and the total excess air ratio (λt) at 2.22. The level of NO_x emissions at the preburner was 1.5 ppm. Moreover, CO and UHC emissions were under 6 ppm, while combustion efficiency was nearly 100 percent. ΔP was 6.7 percent, which was somewhat higher than the level targeted. Meanwhile, when Tg was under 1250°C ($\lambda t = 2.38$), premixed combustion became unstable and was eventually extinguished. The pattern factor ($P.F.$) of the combustor exit gas was below 7 percent, indicating that the temperature distribution was favorable.

The temperature of the ceramic fiber layer of the inner liner wall was below 1000°C, while that of the metal surface of the outer liner wall was below 400°C, indicating that the temperature at each of these locations was low enough.

There was absolutely no backfire either in the catalyst upstream or inside the premixing nozzles.

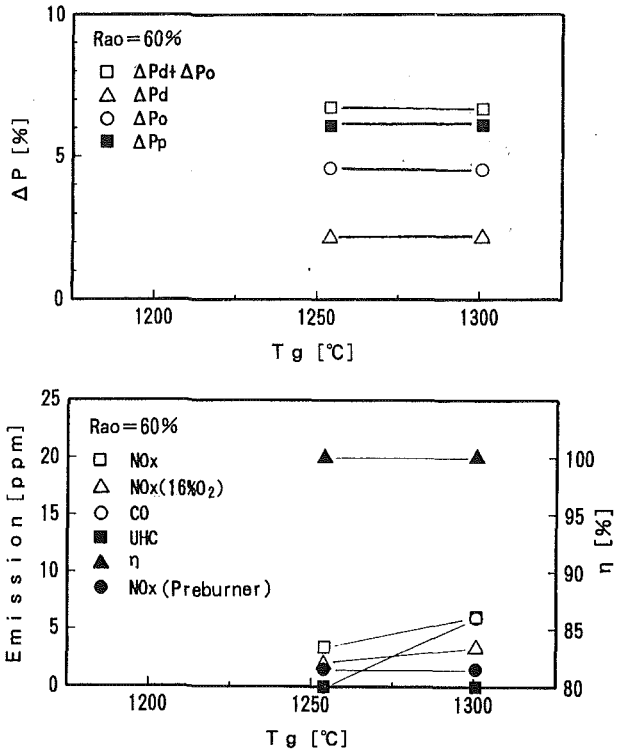

Fig. 6 Combustor performance (CCT)

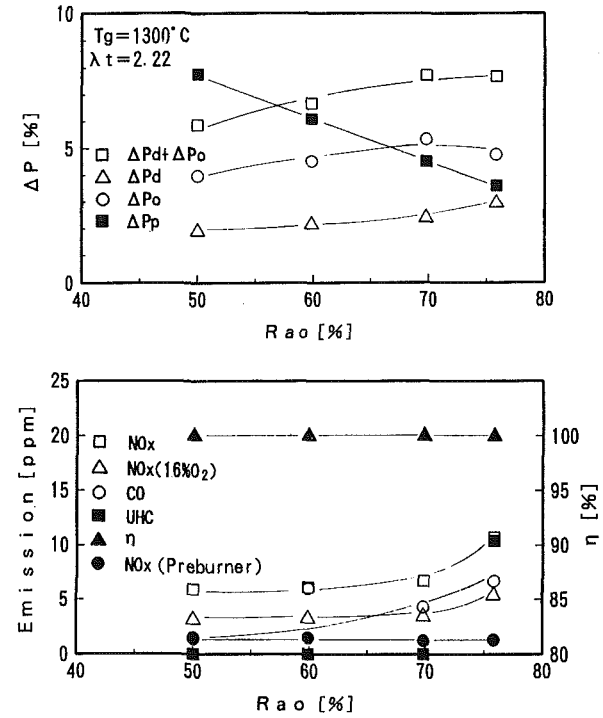

Fig. 7 Effect of air flow distribution (CCT)

Effects of Air Flow Distribution. In this combustor, the air flow distribution for catalytic segment and premixing nozzles affect its combustion characteristics. Figure 7 shows the effects of air flow distribution. This result was obtained by keeping the combustion loading rate (*Lb*), *Ta*, *Tg*, and λt constant while varying *Rao*. In this case, the reaction load of the catalyst increases with an increase in *Rao*. No_x, CO, and UHC emissions tended to increase somewhat with an increase in *Rao*, and when the range of *Rao* was 50–70 percent, NO_x emissions were under 8 ppm (4 ppm at 16 percent O_2), CO emissions under 7 ppm, and UHC under 1 ppm. When *Rao* is higher than 70 percent, NO_x, UHC, and other emissions tend to be accelerated.

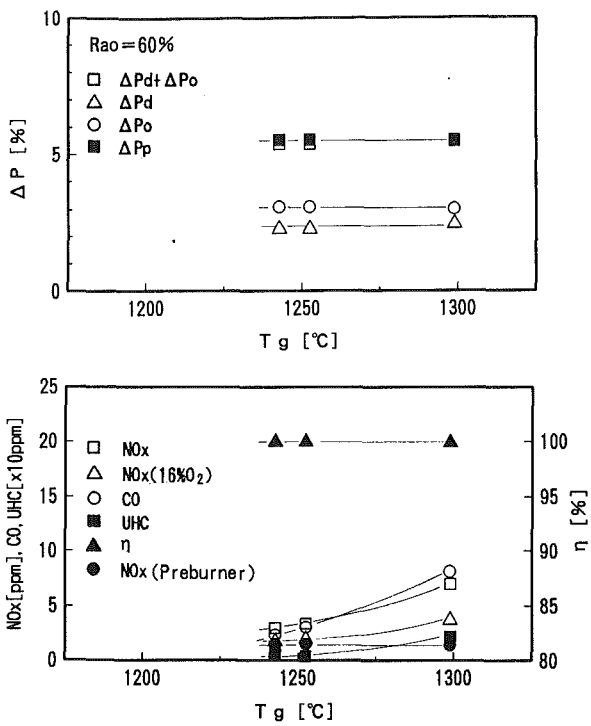

Fig. 8 Combustor performance with no baffle plate (CCT)

Since the catalyst temperature is controlled under 1000°C, concentration of the fuel fed into the catalyst is kept low. As a result, it can be inferred that the increase in NO_x emissions was because the fuel concentration in the premixing nozzles increased with an increase in *Rao*, and partial high-temperature areas increased in the premixed combustion zone.

Effects of Baffle Plate. In order to examine the effects of the baffle plate installed at the catalytic segment exit, a combustion test was conducted by removing the baffle plate. The results are shown in Fig. 8.

NO_x, CO, and UHC emissions increased when the baffle plate was removed. When *Tg* was 1300°C and λt was 2.22, NO_x emissions were 7 ppm (4 ppm at 16 percent O_2), those of CO 80 ppm, and those of UHC 20 ppm. Additionally, to make matters worse, removing the baffle plate caused oscillating combustion. On the other hand, the level of pressure loss was reduced to 5.5 percent, while *P.F.* was kept at about the same level as the case of the existing baffle plate.

Moreover, combustion performance was significantly influenced by *Rao*; when *Rao* exceeded 60 percent, NO_x, CO, UHC, and *P.F.* increased sharply.

Catalyst Performance. The same catalyst was used throughout the test, and the total reaction time was 18 hours and 30 minutes. During this time, the fuel was stopped abruptly 11 times, but no abnormality was observed.

From the above-mentioned results, it was confirmed that with a CCT-type combustor it was possible to achieve, while maintaining the catalyst temperature under 1000°C, low NO_x emissions and high combustion efficiency when the combustor exit gas temperature was at 1300°C. However, the results also indicated some problems, including: (1) Combustion performance declined when the ceramic baffle plate with uncertain reliability was removed; (2) the combustion temperature range of stable premixed combustion was narrow; and (3) pressure loss was at a high level.

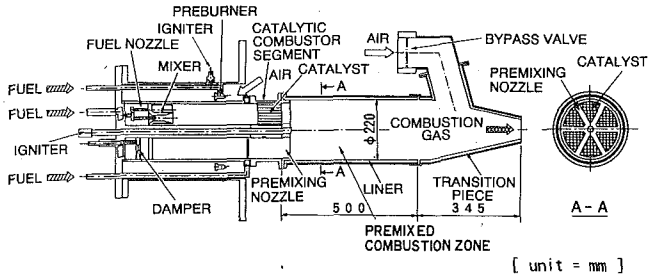

Fig. 9 ACC combustor

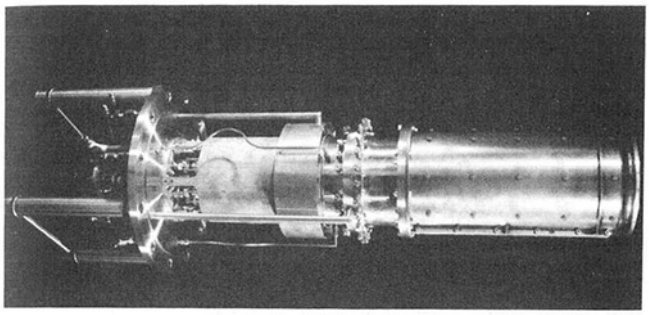

Photo 2 ACC combustor

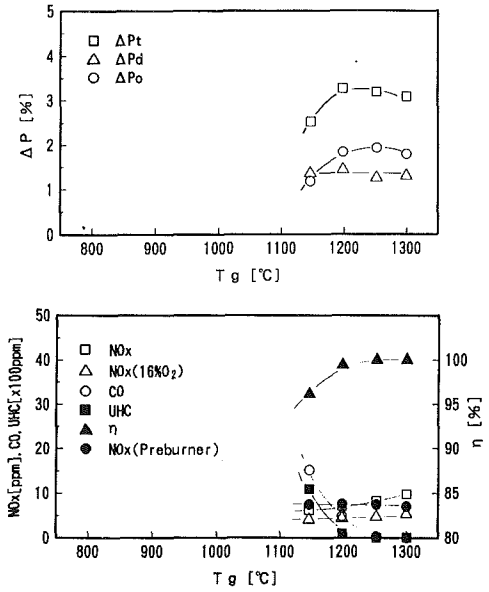

Fig. 10 Combustor performance with no bypass air (ACC)

ACC Combustor Design

In order to overcome these problems, without fitting the baffle plate, we designed an ACC combustor capable of promoting mixing of catalytic combustion gas and premixed gas. Figure 9 shows the ACC combustor, and Photo 2 its outlook.

The combustor consists of an annular preburner, catalytic combustor segments comprised of mixers and catalysts, premixing nozzles, a premixed combustion zone, and a transition piece fitted with an air bypass valve. Six catalytic segments and six premixing nozzles are arranged alternately to form a circle. The premixed combustion chamber and the transition piece are made by using ceramic fiber-type liners.

Air is fed into the combustor through the preburner, some of which is used to cool the liner. The air is heated to 450°C by the preburner, and is distributed to the catalytic segments and premixing nozzles. Combustion air for premixing nozzles is adjusted with a damper. In this test, however, the damper was left completely open. The air fed into the catalytic segments is mixed with the fuel by using the three venturi-type mixers that have been installed in each catalytic segment. The resultant mixture is then fed into the catalysts and catalytic combustion is conducted below 1000°C. The premixed gas from the premixing nozzles is injected around the axis of the combustor at a 60 deg angle counterclockwise to the flow of the catalytic combustion gas. The air bypass valve method used in conventional gas turbine combustors is adopted to deal with the low load operation [10]. The components of the catalysts are the same as those applied to CCT combustor. The sectional form of the catalyst is a concentric circle 204 mm in major diameter and 44 mm in minor diameter and radially divided into six parts. The catalyst 25 mm in length and 3.3 mm in cell pitch is charged in one stage.

Test Results

Effects of Combustor Exit Gas Temperature. Figure 10 shows the effects of Tg on emission properties, η, and ΔP. At 1300°C of Tg ($\lambda t = 2.22$) NO_x emissions were 10 ppm (5 ppm at 16 percent O_2), CO and UHC emissions were under 4 ppm, and η was nearly 100 percent. The level of NO_x emissions at the preburner was 7 ppm (λ of preburner = 20). Also, ΔP was 3 percent and *P.F.* was 21 percent. Moreover, while η dropped, stable combustion was maintained even when Tg was 1150°C ($\lambda t = 2.57$).

Since the level of NO_x emissions in the preburner was higher than those of the CCT-type combustor, NO_x emissions at the combustor exit increased, but they were within the targeted 10 ppm. By improvement of the preburner, NO_x emissions will be able to be reduced. By the way, as the test results of the CCT combustor indicate, NO_x emission in the premixed combustion zone is affected by *Rao*. In the case of the ACC combustor, *Rao* was estimated to be about 70 percent, but by readjusting proper *Rao*, NO_x emissions might be improved too.

The range of stable combustion expanded, and pressure losses were within the targeted 5 percent. However, the target of 15 percent for *P.F.* was not achieved. One possible reason is that the temperature of the central region in the premixed combustion zone rose because the ratio of premixed gas, of which the fuel concentration was high, grew high in this region.

Effects of the Air Bypass Valve. Figure 11 shows the results obtained when, keeping *Ta* and *Vat* constant, the combustion load was varied by controlling the air bypass valve and, at the same time, controlling the fuel flow so that *Tao*, *To*, and the inlet gas temperature of transition piece (*Tti*) were kept constant. By using the air bypass valve, it was possible to maintain stable combustion where NO_x emissions were kept below 10 ppm (6 ppm at 16 percent O_2) when Tg ranged from 1000°C ($\lambda t = 4.10$) to 1300°C ($\lambda t = 2.22$) and η was under 99.92 percent. Meanwhile, *P.F.* increased with an increase in the position percent of the bypass valve.

Figure 12 shows the results obtained when Tg was varied by adjusting the fuel for premixing nozzles with the air bypass valve left completely open. Premixed combustion was maintained when Tg ranged from 750°C ($\lambda t = 5.28$) to 1000°C ($\lambda t = 4.10$), while NO_x emissions were under 7 ppm (7 ppm at 16 percent O_2). Because combustion gas was diluted with bypass air, NO_x emissions at the combustor exit were lower than the preburner NO_x emission. Meanwhile, η declined with a fall in Tg, and η was below 99 percent when Tg was 910°C ($\lambda t = 4.71$).

By continually performing the operations described in Figs. 11 and 12, it is possible to achieve combustion performance where η is over 99.9 percent with Tg over 970°C ($\lambda t = 4.29$) and η is over 99 percent with Tg over 930°C ($\lambda t = 4.55$). The condition where λt is 4.55 is virtually equivalent to the 50 percent load of a gas turbine.

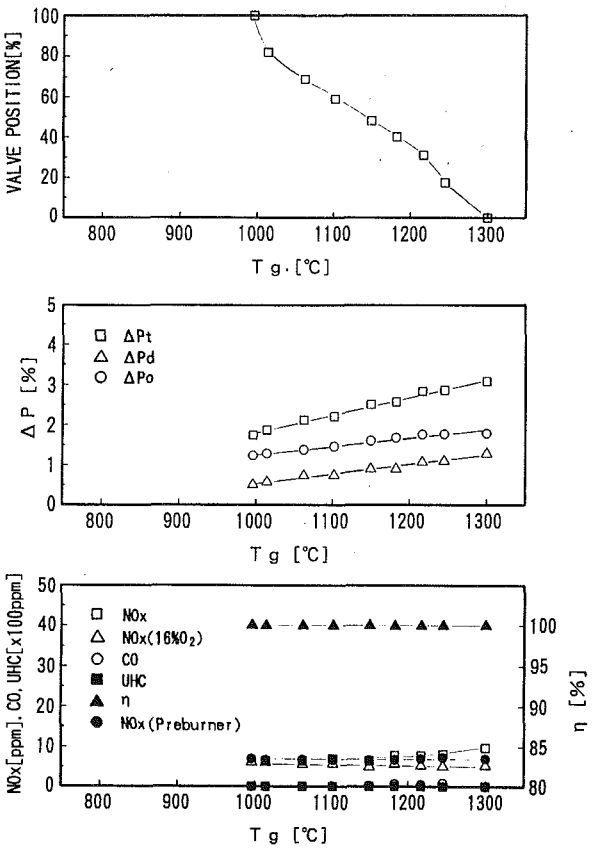

Fig. 11 Combustor performance using air bypass valve (ACC)

The temperature of the ceramic fiber layer of the inner liner wall was below 710°C, while that of the metal surface of the outer liner wall was below 400°C, indicating that the temperature at each of these locations was low enough.

There was absolutely no backfire throughout the test.

The total reaction time of the catalyst was 24 hours and 10 minutes. During this time, the fuel was stopped abruptly 13 times, but no abnormality was observed.

From these results it was confirmed that, while it was necessary to lower the amount of NO_x emissions formed in the preburner and *P.F.*, with an ACC combustor it was possible to achieve NO_x emissions under 10 ppm and a combustion efficiency over 99.9 percent without installing a ceramic baffle plate at the catalytic segment exit. By using the air bypass valve, it was possible to expand the load range of stable premixed combustion.

Conclusion

In order to relax the operating conditions of a catalyst, two types of catalytic combustor combined with premixed combustion were designed. Combustion performance was investigated at atmospheric pressure using natural gas.

In the case of the CCT combustor where catalytic combustor segments were arranged at the center of the burner system, around which was arranged a concentric circle of premixing nozzles, NO_x emissions of about 6 ppm and combustion efficiency of nearly 100 percent were obtained under the rated load condition where the combustor exit gas temperature was set at 1300°C. However, pressure losses exceeded the targeted level, stable combustion range was narrow, and combustion performance declined when the ceramic baffle plate was removed from the catalytic segment exit.

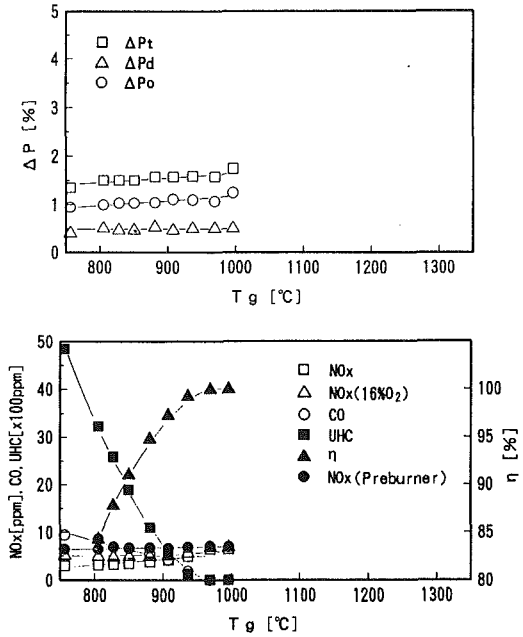

Fig. 12 Combustor performance with fully opened air bypass valve (ACC)

In the case of the ACC combustor, which installed no baffle plate and where catalytic combustor segments were arranged alternatively with premixing nozzles, the amount of NO_x emissions increased to 10 ppm, which was within the targeted level, and it was possible to achieve stable combustion within a wide loading range.

In the future we plan to improve NO_x emissions in the preburner and *P.F.* of the combustor exit gas, examine the effects of pressure, and evaluate catalytic performance.

Acknowledgments

Our deepest gratitude goes to T. Hisamatsu of CRIEPI, who helped us in promoting this research project, T. Yamanaka of KEPCO, who, for a period of time, joined us in carrying out this research, and H. Fukuzawa of CRIEPI, who helped us in experimentally producing the catalysts.

References

1 Pfefferle, W. C., Carrubba, R. V., et al., "Cata Thermal Combustion: A New Process for Low-Emissions Fuel Conversion," ASME Paper No. 75-WA/FU-1, 1975.

2 Anderson, D. N., Tacina, R. R., et al., "Performance of a Catalytic Reactor at Simulated Gas Turbine Operating Conditions," NASA TM X-71747, June 1975.

3 Blazowski, W. S., and Walsh, D. E., "Catalytic Combustion: An Important Consideration for Future Application," *Combustion Science and Technology*, Vol. 10, No. 5/6, 1975.

4 Krill, W. V., Kesselring, J. P., et al., "Catalytic Combustion for Gas Turbine Applications," ASME Paper No. 79-GT-188, 1979.

5 Fukuzawa, H., Ishihara, Y., "Catalytic Combustion for Gas Turbines," *Proceedings of a 4th Workshop on Catalytic Combustion*, EPA-600/9-80-035, Aug. 1980, pp. 349-364.

6 Orenstein, R. M., Hara, Y., et al., "Catalytic Combustion for Advanced Gas Turbines," Paper No. 91-YOKOHAMA-IGTC-108.

7 Yoshine, T., Hara, Y., et al., "Development of Gas Turbine Catalytic Combustor," Paper No. 91-YOKOHAMA-IGTC-109.

8 Ozawa, Y., Saiga, M., et al., "Design and Testing of Low NO_x Catalytic Combustor for Gas Turbine," Paper No. 91-YOKOHAMA-IGTC-107.

9 Hisamatsu,T., Abe, T., "Development of Ceramic Fiber Combustor of Gas Turbines," CRIEPI Report No. EW88004, Jan. 1989.

10 Pillsbury, P. W., Rieke, K. L., et al., EPRI Rep. AP-2584.

Detailed Performance Comparison of a Dump and Short Faired Combustor Diffuser System

J. F. Carrotte

P. A. Denman

A. P. Wray

Department of Transport Technology,
Loughborough University,
Loughborough, Leics, United Kingdom

P. Fry

Combustion Department, Rolls Royce plc,
Derby, United Kingdom

A rectangular model simulating four sectors of a combustion chamber was used to compare the performance of a standard dump diffuser, of overall length 180 mm, with that of a faired design 25.5 mm shorter. The performance of each system was assessed in terms of total pressure loss and static pressure recovery between prediffuser inlet and the annuli surrounding the flame tube. Since the program objective was to test design concepts only, no allowance was made for the presence of burner feed arms or flame tube support pins. In addition, tests were performed with relatively low levels of inlet turbulence and no wake mixing effects from upstream compressor blades. Relative to the dump design, the mass weighted total pressure loss to the outer and inner annuli was reduced by 30 and 40 percent, respectively, for the faired diffuser. Measurements around the flame tube head were used to identify regions of high loss within each system and account for the differences in performance. Within a dump diffuser the flow separates at prediffuser exit resulting in a free surface diffusion around the flame tube head and a recirculating flow in the dump cavity. This source of loss is eliminated in the faired system where the flow remains attached to the casings. Furthermore, the faired system exhibited similar velocity magnitudes and gradients around the combustor head despite its shorter length.

Introduction

One of the main objectives in aircraft engine design is to minimize weight. In the context of the combustor, this has led to the requirement for minimum length consistent with an acceptable total pressure loss and outlet temperature distribution. Since reducing the combustor burning length is prohibited by the need to meet pollution regulations, attention has therefore been focused on the diffuser system.

The primary function of a gas turbine combustor diffuser system is to distribute air issuing from the compressor around the flame tube. In current advanced core engines this objective is usually met with dump diffuser systems, which incorporate a prediffuser upstream of a recirculating dump region. Although such systems have relatively high losses, they are favored because of their inherent flow stability and insensitivity to manufacturing tolerances and thermal expansions. Such systems were initially investigated by Fishenden and Stevens [1] who monitored overall system performance while varying the prediffuser area ratio, dump gap, and mass-flow split to the inner and outer annuli. All tests were conducted with a flame tube that had a radial depth, expressed in terms of prediffuser inlet height (W/h_o), of 3.5. It was concluded that the principal determinants of total pressure loss in such systems are the amount of diffusion being attempted and the radius of curvature undertaken by the flow as it passes around the flame tube. This latter effect is a function of the size and shape of the flame tube and the dump gap. The more recent work of Young et al. [2], Stevens et al. [3], and Srinivasan et al. [4] illustrates the trend for flame tubes of increasing depth with values (W/h_o) in excess of 4.0. This implies a significant increase in the amount of turning and curvature that must be undertaken by the flow in the vicinity of the combustor head. Hence, although these modern systems have been optimized to produce an acceptable pressure loss in the shortest length possible, further reductions in length or increases in flame tube depth will result in relatively large increases in pressure loss. One possible method of maintaining system performance while achieving significant length reductions is therefore to define an alternative diffuser geometry.

A facility has been built at Loughborough (Fig. 1) that allows diffusers of different geometries to be tested. All models are four burner sectors wide and of rectangular cross section. Thus, it should be noted that diffusion of the flow in the circumferential direction present within annular systems is not simulated here. However, it is thought the relative performance of different diffusers can be accurately assessed while the rectangular geometry allows a large number of designs to be tested relatively easily. This paper outlines results relating to a standard dump diffuser (Fig. 2*a*), which is typical of current engine design practice. Its performance is compared with a faired design, which is 25.5 mm shorter (Fig. 2*b*), this representing

Contributed by the International Gas Turbine Institute and presented at the 38th International Gas Turbine and Aeroengine Congress and Exposition, Cincinnati, Ohio, May 24–27, 1993. Manuscript received at ASME Headquarters March 17, 1993. Paper No. 93-GT-331. Associate Technical Editor: H. Lukas.

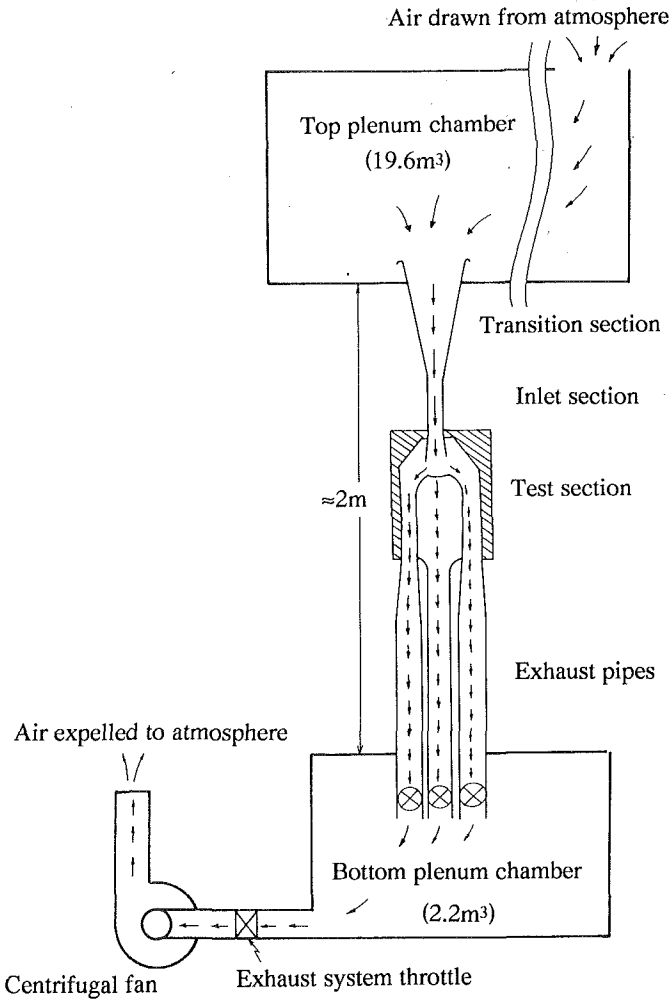

Fig. 1 Test facility—airflow paths

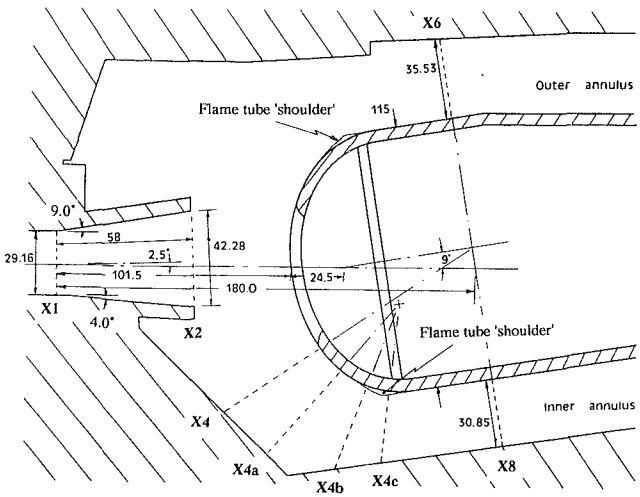

Fig. 2(*a*) Dump diffuser geometry

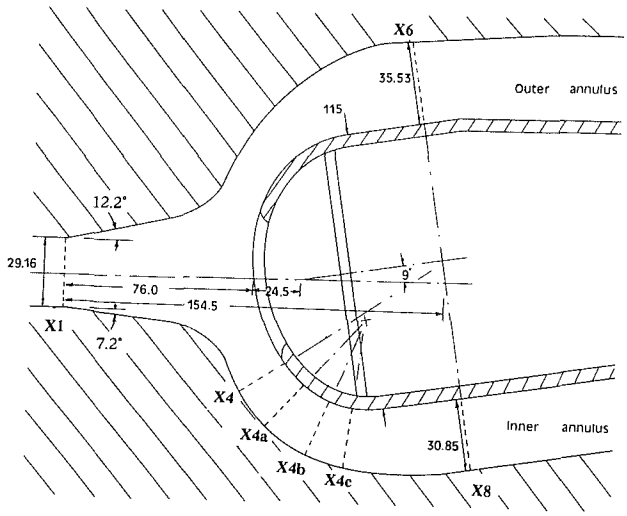

All dimensions in mm

Fig. 2(*b*) Faired diffuser geometry

a 14 percent reduction of overall system length. The performance of these systems is assessed in terms of the total pressure loss and static pressure recovery between prediffuser inlet and the annuli surrounding the flame tube head. Detailed measurements around the combustor head are also presented and used to identify the important processes and loss-generating mechanisms within both systems and thereby offer some explanation for any observed differences in performance.

Experimental Facility

Although of rectangular cross section, for ease of understanding the facility is described using terminology associated with the annular system it is trying to simulate. Hence, rectangular flow passages are described as annuli while at a given axial plane, locations are described in terms of radial and circumferential components. Furthermore, since the overall program objective was to investigate diffuser design concepts, all tests were performed without simulation of the burner feed arms, flame tube supports pins, and other detailed features that would be present within an operational system.

The test facility was manufactured predominantly out of Perspex, its modular design incorporating an inlet section, test section, and three exhaust pipes. Air was drawn from atmos-

Nomenclature

B = hot-wire calibration coefficient
C_p = static pressure recovery coefficient
E = mean hot-wire voltage
E_o = hot-wire voltage with no flow
h_o = prediffuser inlet height
h_1 = prediffuser exit height
K = button hook calibration factor
L = diffuser overall length
M = Mach number
n = hot-wire calibration coefficient
p = local mean static pressure
p_{ps} = local "pseudo" static pressure (Fig. 3)
P = local mean total pressure
q = dynamic head
R_n = nondimensional annulus height
r = radius relative to the center of curvature
t = static temperature
u_i = instantaneous velocity
u = local mean velocity
u' = fluctuating (rms) velocity component
α = kinetic energy flux coefficient
λ = total pressure loss coefficient
ρ = density

Superscripts

$\bar{}$ = mass-weighted mean value
$\tilde{}$ = momentum mix mean value

phere into a plenum box (Fig. 1), located above the vertically mounted rig, prior to entering the inlet section and passing through the test rig. This air was then exhausted into a plenum box, below the facility, prior to being expelled to atmosphere. A centrifugal fan, driven by an 11 kW variable speed motor, was located in the exhaust system and provided the pressure rise required to draw air through the facility.

The scale of the working section was such that diffuser dimensions were typical of those likely to be found within a large turbofan engine. For the standard dump geometry a 2.5 deg outwardly canted prediffuser was incorporated of length 58 mm, inlet height 29.16 mm, and an area ratio of 1.45 (Fig. 2*a*). This was designed according to the current rules for diffusers [6] and projected into the dump cavity. The gap between prediffuser exit and the combustor (i.e., dump gap D/h_1) was approximately 1.0, with the flame tube head being canted outward by 9 deg. Head porosity was provided by holes of diameter 50 mm, the flow then passing through the cowl back plate prior to entering the combustor primary zone. The total width of the rig was 360 mm and consisted of four burner sectors, each sector containing a cowl hole. However, measurements were limited to the central sector, 90 mm wide, where the effects due to the presence of the sidewalls were at a minimum. The faired system (Fig. 2*b*) was 25.5 mm shorter, which was achieved by moving the flame tube closer to prediffuser inlet. Hence, the amount of overall diffusion between the inlet plane and the annuli surrounding the flame tube was the same for both designs. In addition, liners were attached to alter the profile of the inner and outer casings while also modifying the prediffuser geometry. It should also be noted that the diffuser systems incorporated slight variations in flame tube head geometry. In the dump system, sharp edged "lips" or shoulders on the combustor at entry to the outer and inner annuli reflected current engine hardware, their presence being due to flame tube manufacturing techniques. These were found to have virtually no effect on the performance of the dump system [5], and were not present for the tests on the faired system.

All measurements were obtained with low levels ($Tu < 1$ percent) of inlet turbulence and in the absence of compressor blade wakes. The distribution of mass flow to the flame tube, inner and outer annuli was controlled by throttles located in the downstream exhaust pipes. In addition to these three individually controllable flow paths, a further throttle in the exhaust system was used to control the total mass flow passing through the test rig. The facility was operated at a constant prediffuser inlet Mach number of 0.14, which corresponded to a Reynolds number based on the prediffuser inlet hydraulic diameter of 1.8×10^5. The mass flow split around the flame tube head was nominally set to

Inner annulus	43.1 percent
Flame tube	14.9 percent
Outer annulus	42.0 percent

This mass flow split was maintained within ±0.3 percent of these values, thereby ensuring that the amount of flow diffusion to the outer and inner annuli was the same in all tests.

Instrumentation and Data Acquisition

The quantitative performance was mainly assessed using "button hook" pitot probes (Fig. 3), which could be inserted into the facility through holes of the same approximate diameter as that of the probe stem. Radial movement of each probe was controlled by a stepper motor, whereas a probe was circumferentially located either through discrete holes or small slots within which the probe and an associated blanking plate could slide. At any point in the flow the "button hook" pitot probes were used to obtain static as well as total pressures and this information was complemented by numerous wall static

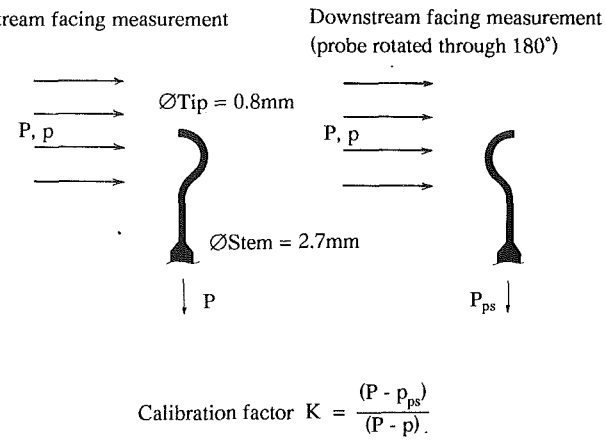

Fig. 3 Button hook probe operation

tappings located around the flame tube head and within the outer and inner annuli. In addition, constant temperature anemometry using a single hot-wire probe (Dantec type 55P11) was also used to give information on the turbulence levels within each diffuser system.

The overall performance of each system was assessed from measurements made at prediffuser inlet (X1) and the traverse planes farthest downstream within the outer and inner annuli (X6, X8). The axial location of these latter planes coincided with that of the primary port admission holes that would be present in engine hardware. At these planes some 20 data points were recorded for each radial traverse, this being repeated at 21 circumferential locations spaced over the 90 mm between burners. Measurements were also made at traverse planes X4 to X4c in order to indicate the nature of the flow passing around the flame tube head. However, in this case measurements were restricted to a single circumferential position located midway between burners, with approximately 20 data points being collected at each traverse plane.

All pressures were measured using transducers, which produced an analogue output signal proportional to the pressure measured. These voltage signals were digitized using an analogue to digital convertor (ADC), with the 5 second averaging of each signal being based on 250 samples at intervals of 20 milliseconds. Hot-wire voltage signals from a Dantec CTA 56C17 bridge circuit were similarly recorded, although these values were based on a 10 second averaging of the data.

Data Reduction

The curvature of flow around the flame tube head means that conditions in this region could not be defined using a pitot probe and wall static tapping. Instead, the technique outlined by Fry [7] was adopted in which the "button hook" probe, as well as being used as a conventional pitot probe, was also used to obtain local static pressure within the flow field. By recording the upstream (total) pressure and the value obtained when the "button hook" probe was rotated through 180 deg, into the downstream direction, the static pressure could be deduced with the aid of a suitable calibration. The calibration factor was assumed constant for a given probe and was defined as:

$$K = \frac{(P - p_{ps})}{(P - p)} \tag{1}$$

where P is the total pressure of the flow measured by the probe when facing upstream, p_{ps} is the "pseudo" static pressure recorded by the probe when pointing downstream, and p is the flow true static pressure (Fig. 3). Since the probe was calibrated prior to its use on the test rig, at a given point in

the flow the true static pressure could be calculated from the measured values of P and p_{ps}. Calibration of each probe was performed in a low-turbulence calibration facility for which the conditions at the working section could be accurately defined. Over the speed range of 10 m/s to 40 m/s the values of K were within ± 1 percent of the mean value.

Calibration of each single hot-wire was based on the law:

$$E^2 - E_o^2 = Bu^n \tag{2}$$

where E is the measured voltage and E_o the "wind off" voltage of a hot wire with calibration coefficients B and n. Turbulence intensity was calculated using the formula:

$$Tu = \frac{u'}{u} = \frac{E_{\text{rms}}}{E^2 - E_o^2} \cdot \frac{2E}{n} \tag{3}$$

where E_{rms} is the root mean square of the fluctuating voltage component. The fluctuating (rms) velocity (u') was calculated from the turbulence intensity and the mean velocity at that point in the flow field.

At any measurement plane the mass flow rate and mean velocity were defined as:

$$m = \int \rho u dA = \rho \bar{u} A \tag{4}$$

while spatially averaged values of total and static pressure at each plane were derived using both mass-weighted and momentum mix techniques [8].

Mass Weighting

$$\bar{P} = \frac{1}{m} \int P dm = \frac{1}{\rho \bar{u}} \int P \rho u dA$$

$$\bar{p} = \frac{1}{m} \int p dm = \frac{1}{\rho \bar{u}} \int p \rho u dA \tag{5}$$

In addition, a kinetic energy flux coefficient (α) is defined that compares the kinetic energy flux of the measured velocity profile with that of a uniform profile with similar mass flow:

$$\alpha = \frac{\int \frac{1}{2} u^2 \rho u dA}{\frac{1}{2} \bar{u}^2 \rho \bar{u} A} \tag{6}$$

so that

$$\bar{P} = \bar{p} + \alpha \frac{1}{2} \rho \bar{u}^2 = \bar{p} + \bar{q}$$

It should be noted that it is the pressures derived from this technique that are used to define the performance of each diffuser system.

Momentum Mix. The spatially averaged total and static pressures obtained from this method are the values that would be recorded if a nonuniform flow mixed out to uniformity in a duct of constant area and in the absence of heat transfer and wall friction. Hence, the momentum mix total pressure is always lower than the mass-weighted value since it includes the pressure loss associated with the mixing out of the nonuniform profile. As outlined by Livesey and Hugh [8], the calculation of the equivalent uniform stream is based on continuity of mass, momentum, and energy flux.

Momentum:

$$\int p(1 + \gamma \mathrm{M}^2) dA = \tilde{p} A (1 + \gamma \tilde{\mathrm{M}}^2) \tag{7}$$

Mass:

$$\int \frac{p}{Rt} u dA = \tilde{p} \tilde{\mathrm{M}} A \sqrt{\frac{\gamma}{R\tilde{t}}} \tag{8}$$

Energy Flux:

$$\int C_p \left(t + \frac{u^2}{2C_p} \right) \frac{p}{Rt} u dA = m C_p \tilde{t} \left(1 + \frac{\gamma - 1}{2} \tilde{\mathrm{M}}^2 \right) \tag{9}$$

The three unknowns ($\tilde{p}$, $\tilde{\mathrm{M}}$, $\tilde{t}$) can be obtained using these three equations, which allows the momentum mix total pressure to be calculated from compressible flow relationships. It should be noted that in this paper, these pressures are mainly used to assess the loss in the outer and inner annuli that is associated with the mixing out of the highly distorted profile in these regions.

Changes in the spatially averaged pressures between plane "b" and an upstream plane "a" within each diffuser system are expressed in terms of the total pressure loss (λ) and static pressure recovery (C_p) coefficients:

$$\lambda_{a-b} = \frac{P_a - P_b}{P_a - p_a} \qquad C_{p_{a-b}} = \frac{p_b - p_a}{P_a - p_a} \tag{10}$$

Note that these coefficients can be based on either mass-weighted or momentum mix spatially averaged pressures.

Information concerning the radial distribution of flow properties at a measurement plane is given in terms of pitch-averaged profiles, which are derived by averaging the relevant flow parameter in the circumferential direction. At a specific annulus height, a pitch-averaged velocity therefore represents the area-weighted mean value of the velocities measured at that height and is nondimensionalized by the overall mean velocity for that traverse plane. Around the flame tube head, the total pressure distributions are nondimensionalized with respect to the mass-weighted total pressure at that plane and the mass-weighted total and static pressures for the short faired design at plane X8.

Estimate of Experimental Errors

Mass-weighted pressures at the traverse plane X1, X6, and X8 were repeatable to better than ± 1 mm H_2O, a variation of less than ± 1 percent of the inlet dynamic head. This results in the derived total pressure loss and static pressure rise coefficients relating to overall diffuser performance being repeatable to better than ± 0.007 of a given value.

Because of flow curvature, turbulence levels, and the shape of the velocity profiles, it is extremely difficult to obtain an accurate definition of the flow parameters around the flame tube head. For example, the maximum velocities derived from the "button hook" probes at planes X4 to X4c were consistently greater, by up to 8 percent, than the values indicated by the hot-wire data. The relatively poor resolution of these data should therefore be considered when viewing the results. Based on these differences in velocity it has been estimated that the spatially averaged pressures in this region are only repeatable to within ± 4 mm H_2O, resulting in loss coefficients being accurate to within ± 0.03 of a given value. However, as will be subsequently shown using the measured pressure values obtained within each diffuser, it is thought the accuracy of these data is better than this estimate.

One problem associated with facilities that only simulate sectors of a fully annular flow field is that of the growth of boundary layers on each sidewall. Due to the diffusing nature of the flow field this is of particular significance in the present investigation and leads to the migration of fluid toward the center of the rig. Detailed measurements of these sidewall boundary layers indicated that at planes X8 and X6 up to 10 percent more flow was passing through the central burner sector, where diffuser performance was assessed, due to this effect. This reduces the amount of diffusion undertaken by the flow in the central measurement region, which will lead to errors in the absolute values of the performance parameters. However, measurements indicated the sidewall boundary layer effect was the same for each diffuser geometry tested therefore

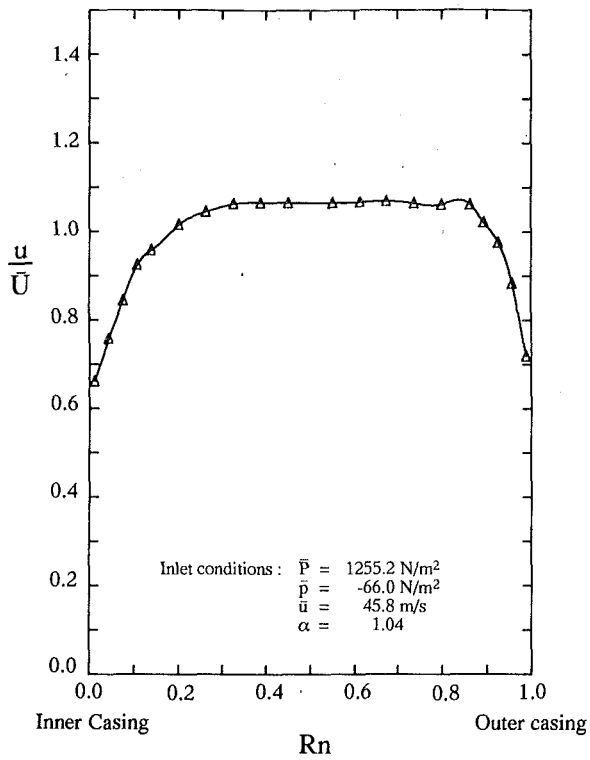

Fig. 4 Pitch-averaged velocity profile—diffuser inlet (X1)

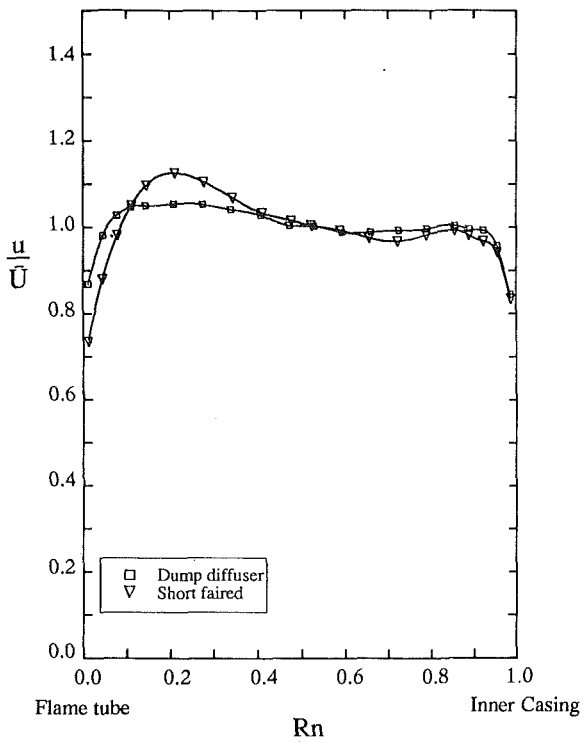

Fig. 5 Pitch-averaged velocity profiles—inner annulus (X8)

Table 1 Overall diffuser performance data (mass weighted)

	Dump diffuser	Faired diffuser
Outer annulus:	λ_{1-6} = 0.318	λ_{1-6} = 0.221(-30%)
	C_{p1-6} = 0.469	C_{p1-6} = 0.519
Inner annulus:	λ_{1-8} = 0.302	λ_{1-8} = 0.181(-40%)
	C_{p1-8} = 0.454	C_{p1-8} = 0.535
Flux coefficients:	α_1 = 1.04	α_1 = 1.04
	α_6 = 1.09	α_6 = 1.26
	α_8 = 1.02	α_8 = 1.04

allowing the relative performance of each system to be evaluated.

Results and Discussion

Inlet Conditions. Tests were performed with a clean upstream geometry resulting in relatively thin boundary layers (Fig. 4) at prediffuser inlet with no simulated compressor blade wakes. Turbulence intensity was less than 1 percent in the midpassage region. Stevens et al. [9] have already indicated the favorable mixing effects on diffuser boundary layers that can be produced when blade wakes are present. Within experimental error these inlet conditions were the same for the two geometries tested.

Overall System Performances. For the standard dump design, the mass-weighted total pressure loss (λ) to the outer (X6) and inner (X8) annuli was 0.318 and 0.302, respectively (Table 1). Allowing for differences in the geometry tested, these values are thought to be in reasonable agreement with previous results. For example, with no head porosity and a smaller flame tube depth ($W/h_o = 3.5$) Fishenden and Stevens [1] recorded loss values to each annulus of 0.24. In contrast, on a deeper flame tube ($W/h_o = 5.5$) but at a larger dump gap ($D/h_1 = 1.1$) Stevens et al. [31] recorded losses of 0.336 (outer) and 0.313 (inner). In these latter tests, however, the losses are thought to be relatively low, since performance was not evaluated from area traverses, but at a single circumferential location midway between burners.

Results from the faired diffuser show a significant reduction in total pressure loss and an associated improvement in static pressure recovery relative to the dump system (Table 1). For the flow passing to the outer annulus the mass-weighted pressure loss was reduced by 30 percent while a 40 percent loss reduction was observed for the inner annulus flow. This improvement in performance is, of course, in addition to the length reduction of 25.5 mm offered by the short faired design. For a dump diffuser this length reduction would have been obtained by an effective change in the dump gap (D/h_1) from 1.03 to 0.43. On tests with a flame tube of relatively small depth ($W/h_o = 3.5$), Fishenden and Stevens [1] observed a 15 percent loss increase for a dump gap reduction of this magnitude. However, Srinivasan et al. [4] using a flame tube of more comparable geometry ($W/h_o = 4.1$) indicated loss increases of between 30 and 60 percent depending on mass flow split.

The radial distribution of fluid within the outer and inner annuli of each diffuser system is shown by the pitch-averaged velocity profiles at the measurement planes (X6, X8). For both diffusers, the flow within the inner annulus appears to be relatively well mixed out (Fig. 5) with virtually no difference between the two systems. However, this is not the case within the outer annulus, where the profiles show a noticeable bias toward the flame tube (Fig. 6). Furthermore, the lower loss associated with the faired system has resulted in a more distorted profile in this region, and this is also confirmed by the kinetic energy flux coefficients (Table 1). It could be argued that this profile reflects an inherent loss that has yet to be realized, so that a relatively high pressure loss will occur within the outer annulus, downstream of plane X6, as the more distorted profile mixes out. However, estimates based on the momentum mix values indicate this could only result in the loss reduction for the faired diffuser falling from 30 to 27 percent.

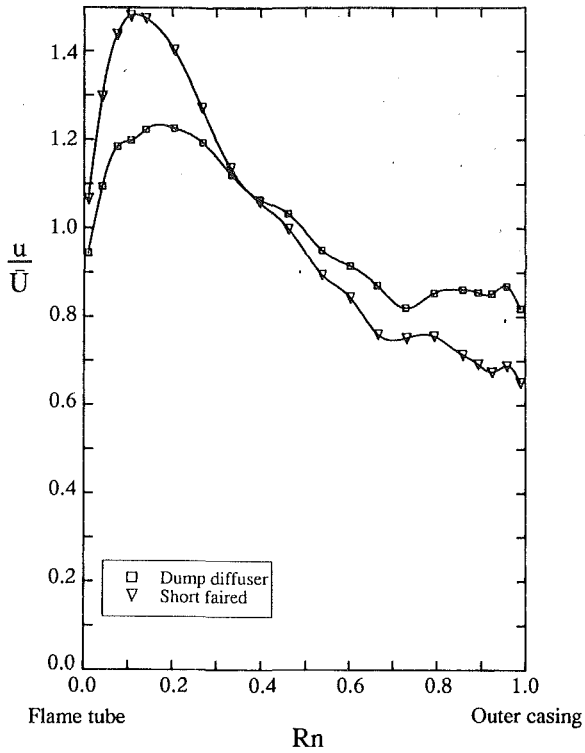

Fig. 6 Pitch-averaged velocity profiles—outer annulus (X6)

Table 2 Flame tube head pressure loss data

	Dump diffuser	Faired diffuser
Mass weighted :	λ_{1-2} = 0.03 (10%)	–
	λ_{1-4} = 0.09 (30%)	λ_{1-4} = 0.01 (5.%)
	λ_{1-4a} = 0.15 (50%)	λ_{1-4a} = 0.06 (30%)
	λ_{1-4b} = 0.21 (70%)	λ_{1-4b} = 0.10 (50%)
	λ_{1-4c} = 0.26 (87%)	λ_{1-4c} = 0.17 (85%)
	λ_{1-8} = 0.30 (100%)	λ_{1-8} = 0.20 (100%)
Momentum mix :	λ_{1-4} = 0.15 (48%)	λ_{1-4} = 0.05 (25%)
	λ_{1-4a} = 0.22 (71%)	λ_{1-4a} = 0.12 (60%)
	λ_{1-4b} = 0.26 (84%)	λ_{1-4b} = 0.16 (80%)
	λ_{1-4c} = 0.30 (97%)	λ_{1-4c} = 0.19 (95%)
	λ_{1-8} = 0.31 (100%)	λ_{1-8} = 0.20 (100%)

Detailed Diffuser Performances. Using a hot wire and button hook probe, attempts have been made to define the flow field around the flame tube head of each diffuser system and thereby account for differences in their overall performance. Measurements were restricted to the rig centerline, midway between cowl holes, and concentrated on the inner annulus flow, which exhibited the greatest differences in loss. Up to six planes were traversed within each system, although for reasons of brevity only a limited number of the measured distributions are presented here. It should also be noted that in the dump diffuser, no attempt was made to define the recirculating flow field within the dump cavity. Hence, for this system spatially averaged pressure values at each plane (Table 2) were only evaluated for the flow passing directly into the downstream annulus. The streamline dividing the mainstream and recirculating flow was defined as that which gave the required mass flow upon integration of the velocity profile between this location and the flame tube surface.

In the past, very few measurements have been made on the flow field around a flame tube head due to the difficulty of making accurate measurements in such regions. Concern has also been expressed as to the quality of data obtained from this investigation, since differences in velocity of up to 8 percent were recorded between the hot wire and button hook probes. However, the mass-weighted and momentum mix pressure data for each plane (Table 2) appear to correlate reasonably well and agree with the measurements of relatively high accuracy at plane X8. This has been expressed graphically in terms of the position of each plane within the dump and faired systems (Fig. 7), their location being defined as the intersection point along a streamline passing down the center of the prediffuser and through the maximum velocity points around the flame tube head. It can be seen that both the mass-weighted and momentum mix pressure loss data lie on reasonably smooth curves with no significant discontinuities. This correlation of the data between planes therefore gives some degree of confidence in the pressure measurements and of the loss values quoted for each station.

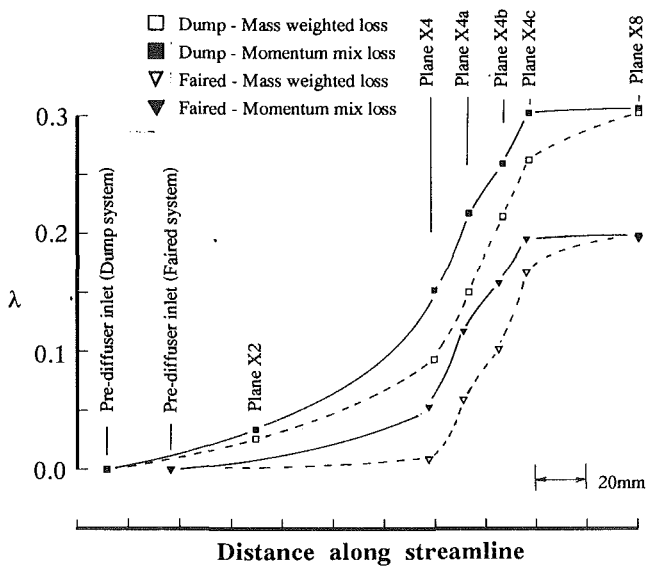

Fig. 7 Pressure loss (λ) through each diffuser system

Dump Diffuser. For the dump system approximately 10 percent of the mass-weighted total pressure loss ($\lambda_{1-2}=0.03$) occurs within the prediffuser and is confined to the fluid within the boundary layers adjacent to each casing. At prediffuser exit the flow then separates and rolls up to form a recirculation zone in the dump cavity. The size of this region is indicated by the velocity profile at plane X4 (Fig. 8*a*), with reattachment of the flow to the inner casing occurring in the region of plane X4c (Fig. 8*b*). This vortex in the dump cavity bounds the mainstream flow, which is discharged into the dump region and impinges on the flame tube head.

At plane X4 (Fig. 8*a*), the high-velocity region close to the flame tube surface indicates acceleration of the flow away from the stagnation point, with velocities in excess of 40 m/s being recorded. This acceleration continues around the flame tube head with the maximum velocity occurring in the vicinity of plane X4b. However, at greater distances from the surface, the velocity decreases rapidly, producing a highly sheared profile with kinetic energy flux coefficients in excess of 1.7. The distorted profile is mainly associated with the curvature of the flow that is required in order for it to pass around the flame tube head. Since flow curvature is still present at plane X4c the profile is still highly sheared (Fig. 8*b*), but downstream of this location the turning is complete with the flow entering the inner annulus. Comparison of the velocity distributions at planes X4c and X8 indicate a rapid mixing out of the profile in this region.

The measured fluctuating velocities were recorded with a

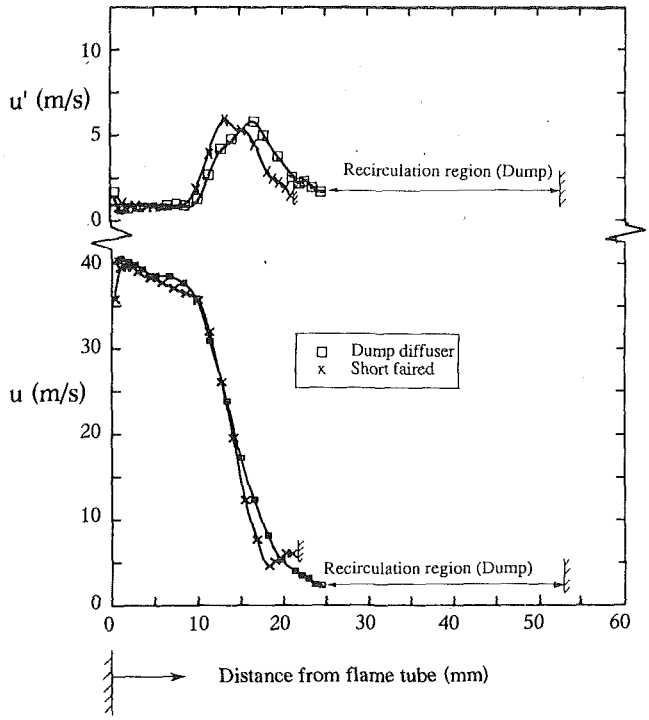

Fig. 8(*a*) Velocity profiles—plane X4

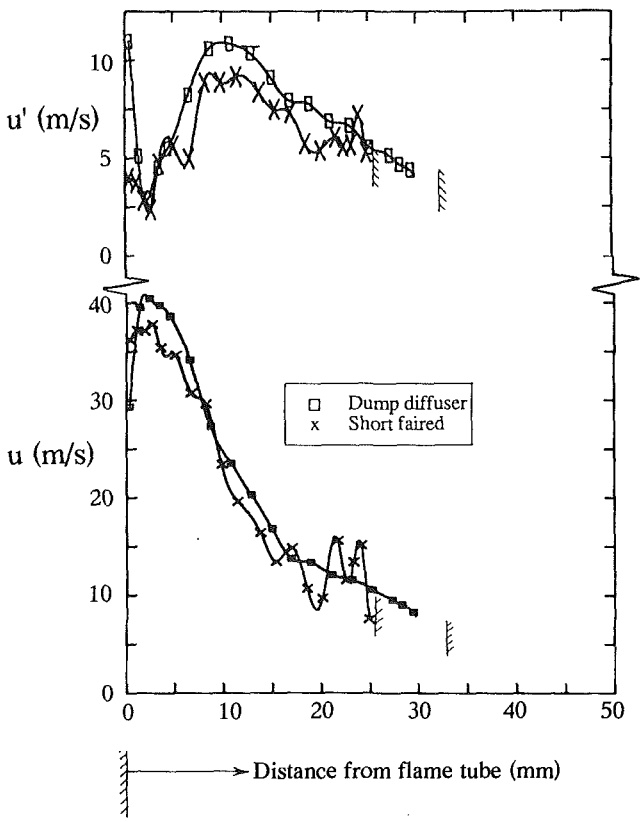

Fig. 8(*b*) Velocity profiles—plane X4c

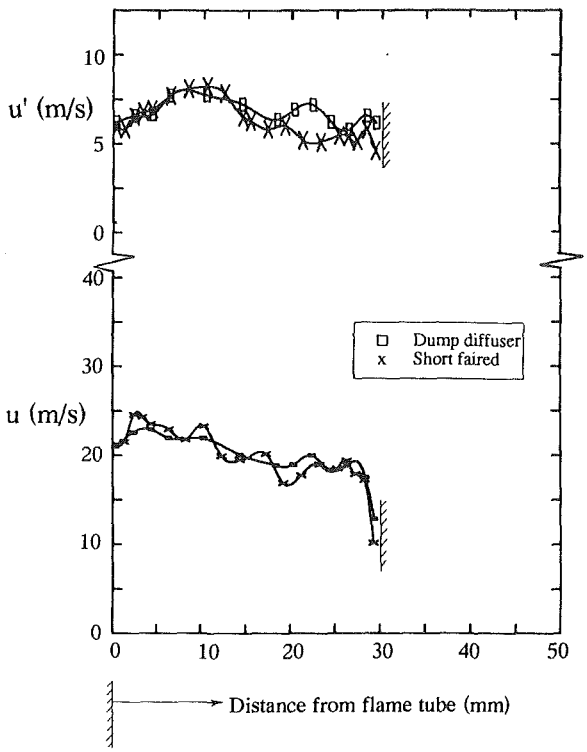

Fig. 8(*c*) Velocity profiles—plane X8

hot wire, which was sensitive to the components both parallel and perpendicular to the flame tube head but not to the component in the circumferential direction. These velocities are therefore thought to be a good indication of the turbulent kinetic energy levels and at plane X4 (Fig. 8*a*) it can be seen that, as expected, this corresponds to the region of highly sheared flow. This continues to be the case around the flame tube head, with the turbulent energy levels increasing steadily to reach a maximum value at plane X4c (Fig. 8*b*). In addition, the growth of the boundary layer on the flame tube head also produces turbulent flow, which can be observed at this plane. These high turbulence levels then assist in the rapid mixing out of the velocity profile between plane X4c and X8.

Since the turbulent energy is extracted from the mean flow there is a good correlation between regions of high turbulence and pressure loss. For example, approximately 30 percent of the system loss has occurred by plane X4, but the measured pressure levels close to the flame tube (1 mm–8 mm) are virtually the same as the maximum pressures recorded at prediffuser inlet (Fig. 9*a*). Hence, at this plane the loss is not associated with this high-velocity fluid but with the shear layer farther away from the surface. The fluid in this shear layer continues to exhibit large pressure losses farther around the head, with over 50 percent of the total system loss being generated within the relatively small region between plane X4 and X4c (Table 2). This region of sheared flow and relatively high pressure loss is thought to be associated with two important loss generating mechanisms:

(*i*) Dump loss: Energy has to be extracted from the mainstream flow passing through the diffuser in order to drive the recirculating flow in the dump cavity. This energy is extracted from the flow adjacent to the recirculation region, thereby increasing local velocity gradients and accounting for some of the observed turbulence and pressure loss.

(*ii*) Turning loss: As already observed, a heavily distorted velocity profile is observed as the flow is deflected around the flame tube head. This sheared flow must lead to the production of turbulent kinetic energy. However, as outlined by Fishenden and Stevens [1] this generation process will be significantly enhanced by the effects of streamline curvature. This is due to the unstable nature of a turbulent flow when the product of the local velocity and radius of curvature (ur) decreases with increasing radius of curvature (r). It can be seen that, apart from the boundary layer close to the flame tube head, the bulk

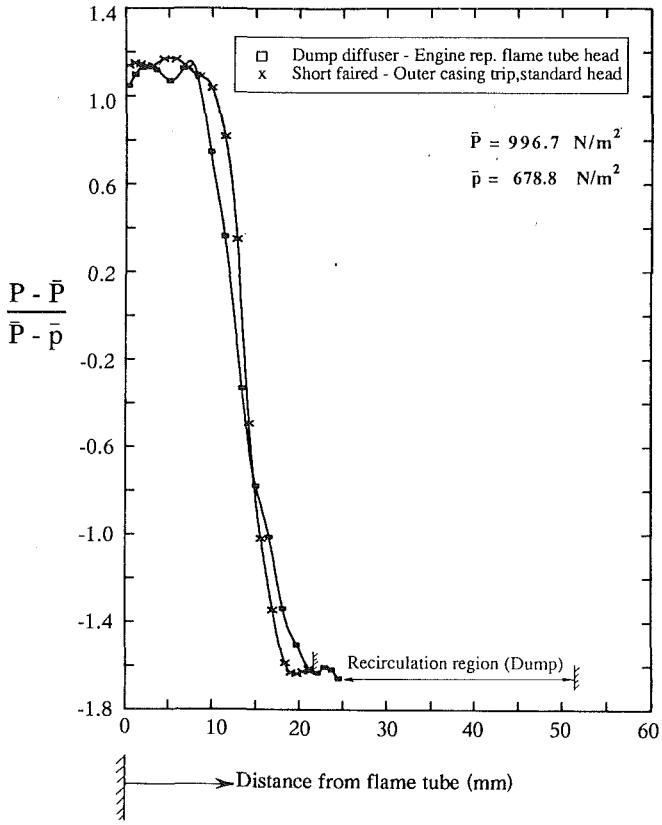

Fig. 9(*a*) Total pressure profiles—plane X4

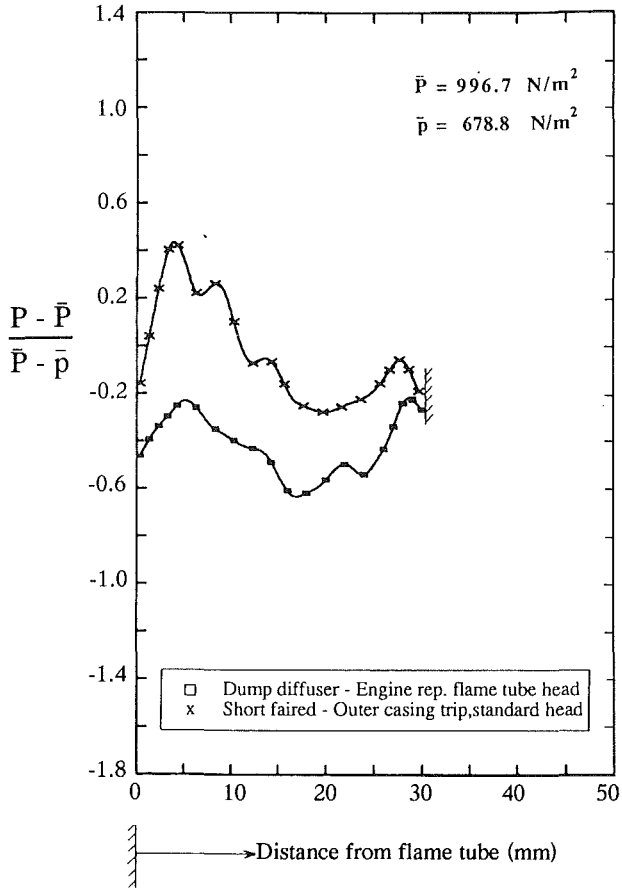

Fig. 9(*c*) Total pressure profiles—plane X8

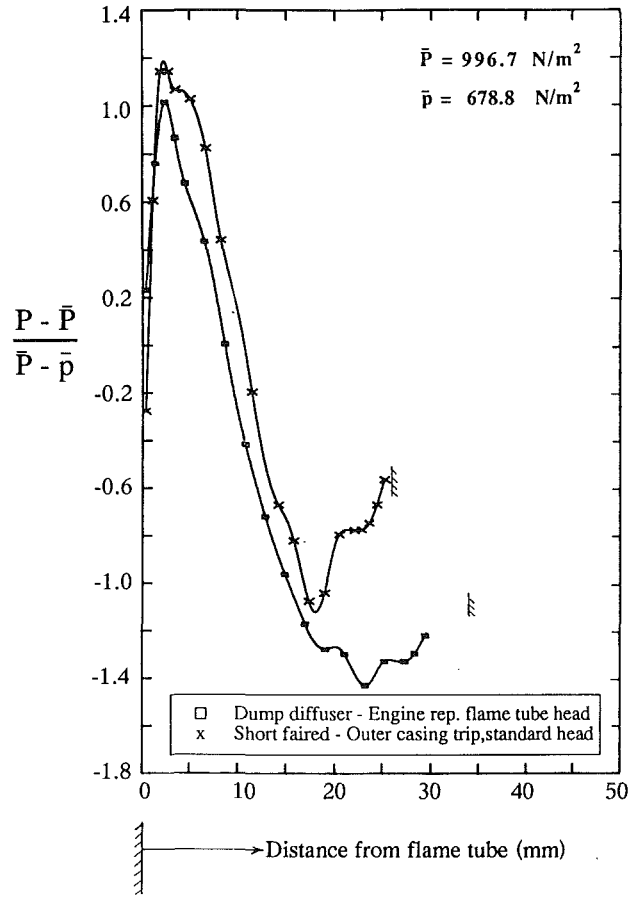

Fig. 9(*b*) Total pressure profiles—plane X4c

of the profile is unstable and will result in a significant enhancement of turbulent energy production.

Downstream of plane X4c a further loss in total pressure of approximately 10 to 15 percent occurs, with the large amounts of mixing in this region also producing a more uniform pressure distribution at X8. However, it can also be seen that between these planes virtually no change is observed in the levels of momentum mix total pressure (Table 2). Hence, the mass-weighted total pressure loss in this region is associated with the mixing out of the distorted profile that was observed at plane X4c and which was generated by the upstream turning of the flow.

Faired System. The faired system has no data available at plane X2 (prediffuser exit), but the total pressure loss up to plane X4 ($\lambda_{1-4}=0.01$) is significantly less than that observed for the dump system ($\lambda_{1-4}=0.09$). However, it should be remembered that within each diffuser system the geometry and flow conditions upstream of plane X4 are extremely different. The faired system incorporates a higher area ratio prediffuser, which may lower the dynamic head at prediffuser exit and thereby reduce losses around the combustor head. But also to be expected with this change in prediffuser area ratio is an increase in loss associated with this component. However, comparison of the dump prediffuser loss ($\lambda_{1-2}=0.03$) with the faired system measurement at plane X4 ($\lambda_{1-4}=0.01$) indicates the reverse effect. This is thought to be due to the flame tube influence on the upstream flow, which, as outlined by Stevens et al. [3], increases the static pressure at the center of a prediffuser passage while reducing the adverse pressure gradient along each casing. In this way prediffuser performance can be improved due to the lower maximum velocities in the passage center and the thinner boundary layers. For the faired system

the closer proximity of the flame tube, due to its 25.5 mm movement toward the inlet plane, is therefore thought responsible for the reduction in prediffuser total pressure loss.

At exit from the prediffuser the close proximity of the flame tube along with the contoured casing profile avoids flow separation within the faired system. In fact, midway between cowl holes the flow initially undergoes a modest acceleration, which will further minimize pressure loss, prior to undergoing a controlled diffusion around the combustor head. This preturning of the flow may reduce local rates of curvature in this region, while the velocity profiles at plane X4 (Fig. 8*a*) show the elimination of the large dump recirculation within the faired system. A significant reduction in pressure loss will therefore occur since no energy is being extracted to drive the recirculating flow within the dump cavity. Comparison of the total pressure distributions at this plane (Fig. 9*a*) shows the reduction in mass-weighted pressure loss at plane X4 is associated with the flow between 9 mm and 15 mm from the flame tube surface. However, this difference in pressure loss is not reflected by the measured overall levels of fluctuating velocity and hence turbulent energy at this location (Fig. 8*a*). It is therefore thought that a significant proportion of the turbulent energy generated within the dump diffuser is transported into the recirculation region, which is not defined in the results presented here.

Approximately 80 percent of the total loss within the faired system occurs between planes X4 and X4c (Table 2), and it is in this region where flow turning and streamline curvature effects are dominant. However, the absolute loss value in this region ($\Delta\lambda = 0.16$) is virtually the same as that recorded for the dump diffuser ($\Delta\lambda = 0.17$). It has already been noted that reducing the dump diffuser length by 25.5 mm would significantly increase the system loss and this would be associated with higher velocities and steeper velocity gradients around the flame tube head. However, despite the shorter length of the faired system, at plane X4 the velocity profiles are remarkably similar to that of the longer dump diffuser (Fig. 8*a*). This continues to be the case farther downstream at plane X4c (Fig. 8*b*), where the fluctuating velocities are also reduced and the difference in pressure loss between the two systems is more apparent (Fig. 9*b*). The similarity of the velocity profiles around the flame tube head is also confirmed by the previous diagram (Fig. 7), which showed the mass-weighted and momentum mix pressures at each plane. The difference between these curves reflects the total pressure loss due to the distorted velocity profiles mixing out and is seen to be remarkably similar for each design. Thus, in addition to eliminating the energy loss required to maintain the recirculation within the dump cavity, it appears that preturning the flow at prediffuser exit and keeping it attached to the inner casing helps reduce the velocity magnitudes and gradients around the flame tube head. In this way, relative to the dump design, a length reduction of 25.5 mm has been achieved for the faired system without increasing the loss between planes X4 and X4c.

A further mass-weighted pressure loss ($\Delta\lambda = 0.03$) occurs between planes X4c and X8 (Table 2). However, as was also the case for the dump system, the momentum mix total pressures are virtually constant in this region, and so this loss is mainly associated with the mixing out of the distorted profile that was generated around the flame tube head. The fact that this profile appears not to be as well mixed out in the faired system is thought to be due to the lower upstream turbulence levels.

Stability of the Faired System. Although the dump diffuser system has always exhibited relatively high losses, its use has been widespread due to its inherent flow stability and insensitivity to manufacturing tolerances and thermal expansions. In contrast the faired system can be unstable, and this was illustrated in the present investigation by reducing the amount of air passing down the outer and inner annuli by increasing the flame tube mass flow. This off-design-point operation increased the amount of flow diffusion being attempted by the flow passing to each annulus and resulted in a flow separation that had no clearly defined location. This led to an instability with the flow switching between the inner and outer annuli and would have been an unacceptable occurrence under operational conditions [5]. In contrast the dump system has a clearly defined separation point at prediffuser exit and allows stable operation over a wide range of conditions. However, with the trend for flame tubes of greater depth and diffusers of shorter length so the difference in total pressure loss and static pressure recovery between the two systems will to continue to grow. It is thought the present results merely reflect this trend and so a point may be reached where the potential gains are sufficient to merit the use of a faired system so long as the instability problems can be addressed. Alternatively a hybrid design may be possible that offers some of the performance improvements of a faired system but that maintains the stability characteristics of a dump diffuser.

Conclusions

The performance of a standard dump diffuser system has been investigated and compared with a faired design that was 25.5 mm shorter. The following conclusions have been drawn:

- The mass-weighted total pressure loss coefficients (λ) between prediffuser inlet and the inner and outer annuli were reduced by 40 percent (inner) and 30 percent (outer) for the faired system. This improvement in overall performance is in addition to the 25.5 mm length reduction offered by this system.
- In the dump diffuser the flow separated at prediffuser exit and reattached to the inner casing at entry to the inner annulus. However, this recirculation loss was eliminated in the faired system with the flow remaining attached to the casing.
- Highly sheared velocity profiles were observed around the flame tube head in both systems due to the deflection and flow curvature in this region. These profiles were virtually the same within each system, despite the shorter length of the faired diffuser.
- The mass-weighted pressure loss within the inner annulus is associated with the mixing out of the profile generated around the flame tube head.
- Relative to the dump diffuser, the faired system is more prone to aerodynamic instabilities. Any reduction in pressure loss by using a faired geometry can therefore only be achieved after a full investigation of system stability.

This work is the subject of a continuing investigation involving both experimental measurements and computational predictions. The aim is to optimize diffuser geometries for a given length, combustor depth, head shape, etc.

Acknowledgments

This work was supported by Rolls Royce, Derby, Contract Nos. PVF1-250DM. The authors would also like to express their appreciation to Messrs. R. Marson, D. Glover, and L. Monk for their assistance in the numerous modifications incorporated into the test rig.

References

1 Fishenden, C. R., and Stevens, S. J., "Performance of Annular Combustor Dump Diffusers," *Journal of Aircraft*, Vol. 14, No. 1, Jan. 1977.

2 Young, K. F., Wray, A. P., and Stevens, S. J., "An Integrated Approach to the Design of Compressor OGVs and Combustor Pre-diffusers," Dept. of Transport Technology, Report No. TT89R03, Loughborough University, 1989.

3 Stevens, S. J., Wray, A. P., and Price, P. D., "The Aerodynamic Performance of a Modern Vaporising Combustor Dump Diffuser," Paper No. AIAA-88-3273, 1988.

4 Srinivasan, R., Freeman, G., and Grahmann, J., and Coleman, E., "Parametric Evaluation of the Aerodynamic Performance of an Annular Combustor-Diffuser System," Paper No. AIAA-90-2163, July 1990.

5 Carrotte, J., Denman, P., and Wray, A. P., "Performance Comparison

of a Dump and Short Faired Diffuser System," Dept. of Transport Technology, Report No. TTR92R02, Loughborough University, 1992.

6 Carrotte, J., and Wray, A. P., "Research Into Short Combustor Diffusers," Dept. of Transport Technology, Report No. TTR91R03, Loughborough University, 1991.

7 Fry, P., Private Communication, Rolls Royce, Derby, United Kingdom.

8 Livesey, J. L., and Hugh, T., "Suitable Mean Values in One-Dimensional Gas Dynamics," *Journal of Mechanical Engineering Science*, Vol. 8, No. 4, 1966.

9 Stevens, S. J., and Wray, A. P., "The Influence of Blade Wakes on the Performance of Outwardly Curved Combustor Pre-diffusers," Paper No. AIAA-85-1291, 1985.

Control Requirements for the RB 211 Low-Emission Combustion System

N. C. Corbett

N. P. Lines

Control Systems & Accessories,
Rolls-Royce Industrial
& Marine Gas Turbines Ltd.,
Ansty, Nr Coventry,
United Kingdom

The RB 211 DLE series staged, premix, lean burn combustor demands total integration of control system and combustion hardware. The controls design process is described from the conception of the Engine Management System (EMS), which provides protection and control in separate environments, through to implementation of engine development testing. The process of devising an acceptable fueling strategy to each combustion stage is discussed. This identified the requirements for the computation of complex routines in order to control combustion zone temperatures. The sensitivity of the control design to external conditions of humidity, ambient temperature, and fuel composition is explored. Extensive simulation was used to determine necessary instrumentation accuracies. The paper concludes with a review of the development testing and the final control system configuration.

Introduction

The legislative requirements to limit or regulate pollutants emitted from land-based fossil-fueled engines is becoming more stringent. This has resulted in the radical redesign of the combustion systems employed on high pressure ratio aero-derived gas turbines. The Rolls-Royce Industrial RB 211 has been developed to minimize emissions using a premixed lean burn staged combustion technique. This has been designated RB 211 Dry Low Emission (DLE).

The performance of the engine in terms of both emissions levels and availability will be a function of the performance of the engine's control system.

Successful implementation of the DLE Staged Combustor relies upon an appropriate control scheme strategy that is accurate, repeatable, and has high reliability.

Staged combustion inevitably requires an increase in hydromechanical control equipment and computational capacity with possible reduction in overall system reliability. Thus the redesign of the engine control system has addressed architecture and redundancy of sensors and systems in order to maintain the total installation availability requirements.

From these requirements and the structured design process, an "Engine Management System" concept has evolved. This has produced a total validated control system environment to ensure design integrity and reliability and an emission compliant package.

The "Engine Management System" has integrated power envelope control, emission control, and protection and provides a Dry Low Emission solution for the Industrial RB 211.

Contributed by the International Gas Turbine Institute and presented at the 38th International Gas Turbine and Aeroengine Congress and Exposition, Cincinnati, Ohio, May 24–27, 1993. Manuscript received by the ASME Headquarters February 13, 1993. Paper No. 93-GT-12. Associate Technical Editor: H. Lukas.

DLE Combustion System

The pollutants emitted from gas turbine engines are directly related to the temperature at which the air and fuel reactants are burned in their combustion systems. The principal pollutants are oxides of nitrogen (NO_x), which begin formation at high temperatures and with rates that grow exponentially with increasing temperatures; and carbon monoxide (CO) and unburned hydrocarbons (UHC), which are produced due to incomplete or weak combustion, typically at low combustor temperatures.

The only viable method of limiting the production of NO_x and CO emissions is by controlling the combustion temperature. There are two techniques available to control temperature, namely "rich-burn rapid quench" and "premix lean burn," as both avoid the high temperatures generated at near-stoichiometric conditions. The terms "rich" and "lean" convey the magnitude of the fuel-to-air mixture strength with respect to stoichiometric conditions; the RB 211 DLE employs the premix lean burn option.

However, the employment of "lean" fuel-to-air mixtures requires operating the combustion system in closer proximity to the reactants' weak extinction limit. Therefore, providing low emissions over a wide operating range demands that the air-to-fuel ratio (AFR) be modulated in some way to sustain combustion, particularly at part-load conditions where the mixture would be too weak to burn.

The idealized low emission combustor design would have the ability to modulate the air *and* fuel flow being used in the combustion process. Such designs were discarded on economic and reliability criteria.

A compromise is to divide the combustor into a number of discrete combustion stages, where at any power condition the proportion of the total air flow to each stage is fixed. Fuel can now be injected into each of these stages as a function of the

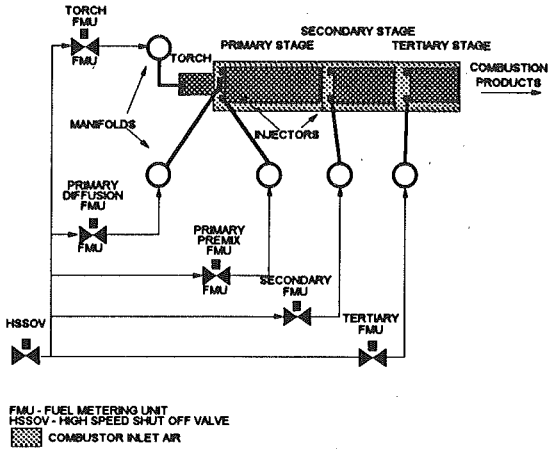

Fig. 1 Schematic of DLE staged combustion system

power output demand and combustor inlet conditions. Thus, the ratios of the fuel and air reactants in each stage can be individually apportioned to control their respect temperatures of combustion within the close temperature bands established to meet the emission targets.

The greater the number of stages, the closer is the approximation to the idealized system, and the turndown of the premix lean burn operating range is increased. However, as the air supply to the combustor is finite, an optimum number of stages can be determined; the RB211 DLE has three stages.

Whenever operational conditions determine that premix lean burn is not practicable (starting and low power operation), the primary stage incorporates a diffusion flame injector.

RB 211 DLE Staged Combustion Description

The DLE combustion system designed for the Industrial RB 211 is a staged combustor in series, Fig. 1, which consists essentially of a number of separate combustion zones arranged in cascade, primary, secondary, and tertiary, respectively, each independently fueled, where the fueling and the required number of active stages depends upon the ambient temperature and load range that must be covered.

With this design only the first stage operates closer to the weak extinction conditions, as the burned products are cascaded through the combustor and any subsequent stage receives preheated gases. Although the temperature rise required in these stages to achieve the design temperature is much reduced, the preheat significantly improves their respective weak extinction margins. Consequently this extends the range of premix lean burn operation and turndown.

The RB 211 DLE design has 9-off combustors, which are projected radially outward of the engine casing, replacing the inherited aero-annular combustor. Each combustor is separate and independent, i.e., there are no flame tube interconnectors, and each combustor requires its own individual ignition source.

Located adjacent to each of the main combustors are separate gas-fueled torch combustion chambers, each of which is ignited from an electrical ignition source. The resulting combustion in the torch chamber propagates a flame into the main combustor primary stage where it ignites the fuel emitted from a diffusion flame type injector.

The primary zone is fueled from a diffusion flame injector, for starting and low power operation, until lean burn is selected. Fueling of this zone is then transferred to a premix type injector. During the normal operational cycle of the engine the control scheme is required to transfer between the two primary stage combustion modes of diffusion and premix lean burn without loss of availability.

The premix injector carefully premixes the air and fuel reactants in ratios weaker than stoichiometric before they enter the combustion zone. Similar pre-mix injectors fuel the secondary and tertiary zones.

As the primary stage does not receive any preheat, as the air reactant is at a relatively low temperature (650 to 750 K), its turndown range is too small, less than 10 percent variation in AFR. Consequently the primary premix stage has been designed to operate at a constant zone temperature, approximately 1800 K to minimize emissions, thereby its stability margin does not become dependent on the operating conditions, and the narrower limit is therefore acceptable.

Whenever premix lean burn operation is selected the primary and secondary premix stages are always concurrently active to achieve the required power turndown.

When the tertiary stage is active the temperature of the secondary combustion zone is modulated between its lower and upper limits of 1600–1800 K, respectively, to produce tertiary combustion temperatures within the same band, thus minimizing the levels of CO and UHC emissions while preventing any further NO_x being produced.

Although each of the combustors is independent, the fuel manifolding system located circumferentially around the engine connects each fuel injection lane of the nine combustors together. Thus the control scheme is only required to modulate the fuel individually to each combustion stage, as each of the five manifolds performs the distribution to each combustor.

Control System Task

Definition of Control System Task. The control system task for DLE can be summarized as:

> "Design and validate an appropriate control system strategy to start the gas generator and proceed to a suitable power level to select premix lean burn operation. From this point to modulate the fuel flow to the gas turbine combustion system to perform engine output power/load control AND staged combustion fuel management simultaneously to minimize emissions of both NO_x and CO.
> To define the control system configuration to achieve the current RB211's availability and reliability and maintain system integrity and safety."

DLE Combustion Temperature Control. Closed-loop control using direct temperature measurement would provide an easy DLE control scheme basis; however, there are some problems.

The design of the DLE combustor relies upon careful and precise homogeneous mixing of the air and fuel reactants with the products of the upstream stage to control the amount of pollutants. Any additional disturbances introduced by the insertion of a device into the combustor, or placement of any holes in the combustor wall, will upset the internal flows, which will consequently affect the mixture temperature and hence pollutants.

Intrusive techniques currently available will not survive the environment; an alternative nonintrusive technique was required, which has resulted in an open-loop technique being employed.

The control scheme developed requires the measurement of a number of parameters in order to control AFR. Some of the problems and methods are discussed.

Air and Fuel Equivalence. Combustion temperature can be determined from the thermodynamic properties and flow rates of the air and fuel reactants; therefore, measurement of these quantities for each combustor stage allows the control system to compute and modulate the individual fuel flows to perform the required stage temperature control. This technique, however, is dependent upon the fuel composition and the states of both the air and fuel reactants.

Combustion engineers traditionally use a "dimensionless

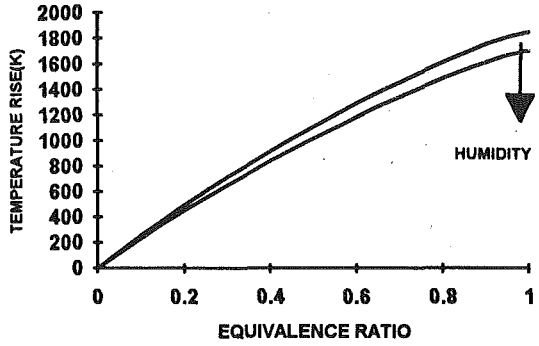

Fig. 2 Fuel and air equivalence ratio

property," air and fuel equivalence (ϕ), Fig. 2, to assist with designs. The relationship is based upon direct proportionality of the air to fuel reactant ratios at stoichiometric (STOI) and actual (AFR) conditions, Eq. (1).

$$\phi = \frac{\text{Stoichiometric Air Fuel Ratio (STOI)}}{\text{Actual Air Fuel Ratio (AFR)}} \tag{1}$$

The equivalence relationship ϕ can then be used to determine the combustion temperature rise for various AFR combinations, thereby only requiring the constant STOI to be determined.

Where the fuel composition is known, this can be included in control calculations as an input variable. A study has been made of gas fuels in the category "Pipeline Natural Gases." This indicates that the variation in STOI is small and the temperature control error introduced by ignoring variations in composition would be approximately ± 10 K.

Effects of the Air Reactant State With AFR Equivalence. Although the equivalence relationship can be applied to various fuel compositions, the temperature rise is also dependent upon the state of the air reactant, particularly the moisture content.

As the water content in the air increases, the resultant combustion temperature for a given AFR reduces, which has consequences if it is not quantified and incorporated into the staging scheme. If ignored this has the undesirable effect of increasing the emissions produced, both CO and NO_x, and moving the primary stage into closer proximity to its weak extinction point.

Whenever the gas turbine is required to operate in environments that have a wide range and varying absolute air moisture content, particularly near saturation conditions, continuous air moisture measurement, at the gas turbine air intake, is required as an input variable to the equivalence relationship.

The selection of an appropriate "humidity" measurement device will be defined from the DLE control design and development program where primary and secondary measurement devices are being evaluated. As this measurement is fundamental to the reliability of the total DLE system, our device specifications will demand minimum recourse for recalibration or maintenance: a minimum 8000 hour service interval, and a certification standard compatible with hazardous area classification.

Combustor Air Flow. In order to control AFR, accurate knowledge of stage air flow is essential. The proportioning of the air flow to the respective stages will be set by combustor geometry but there is no easy method to measure directly the total air flow to the nine combustors.

The total air flow could be measured using a number of techniques, intake depression for example. However, not all the air is used within the combustion process. Various amounts are used throughout the power range for cooling, sealing, and compressor bleed.

Estimation of this "service" air is difficult and the method was not adopted due to the uncertainty on accuracy, reliability, and measurement turndown.

Therefore, a unique algorithm has been developed that determines the flow appertaining to the combustion system only, hence removing any bleed effects, and is valid over a wide power turndown and during transient operation.

The combustion system discharges into the high-pressure turbine nozzle guide vanes (HPNGV) whose capacity remains fixed during the self-sustaining speed range of the engine and is independent of any engine bleeds. Therefore, from the knowledge of the HPNGV capacity, Eq. (2), combined with the fuel flow demand to the engine, the air flow to the combustor can be determined.

$$\text{HPNGV capacity } \frac{w\sqrt{T}}{A \cdot P} = \text{const} \tag{2}$$

where

w = HPNGV flow (air and fuel)
T = HPNGV temperature
P = HPNGV pressure
A = HPNGV area

Combustor inlet pressure and temperature are measured and input to the EMS, where the values for P and T are determined from look-up curves of combustion pressure loss and overall combustor temperature rise. The HPNGV area, A, is input from engine build data. The control system total fuel flow demand is then subtracted from the HPNGV flow, w, to yield the combustor air flow, and with the knowledge of combustor geometry, the stage air flow can be evaluated at any running condition.

Control Scheme Strategy

The primary task of the combustor irrespective of whether it is a conventional or staged combustor is to provide the energy to drive both compressor and power turbines. The overall temperature rise across the combustor will be identical between both types of combustor, hence the turbine inlet conditions will be no different with a staged combustor.

Therefore, the basic control loop, Fig. 3, for the staged combustor is essentially the same "governors in parallel" scheme currently used on conventional engines. In such schemes the total engine fuel flow demand, *Wfe*, is scheduled by lowest and highest wins gate logic selecting the appropriate output demand from the various engine limiters, governors, and transient schedules.

For the staged combustor *Wfe* is apportioned by the staging scheme to each of the respective combustion stage's fuel metering units Wf_1, Wf_2, Wf_3, etc.

The thermodynamic heat balance of the control loop remains the same, and if the dynamics of the individual fuel metering units are identical, the response of the engine will also be similar.

The selection of individual fuel metering units for the staged scheme provides maximum flexibility to schedule the individual stages of the combustor consistent with variations in power output demands and ambient conditions and their effect upon the combustion operating point. The methodology employed to apportion the individual AFRs within each stage requires that the strategy of the "staging scheme" does not affect the forward path dynamics of the flow demand loop with delays or lags that may impair both engine and the system performance.

The control scheme is required to modulate the heat input to the engine to meet changing load demands, no matter how sudden, but as the lean burn combustion process demands operating in closer proximity to weak extinction limits, the

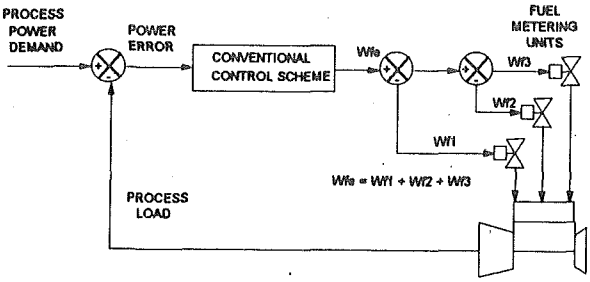

Fig. 3 Staged combustion control basis

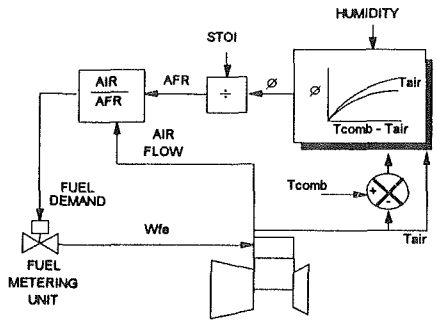

Fig. 4 DLE staging scheme principle

staging scheme must respond with adequate margins to ensure combustion is always sustained.

The staging scheme strategy is required automatically to enable the primary diffusion injector whenever the conditions are outside the range of premix lean burn operation but transfer back whenever the conditions are satisfactory.

Primary Premix Temperature Control. As the primary premix stage is operating close to its combustion stability limit, it is paramount to decouple the primary premix flow demand from the forward path of the power demand control loop to obviate reaction to any sudden load changes.

However, the primary premix flow demand must respond whenever the air flow conditions within its stage alter in order to maintain optimum primary zone temperature.

Provided that the fuel flow scheduled to the primary premix stage sustains combustion, the temperature rise of the stage is dependent upon the proportions of the reactants, Fig. 2.

The basic scheme principle is shown in Fig. 4, where at any operating condition, the maximum permissible temperature rise of the stage is determined from the difference between the temperature of the air reactant, T_{air} and the defined temperature limit for that stage, T_{comb}.

As T_{comb} is set to a constant primary combustion temperature, the fuel flow scheduled to the stage is determined by the combustor inlet state and air flow rate.

The limiting AFR is determined by using an inverted equivalence curve, from input measurements of humidity and combustor air inlet temperature, and the input value of stoichiometric constant, STOI.

The stage air flow is calculated using the method described in Eq. (2) and hence the fuel flow required to maintain a constant primary premix combustion temperature is scheduled, which will only modulate as the engine condition changes as sensed by variations in combustor inlet temperature and the air flow.

Secondary and Tertiary Stage Temperature Control. As each of the successive premix lean burn stages can operate within a wider turndown range, they can be directly placed into the forward path of the fuel flow demand. The fuel sched-

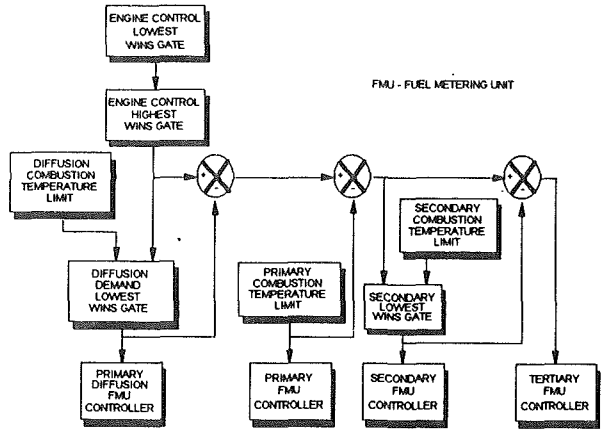

Fig. 5 DLE staging scheme

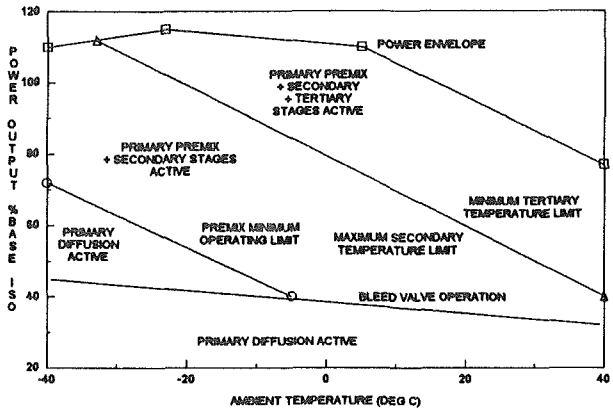

Fig. 6 RB211 DLE operating regime

uled is the difference between the total fuel energy and the preceding stage's fuel flow demand, Fig. 5.

The maximum secondary stage combustion temperature is controlled by comparing the forward path flow demand with that determined from the secondary combustion temperature limit; whichever of these is the lowest in magnitude is scheduled to the combustor. This is determined by "lowest fuel demand wins" voting logic selection.

The secondary combustion temperature limit uses an equivalence curve similar in principle to the primary premix limit, Fig. 4.

Thereby secondary stage fuel flow is free to modulate in response to the power demand until the limiting conditions are reached. Subsequent modulation is determined by the combustor inlet temperature and air flow.

Whenever the forward path demand is in excess of the limiting flow to both primary and secondary combustion zones, the staging scheme strategy automatically enables the tertiary stage. This shortfall in fuel flow from the first and second stages is allowed to modulate freely in response to the power output demand.

Therefore the forward path of the control loop has essentially only one metering unit that is directly responding to load changes. The stages operating at their respective temperature limits respond in accordance to conditions and states dictated by the resultant engine conditions, Fig. 6.

However, these stages must be responsive to avoid flameout as previously described.

To ensure that the tertiary combustion temperature is not too low when a small error in flow demand activates the stage, the secondary combustion temperature limit is reduced with the effect of increasing tertiary stage flow.

The scheme automatically accommodates power reduction by smoothly transferring control between stages. The controller will not allow very low flows into the tertiary zone because incomplete combustion may occur. It avoids this by raising the secondary stage temperature limit to allow the total flow to be scheduled to the primary and secondary stages.

Similarly, at constant power with varying ambient conditions, Fig. 6, the fuel proportions between stages will be automatically adjusted due to changes in air flow and combustor inlet temperature. Also low flow levels will be avoided in any stage by adjustment of zone temperature limits.

Diffusion Injector Operation. The low emission mode is only operative over a defined power turndown, Fig. 6. During starting and very low power operation the primary diffusion injector is used to fuel the engine.

A similar equivalence curve to the primary premix limit, Fig. 4, can equally be applied to this injector as this too has a limited range of operation, due to both temperature and emissions limitations.

Primary Diffusion Mode. Until the primary diffusion temperature limit is reached, the flow via its injector is free to modulate the power output of the engine. Whenever the maximum temperature rise is determined, the flow is again limited and only modulated in accordance with combustor inlet temperature and air flow changes (Fig. 5).

If the primary zone temperature limit with diffusion burning is reached before the engine is at a power level to enable low emission mode; the shortfall in fuel flow demand is accommodated by the secondary premix stage.

Therefore, the engine operates with both primary diffusion and secondary premix injectors whenever the flow exceeds the primary combustion stage temperature limit, until full premix mode is enabled.

The secondary stage flow demand is determined by subtracting the controlling primary diffusion and premix flows from the total flow demand. During this mode of operation, the primary premix is disabled with its flow demand set to zero. This is accomplished by equating the primary premix combustion limit and the measured combustor inlet temperatures, i.e., zero temperature rise.

Transfer to Premix Lean Burn Mode. When premix mode is required, the scheme transfers control from primary diffusion to primary premix by modulating *both* equivalence curves temperature of combustion limits. The diffusion injector temperature rise is reduced to zero by equating its combustor limit and inlet temperatures, while the premix's is increased to its limit of approximately 1800 K.

As the air flow in the primary stage is common to both injectors equivalence curves, the total stage fuel flow remains essentially constant by selecting a common rate of change in the respective combustion temperature limits, dT/dt. Any shortfall in power created by the differences in combustor efficiency will automatically be met by the secondary stage flow, which is allowed to modulate according to the power demand.

When complete transfer is achieved, the diffusion injector combustion temperature rise limit remains at zero, and its fuel metering unit remains closed.

Transfer Back to Diffusion Mode. Transfer of the fueling back to the diffusion injector is achieved by detecting that the engine operating condition is too low to maneuver with primary lean burn premix, and at this point, the temperature data of both primary diffusion and premix are respectively changed at the same rate dT/dt to close off fueling via the premix injector, and establishing primary zone combustion totally through the diffusion injector.

Simulation in Control Scheme Development and Validation

Simulation is an essential tool in the deployment of control ideas and the validation of the final product. Various types of model have been utilized to explore different aspects of the project.

Thermodynamic Non-Real-Time Engine Models. The effectiveness of combustion control relies upon the accurate computation of the air flow. A number of calculation methods were evaluated using a transient component based thermodynamic model. The model was used to quantify the accuracy of selected algorithms under steady-state and transient conditions. It is important to understand the error magnitudes and vectors in order to compensate within the control scheme.

DLE control demands accuracy of fuel metering unit positioning, to maintain the optimum zone temperature. The scheme also relies on a number of gas generator measured performance parameters. The thermodynamic model has been used to assess the sensitivity of measurement error and the cumulative effect on zone temperature. This work assisted in the definition of instrumentation accuracies necessary for the total control scheme implementation.

The control laws were integrated with the thermodynamic model to evaluate system performance under a number of operational conditions, both transient and steady state.

Combustor Models. Much of the initial assessment of the control task and its solution was performed on an IBM PS/2 personal computer (PC). The model represented the combustion methodology and equivalence curves for predicting the individual zone temperatures and the relative weak extinction limits. This provided the basic understanding of the combustion process and provided a mechanism for initial assessment of the developed strategy.

The model proved invaluable when studying operation at conditions where fuel stages were introduced or closed down. This in fact led to the incorporation of hysteresis control by modulating the zone temperature limit at stage overlap conditions.

This was found to be necessary to prevent the system becoming unstable and cycling between stages, which with narrower primary lean burn combustion stability margins could create availability problems.

Real-Time Transfer Function Models. This model form is predominantly used to evaluate the actual control system.

The engine is represented by second-order transfer functions and nonlinearities such as bleed valve operation have been included.

An engine model has been developed to run on a PC and generate all the necessary parameters for control. The PC drives interface cards, which simulate analogue signals necessary for control. This equipment is situated with the controller in the engine test cell. In this way the simulator is used to qualify the control program before engine testing commences, and is resident at run time to evaluate any problems, should they arise, without the need to run expensive engine tests.

Modeling Results. The transfer function model of the engine was validated by comparison with real engine test data collected from an RB 211 with a conventional combustion system. Rapid transients were compared and the agreement between model and engine was excellent, well within expected engine to engine deviations.

Experience from previous projects has demonstrated that controls developed against the transfer function model have required little optimization when fitted to a real engine.

Simulation of rapid maneuvers, such as "slam decel" (Fig. 7), were modeled and indicate that the scheme response main-

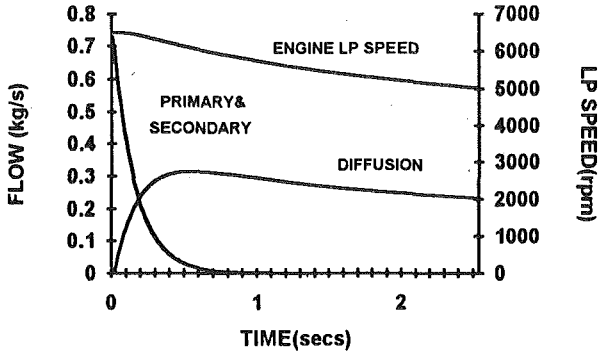

Fig. 7 Simulation of "slam decel"

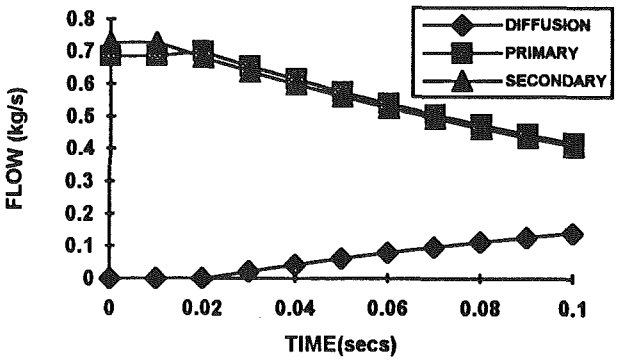

Fig. 8 Detail of simulation "slam decel"

tains sustainable combustion by virtue of all the aforementioned techniques.

The "slam decel" poses the biggest challenge; however, the scheme performed as designed by ensuring that the tertiary followed by the secondary mainly responded to the reduction in total flow demand while the primary premix fueling sustained combustion by only responding to the variation in the air flow and temperature into the combustor.

As the scheme does not allow the engine to be controlled solely by the primary premix injector, whenever the secondary flow reaches its minimum injector flow or temperature of combustion, the diffusion injector is automatically enabled. A small flow of fuel from this injector is sufficient to increase the stability margin of the premix injector until complete transfer to the diffusion injector is accomplished, Fig. 8.

Implementation of Control System. The Dry Low Emission combustor design has placed the task of the engine's control system into a more prominent role with regard to the performance of the total engine package, particularly with respect to the qualitative task of emission compliance.

The size of the control task has significantly increased the amount of input and output communication and the various algorithms to be processed. However, the increased component count and the interdependency of the combustor staging with simultaneous modulation of multivalve systems poses a challenge in terms of reliability. The operator wants a machine that produces reduced pollutant emissions yet has availability as good as the conventional engines.

The size of the task and technical requirements to implement various algorithms, look up tables, etc., and provide flexibility, is most readily realized by the potential that Programmable Electronic Systems (PES) provide. The reliability requirement of the DLE engine has not only enforced a reappraisal and redefinition of previously established control architecture rules, but the development of PES type equipment has required the

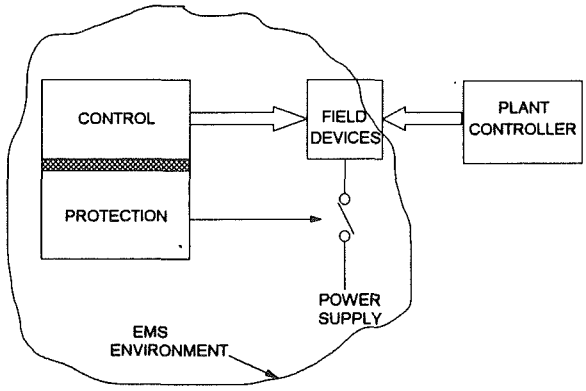

Fig. 9 Engine management system environment

evaluation of a fundamentally different approach that has to be taken with respect to integrity and safety aspects.

In providing a "total" DLE product, Rolls-Royce has adopted the principle of defining the organization or configuration of the PES for controlling and protecting the DLE engine/installation. This has been termed the Engine Management System (EMS), Fig. 9.

The EMS brings together the arrangement of electronic hardware that is totally responsible for the control and protection of the DLE engine. It is a completely separate environment to the remaining plant controls but is designed to interface to it through simple command links.

The EMS is subdivided into two environments:

- The control system, which is the method of governing the operation of the machinery using closed-loop, open-loop control, and specific gas generator sequencing.
- The protection system, which responds to gas generator conditions that require preventive action by immediate shutdown.

The EMS concept is designed to provide a stand-alone unit, which is supplied as a totally validated system to assure that both the integrity and qualitative control of emission requirements are realized, while also improving the overall plant configuration.

This broadly means that changes or effects from the plant control(s) do not have any repercussions on the EMS and vice versa, thereby maintaining gas generator integrity.

Safety policy dictates that the EMS be constructed from two totally separate control and protection system environments, which are independently linked to the operating equipment.

The protection system independently monitors the operating conditions of the engine as determined by the control system, and can separately shut down the engine by taking preventive action.

The protection system may be constructed of a number of separate dedicated tasks or units, each with a specific protection function, i.e., flameout, overspeed, etc.

If the control and protection functions were not separate or independent and incorporated into a single integrated unit, then any failure within this system could simultaneously cause a failure in the protection features.

The EMS is constructed with independent PES control and protection systems with independent inputs, outputs, and power supplies, ensuring that this philosophy is adhered to.

Some operational information is required to be communicated between them, which is accomplished via fully isolated communication between the respective environments.

The reliability of the engine combustion and control system to comply with emission requirements can only be fully realized by the organization of the EMS and associated sensors and systems.

Operational reliability has been achieved by selection of components and units with high MTBF (mean time between failure), redundancy of sensors, and back-up control modes. In all cases the MTTR (mean time to repair) has been minimized.

By taking a planned and systematic approach to the development of the EMS, both hardware and software, the overall quality control ensures that the system responds in a safe and controllable manner.

Activity will continue to develop the EMS in all aspects, both technical and quality, and with the experience gained will be designed into the final production scheme.

Conclusion

The staged combustor introduces an increased qualitative control task for the engine's control system where the total fuel demand is required to be accurately scheduled or apportioned to the respective stages by simultaneous modulation of multivalve combinations to meet the design emission levels.

The role of the engine control system is now fundamental to the performance of the combustor.

The increased interdependency and number of components requiring simultaneous operation necessitates a planned and systematic approach to the architecture of the system in order to realize the requirements of system reliability, availability, and integrity.

Modeling has demonstrated that control schemes that have been conceived satisfactorily control the engine under a variety of maneuvers.

At the time of writing the control hardware had been built and installed in the engine test cell. Basic software has been validated using a standard RB 211 engine. The first DLE development engine is built and will go to test toward the end of 1992.

References

Owen, D. A., and Willis, J. D., 1991, "Low Emission Combustor Design Options for an Aero Derived Industrial Gas Turbine," presented at the Canadian Gas Association Symposium on Industrial Application of Gas Turbines, Banff, Alberta, Canada, Oct. 16–18.

Flex Cycle Combustor Development and Demonstration

M. M. Harris

D. N. Marsh

E. A. Vos

Allied-Signal Aerospace Company,
Garrett Auxiliary Power Division,
Phoenix, AZ 85010

E. Durkin

U.S. Air Force Wright Laboratory,
Wright-Patterson AFB, OH 45433

An innovative, "flex-cycle" combustion system has been developed for the Garrett Model 400-1 Integrated Power Unit (IPU), a 425 shp (317 kW) gas turbine engine designed for use on future fighter aircraft. Demonstration of this system required real-time transient operation of the combustor in a full-scale test rig. The transient testing was unique, having been performed with an electronic control, which modulated all combustor operating parameters according to programmed engine component maps, drag curves, fuel schedules, and selected ambient test conditions. The axially injected annular combustor is capable of engine starts in two seconds, as well as producing 200 shp (149 kW) for emergency use at all altitudes up to 50,000 ft (15,240 m). The combustion system is capable of switching operation from the emergency power stored energy (SE) mode to the normal-air breathing (NAB) auxiliary power mode without loss of engine power. The flex-cycle combustor supplies emergency power in the SE mode with a temperature rise of 2200°F (1222°C) and in the NAB mode with a temperature rise of 1600°F (889°C). Specific features that make these requirements possible include air-assisted simplex airblast fuel atomizers with integral check valves, and effusion-cooled combustor liner walls. This paper describes the flex-cycle combustion system design, test methods used, and significant test results. Steady-state performance, in both the SE and NAB operating modes, and real-time transient test results are discussed. The transient testing included rapid starts as well as transitions from the SE to NAB operating regimes.

Introduction

The flex-cycle combustion system was designed as part of the advanced-concept Garrett Model 400-1 Integrated Power Unit (IPU). For a complete description of this IPU, see Klaass et al. [1, 2]. Figure 1 presents a schematic of the IPU concept, showing the two modes of operation. The IPU is designed to operate from a stored air supply to deliver 200 hp (149 kW) emergency power within two seconds of start initiation at any altitude up to 50,000 ft (15,240 m). This mode of operation is referred to as the stored energy (SE) mode. The IPU is capable of transitioning from this emergency power mode to the normal-air-breathing (NAB) mode without power interruption, performing auxiliary power unit (APU) functions of pneumatic and electrical energy supply at low altitudes and on the ground.

Rapid IPU starts at both sea level and high altitudes are accomplished using the SE start system as the primary IPU start system. The SE system is used to accelerate the turbomachinery to 100 percent speed, at which point the aircraft load can be supported using the SE system, or the IPU can transition to the NAB mode and continue to support the aircraft load indefinitely, independent of the stored air source.

IPU engine concept design work established the characteristics required for development of the flex-cycle combustor, which subsequently was developed as a stand-alone component. Engine-specific details, such as physical size and envelope constraints, and cycle conditions giving the required power unit performance were used to define the combustion system geometry and steady-state test conditions. Cycle conditions, as well as turbomachinery maps, engine drag characteristics, rotor inertia, and other factors derived from the Model 400-1 IPU design were used to set control parameters for transient testing.

The flex-cycle combustor was refined through a series of steady-state development rig tests; then combustor performance was validated for both two-second start sequences and SE to NAB transitions in the transient test rig. Steady-state combustor performance, development of the transient test rig, and the transient test results are presented in later sections.

Background

Aircraft designs for the future are placing demands for increased capability upon emergency power, emergency main engine restarting, and auxiliary power systems. For military applications, designs are being evolved for highly maneuverable aircraft [3–5] operating at altitudes up to 60,000 ft (18,288 m). Concepts such as highly maneuverable, aerodynamically unstable, fly-by-wire aircraft employing full-time computer

Contributed by the International Gas Turbine Institute and presented at the 38th International Gas Turbine and Aeroengine Congress and Exposition, Cincinnati, Ohio, May 24–27, 1993. Manuscript received at ASME Headquarters March 17, 1993. Paper No. 93-GT-320. Associate Technical Editor: H. Lukas.

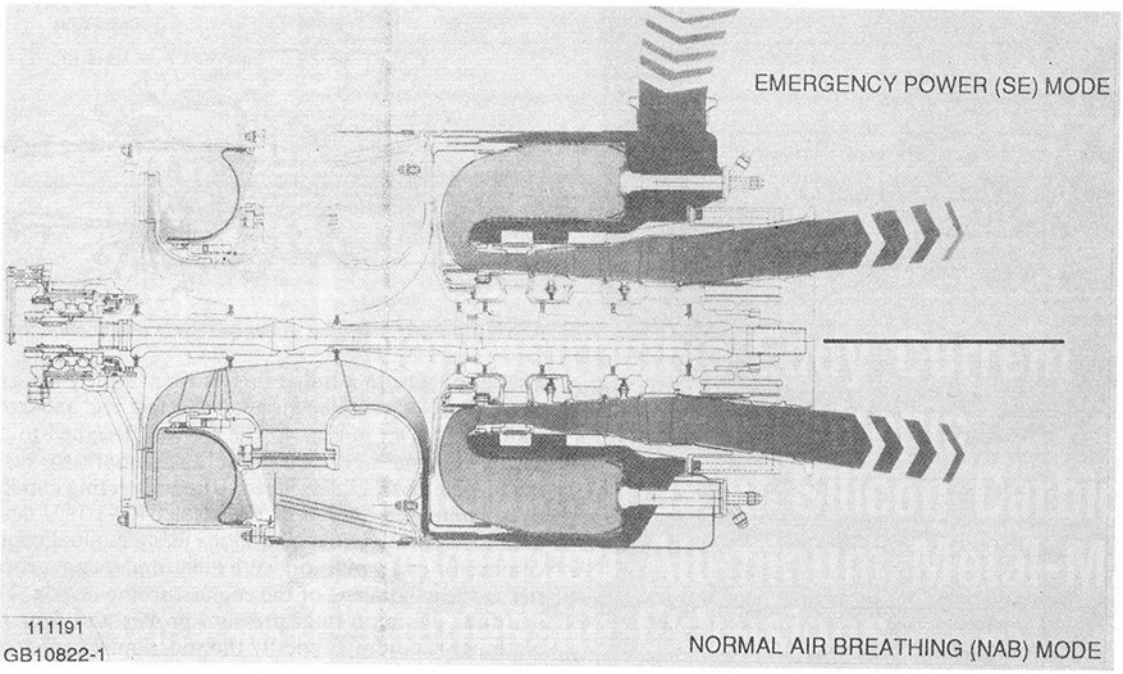

Fig. 1 The Garrett IPU concept, showing the two modes of operation

control and electric actuation systems are being developed. Higher output power and decreased start time are being demanded for main engine restarting at high altitudes; greater auxiliary power system reliability and faster starting response will also be needed.

The start time requirement for present fighter aircraft APU/emergency power systems is four seconds (F-22 ATF) and is being specified as two seconds for the next generation of advanced fighter aircraft. Electrical power interruption to the aircraft systems cannot be tolerated, since this would result in loss of aircraft control during an engine-out emergency. While the main engine(s) are decelerating, the emergency power system *must* start and come on line quickly. For these applications, Garrett Auxiliary Power Division is developing an advanced Integrated Power Unit (IPU) system capable of reliably starting at 50,000 ft (15,240 m) altitude and acceleration to full speed (>60,000 rpm) in less than two seconds. Starting and stored energy (SE) operation supplying up to 200 shp (149 kW) for several minutes will be accomplished using jet fuel and air from onboard tanks. The system will transition automatically to normal air breathing (NAB) operation and continue to perform APU functions at lower altitudes and on the ground.

The key technology in developing an emergency power system with these capabilities is the flexible-cycle (flex-cycle) combustor.

Combustion System Description

A cross section of the flex-cycle combustion system is shown in Fig. 2. This system has been described in detail by Klaass et al. [1, 2]. A photograph of the combustor is presented in Fig. 3. The combustor is axially injected and has two ignitors. Flame stabilization is achieved by dome swirlers surrounding each fuel atomizer. The airblast atomizers have air assist ports for good atomization and stable burning during starting, SE mode operation, and SE to NAB transition. Internal check valves in the atomizer inlet fittings maintain full fuel manifolds, to ensure rapid ignition. The liner walls are cooled by conventional cooling skirts in the primary zone region and by effusion cooling (multiple small-diameter, angled holes) elsewhere. Use of effusion cooling reduces the amount of air

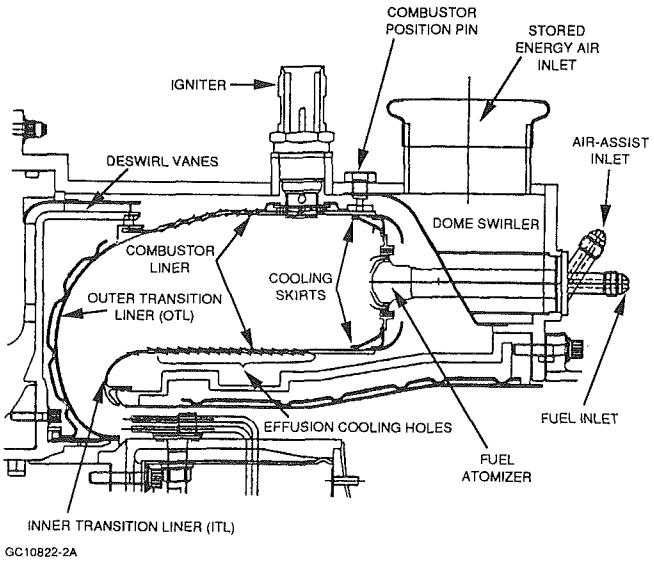

Fig. 2 Cross section of the flex-cycle combustion system

needed for wall temperature control to about half that of a conventional cooling scheme. This reduction in cooling air allows more air to be used for exit temperature control.

The combustor operates as a throughflow combustor during SE mode operation. Air from a storage bottle is regulated to 300 psi (2070 kPa), passes through a modulating valve that controls the flow and further reduces the pressure, then enters the combustor case. This air [20–40 psia (140–280 kPa) at −70°F (−57°C)] is then fed into the combustor annulus through holes in a baffle plate separating the annulus from the air inlet torus. The baffle plate provides a circumferentially uniform air distribution to the combustor annulus with minimal pressure loss. Air passes into the combustor through both the dome swirlers and the liner cooling and air feed holes.

The low air flow and temperature during SE operation result in a low pressure drop across the combustor liner, requiring fuel atomization to be air-assisted. Assist air is provided down

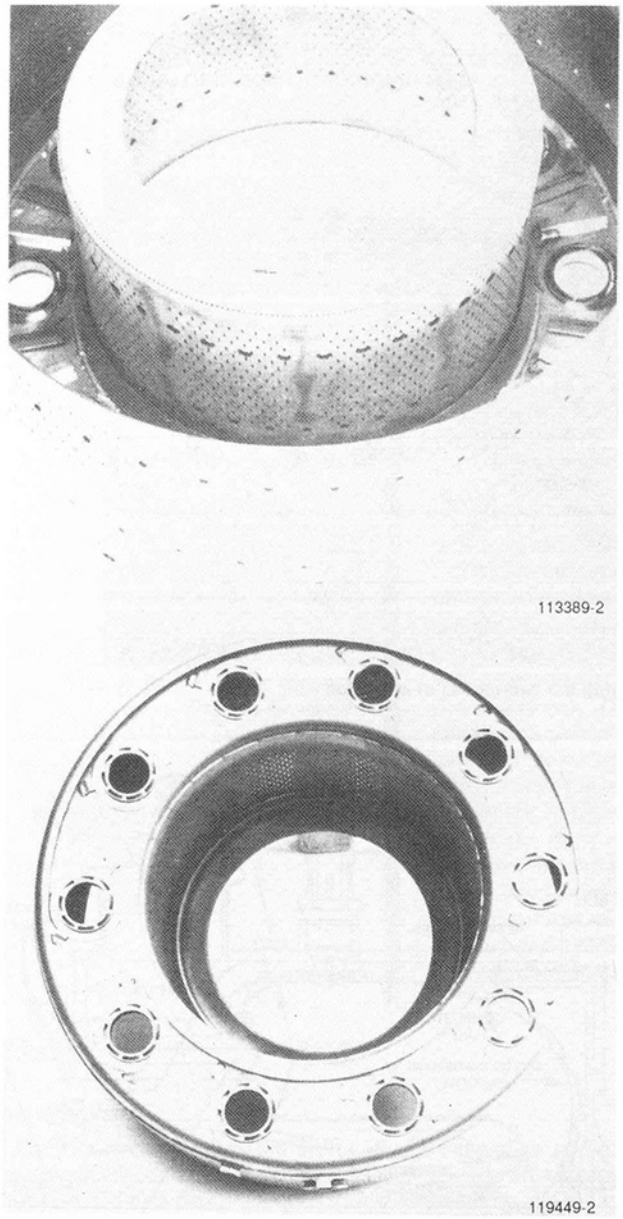

Fig. 3 Photographs of the flex-cycle combustor

the center of each injector. This air is regulated at a pressure of 5 to 10 psi (34 to 69 kPa) above the combustor exit pressure and creates a small recirculation region at the tip of each fuel injector. The use of air assist is easily accomplished with the flex-cycle combustor, since high-pressure air is readily available from the stored air source. The air-assist passages are small, and the air-assist flow rate is less than 2 percent of the combustor airflow.

During NAB operation, the combustion system operates as a reverse-flow system, typical of a small gas turbine auxiliary power unit (APU). Air enters the annulus from the compressor deswirl vanes at 132 psia (910 kPa) and 626°F (330°C), passes into the combustor through the swirlers and various holes in the liner walls, and mixes with atomized fuel, which is burned. Fuel atomization is achieved through an airblast feature, which is driven by the combustor pressure drop. The airflow, fuel flow, and inlet temperature for NAB operation are significantly higher than for SE operation.

Steady-State Testing

Test Methods. The flex-cycle combustor was developed in a series of tests in a full-scale test rig at steady-state operating conditions. A cross section of the test rig and combustion system is shown in Fig. 4. The rig was designed to match the engine flow-path geometry from the compressor discharge to the turbine nozzle inlet. Steady-state operating conditions, derived from cycle studies of the Model 400-1 IPU design, were used to set the rig flow conditions using manual controls. The combustor exit condition were measured using a rotating carrier at the axial plane of the engine turbine nozzle. The carrier had four platinum total pressure probes and four platinum/platinum-rhodium (Type S) thermocouples. Inlet conditions were measured using total temperature (Type K) probes, total pressure probes, and static pressure wall taps. Metal temperatures were measured using temperature indicating paint, which allowed complete mapping of combustor wall temperatures.

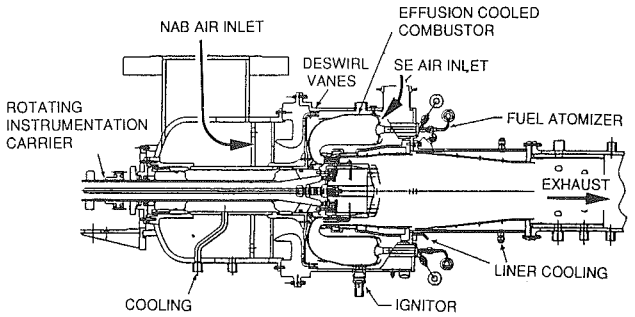

Fig. 4 Cross section of the flex-cycle combustion test rig

Pattern Factor. Combustor exit temperature uniformity is characterized by the pattern factor (PF) relationship:

$$PF = \frac{(T_{max} - T_{avg})}{(T_{avg} - T_{inlet})} \quad (1)$$

A complete exit temperature map was generated from temperature measurements made by rotating the instrumentation carrier through 360 deg in 10-deg increments. The reported pattern factors given below are averages from more than one set of temperature measurements and more than one rig build.

Ignition Characteristics. Ignition delays were measured for a range of fuel/air ratios at several combustor inlet conditions. For this testing, the ignition delay was defined as the time required to see a significant, sustained rise in combustor exit temperature after initiating fuel flow and ignitor spark. This ignition delay includes the delay associated with igniting the combustor, as well as delays associated with the fuel and ignition systems. The fuel system consisted of a boost pump, an on/off solenoid valve, and an electrical torque motor for flow control. The high-tension ignition system consisted of standard APU components. The spark frequency for these tests was 6–8 Hz. The ignition unit provides a minimum of 1 Joule/pulse to the igniter. A voltage of 18,000 to 24,000 volts is required to produce a spark at the ignitor gap.

Smoke and Emissions. Combustor smoke and emissions were measured using a 13-element, averaging gas sample probe located in the rig exhaust. The sampling was performed according to the Society of Automotive Engineers (SAE) Aerospace Recommended Procedure ARP1179 [6] for smoke, and ARP1256 [7] for emissions. The emissions data were used to calculate combustion efficiency per SAE AIR1533 [8]. Combustion efficiency was measured for a range of combustor operating conditions and fuel/air ratios.

Pressure Drop. Combustion system pressure drop was measured using total and static pressure probes in the combustor/plenum annulus and at the combustor exit. Pressure drop (DP) is defined as:

$$DP = \frac{(\text{Upstream pressure} - \text{Downstream pressure})}{\text{Upstream pressure}} \times 100 \text{ percent} \quad (2)$$

Table 1 Flex-cycle combustor operating conditions

Parameter	Units	NAB Sea Level		SE 50,000 ft (15.000 m)		SE 25,000 ft (7.500 m)	
Air Flow	lbm/s (kg/s)	2.39	(1,08)	0.59	(0,27)	0.73	(0,33)
Fuel Flow	lbm/hr (kg/hr)	216.3	(98,1)	69.4	(31,5)	85.6	(38,8)
Inlet Pressure	psia (kPa)	132	(910)	32.8	(226)	40.0	(276)
Inlet Temperature	F (C)	626	(330)	-70	(-56,5)	-70	(-56,5)
Exit Temperature	F (C)	2249	(1232)	2123	(1162)	2124	(1162)

Table 2 Measured flex-cycle combustor steady-state performance values

Parameter	Units	NAB Sea Level		SE 50,000 ft (15.000 m)		SE 25,000 ft (7.500 m)	
Liner Pressure Drop	percent	2.55		0.72		0.73	
Combustion Efficiency	percent	99.99		99.95		--	
Pattern Factor	--	0.15		0.15		0.15	
Lean Stability Fuel/Air Ratio	--	--		<0.009		<0.009	
Ignition Fuel/Air Ratio For 1/2 Second Light-Off	--	0.019		0.023		--	
Maximum Wall Temperature	F (C)	1350	(732)	1300	(705)	1300	(705)
Fuel Pressure Drop	psid (kPa)	116	(800)	24	(165)	29	(200)
Smoke	SAE Smoke #	2.0		2.8		--	
Carbon	--	None		None		None	

The pressure drops reported below are based on the pressure in the ignitor plane and the combustor exit pressure.

Steady-State Test Results. The three most important operating conditions for the flex-cycle combustor are given in Table 1. These represent three different altitudes and two operating regimes: sea level, maximum power NAB operation; 50,000 ft (15,240 m) altitude SE operation; and SE operation near the SE/NAB transition altitude. The sea level, maximum power condition is characterized by high inlet air temperature and high fuel and air flows, conditions that are typical of normal aircraft gas turbine APU operation. The emergency power (SE mode) conditions have low inlet air temperatures, low fuel and air flows, and high fuel/air ratios; these conditions are consistent with low stored air usage and high-altitude operation. The emergency power conditions were set by the hot gas temperature limits for the IPU turbine stator.

Table 2 shows the measured combustor performance for the three conditions listed in Table 1. The reported performance data are for an optimized combustion system, which differs slightly from that discussed by Klaass et al. [1, 2]. The pressure drop given in Table 2 is the total pressure drop across the combustor liner. The upstream pressure is measured in the combustor annulus at the ignitor plane for both operating modes, allowing direct comparison of SE and NAB performance. The ignition fuel/air ratios are quoted for a delay of 1/2 second. This is the maximum ignition time permissible if a two-second engine start is to be achieved. The pattern factors are consistent with turbine life requirements. The SAE smoke number is low and well below the visible limit for both SE and NAB operation. All of the performance parameters are well within the acceptable limits for a high-performance, long-life IPU.

Transient Testing

Test Methods. Figure 5 is a schematic of the transient test setup showing the combustor rig, electronic control box, fuel control system, air control valves, air and fuel measuring sections, an ignition unit, and instrumentation. The combustor rig is similar to that shown in Fig. 4, but with modifications to simulate the transient response of the 400-1 better. The rotating instrumentation carrier was replaced by an instrumented orifice plate, located in the same plane as the turbine nozzle in the 400-1 engine, which restricts the combustor exit flow and produces the desired combustor pressure. The orifice plate effective area matches that of the 400-1 engine turbine nozzle. The deswirl vane assembly was modified to simulate an aerodynamically isolated engine compressor. A small amount of backflow was allowed to flow through the modified deswirl to simulate the compressor backflow. The flow split between the forward flow through the combustor and the flow through the deswirl system was set by the flow area ratio of the controlling orifices.

The fuel flow was metered using an off-the-shelf APU torque motor. Air flows were modulated by rapid-response valves using a closed-loop proportional/integral control. These valves were specially designed for the flex-cycle program. Air flow was measured using Dieterich Standard Diamond II annubar flow meters. These devices have the advantages of low pressure loss, rapid response, and insensitivity to Reynolds number. Fuel flow was measured using a turbine flow meter. Other piping and valving shown in the setup was used manually to set the rig conditions prior to each transient run (i.e., cold soak the rig prior to the cold SE starts).

Command signals from the control box operated the fuel torque motor, air modulating valves, SE and NAB air shutoff valves, fuel shutoff valve, and fuel atomizer air-assist shutoff valve. Instrumentation was used for control of the rig as well as for system monitoring and engine simulation.

Demonstration of two-second engine starts and SE/NAB transitions required incorporation of a real-time engine model into the electronic controller. Engine speed data were crucial for establishing the success of the transient test and for controlling the combustion system. The engine model included aerodynamic performance maps for the load compressor, engine compressor and turbine, as well as predicted engine drag characteristics. The operating conditions for each of the component maps were based on the engine model parameters that were derived from combustor rig measurements.

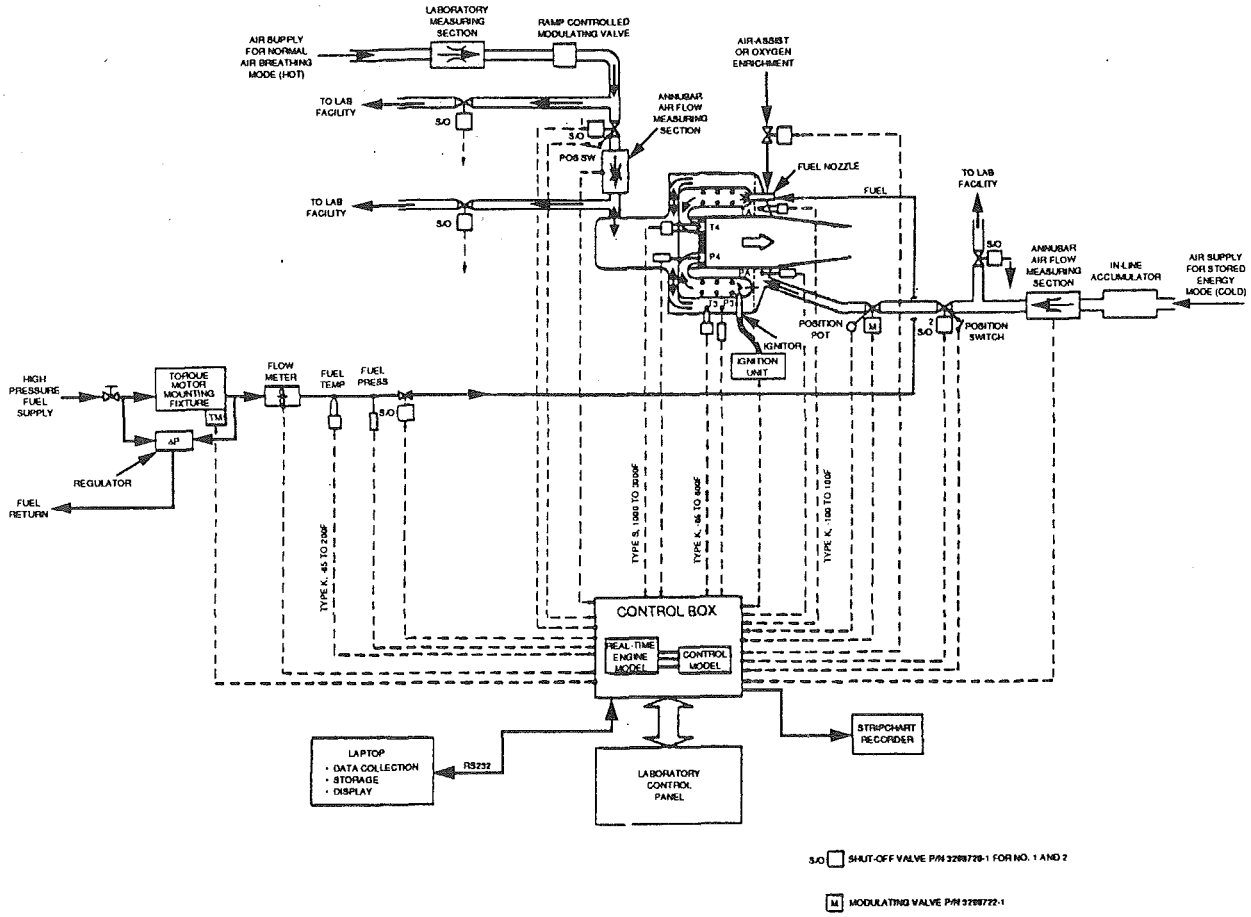

Fig. 6 Schematic of computerized 400-1 IPU engine model used in flex-cycle test rig controller

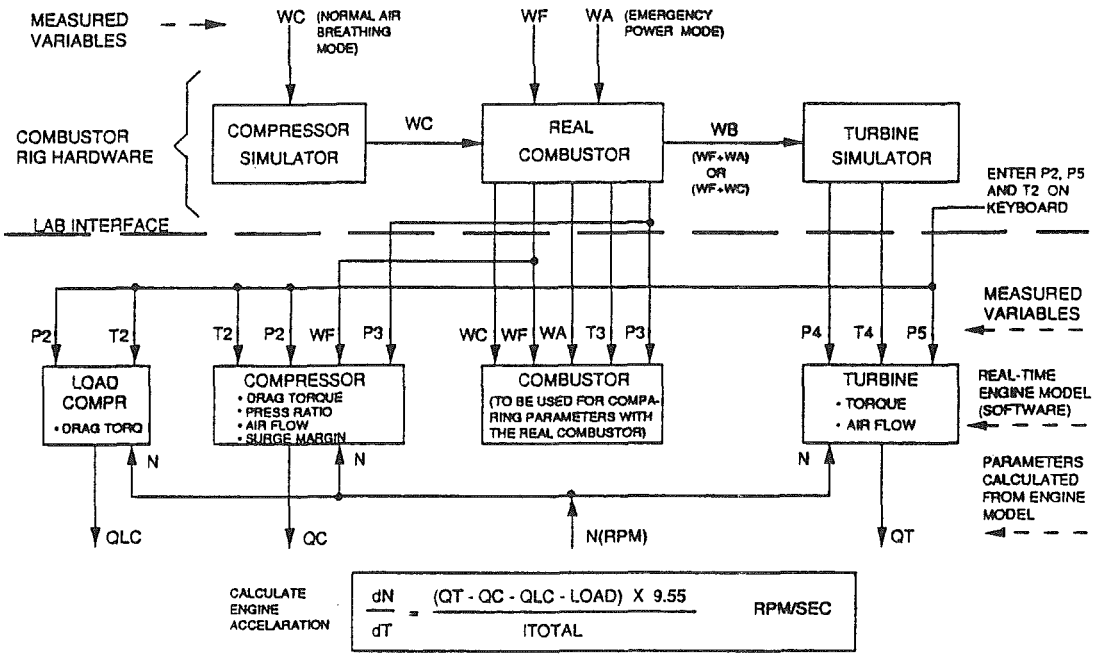

Fig. 5 Flex-cycle combustor test rig control schematic

Figure 6 shows the configuration of the engine model implemented in the controller. The model relies on measurements of combustor pressure, temperature, fuel flow, and air flow. Engine characteristics are calculated and used to update the real combustor conditions at each time step. Calculations and adjustments are made in real-time to make the combustor/simulator dynamically correct. Measured and calculated values are stored electronically. Engine ambient test conditions are input from a laptop computer, which also facilitates data storage.

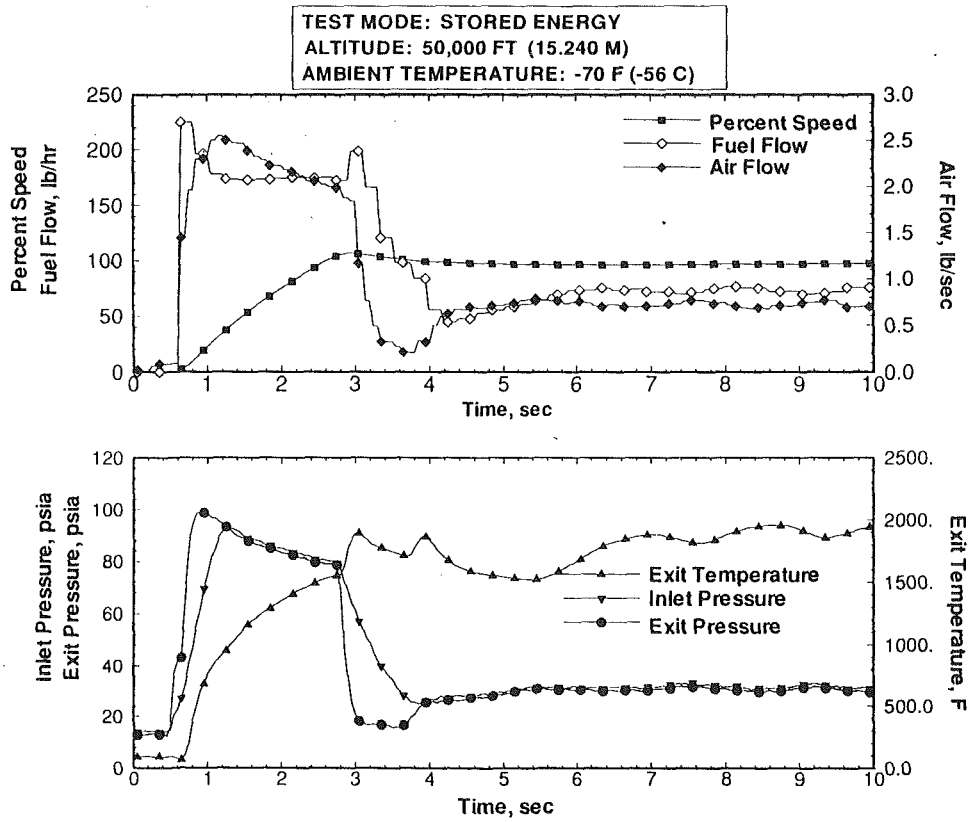

Fig. 7 Sample test data acquired during stored energy (SE) mode rapid start at 50,000 ft (15.000 m) simulated test altitude

Since the 400-1 APU must operate in two modes, each mode requires its own control function for optimum performance. During NAB operation, only the fuel flow is controlled, to maintain the desired engine shaft speed. In the SE mode, both air flow and fuel flow are controlled, to maintain the required fuel/air ratio for optimum combustion, air usage, and power output; and to maintain constant-speed operation.

The SE control consists of both starting and on-speed logic. The control during a start is closed-loop on combustor inlet pressure (P3), not exit temperature (T4). The start cycle is considered complete when the model engine speed reaches 100 percent; the control logic then switches to governing mode to maintain on-speed operation. In the governing mode, the control logic is closed-loop on speed. When speed changes are large, such as when loads are added or removed from the IPU, corrections are made in both the fuel and air flows. Modulating the air flow improves response time by changing the pressure ratio across the turbine nozzle.

The SE start and SE/NAB transition sequences were demonstrated during separate tests. For the SE/NAB transition tests, only the control logic for speed governing was used prior to transition. When a command was given to execute a transition, the NAB control took over the fuel control operation, and SE control operation was deactivated. For a transition, the control closed the SE air shutoff valve, then opened the NAB air shutoff valve to simulate air flow reversal and normal engine compressor operation.

Instantaneous data was collected using the electronic control box and two eight-channel recorders. The data stored in the control box memory were retrieved and copied to diskette following each run. Thirty-six parameters were measured for each transient run at a sampling frequency of 20 Hz.

Transient Test Results. Real-time transient runs were performed at simulated altitudes from sea level to 50,000 ft (15,240 m). These include rapid starts in SE mode, continuous operation in SE mode with simulated engine shaft load changes, and transitions from SE to NAB operation with a constant shaft load.

Three of the transient runs are presented here: The first is a rapid start at 50,000 ft (15,240 m) in the SE operating mode; the second is a transition from SE to NAB operation at 20,000 ft (6096 m); and the third is a sea level start in SE mode, followed by a transition to NAB mode. These conditions are representative of the mission of the SE/NAB system, which includes an emergency power start, SE operation with a 200 shp (149 kW) load, then an SE/NAB transition at an altitude at which the IPU can produce 200 shp in NAB mode alone.

Figure 7 is a plot of engine speed and five key combustor operating parameters during an SE start at 50,000 ft (15,240 m) simulated altitude. The engine start time is two seconds from the first indication of engine speed. The start is characterized by a rapid pulse of air and fuel to provide fast engine acceleration. Ignition occurs at 1/2 second, after which the combustor exit temperature rises quickly. A rapid increase in combustor pressure accompanies the start, resulting in a load-limited turbine throughout engine acceleration.

Initially, the combustor exit pressure is higher than the inlet pressure for two reasons: (1) The response time of the exit pressure is shorter than that of the inlet pressure, and (2) the rapid rise in combustor exit temperature results in a rise in pressure at the combustor exit that is not seen at the inlet until a short time later. In order to prevent engine over-speed, at 100 percent shaft speed the air and fuel flows are cut back drastically and the 200 shp (149 kW) shaft load is applied. The exit temperature and pressure respond to this cutback. Once at 100 percent shaft speed, the combustor settles out to a steady-state operating condition similar to that given in Table 1. The combustor lights rapidly and maintains stable burning throughout the rapid acceleration.

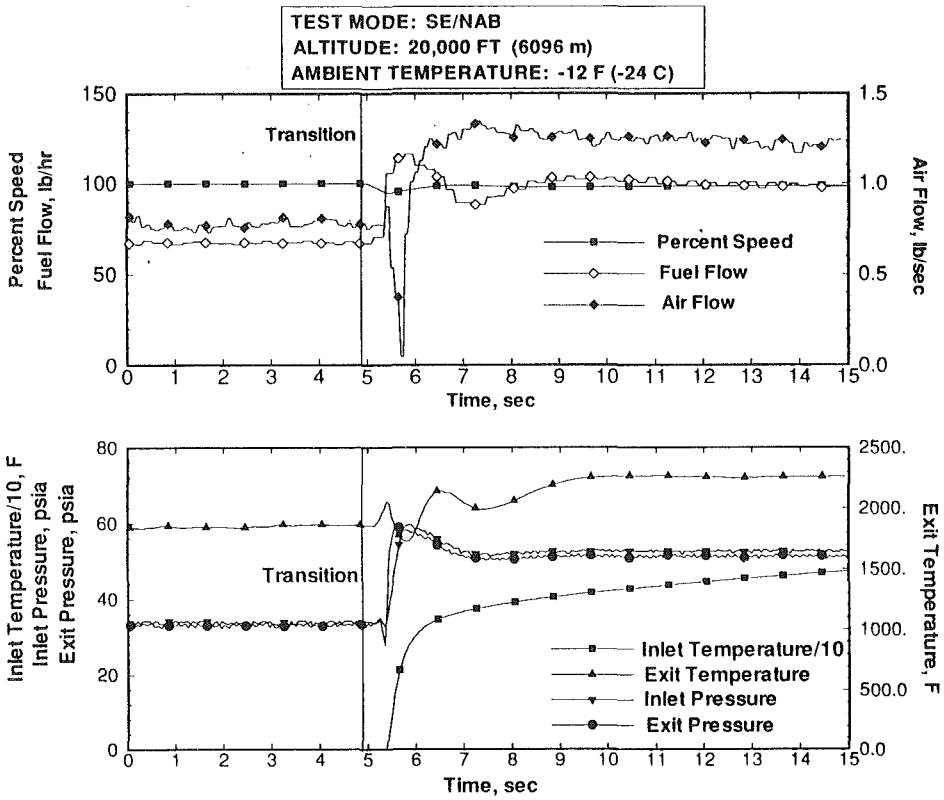

Fig. 8 Sample test data acquired during transition from SE to NAB mode at 20,000 ft (6,100 m) simulated test altitude

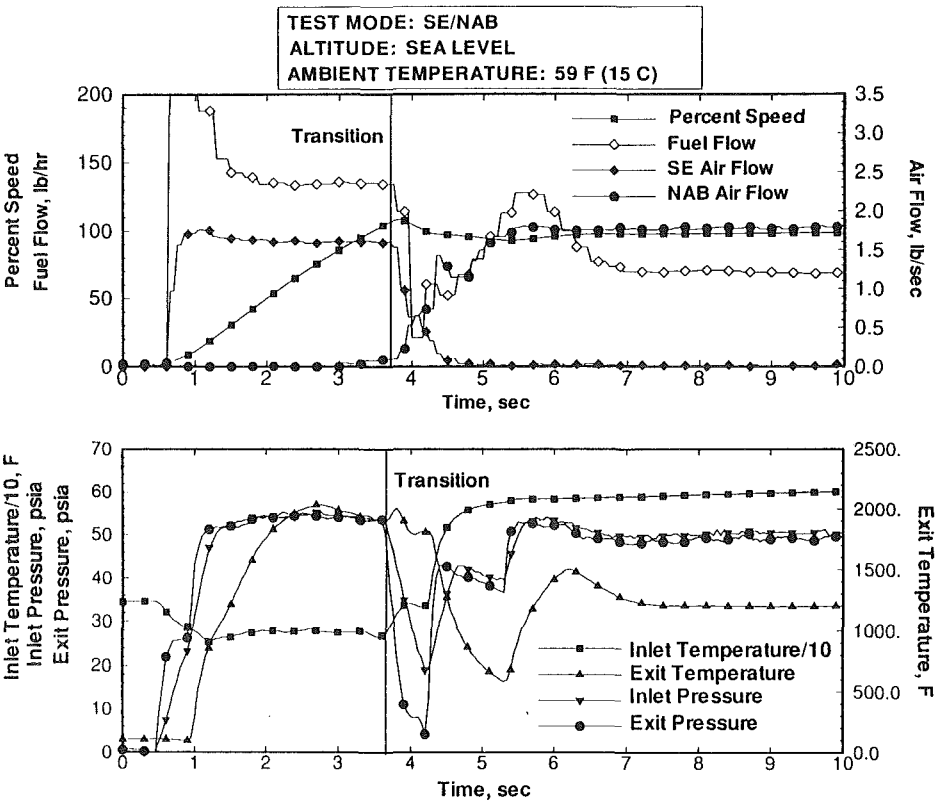

Fig. 9 Sample test data acquired during rapid sea level start and transition to 100 percent speed, no-load operation

Figure 8 shows engine speed along with six combustor operating parameters versus time during a transition from SE to NAB operation. Before the transition the combustor is operating in the SE mode with a 200 shp (149 kW) shaft load. When given the transition command, the control box instantaneously shuts off the SE airflow and there is a momentary

speed droop and a rise in exit temperature. A drop in combustor inlet and exit pressure is shown just before the NAB air valve is opened and the flow in the combustor annulus transitions from throughflow to reverse-flow. The combustor inlet temperature rises rapidly after the transition, as the NAB air system supplies air at conditions identical to the engine compressor discharge air. This conditioning is achieved by mixing hot and cold air upstream of the NAB air flow measuring section. During the SE/NAB transition the fuel control responds to the increased compressor load, which was decoupled during SE operation, and compensates for any deviations from 100 percent speed. Combustor operation is stable throughout the transition and there is no significant speed droop or associated loss in engine power output.

Figure 9 shows engine speed along with seven combustor operating parameters versus time during a rapid, sea level SE start and transition to NAB mode, 100 percent speed, no-load operation. In this figure the stored air flow and engine compressor air flow are shown separately. The APU shaft speed reaches 100 percent after 3.5 seconds. At 3.75 seconds after start initiation, the transition from SE to NAB mode begins. The APU is ready to load within 5 seconds from start initiation. The entire start sequence requires 5.5 lb (2.5 kg) of stored air, and is made with a maximum combustor exit temperature less than 2100°F (1150°C), demonstrating a simple, rapid-start capability consistent with long hot section life.

Conclusions and Summary

Increased demands for greater capability in secondary power systems for future aircraft are being met through new engine system architectures and design innovations. Development of a flex-cycle combustor is the key to meeting the demand for rapid and reliable IPU starts at all altitudes and immediate delivery of emergency power for critical flight control. Extensive development and refinement of the flex-cycle combustor during steady-state testing, and verification of the performance of the entire combustion system during transient rig testing have demonstrated the viability of this combustor concept.

Acknowledgments

Development of the flex-cycle combustor was supported by the U.S. Air Force under the Dual Mode Combustor Development Program, Contact No. F33615-87-C-2807.

References

1 Klaass, R. M., "Power System for 21st Century Fighter Aircraft," SAE Technical Paper 892253, SAE International, Warrendale, PA, Sept. 1989.

2 Klaass, R. M., Harris, M. M., and Marsh, D. N., "Flex-Cycle Combustor Component for Rapidly Starting an Integrated Power Unit," SAE Technical Paper 902022, SAE International, Warrendale, PA, Oct. 1990.

3 Kalviste, J., "Measures of Merit for Aircraft Dynamic Maneuvering," Society of Automotive Engineers (SAE) Technical Paper 901005, SAE International, Warrendale, PA, Apr. 1990.

4 Skow, A. M., "An Analysis of SU-27 Flight Demonstration at the 1990 Paris Airshow," SAE Technical Paper 901001, SAE International, Warrendale, PA, Apr. 1990.

5 Riley, D. R., and Drajeske, M. H., "Relationships Between Agility Metrics and Flying Qualities," SAE Technical Paper 901003, SAE International, Warrendale, PA, Apr. 1990.

6 Anon., "Aircraft Gas Turbine Engine Exhaust Smoke Measurement," Aerospace Recommended Practice ARP1179B, SAE International, Warrendale, PA, Apr. 19, 1991.

7 Anon., "Procedure for the Continuous Sampling and Measurement of Gaseous Emissions From Aircraft Turbine Engines," Aerospace Recommended Practice ARP1256B, SAE International, Warrendale, PA, Aug. 1, 1990.

8 Anon., "Procedure for the Calculation of Basic Emission Parameters for Aircraft Turbine Engines," Aerospace Information Report AIR1533, Society of Automotive Engineers, Inc., Warrendale, PA, Apr. 30, 1982.

Development of an Aeroderivative Gas Turbine Dry Low Emissions Combustion System

G. Leonard

J. Stegmaier

GE Aircraft Engine Business,
Cincinnati, OH 45241

This paper gives the development status of GE's new aeroderivative premixed combustion system. This system consists of a new fuel staged annular combustor, compressor rear frame, first-stage turbine nozzle, electronic staging controller, and fuel delivery system. Component test results along with a description of the combustion system are presented. This new system will reduce NO_X emissions by 90 percent relative to the original aircraft engine combustion system while maintaining low emissions of CO and UHCs. Tests of a LM6000 gas turbine equipped with the new system are planned for early 1994.

Introduction

In January 1990, GE embarked on the detailed design of a new gas-fired premixed combustion system for its family of aeroderivative gas turbines. This new lean premixed system, sometimes referred to as a Dry Low NO_X or a Dry Low Emissions combustion system, will reduce emissions of NO_X to less than 25 ppm. Emissions of other pollutants, such as CO, unburned hydrocarbons, and particulates are also expected to be extremely low.

The technical background required to launch the development of this new combustion system has been acquired over the past 25 years. Research directed at understanding NO_X formation in premixed flames was initiated in the mid-60s (Fenimore, 1970) and continues through today (Correa, 1992). Prototype premixed combustors for GE's aircraft engines and heavy frame gas turbines were first built and tested in the later 1970s (Ekstedt, 1987) and early 1980s (Walsham, 1983), respectively. These pioneering efforts have led to the development of GE's new premixed combustors for its heavy frame gas turbine product line. That development is described elsewhere (Davis, 1992).

This paper presents the development status of GE's new aeroderivative premixed combustion system. It begins with a review of recent test results that have contributed to the design of the new premixed combustion system. The design of this system is then described in some detail. The discussion includes all major engine components impacted by the introduction of the premixed combustion system, including the combustor, compressor rear frame, turbine nozzle, control system, and fuel delivery system.

GE has initiated a series of full-scale premixed combustor tests, which will culminate in a LM6000 factory engine test in early 1994. A brief summary of these tests is presented along with a discussion of the test objectives. Finally, opportunities exist for future improvements in premixed combustion systems. These opportunities are described at the end of this paper.

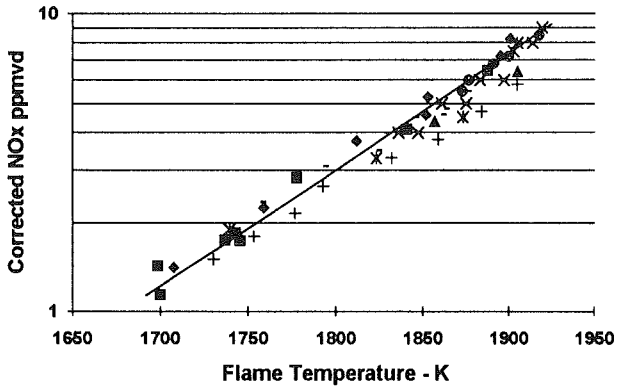

Fig. 1 Corrected NO_X versus flame temperature

Technology Development

The establishment of new design criteria for an aeroderivative premixed combustion system was an important initial phase of this program. These design criteria were established by conducting analytic studies and laboratory tests that focused on how NO_X, CO, and UHC are formed in premixed flames. In addition, the effects of engine operating conditions and combustor film cooling on emissions and lean flame stability were studied in some detail. The results of these tests are described below.

Figure 1 gives NO_X, in ppm by volume corrected to 15 percent O_2 as a function of flame temperature. These data were taken over a wide range of test conditions with a variety of flame holders used to stabilize the premixed flames. The operating pressures, inlet air temperatures, and residence times were varied from 1 to 30 bar, 300 to 800 K, and 2 to 100 ms, respectively.

Contributed by the International Gas Turbine Institute and presented at the 38th International Gas Turbine and Aeroengine Congress and Exposition, Cincinnati, Ohio, May 24–27, 1993. Manuscript received at ASME Headquarters March 10, 1993. Paper No. 93-GT-288. Associate Technical Editor: H. Lukas.

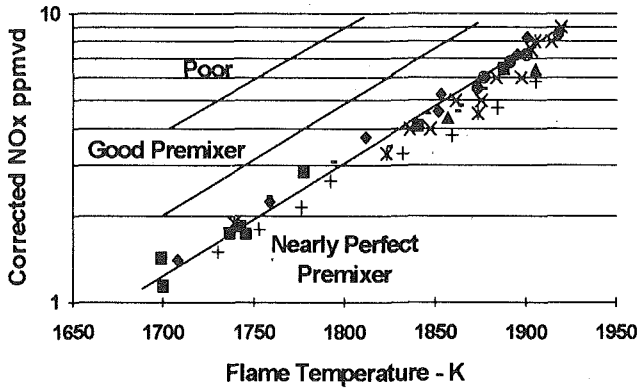

Fig. 2 Effects of nonuniform fuel and air mixing on NO_X formation

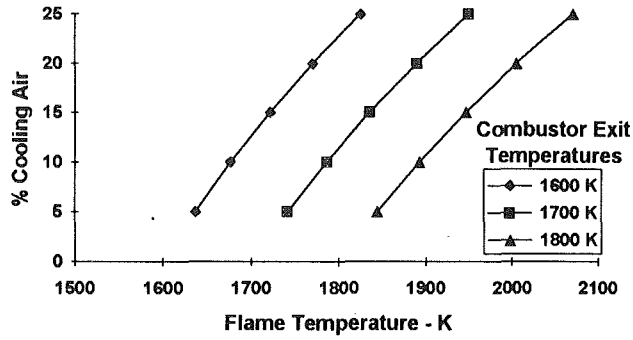

Fig. 3 Available film cooling air versus flame temperature; cooling air presented as a percentage of total combustor air flow

Uniform mixing of the fuel and air prior to combustion is the only feature shared by the data given in Fig. 1.

These data have three important ramifications for premixed systems. First, in extremely well premixed flames operating at less than 1900 K the amount of NO_X formed does not vary with gas pressure. Thus, the traditional guideline that NO_X increases with pressure does not apply to well-designed lean premixed systems. Therefore, high pressure ratio gas turbines with premixed combustion systems will not inherently produce more NO_X than low pressure ratio machines.

Second, the data confirm that NO_X is not a function of combustor inlet temperature. This was expected since the flame temperature of a premixed combustor, unlike a conventional diffusion flame combustor, can be varied independently of combustor inlet temperature. Thus, high pressure ratio gas turbines are not inherently disadvantaged because of their high combustor inlet temperatures.

Finally, in extremely well premixed flames operating at less than 1900 K the amount of NO_X did not increase with increasing residence time. Therefore, lean premixed combustors can have long residence times, to achieve low CO and UHC, while maintaining low NO_X levels. Thus, CO and UHC emissions can be minimized by increasing the size of traditionally compact aeroderivative combustors without impacting NO_X emissions.

Figure 2 shows NO_X as a function of average flame temperature for varying degrees of premixing. Nonuniformities are the result of fluctuations in time as well as variations in space. Figure 2 gives data for a nearly perfect premixer, well-designed premixer, and nonoptimized premixer. The design point flame temperature of the new premixed combustion system was obtained from data similar to those presented in Fig. 2.

It is of interest to note that the amount of NO_X formed in a nonoptimized premixer does increase with increasing pressure. This occurs because reactions taking place in the hot spots (greater than 2000 K) of poorly premixed flames are pressure dependent.

Once the design point flame temperature is set, the combustor residence time necessary to achieve complete reaction of the UHCs and CO is established. The precise value is a function of the engine operating cycle. GE has determined the required residence time for its family of engines from small-scale combustor tests and chemical kinetics models of the combustion process. The results demonstrated the need to double the residence time relative to conventional aeroderivative combustor design practice. As a result, the new premixed combustor's volume is approximately twice that of a conventional combustor.

Traditionally, aeroderivative combustors are cooled by a film of air that keeps hot products of combustion away from the dome and liner of the combustor. Premixed combustor tests have demonstrated that reaction zone film cooling leads to the formation of large quantities of CO and UHCs. The reaction zone film cooling air also results in early flame blowout in premixed combustors.

In lean premixed combustors most of the air must be mixed with the fuel, so little air is left for film cooling. Figure 3 shows combustor film cooling air as a function of flame temperature. The curves correspond to different combustor exit temperatures. The data are for a 30 to 1 pressure ratio gas turbine. At a flame temperature of 1900 K and a combustor exit temperature of 1700 K only 20 percent air remains for combustor film cooling. This amount of air is insufficient to film cool a combustion liner. Therefore, nontraditional liner cooling techniques must be applied.

To summarize, the following conclusions can be drawn from the aforementioned tests. First, low NO_X can be obtained in any gas turbine, low or high pressure ratio, if the fuel and air are uniformly mixed and the flame temperature is kept below 1900 K. Second, low CO and UHC can also be achieved by increasing combustor residence time and eliminating reaction zone film cooling. Finally, modern high firing temperature gas turbines must use nontraditional combustion liner cooling techniques.

LM6000 Lean Premixed Combustion System

The transition from a conventional combustor to a low emissions premixed combustor impacts more components than just the combustor. For example, the compressor rear frame, compressor diffuser, high pressure turbine nozzle, control system, and fuel delivery system must all be re-optimized for use with the premixed combustor. The re-optimization of these components is described below.

Premixed Combustor. Figure 4 shows GE's new LM6000 premixed combustor along with the conventional LM6000 combustor. The premixed combustor has a larger volume to achieve increased combustor residence time for complete reaction of CO and UHCs. The new premixed combustor fits within a new engine frame, called the compressor rear frame, which replaces the existing frame. This modular design approach, as described in the next section, facilitates retrofitting of the new premixed combustion system into existing LM6000 installations.

Figure 5 shows the combustor dome from an aft view. The combustor dome consists of three annular rings of premixers separated by partitions referred to as "centerbodies" in Fig. 4. The outer two annular zones each have 30 premixers while the inner annular zone has 15. This arrangement of 75 premixers facilitates fuel staging during part power gas turbine operation.

Figure 6 gives a cross section of a single premixer. Air enters and passes through a set of axial flow swirlers that induce highly sheared counterrotating flow. The resulting turbulent

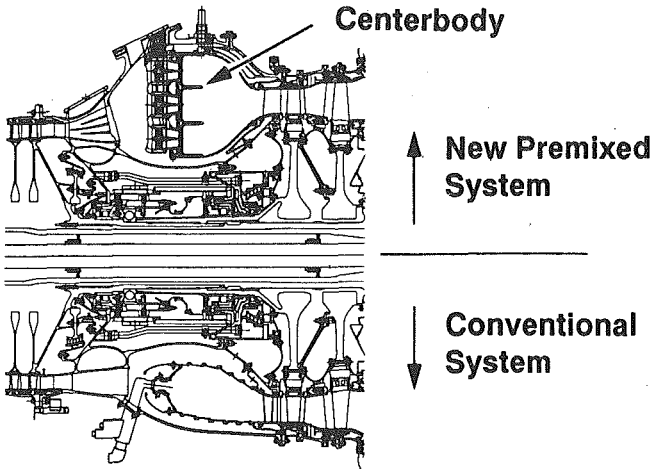

Fig. 4 Comparison of new premixed combustion system with conventional combustion system

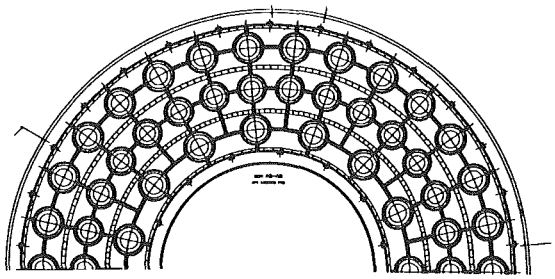

Fig. 5 Premixed combustor dome

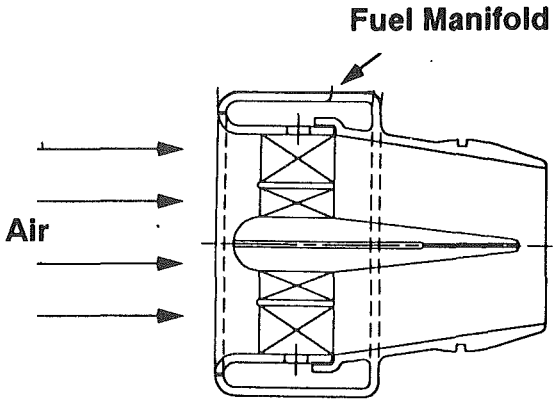

Fig. 6 Fuel-air premixer cross section

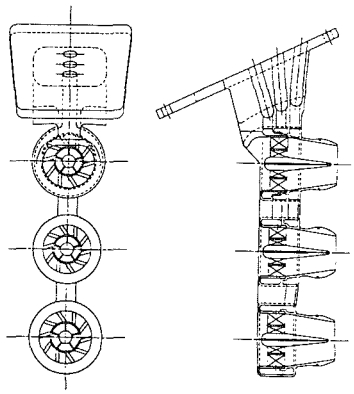

Fig. 7 Fuel nozzle assembly

flow mixes the fuel and air. The fuel enters the premixer through the hollow axial swirl vanes and then passes through trailing edge orifices before mixing with the air. Residual swirl remaining at the exit of the premixer helps stabilize the downstream premixed flame. This design produces a very uniform mixture of fuel and air, which is a primary requirement for achieving low NO_X levels.

Fifteen of the gas turbine's 30 fuel nozzles are formed by combining three premixers on one stem. The stem includes three separate fuel circuits for independently fueling the three premixers. The other 15 fuel nozzles are formed by combining two premixers on one stem. Figure 7 shows a fuel nozzle assembly with three premixers. This fuel nozzle concept was selected because it provided a configuration with readily removable premixers and eliminated the need for fuel lines upstream of the premixer. The elimination of fuel lines and their associated wakes provides a more uniform air flow distribution immediately upstream of the premixers.

As can be seen in Fig. 4, other than the premixers, the primary combustor components are the dome assembly and the liner. The dome assembly consists of a dome plate and a number of heat shields with integral "centerbodies." These heat shields are attached to the dome plate to protect it from the hot product of combustion. The heat shields and "centerbodies" are backside convectively cooled with air that exits downstream of the primary zone of the combustor at the "centerbody" tips. The centerbodies isolate the three annular regions from one another during fuel staged operation at low power. Isolating these regions is necessary to maintain low levels of CO and UHCs over a wide power range.

A short annular combustion liner design was adopted in order to minimize the amount of air required for convective cooling. This liner is cooled by air that exits the compressor diffuser, passes over the external surface of the liner, and then cools the first-stage turbine nozzle. Since only backside cooling is used in the combustor, a thermal barrier coating is applied to both the dome heat shields and the liner to maintain acceptable metal temperatures.

Compressor Rear Frame. To accommodate the new larger volume premixed combustor a new LM6000 compressor rear frame assembly was designed; see Fig. 4. Its diameter was increased by several inches relative to the conventional design. The new compressor rear frame includes a new split compressor diffuser that helps deliver air to the large combustor dome with a minimum of pressure loss. In addition, 30 large access panels were added to aid installation and removal of the fuel nozzles. The new rear frame, which houses the first-stage turbine nozzles as well as the combustor and compressor diffuser, is a direct replacement for the conventional compressor rear frame, thus making retrofitting conventional combustion systems with new premixed systems relatively straightforward.

High Pressure Turbine Nozzle. The temperature profile exiting the LM6000 lean premixed combustor is extremely flat relative to the temperature profile of a conventional combustion system. The cooling flow circuit of the first-stage turbine nozzle was modified in order to maximize the life and performance of the high pressure turbine. In addition, the modification restored the temperature profile entering the first stage rotor to its original shape, which eliminated the need to make changes to downstream turbine components.

Control System. During full power operation, fuel flows to all premixers, and the flame temperature is at its design point. As the gas turbine power is reduced the engine control system must keep the flame temperature near its design point. If the flame temperature significantly exceeds the design point value, then the NO_X will exceed the 25 ppm objective and the combustor liner could be damaged. If the flame temperature

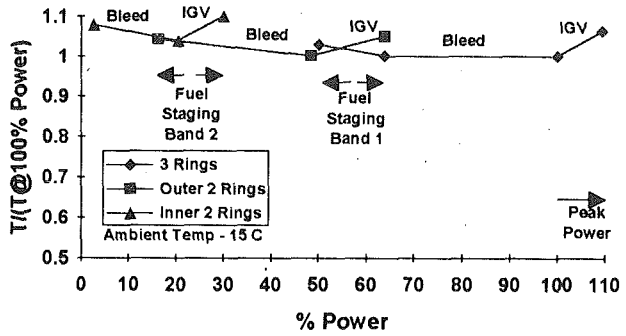

Fig. 8 Flame temperature normalized by design point flame temperature versus power

is too low, then CO and UHCs will exceed the 25 ppm objective, and lean blowout could occur.

The premixed combustion system uses parallel fuel staging, inlet guide vane modulation, and compressor bleed to maintain a nearly constant flame temperature over the engine operating range. Figure 8 shows flame temperature as a function of gas turbine power for this new control scheme. The LM6000 inlet guide vanes will be controlled, so that nearly constant flame temperature is maintained as power is initially reduced. Once the inlet guide vanes are completely closed, compressor air bleed will be used to maintain a nearly constant flame temperature as the power is further reduced. When the bleed limit is reached, the fuel to the inner ring of premixers is shut off. The fuel that was flowing to these premixers is then routed to the outer two rings of premixers. Simultaneously, the compressor bleed is shut off and the flame temperature downstream of the fueled premixers is restored to near its design point value to keep emissions low. As power is reduced further, this sequence is repeated until only the middle ring of premixers is fueled. Using this control strategy, it is possible to operate from start to full power in a premixed mode with the flame temperature varying little from its design point value.

In addition to the conventional system elements, the new control system includes 26 solenoid actuated fuel staging valves, two compressor bleed valves, an electronic NO_X controller, and the instrumentation and sensors required to calculate flame temperature. The main engine control unit retains overall engine control, including fuel metering, guide vane modulation, and compressor bleed valve modulation. The new electronic NO_X controller calculates the flame temperature from measured engine parameters, controls the fuel staging valves, and interfaces with the main engine control unit.

It is theoretically possible to stage between the three annular rings of the new premixed combustor using only two staging valves. The use of 26 staging valves, however, significantly helps to smooth engine operation when staging occurs between the annular combustor rings. To assure high overall engine reliability, these staging valves have been designed to be extremely reliable, with each containing only three moving components. In addition, the control system can detect when a staging valve is faulty and automatically modify the fuel staging schedule so engine operation is not disrupted.

Fuel Delivery System. To accommodate the fuel staging requirements, a new fuel delivery system was designed. This system consists of a base-mounted gas manifold and 30 flexible hose assemblies connecting the manifold to the premixing fuel nozzle assemblies.

The manifold (see Fig. 9), which is a cast design, consists of five circumferential segments, each internally cored to provide fuel to the three premixer rings. The fuel staging valves are mounted on the manifold. Figure 10 shows the external configuration of the fuel delivery system.

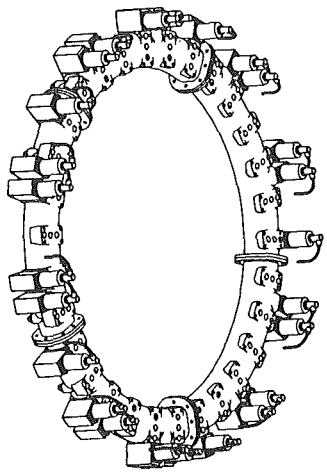

Fig. 9 Fuel manifold

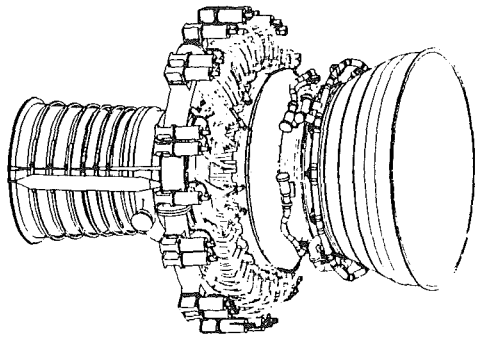

Fig. 10 External fuel delivery system

Development Testing

Development tests are currently being conducted prior to introducing the new premixed combustion system into production. These are being used to assist in the design verification of the compressor diffuser, premixer, heat shield, combustion liner, fuel staging valve, NO_X controller, and control concept. The major system tests are described below.

A 72 deg sector of the full-scale premixed combustor will be tested at LM6000 engine conditions of 800 K inlet temperature and 30 bars of pressure. The flow through the combustor will be 20 percent of the LM6000's combustors 90 kg/s air flow. The fuel staging system, including the NO_X controller, will be used during these tests.

The purpose of these sector tests is to demonstrate that significantly less than 25 ppm NO_X, CO, and UHCs can be achieved with the production premixed combustor design. In addition, a complete lean blowout map and combustor dome and liner temperature profiles will be obtained. The fuel staging valves and NO_X controller will also be evaluated during the fuel staging tests.

A production combustor will be evaluated in a test stand capable of operating at 10 atm prior to engine tests. The purpose of this test is to demonstrate engine starting and low power fuel staging. Combustor exit temperature profiles, pressure drops, and combustor dynamics will also be determined.

In early 1994 a LM6000 equipped with the new premixed combustion system will be tested. The tests will be designed to demonstrate overall engine performance with particular emphasis on engine emissions, control system performance, combined diffuser and combustor performance, combustion dynamics, combustor and casing temperatures, turbine performance during staged operation, and verification of all vari-

able geometry schedules. Transient as well as steady-state engine performance will be determined.

Summary

The technology development, detailed design, and component test phases of GE's premixed combustion system development program are complete. Laboratory-scale tests have demonstrated that NO_X formation in a well-designed premixed combustion system is not a function of operating pressure, combustor inlet temperature, or combustor residence time for flame temperatures less than 1900 K. These tests demonstrated the feasibility of ultralow emissions levels in high pressure ratio aeroderivative gas turbines, and helped establish new design criteria for premixed combustion systems.

The new premixed combustion system design includes an annular combustor with a volume about twice that of a conventional aeroderivative combustor. This added volume should provide the necessary residence time to assure complete reaction of CO and UHCs. This new combustor also uses an advanced backside cooling system that allows most of the combustor air to be routed through the premixer. The resulting lean mixture of fuel and air will combust at a flame temperature of less than 1900 K, thus assuring low levels of NO_X formation. Component testing has demonstrated that less than 25 ppmvd each of NO_X, CO, and UHCs should be attained with the new combustion system over a broad power and ambient temperature range.

The worldwide demand for cleaner burning gas turbines is growing. Design refinements to future premixed combustion systems will lead to even lower emissions. Improved premixer designs, tighter manufacturing tolerances, better flame temperature sensing systems, and a reduction in combustor liner and turbine cooling air flows should all result in lower emissions of NO_X, while maintaining low CO and UHC emissions. NO_X, CO, and UHC levels below 10 ppmvd should be achieved sometime later this decade with advanced aeroderivative premixed combustion systems.

Acknowledgments

The authors would like to acknowledge (1) the aeroderivative Dry Low Emissions design team for the work described in this paper, (2) the GE heavy frame gas turbine Dry Low Emissions design team for their timely and excellent program assistance, and (3) The GE Corporate Research Dry Low Emissions development team for much of the basic research, which laid the foundation for the launch of the new aeroderivative premixed combustion system.

References

Correa, S. M., 1992, "A Review of NO_X Formation Under Gas-Turbine Combustion Conditions," *Combustion Science and Technology*, Vol. 87, pp. 329–362.

Davis, L. B., 1992, "Dry Low NO_X Combustion System for GE Heavy-Duty Gas Turbines," *1992 ASME Cogen-Turbo Conference*, ASME IGTI-Vol. 7, pp. 255–270.

Ekstedt, E. E., 1987, "Advanced Low Emissions Combustor Program," Paper No. AIAA-87-2035.

Fenimore, C. P., 1970, "Formation of Nitric Oxide in Premixed Hydrocarbon Flames," *13th Symposium (International) on Combustion*, Combustion Institute, Pittsburgh, PA, pp. 373–380.

Walsham, R. M., 1983, "Dry Low NO_X Combustion Systems for Utility Gas Turbines," ASME Paper No. 83-JPGC-GT-13.

K. Y. Sokolov

A. G. Tumanovsky

M. N. Gutnik

A. I. Mechanikov

All-Russian Heat Engineering Institute (VTI), Moscow, Russia

V. P. Reshitko

M. I. Grinshtein

Turbineworks Turboatom, Charkov, Ukraine

Experimental Investigation of GTE-115 Combustor With Premixed Burner Unit

The results of experimental investigation of the basic parameters of one-burner, 1/18 sector of a full-scale annular combustor of the "Turboatom" GTE-115 gas turbine unit are presented. Specifics of fuel burnup and formation of toxic pollutants in premixed combustion using a pilot diffusion burner are presented. Generalized dependences of combustor characteristics versus flow parameters and an optimized algorithm of combustor loading are illustrated.

Introduction

The comprehensive investigations conducted at VTI to reduce NO_x emissions with utility GT unit exhaust gases showed the lean fuel combustion ($\alpha = 1.7$–2.3 in the combustion zone) and subsequent intensified diffusion combustion with application of multiburner combustor and microflame burners to be the most promising approach (Hristich and Tumanovsky, 1980). The NO_x concentration was shown to decrease for stationary natural gas GT units as low as 1.5–2.5 times and are at 75–130 ppmv (Tumanovksy, 1973). Even better results (30–40 ppmv) were obtained on GTN-25 units with microflame combustion in opposite-swirled air jets (Tumanovsky et al., 1986; Brevdo et al., 1987; Sokolov et al., 1990). Recently the world's leading gas turbine firms GE, Mitsubishi, ABB, Siemens-KWU, in particular, are paying ever-increasing attention to premixed combustors (Becker et al., 1990; Aigner et al., 1990; Sattelmayer et al., 1990) allowing lower flame temperatures with resultant reduced NO_x concentrations as compared to diffusion combustion.

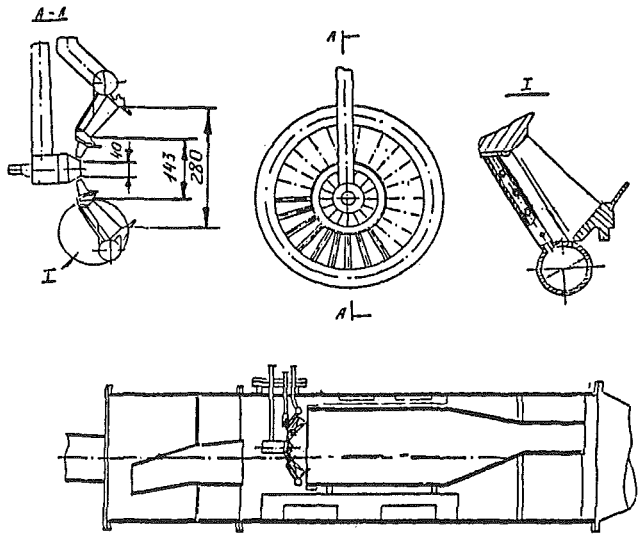

Fig. 1 General view of the test section (*a*) and premixed burner (*b*)

Test Combustor

To realize such a method of combustion in the "Turboatom" GTE-115 utility GT unit, an annular combustor has been designed incorporating a burner unit made up of a central diffusion burner with axial swirler and premixed burner (Fig. 1*a*). The latter is in fact a conical swirler with swirl angle of 45 deg with gas distributer tubes before the swirler and along each blade. The passage areas of central and annular swirlers and the cooling system are related as 0.06, 0.64, 0.3. Thus, in nominal conditions ($\alpha_{tot} = 2.9$–3.1) the air-fuel equivalence ratio in the premixed zone was $\alpha^{pr} = 1.8$–2.0.

Such high values of α_{tot} causing lower NO_x concentrations may lead to problems with flame stability, complete fuel burnup during startup, and adequate levels of hydraulic resistance and fire tube temperature. The tests were conducted on a one-burner 1/18 sector of a full-scale annular combustor (Fig. 1*b*) at 0.11–0.13 MPa with wide variations of other flow parameters.

Contributed by the International Gas Turbine Institute and presented at the 38th International Gas Turbine and Aeroengine Congress and Exposition, Cincinnati, Ohio, May 24–27, 1993. Manuscript received at ASME Headquarters March 1, 1993. Paper No. 93-GT-144. Associate Technical Editor: H. Lukas.

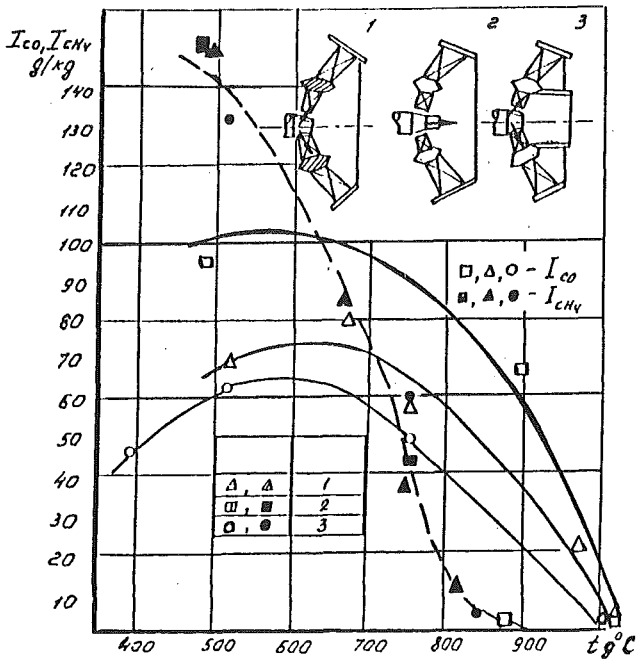

Fig. 2 Emission index of CO and CH_4 versus gas temperature for different diffusion burner designs

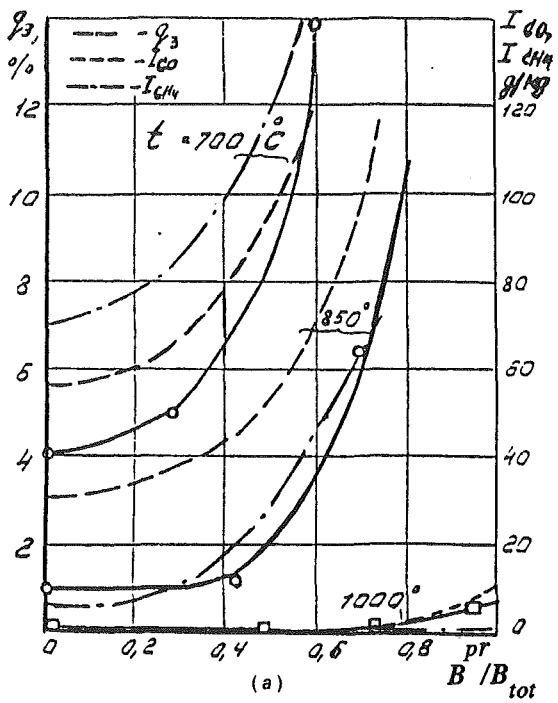

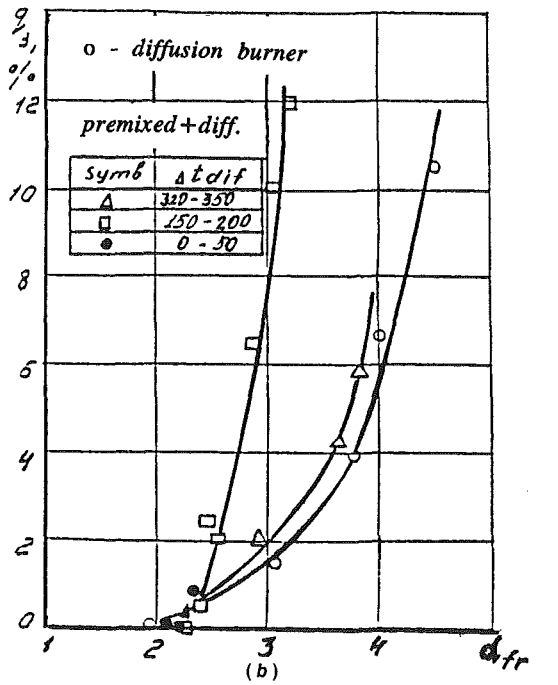

Fig. 3 Incomplete combustion heat loss versus fuel used for premixing (*a*) and burner unit air-fuel ratio (*b*)

Results and Discussion

Stable combustion when using the diffusion burner was found to exist within the range of α_{tot} = 2.5–20, t_{in} = 50–350°C, W_{sw} = 30–80 m/s.

Flame stabilization in the premixed burner with the central burner out operation was not a success up to gas temperature of 1200°C, that is, up to α^{pr} = 1.75 (t_{in} = 350–380°C, W_{sw} = 50–80 m/s).

The main function of the central burner in the burner unit of the proposed design is complete burnup and minimum CO and CH_4 formation during startups and transients. Several options of central burner with different fuel gas injectors and air distribution were tested (Fig. 2).

As one can see from Fig. 2, the use of a division shell allows at the gas temperature of 600–800°C the values of q_3 not exceeding 3–5 percent, CO and CH_4 at 300–400 ppmv to be obtained. This corresponds to emission factors of I_{CO} = 40–60 g/kg and I_{CH_4} = 40–100 g/kg.

The analysis of the results obtained showed that for the given design of the combustor further reduction of incomplete combustion heat loss and CO concentration during transients may be ensured by applying control of air distribution (with

Nomenclature

B^{dif} = diffusion burner fuel flow
B^{tot} = burner unit (front zone) fuel flow
B^{pr} = premixed burner fuel flow
$\overline{B}^{dif} = B^{dif}/B^{tot}$ = relative fuel flow in diffusion burner
G^{fr} = air flow in the front zone
G^{pr} = air flow in the premixed burner
I_{CO} = emission factor (index) of CO
I_{CH_4} = emission factor of CH_4
P_c = combustor pressure
q_3 = incomplete combustion heat loss, percent
T^{pr} = combustion temperature of homogeneous mixture
$T_g(t_g)$ = exhaust gas temperature, K, °C
$T_{in}(t_{in})$ = inlet air temperature
$T_{\alpha=1.1}$ = combustion temperature at α = 1.1
Δt_{dif} = total temperature preheating in combustor by diffusion flame
ΔT^{fr}_{dif} = temperature preheating in front zone by diffusion flame
W_{sw} = swirler exit velocity
α_{tot} = total combustor air-fuel equivalence ratio
α_{fr} = burner unit (front zone) air-fuel equivalence ratio
α^{pr} = premixed burner air-fuel equivalence ratio
α^{dif}_{fr} = front zone air-fuel equivalence ratio with only diffusion burner in operation

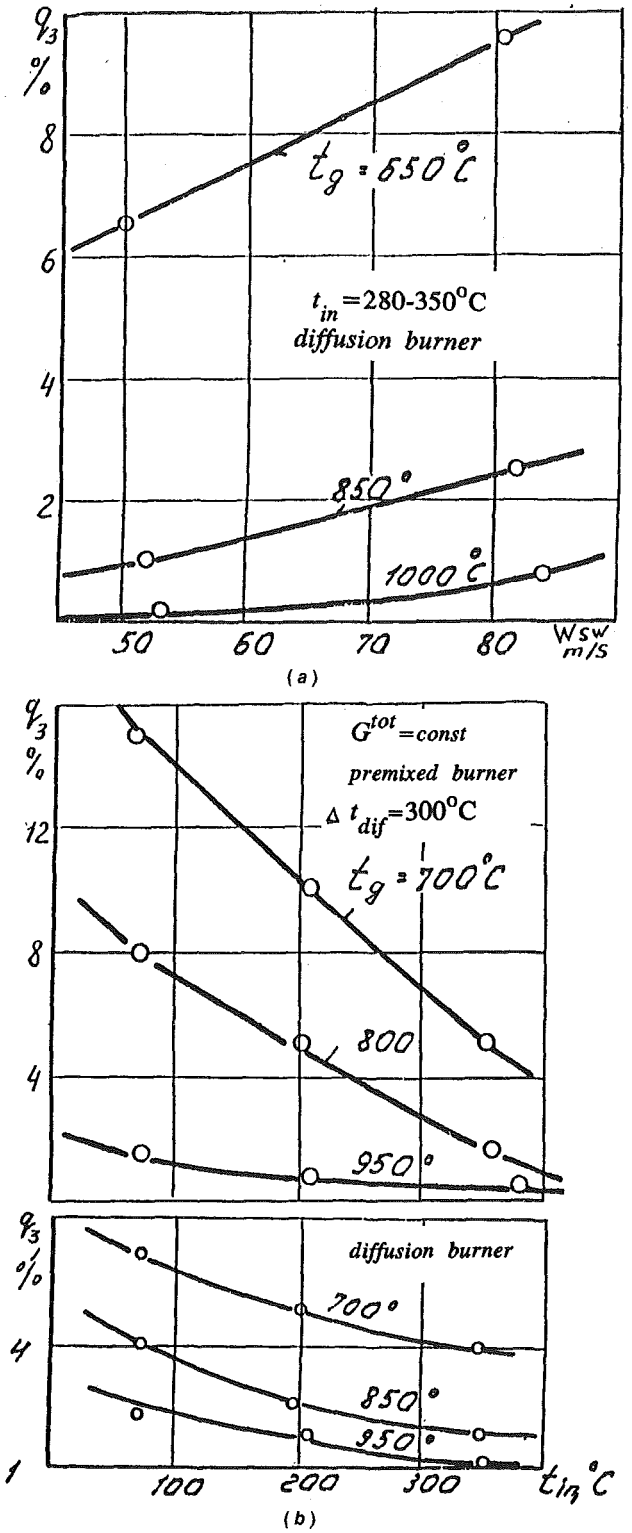

Fig. 4 Incomplete combustion heat loss versus air flow (*a*) and inlet temperature (*b*)

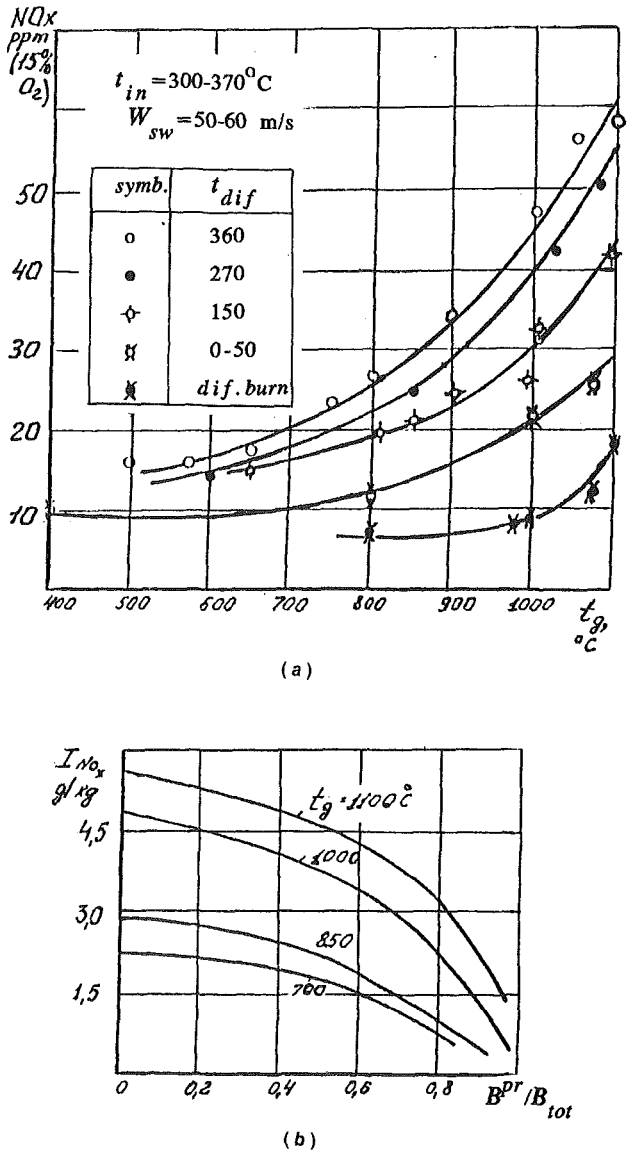

Fig. 5 Concentration (*a*) and emission index (*b*) of NO_x versus exit gas temperature and fuel flow ratio between diffusion and premixed burners

variation of air dilution flow within 0–20 percent of the total air flow). Thus, the air–fuel equivalence ratio in the front zone was found to decrease by 2.5–3 (Fig. 3*a*).

The dependences of q_3 and I_{CO} and I_{CH_4} versus the front zone air–fuel ratio are illustrated in Fig. 3(*b*) for different fuel distribution between two burners. It is evident that with decreasing relative fuel flow for the diffusion burner (T^{fr}_{dif} or $\overline{B}^{dif}$) the fuel burnup during transients drops. However, in nominal conditions (t_g = 1000–1100°C) the fuel burnup is 0.995–1.0 even at minimal (with regard to flame stability) diffusion burner fuel flow.

The influence of air velocity and temperature on q_3 is shown in Fig. 4. The generalized dependence of fuel burnup degree is:

$$\eta_c = 1 - \exp\left[-\frac{0.01\ T_{in}^{1.5}\ (1+B_{pr})}{W_{sw}\cdot \alpha_{tot}^{0.5}}\right] \qquad (1)$$

Another important aspect in our investigation was NO_x formation. For lean fuel–air mixture (α^{pr} = 1.9–2.0) NO_x concentration decreased substantially. At nominal conditions (t_g = 1050–1100°C) with B^{dif} = 5–7 percent, NO_x concentration was 12–15 ppmv and I_{NO_x} = 1.2–1.5 (Fig. 5), which is considerably lower as compared to diffusion combustion (B^{dif} = 100 percent): NO_x = 70–80 ppmv, and I_{NO_x} = 4.5–5.0 g/kg.

One can clearly see from Fig. 6 that the major cause of NO_x reduction with premixed burner is 300–350°C. In this case the maximum NO_x concentration was 150, 40–45, and 15–20 ppmv for B^{dif} of 100, 15, and 6–7 percent, respectively.

The effect of flow conditions on NO_x concentration is given in Fig. 7.

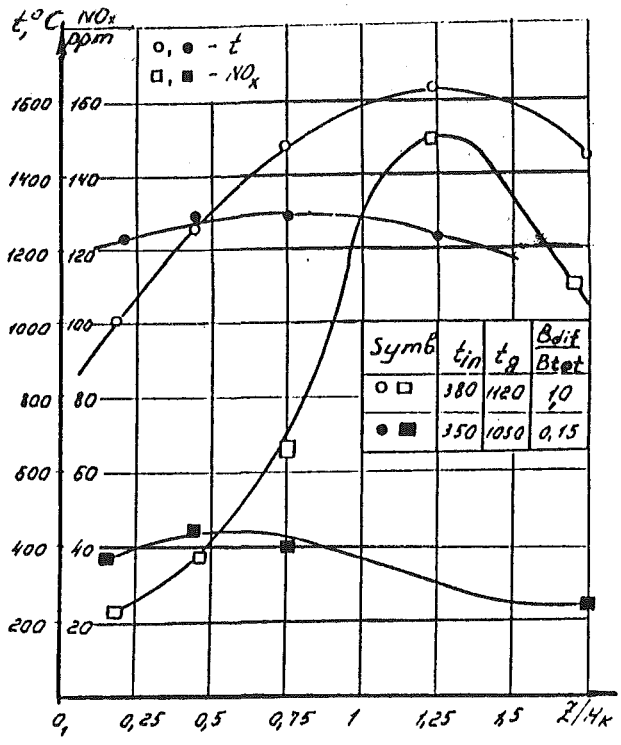

Fig. 6 Change of flame temperature and NO_x concentration along the axis of burner unit

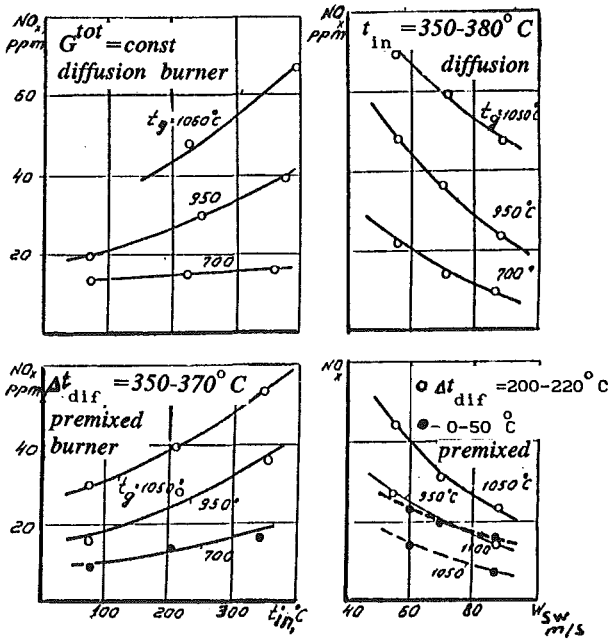

Fig. 7 NO_x concentration versus flow parameters

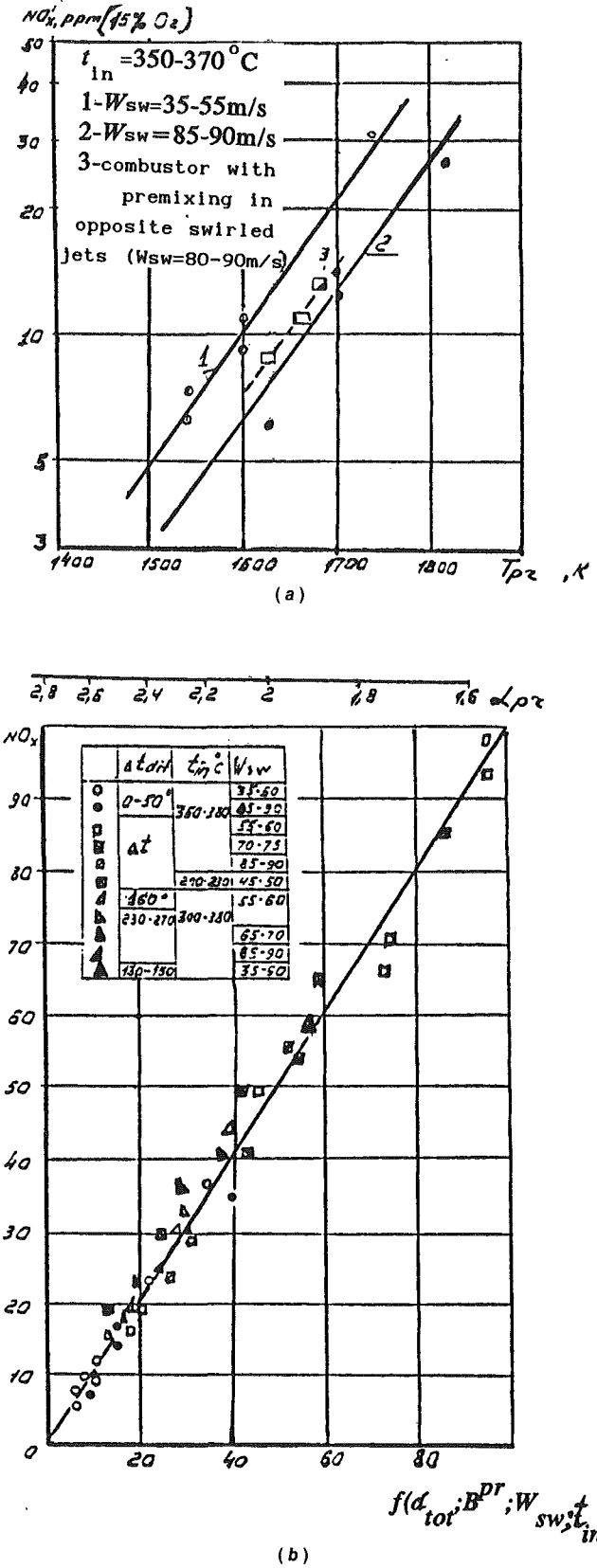

Fig. 8 Generalized dependences of NO_x formation as a function of air-fuel equivalence ratio in premixed burner (*a*) and flow parameters (*b*)

For the case of B^{dif} of 6–7 percent, the NO_x concentration is unambiguously determined by air–fuel equivalence ratio in the homogeneous mixture or by respective combustion temperature (Fig. 8*a*) and can be determined by

$$NO_x\Big|_{O_2=15 \text{ percent}} = 0.0015 \cdot W^{-1} \cdot \exp\frac{T_{pr}}{125} \qquad (2)$$

The dependence above can also be used for generalization of the data for premixed burner with opposite-swirled jets.

For diffusion burners of the considered design the following approximate dependence is obtained:

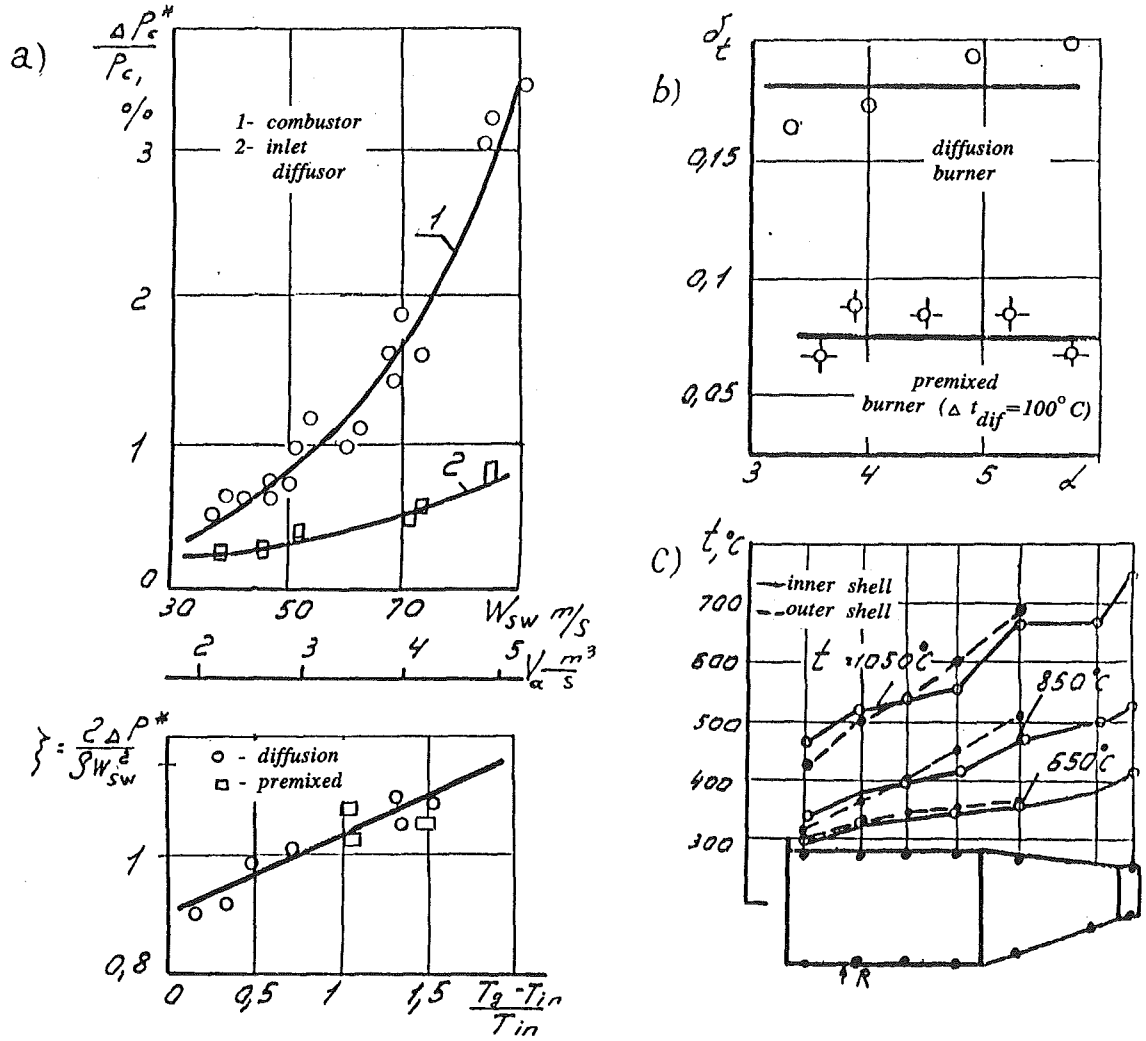

Fig. 9 Combustor characteristics: (*a*) full-pressure loss and hydraulic resistance coefficient; (*b*) exit gas temperature nonuniformity; (*c*) wall temperature

$$NO_x\Big|_{O_2=15\ \text{percent}} = \frac{3.67\cdot 10^{16}}{W_{sw}} \frac{1}{\alpha_{fr}^{1.7}} \exp -\frac{67535}{T_{\alpha=1.1}} \qquad (3)$$

where $T_{\alpha=1.1}$ is found from

$$T_{\alpha=1.1} = 2057 + 0.55\ T_{in} + 0.0001\ T_{in}^2$$

With both types of burner in operation, NO_x concentrations require the mutual influence of the burners to be taken into account, which can be summarized as follows:

1 The use of a premixed burner gives higher air-fuel equivalence ratio in the diffusion flame and front zone

$$\alpha_{fr.\text{dif}}^{\text{eff}} = \frac{G_{fr} - L_o B^{pr}}{L_o B^{\text{dif}}} = 1 + \frac{\alpha^{fr} - 1}{\overline{B}^{\text{dif}}} \qquad (4)$$

The value of $\alpha_{fr.\text{dif}}^{\text{eff}}$ should be used in Eq. (3) for NO_x calculation in diffusion flame ($NO_x^{\text{dif}*}$).

2 The influence of a diffusion flame on NO_x formation for homogeneous flame can be explained by higher combustion temperature due to diffusion burner preheating:

$$T_{pr}^{\text{eff}} = T_{pr} + \Delta T_{\text{dif}}^{fr}$$

The dependence of T_{pr}^{eff} versus T_{in} and B^{pr} may be represented as $T_{pr} = T_{pr}(T_{in}, \alpha_{pr}^{\text{eff}})$.

For the given air flow distribution between the burners, the effective air-fuel equivalence ratio in homogeneous mixture can be obtained from

$$\alpha_{pr}^{\text{eff}} = \frac{\alpha_{fr}}{1 - 0.08\ \overline{B}^{pr}} \qquad (5)$$

Here, one should bear in mind that NO_x concentration in the homogeneous flame with two burners in operation is determined by the difference in NO_x concentrations calculated by Eq. (2) at T_{pr}^{eff} and T_{fr}^{dif}:

$$NO_x^{pr*}\Big|_{O_2=15\ \text{percent}} = \frac{0.0015}{W_{sw}} \exp \frac{T_{pr}^{\text{eff}}(\alpha_{pr}, T_{\text{in}})}{125} - \exp \frac{T_{fr}^{\text{dif}}(\alpha_{fr}^{\text{dif}}, T_{in})}{125} \qquad (6)$$

$t_{in} = 200$–$400°\text{C}$, $W_{sw} = 30$–80 m/s, $\overline{B}_{\text{dif}} = 0$–$1$.

Using Eqs. (2)–(6), one may calculate NO_x concentrations with two burners in operation as follows:

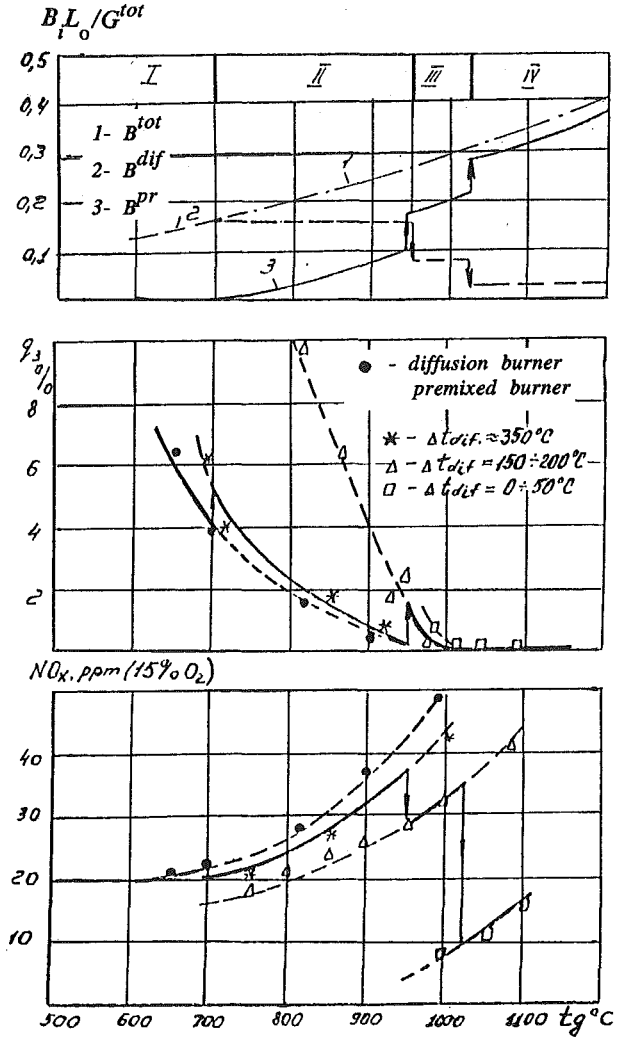

Fig. 10 Burner optimal fuel allocation, incomplete combustion heat loss, and NO_x concentration versus test burner unit gas temperature change of combustor loading

$$NO_x = NO_x^{pr*} + NO_x^{dif*} \quad (7)$$

Comparison of the calculated and experimental results in Fig. 8(*b*) shows the applicability of Eq. (7) for accurate generalization of all the data obtained.

Other combustor characteristics meet today's requirements and can be seen from Fig. 9.

Using the experimental results and Eqs. (1)–(7), the optimal algorithm of the burner unit loading has been developed ensuring minimal formation of harmful substances in combustion products and complete fuel burnup at nominal conditions and during transients (Fig. 10).

For startup and transients the figures were as follows: $NO_x \leq 40$ ppmv, CO ≤ 300–400 ppmv and $q_3 \leq 5$–6 percent while for nominal conditions they were 10–15 ppmv, 10–20 ppmv, and 0–0.05 percent, respectively.

For further NO_x and CO concentration reduction for nominal conditions and transients the burner unit design was optimized:

- α^{pr} was increased to 2.05.
- Share of air fed to the front zone was increased from 0.7 to 0.76.
- Share of air fed to the premixed burner increased from 0.64 to 0.707.
- Swirler exit velocity was increased to 70–72 m/s to improve stability margin with regard to flashback.

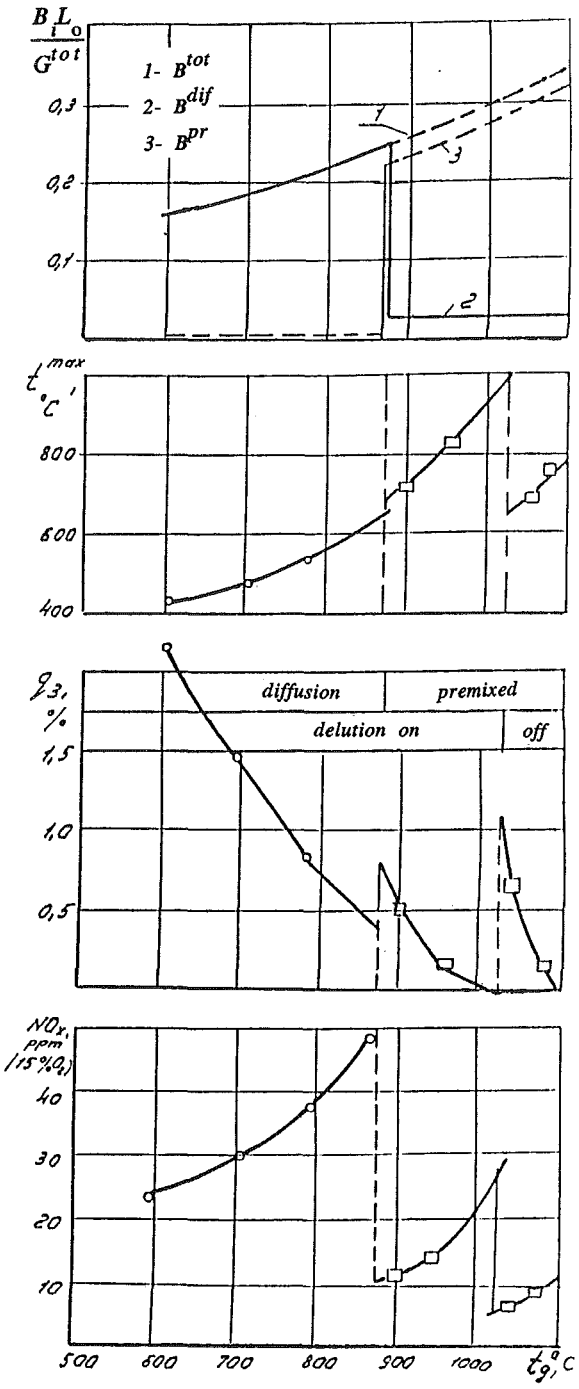

Fig. 11 Burner fuel allocation, wall maximum temperature, incomplete combustion heat loss, and NO_x concentration in loading the combustor with optimized burner unit and controlled air distribution

For more details of the algorithm, using the control of the air flow dilution within 0–20 percent of the total air, the interested reader is referred to Fig. 11.

The test pressure was 0.12–0.13 MPa. Correction for 1.4 MPa pressure was made assuming the pressure influence of NO_x formation for homogeneous flame is described by the formula of Hristich and Tumanovsky (1980) obtained for separate supplies of fuel and air:

$$NO_x \sim \frac{6P_c - 0.23}{P_c + 0.77}$$

The resultant figures for nominal conditions (P_c = 1.4 MPa, t_g = 1100°C, t_{in} = 350°C) are expected to be 23–25 ppmv (15 percent O_2).

Further research is needed to upgrade the burner unit in view of improving premixing, stable operations without flashback and vibrating combustion, opportunity for liquid fuel premixed combustion.

Conclusions

1 The results of experimental investigation of the burner unit incorporating a premixed burner showed opportunities for NO_x concentration reduction down 10–15 ppmv for nominal conditions (t_g = 1050–1100°C) with minimal diffusion fuel flow (B_{dif} = 0.05–0.07).

2 The correlations have been established relating CO and NO_x concentrations and fuel burnup in a wide range of flow conditions and fuel burner distributions.

3 An algorithm has been proposed for loading the burner unit ensuring minimal NO_x and CO formation.

4 The combustor design has been optimized allowing $q_3 \leq 2$ percent during transient and NO_x = 8–10 ppmv (P_c = 0.12–0.15 MPa) in nominal conditions to be obtained.

References

Aigner, M., Mayer, A., and Schissel, P., 1990, "Second Generation Low-Emission Combustors for ABB Gas Turbines: Tests Under Full-Engine Conditions," ASME Paper No. 90-GT-308.

Becker, B., Bonsen, F., and Simon, J., 1990, "A Simple and Reliable Combustion Control System," ASME Paper No. 90-GT-173.

Brevdo, M., Zaharov, U., and Maev, V., 1987, "Operation Experience With Mikroflame 25 MW GT Combustors on Gas Pipelines," *Proceedings, National Conference on Gas Turbines and Combined Cycle Units*, MVTU, p. 124.

Hristich, W. A., and Tumanowsky, A. G., 1980, *GT Units and Enviromental Protection*, Technica, Kiev.

Sattelmayer, T., Felchin, M., and Hauman, J., 1990, "Second Generation Low-Emission Combustors for ABB Gas Turbines: Burner Development and Tests at Atmospheric Pressure," ASME Paper No. 90-GT-169.

Sokolov, K., Tumanovsky, A., and Sudarev, A., 1990, "Mathematical Modeling of Flow, Heat and Mass Transfer and Burning Process in Annular Combustor of a Gas Turbine," *Proceedings 1st Assian-Pacific Conference on Combustion and Energy Utilisation*, Beijing, China, pp. 235–239.

Tumanovsky, A. G., 1973, "On Emissions From GT Combustors," *Teploenergetika*, No. 6, pp. 34–39.

Tumanovsky, A. G., Sudarev, A. V., Zaharov, Y. I., and Sokolov, K. Yu., 1986, "Combustion of Liquid Fuel in Opposite-Swirled Jets of Annular Combustor," *Teploenergetika*, No. 3, pp. 25–28.

T. Nakata
Associate Professor,
Department of Aeronautics and
Space Engineering,
Tohoku University,
Sendai 980-77, Japan

M. Sato

T. Ninomiya

Central Research Institute of
Electric Power Industry,
2-6-1 Nagasaka,
Yokosuka 240-01, Japan

T. Yoshine

M. Yamada

Toshiba Corporation,
Heavy Apparatus Engineering Laboratory,
2-4 Suehiro-cho, Tsurumi-ku,
Yokohama 230, Japan

Effect of Pressure on Combustion Characteristics in LBG-Fueled 1300°C-Class Gas Turbine

Developing integrated coal gasification combined cycle systems ensures that Japan will have cost-effective and environmentally sound options for supplying future power generation needs. Reduction of NO_x emissions and increasing the inlet temperature of gas turbines are the most significant issues in gas turbine development in IGCC. The coal gasified fuel, which is produced in a coal gasifier of air blown entrained-flow type has a calorific value as low as 1/10 of natural gas. Furthermore, the fuel gas contains ammonia when a gas cleaning system is a hot type, and ammonia will be converted to nitrogen oxides in the combustion process of a gas turbine. The study is performed in 1300°C-class gas turbine combustor firing coal-gasifier fuel in IGCC power generation systems. In the previous study [1] the advanced rich-lean combustor of 150-MW class gas turbine was designed to hold stable combustion burning low-Btu gas fuel and to reduce fuel NO_x emission that is produced from the ammonia in the fuel. By testing it under atmospheric pressure conditions, we have studied the effects of fuel parameters on combustor performances and listed the basic data for development applications. In this study, by testing it under pressurized conditions, we have obtained a very significant result through investigating the effect of pressure on combustion characteristics and wish to provide herein a summary of our findings.

Introduction

Research and development of an Integrated Coal Gasification Combined Cycle (IGCC) system as a new technology for coal utilization is being promoted by Japan, the United States, and Europe. In Japan, the government and the electric power companies began undertaking experimental research for a 200T/D pilot plant program in 1986. The calorific value of fuel generated from a coal gasifier is about 1/10 that of natural gas (LNG) and the main combustible component of the fuel is CO. Furthermore, if gas is refined through a hot-type process, it will characteristically contain NH_3, the compound from which fuel NO_x is generated. Thus development of a gas turbine combustor for IGCC with combustion stability and excellent NO_x emission characteristics is highly desirable.

The authors are conducting research and development of a 1300°C-class gas turbine combustor [2–5] under an IGCC system using an air-blown entrained-bed type gasifier. This has been done mainly by designing and experimentally assembling an operating size combustor of a 150 MW-class gas turbine. Up until now, by applying the rich-lean combustion technology of coal gasified fuel, as a method for reducing NO_x fuel, it has been possible to reduce the concentration of NO_x to 60 ppm (the NH_3 concentration in the fuel is 1000 ppm, and O_2 concentration is 16 percent at the combustor outlet), or less than half the level of NO_x concentration obtained when the 1300°C-class gas turbine combustor was first designed [2].

The pressure in combustors affects the emission characteristics of NO_x, combustion efficiency, liner wall temperature, and the like. Thus, in order to introduce on a commercial basis the combustor that CRIEPI has designed, it will be necessary to evaluate its performance under the same high-pressure conditions as a machine actually in operation. This paper reports principally on the results of combustion tests that we conducted under operational conditions and is the final evaluation of the performance of the gas turbine combustor for IGCC that we designed and produced.

Test Facilities

Figure 1 shows a schematic diagram of the test facilities. Low-calorie gas fuel, that is, coal gasified fuel, is manufactured with a fuel reforming system. Raw fuel, made by blending C_3H_8 with CO_2 and steam, decomposes into CO and H_2 in the fuel reformer under the condition of high-temperature 820°C. A hydrogen separation membrane is used to adjust the H_2 concentration in the fuel and the CO/H_2 mole ratio is set within a range of about 1–3. After adjusting the heating value by N_2 dilution, the test fuel is fed into the gas turbine combustor after being preheated by a heater to a temperature of 370°C. In addition, the required NH_3 concentration is fed into the fuel by a NH_3 feeder. A four-stage centrifugal compressor is

Contributed by the International Gas Turbine Institute and presented at the 38th International Gas Turbine and Aeroengine Congress and Exposition, Cincinnati, Ohio, May 24–27, 1993. Manuscript received at ASME Headquarters March 1, 1993. Paper No. 93-GT-121. Associate Technical Editor: H. Lukas.

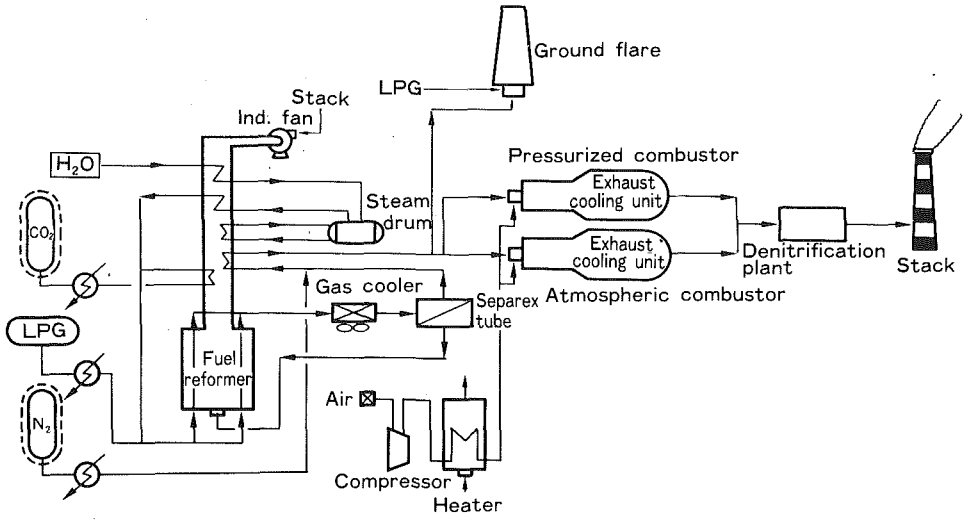

Fig. 1 Schematic diagram of the test facility

Table 1 Standard fuel composition

Composition	CO	18.3	%
	H_2	6.9	%
	CH_4	2.5	%
	CO_2	12.9	%
	H_2O	3.0	%
	N_2	56.3	%
	NH_3	1000	ppm
HHV	1000	kcal/m^{3}N	
	(4190	kJ/m^{3}N)	
LHV	930	kcal/m^{3}N	
	(3890	kJ/m^{3}N)	

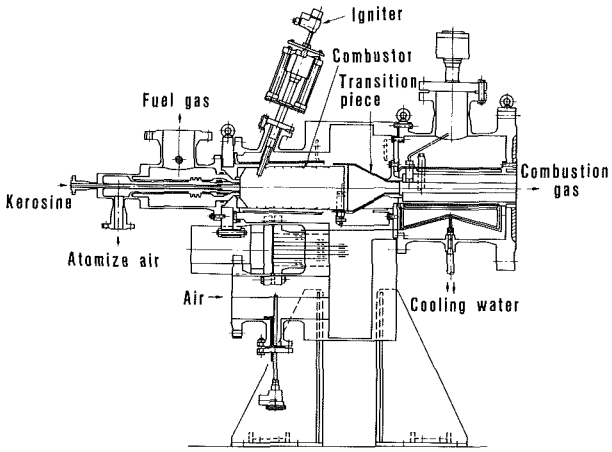

Fig. 2 Cross-sectional view of the test rig

used for air supply to the tested combustor. The standard properties of the sample fuel are shown in Table 1. The high calorific value is set at 1000 kcal/m^{3}N, the CO/H_2 mole ratio is at about 3, the NH_3 concentration is at 1000 ppm and CH_4 is at 2.5 percent.

The combustion testing area has two test rigs, each of which is capable of performing full-scale atmospheric pressure combustion tests as well as half-scale high-pressure combustion tests there. A cross-sectional view of the test rig for pressurized combustion testing is given in Fig. 2. After passing through a transition piece, the exhaust gas from the combustor is introduced into a measuring section for temperature measurement, gas sampling, and analysis. After that, the gas temperature is lowered through a quenching pot using an injection system of a water spray.

Samples are taken from the exit of the combustor through a water-cooled stainless steel probe located on the centerline of the measuring duct. The teflon-coated stainless steel sample lines are thermally insulated with heat tape to maintain the sampling gas system above the dew point of the exhaust gas. The continuous gas samples are introduced into an emission console that measures CO and CO_2 by infrared analysis, NO and NO_x by chemiluminescence analysis, O_2 by paramagnetic analysis, and hydrocarbons by flame ionization. Fuel gas is sampled at the inlet of the combustor, and CO, H_2, CH_4, CO_2, H_2O and N_2 are determined by gas chromatography every 5 minutes. Heating values of the fuel gas are monitored by a calorimeter and calculated from analytical data of gas components obtained from the gas chromatography.

The temperatures of the combustion liner are measured by sheathed type-K thermocouples welded on the liner wall. Gas temperatures at the combustor outlet are measured with R-type thermocouples.

Testing Combustor

Combustion tests are conducted on a half-scale combustor named CGT6001 under pressurized condition. The combustor

Nomenclature

HHV = higher heating value of the fuel, kcal/m^{3}N
Q_a = flow rate of air, m^{3}N/h
Q_f = flow rate of fuel, m^{3}N/h
u = mean sectional flow velocity, m/s
ta = air inlet temperature, °C
tf = fuel inlet temperature, °C
λ = air to fuel ratio = $[(A/F)/(A/F)_{\text{stoichiometric}}]$
C.R. = NH_3 conversion to a NO_x by mass percent
η = combustion efficiency, percent
p = pressure in the combustor, atm
t_{ex} = exhaust gas temperature at the combustor outlet, °C

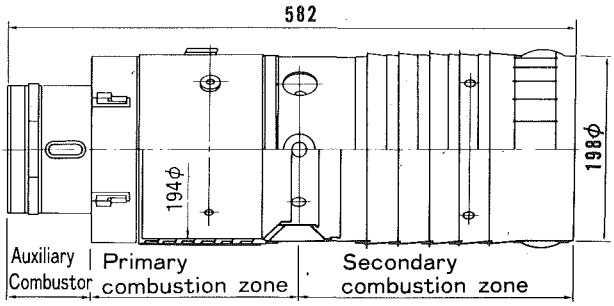

Fig. 3 Tested combustor

Table 2 Standard test conditions

Qa	8400	m^3N/h
Qf	4900	m^3N/h
u	21.3	m/s
λ	2.0	
ta	370	°C
tf	360	°C
p	14	ata
tex	1300	°C

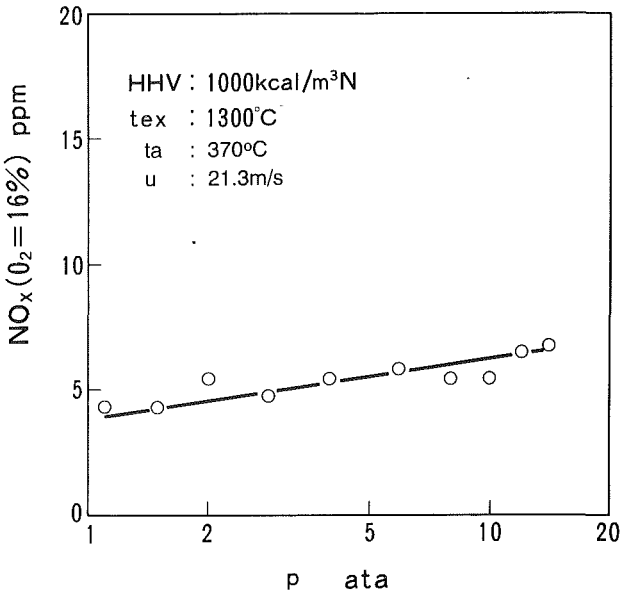

Fig. 4 Thermal NO_x emission characteristics

is designed for advanced rich-lean-combustion. This rich-lean combustion method is effective in decreasing fuel NO_x emissions resulting from fuel-to nitrogen. Figure 3 shows the outline of the tested combustor compared with the full-size combustor CGT-5001 [1]. The CGT-5001 combustor corresponds to the operating size of a multican, 150 MW-class gas turbine combustor. The CGT6001 has developed by using the CGT-5001 as a basis, and halving it, because of the limited capacity of fuel supply of the high-pressure test facilities.

This combustor characteristically consists of three major sections: an auxiliary chamber, a primary chamber, and a secondary chamber. The design of each chamber is based on the following concepts:

1 Auxiliary chamber: To stabilize the combustion flame in the fuel-rich area, a pilot flame is generated. The air-to-fuel ratio in this chamber is designed to be stoichiometric under the rated load condition.

2 Primary chamber: Under the condition of fuel-rich combustion, ammonia contained in the fuel is decomposed to nitrogen in a deoxidized atmosphere. The air-to-fuel ratio in this changer is designed to be 0.6 under the rated load condition.

3 Secondary chamber: Under the condition of fuel-lean combustion, the remaining combustible components are completely burned. The air-to-fuel ratio in this chamber is designed to be 2.0 under the load condition.

Two fuel nozzles are installed: one is at the head of the auxiliary chamber, and the other is set surrounding the exit of the auxiliary chamber. The fuel distribution in the auxiliary chamber is designed to be 15 percent of the total fuel input. Between the primary chamber and the secondary chamber, there is a constricted section where the air for the secondary combustion is fed.

The cooling air for the liner wall is also supplied to each combustion zone. Both the auxiliary chamber and the primary chamber, where the temperature is expected to rise, have liner walls of composites with film and impingement cooling. The inner surface of the combustor has plasma-sprayed ceramic coating.

The overall length of the combustor, including the auxiliary chamber, is 580 mm, and the inside diameter is 200 mm. The loading rate in the combustion chamber at the design point is 2.2×10^7 kcal/($m^3h \cdot atm$).

The standard conditions in the combustion tests are shown in Table 2. After ignition under atmospheric condition, combustion pressure is uprisen by increasing O_a and O_f with sectional flow velocity kept constant.

Test Results and Discussion

Emission Characteristics of Thermal NO_x. The emission characteristics of thermal NO_x under high-pressure conditions, including the operating condition of 14 atm, were examined.

Figure 4 shows the thermal emission characteristics of NO_x when the pressure in the combustor changed from 1 atm to 14 atm. The horizontal axis represents the pressure in the combustor, and the vertical axis represents the thermal NO_x emission concentration with the correction of 16 percent O_2. The total air to fuel ratio of the combustor is set at 2.0, so that the temperature of combustion gas at the combustor outlet would be equivalent to the rated load of 1300°C. The thermal NO_x concentration increased gradually from 4 ppm under atmospheric pressure in tandem with the rise in pressure, reaching 7 ppm under operational conditions of 14 atm.

As an example of the effect that pressure exerts on the level of the thermal NO_x emission in the gas turbine combustor, it is known that the pressure to the power of 1.5 is nearly proportional to the speed at which the Zeldovich NO is produced (mole/cm^3s) and that the emission of NO_x is proportional to the pressure to the power of 0.5 [6]. Moreover, although the equilibrium concentration of NO drops when the pressure rises, since the speed at which NO is produced increases, if the NO concentration fails to reach equilibrium, the NO concentration will tend to rise, when the pressure is high. In the case of the combustor under consideration, the thermal NO_x concentration increased in accordance with approximately the power of 0.2 of the pressure. Thus pressure had a smaller effect on thermal NO_x than is the case with LNG. This is also believed to be because, as shown in Fig. 5, in the case of LNG, the theoretical adiabatic flame temperature will rise significantly if the pressure increases, but in the case of coal gas, the flame temperature will rise only slightly if the pressure increases.

Emission Characteristics of Fuel NO_x. Figure 6 shows the emission characteristics of fuel NO_x, generated from NH_3 in the fuel, when the pressure in the combustor changes. The horizontal axis represents the pressure in the combustor, and

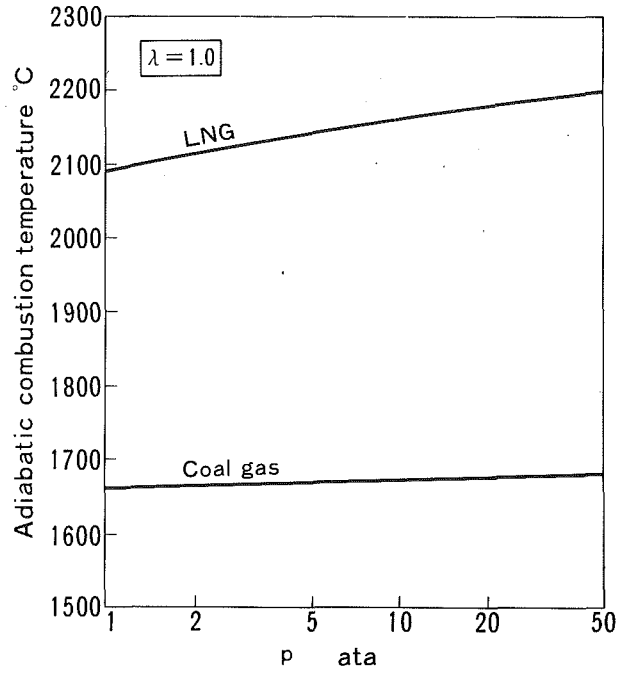

Fig. 5 Adiabatic flame temperature

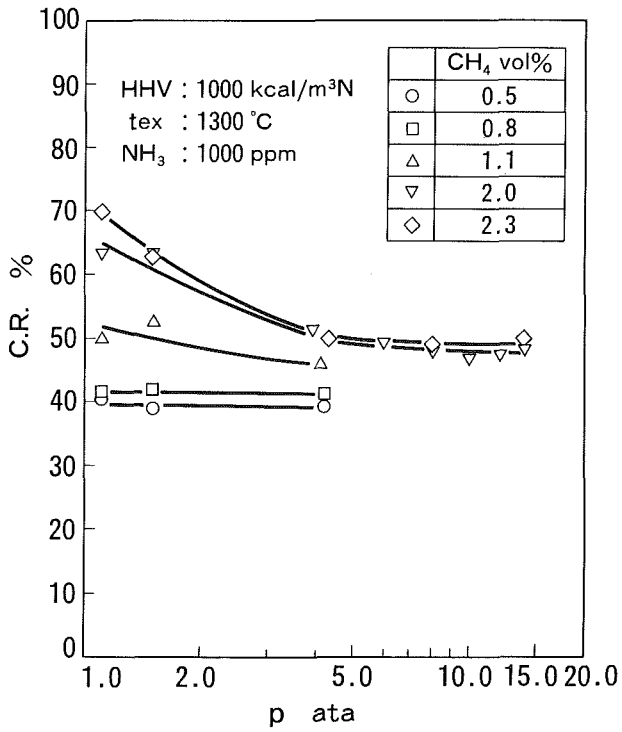

Fig. 6 Relation between pressure and NH_3 conversion to NO_x

the vertical axis represents the ammonia conversion to NO_x in the fuel. The ammonia concentration in the fuel was fixed at 1000 ppm. Furthermore, as a parameter, the methane concentration in the fuel was changed within the range of 0.5 percent to 2.3 percent. Figure 6 reveals the effect of the pressure changes on the fuel NO_x emission characteristics, in accordance with the amount of methane contained in the fuel. In other words, according to the results of our study, if the concentration of methane in the fuel is less than 1 percent, the conversion of NH_3 to NO_x remains virtually unchanged even when the pressure in the combustor rises. On the other hand, if the concentration of methane is 1 percent or more, the conversion

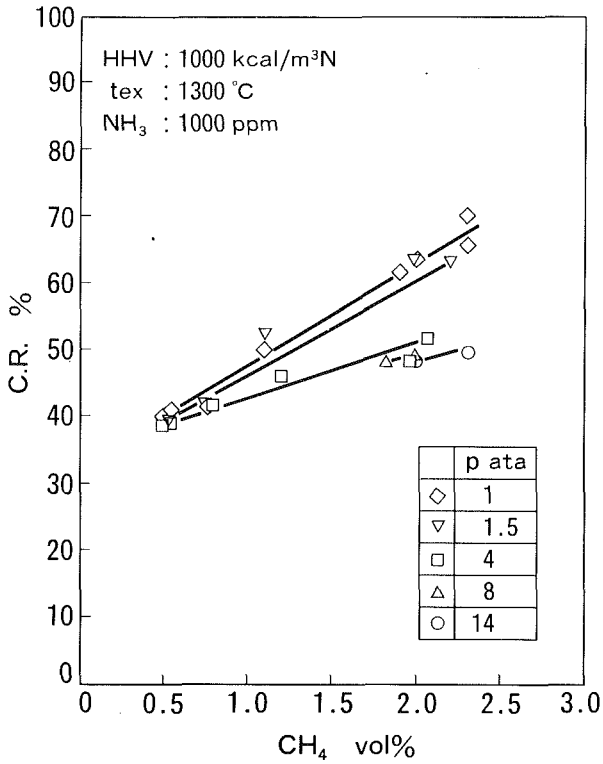

Fig. 7 Relation between CH_4 concentration and NH_3 conversion to NO_x

of NH_3 to NO_x will decrease, in tandem with increases in the pressure. This tendency is particularly noticeable under conditions of 4 atm or below where the pressure is relatively low.

Figure 7 indicates the relationship between the conversion of NH_3 to NO_x and the concentration of methane with the pressure in the combustor as a parameter. The conversion to NO_x tends to increase directly with an increase in the concentration of methane in the fuel. For example, when the pressure in the combustor is 1 atm, the conversion to NO_x will increase significantly, within the range of 40 to 70 percent, if the concentration of methane rises from 0.5 to 2.3 percent. Also, the effect of the concentration of methane on the increase in the conversion to NO_x will be reduced, if the pressure in the combustor rises. For example, when the pressure in the combustor is 14 atm, the conversion to NO_x would increase by only about 10 percent, even if the increases in the concentration of methane rises from 0.5 percent to 2.3 percent.

When the concentration of methane is 0.5 percent, the conversion to NO_x is minimized to 40 percent, which corresponds to about 60 ppm of NO_x (the NH_3 concentration in the fuel is 1000 ppm, an O_2 concentration is 16 percent at the combustor outlet). As the thermal NO_x concentration is 7 ppm under operational conditions of 14 atm, total NO_x emission is expected to reach about 67 ppm.

Since it is different from the generation mechanism of thermal NO_x, it is not fully clear what the formation mechanism of fuel NO_x is like in the gas turbine combustor. In particular, to clarify, among other things, the effect of the pressure, in the combustor, on fuel NO_x and that of methane constituents, it is necessary to examine, in detail, the reaction mechanism and reaction kinetics.

CO Emission Characteristics. We observed the emission characteristics of CO when pressure changes occurred in the combustor. The combustion efficiency is shown in Fig. 8. The concentration of CO tends to decline significantly when the pressure in the combustor increases. For example, although 120 ppm of CO was emitted under atmospheric pressure, the concentration of CO declined sharply, when the pressure in-

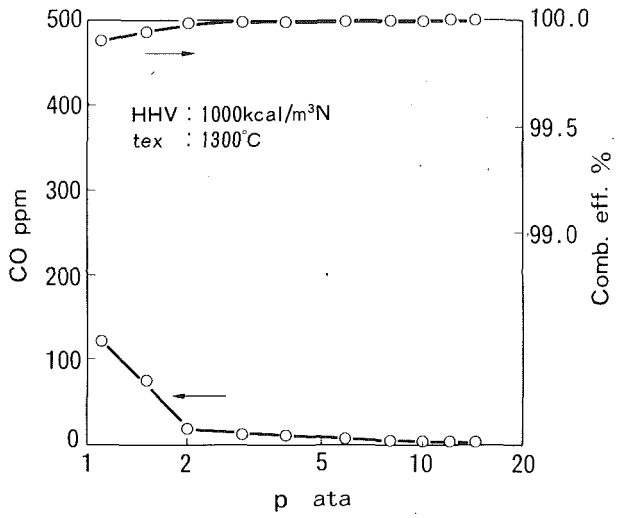

Fig. 8 CO emission and combustion efficiency

creased, and the concentration of CO was 20 ppm or lower when the pressure was at 2 atm or above. The combustion efficiency was nearly 100 percent under rated load conditions.

Characteristics of the Combustor Wall Temperature. The temperature distribution of the combustor liner wall is shown in Fig. 9. By observing the location of combustion region from the wall temperature, we can see that the temperature is adequate in both the auxiliary combustion chamber and the primary combustion chamber, and that the flame stability is maintained. This indicates that, while the amount of heat transferred in the process of flame radiation increases with the rise in pressure, the convection cooling on the combustor wall also tends to increase. It is thus believed that there was no noticeable effect of the pressure on the wall temperature, because the heating values of these components were almost in equilibrium.

We believe the temperature level on the combustor wall just about satisfies the allowable heat resistant temperature of 850°C, or below, and the durability requirement of a 1300°C-class combustor.

Conclusion

The results are summarized as follows:

1 The dependence of thermal NO_x emission on pressure for low-Btu gas combustion is clearly lower than the "$p^{0.5}$—square root of p" law for conventional fuels.

2 The dependence of fuel NO_x emission on pressure depends on the methane content in the fuel. Conversion ratio from the ammonia in the fuel to NO_x is decreasing as pressure increases. This tendency is remarkable when the fuel contains a quantity of CH_4. The possibility of reducing the conversion of NH_3 to NO_x, to 40 percent (60 ppm corrected at 16 percent O_2), even under the operating conditions of 14 atm is confirmed.

3 The combustion performance such as the combustion

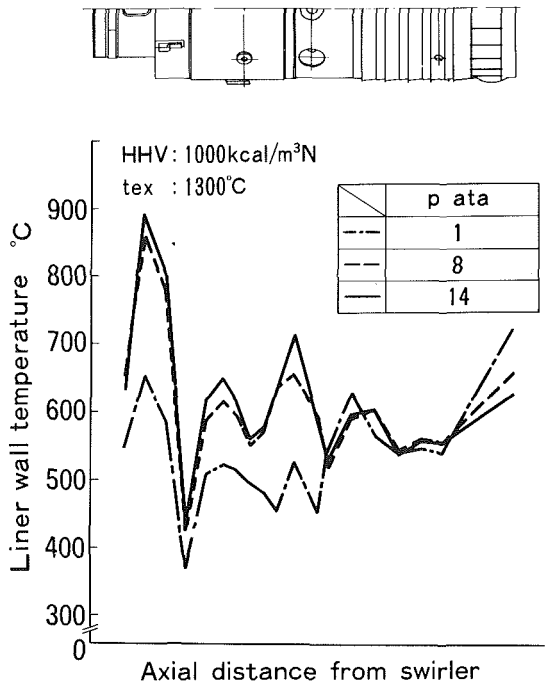

Fig. 9 Liner wall temperature distributions

efficiency and the liner wall temperature are satisfactory under the pressurized conditions. These data will provide useful clues for research and development.

References

1 Nakata, T., Sato, M., Ninomiya, T., Yoshine, T., and Yamada, M., "Design and Test of a Low-NO_x Advanced Rich-Lean Combustor for LBG Fueled 1300C-Class Gas Turbine," ASME Paper No. 92-GT-243, 1992.

2 Sato, M., Abe, T., Ninomiya, T., Nakata, T., Yoshine, T., and Hasegawa, T., "Development of a Low-NO_x LBG Combustor for Coal Gasification Combined Cycle Power Generation Systems," ASME Paper No. 89-GT-104, 1989.

3 Sato, M., Ninomiya, T., Nakata, T., Yoshine, T., Yamada, M., and Hisa, S., "Coal Gaseous Fueled, Low Fuel-NO_x Gas Turbine Combustor," ASME Paper No. 90-GT-381, 1990.

4 Nakata, T., Sato, M., Ninomiya, T., Abe, T., Mandai, S., and Sato, N., "Experimental Evaluation of a Low NO_x LBG Combustor Using Bypass Air," ASME Paper No. 90-GT-380, 1990.

5 Mandai, S., Sato, N., Sato, M., Ninomiya, T., and Nakata, T., "Experimental Evaluation of a Low NO_x LBG Combustor With Air By-pass System," *Proceedings of the 1991 Yokohama International Gas Turbine Congress*, Vol. 3, No. 54, 1991, pp. 73-78.

6 Japan Society of Mechanical Engineers, *JSME Data Book: Formation Mechanism and Controls of Pollutants in Combustion System*, pp. 184-185.

7 Sato, T., and Hilt, M. B., "NO_x Abatement Measures for a Combined-Cycle Plant," *Proceedings of the 1987 Tokyo International Gas Turbine Congress*, Vol. 3, No. 58, 1987, pp. 103-108.

8 Becker, B., Kreutzer, A., and Goebel, K., "GUD Combined-Cycle Power Plants With Integrated Coal Gasification and Low NO_x Emissions," *Proceedings of the 1983 Tokyo International Gas Turbine Congress*, No. 103, 1983, pp. 791-798.

9 White, D. J., Kubasco, A. J., and LeCren, R. T., "Combustion Characteristics of Hydrogen-Carbon Monoxide Based Gaseous Fuels," ASME Paper No. 83-GT-142, 1983.

Low Emissions Combustor Development for an Industrial Gas Turbine to Utilize LCV Fuel Gas

G. J. Kelsall

M. A. Smith

Coal Research Establishment,
British Coal Corporation,
Cheltenham, Glos, United Kingdom

M. F. Cannon

Aero and Technology Products,
European Gas Turbines Limited,
Lincoln, United Kingdom

Advanced coal-based power generation systems such as the British Coal Topping Cycle offer the potential for high-efficiency electricity generation with minimum environmental impact. An important component of the Topping Cycle program is the gas turbine, for which development of a combustion system to burn low calorific value coal derived fuel gas, at a turbine inlet temperature of 1260°C (2300°F), with minimum pollutant emissions, is a key R&D issue. A phased combustor development program is underway burning low calorific value fuel gas (3.6–4.1 MJ/m^3) with low emissions, particularly NO_x derived from fuel-bound nitrogen. The first phase of the combustor development program has now been completed using a generic tubo-annular, prototype combustor design. Tests were carried out at combustor loading and Mach numbers considerably greater than the initial design values. Combustor performance at these conditions was encouraging. The second phase of the program is currently in progress. This will assess, initially, an improved variant of the prototype combustor operating at conditions selected to represent a particular medium sized industrial gas turbine. This combustor will also be capable of operating using natural gas as an auxiliary fuel, to suit the start-up procedure for the Topping Cycle. The paper presents the Phase 1 test program results for the prototype combustor. Design of the modified combustor for Phase 2 of the development program is discussed, together with preliminary combustion performance results.

Introduction

Advanced coal-based power generation systems offer the potential to meet increasing world energy demand burning the world's most abundant fossil fuel. This approach has the advantage of preserving premium fuels, principally natural gas, for applications in which their natural advantages can be exploited most appropriately.

A major assessment study commissioned by British Coal and carried out by Bechtel Limited (Dawes et al., 1989), compared a number of power generation technologies at 200–400 MWe size. This study identified a Topping Cycle, based on a partial fluidized bed gasifier with fluidized bed combustion of the char residue, as the preferred option for development. For this cycle, the potential advantages identified were:

1 A cycle efficiency approaching 47 percent (lower heating value basis) corresponding to around a 20 percent reduction in cost of electricity compared with conventional pulverized fuel fired plant with flue gas desulfurization (pf + FGD).

2 Low nitrogen oxide (NO_x) and sulfur dioxide (SO_2) emissions.

3 20 percent reduction in carbon dioxide (CO_2) per unit of electricity generated compared with pf + FGD, a potential factor in global warming.

Thus, British Coal with technical and financial support from PowerGen plc and GEC ALSTHOM have undertaken a substantial development program. The objective is to establish a commercially available Topping Cycle technology, early in the next century. An intermediate step to achieve this objective is the construction and operation of a demonstration Topping Cycle plant at around the 75 MWe scale.

Topping Cycle System Description. The system has been described in detail elsewhere (Minchener, 1990; Arnold et al., 1991). In brief, the system, shown in Fig. 1, is based on the partial gasification of coal in air using a spouted bed gasifier operating at elevated pressure and temperatures of up to 1000°C (1830°F). Sorbent is added to the gasifier to retain sulfur. The process converts typically 70–80 percent of the coal into a low calorific value (LCV) fuel gas. This gas is cleaned to very low levels of dust using ceramic candle filters at 400–600°C (750–1110°F) and burned in a gas turbine to produce electrical power. The char residue from the gasifier is burned in a Circulating Fludized Bed Combustor (CFBC) at atmospheric pressure to raise steam to produce further electrical power.

The high cycle efficiency and low cost of electricity for the Topping Cycle is due primarily to the use of an air blown

Contributed by the International Gas Turbine Institute and presented at the 38th International Gas Turbine and Aeroengine Congress and Exposition, Cincinnati, Ohio, May 24–27, 1993. Manuscript received at ASME Headquarters March 1993. Paper No. 93-GT-413. Associate Technical Editor: H. Lukas.

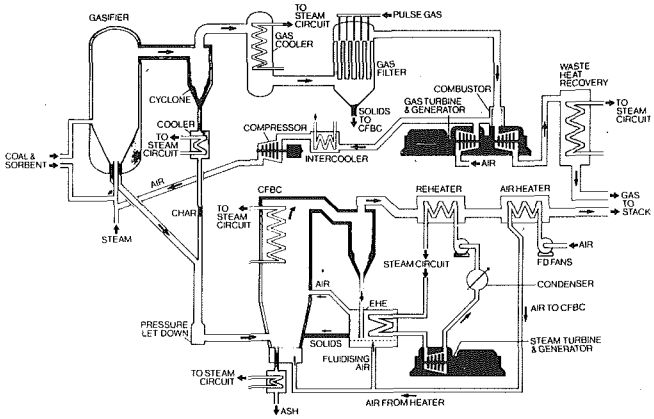

Fig. 1 Schematic of the topping cycle

rather than an oxygen blown system (with its high auxiliary power requirement), the use of hot gas filtration rather than aqueous scrubbing to clean the fuel gas and the relatively high proportion of high-grade steam produced in the cycle allowing the use of a single high pressure steam system. Further, the development of supercritical steam cycles (for which the Topping Cycle is particularly suited) and the ongoing development of industrial gas turbines, have the potential to increase significantly the efficiency of the Topping Cycle. Such advances are predicted to raise the Topping Cycle efficiency to in excess of 52 percent (lower heating value basis).

Gas Turbine Combustion System Requirements. The development of the Topping Cycle based on CFBC char combustion allows conventional gas turbine combustion technology, albeit modified to accommodate the features of the high-temperature coal derived LCV fuel gas to be adopted. However, the duty and demands for the combustion system operating at a combustor outlet temperature (COT) of up to 1360°C (2480°F), required to provide a 1260°C expansion gas after first stage stator cooling, and a fuel gas temperature in the region of 600°C (1110°F) are sufficiently different from conventional technology to require separate development as part of the Topping Cycle development strategy. The particular features of the fuel gas that the combustion system must accommodate are:

1 The calorific value of the fuel gas is predicted to be 3.6–4.1 MJ/m^3 wet gross (approximately 95–110 Btu/ft^3), about one tenth the heat content of natural gas.

2 This low calorific value means that to achieve a COT of 1360°C, low air:fuel mass ratios, typically 2:1 or less, will be required. Consequently the fuel flow will be a significant factor in determining the combustor flow pattern. Further, the low air:fuel ratio will restrict the amount of air available for combustor wall cooling, introducing a potentially significant design constraint.

3 The fuel gas has small but significant amounts of nitrogen containing species present, principally ammonia. The level of ammonia is dependent, primarily, on the coal gasification regime and is predicted to be in the range of 500–1500 ppmv. As the cycle involves cleaning the fuel gas hot, a significant portion of the ammonia will still be present in the fuel gas presented to the gas turbine combustor, so that fuel-NO_x will be the dominant source of the combustor NO_x emission.

Development of a Gas Turbine Combustion System. Combustor development leading to the provision of a combustion system for utility Topping Cycle plant will take place in several phases. Phase 1 of this development is complete. This assessed the performance of a generic prototype combustor design at a nominally 1 MWth scale. The design, manufacture, and testing of this prototype combustor were carried out in conjunction with Aero and Industrial Technology Ltd. (AIT) under contract to British Coal.

Phase 2 of the combustor development will build on the design data base produced in Phase 1. To accommodate the possibility of an early demonstration Topping Cycle plant (to commence construction in 1994–95), the initial development work is being targeted at a currently available, specific industrial engine with a COT of around 1150°C (2100°F). However, the overall development objective for Phase 2, in terms of COT, remains as 1360°C. Thus, at the end of this second phase, it is intended that combustor designs will be available that can be scaled to the size required for a specific gas turbine fired at 1260°C or below.

Phase 3 will include engine specific tests carried out in collaboration with the appropriate turbine manufacturer.

To supplement the experimental development of the combustion system and assist in combustor scale-up predictions, mathematical modeling techniques will also be used and developed where necessary. These models will utilize existing Computational Fluid Dynamics packages, with the inclusion of postprocessing fuel-NO_x prediction capability, being developed specifically for this application.

Detailed discussion of the modeling aspect of combustor development is outside the remit of this paper. Instead, the paper will discuss the design rationale for the prototype combustor and assess results from the completed Phase 1 test program and preliminary results from the first stage of the Phase 2 program.

Combustor Design Rationale

The tubo-annular type of combustor was chosen for Phase 1 development. This was considered the most likely geometry to be adopted in utility size machines with 1260°C turbine entry temperatures; General Electric having developed the Frame 9 machine with tubo-annular combustors. The Frame 9 would provide the correct gas turbine output of the utility size Topping Cycle plant.

The main requirement of the combustor was to achieve high combustion efficiency while maintaining low pollutant emissions, especially NO_x. To this end, the design approach adopted was to stage the combustion by adding the combustion air in

Nomenclature

Conversion Rate = ([Total NO_x] − [Thermal NO_x])/[NH_3] × (Exhaust volume flow)/(Fuel volume flow)

I = combustion intensity, MW/m^{2}bar

Mach number (combined air and fuel) = $WTi^{1/2}/Pi$

OTDF = Overall Temperature Distribution Factor = (Peak temperature − Tex) × 100/($Tex - Ti$)

Pi = mean air and fuel inlet pressure, Pa

RTDF = Radial Temperature Distribution Factor = (Peak circumferential temperature − Tex) × 100/($Tex - Ti$)

Ti = mean air and fuel inlet temperature K

Tex = mean exhaust temperature, K

V = combustor volume, m^3

W = total air and fuel flow, kg/s

Ω = combustion loading = $(W \times 10^9)/(Pi^{1.8} V \exp(Ti/300)$, kg/sm^3 Pa$^{1.8}$

portions along the tube length, such that the primary zone would be fuel rich with the subsequent intermediate and dilution zones being fuel lean. Thus, conditions in the primary zone would be achieved that would promote the reduction of nitrogen-containing species in the fuel to elemental nitrogen, rather than oxidation to fuel-NO_x. Additionally, a beneficial reduction in peak flame temperature would be achieved, thus minimizing thermal-NO_x formation.

To achieve high combustion efficiency, a combustor was designed with sufficient volume in relation to the throughput of fuel and air, to accommodate the high volume of inerts in the fuel gas and the relatively slow burning rate of carbon monoxide (CO). This is of particular significance as operation with staged combustion may augment this problem, as a result of reducing the residence time for CO burn-out in the fuel lean zone. In addition, the length to diameter ratio of the combustor was relatively short at 2:1, constrained by existing hardware limitations. Thus, a combustor design with a relatively modest combustor loading (Ω) to ensure high combustion efficiency was adopted for Phase 1.

Effective mixing within the combustor to promote efficient combustion was achieved, in part, by the use of flow swirlers to impart radial motion to portions of both the air and fuel, and in part by the interaction of the secondary air and the fuel gas jets (see sections on Air Distribution and Fuel Admission).

The particular features of the combustor design have been described previously by Kelsall et al. (1991), but are outlined briefly below for completeness.

Combustor Size. After consideration of the combustor loading and heat release properties of typical small-scale industrial gas turbines, the following nominal values were adopted for the initial combustor evaluation:

Combustor loading (Ω) = 0.6 kg/s $m^3Pa^{1.8}$

Combustion intensity (I) = 6.3 MW/m^2 bar

Air casing Mach number = 0.013

These relatively modest values were adopted, to ensure high combustion efficiency and acceptable flame stability while burning LCV gas. In terms of the combustor size, the constraint was that the data generated should be suitable for scale-up to a size required for the demonstration Topping Cycle plant, typically for a gas turbine in the region of 40 MWe. The minimum size for adequate scale-up was thus determined as a 127 mm (5 in.) internal diameter combustor, approximately half the full geometric scale. Successful combustor performance at this reduced scale, where the flame-tube surface:volume ratio is high, should equate to good performance at the larger scale where the combustor cooling regime is less arduous.

Air Distribution. A conventional air distribution design was chosen with the primary air flow being admitted through a swirler and the secondary, intermediate, and dilution flows being admitted through plain holes along the flame tube surface (Fig. 2).

The primary air swirler and secondary air admission holes were sized in conjunction with the fuel injector to produce a fuel rich, stable primary toroidal recirculation zone. The intermediate air admission was arranged to ensure complete combustion of any CO remaining.

Fuel Admission. The fuel was admitted through an injector positioned at the upstream end of the flame tube, inboard and concentric with the primary air swirler (Fig. 2). To promote rapid mixing of the fuel and air, approximately two thirds of the fuel was admitted through a swirler injecting in a contra direction to the air swirler. This technique had previously been used successfully for low calorific value fuels by Beebe and Blanton (1985).

The remaining fuel was introduced directly into the primary zone through plain holes positioned inboard of the fuel swirler. The injection angle of these holes was arranged to support the primary zone toroidal vortex produced by the flow reversal from the air secondary holes.

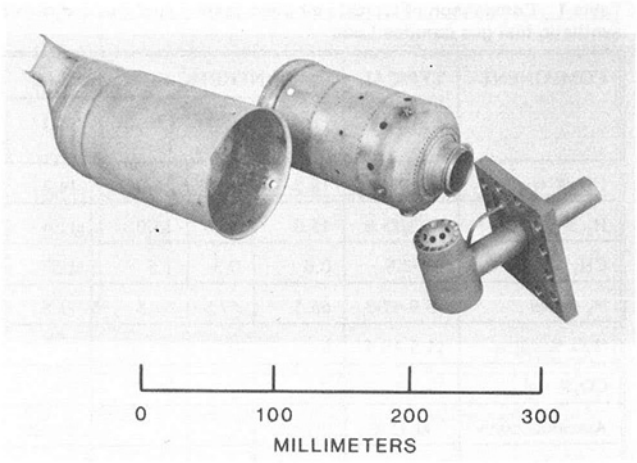

Fig. 2 Prototype turbine combustor and fuel injector

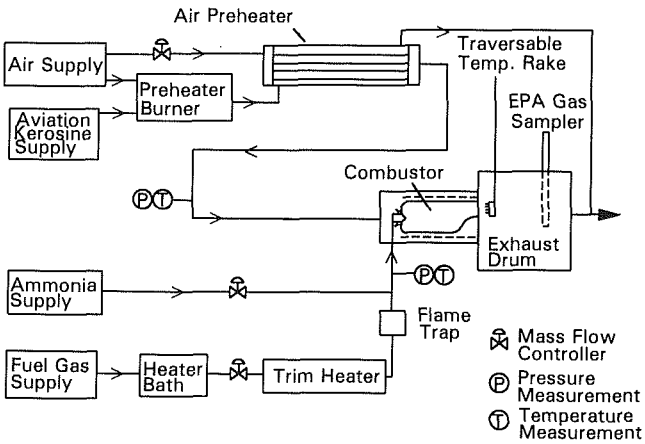

Fig. 3 Schematic layout of the combustion test rig

Combustor Pressure Loss. The low aerodynamic and heat release loadings adopted for the combustor permitted the use of relatively low pressure loss levels.

For the initial design, an air pressure loss of approximately 1 percent was used, with a fuel injection pressure loss of approximately twice this value. However, it should be noted that the cycle efficiency figures for the Topping Cycle, quoted in the introduction to this paper, can be achieved with combustor air pressure loss of greater than 5 percent.

Wall Cooling. Serious consideration of techniques to achieve satisfactory combustor wall temperatures did not form part of the Phase 1 program. However, to avoid premature failure of the flame tube, some 30 percent of the air was distributed through four splash cooling skirts along the flame tube wall and via a number of sweat cooling holes in the exhaust duct. The effect of wall cooling films is of secondary importance in determining the parameters of interest to the Phase 1 program.

Test Equipment

Test Rig Description. The layout of the pressure test rig is shown in Fig. 3. Air is supplied from a compressor at up to 8 bar pressure. The air is metered and the temperature adjusted to 350°C (660°F) by passing through a gas/air heat exchanger, which is heated by a separate liquid-fueled combustor.

Table 1 Comparison of typical air-blown gasifier fuel gas and nominal synthetic fuel gas compositions

COMPONENT	TYPICAL FUEL GAS	SYNTHETIC FUEL GAS			
		PHASE 1A	PHASE 1B		
CO % vol	7.9-14.7	18.5	17.7	16.0	14.3
H_2 % vol	13.2-15.0	15.0	14.3	13.0	11.6
CH_4 % vol	1.5-2.8	0.0	0.5	1.5	2.5
N_2 % vol	45.9-47.3	66.5	67.5	69.5	71.6
H_2O % vol	11.5-18.4	0	0	0	0
CO_2% vol	10.0-12.0	0	0	0	0
Ammonia ppmv	500-1500	0-1000	-	-	0-1500
Gross Calorific Value (MJ/m^3)	3.6-4.1	4.05	4.05	4.05	4.05
Molecular Weight	24.4	24.1	24.3	24.4	24.7

The prototype combustor is designed with a discharge duct of circular to sector cross-sectional area, which is compatible with an existing exhaust plane transverse system. This consists of a water-cooled exhaust drum and adaptor plate. Transverse probes are fitted to monitor either temperature or gas composition at the combustor outlet. The probes are fitted with four sampling points at different radii across the sector and are moved at intervals of 2 1/2 deg across a 36 deg sector. Platinum/platinum 13 percent rhodium Type B thermocouples are used in the thermocouple probes, with appropriate heat shields. Approximately 1 m downstream of the exhaust drum, a crucifix sampler based upon Environmental Protection Agency (EPA) design rules is fitted. All gas samplers are cooled by water at 150°C and the sample transfer lines are electrically heated to 150°C.

Fuel Supply. A synthetic fuel gas, with similar calorific value and average molecular weight to a typical air blown gasifier fuel gas, is supplied in a high-pressure tube trailer. The constituents and properties of this gas are given in Table 1 where they are compared with the composition of a typical fuel gas from an air-blown gasifier. At this stage, for ease of preparation, the inerts are simulated by using nitrogen only. When required, ammonia is injected into the gas supply stream close to the fuel injector. The synthetic fuel gas is supplied to the prototype combustor at temperatures in the range 20–220°C (70–430°F).

Phase 1 Test Program

To assess the performance of the prototype combustor design, an initial three-stage test program (Phase 1) was undertaken. These stages were water flow visualization, ignition and stability tests at atmospheric pressure, and combustion and emissions performance at pressures up to 8 bar. The water visualization and flame stability tests have been described in detail previously, together with the Phase 1A combustion and emissions performance (Kelsall et al., 1991). However, the Phase 1A results are presented briefly in the following sections to allow comparison with the subsequent Phase 1B results.

Elevated Pressure Tests. An initial matrix of experiments (Phase 1A) was carried out at elevated pressure. The nominal operating conditions of this phase of the program are given in Table 2. This first matrix of tests was carried out using a single composition of synthetic fuel gas (Table 1) containing carbon monoxide and hydrogen only as the combustible components. The results achieved during the elevated pressure Phase 1A tests are presented in the following section.

Table 2 Phase 1A elevated pressure test program nominal operating conditions

Pressure 3, 5, 7, 8 bar
Air Inlet Temperature 350°C
Fuel Inlet temperature 20, 120, 220°C
Air:Fuel Mass Ratio 1.7:1 to 4:1
Ammonia doping 0-1500 ppmv

Phase 1A Results

Combustion Efficiency. Over the range of conditions tested, the combustion efficiency as determined by gas analysis was close to 100 percent. This high combustion efficiency was achieved with values of combustor loading (Ω up to 1.5) considerably higher than the design value of $\Omega = 0.6$. These high values of combustor loading were achieved by reducing the operating pressure to 3 bar.

While these values of combustor loading are below those found typically in most industrial gas turbines, the results indicate that there is scope to increase the combustor loading without compromise of high combustion efficiency.

Exhaust Temperature Distribution. The overall temperature distribution factor (OTDF) varied between 4 and 10 percent across the range of conditions tested. The radial temperature distribution factor (RTDF) varied between 2 and 4 percent. This indicates that an acceptable temperature profile to the gas turbine first-stage rotor blades may be achieved with the current design of combustor.

Pressure Loss. The air side pressure loss at the design condition was determined to be 0.8 percent compared with a design value of 1 percent. This relatively low pressure loss is compatible with the low combustor loadings adopted in the initial design.

Metal Temperatures. In assessing the metal temperature it must be noted that no attempt was made, at this stage, to optimize the cooling. When operating at the design COT of 1360°C, a considerable area of the flame tube wall was above 800°C. However, there is considerable scope to reduce the combustor metal temperatures by more efficient utilization of the available cooling air. This issue will be addressed in the Phase 2 program.

NO_x Emissions. *Thermal NO_x.* For all test conditions studied, the NO_x emission in the absence of ammonia addition to the fuel gas, i.e., thermal-NO_x, was below 5 ppmv (dry, 15 percent O_2) with COT in the range 970–1370°C. Although thermal NO_x increased slightly with pressure between 5 and 8 bar (Fig. 4), the effect was negligible and certainly within the accuracy of measurement. However, even when assuming that the thermal NO_x emission is proportional to the square root of the operating pressure, the emission at 14 bar, required for the Topping Cycle application, would be 5–6 ppmv (15 percent O_2, dry).

Fuel NO_x. When ammonia was added to the fuel gas, higher levels of NO_x were produced due to the formation of NO_x from the oxidation of ammonia species (fuel NO_x). The importance of this fuel NO_x component increased as the level of ammonia increased, such that at the 1000 ppmv of ammonia level, fuel NO_x represented around 90 percent of the total NO_x emission (Fig. 5). However, the efficiency at which the ammonia was converted to NO_x decreased as the ammonia level increased, so that the relationship between fuel NO_x and ammonia is nonlinear. Total NO_x emissions in the range 20–45 ppmv (15 percent O_2, dry) were achieved over the range of ammonia doping levels assessed (300–1120 ppmv), corresponding to ammonia to NO_x conversion rates of about 20–50 percent.

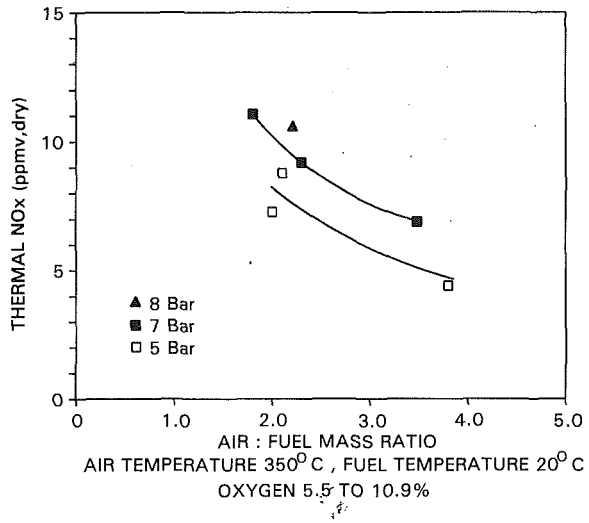

Fig. 4 Effect of pressure on thermal NO_x

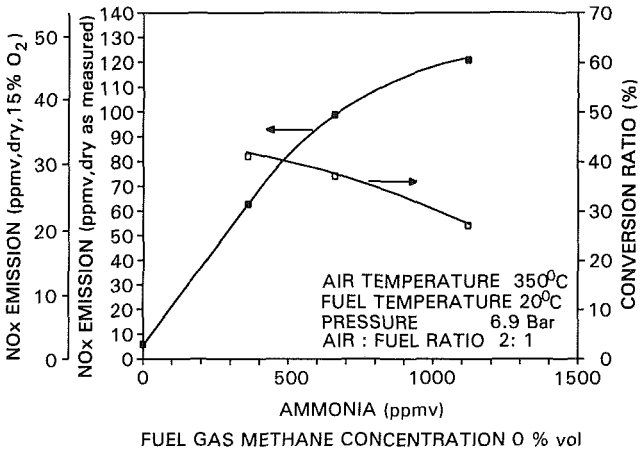

Fig. 5 Effect of ammonia concentration in the fuel gas on NO_x emissions

Nitrous Oxide (N_2O). In addition to measurement of thermal and fuel NO_x, measurements were also made of N_2O. The concentration of N_2O was less than 1 ppmv for all test conditions studied. This indicates that although the flame temperature is lower when burning a LCV fuel gas compared with conventional fuels, it is still above that at which significant levels of N_2O are produced.

Phase 1B Results

At the end of the Phase 1A test matrix, it was concluded that a gas turbine combustor had been designed that merited further development work. A second matrix of tests (Phase 1B) was therefore carried out to assess further combustor performance at higher values of combustor loading and Mach number, to approach those required for industrial and utility applications and thus provide a valuable design link with the subsequent Phase 2 test programs.

This second matrix of tests was also carried out using three compositions of synthetic fuel gas (Table 1). Methane at three different concentrations was now present, with the concentration of the other combustible components, carbon monoxide and hydrogen, adjusted to maintain constant calorific value. In addition, the carbon monoxide:hydrogen ratio and the average molecular weight for each synthetic fuel gas composition were also held approximately constant. The performance information provided by testing these different gas compositions would be twofold:

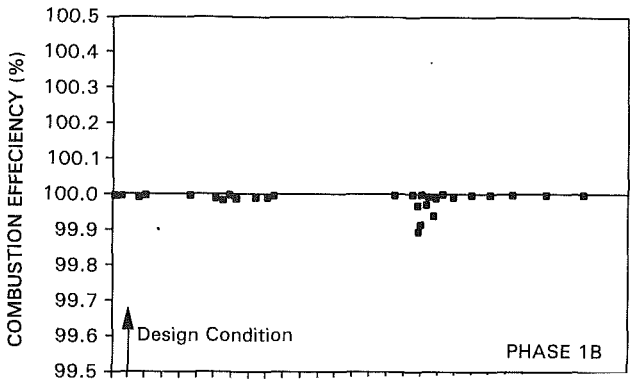

Fig. 6 Effect of combustor loading on combustion efficiency

Firstly, increasing methane concentration and hence decreasing hydrogen concentration (the combustible component with the widest flammability range) to maintain constant calorific value, may indicate a fuel gas composition that cannot be burned in the current prototype combustor configuration.

Secondly, the concentration of methane has been shown to have some adverse effect on the proportion of fuel-bound nitrogen converted to NO_x (Sato et al., 1990).

Combustion Efficiency. Over the range of conditions studied, the combustion efficiency remained close to 100 percent (Fig. 6). This efficiency was achieved with values of combustor loading up to 3.5, some six times higher than the initial design value of 0.6.

In terms of Mach number (based on combined air and fuel flow), the second parameter of consideration, represented for convenience by $WT_i^{1/2}/P_i$, this combustion efficiency was achieved at values up to 0.064, more than four times higher than the design value of 0.015. Operation at these high Mach numbers goes a significant way toward assessing the prototype combustor design at the conditions required for the proposed demonstration Topping Cycle plant.

Further, the high combustion efficiency was achieved burning all three synthetic fuel gas compositions. Thus, the prototype combustor has been shown to be capable of burning efficiently and with a stable flame, fuel gas compositions containing a concentration of hydrogen down to the lowest value tested of 11.6 percent by volume.

NO_x Emissions. Measurement of the NO_x emission was made for the synthetic fuel gas compositions containing zero and 2.5 percent methane. Figure 7 shows the NO_x emissions produced for a range of ammonia doping levels at operating conditions directly comparable with those presented for Phase 1A.

Thermal and Prompt NO_x. The NO_x emission in the absence of ammonia addition was around 5 ppmv (15 percent O_2, dry) for the two gas compositions assessed. This indicates that the presence of methane in the fuel gas composition produced no significant levels of prompt NO_x i.e., where hydrocarbon radicals react with nitrogen molecules in either the air or fuel to produce NO_x via intermediate nitrogenous species. This confirms the statement earlier in this paper that the total NO_x emission is dominated by the fuel-NO_x component.

Fuel NO_x. When ammonia was added to the fuel gas, the effect of methane content in the fuel gas was significant. Total NO_x emissions in the range 75–125 ppmv (15 percent O_2, dry) were produced for ammonia doping levels of 500–1500 ppmv. In terms of ammonia to NO_x conversion rate, this corresponds

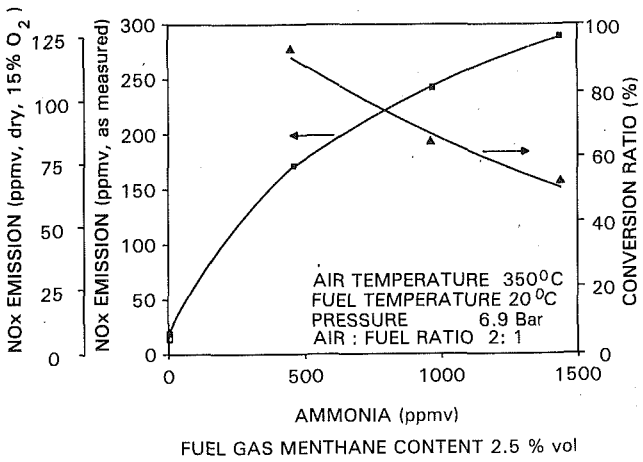

Fig. 7 Effect of ammonia concentration in the fuel gas on NO_x emissions

to conversions of 50 percent to approaching 100 percent at the lower ammonia level. For a fuel gas composition containing zero methane, conversion rates of typically 20–40 percent had been noted (Fig. 5). The exact reason for this effect is not at present clear. It will be investigated in full as part of the Phase 2 program.

Phase 2 Program

The interim conclusion from Phase 1 was that the prototype combustor design, based on a generic industrial gas turbine, had achieved acceptable combustor performance within the operating envelope assessed. The values achieved for combustion efficiency, exhaust temperature profile, ignition and stability, and thermal NO_x were all encouraging. However, the fuel NO_x emission of the combustor, while being very low for synthetic fuel gas compositions containing no methane, was significantly higher where the synthetic fuel gas contained 2.5 percent methane. In addition, the combustor was capable of burning synthetic fuel gases with a range of hydrogen contents between 11.6 and 15 percent.

The basic design principles of the prototype combustor used in the Phase 1 program were therefore retained for the initial stage of the Phase 2 program. The design was modified to allow operation at conditions representative of a currently available, particular industrial gas turbine suitable for application in the proposed demonstration Topping Cycle plant (Table 3). The reason for the adoption of this approach was:

1 To provide a rigorous design datum for the subsequent development of a combustor to achieve very low conversion of fuel nitrogen to NO_x.

2 To provide a design suitable for scale-up within the time frame of an early demonstration Topping Cycle plant, should it be required. In this case, the subsequently designed low-NO_x combustors would be retrofitted to the demonstration plant.

Design Requirements. The modified prototype combustor will be required to demonstrate its ability to operate around the full turbine operating envelope from ignition, through the Full Speed No Load (FSNL) condition to Full Load. Dual fuel capability using natural gas, for part of the operating envelope only, will be required for compatibility with a Topping Cycle start-up strategy.

The issue of flame tube wall cooling will be addressed specifically, with an average wall temperature of below 800°C set as a target.

Air side pressure drop at the full load condition is defined as 3 percent burning synthetic fuel gas, rising to about 6.7 percent at the FSNL condition burning natural gas.

Table 3 Performance data for specific industrial gas turbine suitable for demonstration topping cycle plant

Combustor diameter	- 10.5 inches (267 mm)
Length:diameter ratio	- 3:1
Conditions at 100% load:-	
Air inlet temperature	- 340 °C
Air flow	- 11.7 kg/s
Chamber pressure	- 12 bar
Combustor outlet temperature	- 1150 °C

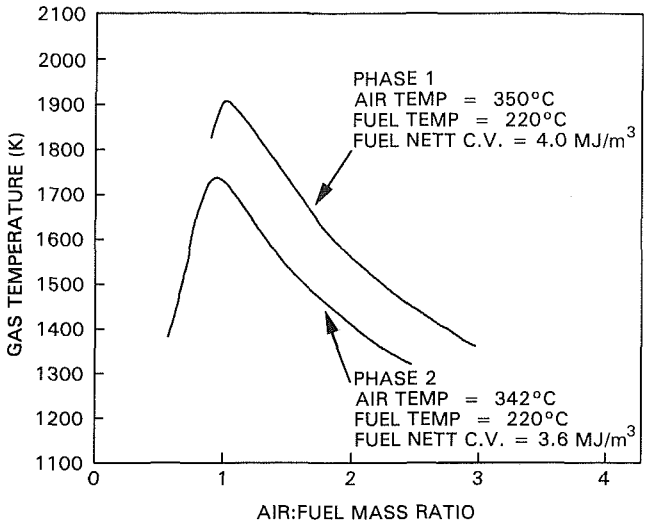

Fig. 8 Effect of air:fuel ratio on adiabatic fuel temperature

The calorific value of the synthetic fuel gas will be reduced to 3.6 MJ/m^3 (wet, gross), to assess performance burning of the lowest fuel gas heat content predicted for an air-blown gasifier in the Topping Cycle application. The effect of this lower heat content on adiabatic flame temperature is shown in Fig. 8, where it is compared with that tested in the Phase 1 program.

Once these performance requirements have been demonstrated adequately, the prototype combustor will be optimized, in terms of NO_x emissions performance, by making relatively small changes to the combustor hardware such as hole size and positioning, and fuel injector orientation. These changes will be made to affect primarily the primary zone stoichiometry and residence time and combustor mixing pattern. The design produced will then form the datum for low-NO_x combustor development.

Test Program. Manufacture of the modified combustor and installation in the pressure test rig at AIT has been completed. Initial tests to assess the combustor burning natural gas have been completed and tests burning synthetic fuel gas initiated. Preliminary results from the natural gas calibration tests are described below.

Natural Gas Tests. The natural gas calibration tests involved the determination of cold flow pressure loss profile, ignition and stability characteristics, combustion efficiency, exhaust temperature profile, metal temperature, and emissions performance at defined ignition and FSNL conditions (Table 4). Provision for the inclusion of a relatively small flow of purge air through a portion of the fuel injector was included. This purge was required to prevent the recirculation of hot primary zone gas into the LCV fuel injector passages when burning natural gas.

Pressure Loss Profile. The combustor pressure loss profile

Table 4 Defined ignition and full speed no load conditions

	FSNL	Ignition
Air Flow (kg/s)	1.6	0.18
Air:Fuel Mass Ratio	105:1	70:1
Pressure (bar)	5.8	2.0
Temperature (°C)	267	72
Air Mach No.	0.064	0.017

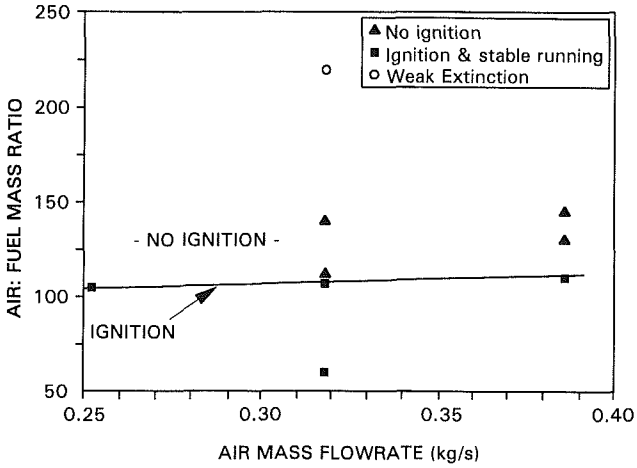

Fig. 9 Ignition and stability performance burning natural gas

was determined at ambient conditions for a range of air Mach numbers corresponding to those to be assessed in the elevated pressure tests. This profile was found to agree closely with the predicted combustor pressure loss, confirming the accuracy of the combustor design and manufacture procedures.

Ignition and Stability. The ignition and stability performance of the combustor were determined using air and fuel at the conditions shown in Table 4. The measured ignition and stability limits are shown in Fig. 9 as a function of air mass flow. Ignition was achieved successfully at air:fuel ratios of up to 110:1. Thus, ignition at the required air:fuel ratio of 70:1 can be achieved. There is some indication that the stability limit is around an air:fuel ratio of 220:1, showing considerable scope to improve further the ignition performance of the combustor burning natural gas.

Combustion Efficiency. Combustion efficiency at a range of air:fuel mass ratios from 65:1 to 115:1 was determined at the ignition and FSNL conditions. Efficiency figures of 95 and 98.5 percent, respectively, were determined. In terms of carbon monoxide (CO) and unburned hydrocarbons (UHC), these combustion efficiencies correspond to 1250 ppmv of CO and 800 ppmv of UHC at the ignition condition, and 250 ppmv of CO and below 50 ppmv of UHC at the FSNL condition.

These efficiencies are considered to be adequate for the combustor operating on its auxiliary fuel for the relatively short periods of time required to meet the Topping Cycle gasifier start-up requirements.

Exhaust Temperature Profile. OTDF and RTDF at the FSNL condition were determined as 18.5 and 2 percent, respectively. While the value of OTDF at first sight appears high, for a mean exhaust temperature of 770°C it represents a maximum temperature in the exhaust profile of 900°C. This temperature would not pose a problem for the gas turbine first-stage stator blades.

TEMP RANGE (°C)	CODE
Below 385	B
385 - 485	C
485 - 515	D
515 - 655	E
655 - 755	F

Fig. 10 Combustor metal temperatures

NO_x Emissions. NO_x emissions were below 35 ppmv (15 percent O_2, dry), for the range of conditions through to FSNL. These relatively low emissions were achieved in a combustor designed primarily for LCV fuel gas.

Metal Temperatures. The combustor wall temperature was assessed using thermal indicator paint (Fig. 10). The flame tube metal temperature was substantially below 500°C, with local hot spots downstream of the dilution holes reaching 650°C. In assessing the metal temperatures, it should be noted that the paint was exposed to a range of conditions through to FSNL, so that the temperature profiles cannot be attributed to a specific operating regime.

Conclusions

A generic, prototype gas turbine combustor for application in the Topping Cycle, based on conventional gas turbine combustion technology, has been designed at a nominal 1 MWth scale. Testing of the combustor has been encouraging, with a high (>99.9 percent) combustion efficiency achieved while maintaining low OTDF and RTDF (less than 10 and 4 percent, respectively) and achieving low NO_x emissions. The NO_x emission achieved for a fuel containing zero methane was typically 30–45 ppmv (15 percent O_2, dry) for a range of ammonia in fuel gas levels of 500–1000 ppmv. However, where the fuel gas contained 2.5 percent methane, NO_x emissions were substantially higher; around 75–110 ppmv (15 percent O_2, dry) for comparable operating conditions and fuel ammonia content. The combustor was capable of burning synthetic fuel gases with a range of hydrogen contents (that component with the widest flammability limits) from 15 to 11.6 percent.

Thus, it was concluded that a combustor had been designed that merited further development work.

Following completion of Phase 1 testing, the prototype combustor was modified to represent closely a currently available, specific industrial gas turbine suitable for application in the proposed demonstration Topping Cycle. The design principles of the generic prototype combustor were retained. Preliminary testing of the modified combustor using natural gas has been encouraging, achieving acceptable combustor performance and metal temperatures at a range of conditions through to FSNL. At the FSNL condition, the combustion efficiency achieved was 98.6 percent with flame tube metal temperatures below 650°C. Assessment of the modified combustor burning synthetic fuel gas is in progress.

Further Work

The remaining tests within the first stage of the Phase 2 program will assess the performance of the modified prototype combustor burning synthetic fuel gas. The performance of the combustor will be optimized, in terms of minimizing NO_x emissions, by relatively small changes to the combustor hardware. This will then form the datum for the subsequent development of a combustor to achieve very low conversion of fuel nitrogen to NO_x at COT's of up to 1360°C.

Development of this low fuel NO_x combustor will be carried out, primarily using a Gas Cleaning and Combustion facility built for the purpose at British Coal's Coal Research Establishment. This facility is capable of providing either a real coal derived fuel gas or a synthetic fuel gas at a pressure and temperature of typically 12 bar and 600°C. It will have the capability to test turbine combustors with flame tube diameters of up to 127 mm.

Studies of the LCV flame chemistry at a fundamental level will be made with emphasis placed on the effects of fuel gas components on fuel nitrogen to NO_x conversion. The information produced will be used in conjunction with mathematical modeling techniques to produce candidate low fuel NO_x combustor designs. These will then be evaluated in the Gas Cleaning and Combustion facility.

Acknowledgments

The studies described in this paper form part of the British Coal Topping Cycle program, being developed by British Coal in collaboration within Power Gen plc and GEC ALSTHOM. Further funding is being provided by the UK Department of Trade and Industry, the Commission of European Communities, the European Coal and Steel Community, and the Electric Power Research Institute. The contributions of colleagues at British Coal, AIT, and European Gas Turbines are gratefully acknowledged.

Any views expressed are those of the authors and not necessarily those of the supporting organizations.

References

Arnold, M. St. J., Kelsall, G. J., and Hudson, D. M., 1991, "Clean and Efficient Electric Power Generation for the next Century—The British Coal Topping Cycle," presented at the First International Conference on Combustion Technologies for a Clean Environment, Vilamoura.

Beebe, K. W., and Blanton, J. C., 1985, "Design and Development of a Heavy Duty Industrial Gas Turbine Combustion System for Low-Btu Coal Gas Fuel," ASME Paper No. 85-GT-45.

Dawes, S. G., Cross, P. J. I., Holmes, J., and Topper, J. M., 1989, "Advanced Coal Burning Systems for Power Generation," presented at Power Plant UK 89, National Exhibition Centre, Birmingham, United Kingdom.

Kelsall, G. J., Smith, M. A., Todd, H., and Burrows, M. J., 1991, "Combustion of LCV Coal Derived Fuel Gas for High Temperature, Low Emissions Gas Turbines in the British Coal Topping Cycle," ASME Paper No. 91-GT-384.

Minchener, A. J., 1990, "Topping Cycle Development," *Energy World*, No. 183, pp. 22–25.

Sato, M., Ninomiya, T., Takata, T., Yoshine, T., Yamada, M., and Hisa, S., 1990, "Coal Gaseous Fuelled, Low Fuel-NO_x Turbine Combustor," ASME Paper No. 90-GT-381.

W. T. Cousins

K. K. Dalton

T. T. Andersen

Performance and Operability,
AlliedSignal Engines,
Phoenix, AZ 85010

G. A. Bobula

U.S. Army Vehicle Propulsion Directorate,
Army Research Laboratory,
Cleveland, OH 44135

Pressure and Temperature Distortion Testing of a Two-Stage Centrifugal Compressor

Altitude pressure and temperature inlet distortion testing of the two-stage centrifugal compressor in the T800-LHT-800 engine is described. The test setup and the testing techniques are reviewed and the results of the test are presented. The generation of classical 180 deg patterns of both pressure and temperature distortion is discussed. Temperature distortion was created using a hydrogen burner system while pressure distortion was created in the classical manner, using screens. Results of both individual and combined temperature and pressure distortions in both opposed and concurrent patterns are shown.

Introduction

Characterizing the effects of inlet airflow distortion on the stability of an aircraft engine is a critical part of any aircraft engine development and qualification program. Understanding the response of the engine compression system to these destabilizing influences enables proper matching of the engine with the aircraft. Throughout an engine program, many influences on engine stability are evaluated. These are used in the formulation of an engine stability assessment. The stability assessment contains all the destabilizing influences of the engine, along with mission analysis information for the particular aircraft. Inlet distortion is a major part of the stability assessment. The engine response to inlet distortion is typically obtained through extensive testing, both at sea level and altitude conditions.

Inlet flow distortion can be separated into two types: pressure and temperature. Often, pressure distortion is considered while temperature distortion is not. This is usually because temperature distortion is more difficult to simulate under test conditions, and depending upon the aircraft mission (for example, civil aircraft), the probability of encountering temperature distortion may be very small. This does not mean that temperature distortion is not important. Much to the contrary, temperature distortion can often have a greater effect on engine stability than pressure distortion. In military applications, the effect of temperature distortion is usually quite critical. Temperature distortion is typically generated by weapons firing, steam ingestion on aircraft carriers, and the exhaust from other aircraft. In rotorcraft, it may even result from ingestion of one's own exhaust during flair and hover.

Generating pressure distortion with screens in a test cell is usually easier than generating temperature distortion. Consequently, pressure distortion testing is a common practice while temperature distortion testing is performed less often. Pressure distortion is due to nonuniform inlets, aircraft maneuvers, crosswinds, inlet/fuselage boundary layers, etc. Often in flight, pressure and temperature distortion are present simultaneously. The effect of this combined distortion can be different from the effect of each separately; therefore, tests were conducted to examine the combined phenomena.

This paper summarizes the altitude inlet distortion testing that was performed on the T800-LHT-800 (T800) engine to examine the effects of pressure and temperature distortion on the compression system surge margin at various altitudes. Testing was conducted to acquire data for the development and qualification of the T800 engine, during the time period from April to August 1991. These data are used in the formation of a stability assessment and performance computer model, thus providing the ability to help customers evaluate the effect of inlet airflow distortion on both performance and engine compression systems stability around the aircraft flight envelope.

This work was performed at the NASA Lewis Research Center in Cleveland, Ohio, with the support of the Army Aviation Systems Command. The T800 is being developed for the U.S. Army by the Light Helicopter Turbine Engine Company (LHTEC), a partnership between Allison Gas Turbine Division of General Motors and AlliedSignal Engines.

Test Vehicle

The T800 (Fig. 1) contains a two-stage centrifugal compression system coupled to a two-stage gas generator turbine with a two-stage free-shaft power turbine. The engine inlet is annular in nature and incorporates an integral inlet particle separator (IPS). The T800 is of the 300-lb, 1200-shaft horsepower class.

For this test series, the full engine was tested with the power

Contributed by the International Gas Turbine Institute and presented at the 38th International Gas Turbine and Aeroengine Congress and Exposition, Cincinnati, Ohio, May 24-27, 1993. Manuscript received at ASME Headquarters March 1, 1993. Paper No. 93-GT-118. Associate Technical Editor: H. Lukas.

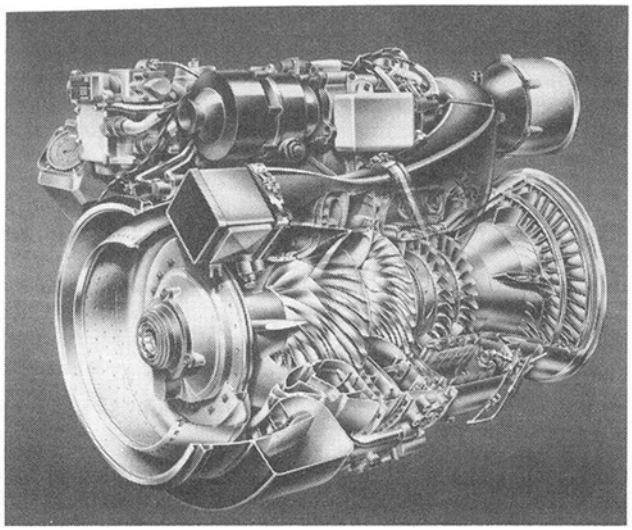

Fig. 1 The T800-LHT-800 engine

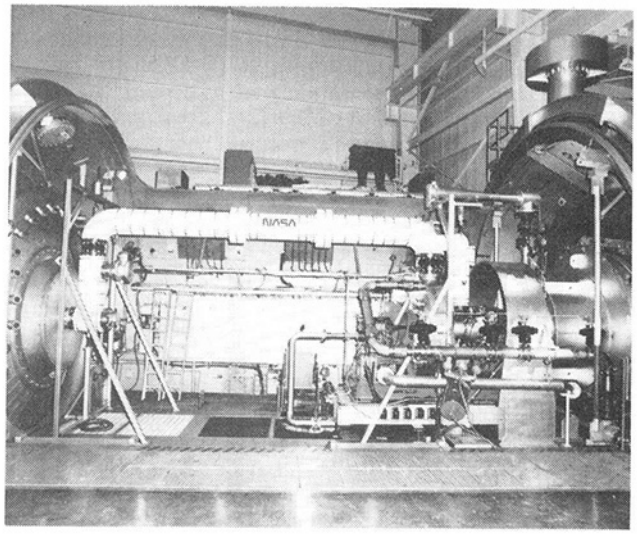

Fig. 2 NASA Lewis Research Center propulsion system laboratory test cell #3

turbine coupled to a dynamometer system. An inflow-bleed system was used to set the pressure ratio of the compression system to obtain data off the normal operating line. Data were obtained along constant speed lines from the operating line to surge.

Test Facility

The inlet distortion was conducted in test cell number 3 of the Propulsion Systems Laboratory (PSL3) at the NASA Lewis Research Center. PSL3 is an air-breathing engine altitude facility capable of simulating the environment for full-scale engines at altitudes up to 70,000 feet (21,336 m) and at velocities up to Mach 3. The altitude tank is 24 feet (7.32 m) in diameter and 38 feet (11.58 m) long (Fig. 2).

Temperature and pressure conditioned air is supplied to the inlet of the altitude chamber from the central air delivery system. A large bulkhead isolates the air delivery side of the test cell from the altitude chamber. Normally, the test engine inlet is connected directly to this bulkhead, with a bellmouth on the upstream side, and the engine, downstream of the bulkhead, subjected to simulated altitude conditions. Altitude conditions are maintained in the chamber by controlling the flow from the test cell to the central air services building. For the T800 installation, the engine could not be mounted directly on the bulkhead since the power turbine shaft exits at the front of the engine and needed to be connected to the dynamometer. To accommodate this configuration, the test cell bulkhead was blanked off and a pipe with a small bellmouth inlet was connected to the bulkhead plate. This led to flow control valving, flow measuring hardware, an inlet settling chamber or airbox, and the engine as shown in Fig. 2. The engine and airbox were mounted directly on a large pallet. This pallet provided the rigid base of a removable test installation upon which the major experimental hardware, including the engine, airbox, and dynamometer were mounted. Using this palletized stand, it was possible to assemble and work on significant portions of the test vehicle before occupying the test cell.

Special Test Hardware

The main items of special test hardware were those related to imposing the inlet flow distortions on the engine. Pressure distortions were generated by inserting a 180 deg circumferential extent screen in the flowpath upstream of the inlet. To raise the velocity at the screen (and therefore the pressure drop through it) the screen was located in a convergent-divergent inlet duct section. The screen was composed of an overlay of two separate screens and was mounted on a large mesh structural grid, or backer screen (Fig. 3). These were located in a rotatable spool piece that permitted circumferential clocking of the screens to enable detailed definition of the resulting distortion pattern with a fixed array of inlet rakes.

The temperature distortions were generated using a gaseous hydrogen burner (Fig. 4) located in the duct ahead of the pressure distortion screen holder. The burner design was based on the work of earlier NASA/Army Propulsion Directorate inlet distortion research (Klann et al., 1984). For this test, modifications based on prior T800 preliminary flight release inlet distortion testing and subsequent government improvements aimed at developing this test device for small engines with annular inlets were incorporated. The burner was divided into six 60-deg segments, allowing the generation of distortions in multiples of 60 deg, including multiple-per-rev patterns. The T800 distortion testing reported herein used only 180 deg circumferential distortion patterns.

Instrumentation

The T800 engine was a fully instrumented test vehicle. The

Nomenclature

N = physical speed
PAV = average pressure
PAVLOW = average pressure in the low-pressure sector
TAV = average temperature
TAVHI = average temperature in the high-temperature sector
Wc = corrected flow = $W\sqrt{\theta/\delta}$
$\Delta Pc/P$ = circumferential pressure distortion intensity
$\Delta Tc/T$ = circumferential temperature distortion intensity
δ = normalized pressure
θ = normalized temperature

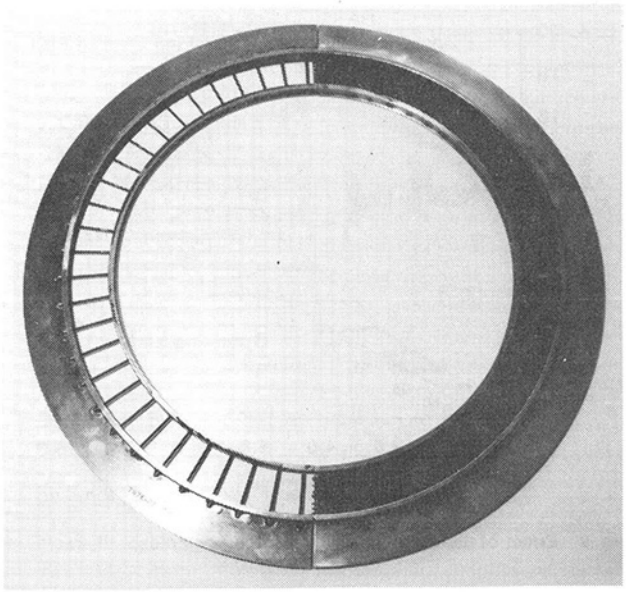

Fig. 3 180 deg distortion screen mounted on the backer screen

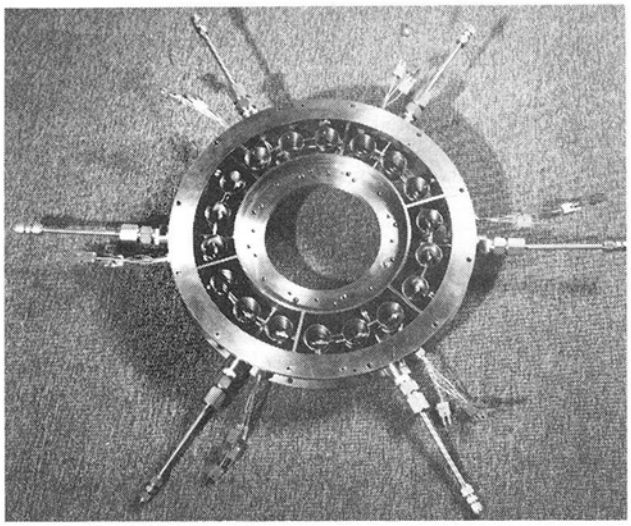

Fig. 4 Hydrogen burner used to generate temperature distortion

inlet airflow distortion level was defined using an array of 40 total pressure and temperature probes (ten rakes with four probes each equally spaced on centers of equal area) at the engine aerodynamic interface plane (AIP). Ten static pressure taps were also arranged on the shroud in this location.

Compressor impeller inlet instrumentation consisted of five rakes with seven total pressure elements per rake, and five shroud static taps. Other static taps were located at the front frame flowpath exit. The compressor exit was instrumented with eleven rakes (each having three total pressure and two total temperature elements), in addition to ten plenum static pressure taps.

Dynamic data were acquired through high-response pressure transducers (Kulites) and high-response temperature thermocouples. This instrumentation was located at the compressor inlet, between the stages, and the compressor exit. The dynamic data were used to assure that the distortions being generated did not produce any separation regions in the inlet particle separator and to examine details of the surge behavior if necessary. Since no anomalies were found in the engine, these data are not discussed in this paper.

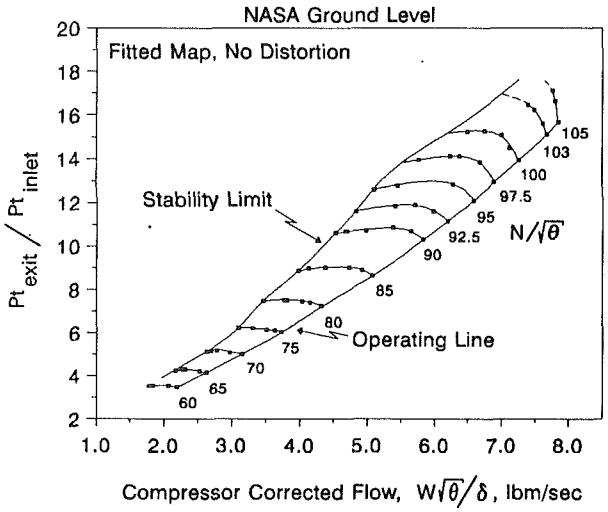

Fig. 5 Clean NASA level map

Test Objectives

The overall objective of the T800 altitude distortion test was to examine compression system stability and gather data to understand the T800 operability characteristics better under both pressure and temperature distortion. The specific objective was to document the changes in surge margin under distorted inflow conditions, at three altitude conditions, so the sensitivity models could be built and used in the stability assessment for various installations. These conditions were sea-level static, three kilometers (9843 ft) Mach 0.6, and nine kilometers (29,528 ft) Mach 0.2.

Four distortion configurations were tested: pressure distortion alone, temperature distortion alone, a concurrent pattern of pressure and temperature distortion, and an opposed pattern of pressure and temperature distortion. All of the patterns tested in this test series were 180 deg distortions. This was to provide the compressor with the most adverse distortion possible. Using 180 deg distortion patterns allows a passing impeller blade a maximum residence time in the low-momentum region of flow. This is the worst case distortion for a machine of this type, since the aerodynamic time constant associated with blade stalling and recovery is a function of blade chord. Incorporating centrifugal impellers, the time constant of the T800 compression system is significantly longer than that of a compression system with axial blades. This is why centrifugal compressors are typically more tolerant to distortion than axial compressors. In addition, dynamic distortion was not investigated with this centrifugal impeller system, due to the aerodynamic time constant.

Temperature changes over time (temperature ramps), while important to the overall operability of the engine, were not run in this test series, since tests of this nature were performed earlier in the engine development program at the NASA facility with no adverse results, while running to the engine specification limits.

Results

Baseline Determination. To determine the baseline operating characteristics of the compressor, data were obtained to develop the "clean" map. Figures 5, 6, 7, and 8 show the clean maps at the three altitude conditions tested, along with the available constant speed surge margin. Next, all of the distortion hardware used to hold the screens and burners was installed and the "backer" map developed (Fig. 9). This was necessary since the hardware has an effect on the characteristics of the compressor. The effect of the temperature and pressure

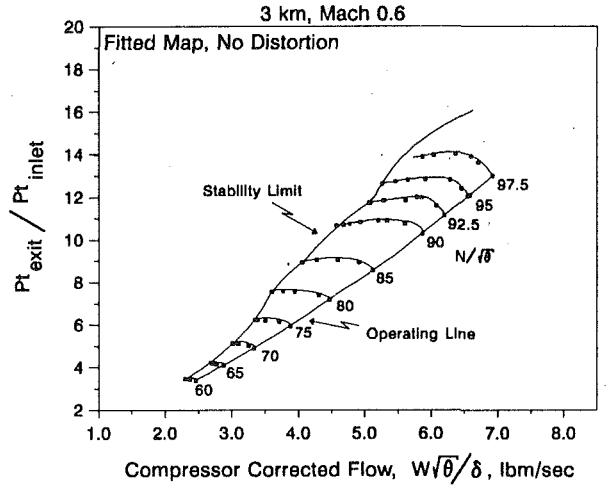

Fig. 6 Clean 3 km, Mach 0.6 map

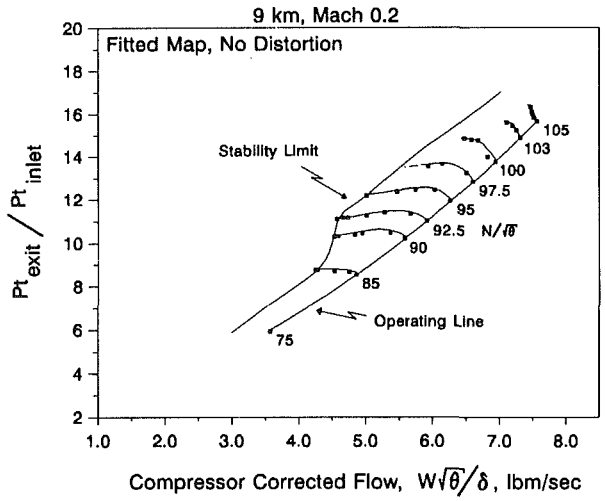

Fig. 7 Clean 9 km, Mach 0.2 map

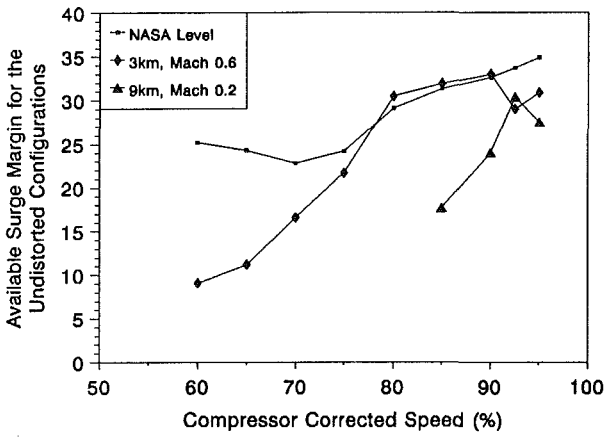

Fig. 8 T800 compression system maintains acceptable available surge margin over the flight envelope

distortion is then compared to the backer map. In later analyses, the changes due to distortion are analytically applied to the "clean" configuration (in other words, the effects of the hardware on the compressor are removed). For purposes of this paper, the data are shown with respect to the backer map, as they were taken.

Prior to the end of the test series, a rub occurred on the second stage impeller. Believed to be a result of running at a

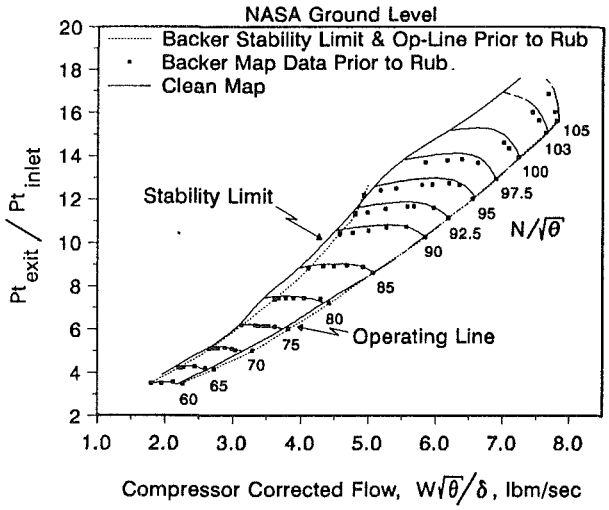

Fig. 9 Effect of distortion hardware on the compressor characteristic

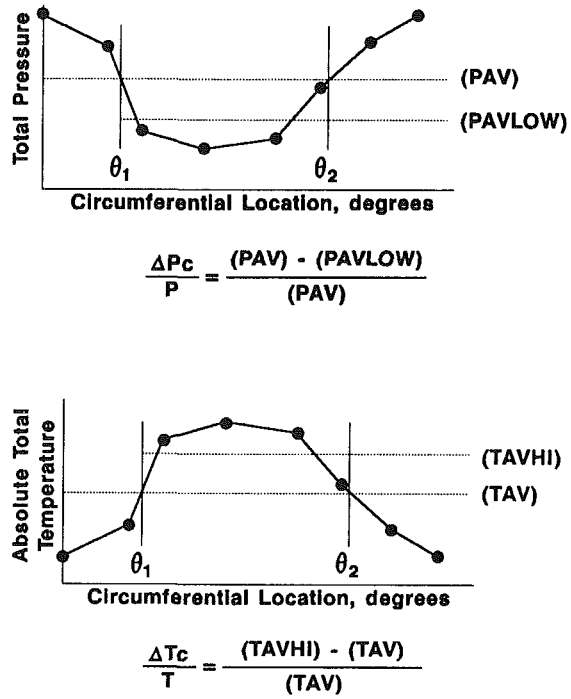

Fig. 10 Distortion intensity definition used in the test series

high inlet Mach number condition (3 km, Mach 0.6) with temperature distortion, it had the effect of reducing the efficiency on the second stage. A second backer map was obtained, so that subsequent distortion data could be properly baselined. The data presented in this paper are always compared with the appropriate backer map.

The distortion testing procedures/analysis techniques performed for the T800 engine follow the practices of the Society of Automotive Engineers (SAE) S-16 Committee on Inlet Distortion (1978, 1983, 1989). These documents describe the convention used in this test series to describe "distortion intensity," $\Delta Pc/P$ and $\Delta Tc/T$, as shown in Fig. 10.

As previously mentioned, the test covered temperature and pressure distortion alone and combined, in both concurrent and opposed configurations. Figure 11 shows the wide range of testing that was performed.

Pressure Distortion—NASA Ground Level. The effect of

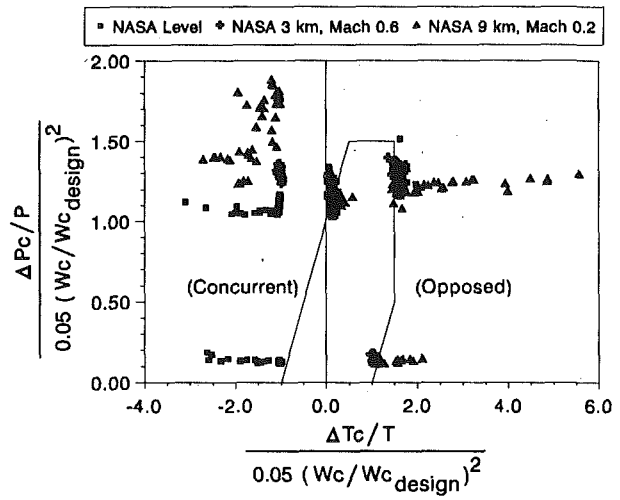

Fig. 11 Tested distortion intensities exceeded the engine specification limits

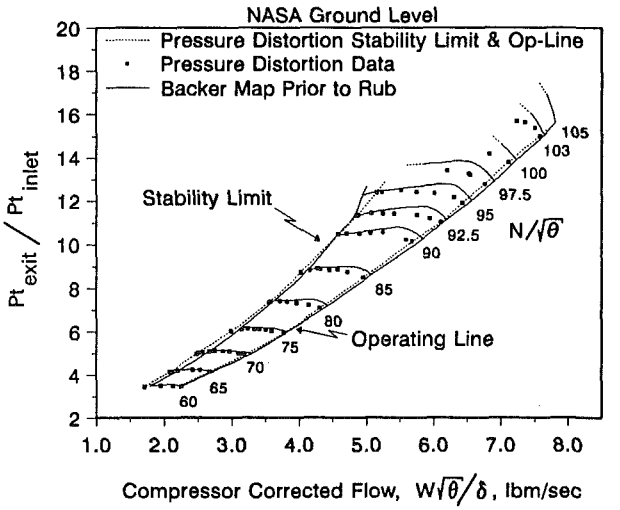

Fig. 12 Pressure distortion has no adverse effect on compressor stability margin in critical low-speed areas

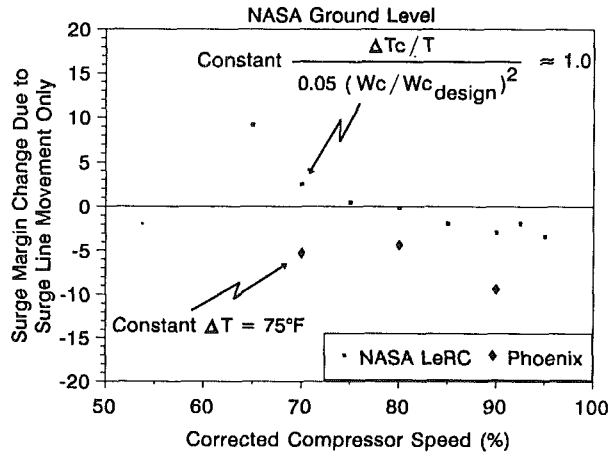

Fig. 13 Different surge margin results between Phoenix and NASA tests are a result of different temperature conditions

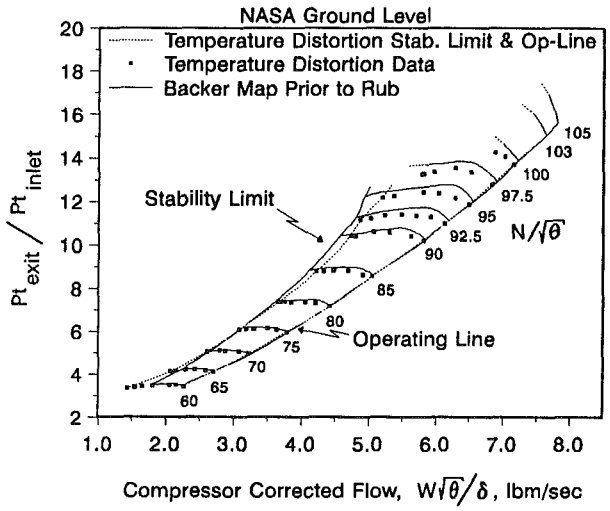

Fig. 14 Temperature distortion reduces the compression system stability limit

pressure distortion on the engine was tested using a 180-deg, 1/rev circumferential wire mesh screen. Previous tests had shown that it was difficult to obtain the desired levels of total pressure loss due to a low inlet Mach number. To increase the pressure loss caused by the screen, the screen was positioned in a converging-diverging section, just upstream of the AIP. The distortion screen produced a distortion intensity ($\Delta Pc/P$) of 4.1 percent at a corrected flow of 8.5 lbm/sec (3.86 kg/s).

At the NASA ground level condition (the closet to sea-level static conditions that could be obtained in the test cell, 14.073 psia [97.03 kPa] Mach 0.08), the distortion caused the compression system surge line to shift to a lower flow, as shown in Fig. 12, below speeds of 92.5 percent.

In addition, the operating line also shifted to a lower flow but the magnitude was smaller than the surge-line shift, resulting in a net gain in surge margin at low speed. At speeds above about 92.5 percent, pressure distortion results in a loss in surge margin. This loss in surge margin at high speed is not critical, since the engine operational transients at these speeds do not use as much of the available surge margin as at low speeds.

Prior to this test, distortion testing was performed at the AlliedSignal Engines facility in Phoenix, Arizona (Cousins et al., 1991), using the same distortion screens. Similar results were obtained in the Phoenix test.

The stabilizing effect of the circumferential pressure distortion is not unlike that seen on some axial-flow machines, where circumferential and radial distortion affect the compression system in opposite ways. While this phenomenon is not well understood, it is possible that the forced, repetitive change in the momentum of the entering flow has a stabilizing effect on the inducer of the centrifugal impeller.

Temperature Distortion—NASA Ground Level. Before the temperature distortion testing at NASA Lewis Research Center, testing had been performed in Phoenix. The Phoenix testing used a hot air injection system to create the distortion, as reported by Cousins et al. (1991). The hot air injection system was not as flexible as the NASA hydrogen burner, so the Phoenix test was run with a constant ΔT across the inlet of 75° Fahrenheit (23.9° C) while the NASA test was run at a constant flow-normalized distortion intensity. Figure 13 shows a comparison of the resulting change in surge margin (due to the surge line movement only) for the two tests. Figure 14 shows the compressor characteristics from the NASA test when under the influence of temperature distortion.

The operating line did not change with temperature distortion, although the intersection of the speed lines with the operating line did change at high speed. Running each of these tests in a different manner allowed covering a wide range of inlet temperature levels that are typical of gun gas ingestion

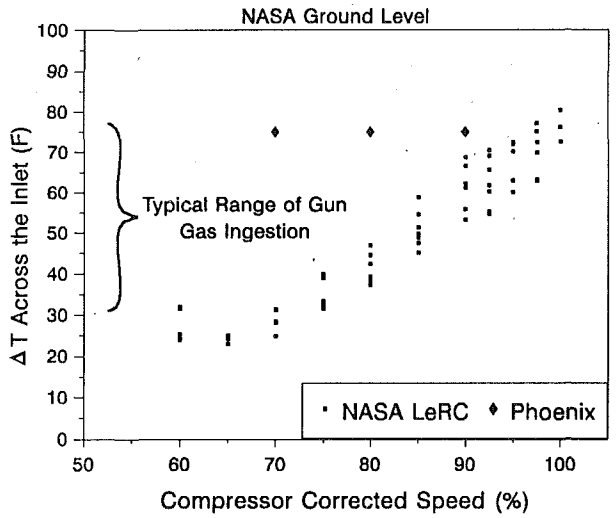

Fig. 15 Temperature distortion tests cover a range of operating conditions

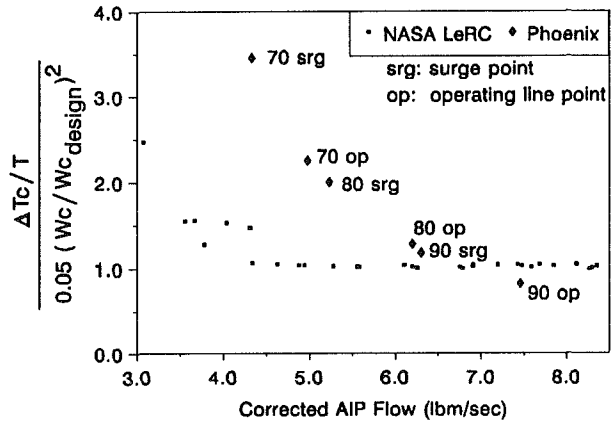

Fig. 16 Flow-normalized temperature distortion intensity is different between Phoenix and NASA tests

(Figs. 15 and 16). Both tests, however, showed that the effect of temperature distortion on the compressor is greater than the effect of pressure distortion.

Opposed Temperature and Pressure Distortion—NASA Ground Level. With the pressure distortion screens in place, temperature distortion was applied to the opposite side of the inlet from the pressure distortion. As shown in Fig. 17, both the stability limit line and the operating lines moved a significant amount. Only at 92.5 percent speed was there a surge margin decrease. As expected, distortions run in this manner do not show as adverse an influence on the compression system as either pressure or temperature by themselves.

Concurrent Temperature and Pressure Distortion—NASA Ground Level. Applying the temperature and pressure distortion in the same 180 deg sector results in an effect on the compression system that is a combination of each separately. The temperature distortion degrades stability while the pressure distortion enhances it, resulting in a net change shown in Fig. 18.

Surge Margin Determinations—All Altitude Conditions. Figures 19, 20, and 21 show the surge margin changes that were measured for all of the distortion patterns at the three altitude conditions, NASA ground level, 3 km Mach 0.6, and 9 km Mach 0.2. Figure 19 shows the surge margin calculated from the previously presented maps.

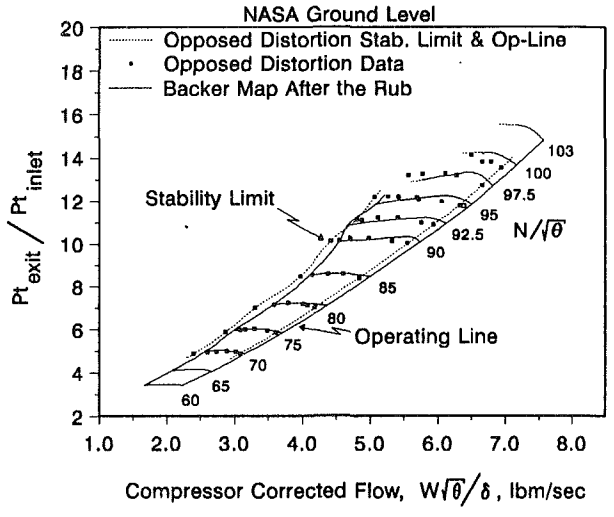

Fig. 17 The effects of opposed temperature and pressure distortion are not as great as temperature distortion alone

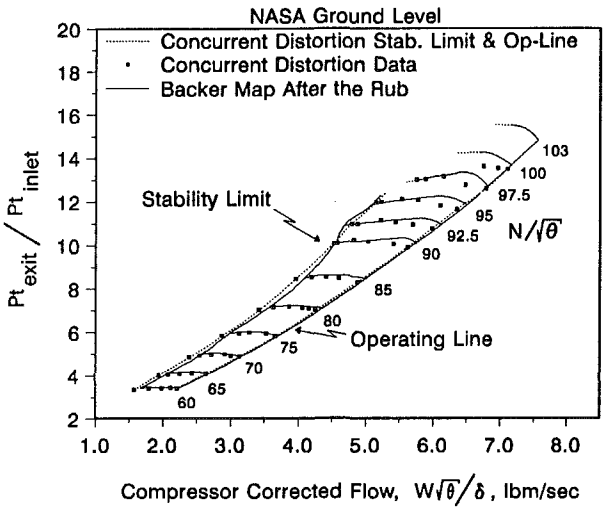

Fig. 18 Concurrent distortion causes a shift in both the operating line and the stability limit

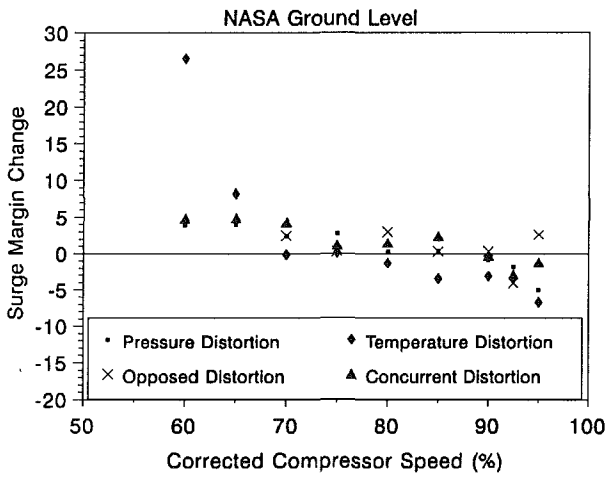

Fig. 19 Temperature distortion causes the most adverse effect on surge margin at low altitude

For the NASA level testing, pressure distortion begins to affect the stability of the compressor adversely above about 90 percent speed, with a surge margin decrease of about 6

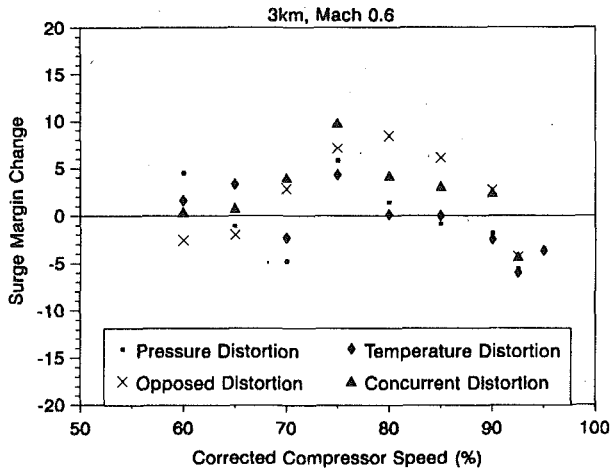

Fig. 20 Temperature and pressure distortion have similar effects above 80 percent speed at 3 km, Mach 0.6 conditions

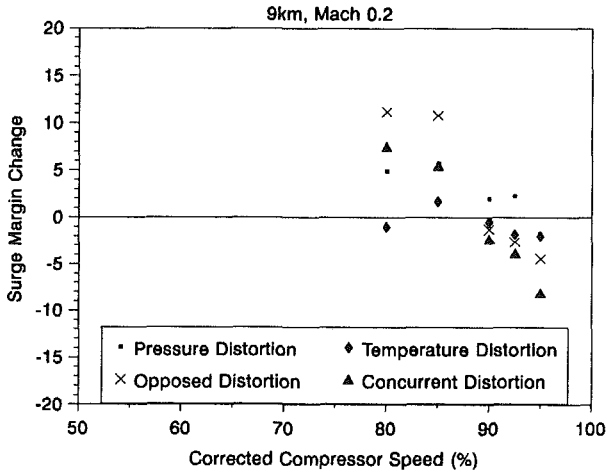

Fig. 21 Concurrent distortion generates the largest surge margin degradation at high altitude

percent. The most critical region for operation of the engine is from 70 to 85 percent speed, where transient accelerations require the most surge margin. In this region, pressure distortion enhanced stability, showing the compressor to be very tolerant of pressure distortion. This is similar at the other altitude conditions, although at 3 km Mach 0.6 there was also a low-speed loss in surge margin of about 5 percent. Examination of the compressor map for this condition (Fig. 6) shows that the stability limit line drops at low speeds, causing the low-speed surge margin effect with pressure distortion. This is not much concern because if one were to operate at a 3 km Mach 0.6 condition, the engine would have to be at high power and not operating in this portion of the map.

Temperature distortion has the most consistent and adverse effect on the compression system, losing about 3 percent surge margin in the critical map area around 70 to 85 percent speed. From the previous Phoenix test, this was also the case, but the magnitude of the surge margin degradation was larger (approximately 5 percent), due to the higher temperature distortion intensity levels run at low speeds.

Concurrent distortion had the greatest adverse effect at 90 to 95 percent speed, using as much as 9 percent surge margin at the 9 km condition, but where available surge margin is 25 to 30 percent. Surge margin increases were obtained at other speeds. Similar results were obtained for the opposed distortion patterns. Generally, the opposed distortion patterns did not affect the surge margin to the magnitude of the concurrent distortion patterns.

In general, pressure distortion causes an increase in the stability characteristics of the engine at low speed and a slight decrease at high speed, while temperature distortion seems to cause a decrease overall. Comparisons of the distortion results presented in this paper with the results of the Phoenix test series (Cousins et al., 1991) suggest that the overall effect of the combined patterns is a function of both the level of each type of distortion and the particular pattern position (concurrent or opposed).

Summary

The inherent stability of a two-stage centrifugal compression system has been demonstrated. Testing has shown the T800 engine to be very tolerant of inlet airflow distortion, losing the most stability where there is the most available surge margin. This provides the engine with the capability to be installed in many different rotorcraft applications.

The effect of pressure distortion on compression system stability is minimal, and in most cases, causes an increase in stability margin. Temperature distortion reduces the stability of the engine, but the largest degradation is in regions of the compressor map where the largest stability margin exists. Patterns of combined pressure and temperature distortion affect the stability in different ways, depending upon the screen orientation and the altitude conditions. Although this is the case, the combined distortion patterns had a minimal adverse effect on engine stability.

Acknowledgments

The authors wish to thank Brian Takesuye, Christopher Gromek, Tor Henriksen, Joan Doherty, Merritt Thomas, and Donald Palmer of AlliedSignal Engines for their extended efforts and support of this test series. Also, thanks to David Clark and Teresa Kline of the Army Vehicle Propulsion Directorate; and Martin Ginley and Jeffrey Balser of the NASA Lewis Research Center for their dedicated contributions to the performance of this test. It is the effort of these individuals that has made this work possible.

The authors would also like to thank LHTEC for permission to publish these test results, and the NASA Lewis Research Center and the Army Vehicle Propulsion Directorate for the support of this test series.

References

Cousins, W. T., Miller, R. E., and Dalton, K. K., 1991, "Distortion Tolerance of the T800-LHT-800 Turboshaft Engine," *Proceedings, American Helicopter Society 47th Annual Forum and Technology Display*, Vol. 2 (A92-14326 03-01), pp. 1147–1155.

Klann, G. A., Barth, R. L., and Biesiadny, T. J., 1984, "Temperature Distortion Generator for Turboshaft Engine Testing," NASA TM-83478.

SAE S-16 Technical Committee, 1978, "Gas Turbine Engine Inlet Flow Distortion Guidelines," ARP1420.

SAE S-16 Technical Committee, 1983, "Inlet Total-Pressure Distortion Considerations for Gas Turbine Engines," AIR1419.

SAE S-16 Technical Committee, 1991, "A Current Assessment of the Inlet/Engine Temperature Distortion Problem," ARD50015.

The Effect of Seal Width on Regenerator Effectiveness

D. S. Beck
Department of Mechanical Engineering,
Massachusetts Institute of Technology,
Cambridge, MA 02139

The effect of axial conduction on regenerator effectiveness has been studied in the past under the assumption of zero seal width. The effect of axial conduction coupled with finite seal width is presented in this paper. A method for calculating effectiveness assuming axial conduction and finite seal width is presented. Results of sample calculations are presented to give the designer a feel for the dependence of seal-width effects on system-parameter values. It is shown that for typical regenerator designs, reductions in effectiveness due to axial conduction coupled with finite seal width can be twice as great as those due to axial conduction under the assumption of zero seal width. Also, it is shown that the required regenerator size to achieve a given effectiveness can increase dramatically when finite seal width is considered in design procedures. It is concluded that consideration of axial conduction should include finite seal width.

1 Introduction

In theory, regenerated Brayton cycles can achieve significantly higher thermal efficiencies than those of diesel cycles (see Wilson [1]). In practice, however, compressed air leaks under the regenerator face seals that separate the compressed-air flow from the exhaust-gas flow. This direct seal leakage reduces the efficiencies of actual regenerated gas turbines.

For the gas turbine to compete with the diesel engine for automotive applications, the efficiency of the gas turbine must be increased. One way to increase the efficiency of regenerated gas turbines is to reduce direct seal leakage. This leakage can be reduced by increasing the width of the seals (see Harper [2]); however, reductions in regenerator effectiveness are incurred due to seal width. Axial conduction causes the axial matrix temperature profile to degrade toward a mean value while the matrix's passages are under the seals. This degradation reduces regenerator effectiveness. The degree of temperature-profile degradation is directly related to the time the passages spend under seals. Thus, reductions in effectiveness increase with seal width. In summary, direct seal leakage decreases with seal width, but regenerator effectiveness also decreases with seal width. Data are needed so that seals of optimal width can be designed.

The literature contains no design information concerning reductions in effectiveness due to seal width. However, various researchers have addressed the calculation of regenerator effectiveness under various assumptions (including zero seal width). Coppage and London [3] provide a summary of the design theory up to 1953. Lambertson [4] extends the theory by calculating effectiveness data for finite rotation rates ($C_{rot} < \infty$) and other system-parameter ranges, which are commonly experienced in regenerated gas turbines. Bahnke and Howard [5] extend Lambertson's [4] results by relaxing his assumption of zero axial conduction; however, they do not consider axial conduction while the matrix's passages are under the seals. It will be shown that reductions in effectiveness due to axial conduction coupled with finite seal width can be twice as great as those due to axial conduction under the assumption of zero seal width. Also, it will be shown that design procedures that neglect seal width can produce unrealistically small regenerators for given effectivenesses.

In the next section, a method for calculating effectiveness reductions due to axial conduction coupled with finite seal width will be presented. First, the heat transfer problem of axial conduction while matrix passages are under seals will be addressed. Then, the governing equations for calculating effectiveness will be presented. Reductions in effectiveness due to axial conduction coupled with finite seal width are dependent upon system-parameter values. In Section 3, results of example calculations will be presented to show these dependencies. Finally, conclusions will be presented in Section 4.

2 Method

2.1 The Heat Transfer Problem. Consider matrix passages located under a seal as shown in Fig. 1(*a*). We would like to calculate the matrix temperature profile where the matrix exits a seal given the matrix temperature profile where the matrix enters a seal.

While the passages are under the seals, the gas within each passage is essentially trapped.[1] The trapped gas is approxi-

Contributed by the International Gas Turbine Institute and presented at the 38th International Gas Turbine and Aeroengine Congress and Exposition, Cincinnati, Ohio, May 24-27, 1993. Manuscript received at ASME Headquarters March 17, 1993. Paper No. 93-GT-341. Associate Technical Editor: H. Lukas.

[1]The gas flow over each end of the passages due to direct seal leakage is neglected in this analysis. It will be concluded that the trapped gas has a negligible effect on the final axial matrix temperature profile, so small flows into and out of the passages are inconsequential.

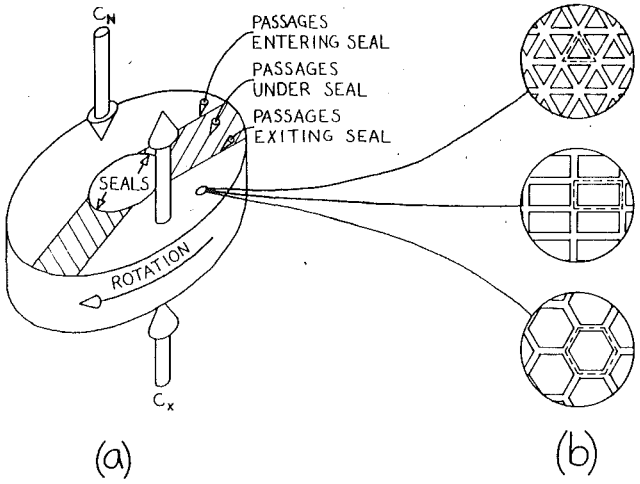

Fig. 1 (*a*) **Rotary-regenerator schematic showing matrix passages under a seal and** (*b*) **alternative passage geometries**

mately stagnant because the typically small hydraulic diameters in gas turbine-regenerator matrices limit free convection. Therefore, the heat transfer problem of interest is three-dimensional heat diffusion in the trapped-gas and matrix-material domains. The temperature distributions in the trapped-gas and matrix-material domains are given by the heat-diffusion equations,

$$\nabla^2 T_{\text{gas}} = \frac{1}{\alpha_{\text{gas}}} \frac{\partial T_{\text{gas}}}{\partial t} \tag{1}$$

$$\nabla^2 T_R = \frac{1}{\alpha_R} \frac{\partial T_R}{\partial t} \tag{2}$$

subject to appropriate boundary conditions.

2.2 Simplifications. Some simplifying assumptions can be made. Consider the alternative passage geometries (equilateral-triangle, rectangular, and regular-hexagon) and the boundaries of individual tubes associated with each passage shown in Fig. 1(*b*). The first assumption is zero heat transfer through passage-tube boundaries. The flows of gas over passage-tube ends due to direct seal leakage are neglected as well as any heat transfer from the matrix material or trapped gas to these flows. In a gas turbine application, the direct-seal-leakage flows are cool compressed air across one matrix face and heated compressed air across the other matrix face. The cooler flow would degrade the matrix temperature profile slightly, while the warmer flow would have a smaller effect. Zero matrix heat conduction through the passage-tube boundaries in the direction of matrix rotation is a reasonable assumption because temperature gradients are small in this direction, especially for high-effectiveness regenerators in which the matrix temperature profile changes little during each rotation at steady state. Zero matrix heat conduction through the passage-tube boundaries in the matrix's radial direction is a reasonable assumption because temperature gradients in this direction are negligible if face seals are not overly large and the flow distribution is sufficiently uniform.

The remaining assumption is that the matrix-material and trapped-gas temperatures are spatially constant at each axial location. The matrix-material temperature is spatially constant at each axial location if the the matrix porosity, p, is sufficiently high. Now, consider the trapped gas. When a matrix passage first enters a seal, the trapped gas has a different average temperature in general than that of the matrix material. However, the trapped gas relatively quickly comes to thermal equilibrium due to its high thermal diffusivity, α_{gas}, compared with that of the matrix material, α_R. For example, for ceramic matrix material,

Nomenclature

As = matrix-material area available for conduction, m^2
As' = As_N/As_X
b = y intercept of a linear temperature profile, K
c = specific heat capacity, J/kg-K
C = heat-capacity rate, W/K
C_{rat} = C_N/C_X
C_{rot} = C_R/C_N
Fo = $\alpha_R t/L^2$ Fourier number
$H_{1\text{-}4}$ = intermediate variables used for axial-conduction and seal-width effect calculations
(hA) = convective conductance, W/K
$(hA)'$ = $(hA)_N/(hA)_X$
j = an index
k = an index
k = thermal conductivity, W/m-K
L = length of a matrix passage (or matrix thickness), m
m = slope of a linear temperature profile, K/m
(mc) = heat capacity, J/K
N = number of elements
NTU = $(hA)_N/\{C_N[1+(hA)']\}$ = number of transfer units
p = $\dfrac{\text{matrix voids volume}}{\text{total matrix volume}}$ = porosity
SC = $As_{SW}/[As_{SW}+As_N+As_X]$ = seal coverage
t = time, s
T = temperature, K
$\overline{T}$ = mean temperature, K
x = axial coordinate, m
α = thermal diffusivity, m^2/s
$(\Delta\epsilon/\epsilon)_{ac}$ = $(\hat{\epsilon}_{ac}-\hat{\epsilon}_{nc})/\hat{\epsilon}_{nc}$ = axial-conduction effect
$(\Delta\epsilon/\epsilon)_{acsw}$ = $(\hat{\epsilon}_{acsw}-\hat{\epsilon}_{nc})/\hat{\epsilon}_{nc}$ = axial-conduction-and-seal-width effect
ϵ = effectiveness, the ratio of the actual heat transferred in a heat exchanger to the heat that would be transferred in a perfect heat exchanger of infinite size
$\mathcal{E}$ = effectiveness output (calculated)
$\hat{\epsilon}$ = effectiveness estimate (calculated by extrapolating effectiveness outputs to zero element area)
ζ = x/L
Θ = $(T_R-\overline{T}_R)/(T_{\max}-\overline{T}_R)$
λ = $k_R As_N(1+1/As')/(LC_N)$ (conduction parameter)
ρ = density, kg/m^3

Subscripts

ac = calculated assuming axial conduction and zero seal width
$acsw$ = calculated assuming axial conduction and finite seal width
e = of a matrix element
fp = for flat-profile condition
gas = of the trapped gas
i = at the inlet of an element
max = maximum
N = on the side of minimum heat-capacity rate
nc = calculated assuming no axial conduction
o = at the outlet of an element
p = evaluated at constant pressure
R = of the matrix material
SW = of a seal
X = on the side of maximum heat-capacity rate

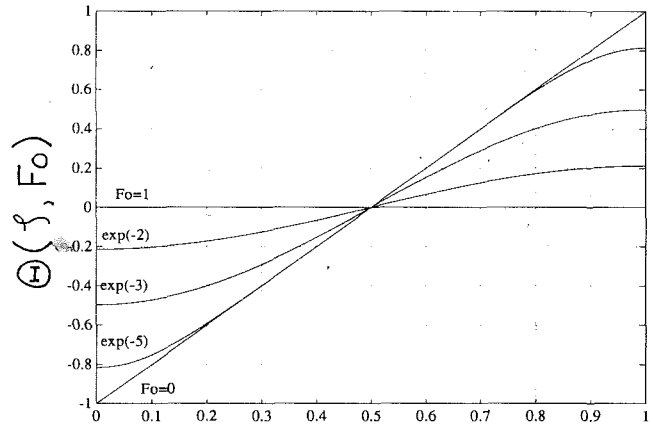

Fig. 2 One-dimensional heat diffusion with a linear initial temperature profile and insulated ends

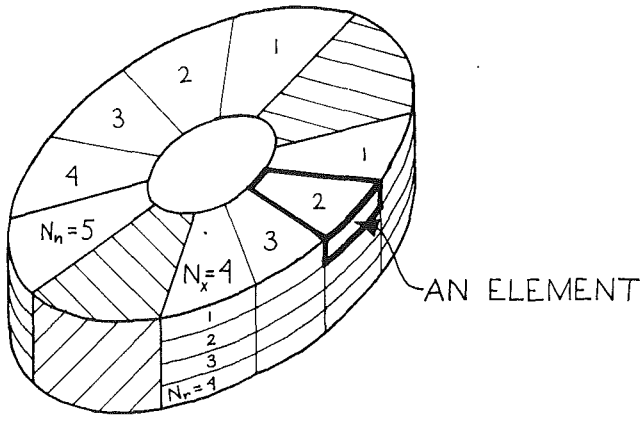

Fig. 3 Schematic of a rotary regenerator showing divisions used in finite-difference computations

$$\alpha_{gas}/\alpha_R = (k_{gas}/k_R)\,(\rho_R/\rho_{gas})\,(c_R/c_{p_{gas}}) \tag{3}$$

$$\alpha_{gas}/\alpha_R \approx 0.3 \times 4000 \times 0.9 = 1000 \tag{4}$$

The trapped gas quickly comes to thermal equilibrium, its average temperature quickly changing to that of the matrix material at each axial location. This happens because the heat capacity of the trapped gas, $(mc_p)_{gas}$, typically is much smaller than the heat capacity of the matrix material, $(mc)_R$. For example, for a ceramic matrix material with $p = 0.7$,

$$(mc_p)_{gas}/(mc)_R = (c_{p_{gas}}/c_R)\,(\rho_{gas}/\rho_R)\,(p/[1-p]) \tag{5}$$

$$(mc_p)_{gas}/(\mathrm{mc})_R \approx 1.1 \times 0.00025 \times 2 = 0.0006 \tag{6}$$

Thus, the temperature distributions in the trapped gas and the matrix material are functions of time and axial location. Therefore, the temperature distributions are independent of each other, and the matrix-material temperature profile is determined by the one-dimensional heat-diffusion equation in the matrix-material domain:

$$\frac{\partial^2 T_R}{\partial x^2} = \frac{1}{\alpha_R}\frac{\partial T_R}{\partial t} \tag{7}$$

2.3 One-Dimensional Heat Diffusion. To gain insight into the heat transfer phenomenon occurring while a passage is under a seal, a one-dimensional heat-diffusion problem subject to boundary conditions typical of regenerators will be solved.

A nearly linear temperature profile usually is established in the matrix material. We will choose the following representative initial temperature profile:

$$T_R(x,\ t=0) = mx + b \tag{8}$$

This yields one boundary condition. The other boundary conditions come from the assumption of no heat transfer from either of the passage-tubes' ends. Thus, our three boundary conditions are:

(1) $\left.\dfrac{\partial T_R}{\partial x}\right|_{x=0,\ t>0} = 0$

(2) $\left.\dfrac{\partial T_R}{\partial x}\right|_{x=L,\ t>0} = 0$

(3) $T_R(x,\ t=0) = mx + b$

The following dimensionless parameters are defined:

$$\zeta \equiv \frac{x}{L} \tag{9}$$

$$\mathrm{Fo} \equiv \frac{\alpha_R t}{L^2} \tag{10}$$

and

$$\Theta \equiv \frac{T_R - \overline{T}_R}{T_{\max} - \overline{T}_R} \tag{11}$$

where $\overline{T}_R = T_R\ (x = L/2,\ t = 0)$, and $T_{\max} = T_R\ (x = L,\ t = 0)$. The heat-diffusion problem is then

$$\frac{\partial^2 \Theta}{\partial \zeta^2} = \frac{\partial \Theta}{\partial \mathrm{Fo}} \tag{12}$$

subject to the following boundary conditions:

(1) $\left.\dfrac{\partial \Theta}{\partial \zeta}\right|_{\zeta=0,\ \mathrm{Fo}>0} = 0$

(2) $\left.\dfrac{\partial \Theta}{\partial \zeta}\right|_{\zeta=1,\ \mathrm{Fo}>0} = 0$

(3) $\Theta(\zeta,\ \mathrm{Fo} = 0) = 2\zeta - 1$

The solution to this problem is

$$\Theta(\zeta,\ \mathrm{Fo}) = \left[\frac{-8}{\pi^2}\right]\sum_{j=1}^{\infty}\left[\frac{1}{(2j-1)^2}\right] e^{-(2j-1)^2\pi^2 \mathrm{Fo}} \cos([2j-1]\pi\zeta) \tag{13}$$

Plots of Eq. (13) are shown in Fig. 2. We can see from the plots that the temperature profile flattens at either end of a passage-tube and gradually flattens for the whole passage-tube as Fo increases. The matrix passage-tubes exit the seals at some Fo with a certain degree of temperature-profile degradation.

2.4 Governing Equations. Bahnke and Howard [5] describe a method for calculating regenerator-matrix temperature distribution. Their method incorporates matrix axial conduction but neglects seal width. Heat diffusion while passages are under seals relies on axial conduction. Therefore, Bahnke and Howard's [5] method is used to calculate the matrix temperature distribution while the matrix is exposed to the flows, and a modification of their method is used to calculate matrix temperature distribution while the matrix passages are under seals.

2.4.1 Equations for Matrix Passages Exposed to Flows. In Bahnke and Howard's [5] method, a regenerator is divided axially N_R times and circumferentially N_X times on the C_X side and N_N times on the C_N side (see Fig. 3). Then, unmixed crossflow with average temperatures at inlets and outlets is assumed for each of the resulting elements.

By extending Bahnke and Howard's [5] method, the matrix

temperature distribution can be expressed by the following vector equations[2]: for the C_X side,

$$\mathbf{x}_{k_X} = \mathbf{A}_X \mathbf{x}_{k-1_X} + \mathbf{b}_X T_{Xi}$$

$$T_{eXo_{N_R,\,k}} = \mathbf{c}_X^T \mathbf{x}_{k-1_X} + d_X T_{Xi}$$

$$1 \le k \le N_X \tag{14}$$

and for the C_N side,

$$x_{k_N} = \mathbf{A}_N \mathbf{x}_{k-1_N} + \mathbf{b}_N T_{Ni}$$

$$T_{eNo_{1,\,k}} = \mathbf{c}_N^T \mathbf{x}_{k-1_N} + d_N T_{Ni}$$

$$1 \le k \le N_N \tag{15}$$

where

$$\mathbf{x}_k = \begin{bmatrix} T_{eRo_{1,\,k}} \\ T_{eRo_{2,\,k}} \\ T_{eRo_{3,\,k}} \\ \vdots \\ T_{eRo_{N_R-1,\,k}} \\ T_{eRo_{N_R,\,k}} \end{bmatrix} \tag{16}$$

and

$$\mathbf{x}_{k-1} = \begin{bmatrix} T_{eRi_{1,\,k}} \\ T_{eRi_{2,\,k}} \\ T_{eRi_{3,\,k}} \\ \vdots \\ T_{eRi_{N_R-1,\,k}} \\ T_{eRi_{N_R,\,k}} \end{bmatrix} \tag{17}$$

The temperatures T_{eRo} and T_{eRi} are, respectively, the outlet and inlet matrix-material temperatures of an element.

2.4.2 Equations for Matrix Passages Under Seals. It is shown in Section 2.3 that the Fourier number, Fo, is the key parameter in describing the degree of heat diffusion that takes place in the matrix material. Therefore, it will be instructive to derive an expression for this parameter in terms of regenerator-system dimensionless parameters. From the Fo definition in Section 2.3,

$$\mathrm{Fo} \equiv \alpha_R t_{SW}/L^2 = k_R t_{SW}/(\rho_R c_R L^2) \tag{18}$$

where t_{SW} is the amount of time that a matrix passage spends under a seal. From the definition of λ, we obtain

$$\mathrm{Fo} = \frac{\lambda C_N A s' t_{SW}}{A s_N (1 + A s') \rho_R c_R L} \tag{19}$$

The value of t_{SW} is

$$t_{SW} = \frac{A s_N (1 + A s') L \rho_R c_R SC}{2 A s' C_R (1 - SC)} \tag{20}$$

Therefore,

$$\mathrm{Fo} = \left(\frac{1}{2}\right)\left(\frac{SC}{1-SC}\right)\left(\frac{\lambda}{C_{\mathrm{rot}}}\right) \tag{21}$$

Let us now derive element equations for passages under seals:

For first-row elements

$$\left[\left(\frac{k_R A s_N}{2L}\right)\left(\frac{SC}{1-SC}\right)\left(\frac{1+As'}{As'}\right)\left(\frac{N_R}{N_{SW}}\right)\right] \times [(T_{eRo_{2,\,k-1}} + T_{eRo_{2,\,k}}) - (T_{eRo_{1,\,k-1}} + T_{eRo_{1,\,k}})] = \left[\frac{C_R}{N_R}\right][T_{eRo_{1,\,k}} - T_{eRo_{1,\,k-1}}] \tag{22}$$

(where N_{SW} is the number of circumferential divisions under a seal), or

$$T_{eRo_{1,\,k}} = \left[\frac{1 - \mathrm{Fo}\left(\frac{N_R^2}{N_{SW}}\right)}{1 + \mathrm{Fo}\left(\frac{N_R^2}{N_{SW}}\right)}\right] T_{eRo_{1,\,k-1}} + \left[\frac{\mathrm{Fo}\left(\frac{N_R^2}{N_{SW}}\right)}{1 + \mathrm{Fo}\left(\frac{N_R^2}{N_{SW}}\right)}\right][T_{eRo_{2,\,k-1}} + T_{eRo_{2,\,k}}] \tag{23}$$

For middle-row elements

$$\left[\left(\frac{k_R A s_N}{2L}\right)\left(\frac{SC}{1-SC}\right)\left(\frac{1+As'}{As'}\right)\left(\frac{N_R}{N_{SW}}\right)\right][(T_{eRo_{j-1,\,k-1}} + T_{eRo_{j-1,\,k}}) - 2(T_{eRo_{j,\,k-1}} + T_{eRo_{j,\,k}})] + (T_{eRo_{j+1,\,k-1}} + T_{eRo_{j+1,\,k}})] = \left[\frac{C_R}{N_R}\right][T_{eRo_{j,\,k}} - T_{eRo_{j,\,k-1}}] \tag{24}$$

or

$$T_{eRo_{j,\,k}} = \left[\frac{1 - 2\mathrm{Fo}\left(\frac{N_R^2}{N_{SW}}\right)}{1 + 2\mathrm{Fo}\left(\frac{N_R^2}{N_{SW}}\right)}\right] T_{eRo_{j,\,k-1}} + \left[\frac{Fo\left(\frac{N_R^2}{N_{SW}}\right)}{1 + 2\mathrm{Fo}\left(\frac{N_R^2}{N_{SW}}\right)}\right][T_{eRo_{j-1,\,k-1}} + T_{eRo_{j-1,\,k}} + T_{eRo_{j+1,\,k-1}} + T_{eRo_{j+1,\,k}}] \tag{25}$$

For last-row elements

$$\left[\left(\frac{k_R A s_N}{2L}\right)\left(\frac{SC}{1-SC}\right)\left(\frac{1+As'}{As'}\right)\left(\frac{N_R}{N_{SW}}\right)\right] \times [(T_{eRo_{N_R-1,\,k-1}} + T_{eRo_{N_R-1,\,k}}) - (T_{eRo_{N_R,\,k-1}} + T_{eRo_{N_R,\,k}})] = \left[\frac{C_R}{N_R}\right][T_{eRo_{N_R,\,k}} - T_{eRo_{N_R,\,k-1}}] \tag{26}$$

or

$$T_{eRo_{N_R,\,k}} = \left[\frac{1 - \mathrm{Fo}\left(\frac{N_R^2}{N_{SW}}\right)}{1 + \mathrm{Fo}\left(\frac{N_R^2}{N_{SW}}\right)}\right] T_{eRo_{N_R,\,k-1}} + \left[\frac{Fo\left(\frac{N_R^2}{N_{SW}}\right)}{1 + \mathrm{Fo}\left(\frac{N_R^2}{N_{SW}}\right)}\right] \times [T_{eRo_{N_R-1,\,k-1}} + T_{eRo_{N_R-1,\,k}}] \tag{27}$$

The following parameters can be defined:

$$H_1 \equiv \frac{1 - 2\mathrm{Fo}\left(\frac{N_R^2}{N_{SW}}\right)}{1 + 2\mathrm{Fo}\left(\frac{N_R^2}{N_{SW}}\right)}$$

[2]The matrix entries can be derived readily from the equations presented by Bahnke and Howard [5], and their values can be deduced from the Matlab commands given in the appendix.

$$H_2 \equiv \frac{\mathrm{Fo}\left(\frac{N_R^2}{N_{SW}}\right)}{1+2\mathrm{Fo}\left(\frac{N_R^2}{N_{SW}}\right)}$$

$$H_3 \equiv \frac{1-\mathrm{Fo}\left(\frac{N_R^2}{N_{SW}}\right)}{1+\mathrm{Fo}\left(\frac{N_R^2}{N_{SW}}\right)}$$

$$H_4 \equiv \frac{\mathrm{Fo}\left(\frac{N_R^2}{N_{SW}}\right)}{1+\mathrm{Fo}\left(\frac{N_R^2}{N_{SW}}\right)} \tag{28}$$

Then, for passages under seals,

$$\mathbf{x}_{k_{SW}} = \mathbf{A}_{SW}\mathbf{x}_{k-1_{SW}}$$
$$1 \le k \le N_{SW} \tag{29}$$

where

$$\mathbf{A}_{SW} \equiv (\mathbf{I}-\mathbf{B}_3)^{-1}\mathbf{A}_3 \tag{30}$$

and

$$\mathbf{B}_3 \equiv \begin{bmatrix} 0 & H_4 & 0 & \cdots & 0 & 0 \\ H_2 & 0 & H_2 & \cdots & 0 & 0 \\ 0 & H_2 & 0 & \cdots & 0 & 0 \\ \vdots & \vdots & \vdots & \vdots & \vdots & \vdots \\ 0 & 0 & 0 & \cdots & 0 & H_2 \\ 0 & 0 & 0 & \cdots & H_4 & 0 \end{bmatrix} \tag{31}$$

and

$$\mathbf{A}_3 \equiv \begin{bmatrix} H_3 & H_4 & 0 & \cdots & 0 & 0 \\ H_2 & H_1 & H_2 & \cdots & 0 & 0 \\ 0 & H_2 & H_1 & \cdots & 0 & 0 \\ \vdots & \vdots & \vdots & \vdots & \vdots & \vdots \\ 0 & 0 & 0 & \cdots & H_1 & H_2 \\ 0 & 0 & 0 & \cdots & H_4 & H_3 \end{bmatrix} \tag{32}$$

Equation (29) gives the outlet temperatures of N_R elements at a circumferential location under a seal as a function of the inlet temperatures.

2.4.3 Initial Temperature Profile Calculation. The equations presented above can be combined to obtain an expression for the matrix-material temperature profile at the location where the matrix passages enter the C_N side. The state equations in Eqs. (14) and (15) can be propagated to obtain the following:

$$(\mathbf{x}_{N_X})_X = \mathbf{A}_X^{N_X}\mathbf{x}_{0_X} + (\mathbf{A}_X^{N_X-1} + \mathbf{A}_X^{N_X-2} + \cdots + \mathbf{I})\mathbf{b}_X T_{Xi} \tag{33}$$

and

$$(\mathbf{x}_{N_N})_N = \mathbf{A}_N^{N_N}\mathbf{x}_{0_N} + (\mathbf{A}_N^{N_N-1} + \mathbf{A}_N^{N_N-2} + \cdots + \mathbf{I})\mathbf{b}_N T_{Ni} \tag{34}$$

Similarly, the state equation of Eqs. (29) can be propagated to obtain

$$(\mathbf{x}_{N_{SW}})_{SW} = \mathbf{A}_{SW}^{N_{SW}}\mathbf{x}_{0_{SW}} \tag{35}$$

For physical compatibility,

$$\mathbf{x}_{0_{SW1}} = (\mathbf{x}_{N_N})_N \tag{36}$$

$$\mathbf{x}_{0_X} = (\mathbf{x}_{N_{SW}})_{SW1} \tag{37}$$

$$\mathbf{x}_{0_{SW2}} = (\mathbf{x}_{N_X})_X \tag{38}$$

and

$$\mathbf{x}_{0_N} = (\mathbf{x}_{N_{SW}})_{SW2} \tag{39}$$

Thus, an expression is obtained for the matrix-material temperature profile where the matrix passages enter the C_N side:

$$\mathbf{x}_{0_N} = [\mathbf{I} - \mathbf{A}_{SW}^{N_{SW}}\mathbf{A}_X^{N_X}\mathbf{A}_{SW}^{N_{SW}}\mathbf{A}_N^{N_N}]^{-1} \times [\mathbf{A}_{SW}^{N_{SW}}\mathbf{A}_X^{N_X}\mathbf{A}_{SW}^{N_{SW}}(\mathbf{A}_N^{N_N-1} + \mathbf{A}_N^{N_N-2} + \cdots + \mathbf{I})\mathbf{b}_N T_{Ni} + \mathbf{A}_{SW}^{N_{SW}}(\mathbf{A}_X^{N_X-1} + \mathbf{A}_X^{N_X-2} + \cdots + \mathbf{I})\mathbf{b}_X T_{Xi}] \tag{40}$$

A value for $\overline{T}_{No}$, the average fluid outlet temperature on the C_N side, can be calculated by propagating Eqs. (15). Then, an effectiveness output[3] can be calculated from

$$\mathcal{E} = \frac{(\overline{T}_{No} - T_{Ni})}{(T_{Xi} - T_{Ni})} \tag{41}$$

Effectiveness is independent of the absolute values of the fluid inlet temperatures. For computational efficiency, T_{Ni} can be set equal to 0 in Eq. (40).

2.4.4 Equations for the Flat-Profile Condition. As the seal coverage approaches 100 percent, $\mathrm{Fo} \to \infty$ (see Eq. (21)). Therefore, the matrix-material temperature profile at the point where a matrix exits a seal is always flat as the seal coverage approaches 100 percent. Thus, the matrix-material temperature is constant axially at this point as the seal coverage approaches 100 percent. This constant temperature, for the flat-profile condition, is the average matrix-material temperature where the matrix enters the seal. This is due to zero heat conduction through passage-tube boundaries. Thus, for this flat-profile condition, Eq. (35) becomes

$$(\mathbf{x}_{N_{SW}})_{SW} = \mathbf{A}_{fp}\mathbf{x}_{0_{SW}} \tag{42}$$

where

$$\mathbf{A}_{fp} = \frac{1}{N_R}\begin{bmatrix} 1 & 1 & 1 & \cdots & 1 & 1 \\ 1 & 1 & 1 & \cdots & 1 & 1 \\ 1 & 1 & 1 & \cdots & 1 & 1 \\ \vdots & \vdots & \vdots & \vdots & \vdots & \vdots \\ 1 & 1 & 1 & \cdots & 1 & 1 \\ 1 & 1 & 1 & \cdots & 1 & 1 \end{bmatrix} \tag{43}$$

and Eq. (40) becomes

$$\mathbf{x}_{0_N} = [\mathbf{I} - \mathbf{A}_{fp}\mathbf{A}_X^{N_X}\mathbf{A}_{fp}\mathbf{A}_N^{N_N}]^{-1}[\mathbf{A}_{fp}\mathbf{A}_X^{N_X}\mathbf{A}_{fp}(\mathbf{A}_N^{N_N-1} + \mathbf{A}_N^{N_N-2} + \cdots + \mathbf{I})\mathbf{b}_N T_{Ni} + \mathbf{A}_{fp}(\mathbf{A}_X^{N_X-1} + \mathbf{A}_X^{N_X-2} + \cdots + \mathbf{I})\mathbf{b}_X T_{Xi}] \tag{44}$$

3 Results

3.1 Mode of Presentation. The majority of the results presented in this section will be represented in terms of an axial conduction and seal width effect,

$$\left(\frac{\Delta\epsilon}{\epsilon}\right)_{\mathrm{acsw}} \equiv \frac{\hat{\epsilon}_{acsw} - \hat{\epsilon}_{nc}}{\hat{\epsilon}_{nc}} \tag{45}$$

where $\hat{\epsilon}_{acsw}$ is an effectiveness estimate calculated assuming axial conduction and finite seal width and $\hat{\epsilon}_{nc}$ is an effectiveness estimate calculated assuming no axial conduction. This mode

[3] An effectiveness (ϵ), an effectiveness output ($\mathcal{E}$), and an effectiveness estimate ($\hat{\epsilon}$) are defined differently. Effectiveness indicates the heat transfer performance of an actual regenerator; an effectiveness output is calculated for a given number of elements; and an effectiveness estimate is obtained by extrapolating effectiveness outputs to zero element area.

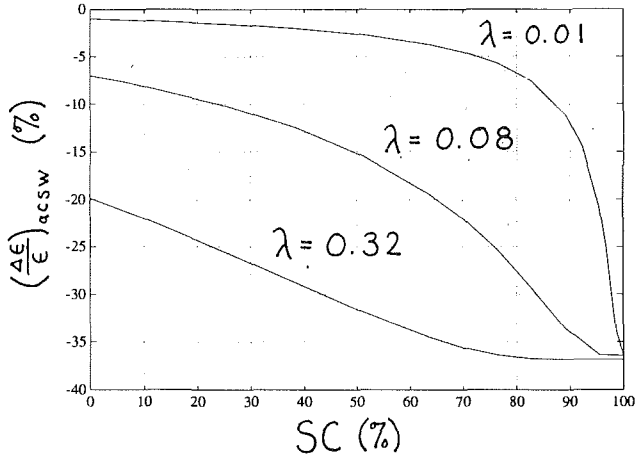

Fig. 4 Reductions in effectiveness with seal coverage for NTU = 20; $C_{rot} = 3$; $C_{rat} = (hA)' = As' = 1$; and $\lambda = 0.01$, 0.08, and 0.32

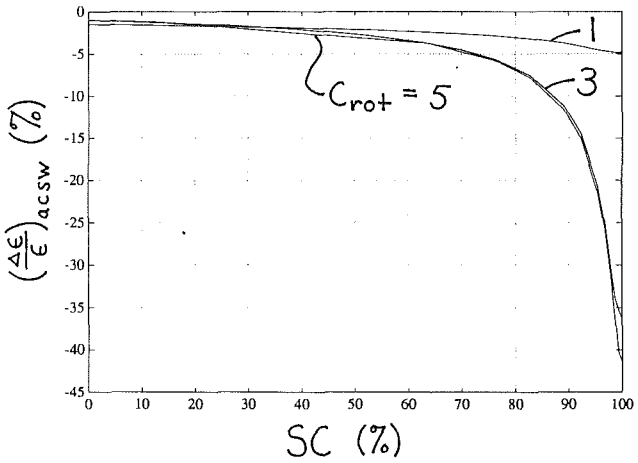

Fig. 5 Reductions in effectiveness with seal coverage for NTU = 20; $C_{rat} = (hA)' = As' = 1$; $\lambda = 0.01$; and $C_{rot} = 1$, 3, and 5

of presentation is similar to that used by Bahnke and Howard [5]; however, reductions in effectiveness are presented as positive effects in Bahnke and Howard's [5] paper, while reductions in effectiveness are presented as negative effects in this paper.

All plots of $(\Delta\epsilon/\epsilon)_{acsw}$ will start at the negative of Bahnke and Howard's [5] axial-conduction effects $[(\Delta\epsilon/\epsilon)_{ac}]$ for Fo = 0 (zero seal coverage). The $(\Delta\epsilon/\epsilon)_{acsw}$ values will then increase in magnitude as the seal coverages are increased and the Fo increase. For very large Fo (for matrices almost completely covered with seals), conditions will be reached for which the matrix-material temperature profiles are completely flat where the passages exit the seals.

Effectiveness-estimate data (similar to Bahnke and Howard's [5], but calculated for various seal coverages) could have been presented in this paper. The numerous[4] data would have been of limited use to the designer, however: only approximate effectiveness values could have been achieved by the designer, by interpolating between system-parameter values. Instead of presenting effectiveness-estimate data, commented listings of Matlab commands are given in the appendix. With these commands, the designer can calculate accurate effectiveness values for her or his application. Matlab commands are given because they are clear and compact and because Matlab has embedded functions that facilitate the required linear-algebra computations.

To give the designer insight for preliminary design, plots of $(\Delta\epsilon/\epsilon)_{acsw}$ versus *SC* will be presented for various system-parameter values. Seal width alone essentially has the same effect on regenerator effectiveness for all system-parameter values. The principal differences between the plots of $(\Delta\epsilon/\epsilon)_{acsw}$ versus *SC* will be due to the following:

1 the (C_{rot}/λ)Fo versus *SC* function (from Eq. (21)) and
2 the dependence of the effects of axial conduction on system-parameter values described by Bahnke and Howard [5].

3.2 λ Effects. Plots of $(\Delta\epsilon/\epsilon)_{acsw}$ versus *SC* for NTU = 20; $C_{rot} = 3$; $C_{rat} = (hA)' = As' = 1$; and $\lambda = 0.01$, 0.08, and 0.32 are shown in Fig. 4. We can see that reductions in effectiveness increase in magnitude with λ. This is because the degree of axial conduction increases with λ. All of the plots start at $(\Delta\epsilon/\epsilon)_{ac}$ for zero seal coverage and drop, near 100 percent seal coverage, to the effectivenesses associated with flat temperature profiles where the matrix exits from under the seals. If the seal coverage is great enough so that the flat-profile condition is reached, the matrix temperature gradients are small for a large part of the time. This leads to small axial-conduction effects for a large part of the time. This is why the flat-profile effectivenesses are nearly identical.

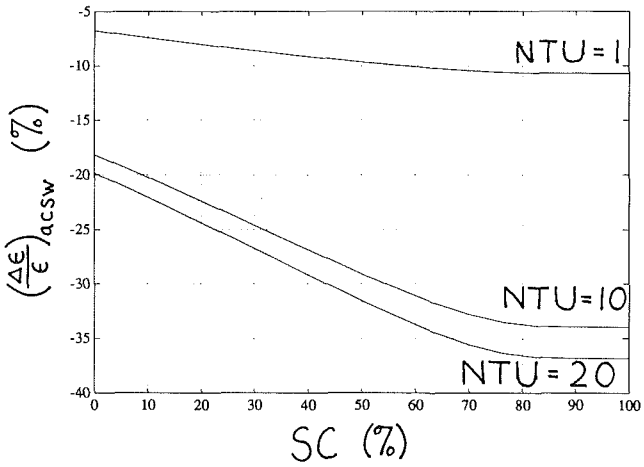

Fig. 6 Reductions in effectiveness with seal coverage for $C_{rot} = 3$; $C_{rat} = (hA)' = As' = 1$; $\lambda = 0.32$; and NTU = 1, 10, and 20

3.3 C_{rot} Effects. Plots of $(\Delta\epsilon/\epsilon)_{axsw}$ versus *SC* for NTU = 20; $C_{rat} = (hA)' = As' = 1$; $\lambda = 0.01$; and $C_{rot} = 1$, 3, and 5 are shown in Fig. 5. We can see that the temperature-profile flattening for high seal coverage is felt most for large C_{rot} (relatively fast matrix rotation). For large C_{rot}, the matrix material's temperature profile does not change appreciably for low seal coverage.[5] This leads to high effectiveness. As the seal coverage approaches 100 percent, however, the flat-profile condition is reached, for which the temperature profile changes drastically. Thus, for high seal coverage, reductions in effectiveness due to axial conduction coupled with finite seal width are greatest for large C_{rot}.

3.4 NTU Effects. The effect of NTU on effectiveness reductions is similar to that of C_{rot}. Plots of $(\Delta\epsilon/\epsilon)_{acsw}$ versus *SC* for $C_{rot} = 3$; $C_{rat} = (hA)' = As' = 1$; $\lambda = 0.32$; and NTU = 1, 10, and 20 are shown in Fig. 6. We see that the effect of NTU

[4]For ten different seal-coverage values, approximately ten times as many data as presented by Bahnke and Howard [5] would have been required.

[5]For zero seal coverage and infinitely fast matrix rotation, the matrix material's temperature profile does not change at all and the regenerator's effectiveness can be calculated from the counterflow-recuperator solution (see Coppage and London [3]).

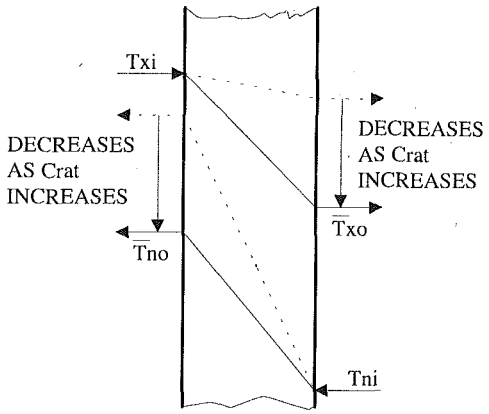

Fig. 7 Effect of varying C_{rat} on regenerator effectiveness

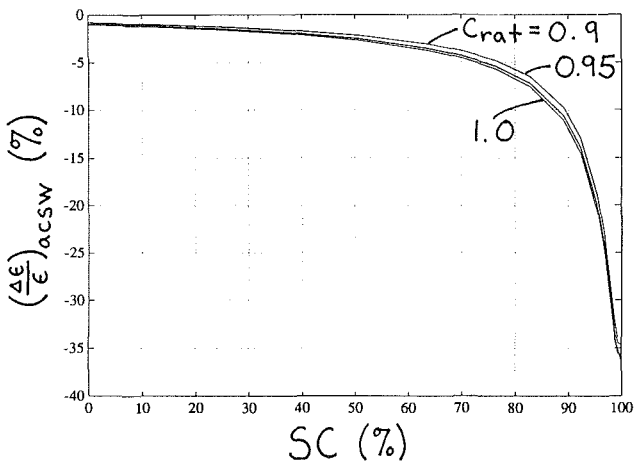

Fig. 8 Reductions in effectiveness with seal coverage for NTU = 20; $C_{rot} = 3$; $(hA)' = As' = 1$; $\lambda = 0.01$; and $C_{rat} = 0.90$, 0.95, and 1.0

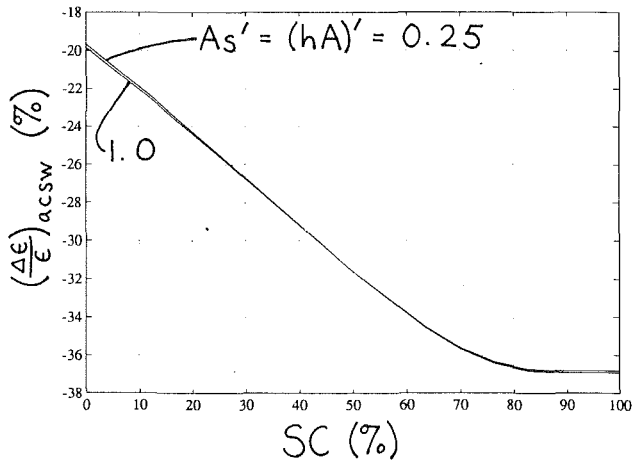

Fig. 9 Reductions in effectiveness with seal coverage for NTU = 20; $C_{rot} = 3$; $C_{rat} = 1.0$; $\lambda = 0.32$; and $(hA)' = As' = 0.25$ and 1.0

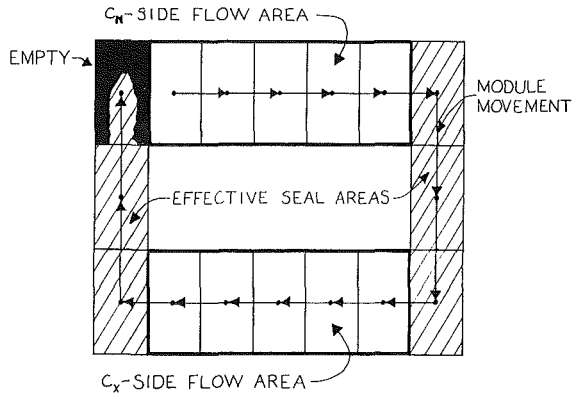

Fig. 10 Schematic of a modular regenerator

on effectiveness reductions is greatest for large NTU. As with C_{rot}, high NTU values produce matrix-material temperature profiles that do not change appreciably throughout a cycle. Therefore, the flat-profile condition produces dramatic effectiveness reductions for high NTU.

3.5 C_{rat} Effects. The effect of varying C_{rat} on effectiveness is shown in Fig. 7. As C_{rat} is decreased (such as by increasing the mass-flow rate on the C_X side of the regenerator), the outlet temperature on the C_X side increases as does the outlet temperature on the C_N side. Thus, the effectiveness increases with decreasing C_{rat}. We would expect that axial conduction would have little influence on this phenomenon. This is the case. Bahnke and Howard [5] report little variation in axial-conduction effect with C_{rat}. Also, we expect little variation in axial conduction and seal width effect with C_{rat} because this effect is dependent upon axial conduction. The plots of $(\Delta\epsilon/\epsilon)_{acsw}$ versus SC for NTU = 20; $C_{rot} = 3$; $(hA)' = As' = 1$; $\lambda = 0.01$; and $C_{rat} = 0.90$, 0.95, and 1.0 shown in Fig. 8 demonstrate that this is the case.

3.6 $(hA)'$ and As' Effects. Bahnke and Howard [5] found little variation in axial-conduction effect when As' differed from $(hA)'$ by ± 30 percent. Also, they found little variation in axial-conduction effect with simultaneous variation of As' and $(hA)'$. Small variation of effectiveness reductions were discovered when axial conduction coupled with finite seal width was considered. Plots of $(\Delta\epsilon/\epsilon)_{acsw}$ versus SC for NTU = 20; $C_{rot} = 3$; $C_{rat} = 1.0$; $\lambda = 0.32$; and $(hA)' = As' = 0.25$ and 1.0 are shown in Fig. 9.

3.7 Sample Calculations. Sample calculations will be presented to show that seal width should be considered in regenerator design.

First, consider the schematic of a modular regenerator shown in Fig. 10. The effective seal coverage (the fraction of the modules not exposed to flows) is

$$SC = 5/15 = 33.3 \text{ percent} \tag{46}$$

The solid-area ratio, $As' = 1$. Let us assume that $As_N = 2$ m^2; $k_R = 0.2$ W/m-K; $C_N = (\dot{m}c_p)_N = (0.25$ kg/s)(1050 J/kg-K; and $L = 0.038$ m. Then

$$\lambda = \frac{(0.2)(2)}{(0.038)(0.25)(1050)}\left(1 + \frac{1}{1}\right) \tag{47}$$

$$\lambda = 0.08 \tag{48}$$

From Fig. 4 we see that $(\Delta\epsilon/\epsilon)_{acsw} \approx -12$ percent and $(\Delta\epsilon/\epsilon)_{ac} \approx -7.5$ percent. Thus, we see that consideration of finite seal width leads to an effectiveness reduction that is significantly greater in magnitude than the one calculated under the assumption of zero seal width.

Kays and London [6] provide a table containing design data from sample calculations. These data were calculated assuming zero seal width. Table 1 is more complete. It includes data calculated assuming a modest seal coverage of 20 percent. All data in Table 1 were calculated for $\epsilon = 0.985$; $C_{rot} \to \infty$; $(hA)' = 1$; and $As' = 1$.

From the results presented in Table 1, it is evident that the detrimental effects of seal width on regenerator effectiveness should be considered in design. For $C_{rat} = 1$, the required NTU to achieve the given effectiveness increases dramatically when

Table 1 Design data from example calculations

C_{rat}	NTU For $\lambda = 0$	NTU For $\lambda = 0.01$; $SC = 0$	NTU For $\lambda = 0.01$; $SC = 0.2$	% increase of NTU, not considering seal width	% increase of NTU, considering seal width
1.00	66.0	190	1400	188	2020
0.95	29.5	40	48.8	36	65

seal width is considered.[6] For $C_{rat} = 0.95$ the required NTU increase is not as dramatic, but is still significant.

4 Conclusions

The following conclusions can be drawn from the results presented in the last section.

1 Seal width should be considered when one considers axial-conduction effects: Reductions in effectiveness due to axial conduction coupled with finite seal width can be twice as great as those due to axial conduction under the assumption of zero seal width; and the required regenerator size to achieve a given effectiveness can increase dramatically when finite seal width is considered in design procedures.

2 The effects due to axial conduction coupled with finite seal width vary greatly with λ and NTU, being greatest for large λ and/or large NTU.

3 The effects differ to a lesser degree with C_{rot}.

4 The effects differ to a small degree with C_{rat}.

5 The effects differ negligibly for variations in As' and $(hA)'$ within limits usually experienced in gas turbine applications.

References

1 Wilson, D. G., *Design of High-Efficiency Turbomachinery and Gas Turbines*, The M.I.T. Press, Cambridge, MA, 1984.

2 Harper, D. B., "Seal Leakage in the Rotary Regenerator and Its Effect on Rotary-Regenerator Design for Gas Turbines," *Transactions of the ASME*, Vol. 79, 1957.

3 Coppage, J. E., and London, A. L., "The Periodic-Flow Regenerator—A Summary of Design Theory," *Transactions of the ASME*, Vol. 75, 1953.

4 Lambertson, T. J., "Performance Factors of a Periodic-Flow Heat Exchanger," *Transactions of the ASME*, Vol. 80, 1958.

5 Bahnke, G. D., and Howard, C. P., "The Effect of Longitudinal Heat Conduction on Periodic-Flow Heat Exchanger Performance," ASME JOURNAL OF ENGINEERING FOR POWER, Vol. 86, 1964.

6 Kays, W. M., and London, A. L., *Compact Heat Exchangers*, 3rd ed., McGraw-Hill, New York, 1984.

APPENDIX

Matlab[7] Listings for Calculating Regenerator Effectiveness

A.1 File "zea.m"

```
clear;format long;
%system parameters (lines beginning with "%" are comments)
NTU=9;Crot=3;Crat=1;hAp=1;Asp=1;lambda=0.1;SC=0.2;
Fo=0.5*(SC/(1.0-SC))*lambda/Crot;
%n1=the highest number of elements used in calculations
n1=40;save vals4 NTU Crat Crot hAp Asp lambda Fo n1;
%n2=the integer part of 80% of n1
n2=modu(0.8*n1);
%appropriately space 1/(n1*n1),1/(n2*n2),and 1/(n3*n3)
n3=modu((2.0/(n2*n2)-1.0/(n1*n1))^(-0.5));N=n3;
%calculate effectiveness output, eff3
sealw;eff3=epsilon;
clear epsilon;save vals3 eff3 n3;clear;load vals4;
n2=modu(0.8*n1);N=n2;
%calculate effectiveness output, eff2
sealw;eff2=epsilon;
clear epsilon;save vals2 eff2 n2;clear;load vals4;
N=n1;
%calculate effectiveness output, eff1
sealw;eff1=epsilon;
clear epsilon;save vals1 eff1 n1;clear;load vals1;
load vals2;load vals3;
%extrapolate effectiveness outputs to zero element area
%to obtain an effectiveness estimate, ehat
ehat=eff1-((eff1-eff2)/(1.0/(n1*n1)-1.0/(n2*n2)))/(n1*n1);
%estimate the number of significant figures to which
%the effectiveness estimate is accurate
nsfhat=(eff1-eff2)/(1.0/(n1*n1)-1.0/(n2*n2));
nsfhat=nsfhat-(eff2-eff3)/(1.0/(n2*n2)-1.0/(n3*n3));
nsfhat=nsfhat/(1.0/(n1*n1)-1.0/(n3*n3));
nsfhat=log(ehat/(2.0*abs(nsfhat/(n1^4))))/log(10.0);
```

A.2 File "sealw.m"

```
%parameters from Bahnke and Howard
C1=Crat*NTU*(1.0+1.0/hAp)/(2.0*N);C2=Crat*Crot;
C3=Crat*lambda*N/(2.0*(1.0+Asp));C4=C1+(1.0+C1)*(C2+2.0*C3);
C5=C1+(1.0+C1)*(C2+C3);D1=2.0*C1/C4;
D2=(C1+(1.0+C1)*(2.0*C3-C2))/C4;D3=(1.0+C1)*C3/C4;
D4=(1.0-C1)/(1.0+C1);D5=C1/(1.0+C1);D6=2.0*C1/C5;
D7=(C1+(1.0+C1)*(C3-C2))/C5;D8=(1.0+C1)*C3/C5;
E1=NTU*(1.0+hAp)/(2.0*N);E2=Crot;
E3=lambda*Asp*N/((1.0+Asp)*2.0);E4=E1+(1.0+E1)*(E2+2.0*E3);
E5=E1+(1.0+E1)*(E2+E3);F1=2.0*E1/E4;
F2=(E1+(1.0+E1)*(2.0*E3-E2))/E4;F3=(1.0+E1)*E3/E4;
F4=(1.0-E1)/(1.0+E1);F5=E1/(1.0+E1);F6=2.0*E1/E5;
F7=(E1+(1.0+E1)*(E3-E2))/E5;F8=(1.0+E1)*E3/E5;
%parameters for seal-width equations
g= Fo*N;H1=(1.0-2.0*g)/(1.0+2.0*g);H2=g/(1.0+2.0*g);
H3=(1.0-g)/(1.0+g);H4=g/(1.0+g);
clear hAp Asp lambda NTU Crat Crot Fo;
%matrices for passages under seals
A3(1,1)= H3;A3(1,2)= H4;A3(N,N-1)=H4;A3(N,N)= H3;B3(1,1)=0.0;
B3(1,2)= H4;B3(N,N-1)=H4;B3(N,N)=0.0;
%matrices for passages exposed to flows
A1(1,1)=-1.0*D7;A2(1,1)=-1.0*F7;A1(N,N)=-1.0*D7;
A2(N,N)=-1.0*F7;A1(1,2)=D8;A2(N,N-1)=F8;
A1(N,N-1)=D5*D6+D8;A2(1,2)=F5*F6+F8;
%matrices
for i=2:N-1,
A3(i,i)=H1;A3(i,i+1)=H2;A3(i,i-1)=H2;B3(i,i+1)=H2;B3(i,i-1)=H2;
A1(i,i)=-1.0*D2;A2(i,i)=-1.0*F2;A1(i,i+1)=D3;A2(i,i-1)=F3;
A1(i,i-1)=D1*D5+D3;A2(i,i+1)=F1*F5+F3;
end
A1(N,N-2)=D4*D5*D6;A2(1,3)= F4*F5*F6;
for i=3:N-1,
for j=1:i-2,
A1(i,j)=D1*(D4^(i-j-1))*D5;A2(j+1,i+1)=F1*(F4^(i-j-1))*F5;
if i==N-1,
A1(N,j)=(D4^(N-j-1))*D5*D6;A2(1,j+3)=F6*(F4^(j+1))*F5;
end
end
end
B1=A1;B2=A2;
for i=1:N,
B1(i,i)=0.0;B2(i,i)= 0.0;
end
g1(1,1)=D6;g2(1,1)=F6*(F4^(N-1));g1(N,1)=D6*(D4^(N-1));
g2(N,1)=F6;
for i=2:N-1,
g1(i,1)= D1*(D4^(i-1));g2(i,1)= F1*(F4^(N-i));
end
for i=1:N,
cv2(1,i)= (F4^(i-1))*F5;
end
```

[6] Attendant high core and header pressure drops probably would make a regenerator with NTU = 1400 impractical.

[7] © Copyright The MathWorks, Inc. 1984–1992.

```
dv2= F4^N;
clear C1 C2 C3 C4 C5 D1 D2 D3 D4 D5 D6 D7 D8 E1 E2 E3 E4 E5;
clear F1 F2 F3 F4 F5 F6 F7 F8 g H1 H2 H3 H4;I=eye(N);
%inv(A) calculates the inverse of A
temp=inv(I-B3);clear B3;At=temp*A3;clear A3;temp=inv(I-B1);
clear B1;Ax=temp*A1;clear A1;bx=temp*g1;clear g1;
temp=inv(I-B2);clear B2;An=temp*A2;clear A2;bn=temp*g2;
clear g2 temp;cn=cv2*(I+An);dn=cv2*bn+dv2;
clear cv2 dv2;Sx=I;
for j= 1:N-1,
Sx=Ax*Sx+I;
end
Afp=(1.0/N)*ones(N,N);AtN= At^N;AxN=Ax^N;AnN=An^N;
%flat matrix-material temperature profile
%where matrix enters C_n side
%xno=inv(I-Afp*AxN*Afp*AnN)*(Afp*Sx*bx);
%profile where matrix enters C_n side
xno=inv(I-AtN*AxN*AtN*AnN)*(AtN*Sx*bx);
clear I AxN AnN Sx Ax bx;u=0.0*ones(N,1);
%[y,x]=dlsim(A,b,c,d,u,x0) propagates the discrete linear
%system given by [A,b,c,d] with inputs u and initial state x0
%(y contains the outputs, and x contains the states).
[y,x]=dlsim(An,bn,cn,dn,u,xno);
epsilon=ones(1,N)*y/N;
```

A.3 File "modu.m"

```
function [out]= modu(num)
j=0.0;
while j<num,
j=j+1.0;
end
if j-num>0.5,
out=j-1;
else,
out=j;
end
```

Contribution of Thermal Radiation to the Temperature Profile of Ceramic Composite Materials

A. Tremante
Departamento de Conversión y Transporte de Energía, Universidad Simón Bolívar, Caracas, Venezuela

F. Malpica
Departamento de Termodinámica y Fenómenos de Transferencia, Universidad Simón Bolívar, Caracas, Venezuela

The steady energy transfer equation for simultaneous conduction and radiation in an absorbing, emitting, and nonscattering gray planar medium is studied theoretically. For extremely high-temperature applications, where radiative transfer plays an important role, ceramic-matrix composites, considered as semitransparent materials, are being explored for potential use in turbine and compressor components, spacecraft structures, engine control systems, and nuclear reactors. Exact solution of the above-mentioned radiative problems is seldom possible and time-consuming numerical approximations are then used. A technique combining an accurate physical formulation, the two-flux model, coupled to a fast numerical procedure for the calculation of the temperature and heat fluxes is described.

Introduction

This is a companion work to the plane layer analysis of Campo and Tremante (1987), and is a continuation of the analysis for semitransparent media (Malpica et al., 1986) extended to ceramic materials, which are also partially transparent (Thomas, 1992) to thermal radiation over a temperature of 650 K.

During the last decade, important efforts have resulted in significant advances in structural materials and analysis. To achieve such advances, developments in high-temperature materials, like ceramic composites, are considered key for potential use in turbine rotor blades, nozzle vanes (Parks et al., 1991), rocket engines, and space structures (Upadhya, 1992). Therefore, fiber-reinforced ceramic matrix composites are receiving increased attention (Tan et al., 1991; Mah et al., 1987) owing to their high-temperature capabilities (Abdullah and Das-Gupta, 1990) and the toughening properties provided by the fibrous reinforcement (Mah et al., 1985).

The purpose of this work is to describe a physical formulation coupled to a numerical procedure for the calculation of the temperature in ceramic composite materials. The system consists of an absorbing and emitting layer contained between two parallel plates. The plates are separated by a distance L and are maintained at uniform temperatures, T_1 and T_2, respectively (Fig. 1).

The exact solution of the nonlinear integro-differential equation involved in this class of problem is seldom possible and typically the analyst resorts to numerical approximations (Viskanta and Grosh, 1962; Crosbie and Viskanta, 1971).

The main goal of this paper is to provide a simple but reliable predictive method to the engineer, faced with the task of analyzing thermal effects and predicting optical properties in semitransparent materials, in which radiation plays an important role, i.e., situations where high-temperature conditions are present. The crucial radiative mechanism is characterized by the undoubtedly simple gray model. Indeed, for systems involving a strongly nongray behavior, it appears that nonmean absorption coefficient can be devised to give a good approximate analysis of the actual radiative transport. The analytical investigations of radiative transport in systems with actual nongray behavior require elaborate time-consuming compu-

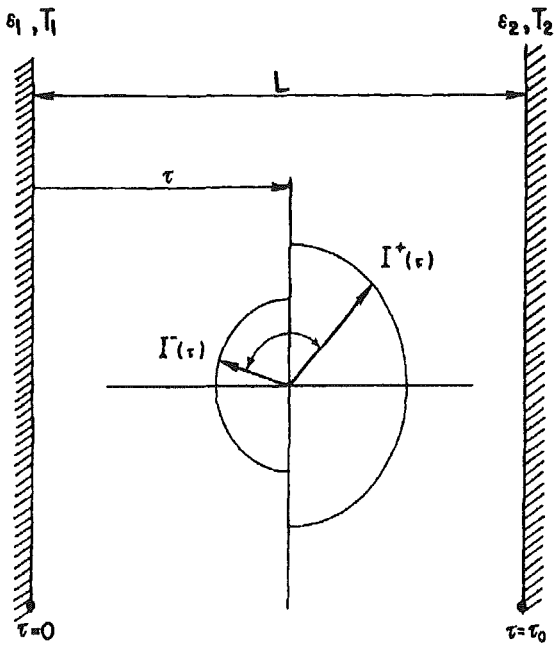

Fig. 1 Physical geometry

Contributed by the International Gas Turbine Institute and presented at the 38th International Gas Turbine and Aeroengine Congress and Exposition, Cincinnati, Ohio, May 24-27, 1993. Manuscript received at ASME Headquarters March 17, 1993. Paper No. 93-GT-325. Associate Technical Editor: H. Lukas.

tations. The results obtained are limited to the specific materials and the specific conditions discussed. For this reason, the gray model combined with a reasonable estimate of the mean absorption coefficient still seems more convenient in making radiative transport calculations (Tien, 1968).

In light of the above, a two-flux model has been employed for the description of radiative transfer (Sidall, 1974). Two different but closely related versions of the model are attempted, namely the Milne-Eddington and Schuster-Schwarzschild versions.

Additionally, the encouraging results obtained for the gray model compared with those obtained by using more complex approaches were a source of motivation for the calculation of equivalent absorption coefficients for real semi-transparent materials based on experimental measurements (Anderson, 1972; Viskanta and Anderson, 1975).

Problem Formulation

The physical system is a plane layer of an absorbing and emitting semitransparent solid of thickness L, placed between two isothermal parallel and infinite plates, which are considered gray and diffuse. It is also assumed that the medium is gray, characterized by a uniform absorption coefficient, with temperature-independent properties, and does not scatter radiation.

At steady state, in the absence of internal heat sources and convection, conservation of energy implies that

$$q_t = -k \cdot \nabla T + q_r. \tag{1}$$

The presence of the conduction mechanism insures continuity of the temperature, and the boundary conditions are then

$$T = T_1 \text{ at } y = 0 \tag{2}$$

$$T = T_2 \text{ at } y = L. \tag{3}$$

As a result of the internal emission of radiation, its intensity is coupled to the temperature distribution of the solid. The interaction between the radiation intensity and the medium gives rise to a nonlinear integro-differential equation of energy as reported by Siegel and Howell (1981).

Alternatively, Eqs. (1), (2), and (3) are solved approximately involving the two-flux model (Sidall, 1974). This model assumes that there are only two uniform fluxes in the medium, one in the forward hemisphere and one in the backward hemisphere, as shown in Fig. 1. This simple assumption reduces the equation of radiation energy to a coupled pair of first-order ordinary differential equations as follows:

$$\frac{dq_r}{dy} = \kappa_a(4\sigma T^4 - G) \tag{4}$$

$$\frac{dG}{dy} = -A\kappa_a q_r \tag{5}$$

where A is a constant, which is 3 for the Milne-Eddington model and 4 for the Schuster-Schwarzschild model.

Combining Eqs. (1), (4), and (5) (Tremante, 1985) and rearranging terms gives the system of equations

$$k\frac{d^2T}{dy^2} = \kappa_a(4\sigma T^4 - G) \tag{6}$$

$$\frac{d^2G}{dy^2} = -A\kappa_a^2(4\sigma T^4 - G). \tag{7}$$

The associated boundary conditions are Eqs. (2) and (3) together with

$$q_1^+ = \epsilon_1\sigma T_1^4 + (1-\epsilon_1)q_1^- \text{ at } y = 0 \tag{8a}$$

$$q_1^- = \epsilon_2\sigma T_2^4 + (1-\epsilon_2)q_1^+ \text{ at } y = L, \tag{8b}$$

where

$$q^+ + q^- = \frac{1}{2}G,\ q^+ - q^- = q_r. \tag{9}$$

In order to simplify the presentation of results, the following set of dimensionless variables:

$$\theta = \frac{T}{T_1},\ N = \frac{k\kappa_a}{4\sigma T_1^3},\ \eta = \frac{\tau}{\tau_0},\ G^* = \frac{G}{\sigma T_1^4} \tag{10}$$

will be adopted to reformulate Eqs. (6) and (7) as follows:

$$\frac{d^2\theta}{d\eta^2} = \frac{\tau_0^2}{N}\left(\theta^4 - \frac{G^*}{4}\right), \tag{11}$$

$$\frac{d^2G}{d\eta^2} = -A\tau_0^2(4\theta^4 - G^*), \tag{12}$$

subject to the following boundary conditions for temperature:

$$\theta = 1 \text{ at } \eta = 0 \tag{13a}$$

$$\theta = \frac{T_2}{T_1} = \theta_2 \text{ at } \eta = 1, \tag{13b}$$

and for intensity:

$$G^* = 4 + \frac{2(2/\epsilon_1 - 1)}{A\tau_0}\frac{dG^*}{d\eta} \text{ at } \eta = 0, \tag{14a}$$

$$G^* = 4\theta_2^4 - \frac{2(2/\epsilon_2 - 1)}{A\tau_0}\frac{dG^*}{d\eta} \text{ at } \eta = 1. \tag{14b}$$

The set of two ordinary differential Eqs. (11) and (12) with the boundary conditions (13*a*), (13*b*), (14*a*), and (14*b*) is solved as two-point boundary value problem, using a variable order, variable step size finite difference method with deferred corrections. In all of the calculations a relative tolerance not greater than 10^{-6} was used at all mesh points as a convergence criterion. Typical values of CPU time were not greater than 3 seconds for a compatible 386 computer.

Finally, the total heat flux transferred by combined conduction and radiation may be computed from the dimensionless relation

$$\frac{q_t}{\sigma T_1^4} = \frac{q_r}{\sigma T_1^4} + \frac{1}{\sigma T_1^4}\left(-k\frac{dT}{dy}\right). \tag{15}$$

Nomenclature

A = constant
G = total intensity of incident radiation, W/cm^2
G^* = dimensionless total intensity of incident radiation
I = intensity of radiation, W/cm^{2}str
k = thermal conductivity, W/cm K
L = layer thickness, cm
N = dimensionless conduction-radiation parameter $= k\kappa_a/4\sigma T_1^3$
q_r = radiative heat flux, W/cm^2
q_t = total heat flux, W/cm^2
Q_t = dimensionless total heat flux
T = temperature, K
t = temperature, °C
y = position coordinate, cm
ϵ = emissivity of the surface
η = dimensionless position coordinate $= y/L$
θ = dimensionless temperature $= T/T_1$
κ_a = absorption coefficient, cm^{-1}
σ = Stefan-Boltzmann constant $= 5.668 \times 10^{-12}$ W/cm^{2}K^4
τ = optical depth $= \kappa_a y$
τ_0 = optical thickness of the medium $= \kappa_a L$

Subscripts

1 = refers to high-temperature plate
2 = refers to low-temperature plate

Table 1 Dimensionless total heat flux

N	0.01			0.1			1.0			10.0		
	(a)	(b)	(c)	(a)	(b)	(c)	(a)	(b)	(c)	(a)	(b)	(c)
ε												
				$\tau_0 =$	0.1		$\theta_2 = 0.5$					
1.0	1.074	1.098	1.077	2.880	2.898	2.877	20.88	20.90	20.88	200.88	200.90	200.88
0.9	0.928	0.949	0.934	2.723	2.749	2.734	20.73	20.75	20.73	200.73	200.75	200.73
0.5	0.524	0.533	0.530	2.332	2.333	2.330	20.33	20.33	20.33	200.34	200.33	200.33
0.1	0.267	0.278	0.278	2.078	2.079	2.079	20.08	20.08	20.08	200.08	200.08	200.08
				$\tau_0 =$	1.0		$\theta_2 = 0.5$					
1.0	0.596	0.594	0.519	0.798	0.808	0.723	2.600	2.616	2.527	20.60	20.62	20.53
0.9	0.523	0.541	0.477	0.743	0.759	0.686	2.555	2.568	2.492	20.55	20.57	20.49
0.5	0.338	0.342	0.317		0.583	0.546	2.397	2.400	2.360	20.39	20.40	20.36
0.1	0.156	0.166	0.161	0.393	0.430	0.415	2.245	2.259	2.239	20.25	20.26	20.24
				$\tau_0 =$	10.0		$\theta_2 = 0.5$					
1.0	0.114	0.114	0.088	0.131	0.133	0.107	0.315	0.316	0.288	2.114	2.116	2.088
0.9	0.111	0.112	0.087	0.130	0.131	0.106	0.314	0.315	0.287	2.113	2.115	2.085
0.5	0.104	0.100	0.080	0.122	0.126	0.103	0.307	0.311	0.285	2.110	2.111	2.085
0.1	0.090	0.077	0.064	0.115	0.166	0.096	0.297	0.307	0.282	2.107	2.108	2.083
				$\tau_0 =$	1.0		$\theta_2 = 0.1$					
1.0	0.658	0.664	0.580	0.991	1.014	0.921	4.218	4.241	4.149	36.60	36.64	36.55
0.9	0.581	0.608	0.538	0.968	0.961	0.882	4.171	4.189	4.110	36.57	36.59	36.51
0.5	0.390	0.400	0.370	0.742	0.770	0.730	3.994	4.006	3.964	36.67	36.40	36.36
0.1	0.222	0.211	0.203	0.591	0.601	0.584	3.752	3.850	3.831	36.22	36.25	36.23

(a) Viskanta-Grosh (b) Milne-Eddington (c) Schuster-Schwarzschild

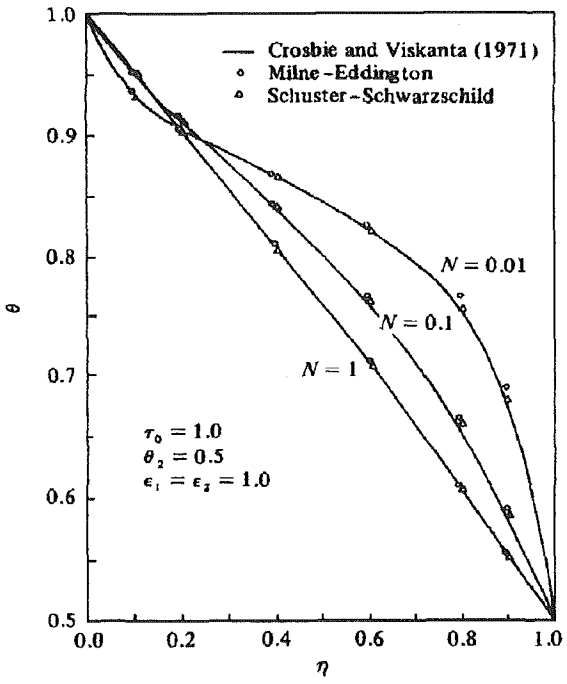

Fig. 2 Dimensionless temperature profiles

This expression rephrased in accordance with the symbols defined in Eq. (10) becomes

$$Q_t = -\frac{1}{A\tau_0}\frac{dG^*}{d\eta} - 4\frac{N}{\tau_0}\frac{d\theta}{d\eta}. \tag{16}$$

Results and Conclusions

In order to evaluate the present method of solution, dimensionless total heat fluxes were calculated for the conditions indicated in Table 1, covering the full range of interest for the coupled conduction-radiation heat transfer through semitransparent solids with diffuse walls, where the emissivity is the same for both surfaces (Tremante, 1985). The results compared reasonably well with those obtained by Viskanta and Grosh (1962) who used a considerable time-consuming numerical procedure.

In addition to heat fluxes, temperature profiles are also calculated for the cases shown in Fig. 2 (Campo and Tremante, 1987). Here again, an excellent comparison with the results from Crosbie and Viskanta (1971) is observed.

At this point, it should be said that the main advantage of the present method is a drastic reduction in time and also accurate enough results for engineering purposes.

As was mentioned before, semitransparent solids are usually not gray but have definite absorption bands for which equivalent gray absorption coefficients have not yet been defined. In the present study, the predicted equivalent gray absorption

Table 2 Predicted equivalent gray absorption coefficient [κ_a] for fused quartz

L [cm]	t_1 °C	t_2 °C	q_t [a]	κ_a [b]
1.27	830	672	6.07	0.137
0.635	804	676	8.02	0.178
0.318	809	741	6.73	0.124
1.27	633	526	2.64	1.789
0.635	618	537	3.14	48.8
0.318	587	554	2.60	19.1
1.27	367	321	0.80	53.1
0.635	344	313	1.03	61.2
0.318	345	331	0.90	57.8

[a] Anderson (1972).
[b] Equivalent predictive gray absorption coefficient using the Schuster-Schwarzschild method.

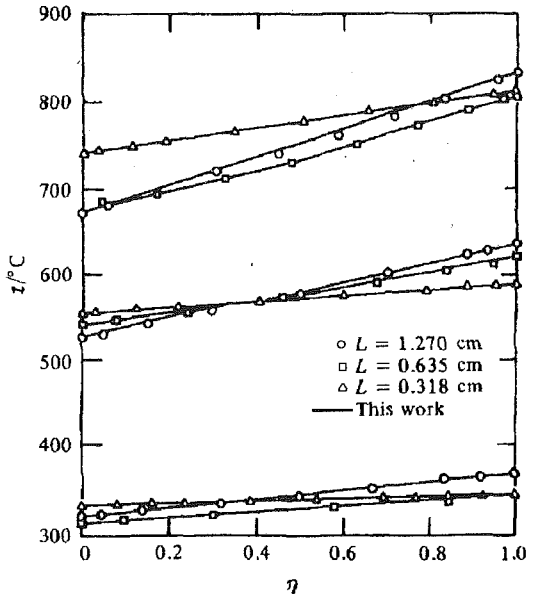

Fig. 3 Comparsion of experimental data by Anderson (1972) and analytically predicted temperature profiles using the Schuster-Schwarzschild method

coefficient is calculated for fused quartz, based on experimental results (Anderson, 1972). This is shown in Table 2.

Additionally, temperature profiles for these cases using the Schuster-Schwarzschild method are in excellent agreement with the experimental results, reported by Anderson (1972) as evidence in Fig. 3, which do not present an error bigger than 1 percent. These results are in better agreement than those reported by Malpica et al. (1986), which presented errors between 2 and 10 percent.

According to the results computed for fused quartz, we are inclined to recommend this predictive procedure for other semitransparent materials, in this case, for ceramic-matrix composites, as long as experimental results are available for ceramic materials.

Thomas (1992) reported different ceramic materials that are good candidates for diesel engine. Two of them, called "BC" and "D" are shown in Table 3, where the scattering coefficient is too small compared with the absorption coefficient. Here again, the gray approximation was used.

An equivalent constant temperature of 880 K for the high-temperature surface was used, taking into account that for diffuse boundaries at isothermal conditions, the maximum temperature drop through the material layer is formed (Aronov, 1984). The equivalent gray absorption coefficients computed with the Schuster-Schwarzschild method do not present an error bigger than 3 percent compared with those reported by Thomas (1992).

Table 3 Gray radiative properties for ceramic materials

Ceramic	κ_a (Thomas, 1992)	τ_0	$1/N$	κ_a (This work)
BC	8854	22.2	178	8901
D	16900	43.0	345	17307

References

Abdullah, M. J., and Das-Gupta, D. K., 1990, "Electrical-Properties of Ceramic Polymer Composites," *IEEE Transactions on Electrical Insulation*, Vol. 25, No. 3, pp. 605-610.

Anderson, E. E., 1972, "Combined Conduction and Radiation in Semitransparent Solids: An Experimental and Analytical Study," Ph.D. Thesis, Purdue University, W. Lafayette, IN.

Aronov, B. I., et al., 1984, "Experimental and Numerical Study of Combined Radiation-Conduction Heat Transfer in a Plane Layer of a Semitransparent Material," *High Temperature—USSR*, Vol. 22, No. 3, pp. 421-426.

Campo, A., and Tremante, A., 1987, "Two-Flux Model Applied to Combined Conduction-Radiation in a Gray Planar Medium," *Wärme und Stoffübertragung*, Vol. 21, No. 4, pp. 221-225.

Crosbie, A. L., and Viskanta, R., 1971, "Interaction of Heat Transfer by Conduction and Radiation in a Nongray Planar Medium," *Wärme- und Stoffübertragung*, Vol. 4, pp. 205-212.

Mah, T. I., et al., 1985, "High-Temperature Mechanical-Behavior of Fiber-Reinforced Glass-Ceramic-Matrix Composites," *Journal of the American Ceramic Society*, Vol. 68, No. 9, pp. 248-251.

Mah, T. I., et al., 1987, "Recent Developments in Fiber-Reinforced High-Temperature Ceramic Composites," *American Ceramic Society Bulletin*, Vol. 66, No. 2, p. 304.

Malpica, F., et al., 1986, "Contribution of Thermal Radiation to the Temperature Profile of Semitransparent Materials," *High Temperature-High Pressures*, Vol. 18, pp. 35-41.

Parks, W. P., et al., 1991, "Potential Applications of Structural Ceramic Composites in Gas Turbines," ASME JOURNAL OF ENGINEERING FOR GAS TURBINES AND POWER, Vol. 113, No. 4, pp. 628-634.

Sidall, R. G., 1974, "Flux Methods for the Analysis of Radiant Heat Transfer," *J. Institution Fuel*, Vol. 47, pp. 101-109.

Siegel, R., and Howell, J. R., 1981, *Thermal Radiation Heat Transfer*, McGraw-Hill, New York.

Tan, T. M., et al., 1991, "Engineering Design of Tough Ceramic Matrix Composites for Turbine Components," ASME JOURNAL OF ENGINEERING FOR GAS TURBINES AND POWER, Vol. 113, pp. 312-317.

Thomas, J. R., 1992, "Coupled Radiation-Conduction Heat Transfer in Ceramic Liners for Diesel Engines," *Numerical Heat Transfer—Part A—Applications*, Vol. 21, No. 1, pp. 109-120.

Tien, C. L., 1968, "Thermal Radiation Properties of Gases," *Adv. Heat Transfer*, Vol. 5, pp. 254-321.

Tremante, A., 1985, "Método de los Flujos Aplicado a Mecanismos Combinados de Conducción y Radiación," M. Sc. Thesis, Universidad Simón Bolívar, Caracas, Venezuela.

Upadhya, K., 1992, "Ceramics and Composites for Rocket Engines and Space Structures," *Journal of the Minerals, Metals & Materials Society*, Vol. 44, No. 5, pp. 15-18.

Viskanta, R., and Grosh, R. J., 1962, "Effect of Surface Emissivity on Heat Transfer by Simultaneous Conduction and Radiation," *International Journal of Heat and Mass Transfer*, Vol. 5, pp. 729-734.

Viskanta, R., and Anderson, E. E., 1975, "Heat Transfer in Semitransparent Solids," *Adv. Heat Transfer*, Vol. 11, pp. 318-441.

Full-Coverage Discrete Hole Film Cooling: Investigation of the Effect of Variable Density Ratio

F. Bazdidi-Tehrani
Department of Mechanical Engineering,
Iran University of Science and Technology,
Tehran, Iran

G. E. Andrews
Department of Fuel and Energy,
University of Leeds,
Leeds, United Kingdom

Experimental results of the overall and adiabatic cooling effectiveness for full-coverage discrete hole film cooling are presented for a range of practical geometries. The results are reported for various hot gas mainstream-to-coolant temperature (density) ratios, in the realistic range of 1.0–3.2. The variation of this ratio was achieved by increasing the crossflow mainstream temperature, over the range 300–930 K. For combustor wall film cooling applications, the overall cooling effectiveness increased significantly with the number of holes per unit wall surface area, over the range of 4306–26910 m^{-2} and with the hole size, in the range of 1.0–2.2 mm, due to the improvement in film cooling. The effect of varying the mainstream-to-coolant temperature ratio, in the present range of 1.0–3.2, on the film cooling performance was shown to be small and no consistent trends were established for various configurations, for the coolant mass flow rates per unit wall surface area, less than 0.4 kg/sm^2. At a higher value of 0.89 kg/sm^2, an increase in the temperature ratio improved the film cooling performance slightly.

Introduction

The steady increase in the combustor exit gas temperature of aero (civil) gas turbine engines to 1800 K and above (Hennecke, 1984) clearly indicates that intensive cooling is required, since the current maximum allowable alloy temperature, for the combustor wall and turbine blades, is some 200°C below the combustor exit gas temperature. A considerable increase in the current cooling airflows is not feasible, since more air is needed for lean burn, low emission combustors. Hence comes the requirement to develop efficient cooling systems, capable of making a better use of the available, or reduced, air.

Full-coverage discrete hole film cooling, often referred to as effusion cooling, is a relatively simple technique for efficient cooling of the combustor wall and turbine blades. The coolant air on its passage through multiple rows of discrete holes cools the wall convectively and then emerges as a film aiming to protect the surface in the region of injection.

Andrews et al. (1990) investigated the influence of the important design parameters, the number of 90 deg injection holes per unit wall surface area, n, and the hole size, D, on the overall cooling performance, for a single crossflow mainstream-to-coolant temperature (density) ratio of 2.5. It is the aim of the present work to extend this study over the range of temperature ratio 1.0–3.2, which is typical of those occurring in gas turbine combustors and turbine blades. Wadia and Nealy (1988) used an array of inclined injection holes with fixed n and D, located in the simulated turbine aerofoil leading edge (showerhead) region. They reported that the effect of the mainstream-to-coolant temperature ratio, in the range of 1.7–2.8, on the average leading edge film cooling effectiveness was negligible.

There have been far more investigations, regarding the effect of the coolant-to-mainstream density ratio, using a single row of inclined injection holes and for turbine blade situation. Forth et al. (1985) showed that, close to the holes, an increase in the density ratio, in the range of 0.81–2.0, obtained by varying the temperature ratio, resulted in an increase in the blowing rate at which maximum cooling effectiveness occurred. Sinha et al. (1991) varied the density ratio, over the range of 1.2–2.0, by cooling down the injected airflow to as low as 150 K. They found that, for a constant momentum flux ratio, Z, jets with a higher density ratio would have a higher blowing rate, which resulted in a greater centerline film cooling effectiveness downstream of injection. Ammari et al. (1989, 1990), unlike the cases above where the temperature changes were employed for the variation of the coolant-to-mainstream density ratio, used foreign gases in the injection flow to simulate density ratios in the range of 1.0–1.52. They reported that for normal injection the heat transfer coefficient, at a fixed blowing rate, was insensitive to the variation of the density ratio, whereas for inclined injection a strong dependence was observed. The results from other foreign gas injection experiments (Goldstein et al., 1974; Pedersen et al., 1977), also employing a single row of inclined holes, indicate a marked effect of the density ratio on the film cooling effectiveness, subject to other parameters such as the blowing rate and the velocity ratio, being taken into consideration. Neither of these

Contributed by the International Gas Turbine Institute and presented at the International Cogen-Turbo Symposium and Exposition, Bournemouth, United Kingdom, September 21–23, 1993. Manuscript received at ASME Headquarters July 1993. Associate Technical Editor: H. Lukas.

investigations, however, investigated the influence of the important design parameters, D, n, and X/D.

Experimental Techniques

The present high temperature, steady-state test facility was described previously by Andrews et al. (1985). It was capable of simulating realistic mainstream-to-coolant temperature ratios, by means of heating the mainstream over the range of 300–930 K, while maintaining the same combustion air mass flow rate (i.e., constant blowing rate, M, at all Tg/Tc, for a fixed test geometry). Hot gas mainstream passed through a 152 mm by 76 mm externally air-cooled rectangular duct, cross-flowing the interchangeable test wall with a square array of 90 deg injection holes. The corresponding ranges for the mainstream velocity, Mach, and Reynolds numbers were 15.0–44.0 m/s, 0.043–0.075, and 4.2×10^4–9.3×10^4, respectively. The variation in the coolant air temperature upstream of the rotameters, Tc, within the range of 288–298 K, in the above-mentioned temperature ratio, was less than 1.0 percent. A range of effusion test walls, having variable hole diameter and hole pitch, flush-mounted in the wall of the duct, was employed. The cooling effectiveness data have been corrected for the radiation interchange between the test wall and the duct walls using the procedure of Andrews et al. (1985).

Overall and Adiabatic Film Cooling Effectiveness

In the present work, the combined influence of the film and internal wall cooling was assessed by the measured overall cooling effectiveness, η_{ov}. That is both modes of heat transfer, namely, convective cooling of the wall as the coolant air passed through it, and film cooling as the coolant air formed a film separating the hot gas from the wall, were taken into account by this parameter. It is defined, in a dimensionless form, by

$$\eta_{ov}=\frac{T_g-T_w}{T_g-T_c} \tag{1}$$

The overall cooling effectiveness was measured in the order of the thermal stations on the test wall. For comparison of various geometries, thermal station 5, 127 mm downstream of the test wall's leading edge in the streamwise direction, was used. This was taken as a fully developed film cooled boundary layer position. Each thermal station corresponded to the location of a type K mineral insulated thermocouple vacuum brazed to the exit (gas) side of the test wall, on its centerline, midway between the cooling holes. This is shown in Fig. 1. In addition, the test walls had thermocouples brazed to their coolant approach side, so as to determine the thermal gradients through the wall. Typical results were presented and discussed previously (Andrews et al., 1985, 1991). Temperature differences across the wall were shown to be below 10 percent of the corresponding difference between the wall and the coolant

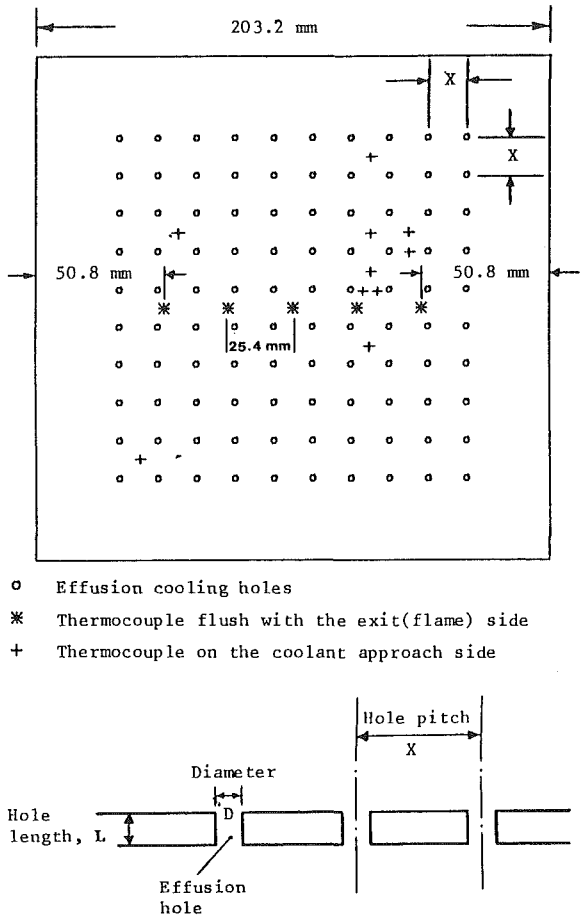

Fig. 1 An effusion test wall configuration

temperatures at all G and were less than 4 percent for G smaller than 0.4 kg/sm^2. The wall temperature could thus be considered to be uniform through the thickness, at all test conditions. The mainstream gas temperature, Tg, was measured on the duct centerline, at the center of the test wall.

The axial variation of the cooling effectiveness, based on five centerline thermocouples at 25 mm intervals, for various test geometries, was presented at a single G value of 0.17 kg/sm^2. The objective of the present work was to achieve a relatively high cooling effectiveness of 0.7 in the coolant flow range of 0.2–0.4 kg/sm^2, which corresponds to a low proportion of the total combustor airflow (i.e., 10–20 percent), used for wall film cooling (Andrews and Mkpadi, 1984).

"Pseudo" adiabatic film cooling effectiveness, η_{ad}, is a dimensionless parameter that was employed to evaluate the performance of the film cooling. It is defined as

Nomenclature

A = heat transfer surface area, m^2
D = hole mean diameter, m
G = coolant mass flow rate per unit wall surface area, kg/sm^2
L = hole length = wall thickness, m
M = blowing rate = $\rho_c u_c/\rho_g u_g$
n = number of cooling holes per unit wall surface area, m^{-2}
N = total number of cooling holes on the test wall
T = temperature, K
Tg/Tc = mainstream-to-coolant nominal temperature ratio = ρ_c/ρ_g
u = velocity, m/s
X = hole pitch, m
X/D = hole pitch-to-diameter ratio
Z = momentum flux ratio = $\rho_c u_c^2/\rho_g u_g^2$
$\Delta P/P$ = coolant pressure loss across the wall, percent
η = cooling effectiveness
ρ = density, kg/m^3

Subscripts

ad = adiabatic film
c = coolant
g = mainstream (gas stream)
gw = gas stream adjacent to the wall
ov = overall
w = wall

Table 1 Test wall design details

Wall	n (m^{-2})	D (mm)	X (mm)	X/D	L (mm)	L/D	ΔP/P (%)	array
I	26910	1.31	6.1	4.7	6.35	4.8	0.1	25x25
E	4306	3.27	15.2	4.7	6.35	1.9	0.1	10x10
V	9688	2.24	10.2	4.6	6.51	2.9	0.1	15x15
K	9688	1.43	10.2	7.1	6.35	4.4	0.5	15x15
U	9688	1.00	10.2	10.2	3.32	3.3	3.0	15x15

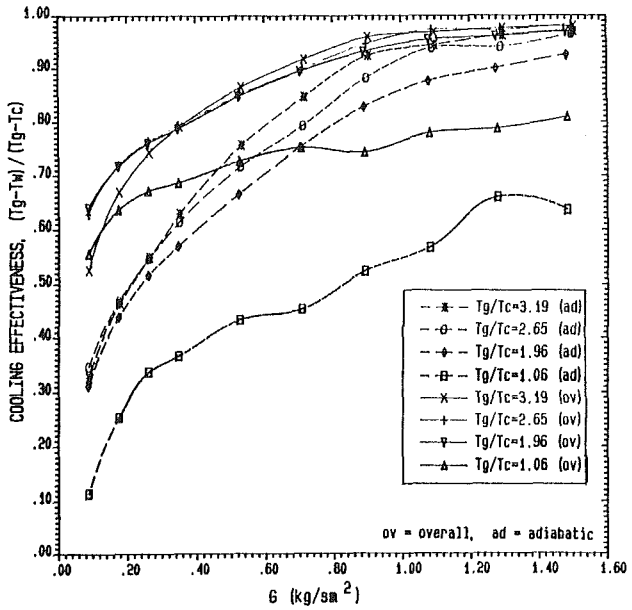

Fig. 2 Cooling effectiveness as a function of coolant injection rate, G, for test wall *I*, at thermal station 5

$$\eta_{ad} = \frac{T_g - T_{gw}}{T_g - T_c} \tag{2}$$

T_{gw} is the gas temperature adjacent to the test wall, at 25, 76, and 127 mm from the wall's leading edge. It is similar to the gas temperature adjacent to an adiabatic wall in studies of adiabatic wall film cooling, where it is taken as the limiting value of the wall temperature in the absence of heat transfer. However, the present measurements of T_{gw} represented a "pseudo" adiabatic wall condition and T_{gw} was shown to be higher than T_w. This difference was small for geometries with good film cooling characteristics, where the film remained attached to the wall with little coolant boundary layer stirring.

A traverse mechanism operated by a stepping motor with a position accuracy better than 0.1 mm was used to measure the gas temperature up to the test wall. It measured T_{gw} on the center of the square hole arrays and hence the minimum adiabatic film cooling effectiveness was evaluated. In the present work, the adiabatic film cooling effectiveness was used to give a quantitative indication of the film cooling performance, separately from the combined influence of the film and internal wall cooling, measured by the overall cooling effectiveness. The difference between the two indicates the importance of heat transfer by the coolant as it passed through the wall. However, there was a small uncertainty associated with the use of η_{ad}, since it was practically impossible to measure T_{gw} at the same position relative to the adjacent holes, for comparison of various geometries with different n and D.

Test Geometries

The test walls' design details are given in Table 1. In the present work, the design pressure loss across the test wall refers to a G value of 0.4 kg/sm^2 bar at a coolant temperature of

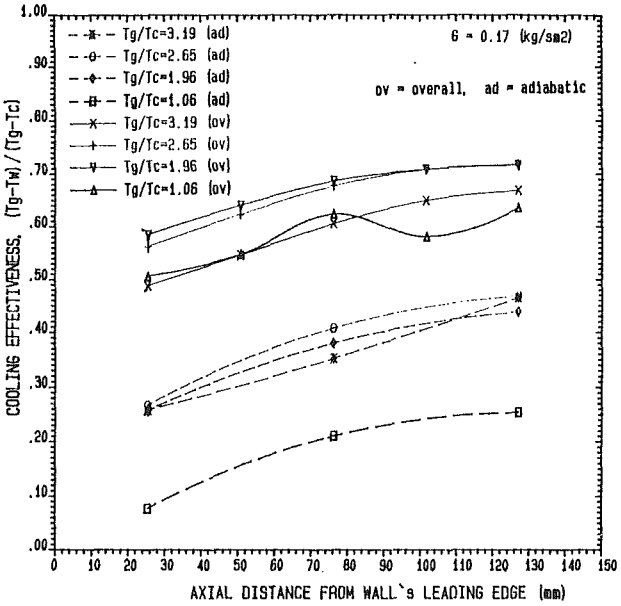

Fig. 3 Axial variation of cooling effectiveness for test wall *I*, at a fixed G, for a range of temperature (density) ratios

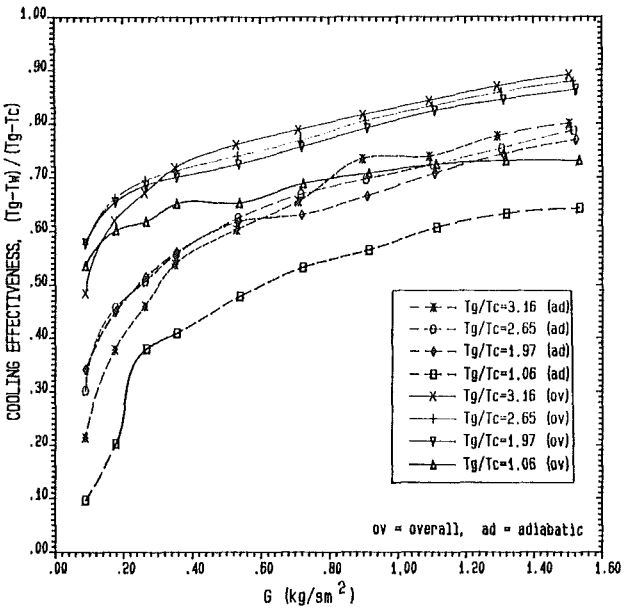

Fig. 4 Cooling effectiveness as a function of coolant injection rate, G, for test wall *V*, at thermal station 5

700 K (Andrews and Mkpadi, 1984). The low coolant pressure loss designs (i.e., 0.1 percent) were all intended to be combined with impingement cooling in a double wall impingement/effusion configuration (Al Dabagh et al., 1990). The higher pressure loss designs were intended for single wall applications where the full combustor wall pressure loss occurred across the effusion wall.

The Influence of the Number of Holes

The influence of the number of holes per unit wall surface area, n, at a constant total cross-sectional area of holes, on the overall cooling performance, was investigated using the test walls *I*, *V*, and *E* listed in Table 1. Increasing n at a constant cross-sectional area of holes, involved a decrease in the hole

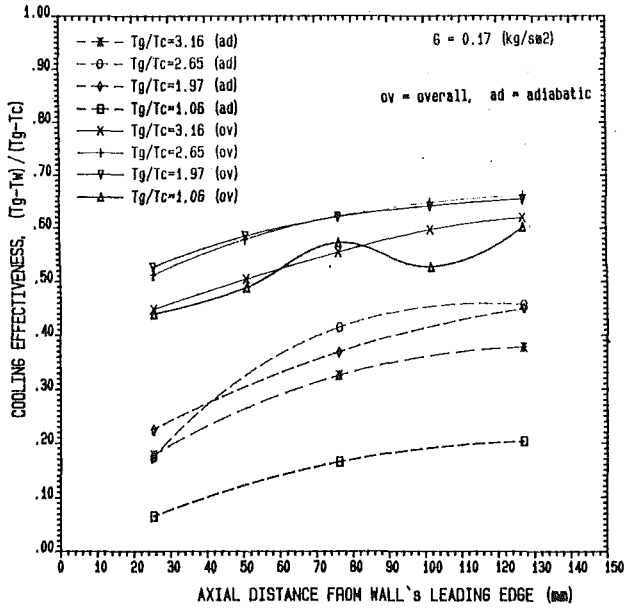

Fig. 5 Axial variation of cooling effectiveness for test wall *V*, at a fixed *G*, for a range of temperature (density) ratios

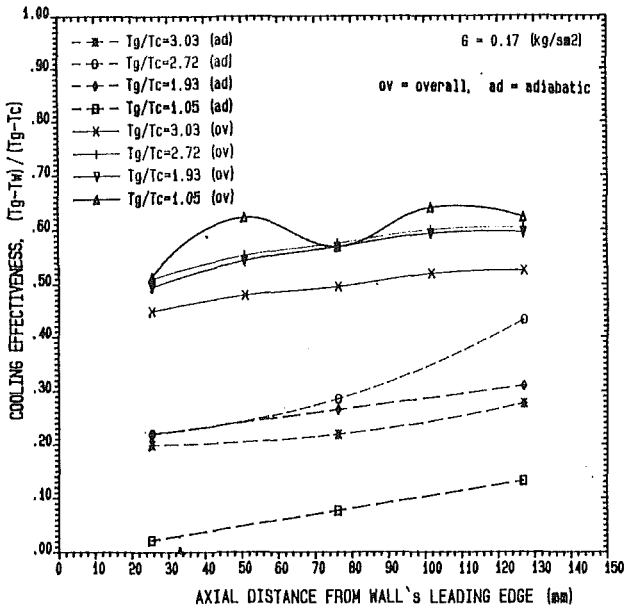

Fig. 7 Axial variation of cooling effectiveness for test wall *E*, at a fixed *G*, for a range of temperature (density) ratios

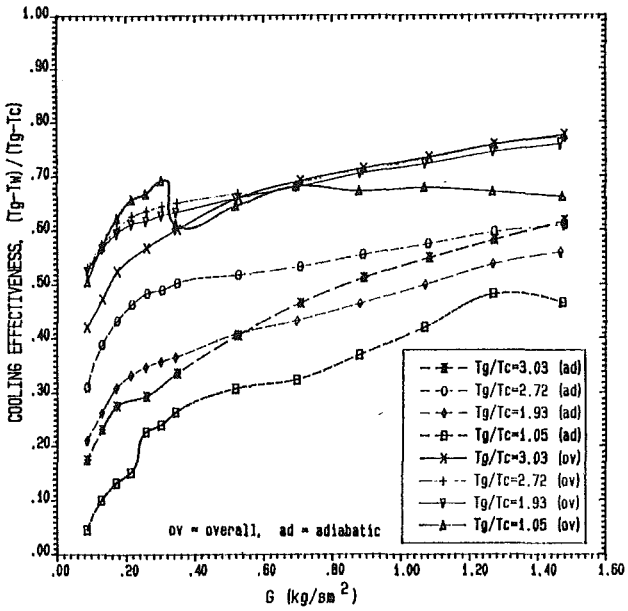

Fig. 6 Cooling effectiveness as a function of coolant injection rate, *G*, for test wall *E*, at thermal station 5

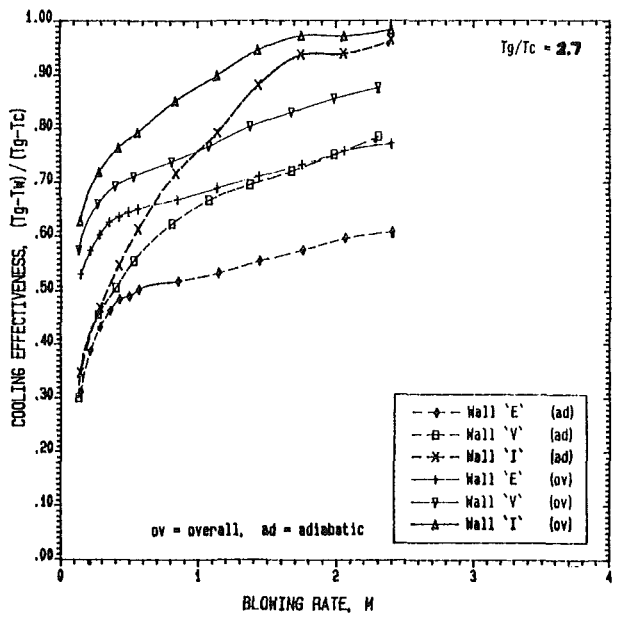

Fig. 8 Cooling effectiveness as a function of blowing rate, for comparison of walls *I*, *V*, and *E*, at thermal station 5

mean diameter, D, resulting in constant coolant jet velocity and pressure loss, for a fixed coolant mass flow rate. It will be shown that the more uniform surface coverage of the higher number of holes, at a fixed X/D of 4.7, gives an enhancement of the film cooling performance.

Results for Walls *I*, *V*, and *E*. Figure 2 shows the overall and adiabatic film cooling effectiveness results for wall *I*, as a function of the coolant mass injection rate per unit wall surface area, G, at four various temperature ratios, T_g/T_c, at thermal station 5. It can be seen that there was an increase in both η_{ov} and η_{ad} with G. The trends are similar at all T_g/T_c, except at the unity temperature ratio showing relatively lower overall cooling effectiveness results. This could be due to a comparatively lower contribution of the film cooling to the overall cooling, which was reflected in the larger difference between η_{ov} and η_{ad} at this temperature ratio. The magnitude of the difference between these two is a rough measure of the importance of the heat transfer by the coolant as it passed through the wall.

The axial variations (i.e., in the streamwise direction) of the overall and adiabatic film cooling effectiveness for wall *I*, at a fixed G value of 0.17 kg/sm^2, are illustrated by Fig. 3. η_{ov} and η_{ad} both increased with the axial distance, due to the coolant boundary layer getting comparatively thicker toward the trailing edge of the wall. This was noticed in the boundary layer temperature profiles (Andrews et al., 1990; Bazdidi-Tehrani, 1990). The target value of 0.7 for η_{ov} was achieved beyond an axial distance of 90 mm from the wall's leading edge, at this low value of G. The effect of varying T_g/T_c was relatively small with no consistent trend. At the unity temperature ratio, η_{ad} was of the lowest magnitude. This indicates the poorest film cooling, but the boundary layer temperature profiles

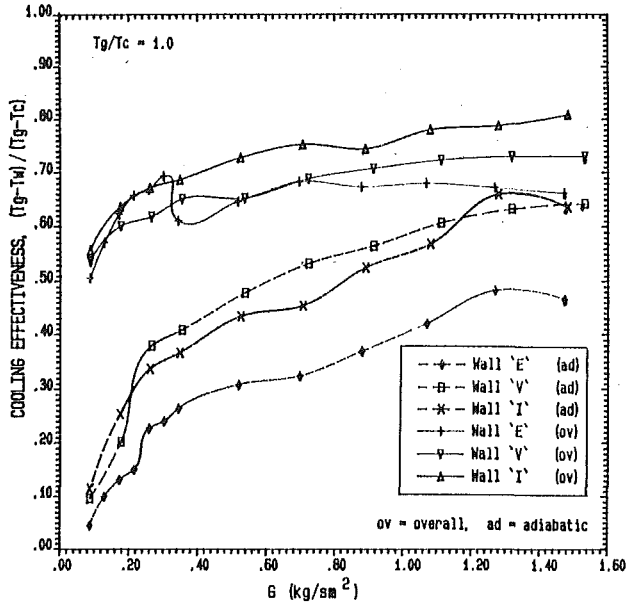

Fig. 9 Cooling effectiveness as a function of G, for comparison of walls I, V, and E, at thermal station 5

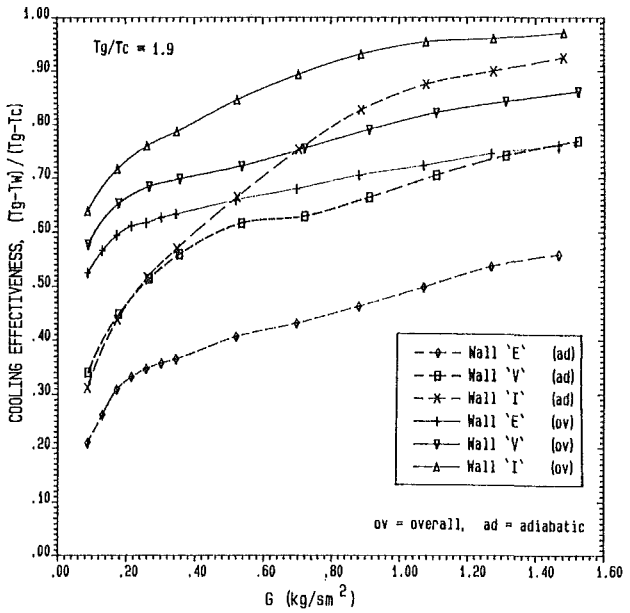

Fig. 10 Cooling effectiveness as a function of G, for comparison of walls I, V, and E, at thermal station 5

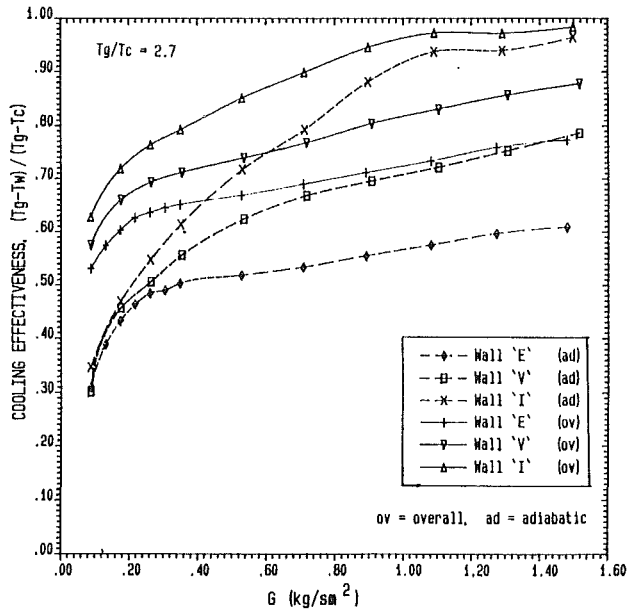

Fig. 11 Cooling effectiveness as a function of G, for comparison of walls I, V, and E, at thermal station 5

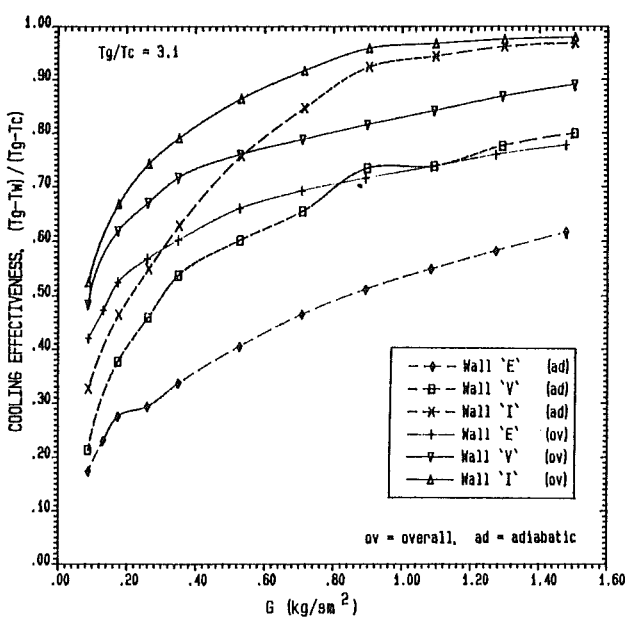

Fig. 12 Cooling effectiveness as a function of G, for comparison of walls I, V, and E, at thermal station 5

showed no sign of jet stirring and T_{gw} was not unusually high. Hence, the above trend could not be significant.

The overall and adiabatic film cooling effectiveness results for wall V, as a function of G, at similar T_g/T_c values to those for wall I, are presented in Fig. 4. η_{ov} and η_{ad} increased with G, but less sharply than that for wall I. At the unity temperature ratio, η_{ov} was lower, due to possibly a lower contribution of the film cooling to the overall cooling. The effect of varying T_g/T_c (except for $T_g/T_c = 1.06$), at thermal station 5, was generally small, at all G. (Figure 5 illustrates the axial variations of η_{ov} and η_{ad} for wall V, at a fixed G value of 0.17 kg/sm^2.) There was an increase in both η_{ov} and η_{ad} with the axial distance, the former reaching the target value of 0.7 at an axial distance of 127 mm, for $G \geq 0.35$ kg/sm^2 (see Fig. 4). η_{ad} was lowest at the unity temperature ratio, indicating the poorest film cooling. The influence of the coolant injection rate, G, on the overall and adiabatic film cooling effectiveness results for wall E, at similar T_g/T_c values to those for walls I and V, is shown by Fig. 6. There was an increase in both η_{ov} and η_{ad} with the G. The trend for the unity temperature ratio is, similar to that for walls I and V, inconsistent. Although η_{ad} is shown to be lowest for this temperature ratio, η_{ov} was slightly higher at low G. Figure 7, representing the axial variations of η_{ov} and η_{ad} for wall E, shows that η_{ad} was lowest at the unity temperature ratio at a G value of 0.17 kg/sm^2. There was a small increase in η_{ov} and η_{ad} with the axial distance. The target value of 0.7 for η_{ov} was not achieved by wall E.

Comparison of Walls I, V, and E. Figure 8 shows the cooling effectiveness results for walls I, V, and E using the blowing rate, M, as the scaling parameter. The coolant mass velocity for walls I, V, and E was the same, at a fixed coolant mass flow rate. This resulted in the blowing rate for these particular geometries to be of a similar order of magnitude,

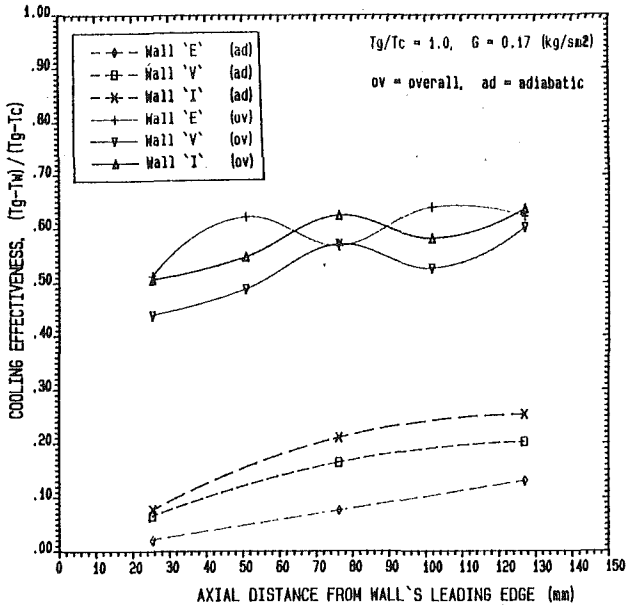

Fig. 13 Axial variation of cooling effectiveness for walls *I*, *V*, and *E*, at fixed *G* and temperature ratio

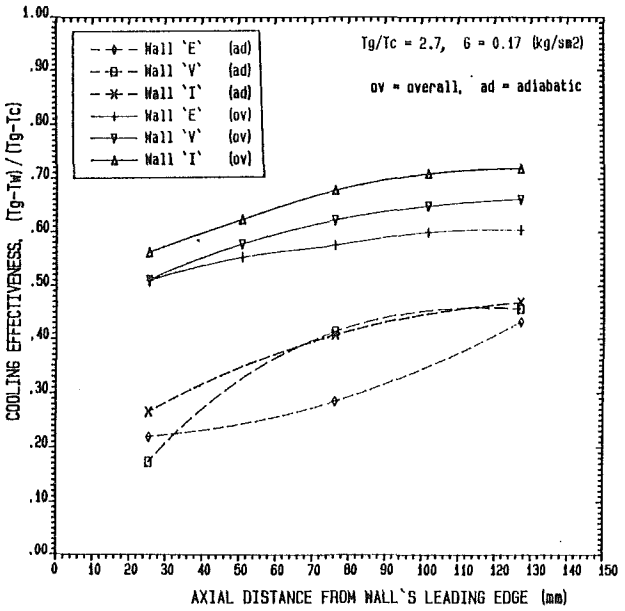

Fig. 15 Axial variation of cooling effectiveness for walls *I*, *V*, and *E*, at fixed *G* and temperature ratio

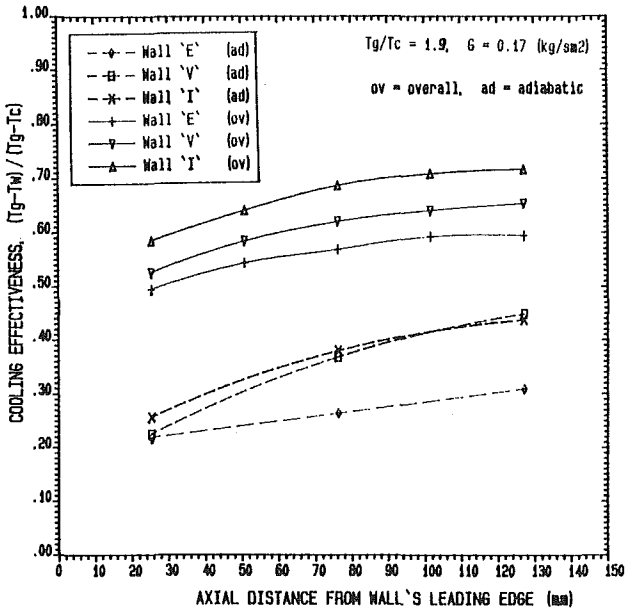

Fig. 14 Axial variation of cooling effectiveness for walls *I*, *V*, and *E*, at fixed *G* and temperature ratio

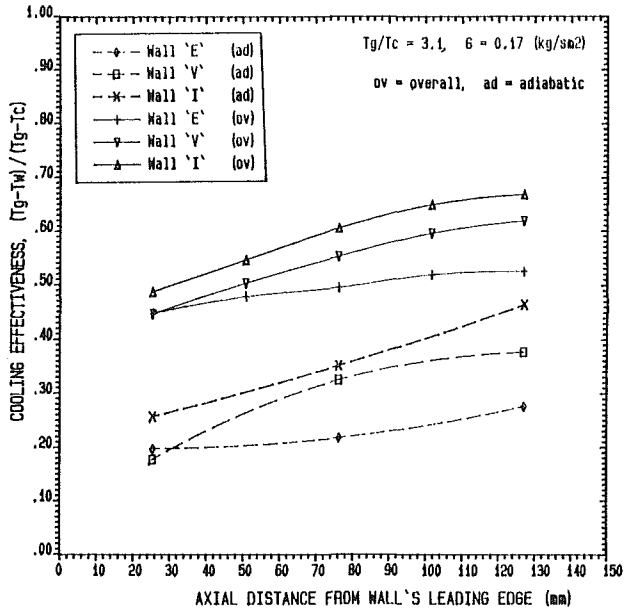

Fig. 16 Axial variation of cooling effectiveness for walls *I*, *V*, and *E*, at fixed *G* and temperature ratio

but the hole size and jet penetration were smaller as n was increased and the blowing rate cannot account for this. It will also be shown later that M could not correlate the results for geometries V, K, and U, with different hole size, at a constant n, and hence difference coolant mass velocities.

Figures 9–12 illustrate the comparisons of the overall and adiabatic film cooling effectiveness results for walls I, V, and E, at four fixed T_g/T_c using G as the scaling parameter. For $T_g/T_c > 1.0$, the results for wall I ($n = 26910$ m^{-2}) were superior to the rest, at all G. This was due to a more uniform surface coverage for this wall with the highest number of holes, leading to a better film cooling performance. The magnitude of this superiority was higher for $G > 0.4$ kg/sm^2. The results indicate that there was a bigger contribution of the film cooling to the overall cooling for wall I, at high G, when compared with those for walls V and E. For the same range of T_g/T_c, wall E ($n = 4306$ m^{-2}) with the lowest number of holes gave lower trends for η_{ov} and η_{ad}, than those for walls I and V. The reason for this was also due to high levels of boundary layer jet stirring, noticed in the temperature profiles, at high G. The trends noted above, regarding wall I, are not quite the same at $T_g/T_c = 1.0$, where this geometry showed a slightly lower η_{ad} than those for wall V, for $G > 0.2$ kg/sm^2. The overall trends, however, indicate that wall V ($n = 9688$ m^{-2}) could be considered as the geometry with the optimum n, in the present range of investigation.

Comparisons of the axial variations of the overall and adiabatic film cooling effectiveness results for walls I, V, and E, at four fixed T_g/T_c, are shown by Figs. 13–16, for $G = 0.17$ kg/sm^2. The trends, regarding η_{ov}, for wall I are highest for $T_g/T_c > 1.0$. The axial increase in η_{ov} was slightly sharper for wall I than those for walls V and E. The trends, concerning

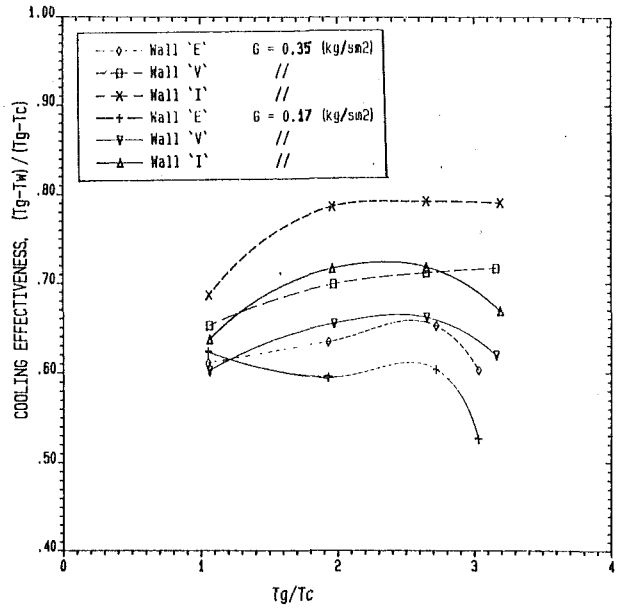

Fig. 17 The effect of nominal temperature ratio on overall cooling effectiveness, for walls *I*, *V*, and *E*, at thermal station 5

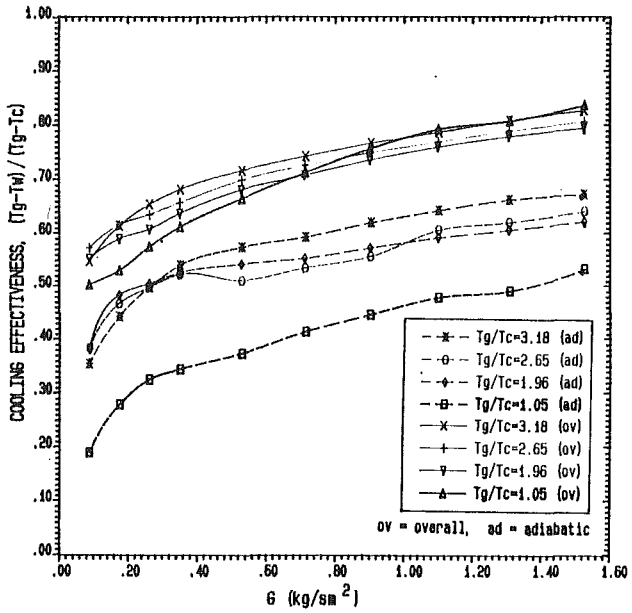

Fig. 19 Cooling effectiveness as a function of coolant injection rate, *G*, for test wall *K*, at thermal station 5

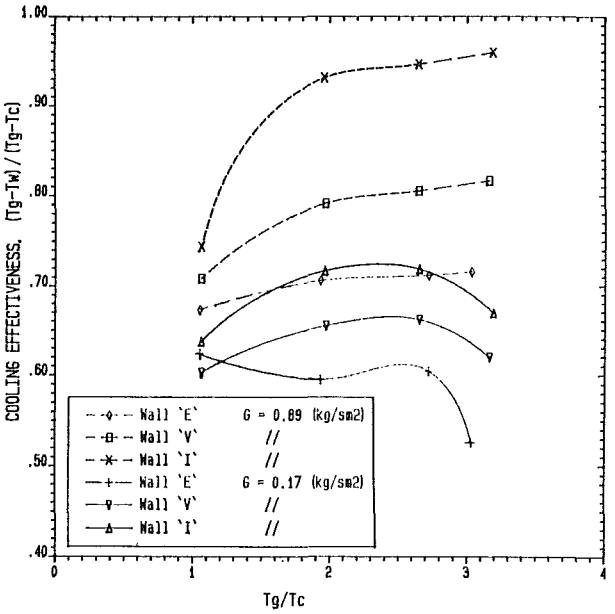

Fig. 18 The effect of nominal temperature ratio on overall cooling effectiveness, for walls *I*, *V*, and *E*, at thermal station 5

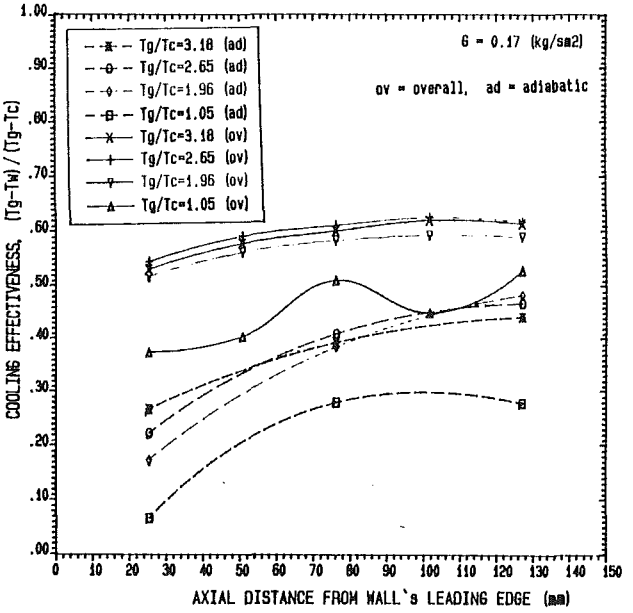

Fig. 20 Axial variation of cooling effectiveness for test wall *K*, at a fixed *G*, for a range of temperature (density) ratios

η_{ad}, are close for walls *I* and *V*, at all T_g/T_c, but with wall *E* being generally the lowest of all. This was due to its comparatively poorer surface coverage.

Figure 17 demonstrates the overall cooling effectiveness results for walls *I*, *V*, and *E*, as a function of the nominal temperature ratio, T_g/T_c, at two fixed *G* values of 0.17 and 0.35 kg/sm^2, at thermal station 5. The results for wall *I* were higher than those for walls *V* and *E*, at both *G* values for the reasons discussed above. The effect of varying T_g/T_c by increasing T_g, at fixed hot gas mainstream and coolant mass flow rates, gave no consistent trends for various geometries and there appeared to be no simple relationship between the temperature ratio and the overall cooling effectiveness. Figure 18 shows that at a higher *G* value of 0.89 kg/sm^2, the trends with regard to the variation of T_g/T_c did not significantly change. There was, however, an indication of a slight increase in η_{ov} with T_g/T_c at this *G* value for all three geometries.

The Influence of the Hole Diameter

The three geometries *V*, *K*, and *U*, listed in Table 1, were employed to study the influence of the hole mean diameter, *D*, at a constant *n* of 9688 m^{-2}, on the overall cooling performance. Increasing *D* and, hence, the total cross-sectional area of holes, resulted in a decrease in the coolant jet velocity and pressure loss, for a fixed coolant mass flow rate. The velocities of coolant jets discharging into the crossflowing mainstream influence the film cooling boundary layer. It will be shown that a larger *D* (i.e., smaller *X/D*), with a lower coolant jet velocity, shows a better film cooling performance.

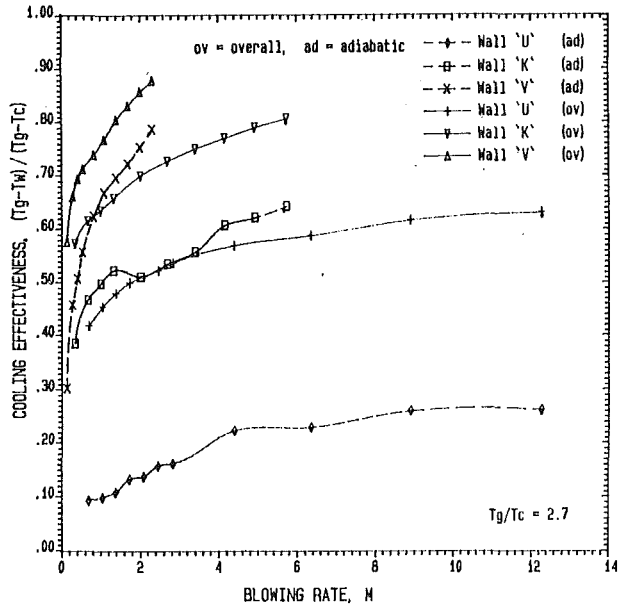

Fig. 21 Cooling effectiveness as a function of blowing rate, for comparison of walls *V*, *K*, and *U*, at thermal station 5

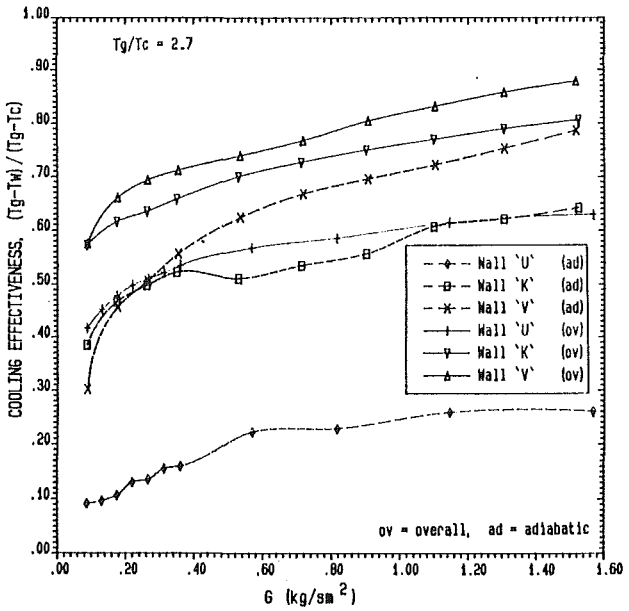

Fig. 23 Cooling effectiveness as a function of *G*, for comparison of walls *V*, *K*, and *U*, at thermal station 5

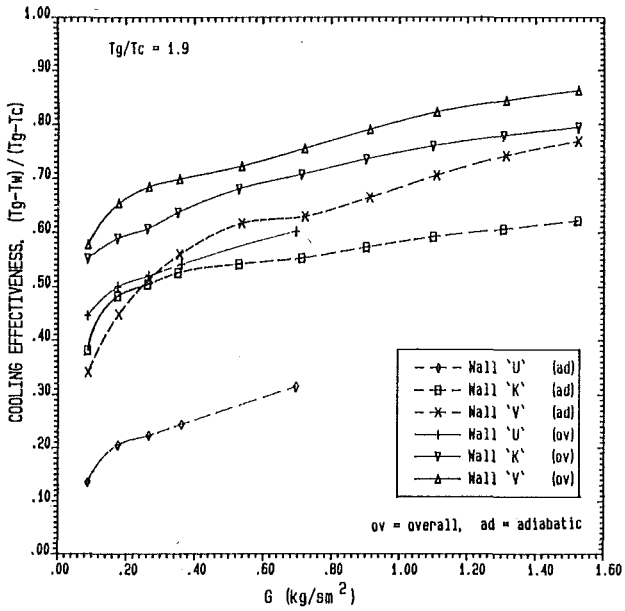

Fig. 22 Cooling effectiveness as a function of *G*, for comparison of walls *V*, *K*, and *U*, at thermal station 5

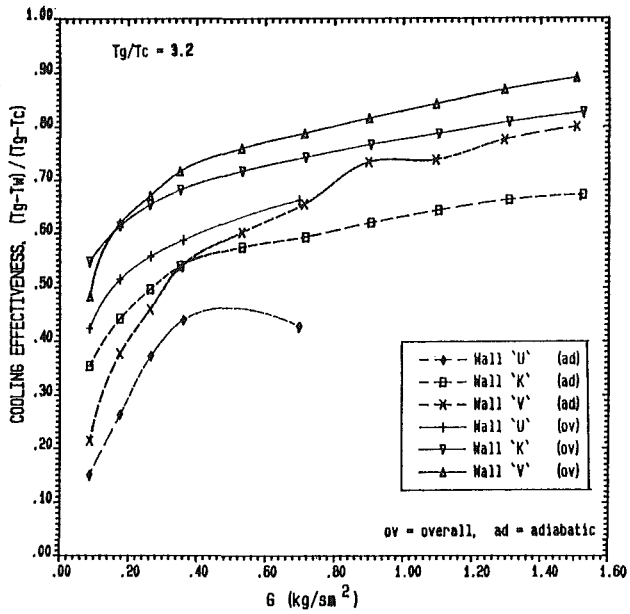

Fig. 24 Cooling effectiveness as a function of *G*, for comparison of walls *V*, *K*, and *U*, at thermal station 5

The choice of $n = 9688\ \mathrm{m}^{-2}$, for the test walls, was aimed at obtaining an optimum overall cooling effectiveness with a lower manufacturing cost, in comparison with higher n. The data for wall U, tested by Asere (1986) at three various mainstream-to-coolant temperature ratios, were used for comparison with those for walls V and K.

Results for Wall *K*. Figure 19 illustrates the overall and adiabatic film cooling effectiveness results for wall K, as a function of the coolant mass injection rate, G, at four various temperature ratios, T_g/T_c, at thermal station 5. Both η_{ov} and η_{ad} increased with G. The trends for η_{ad} are lower than those for η_{ov}, at all T_g/T_c, indicating that the gas temperature adjacent to the wall was generally higher than that of the wall. The magnitude of the difference between η_{ov} and η_{ad} was similar, at all G, except for the unity temperature ratio showing a comparatively lower η_{ad} than other T_g/T_c. The axial variations of the overall and adiabatic film cooling effectiveness for wall K, at a fixed G value of 0.17 kg/sm^2, are shown by Fig. 20. Both η_{ov} and η_{ad} increased with the axial distance, due to a moderate growth of the coolant boundary layer, which was shown in the temperature profiles. The target value of 0.7 for η_{ov} was not achieved by wall K, at the given value of G. The variation of η_{ov} and η_{ad} with T_g/T_c was generally small and no consistent trend is shown. However, at the unity temperature ratio, η_{ad} was lowest, indicating the poorest film cooling. This was not supported by the boundary layer temperature profiles, where no signs of jet stirring or unusually high values of T_{gw} were noticed, at the low G of 0.17.

Comparison of Walls *V*, *K*, and *U*. Figure 21 demonstrates that the cooling effectiveness results for walls V, K, and U

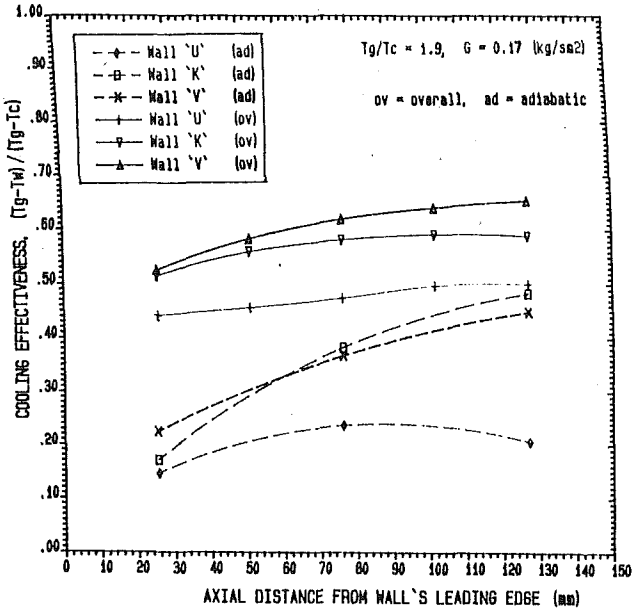

Fig. 25 Axial variation of cooling effectiveness for walls *V*, *K* and *U*, at fixed *G* and temperature ratio

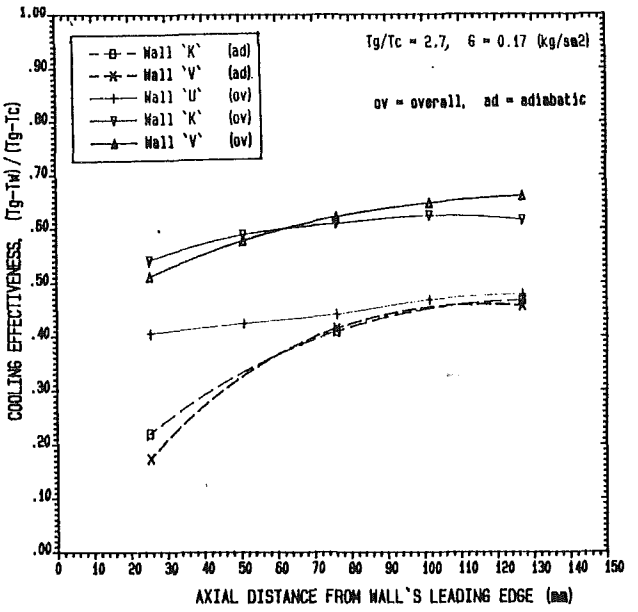

Fig. 26 Axial variation of cooling effectiveness for walls *V*, *K*, and *U*, at fixed *G* and temperature ratio

could not be correlated using the blowing rate, M, as the scaling parameter. The reason for this was that the given geometries, at a fixed coolant mass flow rate, had different total cross-sectional areas of holes and hence coolant mass velocities, which in turn governed the blowing rate. Therefore, comparison of the data at the same blowing rate involved a comparison at different coolant mass flow rates. This, as shown in Fig. 21, gave the incorrect impression of much larger differences in the cooling effectiveness results between these geometries.

Figures 22–24 show the comparisons of the overall and adiabatic film cooling effectiveness results for walls V, K, and U using the cooling mass injection rate, G, as the scaling parameter. The results are presented at three fixed T_g/T_c as there were no data available for wall U, at the unity temperature ratio. Also, apart from $T_g/T_c = 2.7$, the tests on wall U were carried out up to $G = 0.7$ kg/sm^2 only. It can be seen that the cooling effectiveness results increased as the hole size was increased, at all G. For $G < 0.4$ kg/sm^2, both η_{ov} and η_{ad} for wall K were reasonably close to those for wall V, with the largest D, at all T_g/T_c. Wall U, with the smallest D, showed the lowest trends, indicating a poor film cooling performance, at all G. This was due to its higher cooling jet velocity, giving more coolant boundary layer jet stirring and entrainment of hot gases between the injection holes. This was reported for wall U by Asere (1986) in the boundary layer temperature profiles.

Comparisons of the axial variations of the overall and adiabatic film cooling effectiveness results for walls V, K, and U, at three fixed T_g/T_c, are shown by Figs. 25–27, for $G = 0.17$ kg/sm^2. The results concerning η_{ad} for wall U, at $T_g/T_c = 2.7$, were not shown, since there was only data (i.e., T_{gw}) available at thermal station 3. This was also the case in Fig. 23, where the trends shown for η_{ad} represented thermal station 3. However, from the trends shown at other T_g/T_c, the difference was considered to be relatively small. The trends, regarding η_{ov}, for wall V are generally the highest at the fixed value of G. However, at the highest T_g/T_c, wall K showed somewhat higher η than that for wall V. The axial increase in η_{ov} was sharper for wall V than those for walls K and U. This was due to its comparatively better protection by the coolant film. Wall U showed the lowest trends for both η_{ov} and η_{ad}. The trends, regarding η_{ad}, for wall K are generally close to those for wall V and, similar to the trends for η_{ov}, it gave higher η_{ad} at the highest T_g/T_c than that for wall V.

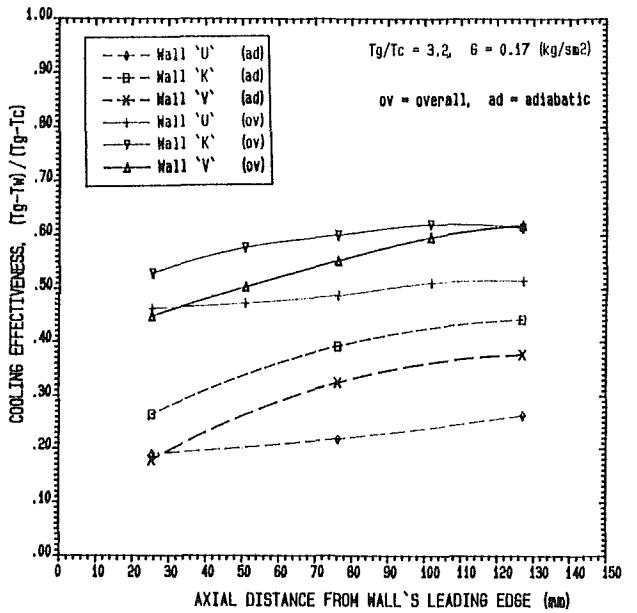

Fig. 27 Axial variation of cooling effectiveness for walls *V*, *K*, and *U*, at fixed *G* and temperature ratio

Figure 28 illustrates the overall cooling effectiveness results for walls V, K, and U, as a function of the nominal temperature ratio, T_g/T_c, at two fixed G values of 0.17 and 0.35 kg/sm^2, at thermal station 5. The results for wall V, with the largest D, were generally higher than those for walls K and U, at both G values for the reasons discussed above. Wall U, with the highest coolant mass velocity and hence blowing rate, at both fixed G values, showed the lowest trends. The effects of varying the temperature ratio by increasing T_g provided no consistent trends for various geometries, at both G values. This was also the case for the influence of n, in the previous section.

Conclusions

1 The overall cooling effectiveness increased significantly with an increase in the number of holes, n, of a full-coverage discrete hole film cooling system, at a fixed X/D of 4.7. This

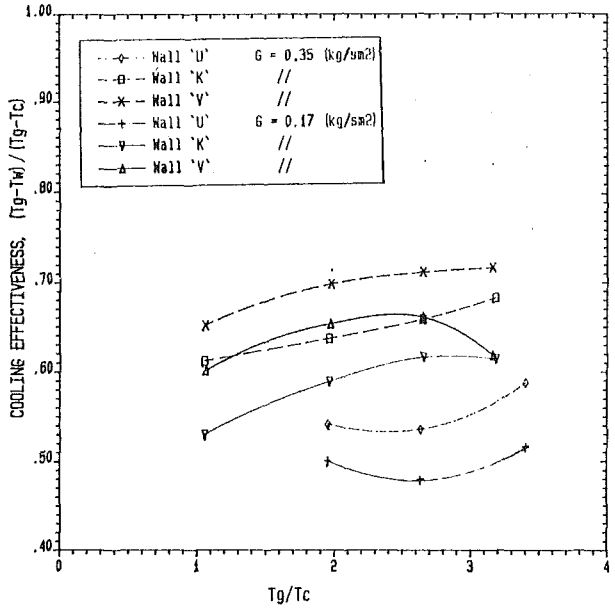

Fig. 28 The effect of nominal temperature ratio on overall cooling effectiveness, for walls *V*, *K*, and *U*, at thermal station 5

was mainly due to the improvement in the film cooling performance, arising from the more uniform surface coverage. A cooling effectiveness of 0.7 was achieved for the 9688 m^{-2} and 26910 m^{-2} configurations, over the low coolant flow rate range of 0.2–0.4 kg/sm^2. This range corresponds to approximately 10–20 percent of the total combustor airflow, demonstrating the potential for a substantial reduction in current wall film cooling uses of around 40–50 percent.

2 The choice of an optimum n, for combustor wall film cooling applications, was dictated not only by a good cooling performance, but also by a relatively low manufacturing cost. For a fixed X/D of 4.7, the optimum n was considered to be approximately 10,000 m^{-2}.

3 The overall cooling effectiveness increased noticeably as the hole size, D, was increased from 1.0 to 2.24 mm, at a fixed n of 9688 m^{-2}. This was because of a reduction in the coolant boundary layer jet stirring. A cooling effectiveness of 0.7, in the coolant flow rate range of 0.2–0.4 kg/sm^2, was not achieved for $D < 2.24$ mm.

4 The effect of varying the nominal mainstream-to-coolant temperature ratio, in the present range of 1.0–3.2, on the film cooling performance was small. No consistent trends were established for various configurations, for $G < 0.4$ kg/sm^2. At a higher G value of 0.89 kg/sm^2, an increase in the temperature ratio improved the film cooling performance slightly.

Acknowledgments

The authors would like to thank European Gas Turbines for the manufacture of some of the test geometries. Thanks are also due to the UK Science and Engineering Research Council for a research grant in support of this work (GR/D/53029).

References

Al Dabagh, A. M., Andrews, G. E., Abdul Hussain, R. A. A., Hussain, C. I., Nazari, A., and Wu, J., 1990, "Impingement/Effusion Cooling: The Influence of the Number of Impingement Holes and Pressure Loss on the Heat Transfer Coefficient," ASME *Journal of Turbomachinery*, Vol. 112, pp. 467–476.

Ammari, H. D., Hay, N., and Lampard, D., 1989, "Simulation of Cooling Film Density Ratios in a Mass Transfer Technique," ASME Paper No. 89-GT-200.

Ammari, H. D., Hay, N., and Lampard, D., 1990, "The Effect of Density Ratio on the Heat Transfer Coefficient From a Film-Cooled Flat Plate," ASME *Journal of Turbomachinery*, Vol. 112, pp. 444–450.

Andrews, G. E., and Mkpadi, M. C., 1984, "Full Coverage Discrete Hole Wall Cooling: Discharge Coefficient," ASME JOURNAL OF ENGINEERING FOR GAS TURBINES AND POWER, Vol. 106, pp. 183–192.

Andrews, G. E., Gupta, M. L., and Mkpadi, M. C., 1985, "Full Coverage Discrete Hole Film Cooling: Cooling Effectiveness," *Int. J. Turbo Jet Engines*, Vol. 2, pp. 199–212.

Andrews, G. E., Asere, A. A., Gupta, M. L., Mkpadi, M. C., and Tirmahi, A., 1990, "Full Coverage Discrete Hole Film Cooling: The Influence of the Number of Holes and Pressure Loss," ASME Paper No. 90-GT-61.

Andrews, G. E., Bazdidi-Tehrani, F., Hussain, C. I., and Pearson, J. P., 1991, "Small Diameter Film Cooling Hole Heat Transfer: The Influence of the Hole Length," ASME Paper No. 91-GT-344.

Asere, A. A., 1986, "Gas Turbine Combustor Wall Cooling," Ph.D. thesis, Dept. of Fuel and Energy, The University of Leeds, Leeds, United Kingdom.

Bazdidi-Tehrani, F., 1990, "Full Coverage Discrete Hole Film Cooling of Gas Turbine Components," Ph.D. thesis, Dept. of Fuel and Energy, The University of Leeds, Leeds, United Kingdom.

Forth, C. J. P., Loftus, P. J., and Jones, T. V., 1989, "The Effect of Density Ratio on the Film-Cooling of a Flat Plate," AGARD-CP-390, *Heat Transfer and Cooling in Gas Turbines*, May.

Goldstein, R. J., Eckert, E. R. G., and Burggraf, F., 1974, "Effects of Hole Geometry and Density on Three-Dimensional Film Cooling," *Int. J. Heat Mass Transfer*, Vol. 17, pp. 595–607.

Hennecke, D. K., 1984, "Heat Transfer Problems in Aero-engines," *Heat and Mass Transfer in Rotating Machinery*, Hemisphere, pp. 353–379.

Pedersen, D. R., Eckert, E. R. G., and Goldstein, R. J., 1977, "Film Cooling With Large Density Differences Between the Mainstream and the Secondary Fluid Measured by the Heat-Mass Transfer Analogy," ASME *Journal of Heat Transfer*, Vol. 99, pp. 620–627.

Sinha, A. K., Bogard, D. G., and Crawford, M. E., 1991, "Film Cooling Effectiveness Downstream of a Single Row of Holes With Variable Density Ratio," ASME *Journal of Turbomachinery*, Vol. 113, pp. 442–449.

Wadia, A. R., and Nealy, D. A., 1988, "Experimental Simulation of Turbine Airfoil Leading Edge Film Cooling," ASME *Journal of Turbomachinery*, Vol. 110, pp. 226–232.

S. Amagasa

K. Shimomura

M. Kadowaki

Tohoku Electric Power Co., Inc.,
Sendai, Japan

K. Takeishi

H. Kawai

Takasago R&D Center,
Mitsubishi Heavy Industries, Ltd.,
Takasago, Japan

S. Aoki

K. Aoyama

Takasago Machinery Works,
Mitsubishi Heavy Industries, Ltd.,
Takasago, Japan

Study on the Turbine Vane and Blade for a 1500°C Class Industrial Gas Turbine

This paper describes the summary of a three-year development program for the first-stage stationary vane and rotating blade for the next generation, 1500°C class, high-efficiency gas turbine. In such a high-temperature gas turbine, the first turbine vane and blade are the most important hot parts. Full-coverage film cooling (FCFC) is adopted for the cooling scheme, and directionally solidified (DS) nickel base superalloy and thermal barrier coating (TBC) will be used to prolong the creep and thermal fatigue life. The concept of the cooling configuration, fundamental cascade test results, and material test results will be presented.

Introduction

The Tohoku Electric Power Co. Higashi Niigata Thermal Power Station Number 3 has operated a combined cycle power plant successfully over 7 years by using six MW-701D gas turbines whose turbine inlet temperature (TIT) is 1154°C. Mitsubishi Heavy Industries, Ltd., and Westinghouse Electric Co. developed the 501F, a 1350°C class gas turbine, and carried out a shop test at full-load conditions to confirm performance and reliability in 1989 [1, 2].

Tohoku Electric Power Co., Inc., and Mitsubishi Heavy Industries, Ltd., started a six-year joint study beginning in 1989. The study was directed at the next-generation high-temperature gas turbine with a TIT of 1500°C. The program included the development of high-performance and high-reliability turbine vanes and blades, and a low-NO_x combustor [3]. Phase 1 of the program was a three-year study in which the key technology and design data necessary to produce a 1500°C class industrial, high-temperature gas turbine were developed. Combined-cycle thermal efficiency of more than 55 percent (LHV) is expected by using the 1500°C class gas turbine. In such a high-temperature gas turbine, the first stationary vane, first rotating blade, and the combustor are the most important hot parts. The concept and combustion test results were reported in [4].

In the case of a 1500°C class industrial gas turbines, the first stationary vane will be exposed to above 1650°C gas temperatures which is higher than the superalloy's melting temperature, when the gas temperature distribution at the combustor exit is considered. More effective and higher reliability turbine vanes and blades should be developed by improving the cooling configuration and adopting stronger materials with anti-oxidation/thermal barrier coatings. The air-cooled turbine vanes and blades are the results of the contributions of aerodynamics, heat transfer, material, structure, vibration, coating and manufacturing, etc., but cooling technology and material contributions are the most significant.

In this paper, the results of the study on full-coverage film cooled turbine vanes and blades and material and TBC research for such hot parts will be presented.

Cooling Scheme of the First-Stage Vanes and Blades

The evolution of increasing turbine inlet temperature of the Mitsubishi-Westinghouse manufactured industrial gas turbines with a comparison with aeroengines is shown in Fig. 1. It is clear from Fig. 1 that there is a strong trend toward

Contributed by the International Gas Turbine Institute and presented at the 38th International Gas Turbine and Aeroengine Congress and Exposition, Cincinnati, Ohio, May 24-27, 1993. Manuscript received at ASME Headquarters March 1993. Paper No. 93-GT-414. Associate Technical Editor: H. Lukas.

increasing TIT of heavy duty gas turbines and that it follows about 10 years after the aeroengine.

The ability to increase TIT strongly depends on the development of superalloys and the improvement of cooling methods. The contribution of superalloys to TIT is only 10°C per year but the cooling technology contribution is over 25°C per year. In addition to keeping the maximum metal temperature under the allowable metallurgical temperature limit, it is also necessary to minimize the cooling air usage to improve gas turbine cycle efficiency. Thus, accelerated development of highly efficient cooling methods is required for the continuing increase of TIT.

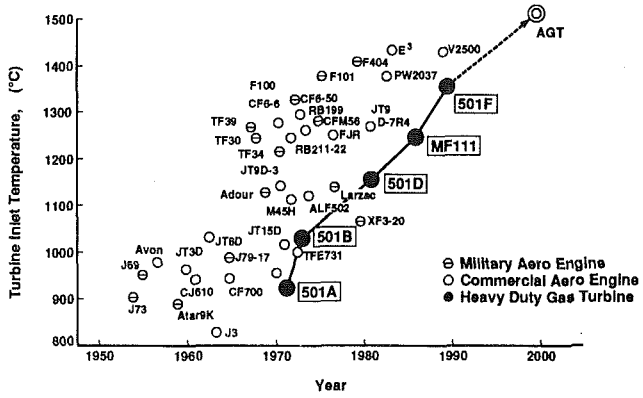

Fig. 1 Evolution of turbine inlet temperature

Figures 2 and 3 show the improvement of the cooling configuration of the first stationary vanes and rotating blades, respectively, adopted for the 501 series gas turbines.

In the case of the stationary vanes, simple impingement cooling was adopted for series A and B vanes. The TIT of the D series is 1200°C, with impingement cooling, pin fin cooling, and film cooling used for the vane. For the higher temperature 1350°C level of the F series gas turbine, three inserts are adopted to optimize the impingement cooling and pin fin cooling by controlling the film cooling pressure difference. Further, showerhead film cooling is adopted at the leading edge where the heat flux is highest.

In the case of the rotating blades, simple multihole cooling is used for the B and D series, but a higher efficiency cooling scheme using serpentine cooling passage with turbulence promoters is used for the first blade of MF-111, whose TIT is 1250°C. The first blade of the 501F is cooled by a combination of techniques via multipass serpentine passages with film cooling on pressure and suction surfaces, and showerhead cooling on the leading edge region with pin fin cooling in the trailing edge exit slots. This maintains the metal temperature and thermal stress under allowable metallurgical limits for maximum temperatures and temperature differences. One candidate of the cooling scheme of the first stage vane and blade for the 1500°C class gas turbine is shown in Figs. 4 and 5, respectively. Full-coverage film cooling is adopted for the vane and blade.

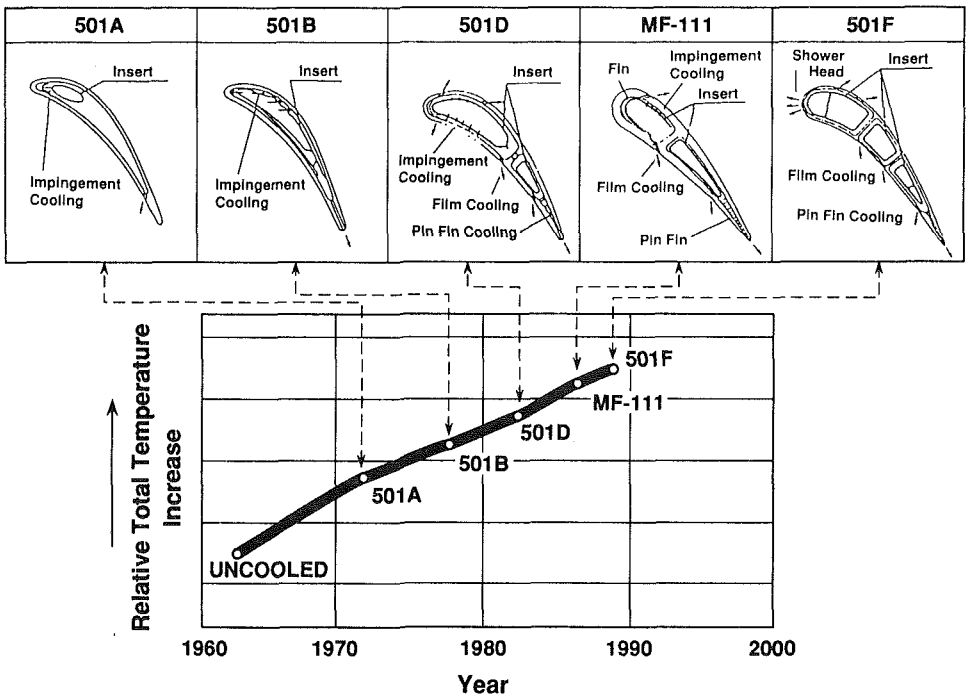

Fig. 2 Improvement of the cooling configuration of the first stationary vane

Nomenclature

d = film cooling hole diameter
G = flow rate
M = blowing flow parameter $= \rho_a U_a / \rho_\infty U_\infty$
P = pitch of the film cooling hole
T = temperature
t = time
U = velocity
x = distance
x_{max} = maximum distance from leading edge
α = injection angle of the film cooling hole
η_f = film cooling effectiveness $= (T_g - T_{aw})/(T_g - T_a)$
ρ = density
τ = mainstream turbulence intensity

Subscripts

a = air
aw = adiabatic wall
f = film
g = gas

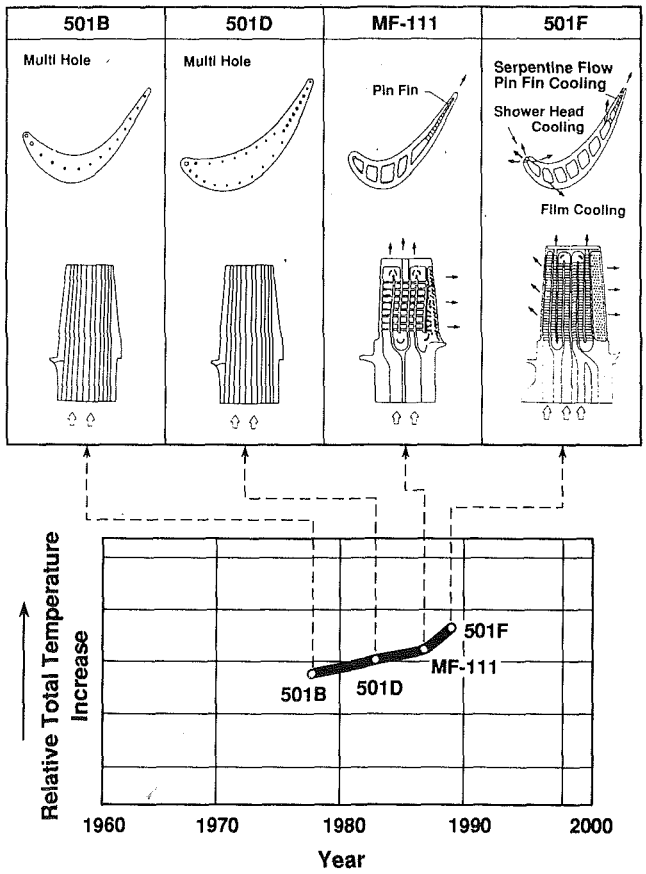

Fig. 3 Improvement of the cooling configuration of the first rotating blade

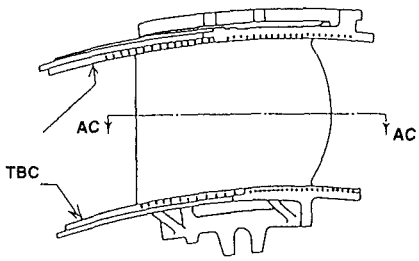

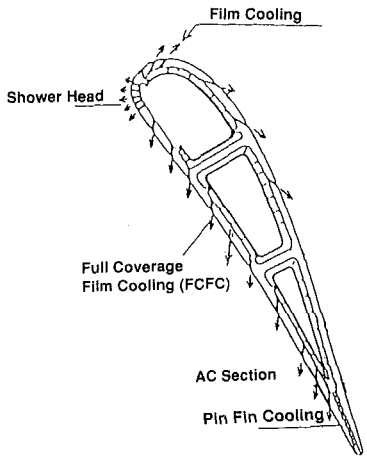

Fig. 4 Cooling configuration of the first stage vane for 1500°C class gas turbine

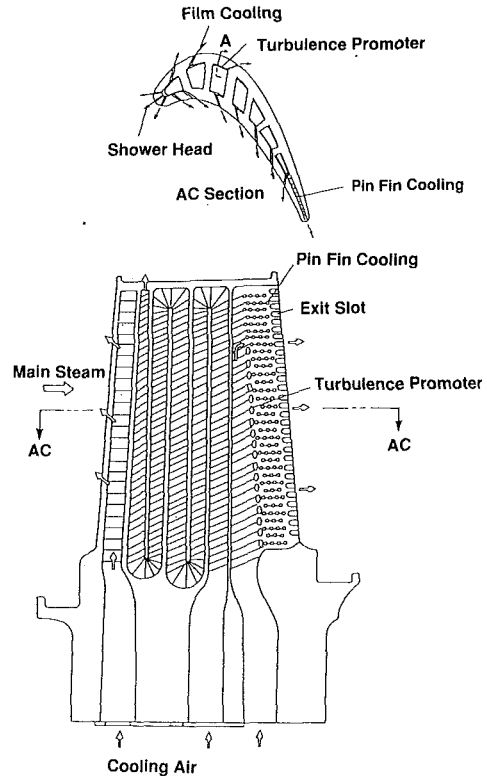

Fig. 5 Cooling configuration of the first stage blade for 1500°C class gas turbine

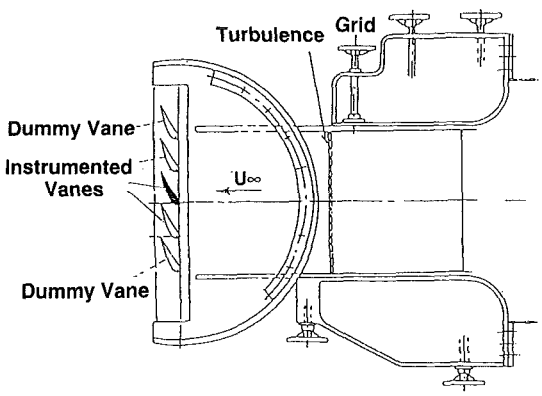

Fig. 6 Schematic geometry of the low-speed cascade

Table 1 Low-speed cascade

Dimension of The Test Section	300W × 600H
Maximum Exit Velocity	50 m/s
Main Steam Temperature	20°C (Room Temp.)
Main Steam Pressure	1.03 ata
Main Steam Turbulence Intensity	0.5~8%

Thermal barrier coating will be used, not only for the shroud but also for the airfoil of the first-stage vane.

As mentioned above, the most suitable cooling schemes are adopted according to the increase in TIT. Even though the heat flux is increasing, creep life and low cycle fatigue life are maintained by keeping the maximum metal temperature under the metallurgical anti-oxidation limit and keeping temperature differences that affect thermal stress low.

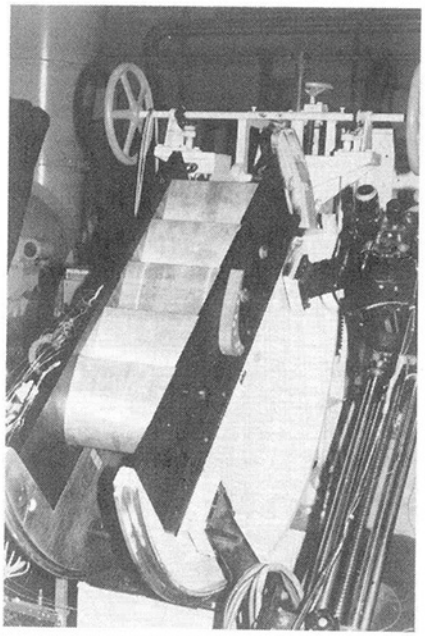

Fig. 7 Low-speed cascade test facility

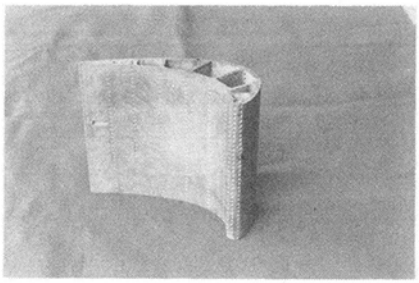

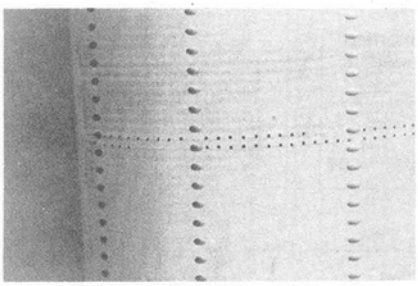

Fig. 8 Model of the full coverage film cooling blade and the instrumentation hole for thermocouples

Low-Speed Cascade Test

Low-speed cascade tests were conducted to measure film cooling effectiveness of the full-coverage film cooling, flow coefficient of the film cooling hole with the mainstream, and aerodynamic performance of the FCFC vane and blade considering the parameter of the cooling air flow rate. The capability of the low-speed cascade is shown in Table 1, Fig. 6 is a schematic of the cascade, and a photograph of the test facility with the mounted FCFC model blades is shown in Fig. 7.

FCFC Heat Transfer Test. The film cooling coefficient of the FCFC vane and blade is measured by the low-speed cascade by keeping the mainstream at room temperature and blowing the heated air through film cooling holes and measuring the adiabatic wall temperature. The model vanes and blades are scaled models of the typical turbine first-stage airfoil mean section, and are made from a low thermal conductivity material, Bakelite. The K type thermocouples of 0.2 mm diameter are embedded along the streamline downsteam of the film cooling hole and between the film cooling holes. Photographs of the model vane are shown in Fig. 8.

The distribution of the adiabatic wall temperature is measured using infrared photography. Also, the embedded thermocouples are used to verify the digital value. Typical

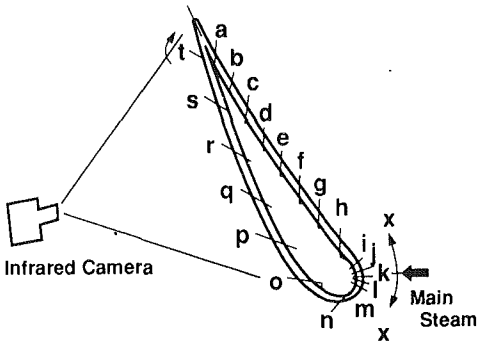

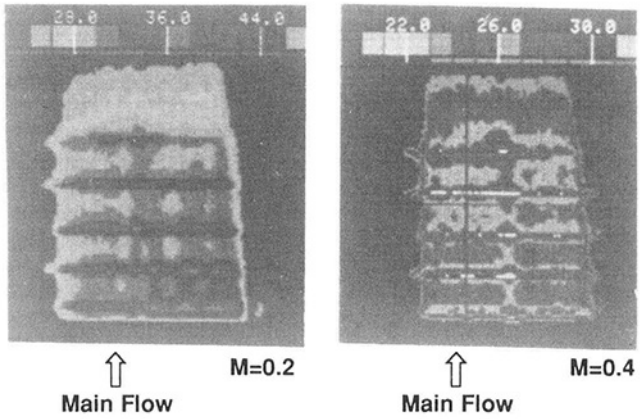

Fig. 9 Distribution of the adiabatic wall temperature measured by the infrared camera

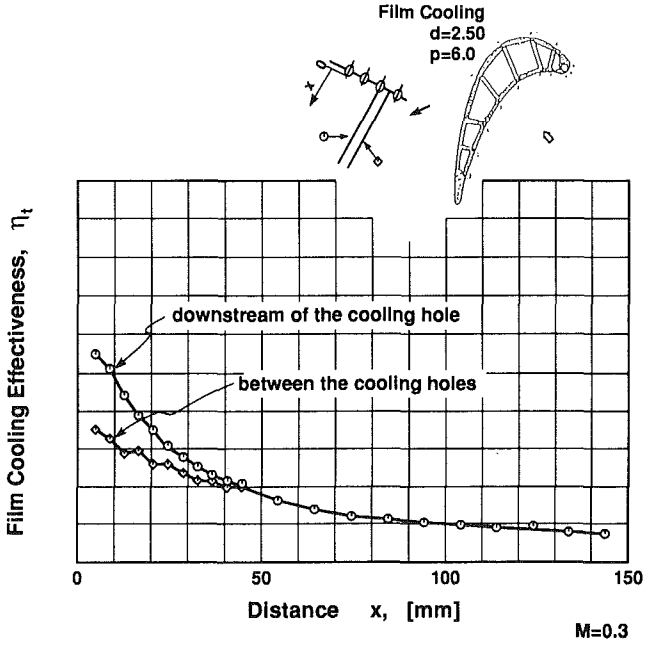

Fig. 10 Film cooling effectiveness on suction surface

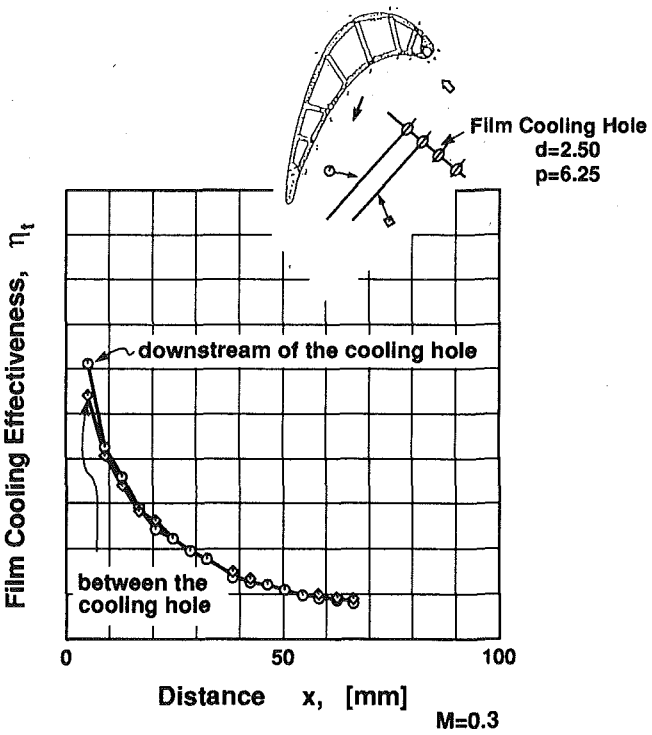

Fig. 11 Film cooling effectiveness on pressure surface

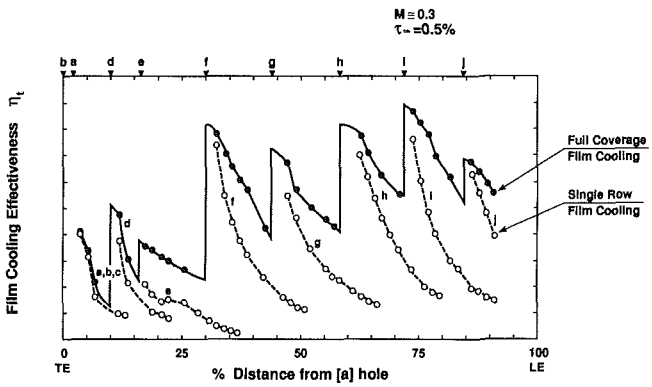

Fig. 12 Full-coverage film cooling effectiveness on pressure surface

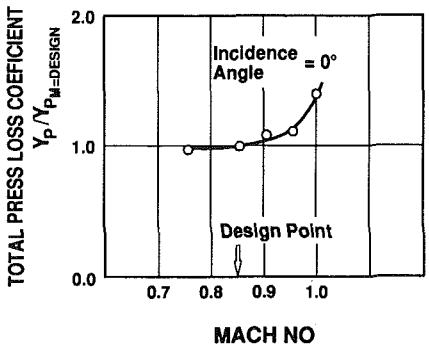

Fig. 13 Total pressure loss coefficient on the FCFC turbine blade

measuring results are shown in Fig. 9. It is clear that an even temperature distribution is attained by using FCFC.

The film cooling effectiveness measured on the suction surface and pressure surface blowing through one row film cooling

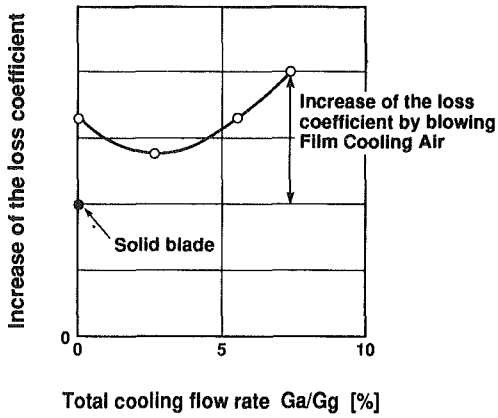

Fig. 14 Influence of the film cooling air on the total press loss coefficient

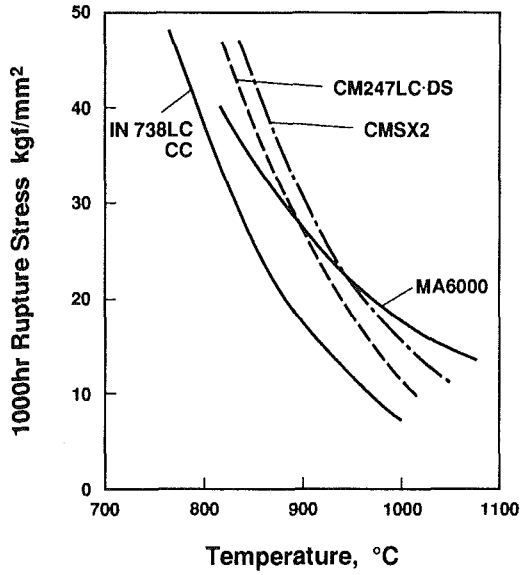

Fig. 15 Creep rupture strength of nickel base superalloys

Table 2 Chemical composition of tested material

Cr	Co	Mo	W	Ta	Ti	Al	C	B	Zr	Hf	Ni
8.20	9.29	0.49	9.50	3.27	0.67	5.68	0.07	0.018	0.010	1.42	Bal.

hole is shown in Figs. 10 and 11, respectively. The film cooling coefficient on pressure surface decreases rapidly as the distance increases, but on the suction surface it persists for a longer distance from the cooling hole. Another characteristic is that there is a difference in film cooling effectiveness between the surface downstream of the film cooling hole and between the holes on suction surface, but there is no such difference on the pressure surface. This is thought to be the result of a strong mixing of the coolant and the mainstream on the pressure surface. The film cooling effectiveness of FCFC on the pressure surface for a mass flow rate of $M=0.3$ is shown in Fig. 12 with comparison of that of single hole film cooling. The additive nature of the film cooling is clear near the trailing edge in Fig. 12. In the design of FCFC turbine vanes and blades, such results should be anticipated.

FCFC Aerodynamic Test. The aerodynamic performance of the full coverage film cooled turbine airfoil was measured

by using the same model but made with a metal airfoil. Typical tests results are shown in Figures 13 and 14. It is clear from Figure 13 that the designed total pressure loss coefficient of the 1st stage blade is low enough at design Mach number. There is a minimum aerodynamic loss when the cooling flow rate is changed as is clear from Figure 14. Aerodynamic loss increases rapidly when the cooling air is increased. Therefore, the FCFC vanes and blades should be designed aerodynamically considering the effect of the film hole position and cooling air flow rate.

Materials for Turbine Vanes and Blades

To develop a 1500°C class gas turbine, it is necessary to develop superalloys, which have superior high-temperature strength in addition to the development of sophisticated cooling systems for turbine vanes and blades. Figure 15 shows the comparison of the candidate superalloy creep rupture strength.

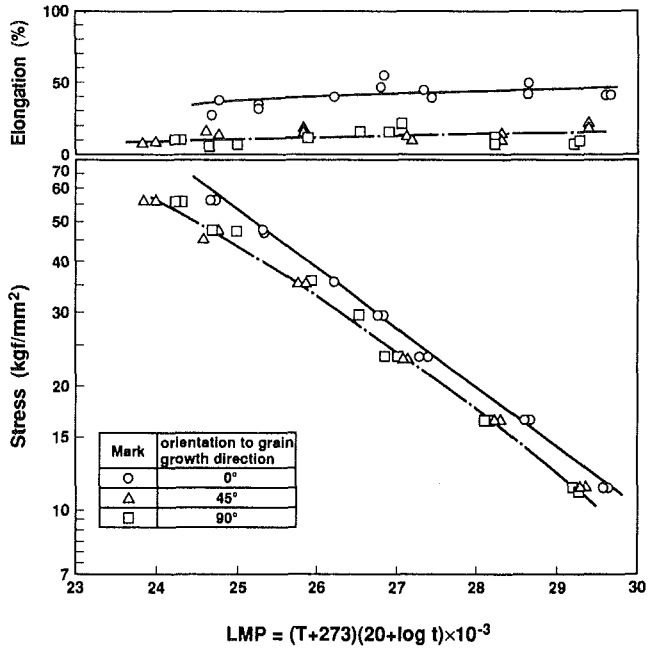

Fig. 16 Creep rupture properties of CM247LCDS (cast to size material)

The creep rupture strength of the CM247LC DS is about 50°C higher than that of IN738 LC CC, and single crystal CMSX-2 has higher strength than CM247LC DS. ODS alloy MA6000 is very strong in the high-temperature region over 950°C. After a feasibility study, it became clear that design demands for materials could be satisfied by the adoption of a DS blade made of nickel base superalloy CM247LC and thermal barrier coating (TBC). Thus, in this materials development program, three goals were established. The first was to collect material data of the nickel base superalloy CM247LC DS for blade and vane design. The second was to optimize casting conditions of large DS vanes and blades. The third goal was to develop a TBC with high-temperature capabilities.

Material Properties. Various material tests are conducted to obtain material data on CM247LC DS. Chemical composition of the tested material is shown in Table 2. The details of the creep rupture properties of CM247LC DS are shown in Fig. 16. It is clear from this figure that there is anisotropy in these properties. Namely, rupture life and elongation in an orientation parallel to grain growth direction (marked 0° in Fig. 16) are better than those in the 45° and 90° orientation.

Figure 17 shows the typical cross-sectional microstructure of test specimen parallel parts after stress rupture tests. From this it is clear that γ' particles become more coarse as LMP (Larson Miller Parameter) increases. γ' particles elongate in an orientation perpendicular to the stress axis and form a raft structure. In the chucking part, γ' particles become coarse, but the raft structure is not observed. Therefore, it is considered that the raft structure is influenced not only by temperature and time, but also by stress. These data are important for life assessment of the blades.

Thermal fatigue and high cycle fatigue data were collected. Physical properties are essential for the design of vanes and blades. Also Young's Modulus, thermal expansion coefficient, thermal conductivity and specific heat were measured in the 0°, 45°, and 90° orientation to grain growth direction. Figure 18 shows anisotropy in Young's Modulus, but no anisotropy in thermal expansion, thermal conductivity, and specific heat.

Trial Manufacturing of Vane and Blade. Trial manufacturing and evaluation of small and large vanes and blades were conducted to optimize casting conditions. Figure 19 shows surface macrostructure of a 150 MW class gas turbine blade. This shows that the morphology of grains is acceptable. Test specimens were taken from the trial blades and vanes and

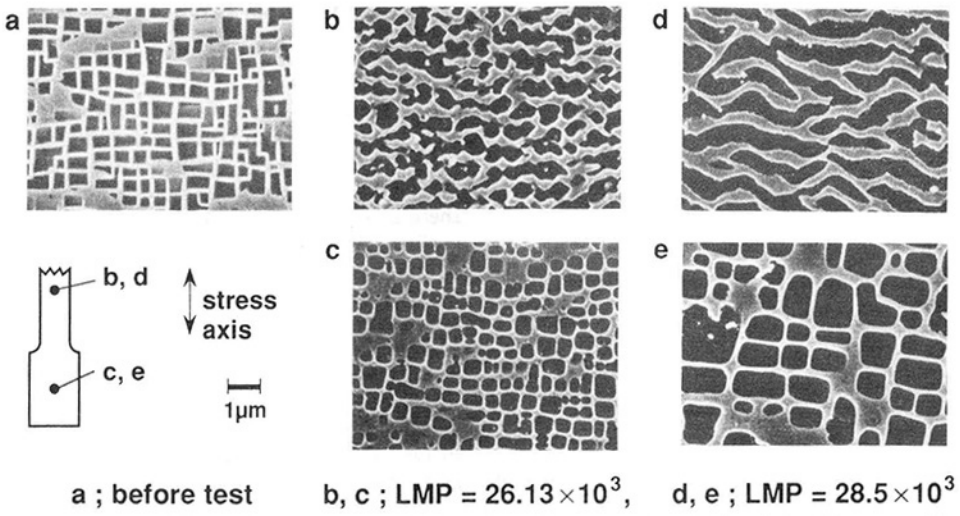

Fig. 17 Cross-sectional microstructure of test specimens' parallel parts (*b*, *d*) and chucking parts after stress rupture tests

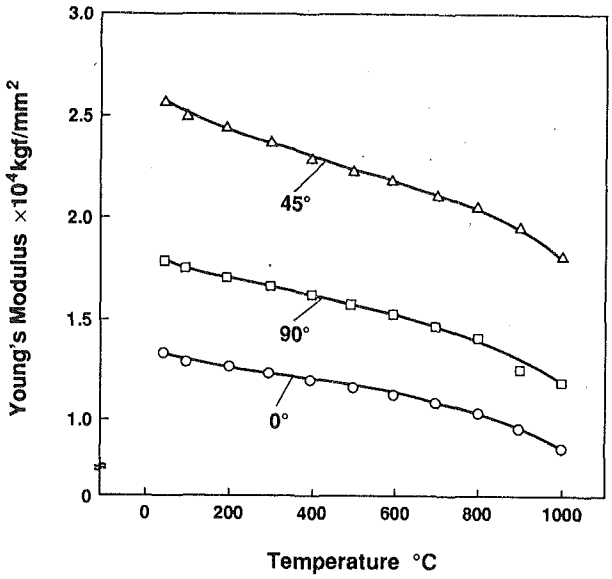

Fig. 18 Young's modulus of DS material

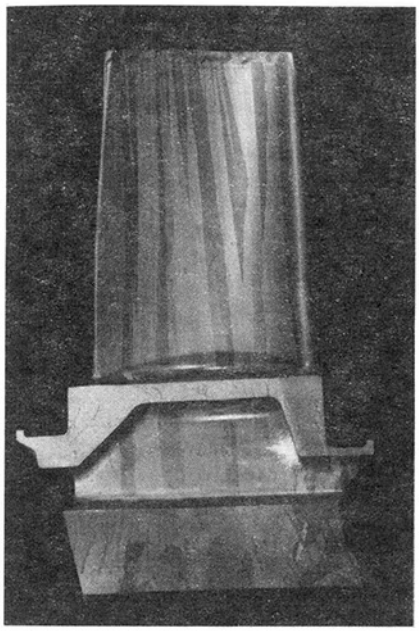

Fig. 19 Macrostructure of trial manufactured DS blade of 150 MW class gas turbine

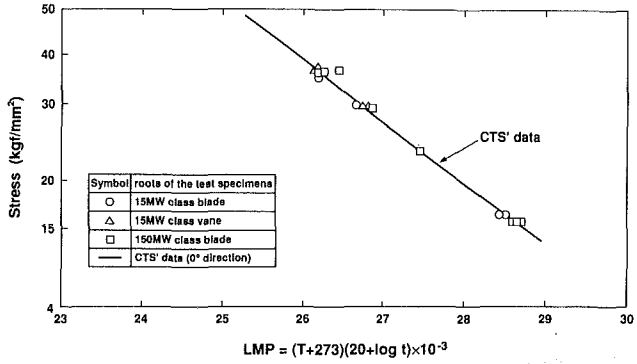

Fig. 20 Creep rupture strength of the test specimens machined from trial manufactured DS blades

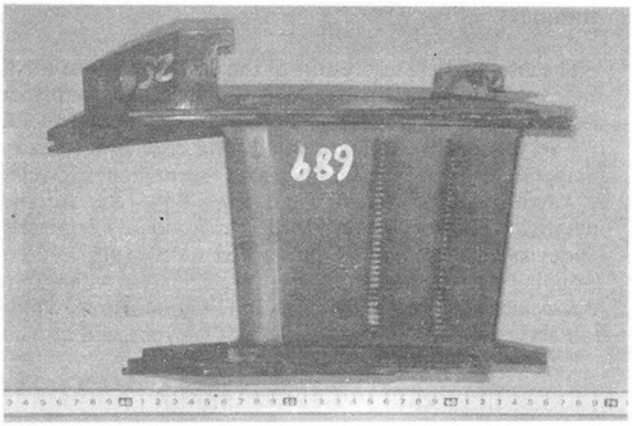

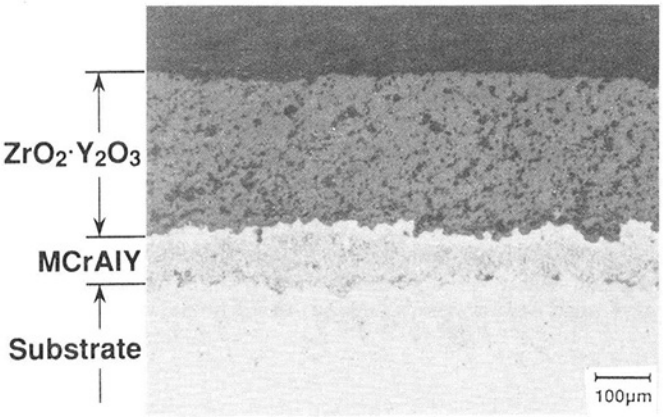

Fig. 21 Appearance and microstructure of TBC-coated vane of 100 MW class gas turbine

metallurgical tests; tensile tests and creep rupture tests were conducted. The creep rupture properties shown in Fig. 20 are acceptable as data for CTS (cast to size) materials.

Development of TBC. To develop a TBC with high-temperature capability, specimen tests were conducted. Also, vanes with TBC are already in use in a 130 MW class gas turbine in 1154°C turbine inlet temperature.

After six months of operation, inspection of these TBC-coated vanes was conducted during a periodic inspection. It was found that there was no damage in the vanes and TBC (Fig. 21) so these vanes are now in commercial use.

Phase II Program

The phase II program of three years started in April, 1992, and will extend through March, 1995. The basic design of the first-stage vanes and blades for the 1500°C class gas turbine will be conducted. In the design of the airfoil, the new aerodynamic data and heat transfer data will be reflected. Also, three-dimensional thermal stress analysis and vibration analysis of the complicated FCFC vane and blade will be completed, and life evaluation will be carried out using the above-mentioned material data.

The cooling performance of the designed FCFC vane and blade are scheduled to be verified through testing in a hot cascade test facility and a high-temperature turbine testing facility with corresponding model vanes and blades. Operating performance data of TBCs will be accumulated via a rainbow test (apply many different kinds of selected TBC) design and applied to the first-stage vane and blade for a 1500°C class gas turbine.

Summary

The intermédiate test results of the development of the first-stage vane and blade for 1500°C class gas turbine are presented describing full-coverage film cooling and material tests. FCFC is a very effective cooling method, and enables a decrease in temperature differences in high heat flux region. However, it is very difficult to control the cooling flow rate. Additional investigations of FCFC are to be carried out. Large size DS blades and vanes were manufactured successfully and corresponding material data showed good correlation with CTS (cast to size material). Reliability data of TBC's will be accumulated by field tests. Tohoku Electric Power Co., Inc., and Mitsubishi Heavy Industries, Ltd., will continue the development of the key technologies for a next generation gas turbine.

References

1 Scalzo, A. J., et al., "A New 150-MW High Efficiency Heavy Duty Combustion Turbine," ASME JOURNAL OF ENGINEERING FOR GAS TURBINES AND POWER, Vol. 111, 1989, pp. 211–217.

2 Entenmann, D. T., North, W. E., Fukue, I., and Mayama, A., "Shop Test of the 501F–A150 MW Combustion Turbine," ASME JOURNAL OF ENGINEERING FOR GAS TURBINES AND POWER, Vol. 113, 1991, pp. 488–494.

3 Kano, K., et al., "Development Study of 1500°C Class High Temperature Gas Turbine," ASME Paper No. 91-GT-297, 1991.

4 Matsuzaki, H., et al., "Investigation of Combustion Structure Inside Low NO_x Combustors for a 1500°C-Class Gas Turbine," ASME Paper No. 92-GT-123, 1992.

Measurement of Residual Stresses in Metal Matrix Composites

P. K. Wright
Aircraft Engine Engineering Division,
GE-Aircraft Engines,
Cincinnati, OH 45215

Metal matrix composites (MMC) are expected to develop internal residual stresses on cooling from fabrication due to the large thermal expansion mismatch between reinforcing fibers and the matrix. This work was undertaken to measure experimentally these residual stresses and compare them with analytical calculations in order to establish clearly their levels and dependence on material parameters. Two techniques for residual stress measurement were investigated: (1) X-ray diffraction (sin^2-psi method) and (2) neutron diffraction. Both techniques gave results in good agreement with analytical predictions for several systems (SCS-6/Ti-24A1-11Nb, W/NiA1, and Al_2O_3NiA1). The results obtained showed a dependence of residual stresses on thermal expansion coefficients, elastic moduli, volume fraction fibers, and matrix yield strengths. The fibers showed compressive stress states, and the matrix, tension. Average stresses were higher in the fiber direction than transverse to fibers.

Introduction

Metal matrix composites (MMC) are expected to develop internal residual stresses due to the large thermal expansion mismatch between reinforcing fibers and the matrix. Calculations of these stresses lead one to expect levels high enough to cause localized matrix yielding in ductile matrices or cracking in some brittle matrices. Besides the obvious undesirable effects of cracking from consolidation, high levels of residual stress in MMC may impact their mechanical properties in service. This work was undertaken to measure residual stresses in MMC experimentally on a microscale and compare them with analytical calculations in order to establish clearly the state of residual stresses existing in MMC.

Approach

Several MMC[1] systems were selected for study. The principal system was a Ti-24A1-11Nb alpha-two titanium aluminide matrix reinforced with approximately 30 percent (by volume) SCS-6 type SiC fibers. The fibers were oriented unidirectionally in four plies and the composite was fabricated by induction plasma deposition (Gigerenzer and Wright, 1991) followed by hot isostatic pressing to yield a dense matrix with about 10 μm grain size. This material was used for comparing the X-ray (XRD) and neutron (ND) diffraction techniques described below. Additional neutron diffraction experiments were performed on two other MMC supplied by NASA Lewis: (1) NiAl matrix (40 μm grain size) reinforced by four unidirectional plies of 35 percent V_f tungsten fibers; (2) NiAl matrix (60 μm grain size) reinforced by four unidirectional plies of 30 percent V_f single crystal Al_2O_3 fibers. The latter two composites were made by the powder cloth method (Bowman and Noebe, 1990).

Two methods for residual stress measurement were investigated: X-ray diffraction and neutron diffraction. X-ray diffraction was performed using the conventional sin^2-psi method, and measurements were taken in the matrix material at the original surface and at various depths from the surface down to the first row of fibers by electropolishing away the matrix. Measurements were taken in both the longitudinal (parallel to fiber) transverse (perpendicular to fiber) directions on both faces of the sample. Raw measurements were corrected for both stress gradients (Koistinen and Marburger, 1959) and sample bending effects (Moore and Evans, 1958).

Neutron diffraction experiments were conducted at the Intense Pulsed Neutron Source at Argonne National Laboratory following the technique outlined by Majumdar et al. (1991). The specimen is placed in the diffractometer with the fiber direction oriented at 45 deg to the beam, and detectors are placed at ± 90 deg to the beam as shown in Fig. 1. Since the beam consists of a range of wavelengths, many diffraction peaks are obtained, representing diffraction from different crystal planes. The spacings from these measurements are compared to those obtained on a stress-free sample, and the residual strain, ϵ_{hkl}, is calculated as

$$\epsilon_{hkl} = (d_{hkl} - d_o)/d_o \quad (1)$$

where d_{hkl} and d_o are the measured interplanar spacings in the stressed and unstressed material, respectively, and hkl are the Miller indices of the diffracting planes. The positions of the two detectors allows measurements to be obtained simultaneously on strains parallel and perpendicular to the fiber directions. Because of the high penetrating power of the beam, sampling of the entire volume of the material (approximately

[1]The term MMC is used here, although all of these matrices are actually intermetallics, rather than true metals.

Contributed by the International Gas Turbine Institute and presented at the 38th International Gas Turbine and Aeroengine Congress and Exposition, Cincinnati, Ohio, May 24-27, 1993. Manuscript received at ASME Headquarters February 18, 1993. Paper No. 93-GT-68. Associate Technical Editor: H. Lukas.

1 cm^3) is possible, including both the fiber and matrix. Since the neutron beam size is appreciably larger than the diameter of the fiber, the average lattice strain in a particular direction of each constituent is obtained. However, this information can be interpreted to give good estimates of some of the local microstrains using knowledge of the nature of the stress distribution within MMC. Specifically, the longitudinal stresses within both the fiber and matrix are expected from micromechanics analyses (see below) to be highly uniform, so that the average stress is also the local stress. In addition, these analyses show that the two transverse stress components within the fiber are equal and also do not vary significantly with position in the fiber. Thus the transverse fiber stress measured should also accurately represent the radial fiber stress at the fiber-matrix interface, and by equilibrium, should be equal to the matrix radial stress at the fiber-matrix interface. The interfacial normal stress is a significant quantity in evaluating the load transfer characteristics in MMC with frictional bonding, such as SCS-6/Ti-24Al-11Nb.

Analytical modeling of the thermal residual stresses expected on the microscale in these composites was conducted using the Concentric Cylinder Model as developed by Hecker (1968). This model has the capability of performing temperature-dependent elastic-plastic analysis of the stresses and strains developed during cooling of the composite from processing. The center cylinder was sized to represent the fiber volume fraction and the fiber (elastic) properties shown in Table 1 were assigned to it. Matrix properties were assigned to the outer rings. The purpose of the multiple rings is to follow the development of plastic flow from the fiber-matrix interface outward during the thermal loading history. The matrix properties used are shown in Table 1 and Fig. 2. Unless otherwise noted, fiber and matrix properties are from internal General Electric programs. Fiber and matrix local and average stresses and strains were computed for the three MMC systems studied to permit comparison to the experimental data. Finite element analysis of these same composites has also been conducted by Saigal et al. (1992). The composite was assumed to be stress free at high temperature and temperature was decreased in increments to room temperature with updating of the temperature-dependent material properties at each step. Bonding between the fiber and matrix was assumed to be complete, i.e., displacement compatibility was enforced in both the axial and radial directions. These composites are known to have relatively weak, frictionally bonded interfaces, but under the state of radial compression interface loading imposed by the cooldown, the clamping forces are high and interface slip is likely only at the very end of these long fibers.

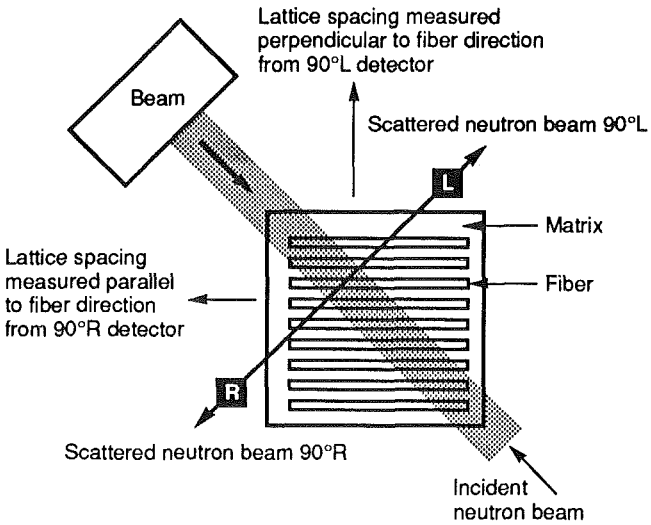

Fig. 1 Neutron diffraction

Results

X-Ray Diffraction. The residual stresses measured in the matrix of the SCS-6/Ti-24Al-11Nb composite are shown in Fig. 3. These results are for both longitudinal and transverse matrix stresses on both sides of the composite sample. At the surface, there appears to be some variability in the stresses, but at depths of 33 and 75 μm, the results are fairly consistent and constant with depth. Tensile stresses were found in both longitudinal (315 MPa average) and transverse (200 MPa average) directions. Longitudinal tensile stresses of this magnitude have been reported in these materials by Cox et al. (1990) and by Jayaraman and Rangaswamy (1993). The variations in surface stresses found here are most likely the result of chemical contamination or surface finishing; it was noted that the X-ray peak widths at the surface were broader than subsurface,

Table 1 Thermal and elastic properties of fibers and matrices used for thermal stress analysis

Material	T(°C)	Elastic Modulus (GPa)	Poisson's Ratio	Thermal Expansion* (mm/mm°/C)
SCS-6	20	414	0.30	4.35 x 10^{-6}
	250	414	0.30	4.35 x 10^{-6}
	500	414	0.30	4.35 x 10^{-6}
	750	415	0.30	5.02 x 10^{-6}
	1000	414	0.30	6.71 x 10^{-6}
W (ASM, 1979)	20	407	0.28	3.86 x 10^{-6}
	500	398	0.29	4.20 x 10^{-6}
	1000	366	0.29	4.60 x 10^{-6}
	1300	351	0.30	4.90 x 10^{-6}
Al_2O_3	20	421	0.20	6.02 x 10^{-6}
	500	413	0.20	9.12 x 10^{-6}
	1000	405	0.20	10.59 x 10^{-6}
	1300	346	0.20	10.67 x 10^{-6}
Ti-24Al-11Nb	20	94.5	0.30	10.11 x 10^{-6}
	250	90.3	0.30	10.44 x 10^{-6}
	500	74.5	0.30	12.05 x 10^{-6}
	750	32.0	0.30	13.77 x 10^{-6}
	1000	6.5	0.30	16.78 x 10^{-6}
NiAl	20	169	0.30	12.91 x 10^{-6}
	500	155	0.30	15.23 x 10^{-6}
	1000	128	0.30	17.12 x 10^{-6}
	1300	81	0.30	17.99 x 10^{-6}

* tangent value

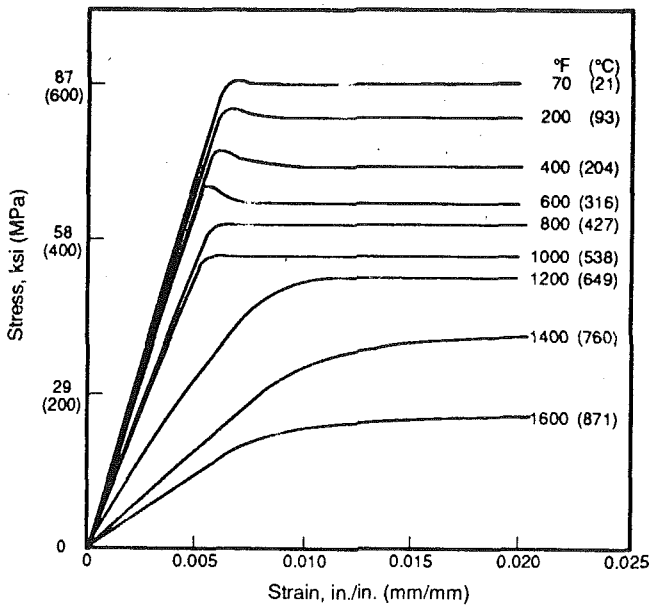

Fig. 2(*a*) Ti-24Al-11Nb

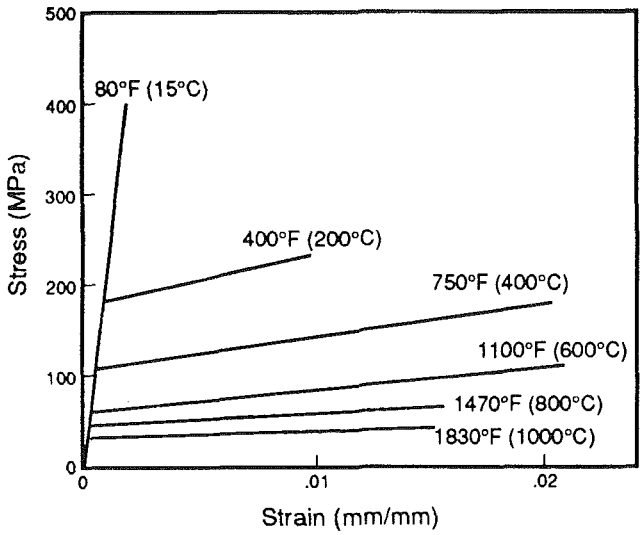

Fig. 2(*b*) NiAl (Noebe et al., 1991)

Fig. 2 Stress-strain properties used in analytical modeling

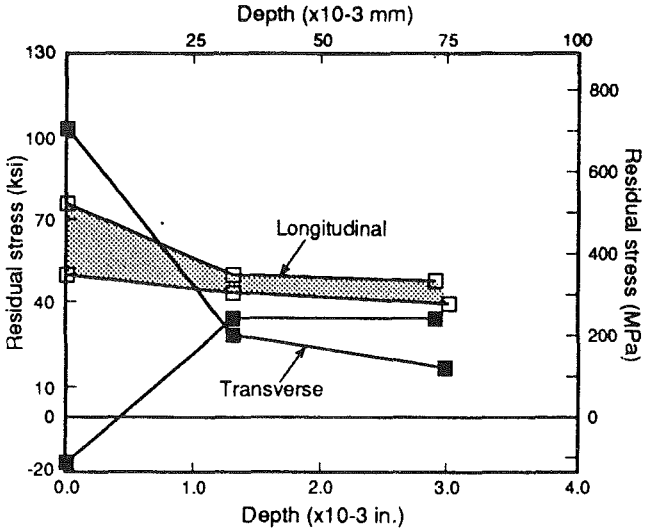

Fig. 3 Matrix residual stresses determined in SCS-6/Ti24Al-11Nb by X-ray diffraction

indicating the presence of disturbed material at the surface. The averages of the measurements at the two subsurface locations are listed in Table 2(*a*) for comparison to the neutron diffraction and analytical model results. Elastic strain values corresponding to these stresses are also presented for purposes of comparison. Attempts were made to obtain diffraction data from the fibers but these were not successful.

Neutron Diffraction

SCS-6/Ti-24Al-11Nb. The residual strains and stresses measured by neutron diffraction are also shown in Table 2(*a*) and Fig. 4. Like the X-ray diffraction results, they indicate the presence of substantial matrix tension in the longitudinal direction and a much lower level of matrix tension in the transverse direction. Quantitatively, the average longitudinal matrix stress measured by neutron diffraction is slightly higher than that measured by X-ray diffraction and the transverse stress is lower. Note that even though the average transverse matrix strain is slightly negative, the average transverse stress is positive because of the strong Poisson effects from the large axial matrix strain component. This effect comes from the Hooke's Law relationship between strain (measured by neutron diffraction) and stress (calculated using elastic constants):

$$\sigma_L^i = \frac{\nu^i E^i}{(1-\nu^i)(1-2\nu^i)}(\epsilon_L^i + \epsilon_T^i + \epsilon_N^i) + \frac{E^i}{(1+\nu^i)}(\epsilon_L^i) \quad (2)$$

$$\sigma_T^i = \frac{\nu^i E^i}{(1+\nu^i)(1-2\nu^i)}(\epsilon_L^i + \epsilon_T^i + \epsilon_N^i) + \frac{E^i}{(1+\nu^i)}(\epsilon_T^i) \quad (3)$$

Here, σ_L^i and σ_L^i are the average longitudinal and transverse stresses, respectively, listed in Table 2 for the fibers ($i = f$) and matrix ($i = m$) phases. E^i and ν^i are the elastic constants at room temperature listed in Table 1, and ϵ_L^i, ϵ_T^i, and ϵ_N^i are the average measured strains in either the fiber ($i = f$) or matrix ($i = m$) in the three principal material directions: longitudinal, transverse, and through-thickness. It was assumed that the composite was transversely isotropic, so $\epsilon_N^i = \epsilon_T^i$. If ϵ_L^i is much larger than ϵ_T^i, as it is in most of the cases here, then the first term in Eq. (3) will dominate the value of σ_T^i. Thus even if ϵ_T^i is slightly negative, σ_T^i can be positive.

In addition to the matrix strains, the fiber strains could be clearly detected, and these are also reported in Table 2. As expected, the fiber is in compression, with the compressive strains and stresses being larger in the longitudinal direction than the transverse.

W/NiAl. The average strains and stresses measured by neutron diffraction in this system are shown in Table 2(*b*) and Fig. 4. Despite the larger thermal expansion and higher stress-free temperature compared to SCS-6/Ti-24A1-11Nb, the elastic strains and stresses were actually lower. The trends among the stresses and strains were similar, however: longitudinal tension in the matrix, longitudinal compression in the fiber, and transverse compression in the fiber and near zero (slightly compressive) transverse stress in the matrix.

Al_2O_3/NiAl. Neutron diffraction results for this system are also shown in Table 2(*c*) and Fig. 4. Even though the thermal expansion coefficient of the alumina fiber is considerably less than that of the tungsten fiber, the residual stresses and strains are approximately the same as the W/NiAl system.

Analytical Modeling. Thermal residual stresses and strains predicted for the SCS-6/Ti-24Al-11Nb composite are shown in Fig. 5 as a function of radial position (distance outward from the axis of the fiber). Because of the radial symmetry of this model, there is no circumferential variation in any of the

Table 2 Measured and calculated average thermal strains and stresses in MMC's

a) SCS-6/Ti-24Al-11Nb (V_f=.25)

		XRD	ND	ANALYSIS
Matrix	Longitudinal Strain (m/m)	+.0032	+.0037	+.0029
	Transverse Strain (m/m)	+.0012	-.0002	-.0004
	Longitudinal Stress (MPa)	+315	+430	+330
	Transverse Stress (MPa)	+200	+160	+ 90
Fiber	Longitudinal Strain (m/m)	------	-.0022	-.0020
	Transverse Strain (m/m)	------	-.0009	+.0003
	Longitudinal Stress (MPa)	------	-1220	-988
	Transverse Stress (MPa)	------	- 770	-270

b) W/NiAl (V_f=.35)

		ND	ANALYSIS
Matrix	Longitudinal Strain (m/m)	+.0013	+.0017
	Transverse Strain (m/m)	-.0005	-.0001
	Longitudinal Stress (MPa)	198	345
	Transverse Stress (MPa)	-36	102
Fiber	Longitudinal Strain (m/m)	-.0012	-.0013
	Transverse Strain (m/m)	+.0001	+.0001
	Longitudinal Stress (MPa)	-584	-640
	Transverse Stress (MPa)	-170	-190

c) Al_2O_3/NiAl (V_f=.30)

		ND	ANALYSIS
Matrix	Longitudinal Strain (m/m)	+.0014	+.0014
	Transverse Strain (m/m)	-.0004	-.0002
	Longitudinal Stress (MPa)	+240	+295
	Transverse Stress (MPa)	+ 6	+ 81
Fiber	Longitudinal Strain (m/m)	-.0011	-.0015
	Transverse Strain (m/m)	+.0003	+.0000
	Longitudinal Stress (MPa)	-445	-689
	Transverse Stress (MPa)	+ 47	-190

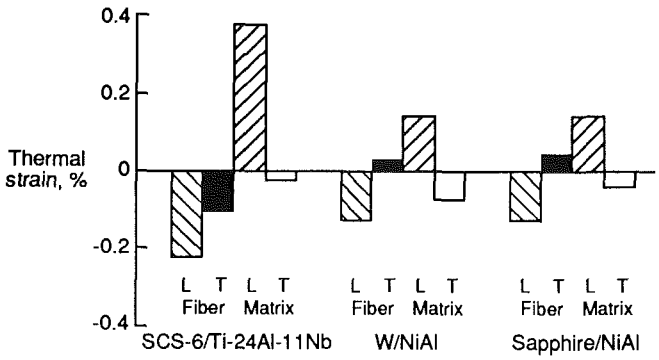

Fig. 4 Residual thermal strains measured by neutron diffraction

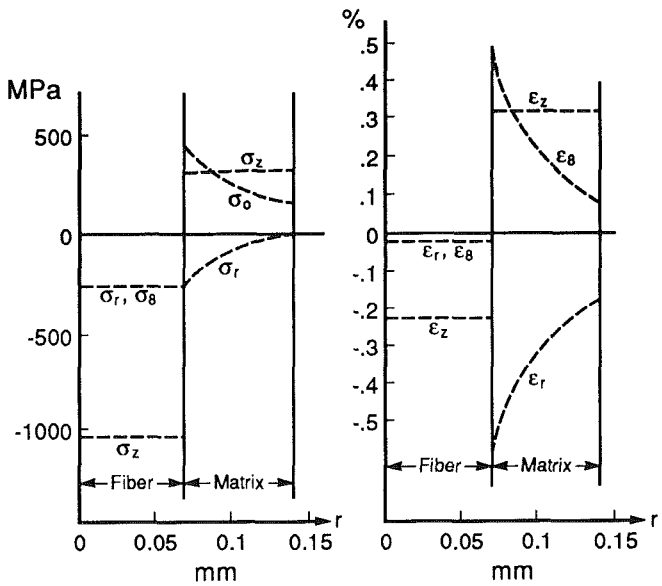

Fig. 5 Fiber and matrix stresses and strains calculated by concentric cylinder model for SCS-6/Ti24Al-11Nb (Vf = 0.25)

stresses. There are also no shear stresses, since the model is for infinitely long fibers for which load transfer is fully complete. As stated above, the stresses in the fiber are compressive and independent of radial location. The longitudinal (z) stresses are considerably higher than the radial (r) and circumferential (θ) stresses. The matrix longitudinal stress and strain are also independent of r, but are tensile in sign. For the material properties and consolidation temperature assumed, the model does not predict yielding in the matrix, but it is quite close. For other conditions studied, the onset of yielding occurs at the fiber-matrix interface and proceeds outward. When yielding does occur, there is a tendency for the axial stress to be lower near the interface and increase with increasing radius. The transverse matrix stresses are predicted to vary with radius, decreasing from their maximum values at the fiber-matrix interface. Note that because of equilibrium condition imposed, the radial stress at the fiber-matrix interface is the same in the fiber and matrix, and the radial stress at the outer radius is zero. Finite element analysis of similar composites shows general similarity of predictions; the stresses now become somewhat dependent on circumferential position, and the average instead of the local radial matrix stress goes to zero at its outer boundary. Predicted average stresses and elastic strains for this system are shown in Table 2 and Fig. 6 for both the concentric cylinder model and the finite element model of Saigal et al. (1992).

Concentric cylinder model predictions were also performed for the two NiAl matrix composites using the properties shown

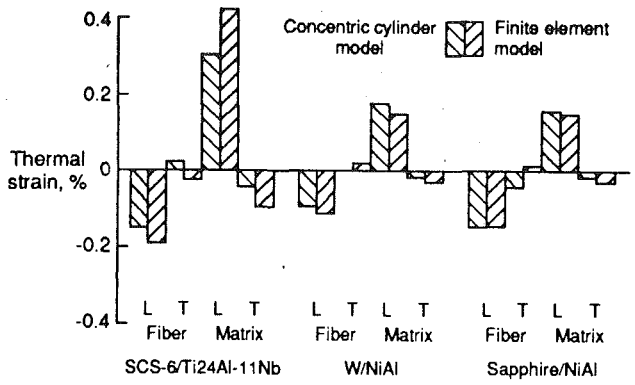

Fig. 6 Comparison of concentric cylinder and finite element models for thermal strain calculations

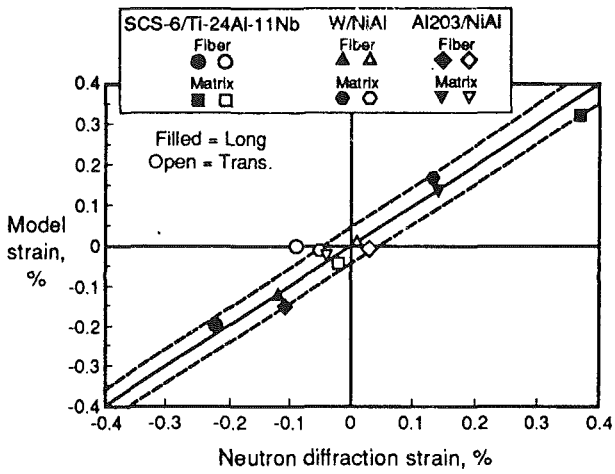

Fig. 7 Comparison of neutron diffraction results with concentric cylinder model

in Table 1 and Fig. 2. The predicted average stresses and elastic strains are shown in Table 2 and Fig. 6. Unlike the SCS-6/Ti24Al-11Nb system, both of these composites show yielding in the NiAl matrix during cooldown, the *W* fiber system showing more yielding than the Al_2O_3 fiber system. Because of this yielding the predicted final matrix stresses in these systems are limited by the flow stress of the matrix at room temperature, and are thus more similar than expected without plasticity. Note that the model calculations for the two NiAl composites were performed at slightly different volume fraction fibers to match the different fiber fractions actually present in the samples tested. The higher fiber fraction in the *W* fiber composite tends to lower the fiber stresses since there is more fiber present to balance the matrix stresses. The fiber fraction difference has a smaller effect on the matrix stresses because of matrix yielding.

Discussion

The average longitudinal and transverse stresses and strains predicted by the concentric cylinder model are given in Table 2 in comparison with the experimental values obtained. These averages were obtained by taking the z, r, and θ coordinate stresses in each cylinder ring, transforming them to a rectangular, z, x and y coordinate system, and then averaging over the volume of each phase (fiber or matrix). For systems in which plastic flow was observed, the strains reported are elastic strain, since this is what is sensed by the diffraction experiments. Stresses for the experimental results were calculated from strains using Hooke's Law and assuming that the strains in the two transverse composite directions were equal.

A graphic comparison of the average analytical and experimental strain values for the three systems studied is shown in Fig. 7. The strains and stresses observed in the fiber by the neutron diffraction method are in generally good agreement with the predictions of the concentric cylinder model, with the correlation being bounded by ± 0.05 percent strain. The transverse fiber strains show the most variation. However, these are also the smallest strains and are thus hardest to measure. The differences between the X-ray and neutron diffraction methods are not large and are probably within experimental scatter.

One check on the validity of the measurements can be obtained by comparing the fiber and matrix longitudinal stresses through the rule of mixtures. Since the net externally imposed stress on the composite is zero, the average fiber and matrix longitudinal stresses should be related through the rule of mixtures:

$$\sigma_L^f V_f + \sigma_L^m (1 - V_f) = 0 \qquad (4)$$

where σ_L^f is the average fiber longitudinal stress, σ_L^m is the average matrix longitudinal stress, and V_f is the fiber volume fraction. Performing this check for the neutron diffraction data shows that the summation of Eq. (4) in all cases gives a net stress ≤ 17 MPa, a value that is equivalent to zero within the experimental error of the measurements. Thus it appears that the experimental data are valid.

For the two NiAl matrix systems studied the development of matrix yielding on cooldown appears to dominate the matrix stresses. Despite rather large differences in fiber thermal expansion, the *W* and Al_2O_3 fiber systems developed very similar stresses. This is predicted by the model (Fig. 6) and confirmed by experiment (Fig. 4).

Finite element predictions performed by Saigal et al. (1992) for the same composite are also shown in Fig. 6. These show slightly better agreement with the experimental results, especially in predicting the sign of the small transverse fiber strain, and the magnitude of the matrix strain and suggest that the concentric cylinder model is slightly inferior in this regard.

Conclusions

1 Neutron and X-ray diffraction techniques for measuring residual stresses in MMC were found to give comparable results to the extent that comparisons were possible. The amount of information available from the neutron diffraction method was greater, and permitted measurement of stresses in both the fiber and matrix.

2 In addition to directly measuring the average stresses and strains in each phase, the local fiber-matrix interfacial stress can be inferred from the average transverse fiber stress.

3 The neutron diffraction method was demonstrated on a variety of composite systems, and consistently gave results in reasonable agreement with analytical predictions. In the SCS-6/Ti-24Al-11Nb system, little or no yielding occurred, and the stresses were controlled by the fiber-matrix thermal expansion mismatch, the elastic properties of the fiber and matrix, and to a lesser extent, the volume fraction fiber. In the NiAl matrix systems, yielding of the matrix occurred well above room temperature, and the fiber-matrix thermal expansion mismatch had little influence on the stresses at room temperature. The yield strength of the matrix controlled stress levels under such conditions.

Acknowledgments

This work was performed under NASA contract NAS3-25790, Alex Vary, Project Manager, and his support in this work is gratefully acknowledged. Drs. Bowman and Noebe of NASA Lewis kindly supplied the NiAl composites. Dr. David Kupperman, Argonne National Laboratory, performed the

neutron diffraction experiments, and Lambda Research, Inc. performed the X-ray diffraction measurements. The efforts of Mark Sensmeier in setting up and running the concentric cylinder model are also appreciated.

References

ASM Handbook Committee, 1979, *Metals Handbook Ninth Edition, Vol. 2, Properties and Selection: Nonferrous Alloys and Pure Metals*, ASM, pp. 816–820.

Bowman, R. R., and Noebe, R. D., 1990, "Processing and Mechanical Evaluation of Continuous Fiber Reinforced NiAl Composites," *HITEMP Review 1990*, NASA Conference Publication 10051, pp. 40–1 to 40–14.

Clark, R. W., and Whittenberger, J. D., 1984, "Thermal Expansion of Binary CoAl, FeAl, and NiAl Alloys," *Thermal Expansion 8*, T. A. Hahn, ed., Plenum Press, pp. 189–196.

Cox, B. N., James, M. R., Marshall, D. B., and Addison, R. C., 1990, "Determination of Residual Stresses in Thin Sheet Titanium Aluminide Composites," *Met. Trans.*, Vol. 21A, pp. 2701–2707.

Gigerenzer, H., and Wright, P. K., 1991, "Plasma Sprayed SCS-6/Titanium Aluminide Composite Test Panels," *Titanium Aluminide Composites*, P. R. Smith, S. J. Balsone, and T. Nicholas, eds., WL-TR-91-4020, pp. 251–264.

Hecker, S. S., 1968, "Elastic-Plastic Analysis of Composite Cylinders in Axial Tension," PhD Thesis, Case Western Reserve University.

Jayaraman, N., and Rangaswamy, P., 1993, "Residual Stresses in Ti_3Al-SCS-6 Fiber Reinforced Metal Matrix Composites," *J. Comp. Res. Technol.*, in press.

Koistinen, D. P., and Marburger, R. E., 1959, *Trans. ASM*, Vol. 51, p. 537.

Majumdar, S., Singh, J. P., Kupperman, D., and Krawitz, A. D., 1991, "Application of Neutron Diffraction to Measure Residual Strains in Various Engineering Composite Materials," ASME *Journal of Engineering Materials Technology*, Vol. 113, pp. 51–59.

Moore, M. G., and Evans, W. P., 1958, "Mathematical Correction for Stress in Removed Layers in X-ray Diffraction Residual Stress Analysis," *Trans. SAE*, Vol. 66, pp. 340–345.

Noebe, R. D., Bowman, R. R., Cullers, C. L., and Raj, S. V., 1990, "Flow and Fracture Behavior of Binary NiAl With Prospects for Future Alloy Development," *HITEMP Review 1990*, NASA Conference Publication 10051, pp. 20–1 to 20–19.

Saigal, A., Kupperman, D. S., and Majumdar, S., 1992, "Residual Strains in Titanium Matrix, High Temperature Composites," *Material Science and Engr.*, Vol. A150, pp. 59–66.

Ceramic Composite Attachments for Transmission of High-Torque Loads

J. W. Brockmeyer

A. C. Straub

E. J. Krieg

Rocketdyne Division,
Rockwell International Corp.,
Canoga Park, CA 91303

The use of fiber-reinforced ceramic matrix composites (FRCMC) for advanced turbopump (T/P) hot-section components offers a number of potential advantages relative to the use of "conventional" materials. Among these advantages are reduced weight, enhanced life with reduced maintenance, and improved performance achievable by increasing the turbine inlet temperature. FRCMC are, however, emerging materials, and their design and analysis present unique challenges. These composites have relatively low thermal expansion coefficients and low strain-to-failure characteristics, and they have nonlinear, anisotropic properties. These characteristics particularly complicate the design of attachments to mating metallic components within a T/P. In an ongoing program,[1] an FRCMC stator and rotor for a rocket engine T/P are being developed for eventual ground test demonstration. The rotor attachment is designed to transmit high-torque loads and provides an example of a design methodology that is compatible with current analytical capabilities. The approach used and described herein applies an empirically derived materials properties data base in combination with macromechanical analysis to reach a solution to this design challenge. This example demonstrates both the capabilities and the limitations of current design and analysis practices and provides direction for future development. A curvic coupling was chosen to meet the specific design goals and will be fabricated and tested to verify the design.

Introduction

Application of FRCMC to rocket engine turbomachinery (T/M) has the potential to: reduce component weights, improve life and decrease maintenance of components subject to high thermal stresses and/or to erosive and corrosive rocket engine environments, and improve performance or efficiency (principally by increasing the turbine inlet temperature) (Brockmeyer and Schnittgrund, 1990). FRCMC are, however, emerging materials, and their ability to withstand the extreme conditions imposed by rocket engine use has not been validated. Of particular concern is the relative lack of anchored design and analysis methods for these complex (nonlinear, anisotropic) materials, which results in the need for substantial levels of empirical verification of analysis predictions. Gaining confidence and eventual acceptance of these materials, then, requires design and analysis of representative components followed by validation through fabrication and testing.

Methods for FRCMC design and analysis continue to be developed and improved. Laminate level analytical methods (Duffy et al., 1993; Thomas and Wetherhold, 1993) for in-plane reliability based on statistical, fast fracture predictions are undergoing rapid development. These analyses are valid for composites composed of unidirectional lamina but are not yet developed and validated for woven laminate structures. Micromechanical analysis methods (Rubinstein, 1993) also have potential to support future designs but are not currently suited to analysis of complex components.

In a NASA Lewis funded program, an FRCMC stator and rotor are being designed and analyzed and, ultimately, will be fabricated for test within a rocket engine T/P. The baseline turbopump selected for this effort is the Mk44F[2] turbopump (Fig. 1), which is a gas generator cycle, liquid oxygen/liquid hydrogen (LOx/LH_2) combustion product propelled T/P. The Mk44F is suitable for demonstrating a number of key characteristics of the FRCMC components on a relatively small, economical scale. To demonstrate the effects of increased turbine inlet temperature, the baseline Mk44F T/P will be modified to increase the inlet temperature from 870°C (1600°F) typically used for conventional stator and rotor materials (e.g., superalloys) to 1200°C (2200°F), which is compatible with currently available and previously identified FRCMC materials. To achieve the increased inlet temperature, current plans

[1]NASA-Lewis Research Center (NASA Lewis) Contract No. NAS3-25468, "Fiber-Reinforced Ceramic Matrix Composites for Earth-to-Orbit Rocket Engine Turbines," Dr. T. P. Herbell, Program Monitor.

Contributed by the International Gas Turbine Institute and presented at the 38th International Gas Turbine and Aeroengine Congress and Exposition, Cincinnati, Ohio, May 24-27, 1993. Manuscript received at ASME Headquarters March 17, 1993. Paper No. 93-GT-324. Associate Technical Editor: H. Lukas.

[2]The Mk44F is a fuel (hydrogen) turbopump originally designed as an auxiliary power unit under Air Force contract.

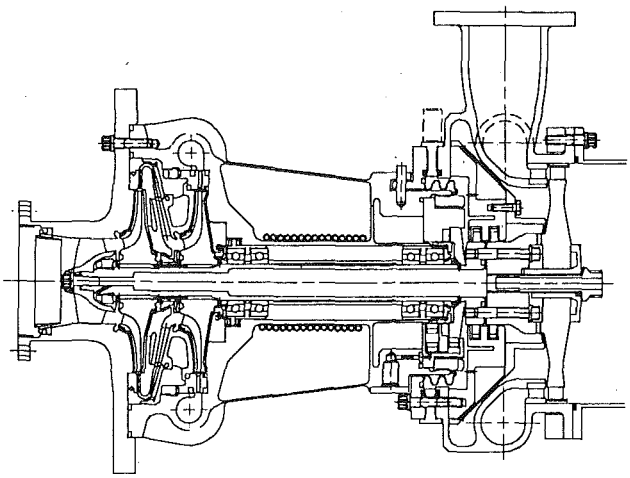

Fig. 1 Modified Mk44F T/P shown with high temperature capability manifold for demonstration of FRCMC stator and rotor

call for the use of a water-cooled turbine inlet manifold fabricated from conventional materials for ground tests. In the future, high temperature capability manifold materials will be used for a flightweight T/P. Also, to simplify and reduce cost of the ground test demonstration, the baseline two-stage turbine will be modified to a single-stage FRCMC turbine.

In previous studies, the preferred material for near-term demonstration of FRCMC materials capabilities was identified to be polar woven, carbon fiber-reinforced silicon carbide (C/SiC) fabricated by chemical vapor infiltration (CVI) (Brockmeyer and Schnittgrund, 1990). Use of polar weaving tailors the in-plane load-bearing capability of the FRCMC to the high in-plane loads encountered in the rotor. C/SiC has been shown to meet the thermal (Eckel and Herbell, 1990) and environmental (Misra, 1990; Herbell et al., 1991) demands imposed by the hydrogen-rich steam combustion environment of the T/P hot section. CVI processing meets near-term, component fabrication requirements.

Design and Analysis Procedures

A structurally acceptable profile for the rotor had previously been designed and analyzed, using an analogous approach to that described for the attachments. Initial concern in profile design focused on the high in-plane mechanical stresses generated during rotor operation, including both bore burst stresses and flow pressure bending stresses expected at the blade tips. However, as the design progressed, out-of-plane stresses (e.g., interlaminar shear and through-thickness tension) were found to have a major influence on the profile design due to the low values of these properties for 2D C/SiC. Throughout the design process, fabrication constraints were also considered. This was accomplished through a concurrent engineering approach with the materials fabricator. For initial analyses, the vendor's (DuPont Lanxide Composites, Wilmington, DE) materials properties data base (Table 1) was used, although this data base has been expanded and refined for subsequent analyses.

The properties data shown are for a 50:50 (balanced), orthogonal, plain woven, fiber architecture. For the initial turbine disk analyses a balanced, 50:50 polar woven fiber architecture was assumed, which is analogous to the balanced orthogonal architecture. That is, the hoop (or circumferential) fibers of the polar weave correspond to the 0 deg orthogonal fibers, and the radial fibers correspond to the 90 deg orthogonal orientation. Future evolutions of the polar layup will further tailor the structure and may employ imbalanced fiber architectures.

Table 1 C/SiC materials properties summary (for 0 deg/90 deg, balanced layup)

PHYSICAL PROPERTIES			
PROPERTY	UNITS	NOMINAL VALUE	
Fiber Content	Vol. %	45	
Density	Gm/cm^3	2.1	
Porosity	Vol. %	10	
MECHANICAL PROPERTIES			
PROPERTY	UNITS	TEMPERATURE	
		23°C	1200°C
Tensile Strength	MPa	425	530
Elongation (Tensile)	%	0.93	1.0
Initial Young's Modulus (Tensile)	GPa	76	120
Compressive Strength (In-Plane)	MPa	520	
Flexural Strength	MPa	454	
Flexural Elongation	%	0.72	
Flexural Modulus	GPa	68.3	
Cross-Ply Tensile Strength	MPa	11.9	
Shear Strength (Interlaminar)	MPa	26	
Fracture Toughness	MPa·m$^{1/2}$	40	
THERMAL PROPERTIES			
PROPERTY	UNITS	TEMPERATURE	
		23°C	1000°C
In-Plane CTE*	10^{-6}/°C	3	3
Thru-Thickness CTE	10^{-6}/°C	5	5
In-Plane Diffusivity	10^{-6}m^2/S	11	7
Thru-Thickness Diff.	10^{-6}m^2/S	5	2
Specific Heat	J/kg°C	620	1400
Total Emissivity	---	0.8	0.8
In-Plane Conductivity	Wm^{-1}•°C^{-1}	14.3	20.6
Thru-Thickness Cond.	Wm^{-1}•°C^{-1}	6.5	5.9

* - Coefficient of Thermal Expansion

Using the torque loads anticipated for the modified Mk44F T/P design, a series of possible attachments were then evaluated. The objectives were to maintain acceptable loads within the rotor profile while simultaneously achieving acceptable loads within the attachments or couplings. In addition to torque transmission, the attachment must maintain rotor centering to the shaft during the severe transient and mainstage operation. Analyses were based on fast fracture criteria. Statistically derived design allowables were used when sufficient data were available, or factors of safety were applied where data were inadequate for statistical analysis. Coupon tests were run that verified durability of C/SiC under the proposed operating conditions and which support use of fast fracture properties. Coupon tests showed that only extreme conditions of thermal shock combined with environmental exposure resulted in degradation of properties.

Analyses were macromechanical and used two-dimensional (2D), ANSYS finite element models. Orthotropic materials properties were input to determine principal in-plane and out-of-plane stresses. Initial cases considered mechanically induced loads and used as-received, room temperature materials properties. Refined analyses of the preferred attachments additionally considered effects of mechanical cycling and thermal

Nomenclature

T/P = turbopump
FRCMC = fiber-reinforced ceramic matrix composites
T/M = turbomachinery
Mk44F = Mark 44 fuel (hydrogen) turbopump
LO_x/LH_2 = liquid oxygen/liquid hydrogen
C/SiC = carbon fiber-reinforced silicon carbide
CVI = chemical vapor infiltration
2D = two-dimensional
OD = outer diameter
ID = inner diameter
WI = Williams International

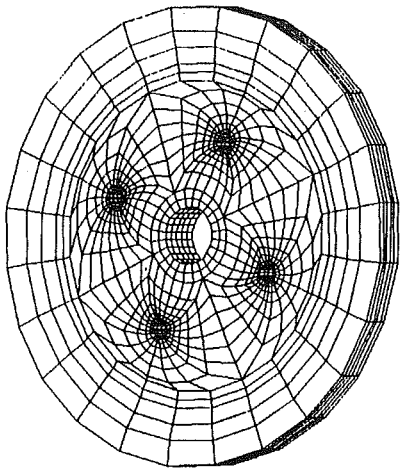

FRCMC ROTOR / Centrif. load • RT / 0.25" diam. hole at r=1.4"

Fig. 2 Stud drive (overview)

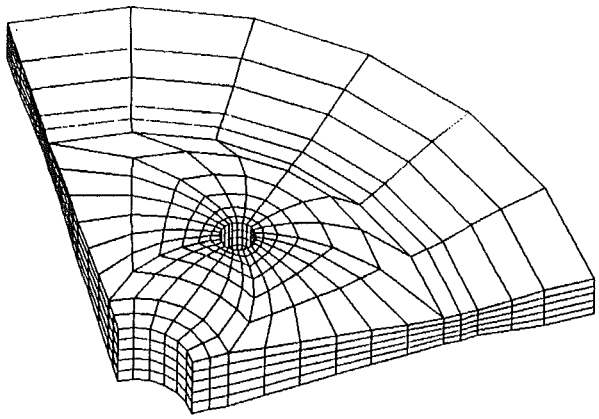

FRCMC ROTOR / Centrif. load • RT / 0.25" diam. hole at r=1.4"

Fig. 3 Stud drive (detail)

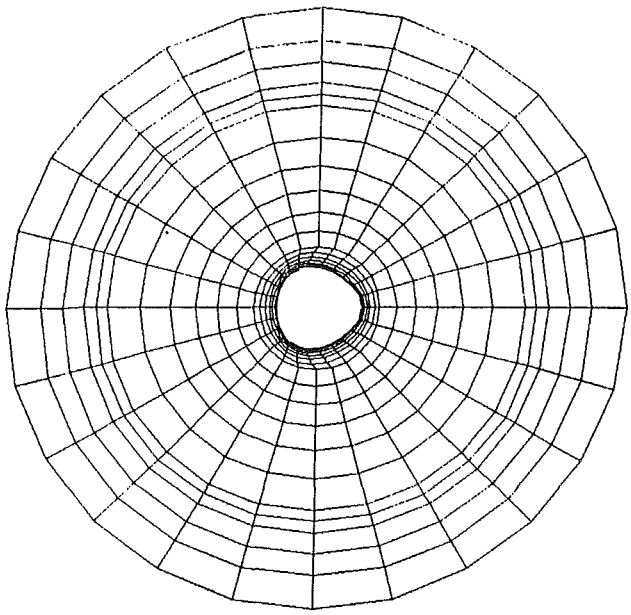

FRCMC ROTOR With 7/8" Polygonal Drive / Centrif. load at RT

Fig. 4 Polygonal shaft drive (overview)

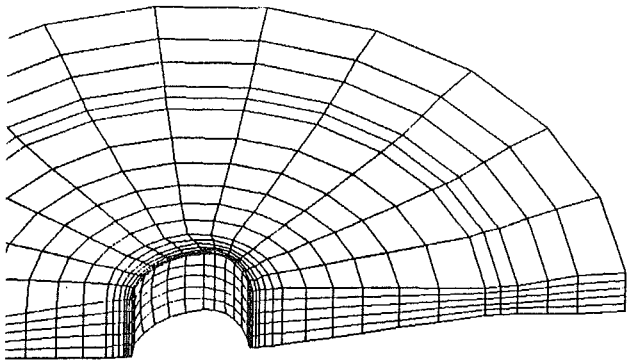

FRCMC ROTOR With 7/8" Polygonal Drive / Centrif. load at RT

Fig. 5 Polygonal shaft drive (detail)

loading effects. The design of the couplings followed an evolutionary approach, drawing upon lessons learned in previous cases until an acceptable, conceptual design was developed.

Results and Discussion

Conventional coupling methods used with metallic rotors were modified for use with the FRCMC rotor profile. Loads were analyzed for representative operating conditions as described below.

Stud Drive. The possibility of using studs to carry the torque loads was evaluated (Figs. 2 and 3). The model included 4 @ 0.64 cm (1.4 in.) diameter through-holes located at a radius of 3.56 cm (1.4 in.) on the 16 cm (6.3 in.) outer diameter (OD) disk. Qualitative consideration was given to other hole diameters. Results were unacceptable primarily due to the high hoop stresses (366 MPa 53.1 ksi]) within the holes. Consequently, the holes were moved outward to avoid the high inertial hoop and radial loads encountered at the 3.56 cm (1.4 in.) radius. Very high Hertzian contact loads (approximately 331 MPa [48 ksi]) for a typical bolt at this location combined with the inertial loading (262 MPa [38 ksi]) also were considered unacceptable.

Polygonal Shaft. Use of a three-lobed polygonal shaft with a nominal 2 cm (0.8 in.) minimum bore (compatible with fabrication constraints) (Figs. 4 and 5) resulted in unacceptable (384 MPa [55.7 ksi]) hoop loads from centrifugal loading only. Consideration of a reduced bore diameter resulted in unacceptable hoop inertial stresses due to the concentration of loads in the reduced radius of the lobes. Torque loading resulted in an additional 69 MPa (10 ksi) hoop stress.

Extruded, Splined Hub. An extruded, splined flange with a 0.8 cm (0.3 in.) fillet was considered (Fig. 6). In addition to centrifugal loading, various hub face preloads were added to reduce through-thickness tension and interlaminar shear loads. The preferred preload was estimated to be 14 MPa (2 ksi). Even with this preload, interlaminar shear and through-thickness tensile loads were unacceptable (40 MPa [5.8 ksi] and 27 MPa [3.9 ksi], respectively) due to the steep taper angles in the vicinity of the flange.

Inner Diameter (ID) Radial "Gear" Use of an ID (hub) spur gear type arrangement (Fig. 7) was also found unacceptable. The stress concentration in the vicinity of the gear teeth resulted in excessive (525 MPa [76.1 ksi]) hoop stresses.

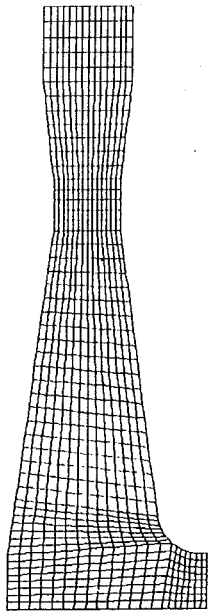

Fig. 6 Extruded, splined hub

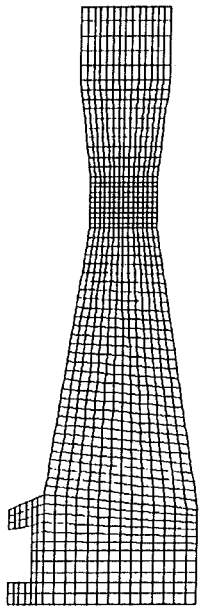

Fig. 8 Hub internal face spline concept No. 1

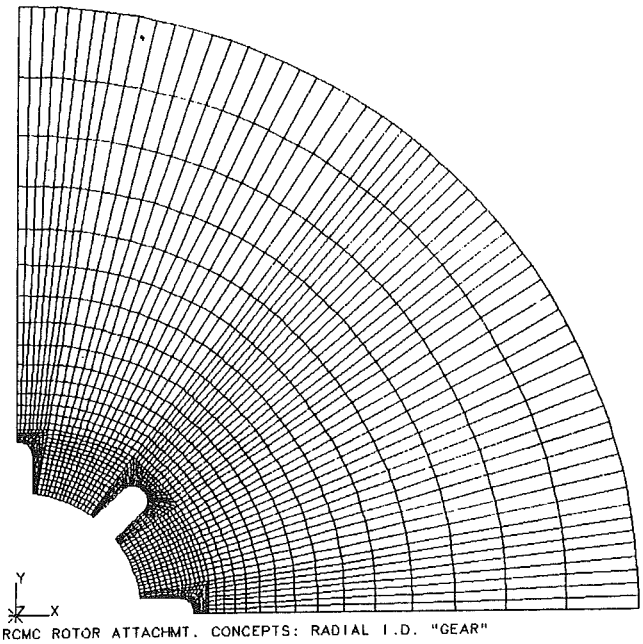

Fig. 7 ID radial "gear"

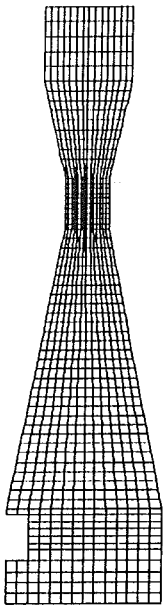

Fig. 9 Hub internal spline concept No. 2

Hub Internal Face Spline. The possibility of using a hub internal spline (Figs. 8 and 9) was evaluated with the previously developed rotor profile. No significant changes were observed in hoop and radial loads versus the profile without couplings, but interlaminar shear (35.2 MPa [5.1 ksi]) and through-thickness tension (39.2 MPa [5.7 ksi]) loads were unacceptable due to the sharp taper in the extruded section of the hub where the splines were located. An alternative was evaluated (Fig. 8) without extrusion of the hub section. Hoop loading was slightly reduced to 277 MPa (40.2 ksi), but isolated areas of unacceptable interlaminar shear and through-thickness tension loading were observed.

Curvic Coupling. A standard curvic coupling, precision face spline with 20 teeth (Fig. 10) was analyzed using the rotor profile. The teeth were located at a 5.3 cm (2.1 in.) ID based on initial T/P conceptual design requirements. Inertial loads (60,000 rpm at room temperature) were analyzed first. Based on inertial loading only, this was determined to be the preferred coupling concept. Hoop loads (325 MPa [47.1 ksi]) were nominally acceptable. Peak radial stress was 163 MPa (23.7 ksi). A peak interlaminar shear load of 32.4 MPa (4.7 ksi) was found in an isolated volume near the curvic fillet. This stress was greater than allowable, but compressive loading from the metallic, mating component had not been factored into the analysis. Also, previous studies had indicated that ability to survive high, calculated interlaminar shear loads in isolated regions may be greater than anticipated and requires experimental verification. Based on these considerations, this curvic design was tentatively considered acceptable, and more extensive analyses were performed.

Additional stresses could be expected to be generated as a

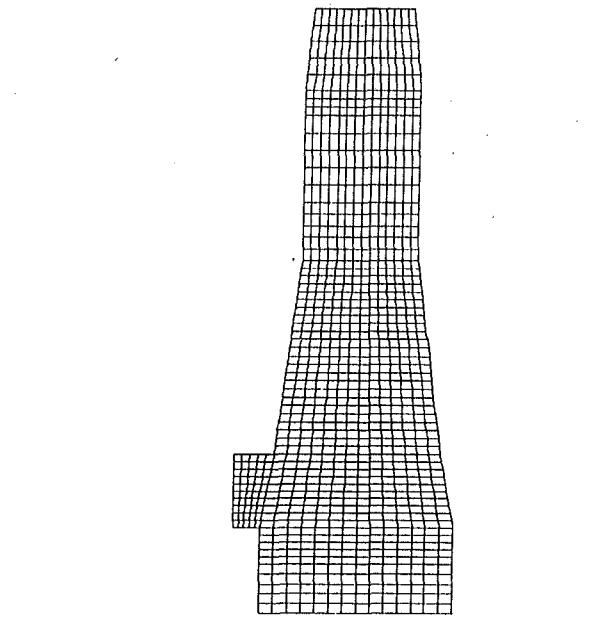

Fig. 10 Curvic coupling

result of thermal expansion mismatch between the FRCMC disk and the mating metallic component. 2D thermal analyses were run of the disk in the vicinity of the curvic. Results of this modeling are being input to a more detailed structural model, which considers the impact of the thermal expansion mismatch. Initial results indicate that the difference in radial growth between the metallic and FRCMC components is acceptable. Further analysis of this concept is in progress. An allowance for limited relative growth can be accommodated within the tooth geometry.

Summary and Conclusions

Use of FRCMC components in advanced T/M requires the development of attachment and coupling concepts that are compatible with the nonlinear and anisotropic properties of these materials and that account for the relatively low thermal expansion and strain-to-failure characteristics of the material. The low interlaminar shear and through-thickness tension strengths of these materials require more detailed analysis than that for conventional, isotropic materials. Current analytical tools are limited to macromechanical analysis and, in practice, an empirical, evolutionary design approach proves to allow for effective utilization of the available tools.

For the example discussed, a curvic coupling provides an apparently effective solution to the challenge of transmitting the high torque loads generated by a rocket engine turbopump. Work is continuing to analyze further the thermal expansion mismatch effects, and preliminary results are promising. Ultimately, experimental validation of these concepts is needed. As a first step in this direction, machining studies are planned to validate capabilities of fabricating curvic couplings as part of an FRCMC component. Following these machining studies, an FRCMC curvic coupling will be fabricated and tested to verify its torque handling capabilities.

Acknowledgments

The authors gratefully acknowledge the support of a number of contributors within Rocketdyne who have provided continuing technical and management support to this effort, including Linsey Orr, Jim Tellier, Gary Tuttle, and John Wooten. They would also like to thank the many personnel at DuPont and Williams International who have played a key role in supporting this concurrent engineering effort. Finally, they wish to thank NASA Lewis for their sponsorship of much of this work.

References

Brockmeyer, J. W., and Schnittgrund, G. D., 1990, "Fiber-Reinforced Ceramic Matrix Composites for Earth-to-Orbit Rocket Engine Turbines, Phase I—Final Report," NASA CR-185624, July.

Duffy, S. F., Palko, J. L., and Gyekenesi, J. P., 1993, "Structural Reliability Analysis of Laminated CMC Components," ASME JOURNAL OF ENGINEERING FOR GAS TURBINES AND POWER, Vol. 115, Jan. pp. 103–108.

Eckel, A. J., and Herbell, T. P., 1990, "Thermal Shock of Fiber Reinforced Ceramic Matrix Composites," *Proceedings of the 13th Annual Conference on Composite Materials and Structures*, NASA CP-3054, Part 1, pp. 153–162.

Herbell, T. P., Eckel, A. J., Hull, D. R., and Misra, A. K., 1991, "Effect of Hydrogen on the Strength and Microstructure of Selected Ceramics," in: *Environmental Effects on Advanced Materials*, R. H. Jones and R. E. Ricker, eds., Proceedings of Fall 1990 TMS/ASM Meeting, The Minerals, Metals, and Materials Society, pp. 159–172.

Misra, A. K., 1990, "Thermodynamic Analysis of Chemical Stability of Ceramic Materials in Hydrogen Containing Atmospheres," NASA Contractor Report 4271, Sverdrup Technology Inc., Cleveland, OH.

Rubinstein, A. A., 1993, "Micromechanical Analysis of the Failure Process in Ceramic Matrix Composites," ibid., pp. 122–126.

Thomas, D. J., and Wetherhold, R. C., 1993, "Reliability Analysis of Ceramic Matrix Composite Laminates," ibid., pp. 117–121.

Stiffness Degradation in Metal Matrix Composites Caused by Thermomechanical Fatigue Loading

S. Aksoy
Textron Lycoming,
Stratford, CT 06497

Damage during thermomechanical fatigue loading of a metal matrix composite is represented by a vector. The undamaged material is characterized by the generalized Hooke's law for transversely isotropic materials. The residual elastic properties of metal matrix composite are related to the initial elastic properties by the damage vector. The residual stiffness properties are then correlated with the number of fatigue cycles to failure. The ability to use this concept to determine the safe strength requirement for a given cyclic life is discussed.

I Introduction

Metal matrix composites (MMC) are currently being considered for advanced gas turbine components because of their high strength-to-density ratio at high temperatures. For safe application of these new materials, their failure mechanisms and modes must be understood and a life prediction method, which incorporates the effects of isothermal and thermomechanical fatigue, must be developed. Figure 1 shows the major building blocks for development of a fatigue life model. The first step in the development of a life prediction model is a characterization of damage done in a given loading event. In general damage is defined as the progressive change in a material's microstructure that eventually results in crack initiation. The second step is to establish the sequential development of the damage mechanisms and to quantify the growth rates of the mechanisms. With this knowledge, models for predicting the fatigue behavior of composites can be developed. The investigation of damage accumulation mechanisms and failure modes requires a data base to develop the relationship between macromechanical parameters and fatigue initiation resistance. In development of a data base, one of the most critical steps is the selection of experimental procedure that simulates the component operating environment.

Hot section components of aircraft gas turbine engines are subjected to severe thermal-structural loading conditions during the engine mission cycle. The most damaging stresses and strains are those induced by the steep thermal gradients, which occur during the start-up and shutdown transients. The thermomechanical fatigue (TMF) damage produced by this thermal mechanical cycling can often shorten component life. Experimental work on monolithic materials in the literature reveals that isothermal fatigue data obtained at various temperatures cannot be readily applied to TMF loading conditions because the mechanics of fatigue are often different at the extremes of temperature in the TMF cycle. Thermomechanical fatigue damage can be investigated by independently cycling mechanical load (stress or strain) and temperature, either "in-phase" or "out-of-phase." For this study, a test is defined as in-phase when the maximum temperature coincides with the maximum positive stress. In contrast, a test is defined as out-of-phase when the maximum temperature coincides with the minimum

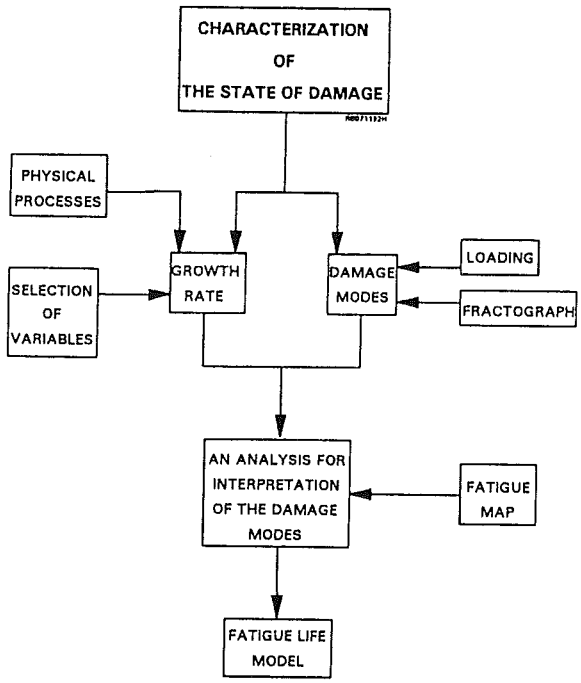

Fig. 1 Metal matrix composite life prediction approach

Contributed by the International Gas Turbine Institute and presented at the 38th International Gas Turbine and Aeroengine Congress and Exposition, Cincinnati, Ohio, May 24-27, 1993. Manuscript received by the ASME Headquarters March 17, 1993. Paper No. 93-GT-318. Associate Technical Editor: H. Lukas.

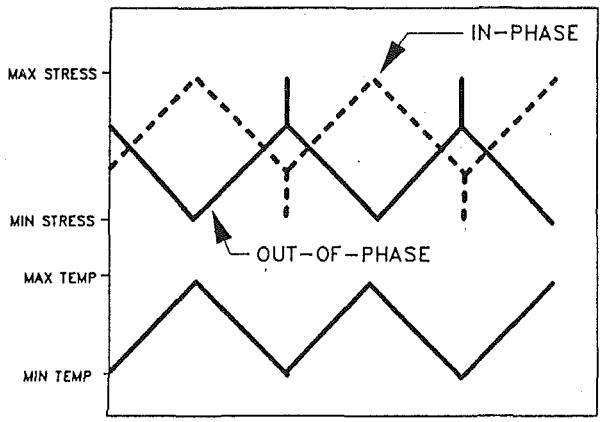

Fig. 2 Thermomechanical fatigue cycles used in this investigation

stress and the minimum temperature coincides with the maximum stress. Figure 2 illustrates the temperature and stress waveforms used for out-of-phase and in-phase tests and their phasing relationship used in this investigation. TMF testing has been used to study fatigue resistance of many monolithic structural alloys [1–6] and, recently, composite systems [7, 8]. Several approaches to the prediction of monolithic material fatigue behavior under TMF conditions have been developed [1, 2, 5, 6]. The resulting complexity of the experimental data has precluded the development of a general model of thermomechanical fatigue. Damage mechanisms in a unidirectional titanium matrix composite with silicon carbine fibers subjected to thermomechanical and isothermal fatigue cycling were reported by several authors [7–11]. It was shown that damage mechanisms leading to failure would be effective in a limited range of applied loading parameters. Based on this observation, the fatigue-life curve would consist of different components, each corresponding to the underlying damage mechanism. Therefore, it is necessary to identify the regions of dominance by damage mechanisms in MMC system under TMF loading and to develop relationships in terms of appropriate parameters, which will allow predictions of structural behavior and life. All these studies show that the damage can take many forms: matrix cracking, fiber breakage, and interface failure during TMF cycling. With this diversity of damage mechanisms, it was observed that the stiffness properties of composites were degraded during fatigue cycling. In other words, static strength, stiffness, and cyclic life are part of the design phenomenon.

In this paper, the overall stiffness properties characterizing the deformation response of a damaged SiC(SCS-6)/Ti-6-4 composite under thermomechanical loading are discussed. Damage is represented by a vector calculated using a continuum mechanics model. The material constants in the damaged stiffness matrix are taken as parameters for investigating the relationship between damage mechanisms and number of cycles to failure. In addition, fatigue-damage diagrams are discussed relative to the roles of the damage mechanisms in determining the damage accumulation mechanisms. The ultimate objective of the ongoing investigation is to understand and relate damage state, stiffness, residual strength, and fatigue life into a life model.

II Continuum Mechanics Characterization of Damage

To date, considerable efforts have been made to define the damage mechanisms in composite systems [7–11]. The results of these investigations revealed the importance of stiffness in characterization of damage in composites and led to intensified search to establish an analytical relationship between stiffness degradation and the extent of damage [12–17]. Among the various approaches that have been proposed in the literature, the first was the expression for the overall elastic constants based on the elastic energy associated with a single crack [15]. Another method, which is based on a general approximate method known as the "self-consistent scheme," assumes the elastic moduli of lamina with matrix cracks to be given by the effective moduli of an infinite medium with the same fiber volume fraction and crack density as in the cracked lamina [16]. In the following, a brief derivation of expressions based on continuum mechanics characterization of damage is given. The detailed discussion can be found in [17].

In [0°] unidirectional metal matrix composites, it is assumed that damage occurs as cracks normal to the fiber. The damage vector is given by

$$V = D_I(1,\ 0,\ 0) \tag{1}$$

The stiffness components of a damaged composite are given by

$$C_{pq} = C^0_{pq} + C^1_{pq} \tag{2}$$

The coefficient matrix C^0_{pq} determines the elastic response of the virgin material, while the coefficient matrix C^1_{pq} characterizes the change in the elastic response of a damaged material whose damage state is described by a vector field V. The coefficient matrix C_{pq}, given by Eq. (2), characterizes the current elastic response of a damaged composite. The coefficient matrix C^0_{pq} is the elastic coefficient matrix for the generalized Hooke's law for transversely isotropic materials. The coefficient matrix C^1_{pq} for this damage takes the form

$$C^1 = \begin{bmatrix} C^1_{11} & C^1_{12} & C^1_{13} & 0 & 0 & 0 \\ C^1_{21} & C^1_{22} & C^1_{23} & 0 & 0 & 0 \\ C^1_{31} & C^1_{32} & C^1_{33} & 0 & 0 & 0 \\ 0 & 0 & 0 & C^1_{44} & 0 & 0 \\ 0 & 0 & 0 & 0 & C^1_{55} & 0 \\ 0 & 0 & 0 & 0 & 0 & C^1_{66} \end{bmatrix} \tag{3}$$

The coefficients of the matrix C^1 are given by the following:

$$C^1_{11} = 2a_4V_1^2 + 2a_5V_2^2 + 2a_6V_3^2$$

$$C^1_{12} = C^1_{21} = a_{10}V_1^2 + a_{11}V_2^2 + a_{12}V_3^2$$

$$C^1_{13} = C^1_{31} = a_{13}V_1^2 + a_{14}V_2^2 + a_{15}V_3^2$$

$$C^1_{22} = 2b_3V_1^2 + 2b_4V_2^2 + 2b_5V_3^2$$

$$C^1_{23} = C^1_{32} = b_9V_1^2 + b_{10}V_2^2 + b_{11}V_3^2$$

$$C^1_{33} = 2c_2V_1^2 + 2c_3V_2^2 + 2c_4V_3^2$$

$$C^1_{44} = \frac{1}{2}d_2V_1^2 + \frac{1}{2}d_3V_2^2 + \frac{1}{2}d_4V_3^2$$

$$C^1_{55} = \frac{1}{2}e_2V_1^2 + \frac{1}{2}e_3V_2^2 + \frac{1}{2}e_4V_3^2$$

$$C^1_{66} = \frac{1}{2}f_2V_1^2 + \frac{1}{2}f_3V_2^2 + \frac{1}{2}f_4V_3^2 \tag{4}$$

where V_1, V_2 and V_3 are the components of the damage vector (see Eq. (1)), and where the coefficients $a_4, \ldots, f_2$ are to be determined.

For the special case of damage given by Eq. (1), the coefficient matrix C^1s are given by

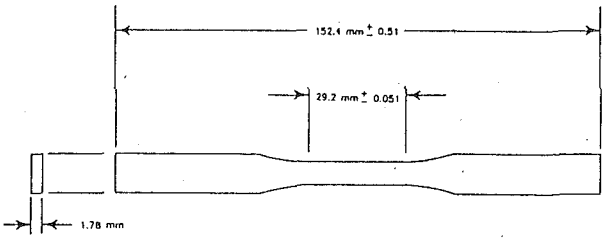

Fig. 3 Specimen detail

$$D_I^2 \begin{bmatrix} 2a_4 & a_{10} & a_{13} & 0 & 0 & 0 \\ a_{10} & 2b_3 & b_9 & 0 & 0 & 0 \\ a_{13} & b_9 & 2c_2 & 0 & 0 & 0 \\ 0 & 0 & 0 & \frac{1}{2}d_2 & 0 & 0 \\ 0 & 0 & 0 & 0 & \frac{1}{2}e_2 & 0 \\ 0 & 0 & 0 & 0 & 0 & \frac{1}{2}f_2 \end{bmatrix} \tag{5}$$

Let us consider an orthotropic composite subjected to damage that preserves the orthotropic symmetry of the elastic coefficients.

The classical elastic constitutive equations for in-plane behavior can now be written as follows:

$$\begin{Bmatrix} \sigma_1 \\ \sigma_2 \\ \sigma_6 \end{Bmatrix} = \begin{bmatrix} C_{11} & C_{12} & 0 \\ C_{21} & C_{22} & 0 \\ 0 & 0 & C_{66} \end{bmatrix} \begin{Bmatrix} \epsilon_1 \\ \epsilon_2 \\ \epsilon_6 \end{Bmatrix} \text{ or}$$

$$\begin{Bmatrix} \epsilon_1 \\ \epsilon_2 \\ \epsilon_6 \end{Bmatrix} = \begin{bmatrix} S_{11} & S_{12} & 0 \\ S_{21} & S_{22} & 0 \\ 0 & 0 & S_{66} \end{bmatrix} \begin{Bmatrix} \sigma_1 \\ \sigma_2 \\ \sigma_6 \end{Bmatrix} \tag{6}$$

where the coefficients of the inverse of the matrix C are given by

$$S_{11} = \frac{C_{22}}{C_{11}C_{22} - C_{12}^2}$$

$$S_{12} = S_{21} = \frac{-C_{12}}{C_{11}C_{22} - C_{12}^2}$$

$$S_{22} = \frac{C_{11}}{C_{11}C_{22} - C_{12}^2}$$

$$S_{66} = \frac{1}{C_{66}} \tag{7}$$

The elastic constants defined by the Young's moduli E_1 and E_2, the shear modulus G_{12} and the two Poisson ratios ν_{12} and ν_{21} are given by

$$E_1 = \frac{1}{S_{11}} = \frac{C_{11}C_{22} - C_{12}^2}{C_{22}}$$

$$E_2 = \frac{1}{S_{22}} = \frac{C_{11}C_{22} - C_{12}^2}{C_{11}}$$

$$G_{12} = \frac{1}{S_{66}} = C_{66}$$

$$\nu_{12} = -\frac{S_{12}}{S_{11}} = \frac{C_{12}}{C_{22}}$$

The coefficients C_{pq}^1 given by Eq. (4) can be substituted in the first of Eqs. (8):

Table 1 Test matrix; out-of-phase minimum cyclic temperature = 120°C

	Maximum cyclic temperature					
	370°C	425°C	450°C	540°C	590°C	650°C
Stress, MPa	1090 1215	1090	1090	1090	1090	1090

$$\nu_{21} = -\frac{S_{12}}{S_{22}} = \frac{C_{12}}{C_{11}} \tag{8}$$

Using the relationship $C_{pq} = C_{pq}^0 + C_{pq}^1$, the relations for the elastic constants are obtained as follows:

$$E_1 = E_1^0 + D_I^2[2a_4 + 2b_3(\nu_{12}^0)^2 - 2a_{10}\nu^0]$$

$$E_2 = E_2^0 + D_I^2[2b_3 + 2a_4(\nu_{21}^0)^2 - 2a_{10}\nu^0]$$

$$\nu_{12} = \nu_{12}^0 + D_I^2\left(\frac{1 - \nu_{12}^0\nu_{21}^0}{E_2^0}\right)(a_{10} - 2b_3)$$

$$\nu_{21} = \nu_{21}^0 + D_I^2\left(\frac{1 - \nu_{12}^0\nu_{21}^0}{E_1^0}\right)(a_{10} - 2a_4)$$

$$G_{12} = G_{12}^0 + 1/2f_2D_I^2 \tag{9}$$

It should be noted here that all elastic constants change with damage considered. To determine the elastic constants, four unknown coefficients are required. Conversely, for a damaged state, measurement of the four independent elastic constants will determine the unknown coefficients. Once these coefficients are determined, the change in the elastic constants can be related to the magnitude of the damage vector. This provides a basis for monitoring damage through elastic coefficient changes.

III Material and Experimental Procedure

The composite system considered in this investigation consists of silicon carbide fibers (SCS-6 produced by Textron Specialty Materials) in a Ti-6Al-4V matrix. Panels were fabricated using the foil-fiber-foil method. The lay-up consisted of eight plies of continuous 0° (longitudinal) oriented fibers in a matrix providing a nominal volume fraction of 35 percent. The overall panel thickness was 1.78 mm. Longitudinally oriented test specimens, Fig. 3, were cut from the panels using wire EDM. The cut surfaces were then polished to remove any surface damage.

All tests were conducted on a computer-controlled, servo-hydraulic test system employing direct induction heating with forced air cooling cycles. All tests were performed on specimens with the fiber oriented in line with the loading axis and in an air environment. All experiments were run to failure under load control, tension-tension conditions with a minimum/maximum stress ratio (R) of 0.05. Here failure was defined as complete fracture (separation of the specimen into two pieces). The test matrix, shown in Table 1, was formulated to investigate the behavior of the composite over its full working temperature spectrum. Throughout each test the maximum and minimum strain were monitored in an attempt to correlate change in compliance with damage accumulation.

The initial load or stress was established by obtaining a maximum strain value of 0.50 percent at the peak point of the initial cycle and a minimum strain of 0.05 percent at minimum point of the initial cycle. This yielded a strain range of 0.45 percent at start-up point for all the out-of-phase tests involved in the study. Heating rates ($\dot{T}$) ranging from approximately 4.4°C per second to approximately 14.4°C per second and stress rates ($\dot{\sigma}$) ranging from 7 MPa per second to approximately 55 MPa per second were evaluated. Due to the length

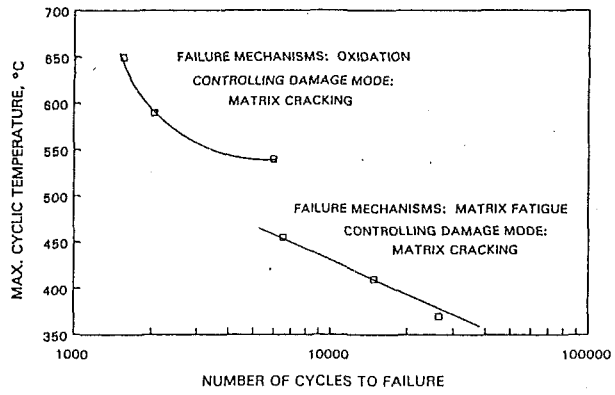

Fig. 4 Fatigue-damage map for SiC/Ti-6-4 composite under out-of-phase TMF loading, σ_{max} = 1090 MPa and T_{min} = 120°C

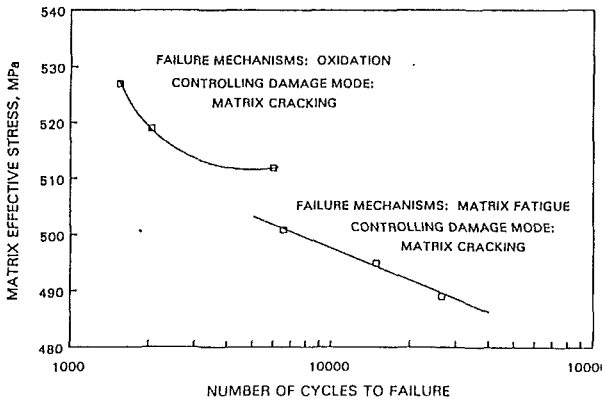

Fig. 5 Fatigue-damage map for SiC/Ti-6-4 composite under out-of-phase TMF loading, σ_{max} = 1090 MPa and T_{min} = 120°C

of time required to remove thermal energy from the test specimen at lower temperature, the fatigue test machine was programmed to vary the loading at 120°C to simulate the strain that would occur if the specimen were allow to cool to room temperature.

IV Fatigue-Damage Diagram

The damage accumulation mechanisms in fibers, matrix, and interface form a complex picture of composite fatigue damage when they occur together. The growth rates of the individual damage mechanisms might be found to be quite different in separate regions. These regions are characterized by certain damage mechanisms, which can be mapped on a diagram. This type of damage map is used to characterize the fatigue behavior of the composite and helps to develop the life prediction model. For monolithic materials, such fatigue-damage maps have been developed in [18], and have then been used to evaluate the fatigue performance of continuous fiber reinforced polymeric matrix materials [19] and SiC fiber-reinforced titanium alloys [20].

This author has characterized damage mechanisms and modes and developed the fatigue-damage map for SiC/Ti-6-4 composite under thermomechanical fatigue loading [11]. A brief summary is given here to provide the background knowledge for damage modeling in this study. The fatigue-damage maps of SiC/Ti-6-4 composite under out-of-phase TMF loading were constructed by using three parameters: (1) strain range increase rate (SRIR) (which is defined as percent of strain range change per cycle), (2) maximum cyclic temperature, and (3) matrix effective stress. The fatigue-damage diagram is shown in Fig. 4 where the maximum cyclic temperature is plotted against the logarithm of the number of cycles to failure. As seen in the figure, the damage mechanism for out-of-phase cycling is dependent upon the maximum cycle temperature. Below a maximum cyclic temperature of 500°C, failure of the composite is controlled by matrix cracking. At long lives, the thermomechanical cycling produces microdamage associated with the matrix–fiber interface, namely microvoids or cracks, often leading to the debonding of the interface. As cycling continues, the external load causes propagation of the crack in the matrix. For tests above a maximum cyclic temperature of 500°C, all damage occurred as surface-initiated environmental damage. It was seen that damage mechanism leading to failure is effective in a limited range of temperature envelope. Therefore, there are two curves in Fig. 4, each representing a different type of damage mechanism that is listed next to each curve. The fatigue-damage diagram, in which the coordinates are the matrix effective stress and the logarithm of the number of cycles to failure, is shown in Fig. 5. The matrix effective stress was calculated using a four concentric cylinder model. As seen in this figure, the classification of failure is consistent with observations from Fig. 4.

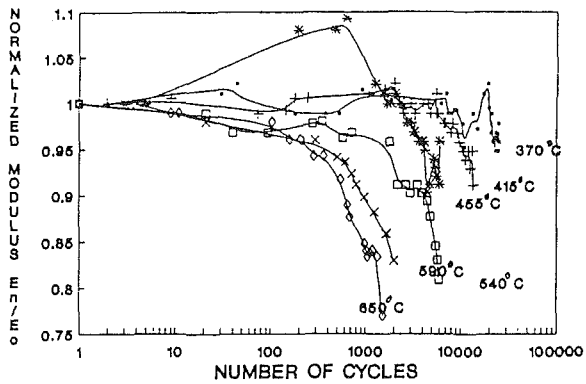

Fig. 6 Changes of modulus for SiC/Ti-6-4 composite under out-of-phase TMF loading, σ_{max} = 1090 MPa and T_{min} = 120°C

At stress levels used in this investigation, failure dominated by fiber breakage was not observed. This mode is significant only at relatively high loads, which usually exceed allowable design magnitudes. It is important to note that the objective of this program was to evaluate and establish properties data for a SiC/Ti-6-4 MMC system operating in a realistic gas turbine component environment. Therefore, only relatively low stresses and design usable temperature ranges were used for the TMF evaluation. In accordance with the fatigue damage diagram, the operating temperature limit to fatigue resistance of SiC/Ti-6-4 MMC system is 500°C and the maximum allowable stress in the matrix is 500 MPa.

V Results and Discussion

In this paper, the analysis of TMF resistance of SiC/Ti-6-4 composites is based on a stiffness degradation for a given loading. Once, damage mode and material constants (a_4, b_3, a_{10}, f_2) are determined, the change in the elastic constants can be related to the magnitude of the damage vector in each loading case. In the following, the experimental determination of the four unknown material constants in the stiffness degradation equations (9) and variation of these constants under TMF loading is discussed.

The current (damaged) modulus at cycle N can be determined experimentally by using the relationship:

$$E_1^N = E_1^0 \frac{\Delta\epsilon_0}{\Delta\epsilon_N} \tag{10}$$

where

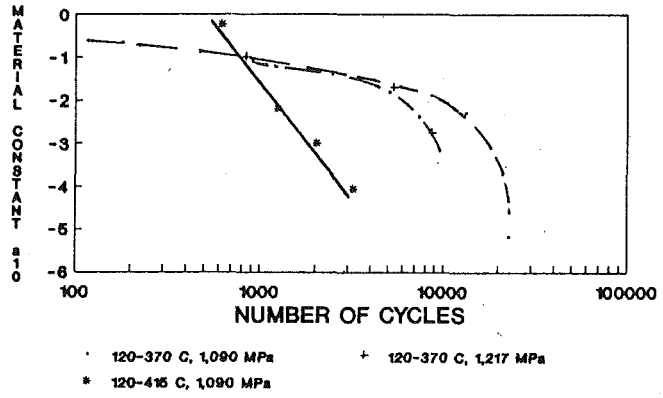

Fig. 7(*a*) Variation of a_4 for SiC/Ti-6-4 composite under out-of-phase TMF loading

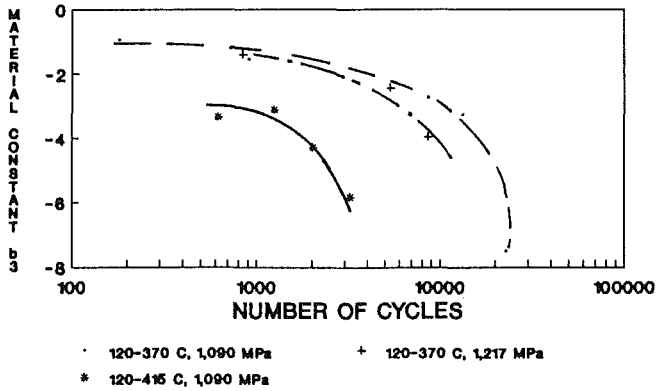

Fig. 7(*b*) Variation of b_3 for SiC/Ti-6-4 composite under out-of-phase TMF loading

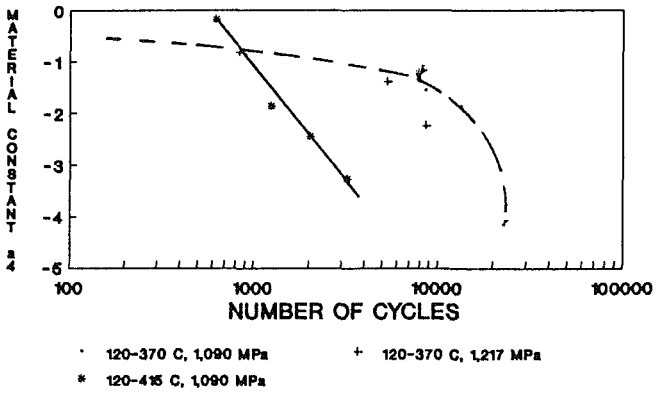

Fig. 7(*c*) Variation of a_{10} for SiC/Ti-6-4 composite under out-of-phase TMF loading

E_1^0 = undamaged modulus
E_1^N = current (damaged) modulus at cycle N
$\Delta\epsilon_0$ = mechanical strain at first cycle
$\Delta\epsilon_N$ = mechanical strain at N cycle

Figure 6 shows experimental data of normalized modulus over a range of applied TMF cycles. As seen in this figure, the elastic response remains essentially constant until the damage due to fatigue occurs.

The unknown material constants in the stiffness reduction Eq. (9) are calculated using the current modulus corresponding to stiffness reduction goal in design. Due to the lack of measurement data on Poisson ratio and shear modulus, they are estimated using classical lamina theory. Using this information in the description of the state of damage under TMF loading,

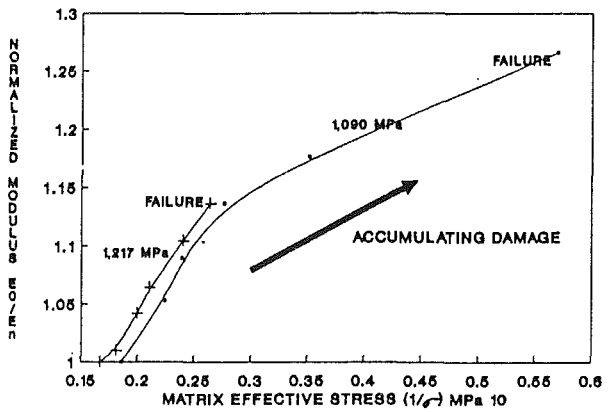

Fig. 8 Relationship between stiffness loss and damage in matrix in terms of matrix effective stress under out-of-phase TMF loading, σ_{max} = 1090 MPa and cyclic temperature range, 120-370°C

the variation of material constants, a_4, b_3, and a_{10}, are plotted as function of number of cycles for constant damage parameter, D_l, in Fig. 7(*a*), 7(*b*), and 7(*c*), respectively. As seen in this figure, the material constants are not a function of the applied stress during early TMF cycles. It becomes a function of stress only when higher number of cycles are accumulated.

From the results described above it is apparent that changes in damaged modulus alone do not reflect damage events in TMF loading. Therefore, a damage characterization of composites cannot be based on the changes in modulus alone. A stiffness-based fatigue damage model requires changes to be related to the damage accumulation mechanisms. In order to take into account the variation of damage mechanisms with stress level and cyclic temperature range in TMF loading. A general form of the damage function is necessary. One approach would be to define a damage rate function as a function of the number of cycles, a cyclic stress level, a cyclic temperature range, and the damage itself.

$$\frac{dD}{dN} = F(N, \sigma_{max}, \Delta T, D) \tag{11}$$

The number of cycles N_f required to increase the damage from an initial value D_i to a final value D_f is

$$N_f = \int_{D_i}^{D_f} \frac{dD}{f(N, \sigma_{max}, D)} \tag{12}$$

The effect of the matrix effective stress on stiffness reduction is illustrated in Fig. 8. In this figure, the variation of the damaged modulus is plotted as the function of the effective matrix stress in case of the applied stresses of 1090 and 1217 MPa. It is clear that the definition of life of a component is uniquely associated with that point in time during the loading history at which control failure is reduced to the level of applied loads. In Fig. 9, this concept is illustrated by plotting stiffness reduction as a function of fatigue cycles and matrix effective stress. The matrix effective stress is calculated using a three-cylinder concentrating cylinder model. This type of graph can be used to establish safe design load based stiffness loss.

V Summary and Conclusions

In development of a life prediction method for composite structures subjected to thermomechanical fatigue loading, an investigator is faced with several tasks. The selection of experimental procedure with the proper parameters, which simulate the component operating environment is one of the most critical steps in the investigation. Another important step is the characterization of the state of damage and its relation to the overall mechanical response. Before choosing parameters to represent the fatigue resistance of a composite, it is necessary

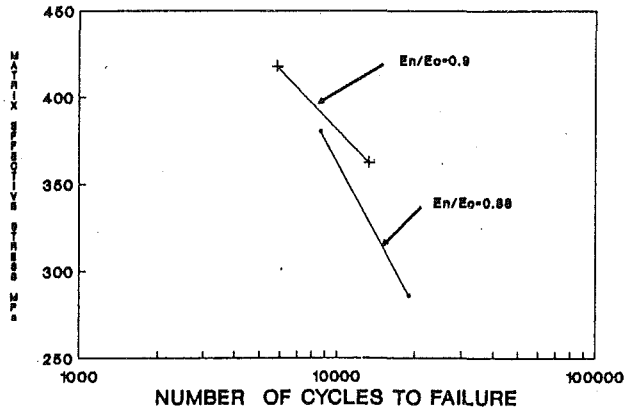

Fig. 9 Residual stiffness degradation as a function of number of cycles

to establish the evolution of damage mechanisms and to quantify the accumulation rate of these mechanisms.

In this paper, damage mechanisms and accumulation, and associated stiffness reduction were studied in SiC/Ti-6-4 composite under out-of-phase TMF loading. To determine the mechanical response in the damaged composite, stiffness-damage relationships based on continuum mechanics were investigated using the results of the load-controlled TMF testing. This study shows that the development of a cumulative damage model cannot rely completely on the experimental determination of residual curve, which was not only a function of the number of cycle. Therefore, residual stiffness alone does not seem to be a good parameter to represent fatigue resistance of composites.

References

1 Sehitoglu, H., and Boismier, D. A., "Thermo-Mechanical Fatigue of Mar-M247: Part 1—Experiments; Part 2—Life Prediction," *Journal of Engineering Materials and Technology*, Vol. 112, Jan. 1990, pp. 68–89.

2 Malpertu, J. L., and Remy, L., "Thermomechanical Fatigue Behavior of a Superalloy," *Low Cycle Fatigue*, ASTM STP 942, H. D. Solomon, G. R. Halford, L. R. Kaisand, and B. N. Leis, eds., 1988, pp. 657–671.

3 Gayda, J., Gabb, T. P., Miner, R. V., and Halford, G. R., "Bithermal Low-cycle Fatigue Behavior of a NiCoCrALY-Coated Single Crystal Superalloy," NASA TM-89831, 1987.

4 Bill, R. C., Verrilli, M. J., McGaw, M. A., and Halford, G. R., "Preliminary Study of Thermomechanical Fatigue of Polycrystalline MAR-M200," NASA TM-2280, 1984.

5 Halford, G. R., and Manson, S. S., "Life Prediction of Thermo-mechanical Fatigue Using Strainrange Partitioning," in: *Thermal Fatigue of Materials and Components*, ASTM STP 612, D. A. Spera and D. F. Mowbray, eds., 1976, pp. 239–254.

6 Cook, T. S., Kim, K. S., and McKnight, R. L., "Thermal Mechanical Fatigue of Cast Rene 80," *Low Cycle Fatigue*, ASTM STP 942, H. D. Solomon, G. R. Halford, L. R. Kaisand, and B. N. Leis, eds., 1988, pp. 692–708.

7 Castelli, M. G., Ellis, R. J., and Bartolotta, P. A., "Thermomechanical Testing Techniques for High-Temperature Composite: TMF Behavior of SiC(SCS-6)/Ti-15-3," NASA TM-103171.

8 Gabb, T. P., Gayda, J., and MacKay, R. A., "Isothermal and Nonisothermal Fatigue Behavior of a Metal Matrix Composite," *Journal of Composite Materials*, Vol. 24, 1990, pp. 667–686.

9 Johnson, W. S., "Fatigue Testing and Damage Development in Continuous Fiber Reinforced Metal Matrix Composites," *Metal Matrix Composites, Testing, Analysis, and Failure Modes*, ASTM STP 1032, W. S. Johnson, ed., 1989, pp. 194–221.

10 Stinchcomb, W. W., and Reifsnider, K. L., "Fatigue Damage Mechanisms in Composite Materials: A Review," *Fatigue Mechanisms*, Proc. ASTM-NBS-Nsf Symp. ASTM STP 679, J. J. Fong, ed., 1979, pp. 762–787.

11 Aksoy, S., "Thermomechanical Damage Development in SiC(SCS6)/Ti-6-4 Metal Matrix Composite," ASME Paper No. 92-GT-342, 1992.

12 Hahn, H. T., "Fatigue Behavior and Life Predictions of Composite Laminates," *Composite Materials: Testing and Design*, 5th, ASTM STP 674, 1979, pp. 383–417.

13 Hahn, H. T., and Tsai, S. W., "On the Behavior of Composite Laminates After Initial Failures," *Journal of Composite Materials*, Vol. 8, 1974, pp. 288–305.

14 Highsmith, A. L., and Reifsnider, K. L., "Stiffness-Reduction Mechanisms in Composite Laminates," *Damage in Composite Materials*, ASTM STP 775, 1982, pp. 103–177.

15 Gotiesman, T., Hashin, Z., and Brull, M. A., "Effective Elastic Moduli of Cracked Fiber Composites," *Advances in Composite Materials*, Vol. 1, A. R. Bunsell et al., eds., Pergamon Press, Oxford, 1980, pp. 749–758.

16 Laws, N., Dvorak, G. J., and Hejazi, M., "Stiffness Changes in Unidirectional Composites Caused by Crack Systems," *Mechanics of Materials*, Vol. 2, 1983, pp. 123–137.

17 Talreja, R., *Advances in Composite Materials*, Proc. ICCM3, A. R. Bunsell et al., eds., Pergamon, New York; *Proc. Roy Soc. London A378*, 1980, p. 461.

18 Ashby, M. F., "Progress in the Development of Fracture-Mechanism Maps," *Fracture 1977*, D. M. R. Taplin, ed., University of Waterloo Press, Waterloo, Ontario, Vol. 1, 1977, pp. 1–14.

19 Talreja, R., "Fatigue of Composite Materials: Damage Mechanisms and Fatigue-Life Diagrams," *Proc. Roy. Soc., London*, Vol. A378, 1981, pp. 461–475.

20 Jeng, S. M., Alassoeur, P., Yang, J. M., and Aksoy, S., "Fracture Mechanisms of Fiber-Reinforced Titanium Alloy Matrix Composites," *Mater. Sci. Eng.*, Vol. A148, 1991, pp. 67–77.

Performance Testing and Strength Prediction of Ceramic-to-Metal Joints

J. H. Selverian

D. A. O'Neil

Osram Sylvania Inc.,
60 Boston Street,
Salem, MA 01970

S. Kang
Valenite,
1711 Thunderbird,
Troy, MI 48084

Brazed joints were made between silicon nitride and Ni-based and Fe-based super alloys. Room temperature shear (torsion) strengths ranged from 75–242 MPa for Si_3N_4-to-Incoloy 909 joints and from 30–127 MPa for the Si_3N_4-to-Inconel 718 joints. At 500°C the joint strength was 120 MPa while at 650°C and 950°C the joint strengths were less than 20 MPa. These low strengths at 650°C and 950°C were attributed to a reduction in the shrink-fit and to low braze strength at these high temperatures. Finite element analysis (FEA) and a probabilistic failure theory (CARES) were used to predict the joint strengths. The predicted joint strengths agreed well with measured joint strengths in torsional loading at 20°C. Torsion tests were also performed at 650°C. Aspects of the material systems, residual stresses, mechanical behavior, and strength predictions and presented. Two new braze alloys based on the Au–Ni–Cr–Fe system were used to overcome the poor high-temperature strength. Joints made with these brazes had good strength (85 MPa and 35 N-m) at 650°C.

Introduction

Ceramics are being considered for structural components in the development of advanced heat engines. A key issue is the problem of joining a ceramic rotor to a metal shaft to transmit power. Design concepts for ceramic-to-metal brazed joints were described in an earlier paper (Selverian et al., 1992).

The major type of loading these joints will experience is torsional and thermal; therefore, the joints were evaluated with torsion, torsion fatigue, and thermal fatigue tests. The joints were tested at room temperature, 500°C, 650°C, and 950°C. The experimental results were linked to the predictions based on the residual stresses calculated by finite element analysis with simplifying assumptions.

The goals of this work were to develop a ceramic-to-metal joint that could withstand 20.9 N-m (50 MPa) of torque at 650°C and 950°C and would have a 2 cm^2 brazed area, and to develop methods to predict joint performance.

Experimental Procedure

Materials. For the 650°C application, an Fe-based superalloy, Incoloy 909, was selected because of its low coefficient of thermal expansion (CTE) as well as its high-temperature properties. For the 950°C application, a Ni-based superalloy, Inconel 718, was chosen solely for its high-temperature capabilities. The CTE of Inconel 718 is approximately 50 percent greater than that of Incoloy 909. In the remainder of the paper Incoloy 909 and Inconel 718 together were referred to as structural alloys.

Silicon nitride (Si_3N_4 + 6 percent Y_2O_3) was selected as the structural ceramic material. The silicon nitride shaft was polished to a 0.1 μm surface finish. A 3-μm-thick Ti coating was electron beam evaporated onto one end of the silicon nitride shaft. This Ti coating served to promote wetting and adhesion between the ceramic and braze alloy.

Nickel and molybdenum were used as interlayer materials between the ceramic and the structural alloy, and a Au-5Pd-2Ni (in wt%) braze alloy was used. The two material systems studied were Si_3N_4/Ni/Incoloy 909 as the 650°C system and Si_3N_4/Mo/Inconel 909 as the 650°C system and Si_3N_4/Mo/Inconel 718 as the 950°C system. The Au–5Pd–2Ni braze alloy was used in both systems.

Joint Geometry. The joint consists of a 1.27-cm-dia silicon nitride rod brazed to a 1.946 cm outer diameter metal shaft with a 2 cm^2 brazed area. The ceramic rod fits into a cup machined into the end of the metal shaft. A schematic of the ceramic-to-metal joint geometry is shown in Fig. 1. Finite element analysis showed that this type of cylindrical lap joint resulted in lower residual stress in the ceramic compared to other geometries (Selverian et al., 1992).

Brazing Process. The entire ceramic-to-metal joint was placed in a graphite brazing fixture for alignment. A thermocouple was placed near the joint, and the brazing setup was placed in a vacuum furnace. The furnace was raised to the brazing temperature, 1180°C, in approximately 1 hour, at which point the vacuum was 10^{-2} to 10^{-3} Pa. The joint was held at

Contributed by the International Gas Turbine Institute and presented at the 38th International Gas Turbine and Aeroengine Congress and Exposition, Cincinnati, Ohio, May 24–27, 1993. Manuscript received at ASME Headquarters March 1993. Paper No. 93-GT-412. Associate Technical Editor: H. Lukas.

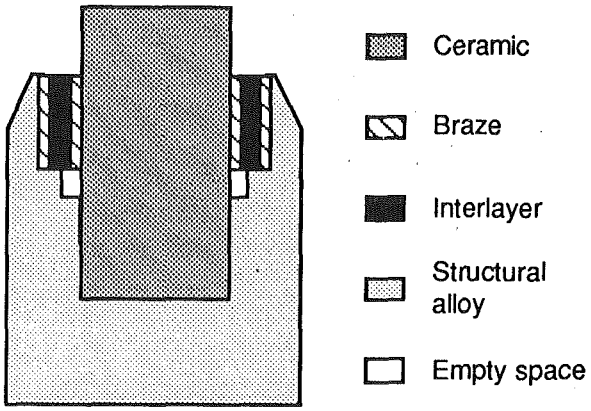

Fig. 1 Schematic of the ceramic-to-metal joint geometry

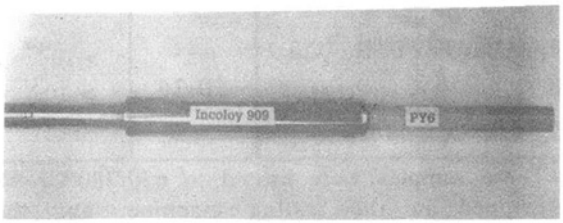

Fig. 2 Brazed Si_3N_4/Ni/Incoloy 909 joint. Test sample for torsion and mechanical fatigue testing. The ceramic is 1.27 cm in diameter and the metal is 1.946 cm in diameter.

temperature for 10 minutes. After brazing, the furnace power was turned off, and the joints cooled to room temperature in approximately 3 hours.

Testing of Brazed Joints. Figure 2 shows a brazed joint between silicon nitride and Incoloy 909. This type of joint was used for the torsion and torsion fatigue tests. All of the mechanical testing of the brazed joints was carried out on a servo hydraulic axial/torsional machine. The top and bottom gripping axes were axially aligned to within 40 μm of one another.

Torsion tests were run at a rate of 0.2°/s and the axial load was controlled to within ±4.5 N of zero to maintain pure torsional loading. An induction furnace, with a SiC susceptor, was used to heat the joints for the elevated temperature tests. Torsion fatigue tests were carried out at minimum and maximum torques of 3.95–20.9 N-m, 6.0–31.7 N-m, or 8.04–42.2 N-m, all with a 1.5 Hz loading frequency. Torques of 3.95–20.9 N-m are typical values found in heat engines currently under development.

The temperature versus time profile used for the 650°C thermal fatigue testing consisted of a maximum temperature of 650°C and a minimum temperature of 335°C with a frequency of 0.07 Hz. The temperature versus time profile used for 950°C thermal fatigue testing consisted of a maximum temperature of 950°C and a minimum temperature of 545°C with a frequency of 0.11 Hz. The thermal fatigue conditions were also developed with the idea of simulating the stresses developed in a heat engine. All of the mechanical and thermal tests were conducted in air.

Results and Discussion

Torsion Testing. The bending moment in the brazed joint, due to misalignment between the ceramic and metal parts of the joint, introduced additional stresses in the joint. There was no strong correlation between the bending moment and the shear stress of a joint for bending moments below approximately 25 N-m.

Table 1 Results of the torsion tests of Si_3N_4/Ni/Incoloy 909 brazed joints

Test Temp. (°C)	Torque (N-m)	Shear Strength (MPa)	Bending Moment (N-m)	Rotation (°)
25	61	151*	7	2.22
	97	242*	14	3.52
	53	132*	11	1.98
	30	75*	13	1.15
	60	148*	10	1.05
	49	121*	23	2.55
	64	158*	14	3.05
	90	222*	12	4.3
	45	111*	2	2.05
650	4.	11.5#	---	---
	1.6	3.9#	---	0.10
	7.0	17.4#	---	---
	4.9	12.1#	---	0.21°

* broke in ceramic.
\# ceramic slipped in joint.

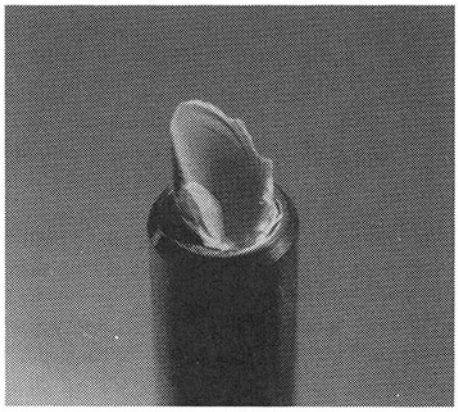

Fig. 3 Fracture surface of a Si_3N_4/Ni/Incoloy 909 joint fractured in a room temperature torsion test. The ceramic is 1.27 cm in diameter and the metal is 1.946 cm in diameter.

Results from room temperature torsion tests of Si_3N_4/Ni/Incoloy 909 joints are shown in Table 1. The measured shear strengths calculated according to Eq. (1) were in the range of 75–242 MPa at room temperature.

The shear stress, τ, for an applied torque, M_T, and a gage diameter, D, was given by

$$\tau = \frac{16\,M_T}{\pi D^3}. \quad (1)$$

Fracture started in the ceramic near the top of the interlayer. Away from the interlayer, the fracture surface formed approximately a 45 deg angle. Near the top of the interlayer, the angle of the fracture surface varied from 45 deg. This suggested that the stress pattern near the interlayer was significantly different than in the bulk silicon nitride away from the interlayer. The initiation site of fracture was in agreement with the finite element prediction that the maximum residual stress would occur at the top of the interlayer (Selverian et al., 1992).

Table 2 Results of the torsion test of Si_3N_4/Mo/Inconel 718 brazed joints

Test Temp. (°C)	Torque (N-m)	Shear Strength (MPa)	Bending Moment (N-m)	Rotation (°)
25	12	30	25*	0.38
	40	98	13*	1.19
	23	56	17*	0.70
	51	127	16*	0.80
	41	101	16*	0.64
950	0.34	0.84#	---	---

* broke in ceramic.
# ceramic slipped in joint.

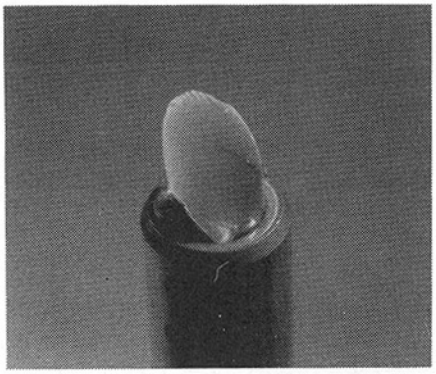

Fig. 4 Si_3N_4/Mo/Inconel 718 joint fractured in a room temperature torsion test. The ceramic is 1.27 cm in diameter and the metal is 1.946 cm in diameter.

Results from the torsion tests at 650°C are also shown in Table 1. In general, the strengths of these joints were very low (3.9–17.4 MPa). During the torsion tests the ceramic would slip without fracturing. Auger analysis of the fracture surface indicated that the fracture path was complex and occurred in the silicon nitride, in the TiN reaction layer, and in the braze alloy. Titanium nitride has been commonly seen as a reaction layer forming between titanium and silicon nitride. For all of the torsion tests at all temperatures studied, the torque versus rotation plots were straight lines, indicating that yielding of the metal components did not occur before final fracture or slippage.

Results from the room temperature torsion tests of the Si_3N_4/Mo/Inconel 718 joints are shown in Table 2. The fracture behavior of these joints, Fig. 4, was similar to the Si_3N_4/Ni/Incoloy 909 joints. However, the Si_3N_4/Mo/Inconel 718 joints were significantly weaker than the Si_3N_4/Mo/Incoloy 909 joints. The shear strengths of the Si_3N_4/Mo/Inconel 718 joints at room temperature ranged from 30 to 127 MPa. This difference in room temperature strength was largely attributed to the higher residual stresses developed in the Si_3N_4/Mo/Inconel 718 joints. The higher residual stresses were due to the higher CTE of Inconel 718 as compared to Incoloy 909, and due to the lower CTE and higher flow stress of molybdenum as compared to nickel.

Table 3 Room temperature fatigue tests of Si_3N_4/Ni/Incoloy 909 and Si_3N_4/Mo/Inconel718 brazed joints

Joint	Torque (N-m)	Rotation (°)	Number of Cycles for Failure
Si_3N_4/Ni/ Incoloy 909	3.95-20.9	±0.31	$> 10^3$*
	"	±0.32	$> 10^3$*
	"	±0.31	$> 10^3$*
	"	±0.32	$> 10^3$*
	"	±0.31	$> 10^6$
	6.0 - 31.7	---	$> 10^6$
	8.0 - 42.2	---	$> 10^6$
Si_3N_4/Mo/ Inconel 718	3.95 - 20.9	---	$> 10^3$*
	"	±0.26	$> 10^3$

* These samples were heated to 650-700°C, then gripped in the testing machine, and then cooled to room temperature before testing, to realign the sample.

Fatigue Testing. Thermal and mechanical fatigue tests were used to evaluate the effects of repeated thermal and mechanical loading on the long-term performance of the brazed joints. Braze joints were made for thermal fatigue tests at 650°C and 950°C. The same joint geometry was used as in Fig. 2. The initial crack distribution in the joint was checked by microfocus x-ray. No cracks were detected in the silicon nitride. The apparent lack of cracks in the silicon nitride could be due to either no cracking or to the cracks being smaller than the 40 μm detection limit of the x-ray equipment. The samples were re-examined by microfocus x-ray after 10, 100, and 1000 cycles. The Si_3N_4/Ni/Incoloy 909 joints survived all 1000 cycles without evidence of cracking. Severe oxidation of the molybdenum interlayer in the Si_3/N_4/Mo/Inconel 718 joints prevented their complete testing.

Several Si_3N_4/Ni/Incoloy 909 and Si_3N_4/Mo/Inconel 718 joints were torsion fatigue tested at room temperature, Table 3. A Si_3N_4/Ni/Incoloy 909 joint was first fatigued at room temperature for 10^3 cycles, then fatigued at room temperature for 10^6 cycles. All of the joints survived 10^6 fatigue cycles at a torque amplitude of 3.95–20.9 N-m. The joints showed no signs of degradation; the rotation required to maintain these torques was unchanged at ±0.32 deg from the start of the test. The torque amplitudes were increased to 6.0–31.7 N-m and to 8.0–42.2 N-m. One joint was tested at each torque level and joints survived 10^6 cycles, Table 2.

Effect of Shrink Fit. For joints that failed in the joint region, the joint strength was broken down into two main parts. The first was the intrinsic strength of the metallurgical bonding across the ceramic/metal interface and the second was the shrink-fit force, which was due to the compressive forces exerted on the ceramic by the surrounding metal. Of these two factors, the shrink-fit was believed to be the most temperature sensitive. However, at high temperatures the temperature-dependent properties of the joint materials also played a role in the joint strength.

Tables 1 and 2 showed that the joints were very weak at 650°C and 950°C. It was uncertain whether the low joint

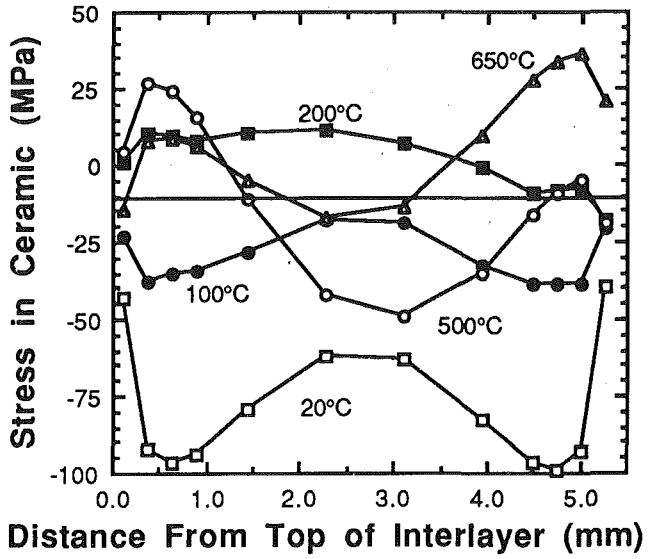

Fig. 5 Centroid stresses in the ceramic at the ceramic/interlayer interface as a function of temperature calculated by finite element analysis for a Si_3N_4/Ni/Incoloy 909 joint. The joint was initially cooled down to 20°C from the brazing temperature then reheated to the different temperatures.

strength was due to a weakening of the braze alloy or to a reduction in the shrink-fit due to the elevate temperature testing. Therefore, the amount of shrink-fit (radial stress) in the final joint geometry was calculated by finite element analysis (Selverian et al., 1992).

The radial stresses were measured from the centroid of the 12 ceramic finite elements at the ceramic/metal interface. In Fig. 5, these radial stresses were plotted as a function of distance along the ceramic/metal interface, for several temperatures. The radial stress distribution in the ceramic changed and became very complicated at temperatures above 200°C.

The stresses in Fig. 5 were used to estimate the loss in joint strength as a result of an increase in temperature and the resultant decrease in shrink-fit. For a shrink-fit joint, the torque (T) the joint can withstand without slipping was approximated by the following equation:

$$T = \mu r A \sum_{i=1}^{n} P_i \qquad (2)$$

where μ was the coefficient of friction between the ceramic and metal (~ 0.1), r was the radius of the ceramic (6.35 mm), A was the area of contact, which was taken as the area/element in the FEA mesh (1.7×10^{-5} m^2) times the number of elements (n) with a compressive stress, and P_i was the radial compressive stress in element i (σ_{rr}). Only compressive stresses were included in this analysis. The radial stresses along the ceramic/metal interface are shown in Fig. 5. The calculated values of the torque due to the shrink-fit stresses were 122 N-m at 20°C, 25 N-m at 500°C, and 1.8 N-m at 650°C, corresponding to shear strengths of 304 MPa, 62 MPa, and 4 MPa, respectively. These torque values are for a shrink-fit joint and are only valid for joints that slipped at the ceramic/metal interface and did not break in the ceramic or fail by deformation of any of the metallic components of the joint.

The total strength of a joint can be thought of as being comprised of two components: the shrink-fit, and the metallurgical bond. The metallurgical bond component is the chemical bonding and mechanical interlocking at the ceramic/metal interface, in this case between the Ti-coating and silicon nitride. The total joint strength is defined as

$$\text{Total joint strength} = \text{Shrink-fit} + \text{Metallurgical bond} \qquad (3)$$

Table 4 Results of the 500°C torsion tests of Si_3N_4/Ni/Incoloy 909 brazed joints. All of these joints were fatigue tested at room temperature before testing at 500°C.

Torque (N-m)	Shear Strength (MPa)	Previous Fatigue Test Conditions (cycles at stress)	Fracture Mode
49.7	123	10^3 at 3.95-20.9	slipped
24.8	61	10^6 at 3.95-20.9	cer. broke
15.3	38	10^6 at 6.0 - 31.7	slipped

where the contribution of the metallurgical bond to the joint strength is approximately constant at 85 MPa for the temperature range studied (Table V in Selverian and Kang, 199b).

For the joints tested at room temperature, the total joint strength is approximately 304 MPa + 85 MPa = 389 MPa. This strength is significantly higher than the measured joint strengths, Table 1, which is supported by the fact that at room temperature the ceramic broke and the joint did not slip, i.e., the joint was stronger than the ceramic. At 500°C the total joint strength is approximately 62 MPa + 85 MPa = 147 MPa, which compares favorably with the experimental value of 123 MPa after 1000 cycles of fatigue testing, Table 3. At 650°C the total joint strength is approximately 4 MPa + 85 MPa = 89 MPa. This value is significantly higher that the experimental value of approximately 10 MPa, Table 1. This discrepancy is attributed to a weakening of the braze alloy at 650°C, indicating that at the higher temperatures the joint strength is controlled by the strength of the braze alloy.

The mechanical properties of the braze alloy at elevated temperatures were expected to play an important role in determining the creep behavior of this joint. However, the creep requirements for this joint were not well defined and were not studied.

Comparison Between FEA Predictions and Experimental Results. Finite element analysis was used to predict the residual stress for each joint component (Selverian et al., 1992). The joints were assumed to have perfect bonding at every interface; the presence of voids in the braze was ignored. Further, the influences of metallurgical reactions due to processing was not accounted for in the analysis. Bulk properties were used for each material in the joint. Also, significant alloying was seen between the braze, interlayer, and structural alloys. This alloying caused a change in the braze alloy's composition and hence in its properties (the most important was the flow stress). Such effects were not accounted for in the finite element analysis.

The comparison between predictions and experimental results was made with a probabilistic approach to joint failure. For the probabilistic approach, the NASA CARES program (Nemeth et al., 1989a, 1989b) was used to calculate the probability of survival (P_s) of the joints and the result was presented in the form of a probability plot. In this approach, the predicted strength value was obtained by superimposing the distribution of an applied torque and the calculated residual stress.

Probabilistic Approach. For this approach, an applied torque was superimposed with the calculated residual stress field as a shear stress. Figure 6 shows the torque distribution used to determine the shear stress. A stress concentration due to the change in cross section at the joint was included as before. The stress concentration was 1.7 at the top of the joint

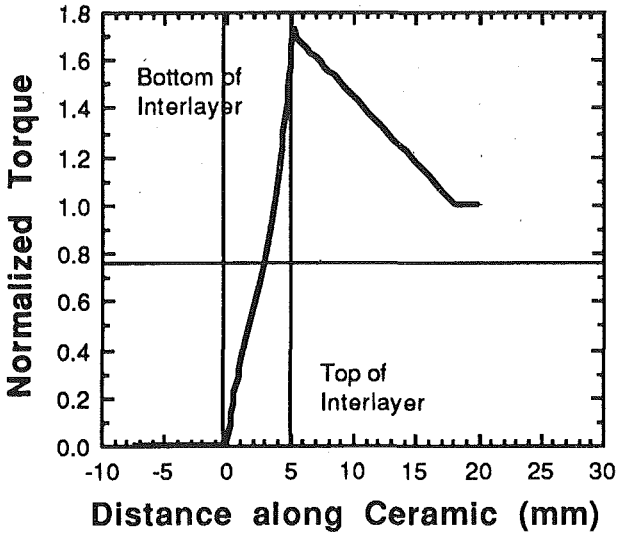

Fig. 6 Plot of the torque distribution in the ceramic portion of the brazed joint. Torque values are normalized to the applied torque.

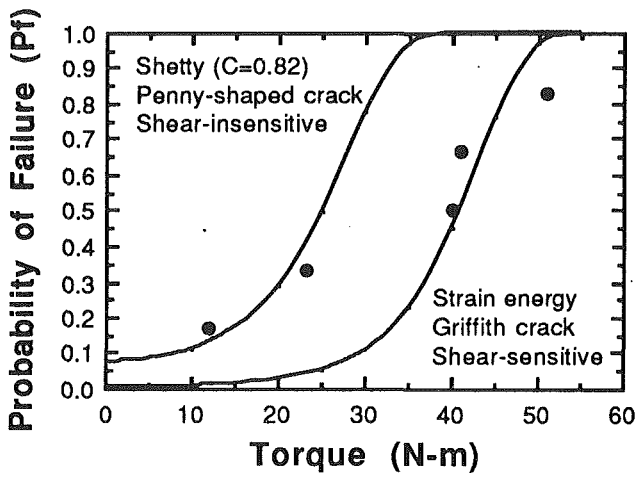

Fig. 8 Predicted and experimental values of the brazed joint strength measured in torsion (Si_3N_4/Ni/Incoloy 718). Two failure theories were used: (1) Shetty criterion with $\bar{c}$ = 0.82, penny-shaped crack, and a shear-insensitive Batdorf crack density, and (2) coplanar strain energy release rate, Griffith crack, and a shear-sensitive Batdorf crack density.

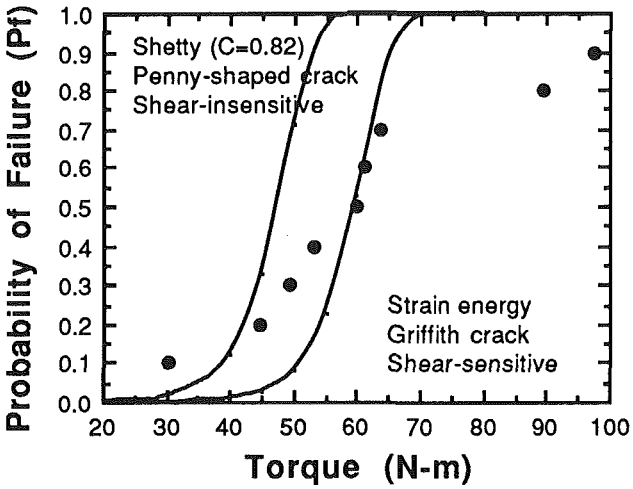

Fig. 7 Predicted and experimental values of the brazed joint strength measured in torsion (Si_3N_4/Ni/Incoloy 909). Two failure theories were used: (1) Shetty criterion with $\bar{c}$ = 0.82, penny-shaped crack, and a shear-insensitive Batdorf crack density, and (2) coplanar strain energy release rate, Griffith crack, and a shear-sensitive Batdorf crack density.

and tapered off to 1.0 a distance of one ceramic diameter away from the joint. Selection of the stress concentration factor depended on the radius of the fillet formed by the braze alloy. A fillet radius of 1 mm was selected; however, the fillet radius varied over the joint area. The stress concentration factor was estimated from Rourk (1971).

The fraction of torque carried by the ceramic and metal components in the joint region was calculated based on the material properties and was also factored into the torque distribution shown in Fig. 6. Once the torque was added to the residual stress field, the combined stress field was used as input to the CARES probabilistic failure computer code (Nemeth et al., 1989a, 1989b) to obtain the probability of survival for the joint at the applied torque level. This same procedure was performed at several different torques and the probability-of-failure (P_f) values were calculated as a function of applied torque. This probabilistic approach to joint strength, unlike the maximum principal stress approach, provided a method to estimate the strength distribution of a ceramic-to-metal brazed joint and can be used as a design aid.

Two failure theories were used to predict the behavior of the ceramic-to-metal joints for comparison. These were: (1) Shetty criterion, with $\bar{c}$ = 0.82, a penny-shaped crack, and a shear-insensitive Batdorf crack density coefficient, and (2) coplanar strain energy release rate, with a Griffith crack, and a shear-sensitive Batdorf crack density coefficient. For these failure theories the Weibull modulus (m_v), the normalized Weibull scale parameter (σ_{ov}), and the Batdorf crack density coefficient (k_{BV}) were calculated from four-point bend tests of the silicon nitride material used in the ceramic-to-metal brazed joints. Twenty-four samples were tested and 1 outlier was detected in the data (Selverian and Kang, 1992a).

A Weibull modulus (m_v) of 21.2 and a normalized Weibull scale parameter (σ_{ov}) of 369.8 $MPa(m)^{3/21.2}$ were used for both failure theories. A shear-insensitive Batdorf crack density coefficient of 43.4 and a shear-sensitive Batdorf crack density coefficient of 22.2 were used for the Shetty and coplanar strain energy release rate theories, respectively. The maximum likelihood method was used to fit the experimental data. The constants described above were required as input variables by the CARES program and are further described by Nemeth et al. (1989a).

Figures 7 and 8 show experimental and predicted results of torsion testing of the brazed joints. The predicted strength distributions surrounded the experimental values and intermediate values of P_f, where $P_f = 1 - P_s$. However, at the low and high regions of the probability distributions the predictions deviated from the experimentally measured strengths. Also, the predicted probability distributions were much steeper (higher Weibull modulus) than the experimental probability distribution. The Weibull modulus decreased from 21.2 for the unbrazed ceramic to ~4 for the Si_3N_4/Ni/Incoloy 909 brazed joints. A similar decrease in Weibull modulus was seen in shear testing of ceramic-to-metal lap joints (Selverian and Kang, 1992b) and in four-point bend tests of ceramic-to-metal butt joints (Lugscheider and Tillmann, 1990). The cause of the difference in the slopes (Weibull modulus) of the probability distributions was unknown.

Development of New High-Temperature Braze Alloy. The results in Tables 1 and 2 point out the need for new braze alloys for application temperature above 500°C to provide high-temperature creep strength as well as oxidation resistance.

A FEA (finite element analysis) study (Selverian et al., 1992) indicated that the alloys need to have low yield strength, high

Table 5 Torsional strength of the PY6/Ni/Incoloy 909 system brazed with SK-1 or SK-2 braze alloy at 1100°C for 30 minutes

Braze Alloy	Test Temp. (°C)	Torque (N-m)	Bending Moment (N-m)	Rotation (°)
SK-1	20	46*	6	1.23
		48*	16	1.30
		35*	10	0.88
		35*	12	---
		45*	12	---
	650	35*	30	1.23
		33*	39	0.95
		38*	39	1.20
		17$	29	---
SK-2	20	46*	41	1.25
		46*	---	---
		36*	10	0.92
		40*	8	0.96
		27*	4	---
	650	37*	19	---
		2$	10	---
		10#	---	---

* broke in ceramic.
\# ceramic slipped in joint.
$ greater than 50% unbonded area.

Table 6 Torsional rupture of PY6/Ni/Incoloy 909 joints with the SK-1 braze at 650°C for an applied torque of 20.9 N-m

Bending Moment (N-m)	Maximum Rotation (°)	Time to Rupture (hrs)	Creep Rate (°/hr)
70	0.580	3.5	4.5×10^{-2}
45	1.260	10.5	6.7×10^{-2}
51	0.640	>100*	8.8×10^{-4}
18	1.317	> 160	4.6×10^{-3}

* Experiment was stopped after 100 hours creep at 650°C due to a planned electrical shut-down.

ductility, and high ultimate strength at low temperature for optimum bonding performance. High ductility and high toughness values of the alloys are extremely important in producing braze foils by rolling. Many of these requirements are in conflict. Interactions between joining components sometimes cause compatibility problems. There is a limit in brazing temperatures to prevent silicon nitride substrates from decomposing, ~1200°C.

Two new braze alloys were developed for high-temperature use. These alloys are based on the Au-Ni-Cr-Fe-Mo system (SK-1) and the Au-Ni-Cr-Fe system (SK-2) (Kang et al., 1992).

The results of some preliminary mechanical tests of joints brazed with these alloys are given in Tables 5 and 6 and Fig. 9. Joints made with these new braze alloys exceed the goal of 20.1 N-m of torque at 650°C.

Summary and Conclusions

Material systems designed for 650°C and 950°C applications were evaluated in terms of torsion, torsion fatigue, and thermal

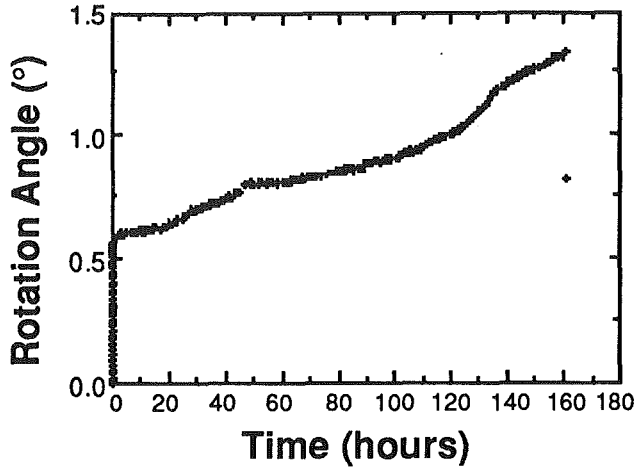

Fig. 9 650°C creep behavior of ceramic-metal joints brazed with the SK-1 alloy

fatigue. Si_3N_4/Ni/Incoloy 909 was selected as the 650°C system while Si_3N_4/Mo/Inconel 718 was selected as the 950°C system. The Au-5Pd-2Ni braze alloy was used in both systems. A cylindrical lap geometry with an interlayer was selected for these joints.

Room temperature and 500°C torsion strengths of the 650°C system were measured in the range of 30-100 N-m with a 2 cm^2 brazed area while the strength at 650°C was significantly lower (1.6-7.0 N-m). This was attributed to a reduction in the shrink-fit at 650°C. The Si_3N_4/Ni/Incoloy 909 joints showed excellent room temperature fatigue behavior. A similar trend was seen in the high-temperature strength of the Si_3N_4/Mo/Inconel 718 joints, which had lower strength than the Si_3N_4/Ni/Incoloy 909 joints due to the high CTE of Inconel 718.

The strength predictions of the finite element analysis were compared with experimental results. Scatter in the measured strengths and the difference between measured and predicted strengths indicated the importance of processing effects and the probabilistic nature of ceramic failure on the fracture process. Fractographs of room temperature torsion specimens showed that the initiation sites for cracking coincided with those for maximum principal stress. This indicated that the maximum principal stress criterion should be a good estimate of the location of probable fracture. However, the probabilistic approach for the ceramic-to-metal brazed joint was a better method for comparing the performance of various braze joints due to the statistical nature of ceramic failure, and it provided an estimate of the strength distribution of the joint for design considerations.

Two new braze alloys were developed and demonstrated to be useful at 650°C. These alloys are based on the Au-Ni-Cr-Fe-Fe system and the Au-Ni-Cr-Fe system and resulted in joints with strengths of ~85 MPa at 650°C.

Acknowledgments

This research was sponsored, in part, by the U.S. Department of Energy, Assistant Secretary for Conservation and Renewable Energy, Office of Transportation Systems, as part of the Ceramic Technology for Advanced Heat Engines Project of the Advanced Materials Development Program, under contract DE-AC05-840R21400 with Martin Marietta Energy Systems, Inc. Special thanks go to M. Santella and D. R. Johnson at ORNL. The support of R. Schulz at the DOE is also appreciated.

The authors wish to thank H. Kim for his support and E. Dunn for contributions. The participation in the experimental program by D. Bazinet and G. McCloud is gratefully acknowledged. Assistance from K. Kim is appreciated.

References

Beer, F. P., and Johnston, E. R., Jr., 1981, *Mechanics of Materials*, McGraw-Hill, New York, p. 398.

Kang, S., Dunn, E. M., Selverian, J. H., and Kim, H., 1989, *Ceramic Bulletin*, Vol. 68, pp. 1608–1617.

Kang, S., Selverian, J. H., and O'Neil, D., 1992, Final Report, Subcontract No. 86X-SB047C, Oak Ridge National Laboratory.

Kim, D. H., Hwang, S. H., and Chun, S. S., 1990, *Ceramics International*, Vol. 16, pp. 333–347.

Nemeth, N. N., Mandersheid, J. M., and Gyekenyesi, J. P., 1989a, "Ceramic Analysis and Reliability Evaluation of Structures (CARES)—User's Guide," NASA Technical Paper No. 2916.

Nemeth, N. N., Mandersheid, J. M., and Gyekenyesi, J. P., 1989b, *American Ceramic Society Bulletin*, Vol. 68, No. 12, pp. 2064–2072.

Lugscheider, E., and Tillmann, W., 1990, *J. American Welding Soc.*, Vol. 69, No. 11, pp. 416s–421s.

Rourk, R. J., 1971, *Formulas for Stress and Strain*, 4th ed., McGraw-Hill, New York, pp. 388–389.

Selverian, J. H., O'Neill, D., and Kang, S., 1992, *American Ceramic Society Bulletin*, Vol. 71, No. 9.

Selverian, J. H., and Kang, S., 1992a, *American Ceramic Society Bulletin*, Vol. 71, No. 10.

Selverian, J. H., and Kang, S., 1992b, *J. American Welding Soc.*, Vol. 71, No. 1.

Microstructural Investigation of the Weld HAZ in a Modified 800H Alloy

C. D. Lundin

C.-Y. P. Qiao

Materials Science and Engineering,
The University of Tennessee, Knoxville,
Knoxville, TN 37996-2200

Detailed metallographic investigations of Gleeble simulated HAZ samples in modified 800H were performed. Precipitate dissolution, gain growth, HAZ liquation and the hardness degradation behavior in modified 800H were also addressed. Results of this study agree with previous HAZ hot cracking and softening behavior evaluations.

Introduction

Modified 800H is one of the newly developed high-temperature alloys for applications in coal-fired power generating systems (Swindeman, 1991). Modified 800H possesses a greater creep and higher temperature tensile strength as compared to standard alloy 800 and conventional austenitic stainless steels. To achieve excellent creep and high-temperature tensile strength a thermomechanical treatment is applied during alloy fabrication (5–10 percent cold work). Therefore, grain growth, recrystallization, and precipitate dissolution and redistribution will occur in the weld HAZ during fabrication. Thus, both mechanical and metallurgical degradation may occur in the HAZ. Additionally, metallurgical reactions adjacent to the fusion boundary, including a partially melted region and constitutional liquation, may occur and influence the hot cracking resistance. In order to minimize these welding-related problems, a significant microstructural investigation of the weld HAZ in modified 800H was carried out.

The Gleeble thermal mechanical simulator was used to prepare simulated HAZ specimens. Using thermally simulated HAZ samples, a careful evaluation was performed to determine the evolutionary processes for precipitates in the HAZ. Scanning electron microscopy (SEM), transmission electron microscopy (TEM), and optical light microscopy (OLM) were utilized to characterize the microstructures. Quantitative image analysis techniques were also applied to interpret the HAZ microstructure carefully. Energy dispersive spectroscopy (EDS) analysis and x-ray diffraction analysis were employed to define the precipitates in the HAZ. The microstructural morphologies revealed, grain size, and hardness measurements results are discussed in this paper.

Sample Preparation

One commercial tubing heat of modified 800H was used to conduct this investigation. The composition of the material is listed in Table 1. The processing condition for the tubing included: (1) the cold finishing of the hollow into tubing with a 21 percent wall thickness reduction; (2) annealing at 2050°F (1120°C) for 30 minutes and cooling in air; (3) annealing at 2175°F (1190°C) for 30 minutes and cooling in air; and (4) cold sinking to an average 5 percent outside diameter reduction.

Table 1 Composition of the material used in this study (wt.%)

C	S	P	Cr	Ni	Mo	Mn	Si	V	Al	Ti	Nb	N	Cu	B
0.10	0.006	0.022	20.13	30.09	1.89	2.00	0.19	0.59	0.01	0.28	0.22	0.007	0.01	0.006

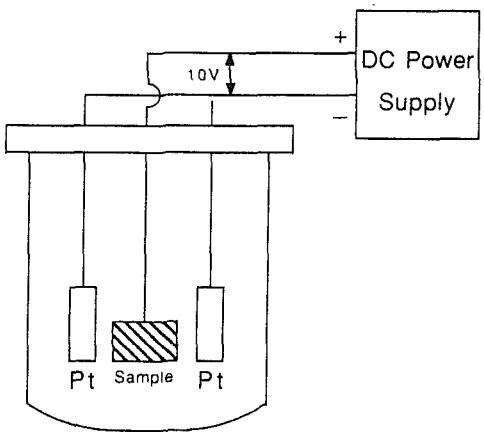

Fig. 1 Schematic illustration of the electrolytic precipitate extraction device

The simulated HAZ samples were prepared by using a Model 1500 Gleeble. The simulation thermal cycle reflects the weld HAZ in a 1-1/2 in. thick stainless steel plate with the SMAW process using 70 kJ/in. energy input and ambient temperature preheat. Seven peak temperatures (1001°C, 1090°C, 1145°C, 1200°C, 1260°C, 1285°C, and 1320°C) were employed representing different locations in the HAZ. Two samples were prepared for each temperature. One sample was utilized to perform metallographic examinations and the other was used for electrolytic precipitate extraction. The precipitate extraction process is schematically illustrated in Fig. 1. The conditions for particle extraction were: voltage: 8 V; current: 2 A/cm^2; and time: 2 hours. The solution used for extraction was

Contributed by the International Gas Turbine Institute and presented at the 38th International Gas Turbine and Aeroengine Congress and Exposition, Cincinnati, Ohio, May 24-27, 1993. Manuscript received at ASME Headquarters March 3, 1993. Paper No. 93-GT-202. Associate Technical Editor: H. Lukas.

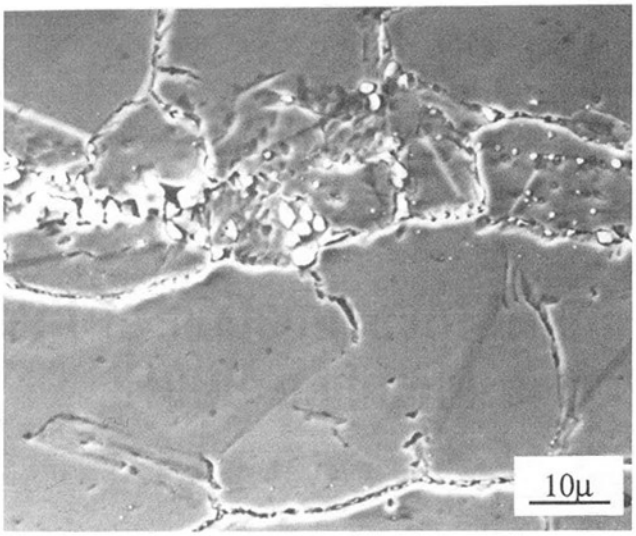

Fig. 2 SEM morphology of base metal microstructure in modified 800H (ht. V988-1)

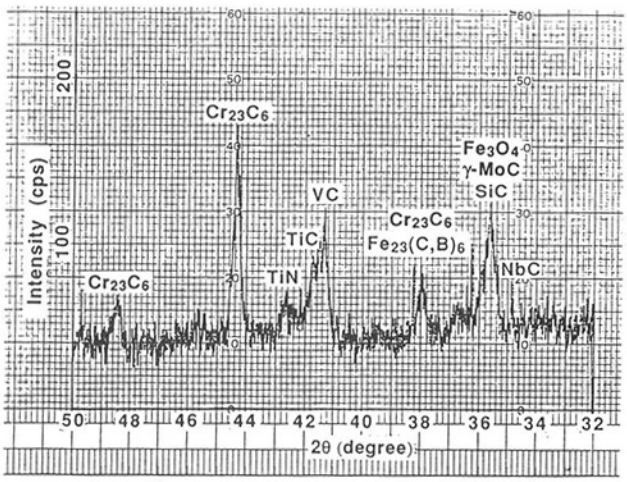

Fig. 3 The x-ray spectrum of particles extracted from as-received base material

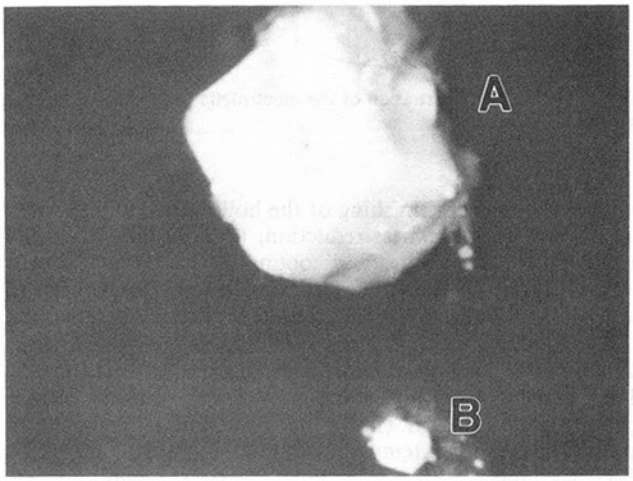

Fig. 4 SEM morphology showing the typical particles existing in base metal of modified 800H (ht. V988-1)

10 percent HCl and 90 percent methanol. A centrifuge was used to separate the particles from the solution. The weight percentage of the extracted particles for each sample was determined. A Rigaku x-ray diffraction apparatus was used to

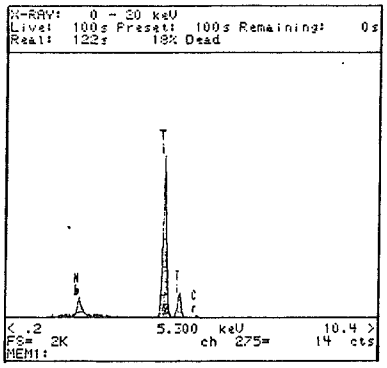

(a)

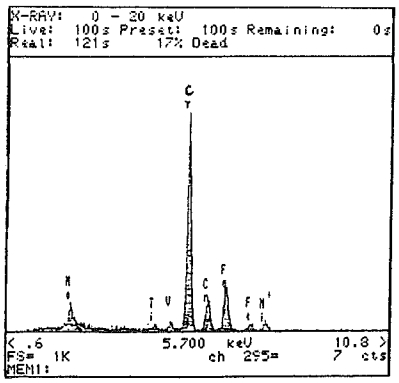

(b)

Fig. 5 EDS spectra of the particles indicated in Fig. 4: (*a*) spectrum for particle A; (*b*) spectrum for particle B

identify the particles. A small amount of the particles was also dispersively placed on sample stool and used to conduct an EDS evaluation.

Results and Discussions

Microstructural Morphologies. The SEM microstructural morphology of the base metal in modified 800H is illustrated in Fig. 2. It is to be noted that the precipitates are nonuniformly distributed. The location where the precipitates are concentrated is generally in the finer grain region, which results from the pinning effect of the particles on grain boundary migration during annealing. The particles electrolytically extracted from the base metal were examined by x-ray diffraction and the results are presented in Fig. 3. In the as-received condition, $M_{23}C_6$ type carbides are the dominant precipitates. Figure 4 shows the SEM morphology of the particles electrolytically extracted from the base material. Most of the precipitates obtained were defined as $M_{23}C_6$ and MC type carbides and/or M(C, N) type carbonitrides by using a Link EDS analytical system with a ZAF-P/B analytical computer program. The typical EDS spectra for TiC and $Cr_{23}C_6$ carbides are shown in Fig. 5.

Figure 6 shows the microstructure in a HAZ sample simulated with a peak temperature of 1001°C. It is clear that initiation of recrystallization is manifested with this thermal history as compared to the base metal. Precipitate dissolution has taken place. However, some large particles still remain as indicated by the arrows in Fig. 6(*b*). Figure 7 shows the microstructure from a simulated HAZ sample with a peak temperature of 1090°C. Significant evidence of recrystallization is observed and the average grain size is clearly finer than that of the base metal. More extensive dissolution of secondary

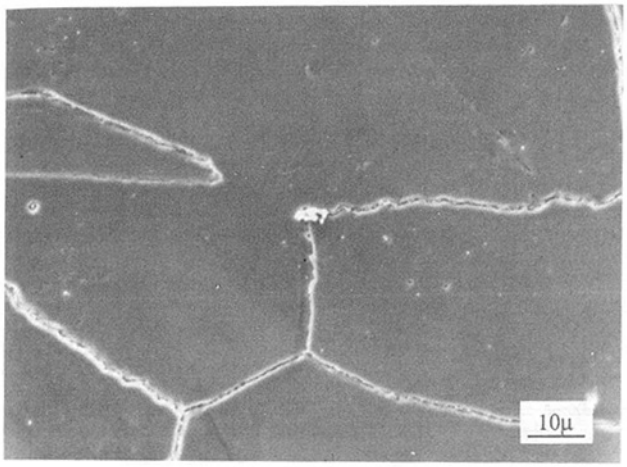

(a)

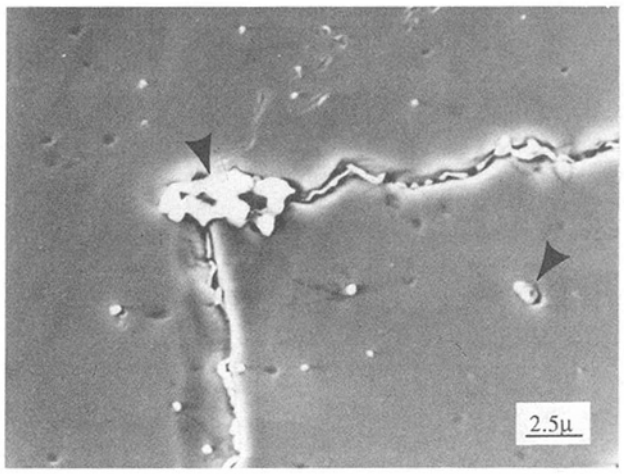

(b)

Fig. 6 Microstructure in the sample thermally simulated with a peak temperature of 1001°C

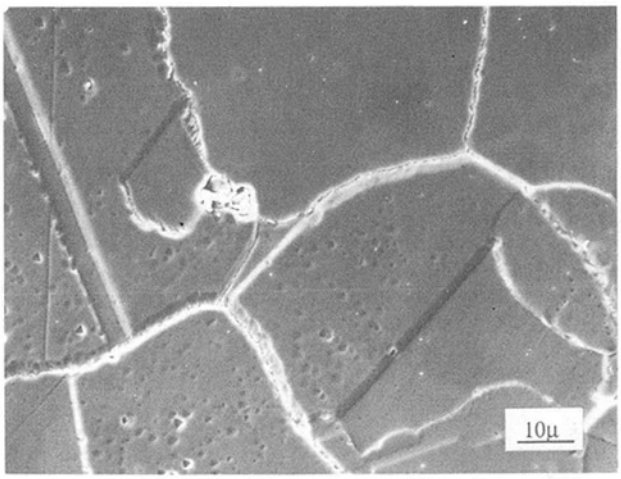

(a)

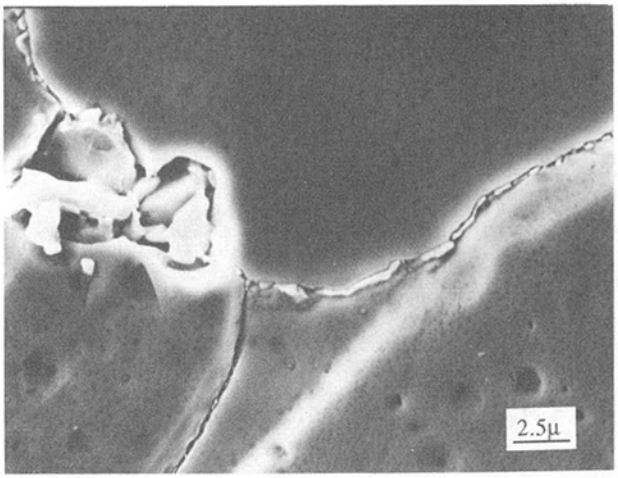

(b)

Fig. 7 Microstructure in the sample thermally simulated with a peak temperature of 1090°C

phase particles is revealed contrasted to the base material and the HAZ sample simulated with a peak temperature of 1001°C. Figure 8 shows the microstructure in a HAZ simulated sample with a peak temperature of 1145°C. A completely recrystallized microstructure is observed. Extensive precipitate dissolution is evident as compared to the HAZ simulated sample with a peak temperature of 1090°C (the triangle features in this figure are etch pits and are not related to precipitates). As indicated in Fig. 9, a microstructure with uniform grain size is revealed in the HAZ simulated sample with a peak temperature of 1200°C. The size of the particles in grain boundaries has decreased as compared to those in the HAZ simulated sample with lower peak temperatures. This can be more clearly observed at a higher magnification in Fig. 9(*b*). However, a fine precipitate is evident in the matrix as well as along the grain boundaries. This is due to the fact that MC type carbides precipitate along the grain boundaries and decorate dislocations in the matrix during cooling from 1200°C. At high temperatures (above 910°C for austenitic stainless steels), MC type carbides show a greater nucleation and growth rate as compared to $M_{23}C_6$ type carbides. Liquation was exhibited in the HAZ simulated sample with a peak temperature of 1260°C (see Fig. 10). The precipitate distribution and grain size in this sample are similar to those simulated with a peak temperature of 1200°C. Significant liquation occurred in the HAZ simulated sample with a peak temperature of 1285°C compared to that in the HAZ simulated sample with a peak temperature of 1260°C (see Fig. 11). Grain boundary migration and constitutional liquation are also noted in this sample. In the HAZ simulated sample with a peak temperature of 1320°C, liquation appears both intergranularly and intragranularly. The constituents produced along the grain boundaries by eutectic reactions are shown in Fig. 12.

The above observations reveal that several reactions can occur in the HAZ of modified 800H. These include grain boundary liquation, grain growth, recrystallization, secondary phase dissolution, and precipitation. All of these reactions may enhance hot crack formation in the HAZ and influence HAZ softening behavior. The metallographic observations also agree with the results of quantitative measurement of the amount of particles electrolytically extracted (Lundin and Qiao, 1992).

Grain Size and Microhardness Measurements

Grain Size Measurement. The grain sizes for all Gleeble thermally simulated HAZ samples were measured and are sum-

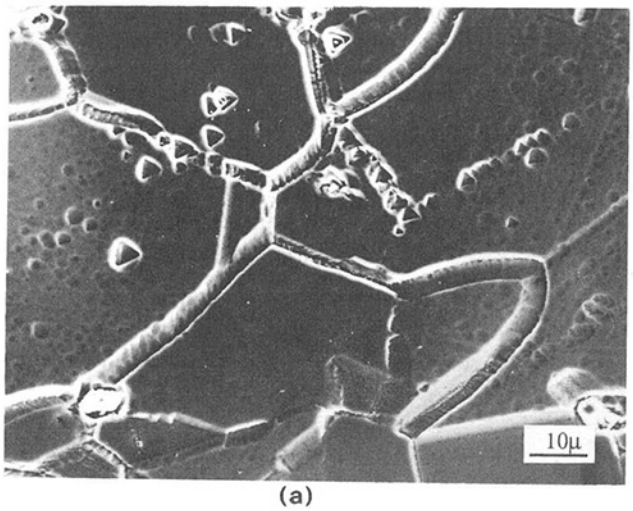

(a)

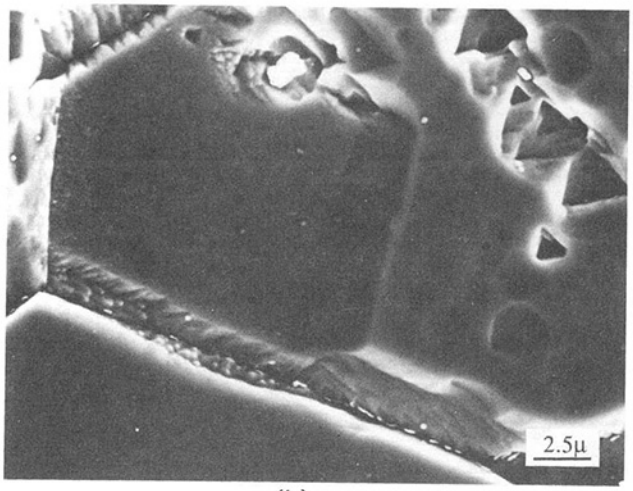

(b)

Fig. 8 Microstructure in the sample thermally simulated with a peak temperature of 1145°C

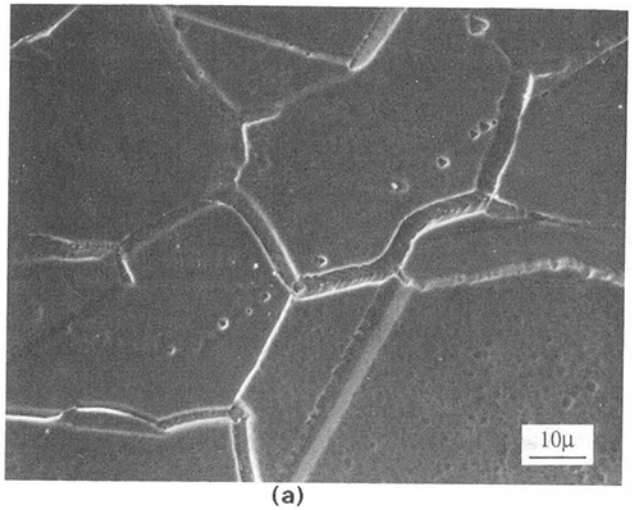

(a)

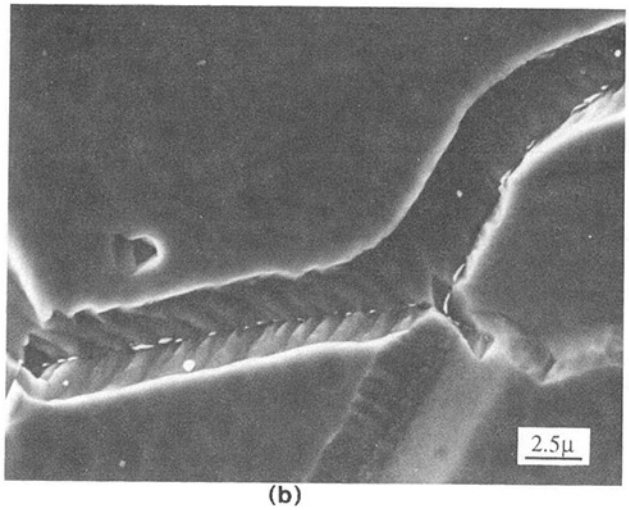

(b)

Fig. 9 Microstructure in the sample thermally simulated with a peak temperature of 1200°C

marized in Table 2. It is clear that changes in the HAZ grain size agree with the metallographic examination results described above. The liquation, at high temperature, that occurs along grain boundaries causes a pinning effect, retarding grain boundary migration. Therefore, there is almost no grain growth (as compared to the base metal) at the HAZ location characteristic of 1320°C and 1285°C peak temperatures. Slight grain growth was observed in the HAZ simulated sample with peak temperatures of 1260°C and 1200°C. Extensive recrystallization was observed in the sample simulated with a peak temperature of 1145°C. In the HAZ simulated sample with peak temperature of 1145°C a clearly reduced grain size was found as compared to that of base material. Recrystallization has occurred in the HAZ simulated samples with peak temperatures of 1090°C and 1001°C. All of these HAZ elevated temperature reactions are important in defining properties. Therefore, an understanding of the combined influence of these reactions on HAZ properties will be beneficial for alloy improvement.

It should be pointed out that an actual weld HAZ occurs over a narrow region and high resolution is required to identify the microstructures in an actual weld HAZ that are related to the simulated HAZ structures. Gleeble simulation techniques provide an approach to evaluate HAZ microstructues and reactions occurring in the HAZ precisely by expanding the HAZ region to a size for ready observation and ease of property measurement.

Microhardness Measurements. A summary of the hardness measurements for the thermally simulated HAZ samples is tabulated in Table 3. As indicated in Table 3, a hardness decrease occurred for all thermally simulated HAZ samples. The hardness decrease results from several factors. These include precipitate growth, precipitate dissolution, grain growth, and recrystallization. The results of hardness measurements indicate that a softened zone will exist in the HAZ adjacent to, but not contiguous with, the fusion boundary in the modified 800H material. The greater hardness value adjacent to the fusion line (1320°C) is a result of liquation segregation, which increases strength. The extent of hardness reduction in the HAZ of modified 800H is dependent on the combined effect of grain growth, recrystallization, precipitate dissolution, and redistribution. Therefore, the hardness values listed in Table 3 reflect this combined influence. It is to be noted

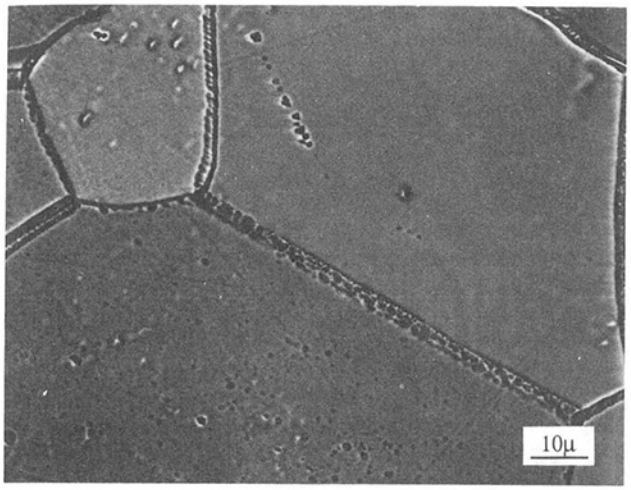

(a)

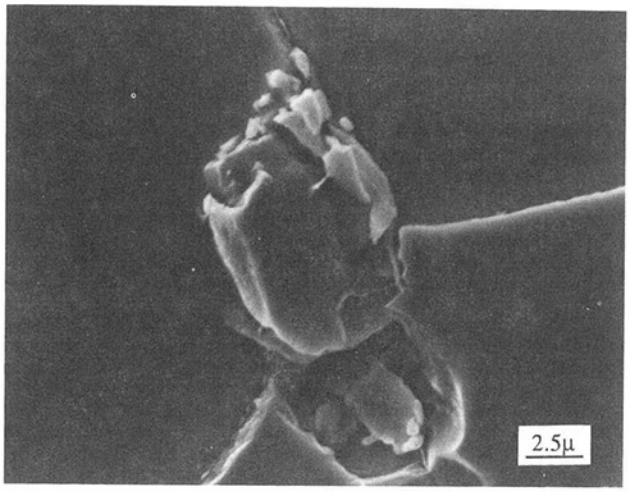

(b)

Fig. 10 Microstructure in the sample thermally simulated with a peak temperature of 1260°C

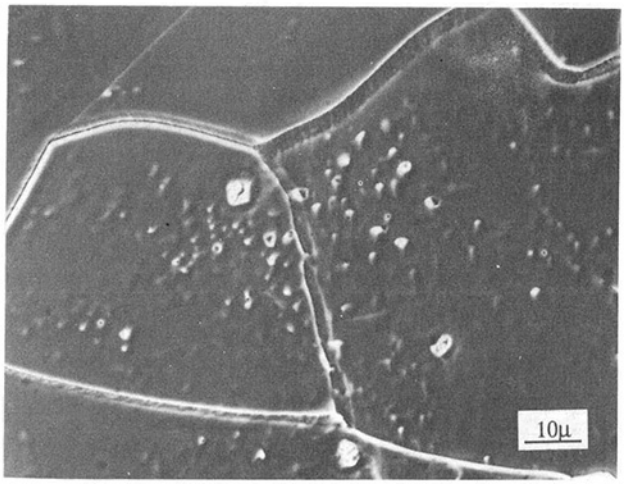

(a)

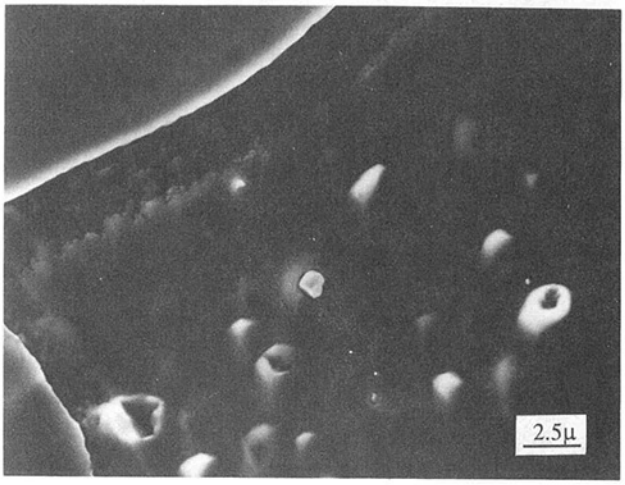

(b)

Fig. 11 Microstructure in the sample thermally simulated with a peak temperature of 1285°C

Table 2 Summary of grain size measurements

Simulated HAZ Peak Temperature (°C)	Grain Size (ASTM No.)
Base Material (22°C)	5
1001	5~5.5
1090	6
1145	6.5
1200	4.5
1260	4.5
1285	5
1320	5

Table 3 Summary of hardness measurement results

Simulated HAZ Peak Temperature (°C)	HV (0.1)
Base Material (22°C)	250
1001	192
1090	199
1145	156
1200	155
1260	156
1285	153
1320	185

that the results of hardness measurements on the Gleeble samples agree with the results of hardness traverses obtained from actual autogenous GTA welds (Lundin and Qiao, 1992).

Summary

Metallographic examination of modified 800H thermally simulated HAZ samples showed that HAZ liquation cracking can be related to HAZ reactions attendant with welding thermal exposure. Grain growth, precipitate dissolution, and reprecipitation along the grain boundaries in the HAZ can significantly enhance grain boundary segregation and affect liquation and thus the cracking tendency.

It is clear that precipitate dissolution and reformation behavior in the HAZ of modified 800H plus grain growth and recrystallization are the major factors that influence HAZ softening. Hardness (strength) loss in the HAZ is caused by a combination of these phenomena. Microhardness measure-

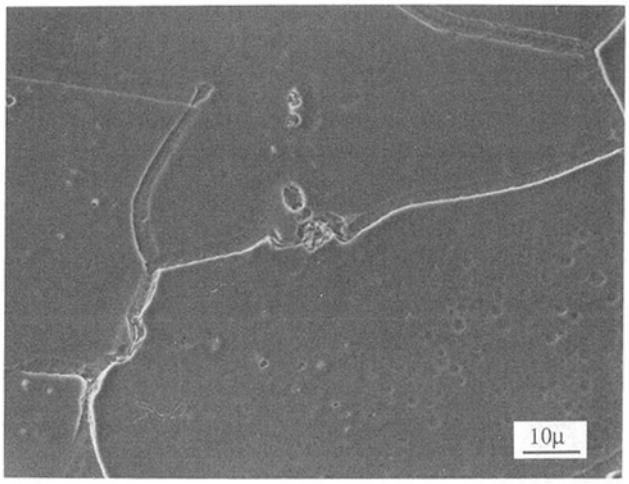

(a)

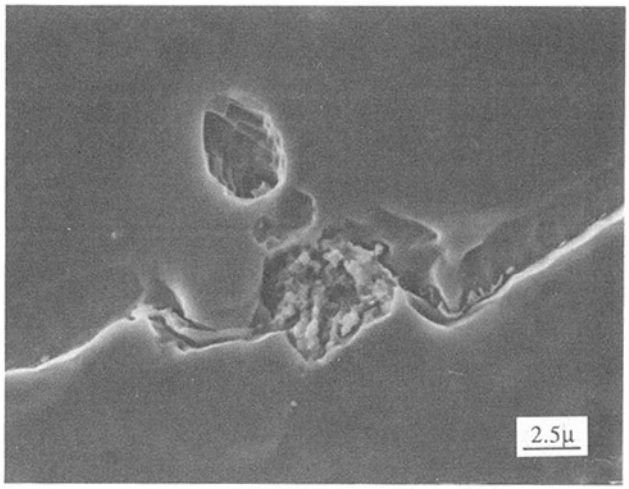

(b)

Fig. 12 Microstructure in the sample thermally simulated with a peak temperature of 1320°C

ments indicate that the location that showed the maximum decrease in hardness (HAZ softened zone) is adjacent to, but not contiguous with, the fusion zone (simulated HAZ with a peak temperature of 1285°C).

Acknowledgments

The authors record their thanks to R. R. Judkins, manager of DOE Fossil Energy Program at Oak Ridge National Laboratory, for his encouragement and review of the paper. The research is sponsored by the U.S. Department of Energy, through the Fossil Energy Materials Program, operated at Oak Ridge National Laboratory managed by Martin Marietta Energy Systems, Inc.

References

Edmonds, D. V., and Honeycombe, R. W. K., 1976, "Precipitation in Iron-Base Alloys," *Proceedings of Conference on Precipitation Processes in Solids*, The Metallurgical Society of AIME, Sept., pp. 121–160.

Lundin, C. D., and Qiao, C. Y. P., 1991, "Weldability of Nuclear Grade Stainless Steels," *Proceedings of the International Conference on New Advances in Welding and Allied Processes*, Vol. 2, May, pp. 3–10.

Lundin, C. D., and Qiao, C. Y. P., 1992, "Evaluation of HAZ Liquation Cracking Susceptibility and HAZ Softening Behavior in Modified 800H," Topical Report, ORNL/Sub/88-07685/03, Nov.

Marshall, P., 1984, *Austenitic Stainless Steels—Microstructure and Mechanical Properties*, Elsevier Applied Science Publishers Ltd., London-New York.

Ogawa, K., Miura, M., and Minami, T., 1986, "Carbide Precipitation and Corrosion Resistance in HAZ of 15Cr-75Ni Alloy," IIW Doc. IX-1411-86, July.

Sumitomo Metal Industries, Ltd., 1987, Technical Report, "Characteristics of a New Steel Tube (HR3C) With High Elevated Temperature Strength and High Corrosion Resistance for Boiler," Dec.

Swindeman, R. W., 1991, "Investigation of Austenitic Alloys for Advanced Heat Recovery and Hot-Gas Clean-up Systems," Technical Report, ORNL/FMP-91/2, Sept., pp. 223–230.

Weiss, B., Grotke, G. E., and Stickler, R., 1970, "Physical Metallurgy of Hot Ductility Testing," *Welding Journal*, Oct., pp. 471s–487s.

Computed Tomography Evaluation of Metal-Matrix Composites for Aeropropulsion Engine Applications

R. N. Yancey
Advanced Research and Applications Corporation,
Dayton, OH 45431

G. Y. Baaklini
NASA Lewis Research Center,
Cleveland, OH 44135

Computed tomography (CT) is a powerful evaluation tool for advanced propulsion engine materials and components. CT uses X-rays nondestructively to produce images of two-dimensional slices or planes through an object. This paper will present data from CT investigations of metal-matrix composite (MMC) ring, rod, and coupon structures. Moderate resolution CT data identified density variations within reinforced sections, which were correlated with fiber packing densities. Also, some composite lay-up features were also imaged. High-resolution CT data provided information on fiber spacing and distribution. Correlation with other NDE techniques and destructive analysis was good. CT proved to provide valuable information on the internal state of these metal-matrix composite components. Use of CT during process development of MMCs and the components made from MMCs is encouraged given the results of this study.

Introduction

Computed tomography (CT) has been called one of the 10 greatest scientific achievements of the past 25 years. Its use in the medical field is well established and accepted. Industrial CT has become a useful inspection and evaluation tool in certain fields and new applications are being identified. One of the promising areas for the application of industrial CT is in the aeropropulsion field. CT can provide useful information during many stages of aeropropulsion system development. Some of the potential areas are in material process development, prototype development, test evaluation and characterization, and final inspection.

CT is a technique whereby a finely collimated X-ray beam passes through a part and X-ray attenuation measurements are made through many angles. These X-ray measurements are then stored and reconstructed with the aid of a computer to generate images representing a two-dimensional slice or plane through the object.

By stacking a series of two-dimensional CT images, one can obtain full three-dimensional coverage. Figure 1 shows a comparison between CT and radiography. It can be readily appreciated that if an internal feature is detected in conventional projection radiography, its position along the line of sight between the source and the film is unknown. Somewhat better positional information can be determined by making additional radiographs from several viewing angles and triangulating. This triangulation is a rudimentary, manual form of tomographic reconstruction. In essence, A CT image is the result of triangulating every point in the plane from many different directions.

Metal-matrix composites have great potential for aeropropulsion engine applications. Ceramic fibers provide added stiffness to aeropropulsion components, especially at elevated

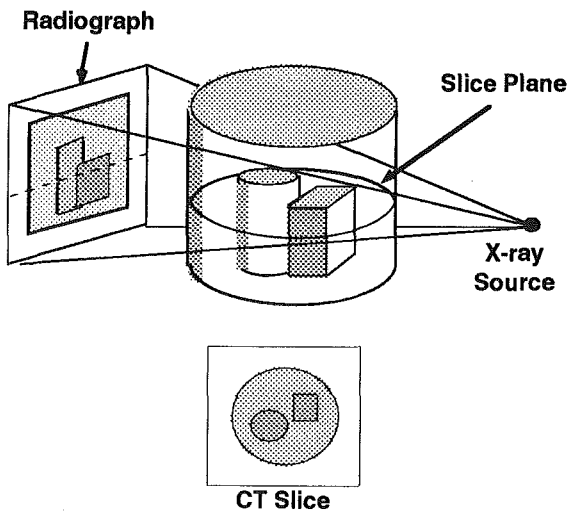

Fig. 1 Comparison between conventional radiography and computed tomography

Contributed by the International Gas Turbine Institute and presented at the 38th International Gas Turbine and Aeroengine Congress and Exposition, Cincinnati, Ohio, May 24–27, 1993. Manuscript received at ASME Headquarters February 12, 1993. Paper No. 93-GT-4. Associate Technical Editor: H. Lukas.

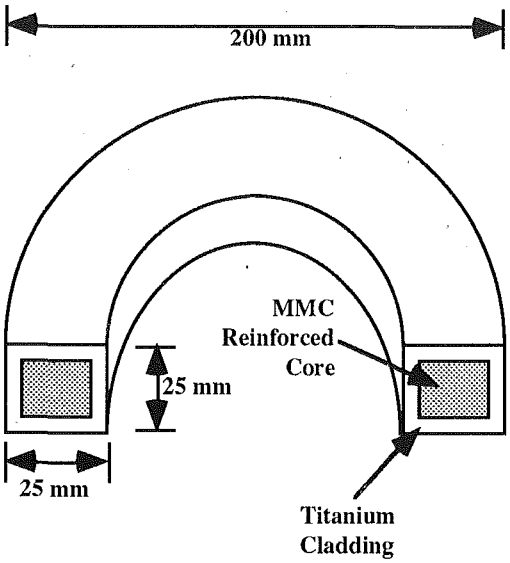

Fig. 2 Sketch of a cut MMC ring showing dimensions and locations of MMC reinforced core and the monolithic titanium cladding

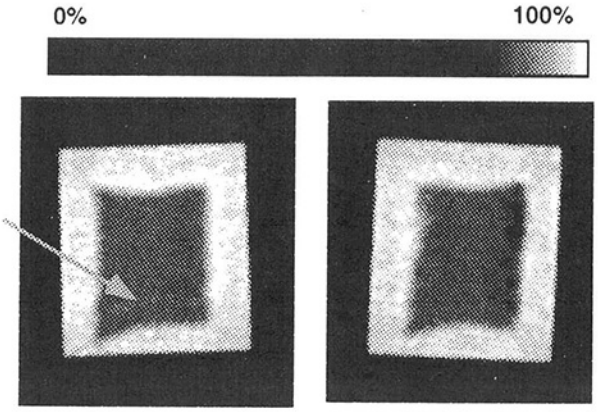

Fig. 3 LAM/DE CT cross sections of MMC ring showing location and shape of MMC core

temperatures. Successful implementation of MMC's into engines can reduce weight and increase engine temperature, which will increase engine performance and efficiency. MMC's are more difficult to process than conventional metal alloys and their composite structure also makes analysis and characterization a more involved task. Methods that can provide quick, accurate information on these materials during process development and/or component testing will speed their introduction into aeropropulsion applications.

This paper will present CT images taken with two industrial CT scanners. LAM/DE® is a CT machine used for applications research. LAM/DE can handle a variety of sizes and configurations of industrial objects and has a spatial resolution of approximately 0.25 mm. The Tomoscope® is a new-generation high-resolution CT scanner that can achieve a resolution of approximately 25 μm. Tomoscope has a limited field of view and can't handle objects bigger than 100 mm in diameter. Its 200-kV X-ray source also limits the amount of material that can be effectively penetrated. LAM/DE does not have the resolution capabilities of Tomoscope but it can handle much larger objects and has a 420-kV X-ray source giving better penetration of X-rays. These scanner hardware differences make Tomoscope useful for small laboratory type samples and LAM/DE useful for full-scale parts. Both LAM/DE and Tomoscope scans of various MMC materials and components will be shown and discussed.

The materials and components utilized for this study include titanium-based metal-matrix composites. In all of the materials and components, a Textron SCS-6 silicon carbide fiber is used. The fiber is 142 μm in diameter and is manufactured using a chemical vapor deposition process utilizing a carbon core. The MMC rings and the test coupon contain a Ti-15-3 titanium alloy for the matrix and the MMC rods and rotor contain a titanium alloy C matrix.

Metal-Matrix Rings

MMC ring structures are being developed for aeropropulsion applications. A sketch of the ring structure is shown in Fig. 2. The ring consists of an MMC core surrounded by a titanium-based cladding. The rings scanned during this study were approximately 200 mm in diameter, 25 mm thick, with a cross section of approximately 25 mm × 25 mm. Ideally, the MMC core is centered in the ring and its cross section is rectangular. The ring is manufactured by spirally winding an SCS-6 fiber bundle with titanium ribbon and then inserting the filament bundle into a titanium alloy slotted disk. Titanium caps are welded to the top of the slotted disk for sealing. The disk is consolidated by hot isostatic pressing and then machined to final shape. The MMC rotor is made in a similar fashion, except consolidation is carried out by vacuum-hot-pressing (VHP).

Half-Scale MMC Rings. Figure 3 shows two LAM/DE CT cross sections of an MMC ring. The color scale used for displaying the data is shown above the image. The total scale goes from 0 to the highest pixel value in the image. The gray level used within this range is shown in the color bar. Brighter shades correspond to higher densities. The images show that the reinforced region (dark) is not well centered within the ring. Also, its shape is irregular and in the bottom left of the left-hand image, the core comes very close to the outside edge. Some density variations are visible within the core regions. Destructive analysis has determined that the density variations within the core are indications of changes in the fiber packing density. The brighter line running horizontally near the bottom of the core (denoted by the arrow) in the left-hand image was found to be where two foil plies overlapped during the manufacturing process. Information on the core shape and location was used in modeling the ring structure to predict its response to high-temperature burst and fatigue life testing. Before the CT data were taken, the models assumed the core was centered and rectangular in shape.

Figure 4 shows a LAM/DE CT cross section with a graph line-out showing the extent of density variations with the reinforced core. The horizontal scale is in pixels, which were 0.25 mm square. The vertical scale is in CT number which is approximately equal to density in mg/cm^3 [1]. The graph shows the higher density titanium cladding, the lower density reinforced core, and the density variations within the core region. In the reinforced core, the left-hand spike of the graph corresponds to the overlapping titanium foil layers. The lower density in the bottom right of the core is also shown in the graph. The density variations within the core are not large but the sensitivity of CT allows these small variations to be imaged. As mentioned above, the density variations within the core were correlated (using destructive analysis) to changes in the fiber packing density [1, 2].

Fracture Surface. Figure 5 shows two LAMD/DE CT cross sections of a fractured specimen that has been cut from a failed MMC ring. The cross sections are perpendicular to the fracture surface yielding a different view from the images shown in

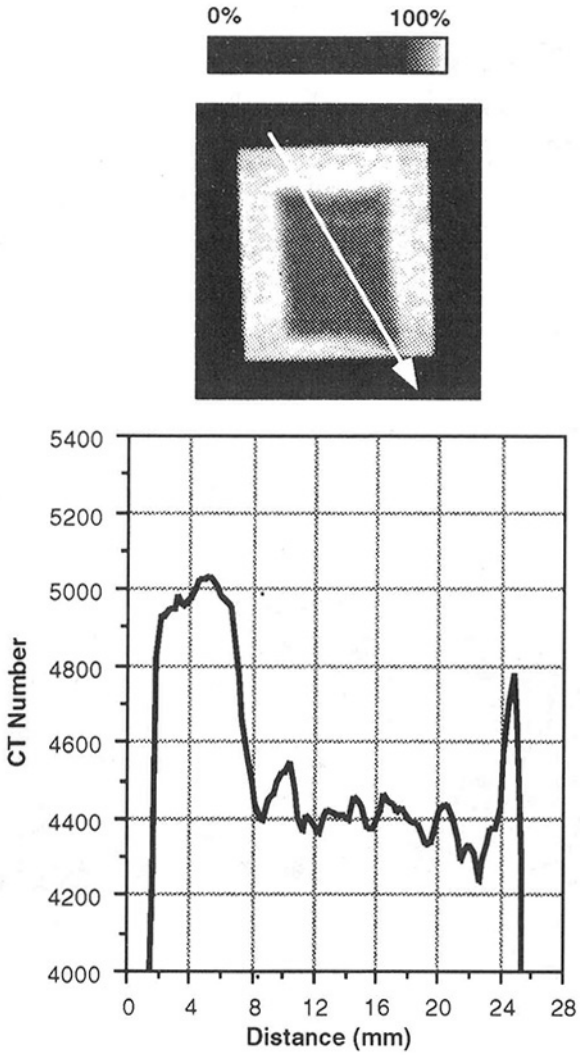

Fig. 4 LAM/DE CT cross section of MMC ring with density line-out graph showing extent of density variations

Figs. 3 and 4. The shape of the fracture surface can be seen in these images. The reinforced core is shown in the middle with the titanium cladding on the two outside edges. A dark vertical line in the right-hand image (denoted by the arrow) shows where a bundle of fibers was pulled out from this side of the fracture.

Figure 6 shows a Tomoscope CT scan of a failed MMC ring section. The CT slice is taken parallel to the fracture surface less than 1 mm below the fracture surface on the top of the image. The added resolution of Tomoscope provides enhanced detail in the image where the individual SiC fibers can be seen. Also, the presence of the extra layer of foil in the reinforced region is clearly imaged and is identified by an arrow in the image. Because of the lower energy X-ray source used on Tomoscope, some ring artifacts appear in the image. A size 25 mm × 25 mm for the MMC material is the limit of penetration for a 200 kV X-ray source. Even with these limitations, important information can still be gathered from the image.

Reinforced Rotor. Figure 7 shows a Tomoscope and LAM/DE image of a MMC rotor section. The Tomoscope image is shown in Fig. 7(*a*) and the LAM/DE image is shown in Fig. 7(*b*). Both images show the shape of the reinforced core. The LAM/DE image shows some density variations within the core, which are correlated in the Tomoscope image to changes in the fiber packing density. Again, the shape of the core is irregular and it is not centered within the rotor.

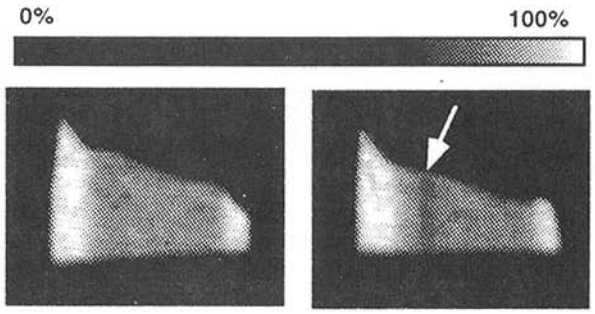

Fig. 5 LAM/DE CT scans of fractured specimen cut from a failed MMC ring

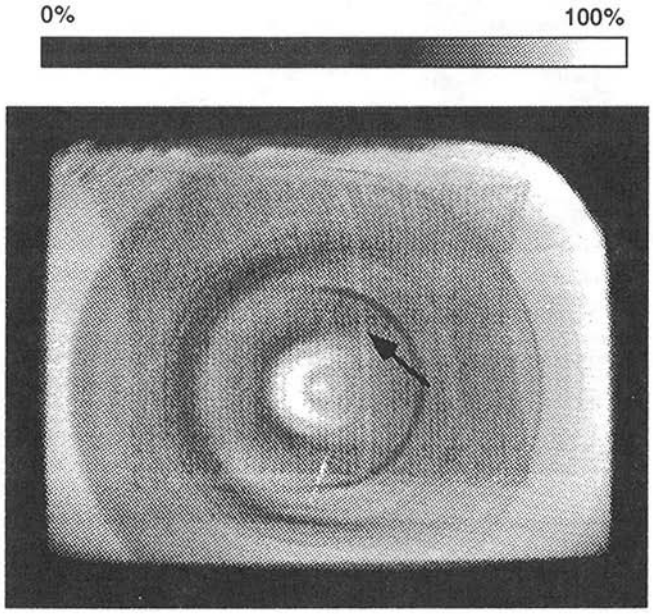

Fig. 6 High-resolution Tomoscope image of a fracture surface specimen cut from a failed MMC ring

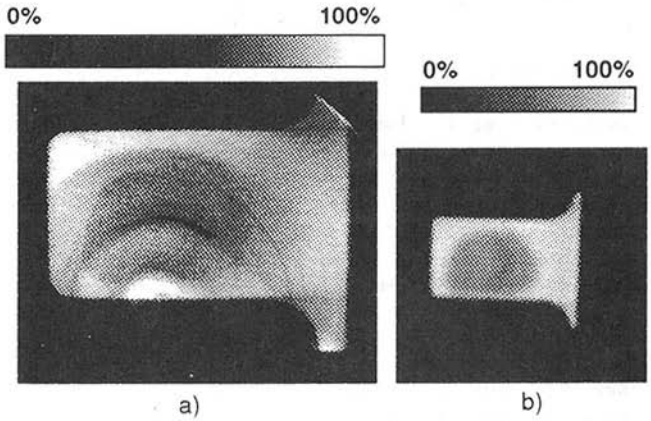

Fig. 7 CT images of MMC rotor with (*a*) a high-resolution Tomoscope image, and (*b*) a higher-energy, lower-resolution LAM/DE image

MMC Test Rods and Coupons

To evaluate various mechanical properties of MMCs, tensile test rods and coupons are fabricated. The test samples are expensive to fabricate and it is desired that the optimum amount of test data be obtained from a minimum amount of test material. CT can therefore play a role in characterizing the test rods and coupons before mechanical testing so that better correlations between material features and mechanical prop-

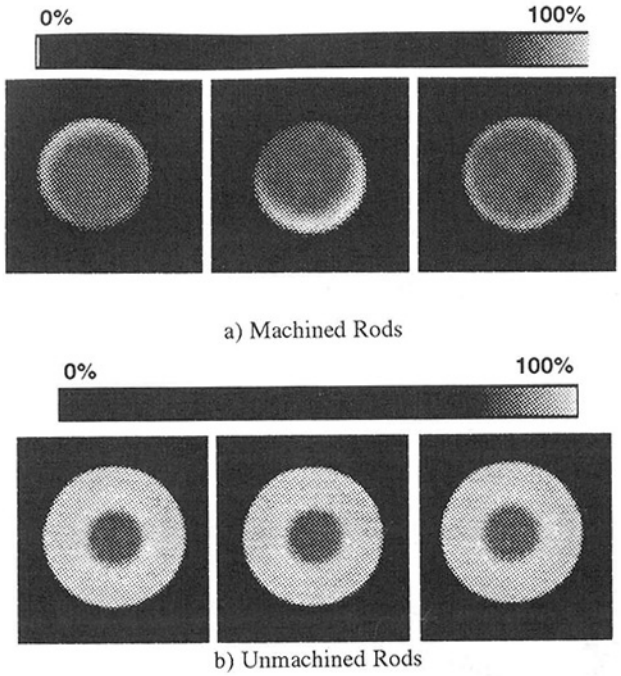

Fig. 8 LAM/DE CT scans of MMC test rods: (*a*) scans show reinforced core not well-centered in machined test rods, (*b*) scans of unmachined test rods to provide information to guide machining operation

erties can be made. In other words, the effect of given "defects" can be determined, which can then be provided as feedback to the material process development staff. In addition, CT can be used after various stages of testing to evaluate the growth or propagation of damage throughout a material.

The test rods are made by winding a bundle of SCS-6 fibers with titanium ribbon and then inserting this bundle into a titanium alloy cylinder. Titanium caps are welded to each end and the rod is consolidated by hot isostatic pressing. The rod is then machined to its final shape. The test coupons are made by laying down alternate layers of SCS-6 fibers and titanium alloy foils and then hot pressing.

MMC Rods. Figure 8(*a*) shows LAM/DE scans of three MMC test rods. The test rods are cylindrical dog-bone-type specimens. Like the MMC ring, an MMC reinforced core is surrounded by a monolithic titanium cladding. In this case, the CT scans reveal that the machining operation actually cut into the reinforced core of the left two samples. This information was documented for consideration in the test analysis and initiated the use of CT to guide machining future rods. Figure 8(*b*) shows LAM/DE scans of three MMC test rods before the rods were machined to their final configuration. The reinforced region can be seen within the thick titanium cladding. Given the data in Fig. 8(*a*), CT scans were taken of these unmachined rods to provide guidance to the machining operation. The reinforced core location was identified from the CT data and the rods were then machined to maintain the reinforced core in the center of the rod. This resulted in a significant cost savings.

MMC Test Coupon. Figure 9(*a*) shows a high-resolution Tomoscope scan of an MMC test rod. The corresponding LAM/DE image is shown in Fig. 9(*b*). Again, the higher resolution provides an image that shows the individual SiC fibers (142 μm diameter). This is a more accurate method to determine if machining actually cut into fibers. This type of data can also provide information on fiber distribution and identify regions where fibers may be widely spaced or touching.

Figure 10 shows another high-resolution Tomoscope scan

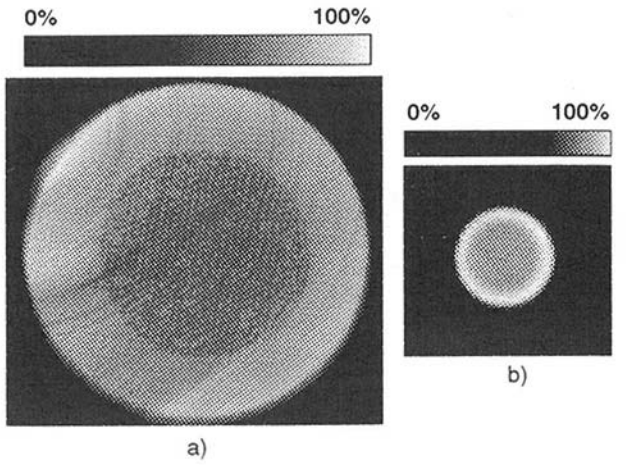

Fig. 9 High-resolution Tomoscope scan of MMC test rod showing arrangement of individual SiC fibers

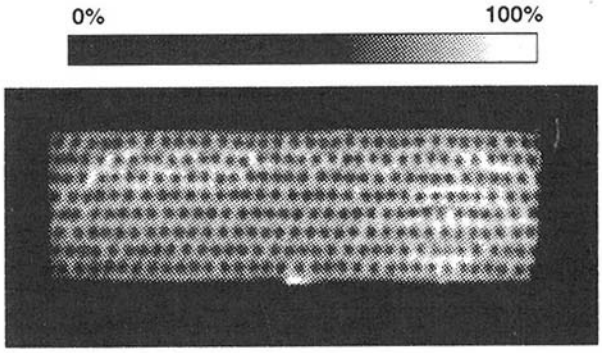

Fig. 10 High-resolution Tomoscope scan of eight-ply MMC test coupon showing uniform arrangement and distribution of SiC fibers

of an eight-ply MMC test coupon. The SiC fiber arrangement and distribution in this sample is very good. For this particular study, CT data were taken after the cycle had undergone several thermomechanical fatigue cycles. CT did not detect any damage in the sample and the coupon went on to withstand several additional thermomechanical fatigue test cycles.

Discussion of Results

CT data of these MMC materials and components have proved very useful in many respects. Three specific areas where the CT data were helpful were identified. These areas are explained briefly below.

Substitution for Destructive Analysis. Destructive analysis is often used to obtain detailed information on the internal structure of the materials and components. Information from destructive analysis can be very useful in determining failure modes in failed components. These methods have two main disadvantages: (1) They are time-consuming and expensive, and (2) they limit the viewing plane to the sectioned surface. CT, on the other hand, can be quick and can cover the entire part. Here, costly sample preparation steps are eliminated and the data can be viewed along any desired plane. In addition, CT data can be used to guide the destructive analysis so that it is more efficient and effective. CT does not have the resolution of SEM, so in some cases, destructive analysis will still be needed. For the MMCs, CT provided information on fiber distribution, fiber lay-up, and shape and location of reinforced regions. In many cases, that information may be sufficient to characterize a component. CT can definitely act as a substitute for a number of destructive analysis techniques currently used and point to the critical location where destructive analysis must be used.

Pedigree Evaluation. MMCs currently undergo a number of processing steps. Using CT during process development can help define where in a process a problem may be occurring. In other words, a single part is followed throughout a process so that the prior history of the part is known before each CT evaluation, hence the name pedigree evaluation. If parts are only inspected at the end of the process or at selected stages, the cause of certain defects cannot be ascertained easily. Also, certain features in a part during the early stages of processing may be causing the defect and pedigree evaluation methods allow for this to be determined. CT data used in this manner can significantly decrease the process development time period. Scanning the lay-up of foil and fiber mats before consolidation could have identified the overlapping foil layer shown in Figs. 3 and 4. CT used in this way can help better define processing procedures and also catch problems early on in a process where they can be fixed.

Effect of Defects. The term "defect" is often a very difficult one to define. A crack may be termed a defect but that may not necessarily mean that the crack is detrimental to the part. This concept is very important in MMC's since traditionally defined damage such as cracks may actually enhance performance rather than hinder it. For example, cracks or fiber-matrix disbonds in an MMC may relieve residual stresses, which might affect material properties in a positive manner or in a negative manner depending on the lay-up [3, 4]. As materials become more and more complex, the term "defect" needs to be used very carefully. CT can assist here since it can identify features in a material before the part or material is tested. The CT data can then be correlated with test results and the effect of the features can be determined. In this way, "defects" can be accurately defined. This may prevent unnecessary process development work, which tries to eliminate a feature that is not actually degrading the part performance. A proper understanding of which defects are important and which are not in the performance of the part is a critical step in process development.

Conclusions

CT provided very useful information on the MMC materials and components that were scanned. Data on fiber packing density, fiber distribution, lay-up configuration, and geometric properties were obtained with the CT scans. Those data were correlated with destructive and other nondestructive evaluation data on the same components. More of this correlation work is needed to provide the necessary confidence in the CT data. Continued work is encouraged with MMC's to establish further guidelines and procedures for using CT data. Also, development of high-energy, high-resolution CT scanners will be needed in the future to scan full-scale MMC engine components.

Acknowledgments

The Tomoscope® was developed under funding from the Defense Nuclear Agency, the Defense Advanced Research Projects Agency, and the Air Force Wright Research and Development Center. The LAM/DE® scanner was developed under funding from the Air Force Wright Research and Development Center. The CT scans in were taken under Air Force contract No. F33615-89-C-5618. This support is gratefully acknowledged.

References

1 Baaklini, G. Y., "X-Ray Attenuation Measurements for High-Temperature Materials Characterization and In-Situ Monitoring of Damage Accumulation," NASA TM-105577, Mar. 1992.

2 Baaklini, G. Y., and Bhatt, R. T., "Characterization of MMC Subscale Engine Components Using X-Ray Computed Tomography," HITEMP Review 1991, NASA CP-10082, 1991, pp. 33-1-33-14.

3 Johnson, W. L., Lubowinski, S T., Highsmith, A. L., Brewer, W. D., and Hoogstaten, C. A., "Mechanical Characterization of SCS6/Ti-15-3 Metal-Matrix Composites at Room Temperature," NASP Technical Memorandum 1014, NASA Langley Research Center, Hampton, VA 1988.

4 Sun, C. T., Chen, J. L., Sha, G. T., and Koop, W. E., "Mechanical Characterization of SCS-6/Ti-6-4 Metal-Matrix Composite," *Journal of Composite Materials*, Vol. 24, No. 10, Oct. 1990, pp. 1029-1059.

5 Yancey, R. N., Baaklini, G. Y., and Klima, S. J., "NDE of Advanced Turbine Engine Components and Materials by Computed Tomography," ASME Paper No. 91-GT-287, 1991.

6 Armistead, R. A., and Yancey, R. N., "Computed Tomography for the Nondestructive Evaluation of Advanced Engineering Materials," *Materials Evaluation*, Vol. 48, No. 5, May 1990, pp. 604-608.

7 London, B., Yancey, R. N., and Smith, J. A., "High-Resolution X-Ray Computed Tomography of Composite Materials," *Materials Evaluation*, Vol. 48, May 1990, pp. 604-608.

8 Yancey, R. N., and Klima, S. J., "High-Resolution Computed Tomography of Advanced Composite and Ceramics Materials," *Proceedings of the 15th Annual Conference on Composites and Advanced Ceramics*, ACerS, Cocoa Beach, FL, Jan. 13-16, 1991.

Calibrating Ultrasonic Images for the NDE of Structural Materials

R. S. Gilmore
GE Corporate R&D,
Schenectady, NY 12301

A. M. Glaeser
University of California,
Berkeley, CA 94720

J. C. Wade
Garrett APD,
Phoenix, AZ 85034

Ultrasonic imaging is taking a larger and larger role in the NDE of turbine engine materials and in support of fracture mechanics calculations. It is also playing an increasing role in quality and process control. For most fracture toughness calculations, it is necessary to establish the accuracy with which a flaw's size and shape are imaged, whether single or multiple flaws are involved, and the spacing of multiple flaws. Because of these requirements, resolution, as well as detection sensitivity, has become an issue. There are a number of resolution targets that can provide this type of calibration information for an ultrasonic imaging system. A fused quartz USAF 1951 target, similar to the patterns used in this work, was first used by Gilmore (1986), but Gilmore's pattern was superficial and subsurface evaluations were limited to focusing on the pattern from the opposite side of the blank and monitoring the reflection from what is now the target backwall. Work by Paton (1977) did produce buried targets in titanium samples, but there was no practical method to produce buried targets in high-temperature ceramics until the techniques developed by Rodel and Glaeser (1987) were used to produce the targets described in this paper. Optically transparent resolution targets make it feasible to verify visually that the resolution target has been correctly fabricated. An image of the target with a candidate ultrasonic transducer then permits quantitative image resolution estimates to be made even when the interrogating acoustic beam contains significant refractive aberration. This is important because useful subsurface images can be acquired with the use of acoustic beams that are aberrant to the point that diffraction-limited beam-width calculations are meaningless. This work also demonstrates how the interdisciplinary skills of manufacturing companies can be combined with those of universities to produce results that any one of the individual members of the team could not have produced alone, without significant increases in labor, time, and cost.

Introduction and Historical Review

The resolution target work was initiated to meet a specific need. In 1989 an extensive testing and evaluation project on silicon nitride as an engine structural ceramic was initiated by the Department of Energy through the Oak Ridge National Laboratory.

Allied Signal's Garrett Auxiliary Power Division was chosen as prime contractor by Oak Ridge. In order to solve the ultrasonic imaging problems posed by the necessity to detect and characterize very small flaws in silicon nitride test samples, a team was assembled that included the above-mentioned authors. The calibration concept, proposed by this team, was straightforward. A USAF 1951 image resolution target (Fig. 1) was to be imbedded in a transparent material that had the same ultrasonic velocity as the Norton NT-154 silicon nitride ceramic used for the bulk of the testing program. The smallest resolvable line-space combination would then define the resolution.

Military Standard 150-A describes this basic pattern, which has become known as the USAF-1951 or simply the "Air Force" target. Each element consists of two patterns oriented at right angles to each other, each containing three lines and two spaces. The line and spacing width are equal; the line length is equal to five times the line width. The change in pattern size is based on the sixth root of two; i.e., for every six target elements the number of line spaces per millimeter doubles. Each six-target element set is known as a group, and the group number (0, 1, 2, 3, and 4 for the targets used in this paper) is the power of two to which the first element in the group is raised to express the number of lines per millimeter. Therefore, the numbers 0 to 4 for these targets correspond to 1, 2, 4, 8, and 16 lines per millimeter as shown in the table in Fig. 1.

Targets were fabricated from transparent materials with acoustic longitudinal and shear velocities similar to those of the optically opaque NT-154. This assured that the refractive aberration (as shown in Fig. 2) affecting the acoustic beam in the target would be similar to that produced in NT-154. The longitudinal (C_L) and shear (C_S) velocities in the C-axis direction in single-crystal sapphire (C_L = 11.22 mm/μs, C_S = 6.10 mm/μs) closely match the velocities in NT-154 (C_L = 11.15 mm/μs, C_S = 6.16 mm/μs).

Contributed by the International Gas Turbine Institute and presented at the 38th International Gas Turbine and Aeroengine Congress and Exposition, Cincinnati, Ohio, May 24-27, 1993. Manuscript received at ASME Headquarters March 10, 1993. Paper No. 93-GT-300. Associate Technical Editor: H. Lukas.

Number of lines per millimeter in USAF resolving power test target 1951

Element No.	Group Number									
	−2	−1	0	1	2	3	4	5	6	7
1	0.250	0.500	1.00	2.00	4.00	8.0	16.0	32.0	64.0	128.
2	.280	.561	1.12	2.24	4.49	8.98	17.95	36.0	71.8	144.
3	.315	.630	1.26	2.52.	5.04	10.1	20.16	40.3	80.6	161.
4	.353	.707	1.41	2.83	5.66	11.3	22.62	45.3	90.5	181
5	.397	.793	1.59	3.17	6.35	12.7	25.39	50.8	102.	203.
6	.445	.891	1.78	3.56	7.13	14.3	28.51	57.0	114.	228.

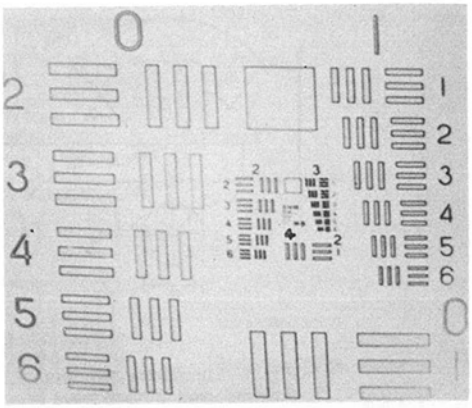

Fig. 1 Table of sizes and image format for USAF resolving power test target 1951 as provided by Teledyne-Gurley Inc., Troy, NY

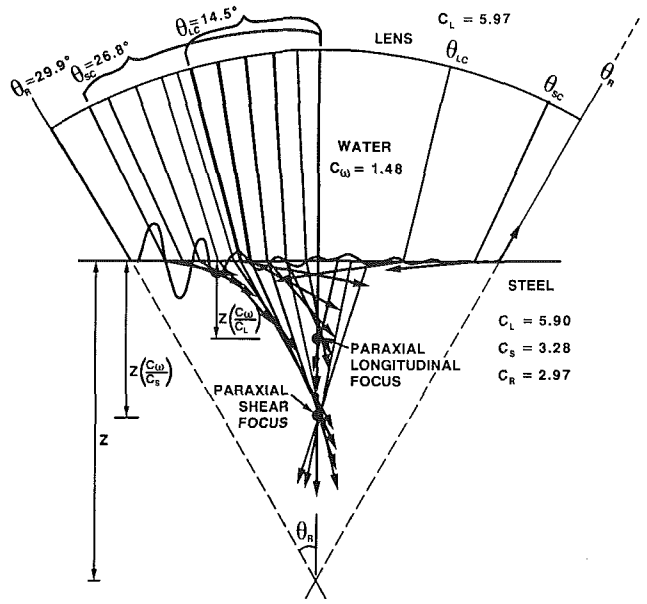

Fig. 2 The angular spectrum for a water-steel interface showing the critical θ_i angles for the longitudinal (θ_{LC}), shear (θ_{SC}), and Rayleigh (θ_R) wave, and the refractive aberration caused by incidence to the water-steel interface at angles approaching $\theta_i = \theta_{LC}$, and $\theta = \theta_{SC}$

Widespread interest in these resolution targets by other ultrasonic groups suggests that this is an effective strategy. This paper discusses work that has continued beyond the effort to develop the structural ceramic standards. The Rodel and Glaeser diffusion bonding techniques have also been used to produce buried 1951 USAF resolution targets in lead borosilicate glass and in [100] cut silicon. These additional target materials permit the velocities in a number of test materials to be matched to the velocity in the resolution standard. In addition to silicon nitride, sapphire can also be used to match other structural ceramics such as polycrystalline Al_2O_3, BeO, MgO, and SiC. Lead borosilicate glass produces targets that match the zirconium alloys and other lower velocity materials. The [100] cut silicon wafer sample was prepared to provide a standard to evaluate heat sink bonding integrity in silicon chip carriers for integrated circuit applications. The fused quartz resolution target used by Gilmore et al. (1986) is a good velocity match to most structural steels, including those used for high-temperature turbine engine disks and blades. Fused quartz also is a good velocity match to the oxide loaded glasses used in computer chip carrier applications.

Ultrasonic C-Scan Imaging

The method of mechanically scanning ultrasonic images was first used for NDE in 1954 (Buchanan and Hastings, 1955). Since then it has been further developed by Lemons and Quate (1973), Tsai et al. (1977) and by many others (some listed in Liang et al., 1985), for materials characterization and evaluation, and for manufacturing process and quality control. In addition to providing a visual estimate of bond integrity, material integrity, and flaw size, the spatial correlation of the ultrasonic echoes from a flaw provides a higher probability of detection (PoD). PoD is improved, first, because the multiple echoes are spatially correlated and identified, by the imaging process, to come from single or multiple discontinuities. In addition, the signal-to-noise ratio is improved when signals scattered by the material microstructure (N) add algebraically to the flaw discontinuity signals (S) producing a $(S + N)/N = S/N + 1$ ratio in the image.

Ultrasonic images generally fall into one of two categories: surface images or volume images. The type of image is determined by how the incident beam is focused and how the signals are gated. These are in turn established by the transducer lens and the velocities in the material being imaged. The key considerations are summarized in Figs. 3 and 4.

By restricting this discussion to quasi-isotropic materials, the acoustic properties of the material can be described by the density and three velocities. These are the longitudinal (C_L), the shear (C_S), and the surface or Rayleigh (C_R) velocities, respectively. For the materials listed in Table 1, the ratio C_L/C_S is typically about 1.6, and the ratio C_R/C_S is typically about 0.92. When an acoustic ray is incident through a fluid with a velocity C_2 onto a multiple velocity substrate with two or more refracted velocities C_L, C_S, and C_R, then the direction of the refracted rays shown in Fig. 2 is described by Snell's law

$$\sin \theta(L, S, R) = \frac{C(L, S, R)}{C_i} \sin \theta_i$$

where θ_i is the angle of the incident ray in the fluid and $\theta(L, S, R)$ are the angles of the refracted longitudinal, shear, and surface rays. The values for which $\sin \theta(L, S, R) = 1.0$ are called the critical angles for each of the respective velocities. Neglecting the occurrence of nonpropagating waves and their behavior, for C_L and C_S, the critical angles of incidence are those at which longitudinal, shear, and surface waves are refracted parallel to the entry surface. For the longitudinal and shear modes, the fluid–solid interface dramatically increases in reflectance as the critical angle is approached, and since neither the longitudinal nor the shear modes develop surface propagating waves, the ability of those modes of propagation to interact with the substrate material is limited by their critical

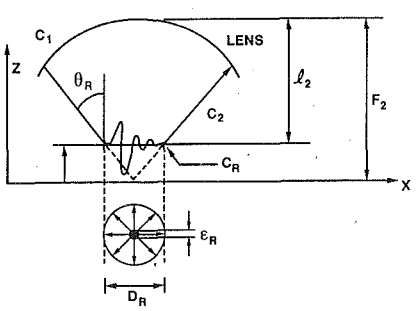

$D_R = 2Z \tan \theta_R$

$= 2[F_2 - \ell_2] \tan \theta_R$

λ_R = SW WAVELENGTH

C_R = SW VELOCITY

$\varepsilon_R\big|_{-3dB} = 0.32\ \lambda_R$

$\varepsilon_R\big|_{-1dB} = 0.16\ \lambda_R$

$\varepsilon_{RZ}\big|_{-3dB} = \lambda_R$ (BROADBAND PULSES ONLY)

D_R = Diameter of entry circle produced by the intersection of the Rayleigh critical angle cone with the entry surface.

λ_R = Wavelength of the Rayleigh wave on the entry surface.

C_R = Velocity of the Rayleigh wave on the entry surface.

ε_R = -3 dB diameter of the amplitude maximum caused by the convergence of the Rayleigh waved at the center of the Rayleigh entry circle. Defines 1 shade of gray or resolution produced by the beam convergence.

ε_R = -1dB diameter of the amplitude maximum described above. Used to specify the pixel size/spacing for the image.

ε_{RZ} = -3 dB sensitivity drop of a broadband Rayleigh wave (less than 2 wave pulse length) beneath the surface of propagation.

Fig. 3 Summary of the equations and the parameters describing the diffraction limited resolution for a time-resolved surface wave image

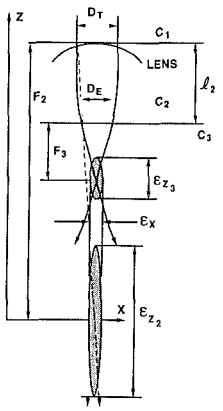

SPHERICAL FOCUS $F/D \geq \frac{C_3}{C_2}$

$\varepsilon_X\big|_{-3dB} = 1.03\ \lambda_2 \frac{F_2}{D_T} = 1.03\ \lambda_3 \frac{F_3}{D_E}$

$\varepsilon_X\big|_{-1dB} = 0.4\ \lambda_2 \frac{F_2}{D_T}$

$\varepsilon_{Z_2}\big|_{-3dB} \simeq 4\ \lambda_2 \left[\frac{F_2}{D_T}\right]^2$

$\varepsilon_{Z_3}\big|_{-3dB} = 4\ \lambda_2 \left[\frac{F_2}{D_T}\right]^2 \frac{C_2}{C_3} = 4\ \lambda_3 \left[\frac{F_3}{D_E}\right]^2$

$F_3 = [F_2 - \ell_2] \frac{C_2}{C_3} \quad \lambda_3 = \frac{C_3}{C_2} \lambda_2$

$D_E = \frac{F_2 - \ell_2}{F_2} D_T$

$\frac{F_3}{D_E} = \frac{F_2}{D_T} \frac{C_2}{C_3}$

C = Ultrasonic velocity in the lens (C_1), the water or coupling fluid (C_2), and the part (C_3), respectively.

λ = Ultrasonic wavelengths (velocity/frequency), for the lens (1), water (2), and part (3), respectively.

F = Focal length produced by the transducer lens in the water (F_2), and part (F_3), respectively.

D_T = Diameter of the transducer element and/or lens.

D_E = Diameter of ultrasonic beam on entry into the part.

ε_X = -6 dB and/or -1 dB beam diameters of diffraction limiter focal zones in either the water or the part. -6 dB is industry standard for transducer characterization, -1dB is used to determine pixel size for imaging.

ε_Z = -3 dB depths of the focal zones produced by the transducer lens in the water (ε_{Z_2}), and part (ε_{Z_3}).

l = Transducer lens to part distance (water path).

X = Coordinate axis perpendicular to acoustic axis.

Z = Coordinate axis parallel to acoustic axis.

Fig. 4 Summary of the equations and the parameters for the lateral resolution produced by a diffraction limited focused acoustic beam in a beam forming fluid or in a high-velocity substrate

Table 1 Longitudinal, shear, and surface wave velocities of selected materials and the respective critical angles; the C-axis sapphire is reported as if it was transversely isotropic for the shear and surface wave velocities—this is only approximate

Material	Density	C_L mm/μsec	C_S mm/μsec	C_R mm/μsec	θ_L (degrees)	θ_S (degrees)	θ_R (degrees)
H_2O (22°C)	1.0	1.48					
[001] sapphire	3.99	11.22	6.10	5.50	7.6	14.0	15.5
[100] silicon	2.33	8.90			9.6		
[111] silicon	2.33	9.37			9.1		
NT-154 SiN	3.25	11.15	6.16	5.54	7.6	13.9	15.5
SiC (HIP'ed)	3.25	12.65	6.25	5.92	6.7	13.7	14.5
Fused SiO_2	2.22	5.97	3.74	3.44	14.2	23.3	25.5
Sintered Diamond	3.87	16.49	11.20	9.89	5.2	7.6	8.6
Steel	7.9	5.90	3.28	2.97	14.4	26.8	29.9
Inconel 718	8.3	6.10	3.18	2.95	14.0	27.7	30.1
Lead Glass	3.65	4.21	3.12	2.90	20.5	28.3	30.7
Zirconium	6.49	4.80	2.40	2.22	18.0	38.1	41.8

angles. In comparison, the Rayleigh critical angle θ_R is the angle at which a propagating surface wave mode is generated. When the acoustic rays are considered at monotonically increasing angles of incidence (such as for the water–steel interface shown in Fig. 2), a plot of the acoustic amplitudes, modes of propagation, and critical angles for the modes is often called the angular acoustic spectrum of that substrate material. Therefore, when the cone of focus is made large enough to include the Rayleigh critical angle (so that surface wave images can be made), reflections from discontinuities in the vicinity of the longitudinal and shear subsurface foci can also contribute to the image by interacting with the surface wave.

This discussion will not redevelop the beam diameter cal-

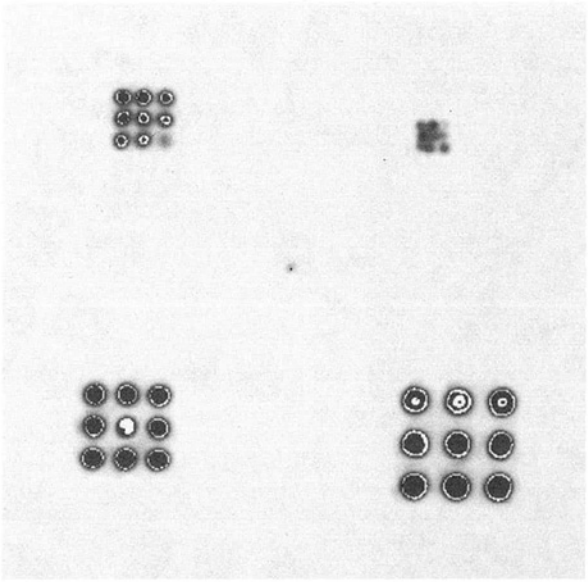

Fig. 5 Acoustic image of a block with multiple flat-bottomed holes. There are four 3 × 3 arrays of holes spaced at the hole diameter, and a single hole at the block center. Each array has nine holes with diameters of 400, 800, 1200, and 1600 μm, respectively. The single hole is 400 μm. Note that the 400 μm holes are detected but not resolved (separated) by the 20 MHz, F/7.0 acoustic beam, which is 500 μm in diameter.

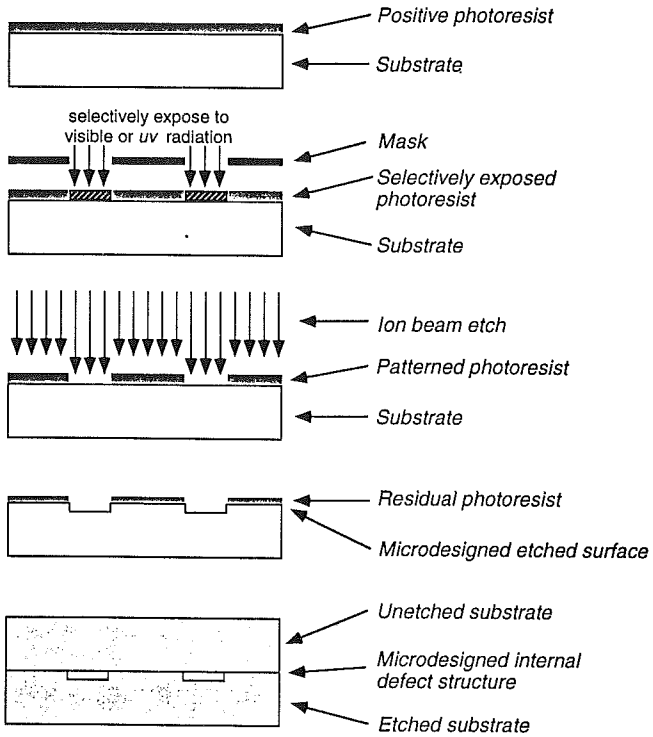

Fig. 6 Schematic illustration of the procedure used to produce the subsurface target pattern in single-crystal sapphire blanks 1.5 mm and 3.0 mm thick: (*a*) coated substrate, (*b*) selective exposure through a USAF 1951 mask, (*c*) ion beam etching of substrate and patterned photoresist, (*d*) etched photoresist and sapphire, and (*e*) bonding of etched and unetched sapphire blanks

culations summarized for surface wave imaging in Fig. 3 and for volumetric imaging in Fig. 4. Similar calculations have been well discussed by Liang et al. (1985) and references cited therein, and by Gilmore (1986, 1988). What this paper wishes to emphasize is that subsurface foci in high-velocity substrates almost always contain significant refractive aberration, such as shown in Fig. 2. In addition, they also contain micro-aberrations due to grain-to-grain anisotropy. The use of single crystal and glass resolution standards eliminates grain anisotropy from the resolution standard images. However, grain-to-grain anisotropy is the mechanism that permits all acoustic images, and particularly surface waves, to image the microstructure. In fact, surface wave images of microstructure are simply micro-aberration images. For volumetric imaging, unless the ratio of transducer focal length to diameter in the fluid is equal to or greater than the velocity ratio of the substrate/fluid interface, (F/D C_3/C_2, Fig. 4), the most straightforward method to determine the resolution produced at a subsurface plane in a high-velocity solid is to scan a resolution target fabricated from the subject material or a velocity-matched material.

Standards for Ultrasonic Inspection Methods

The development of standards for establishing the sensitivity and resolution of all ultrasonic NDE inspection methods has proven to be an ongoing problem for the testing industry. The traditional sensitivity standard is a flat-bottomed hole (FBH), first proposed by the Krautkramers (1977). Drilled into materials that are identical in composition and in microstructure to those being inspected, the FBH provides a reflector of known circular (and therefore mathematically definable) scattering cross section. Since, as a first-order approximation, pulse-echo amplitude is linearly proportional to the area of a compact flat reflecting void perpendicular to the acoustic axis of the interrogating beam, the FBH area establishes the reflecting area that can be detected, hence the test sensitivity. However, an ultrasonic image of a single hole can only show that it was detected; no resolution information is supplied. Another drawback is that the circular bottom of the hole is always accompanied by a cylindrical shaft connecting it to the drilled surface, and therefore it is surface connected and only approximates the buried circular void/crack it is intended to represent. In addition, for materials with scattering microstructures (i.e., materials with grains, or more than one material such as composites) the echoes from the bottoms of small holes add algebraically to the grain boundary reflections, producing significant echo amplitude variations from holes of precisely the same size. Therefore, single reflector calibration blocks can overcalibrate or undercalibrate depending on the location of the FBH in the material microstructure. In order to meet these problems and to solve the sensitivity/resolution dilemma, standards have been developed with multiple hole patterns (Mitchell and Gilmore, 1992, Fig. 5). These hole patterns can determine the variance in amplitude and resolution produced by scattering materials and are easy to make for materials that can be drilled, such as titanium, steel, and zirconium. But ceramics are difficult to drill, and holes only a few microns in diameter, such as are required to calibrate inspections for small voids in structural ceramics, are especially difficult.

Development of Imaging Standards With Photolithography

Lithography has furnished a new tool for studying and for creating subsurface void arrays with very precise geometries. These arrays may be produced in high-temperature structural ceramics, in many glasses, and at ceramic–metal interfaces. The combination of photolithographic methods with ion beam etching and hot pressing provides the ability first to produce surface features with highly precise geometries and locations and then to transform these features into internal features without losing this detail. The methods summarized here are reported in greater detail elsewhere (Rodel and Glaeser, 1987, 1989).

The basic steps for the manufacture of subsurface target-void patterns are shown schematically in Fig. 6. A flat, optically

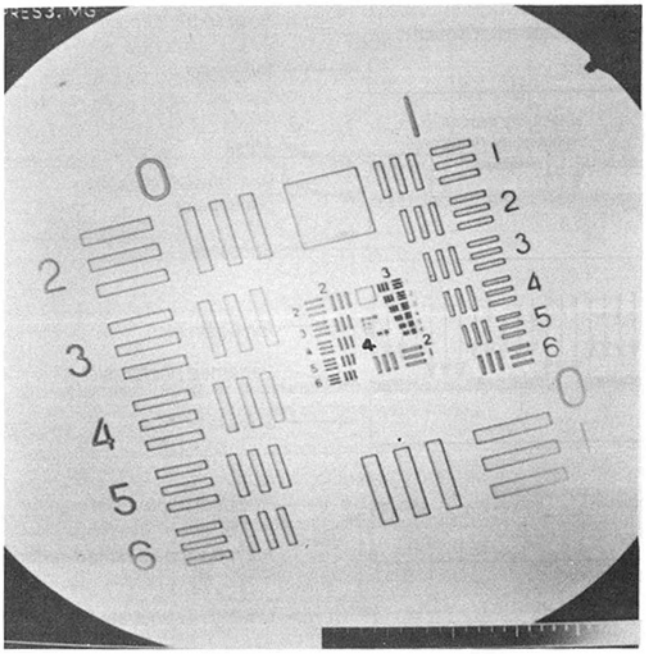

Fig. 7(*a*) 50 MHz, F/0.8 image of USAF 1951 pattern etched on the surface of a fuzed quartz plate. The 1024 × 1024 image covers 25.4 × 25.4 millimeters, making the pixel size 25 μm, which is also the transducer beam diameter.

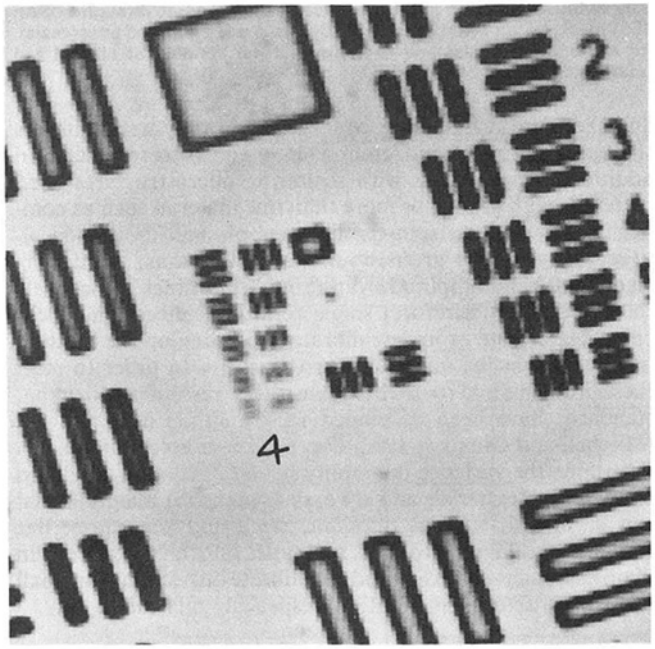

Fig. 7(*b*) Magnified image of the Group 4 segment of Fig. 7(*a*). The 25 μm pixels are now visible, as is the loss of resolution as the line pairs approach 32 lines/mm.

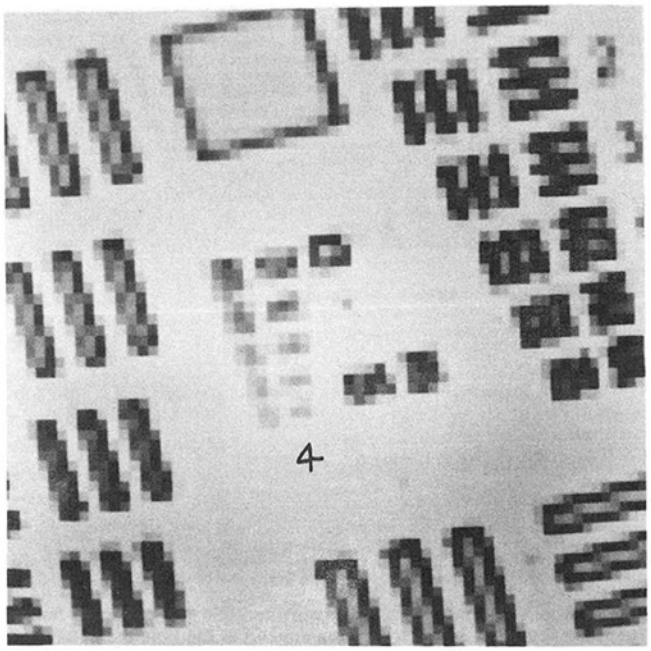

Fig. 7(*c*) Image of the same area as in Fig. 7(*b*) but undersampled in two directions by a factor of two. The image now displays Group 3 patterns with the same relative resolution as in Fig. 7(*b*) resolved in Group 4.

polished substrate (single-crystal or polycrystalline) is coated with a uniformly thick photoresist layer. Using typical process conditions, the photoresist layer may be from 1.3 to 2.6 μm in thickness. The photoresist is then selectively exposed to ultraviolet radiation using a mask to control the shape of the exposed features. This mask is produced by pattern generation software, and in this case the USAF resolution target (purchased from Teledyne-Gurley, Troy, NY) provided the design. For positive photoresists, exposure increases the solubility of the layer and therefore permits its selective removal, exposing the substrate. Ion beam etching is then used to etch the exposed ceramic surface and thereby transfer the pattern to the ceramic substrate. After removal of the remaining photoresist, an etched and unetched sample may be bonded to place the void pattern at an internal interface.

For the sapphire target used to produce the acoustic images in Figs. 8(*a*), 8(*b*), and 8(*c*), vacuum hot pressing (1370°C, 15 MPa, 2.6 mPa) was used to bond a 1.5-mm-thick unetched single crystal [001] sapphire slab to a 3.0-mm-thick etched slab of the same [001] orientation. This produced the USAF-1951 target embedded in a volume of single-crystal sapphire. The target contains bar-space patterns 0, 1, 2, 3, and 4, as described in Fig. 1, with an entry surface to target-pattern depth of either 2.0 or 4.0 mm. Referring to the table in Fig. 1, these range from 1 to 28.5 lines per mm. Note that in addition to possessing the geometric precision required for image calibration, these void arrays are truly buried flaws surrounded by intact solid material. They scatter sound like the subsurface cracks they are.

Results

Figure 7(*a*) shows a 1024 point × 1024 point image of an area 25.4 × 25.4 mm of the USAF 1951 pattern etched into the surface of a fused quartz plate. The 50 MHz, F/0.8 acoustic beam was focused by a lens 6.37 mm in diameter and with a 4.8 mm focal length in water at ambient conditions. The resolution target (consisting of groups 0, 1, 2, 3, and 4, as discussed above) is etched into the surface of a fused quartz plate 1.5 mm thick. The image was acquired by focusing the acoustic beam directly on the patterned water–quartz interface, gating the back-reflected amplitude, and acquiring a pixel every 25 μm. Focused in this manner, the transducer produces a −6 dB diffraction limited beam that is also 25 μm in diameter.

Figure 7(*b*) is a magnified image of the same data file displaying the full resolution of that file. The 25 μm beam and pixels show good resolution for the largest bar-space patterns in Group 4 (16 lines/mm or 62.5 μm line-line spacing), but the smallest patterns in the group (almost 32 lines/mm, 31.2 μm line-line spacing) are not resolved. This observation provides one more verification of the Nyquist theorem applied to spatial resolution. Stated simply: in order to resolve dimension "*d*,"

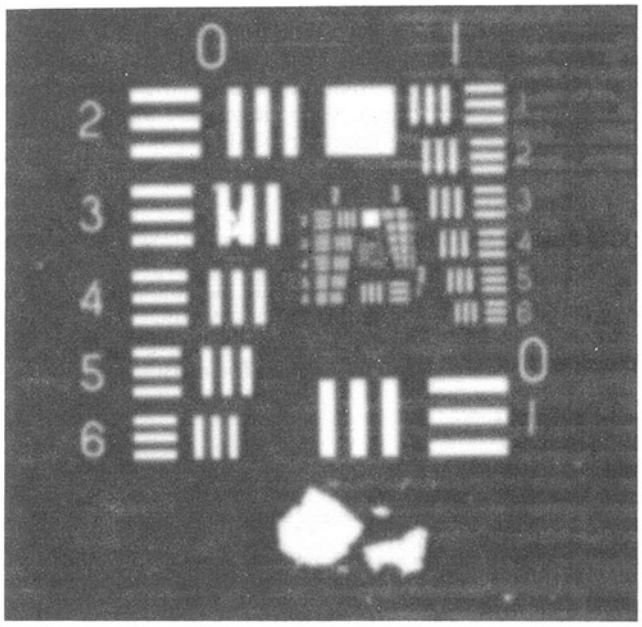

Fig. 8(*a*) 50 MHz, F/3.0 image of the sapphire resolution target taken from the 1.5 mm surface to pattern depth. The flaws evident in the image were actually very useful. One of the smallest was used to define the point-spread beam function used to provide the image enhancement shown in Fig. 8(*c*).

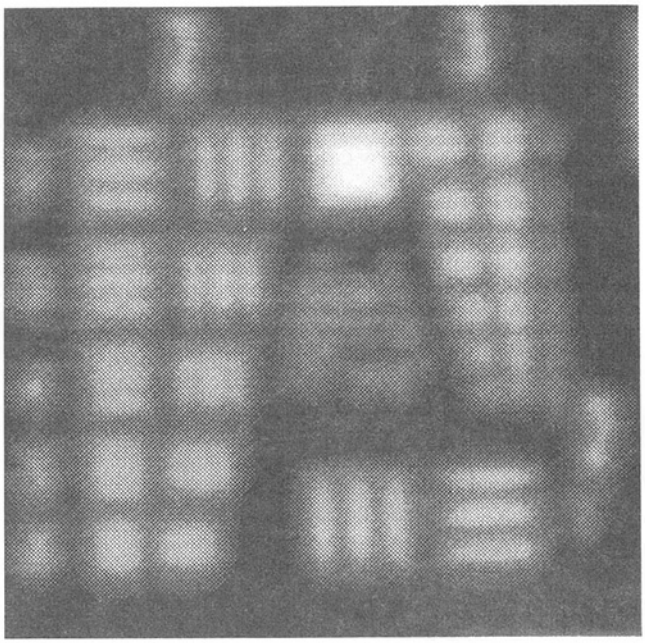

Fig. 8(*b*) Magnified image of the central portion of Fig. 8(*a*)

image data must be acquired at a sampling interval less than or approaching "$d/2$." Applying Nyquist to the 25 μm acoustic beam used to acquire the data file for Figs. 7(*a*) and 7(*b*) indicates that the micron pixels do not support the 25 μm resolution provided by the beam. In order to support the beam, the pixel size/spacing should be less than 12.5 μm. However, this was beyond the capability of the scanner at the time this file was acquired.

Figure 7(*c*) shows the same data file undersampled by two in each direction, increasing the pixel size to 50 μm. Note that it is now not possible to resolve even the largest pattern in Group 4 of the resolution target. However, looking at the next largest group, it can be observed that the patterns in Group 3

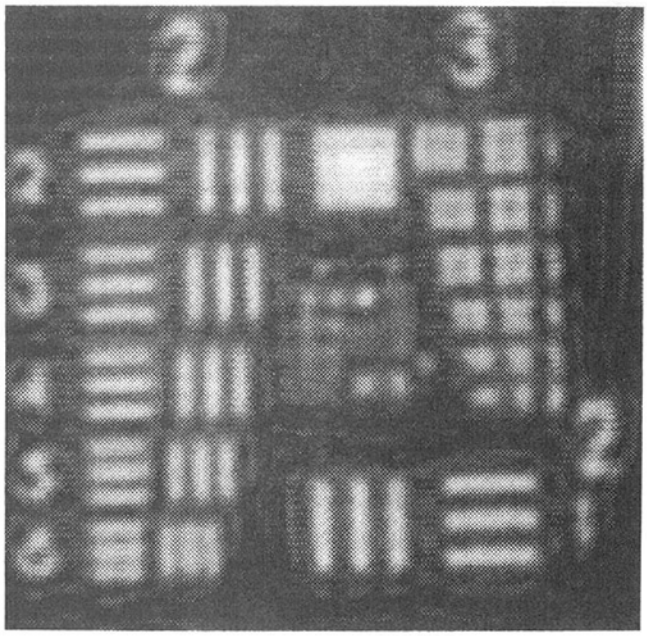

Fig. 8(*c*) Wiener filter enhancement of Fig. 8(*b*) showing approximately a factor of two improvement in resolution

(upper right in the Fig. 7(*c*) image) show the same respective definition that Fig. 7(*b*) displayed for Group 4. Since the spatial resolution was decreased by a factor of two the result should be expected.

Figure 8(*a*) shows a 1024 $\times$ 1024 longitudinal wave image of the 25.4 mm $\times$ 25.4 mm sapphire target described above. The 50 MHz, F/3.0 transducer used to acquire the image used a 6.37-mm-dia lens focusing the beam at 19.05 mm in water. This produces a half-angle of incidence of 9.5 deg, well beyond the 7.6 deg critical angle of incidence for longitudinal waves in water incident on a C-axis sapphire substrate (Table 1). The longitudinal focus produced in sapphire is similar to that shown for steel in Fig. 2 (between 0 and 14.5 deg). Clearly, diffraction limiting conditions do not control the resolution in this image.

A display of the raw data as shown in Fig. 8(*b*) is able to resolve only the first two patterns in Group 2 (a little better than 4.5 lines/mm or 220 μm). The resolution inherent to the high spatial frequency of the image (25 μm pixel size), however, can still be utilized. Figures 8(*b*) and 8(*c*) show a magnified view of the outlined portion of Fig. 8(*a*) and then enhance the resolution using a Wiener filter image processing technique described elsewhere (Mitchell and Gilmore, 1992). Note that in Fig. 8(*c*) the patterns resolved in Group 3 suggest that the processed image shows twice the resolution of the unprocessed image.

Figure 9 shows a 50 MHz, F/4.0 image of a target fabricated from lead borosilicate glass. The image was made at a surface to pattern distance of 8.06 mm. The transducer lens is 6.35 mm in diameter and focuses at a distance of 25.4 mm in water, producing an angle of incidence for the marginal rays of 7.2 deg. Since this is well within the 20.7 deg first critical angle of the material, the resolution in the image will be controlled by the -6 dB transducer beam diameter (120 μm). Applying the Nyquist criterion to the 120 μm beam diameter, i.e., doubling the beam diameter (240 μm) should indicate the approximate resolution limit in the image. Note that in Fig. 9 the first four elements in Group 2 are resolved and that the largest element in Group 2 is spaced at 4.0 lines/mm (250 μm) and that elements spaced less than 5.66 lines/mm (177 μm) cannot be readily resolved (from list in Fig. 1).

Figure 9 also shows, however, that in this target all the lines in Group 0, the lines in the largest element in Group 1, and

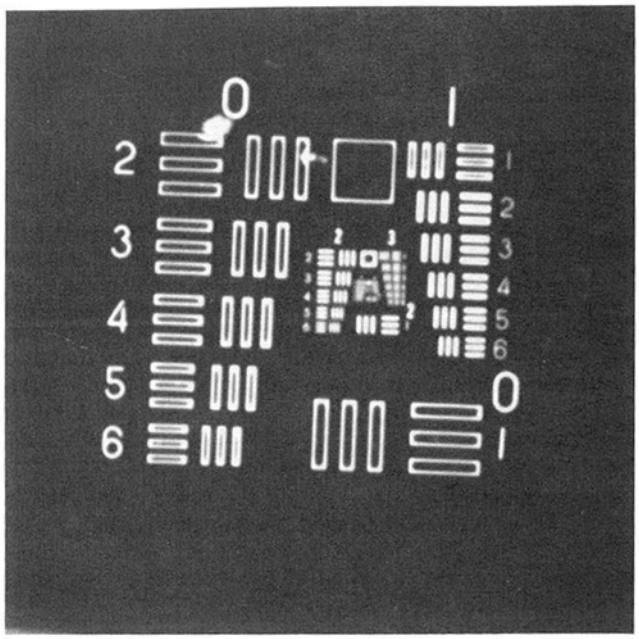

Fig. 9 50 MHz, F/4.0 image of the lead borosilicate glass target from the 8.1 mm surface to pattern distance

all of the solid squares have had their central regions bonded by the hot pressing process. Therefore just as the target can be used to evaluate the acoustic image, the image can also be used to evaluate the target (fabrication process). A somewhat more moderate temperature/pressure combination is indicated for future targets fabricated from lead borosilicate glass.

Conclusions

For subsurface ultrasonic imaging, high-velocity materials result in low numerical apertures for the penetrating acoustic beam and therefore low resolution for an image of an interior plane. The purpose of this discussion was to demonstrate a pragmatic method for establishing the resolution that can be achieved at depth in high-velocity substrates, even in the presence of considerable refractive aberration. The velocity range available in transparent materials (glasses, oxides, and silicates) combined with the possibilities to create buried target patterns by diffusion bonding makes it possible to develop resolution standards for most materials. Standards such as those discussed here have been of considerable use to the authors of this paper for characterizing the resolution in their ultrasonic imaging systems. As demonstrated, these targets are also of considerable use in evaluating image processing techniques.

Acknowledgments

Part of the work to develop the sapphire targets was funded by DoE Contract 86X-SC674C through the Oak Ridge National Laboratory. The authors would like to thank Jeffrey B. Platt and Patrick J. Howard for their assistance in the display and processing of some of the ultrasonic images used in this discussion and to Harold D. Ackler for assistance in making the targets.

References

Buchanan, R. W., and Hastings, C. H., 1955, "Ultrasonic Flaw Plotting Equipment: A New Concept in Industrial Inspection," *Nondestructive Testing*, Vol. 13, No. 5, pp. 17–25.

Gilmore, R. S., Tam, K. C., Young, J. D., and Howard, D. R., 1986, "Acoustic Microscopy From 10 to 100 MHz for Industrial Applications," *Philosophical Transactions of the Royal Society, London*, Vol. A320, pp. 215–235.

Gilmore, R. S., Hewes, R. A., Thomas, L. J., III, and Young, J. D., 1989, "Broadband Acoustic Microscopy: Scanned Images With Amplitude and Velocity Information," *Proceedings of the 17th Annual Symposium on Acoustic Imaging*, H. Shimizu, N. Chubachi, and J. Kushibiki, eds., Vol. 17, Plenum Publishing, New York, pp. 97–110.

Krautkramer, J., and Krautkramer, H., 1977, *Ultrasonic Testing of Materials*, Springer-Verlag, Berlin, Federal Republic of Germany.

Lemons, R. A., and Quate, C. F., 1973, "Acoustic Microscopy by Mechanical Scanning," *Applied Physics Letters*, Vol. 24, pp. 165–167.

Liang, K. K., Kino, G. S., and Kuri-Yakub, B. T., 1985, "Material Characterization by the Inversion of $V(z)$," *IEEE Transactions on Sonics and Ultrasonics, Special Issue on Acoustic Microscopy*, Vol. SU-32, No. 2, pp. 213–224.

Mitchell, K. W., and Gilmore, R. S., 1992, "A True Wiener Filter Implementation for Improving the Signal to Noise in Acoustic Images," *Review of Progress in Quantitative NDE*, Vol. 11, D. O. Thompson and D. E. Chimenti, eds., Plenum Press, New York.

Paton, N., and Tittmann, B., 1977, "New Ultrasonic Standards," *Review of Progress in Quantitative NDE*, June, NTIS Report #80-A060-783.

Rodel, J., and Glaeser, A. M., 1987, "Production of Controlled-Morphology Pore Arrays: Implications and Opportunities," *Journal of the American Ceramic Society*, Vol. 70, No. 8, pp. c172–c176.

Rodel, J., and Glaeser, A. M., 1989, "Photolithography: A New Tool for Ceramic Science," *Materials Research Society Symposium Proceedings*, Vol. 155, pp. 293–306.

Tsai, C. S., Wang, S. K., and Lee, C. C., 1977, "Visualization of Solid Material Joints Using a Transmission Acoustic Microscope," *Applied Physics Letters*, Vol. 31, pp. 791–793.

P. K. Liaw[1]
Department of Materials Science and Engineering,
The University of Tennessee,
Knoxville, TN 37996-2200

R. Pitchumani
Center for Composite Materials,
University of Delaware,
Newark, DE 19716

D. K. Hsu
Center for Nondestructive Evaluation,
Iowa State University,
Ames, IA 50011

H. Jeong[2]
Agency for Defense Development,
DaeJon, Korea

S. C. Yao
Department of Mechanical Engineering,
Carnegie Mellon University,
Pittsburgh, PA 15213

Nondestructive Eddy Current Evaluation of Anisotropic Conductivities of Silicon Carbide Reinforced Aluminum Metal-Matrix Composite Extrusions

Nondestructive eddy current methods were used to evaluate the electrical conductivity behavior of silicon-carbide particulate (SiC_p) reinforced aluminum (A1) metal-matrix composite extrusions. The composites investigated included 2124, 6061, and 7091 A1 base alloys reinforced by SiC_p. The composite extrusions exhibited anisotropic conductivities with the maximum conductivity occurring along the extrusion plane. Microstructural characterization showed that the observed anisotropic conductivities could result from the preferred orientation distribution of SiC_p. A theoretical model was formulated to quantify the influence of composite constituents (SiC_p, intermetallics, and A1 base alloy) on the anisotropic conductivities of the composites. The theoretical predictions of conductivities were found to be in good agreement with the experimental results.

1 Introduction

Metal-matrix composites (MMCs) are rapidly becoming one of the strongest candidates as structural materials for actual applications, in the transportation and aerospace industries (e.g., automobile and turbine engine components), and in the electronic and magnetic packaging industries. The widespread applications of MMCs are generally limited by the absence of reliable material qualification techniques. In particular, MMCs offer a significant challenge for traditional nondestructive evaluation (NDE) methods [1–22].

If NDE methods can be used to evaluate microstructural characteristics of MMCs, this kind of technology can be applied to assess microstructural features of composite gas turbine components. Moreover, NDE techniques are effective in determining material properties of turbine components. For example, eddy current methods can be used to measure conductivity of turbine components.

The prime objectives of this present paper are to: (1) evaluate the applications of nondestructive eddy current techniques for the characterization of the electrical conductivity behavior in MMCs, (2) thoroughly characterize the microstructures of the composites, and (3) formulate theoretical models to quantify the influence of composite constitutents on the conductivities of composites.

2 Material

Silicon-carbide-particulate (SiC_p) reinforced A1 MMCs extruded plates were provided by DWA Composite Specialties, Inc. The composities were manufactured by the powder metallurgy (P/M) method. The A1 base alloys were 2124, 6061, and 7091, and the volume percentages (v/o) of SiC_p reinforcement covered a wide range of 0, 10, 20, 25, 30, 40 and 55 percent. The composite extrusions were received in an extruded-plate form with the final extrusion ratios ranging from 10:1 to 39:1.

3 Experimental Procedure

3.1 Microstructural Characterization. Figure 1(*a*) presents the orientation of a composite extrusion, where x_1 is the extrusion direction, x_2 is the in-plane (extrusion plane) transverse direction, and x_3 is the out-of-plane thickness direction. Moreover, the x_1–x_2 plane is the extrusion plane, and both x_1–x_3 and x_2–x_3 planes are perpendicular to the extrusion plane.

Metallographic specimens were machined from the extrusions along the x_1–x_2, x_1–x_3 and x_2–x_3 planes, and prepared for microstructural characterization using scanning electron microscopy (SEM). Initial polishing of the specimens was con-

[1]Formerly with Westinghous Electric Corporation.
[2]Formerly with Iowa State University.

Contributed by the International Gas Turbine Institute and presented at the 38th International Gas Turbine and Aeroengine Congress and Exposition, Cincinnati, Ohio, May 24–27, 1993. Manuscript received at ASME Headquarters February 12, 1993. Paper No. 93-GT-15. Associate Technical Editor: H. Lukas.

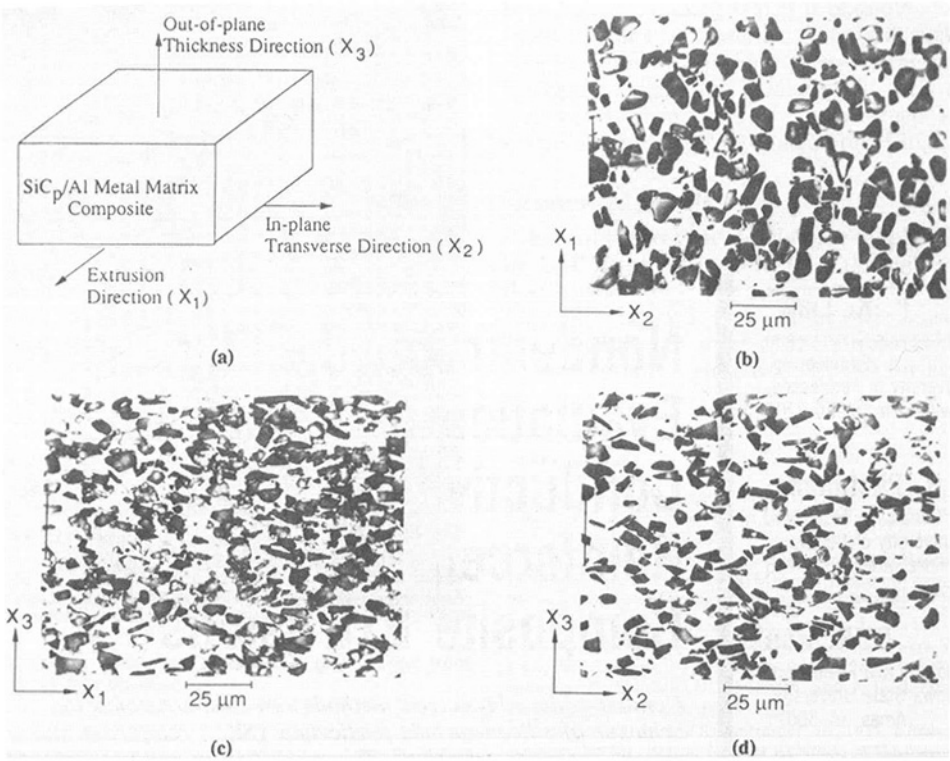

Fig. 1 (*a*) Schematic of a SiC_p composite extrusion showing three symmetry axes; (*b*)-(*d*) micrographs of a 7091/SiC/30p composite on the x_1–x_2, x_1–x_3, and x_2–x_3 planes, respectively

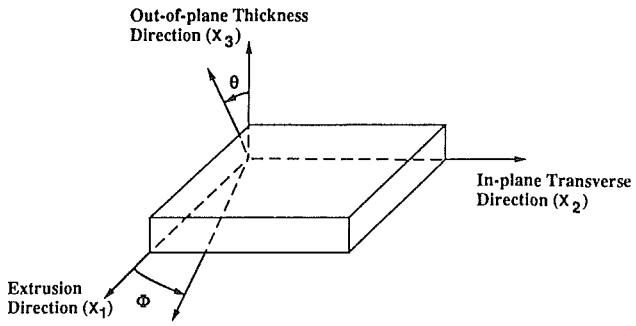

Fig. 2 Coordinate system for measuring the orientation of SiC_p

ducted using 240 to 600 grit emery paper. Fine-diamond pastes were subsequently used to polish the specimen further to approximately 1 μm finish (i.e., with a polishing paste composed of 1 μm diamond particles). Final polishing was accomplished using cerium oxides with a particle size of approximately 0.05 μm.

The microstructural characteristics examined included the assessment of the volume percentages (fractions) of SiC_p, intermetallics, and porosity. An energy-dispersive X-ray (EDS) spectroscopy analysis was used to identify the chemical compositions of intermetallics. The volume percentages of SiC_p, intermetallics, and porosity were quantitatively determined by the point counting techniques [24]. Additionally, the size and the aspect ratio of SiC_p were determined.

To quantify the orientation of SiC_p, Fig. 2 presents the coordinate system employed to determine the orientation angle distribution of SiC_p on the x_1–x_2, x_1–x_3, and x_2–x_3 planes. Using an image analysis system [25], the orientation angle of SiC_p on the x_1–x_2 plane was measured with respect to the x_1 direction, i.e., Φ angle, while those on the x_1–x_3 and x_2–x_3 planes were determined against the x_3 direction, i.e., θ angle.

3.2 Eddy Current Measurements. Eddy current test techniques were used to determine the electrical conductivities of MMCs [26–28]. The NDE methods based on the eddy current principles involve the use of special probes (A.C. coils) designed to detect the impact of discontinuities and microstructural characteristics on the electromagnetic behavior. When an alternating current test coil is brought near an electrically conducting material, an eddy current field is generated in the material as a result of electromagnetic induction. This electrical field, in turn, can affect the performance of the exciting coil itself, such that careful measurements of the coil response can be related to the properties of the test sample. In particular, changes in coil impedance can be used to deduce material properties. Many factors can affect the magnitude of eddy current and thus, coil impedance. In addition to coil design characteristics (size, shape, etc.) and energizing parameters (frequency, current magnitude, etc.), the electrical conductivity and magnetic permeability of the test material as well as the presence of discontinuities can affect impedance measurements. The high sensitivity of eddy current tests to conductivity and permeability parameters and the relationship between these factors and material properties provide the rationale for the direct evaluation of material properties with eddy current NDE techniques. Since the magnetic permeability of A1 MMCs is essentially unity, the eddy current method can be used to determine the electrical conductivities of MMCs [26–28].

Eddy current measurements were made using a Nortec NDT-16 eddyscope and a 10 kHz (SP-10A) probe with a solenoid coil size of 1 cm. The frequency was selected so that the field samples the interior as well as the surface of the material, while avoiding effects due to the finite sample thickness. Note that at the frequency of 10 kHz, the penetration depth of eddy current equals 1.4 mm for A1 composites with 25 percent SiC_p [19]. The samples were parallelepipeds machined from the extrusions, and their faces made parallel to the symmetry planes (x_1–x_2, x_1–x_3, and x_2–x_3 planes), shown in Fig. 1(*a*). The smallest

Table 1 Microstructural features of SiC_p reinforced A1 metal-matrix composite extrusions

Base Alloy	Billet Number	Volume Percentage (v/o) of SiC_p (%)	SiC_p Size (μm)	SiC_p Aspect Ratio	Volume Percentage (v/o) of Intermetallics (%)	Volume Percentage (v/o) of Porosity (%)
2124	PE-2600	0	-	-	7.4	0
2124	PE-3025	20	4.1	3.3	7.6	0
2124	PE-2404	25	2.5	2.3	4.4	0
2124	PE-2229	25	2.4	2.2	10.0	0
2124	PE-2488	30	3.9	2.1	6.7	1.4
6061	PE-2045	0	-	-	5.2	0
6061	PE-2047	20	2.3	2.1	15.5	0
6061	PE-2099	25	2.6	2.2	2.9	0
6061	PE-2731	30	2.8	2.3	1.2	2.6
6061	PE-2869	40	3.9	2.8	3.3	1.6
6061	PE-3235	55	4.3	2.4	7.0	2.8
7091	PE-2730	0	-	-	6.9	0
7091	PE-2711	10	2.4	2.8	6.9	0.5
7091	PE-2712	20	2.3	2.5	4.4	0
7091	PE-2713	30	3.5	2.2	3.2	4.2
7091	PE-2665	30	3.7	2.5	6.9	1.6

of the parallelepipeds measured were 40 mm × 15 mm × 12 mm.

A calibration curve was developed to correlate the eddyscope output voltage of the "lift-off" signal to the electrical conductivity in units of percent IACS (International Annealed Copper Standard). The calibration standards used covered a conductivity range of 12–46 percent IACS. The output voltages were read from a Fluke 27 digital multimeter connected to the rear panel output of the eddyscope. Note that surface roughness to test samples affects eddy current measurements. It is important that both test samples and calibration standards have similar roughness levels. Although the surface of composite extrusions was relatively smooth, eddy current measurements were conducted on polished test samples.

Owing to the circular symmetry of the eddy current coil, the measurements gave planar conductivity (relative to the conductivity along a specific direction) that was an average of the conductivities along different directions on the plane. Measurements were determined on the x_1–x_2, x_1–x_3, and x_2–x_3 planes to obtain their respective planar conductivities. On each plane, three to five repeated measurements were made to determine the mean and standard deviation. The standard deviations were found to be generally much less than 0.5 percent IACS.

4 Results

4.1 Metallography. In Table 1, the average size of SiC_p varied from approximately 2 to 4 μm for each series of the composite system (2124, 6061, or 7091 A1 MMCs). It seemed that in each composite system, the average particle size was somewhat larger for the greater volume percentage of SiC_p. The aspect ratio of SiC_p ranged from approximately 2 to 3.

All the composites including the base alloys exhibited the presence of intermetallics (Table 1). The EDS analysis in the SEM identified that the intermetallics contained various combinations of elements, such as A1, Si, Mn, Fe, Cu, Cr, Mg, Co, Zn, Ti, and Zr, depending on the base alloy [14].

Figure 1 presents the example microstructural features of a typical extrusion (7091/SiC/30p, where 7091 is the A1 base alloy, SiC is the silicon carbide reinforcement, and 30p is the thirty volume percentage of particulate reinforcement) on the three symmetry planes.

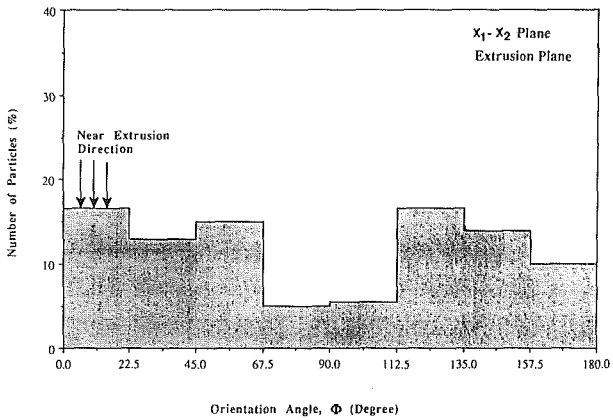

Fig. 3 Orientation distribution of SiC_p on the x_1–x_2 plane of a 7091/SiC/30p composite

In Fig. 1, the micrographs of the cross sections of the composite along the three symmetry planes reveal that the SiC_p cross sections are flat and nearly rectangular in shape on the extrusion (x_1–x_2) plane [Fig. 1(*b*)], while observed on the x_1–x_3 and x_2–x_3 planes, they are elongated and approximately elliptical and narrow-rectangular in shape [Figs. 1(*c*) and 1(*d*), respectively]. Futhermore, on the x_1–x_3 and x_2–x_3 planes [Figs. 1(*c*) and 1(*d*)], SiC_p is randomly distributed, but preferentially oriented in the extrusion (x_1) and the in-plane transverse (x_2) directions, respectively. Nevertheless, on the x_1–x_2 (extrusion) plane, both the distribution and the orientation of SiC_p are random [Fig. 1(*b*)]. Thus, it may be assumed that the arrangement of SiC_p is predominantly planar along the extrusion plane.

The example results on the orientation angle distributions of SiC_p in the 7091/SiC/30p composite extrusion are shown in Figs. 3 and 4 for the x_1–x_2 and x_1–x_3 planes, respectively. In each figure, the number of SiC_p in percent is plotted versus the orientation angle. On the extrusion (x_1–x_2) plane in Fig. 3, the number of SiC_p was found to be relatively insensitive to the orientation angle, Φ. Therefore, on the extrusion plane, SiC_p appears to be randomly oriented, as found in Fig. 1(*b*). On the x_1–x_3 plane, the number of SiC_p is the greatest, when

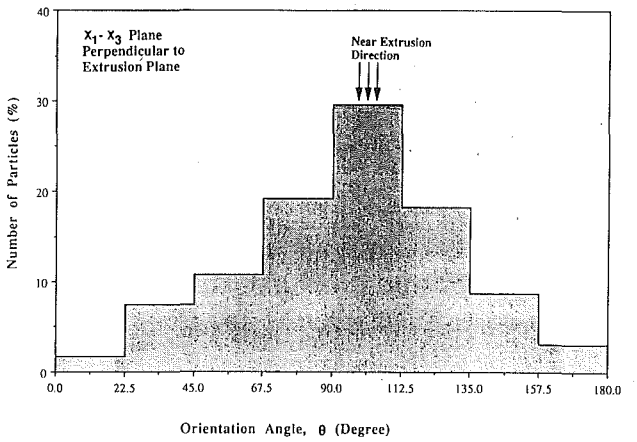

Fig. 4 Orientation distribution of SiC_p on the x_1–x_3 plane of a 7091/SiC/30p composite

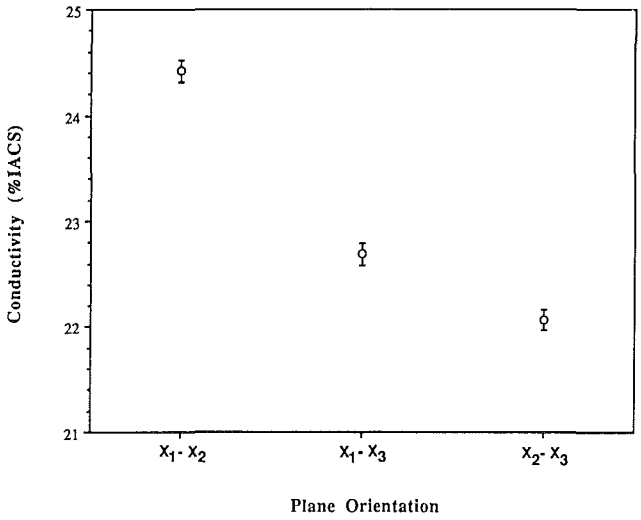

Fig. 5 Conductivities of a 2124/SiC/20p composite on the x_1–x_2, x_1–x_3, and x_2–x_3 planes, respectively

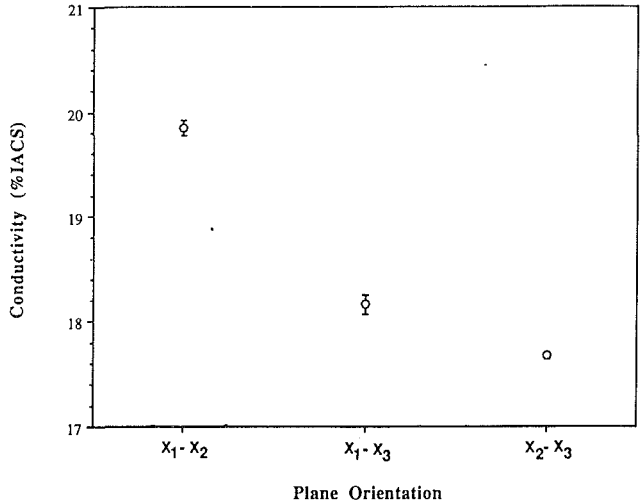

Fig. 6 Conductivities of a 6061/SiC/20p composite on the x_1–x_2, x_1–x_3, and x_2–x_3 planes, respectively

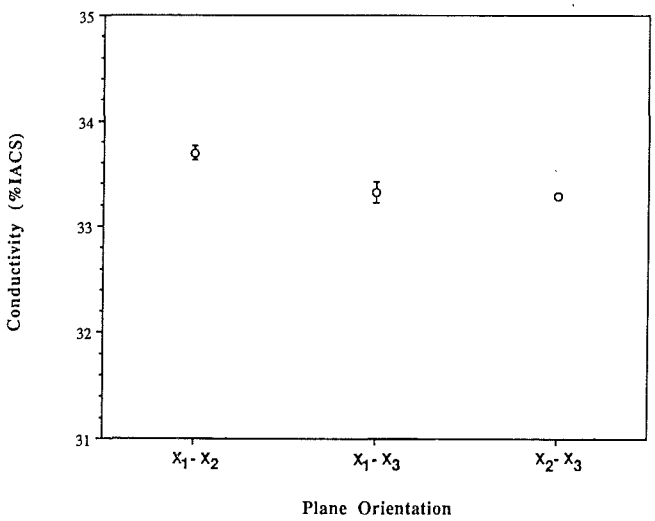

Fig. 7 Conductivities of a 2124/SiC/0p composite on the x_1–x_2, x_1–x_3, and x_2–x_3 planes, respectively

the orientation angle (θ) is near the extrusion direction (θ = 90 deg). This behavior indicates that SiC_p tends to align along the extrusion direction, as observed in Fig. 1(*c*). Similar results were found on the x_2–x_3 plane, i.e., SiC_p tends to orient along the x_2 direction. The results presented in Figs. 1, 3, and 4 clearly demonstrate the anistropic orientation distribution of SiC_p in the composite extrusions.

4.2 Eddy Current. The example results of the conductivity measurements are presented in Figs. 5 and 6 for the 2124/SiC/20p and 6061/SiC/20p composite extrusions, respectively. In each figure, the conductivity on the x_1–x_2 plane was found to be greater than that on the x_1–x_3 or x_2–x_3 plane. Futhermore, the conductivities on the x_1–x_3 and x_2–x_3 planes seem to be comparable. Thus, the composite extrusions exhibit anisotropic conductivities, i.e., the conductivity on the extrusion plane (x_1–x_2 plane) is greater than that on the other orthogonal planes (x_1–x_3 and x_2–x_3 planes). Similarly, the anisotropic elastic constants were also observed in the present composite extrusions [20, 22]. Note that in the base alloy (e.g., 2124/SiC/0p), the anistropic conductivity behavior is minimal, as presented in Fig. 7.

The anisotropic conductivity can be correlated with the anisotropic orientation distribution of SiC_p, as shown in Figs. 1, 3, and 4. The different SiC_p orientation distribution between x_1–x_2 and x_1–x_3 (or x_2–x_3) planes (Figs. 1, 3, and 4) results in the different conductivity on these two planes. Furthermore, the similar SiC_p orientation distribution on the x_1–x_3 and x_2–x_3 planes corresponds to the comparable conductivity on both planes.

As described below, a theoretical model was formulated to incorporate the anisotropic characteristics of the SiC_p orientation distribution, which can, in turn, be used to quantify the influence of the SiC_p orientation distribution on the conductivity behavior.

5 Theoretical Modeling

5.1 Two-Phase (SiC_p and A1) Model. The two-phase model was developed in earlier work by the authors [29]. However, since the three-phase model presented in section 5.2 is based on the two-phase model, the important steps and results of the two-phase model are repeated here for the sake of clarity in understanding the three-phase model. For additional details on the two-phase model, the readers are referred to [29].

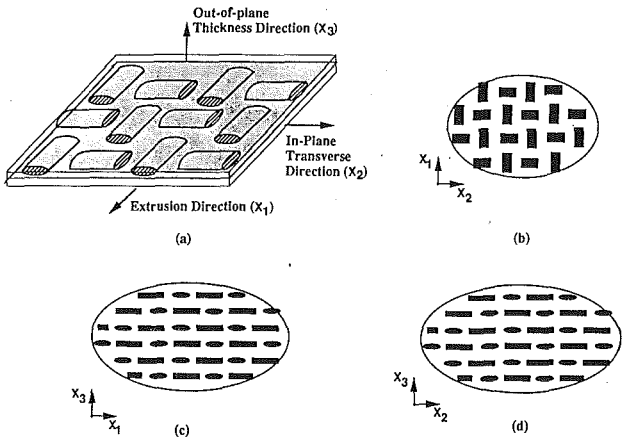

Fig. 8 *(a)* **Two-phase model for the planar arrangement of SiC_p; *(b)*-*(d)* model representations for the SiC_p cross sections on the x_1-x_2, x_1-x_3, and x_2-x_3 planes, respectively**

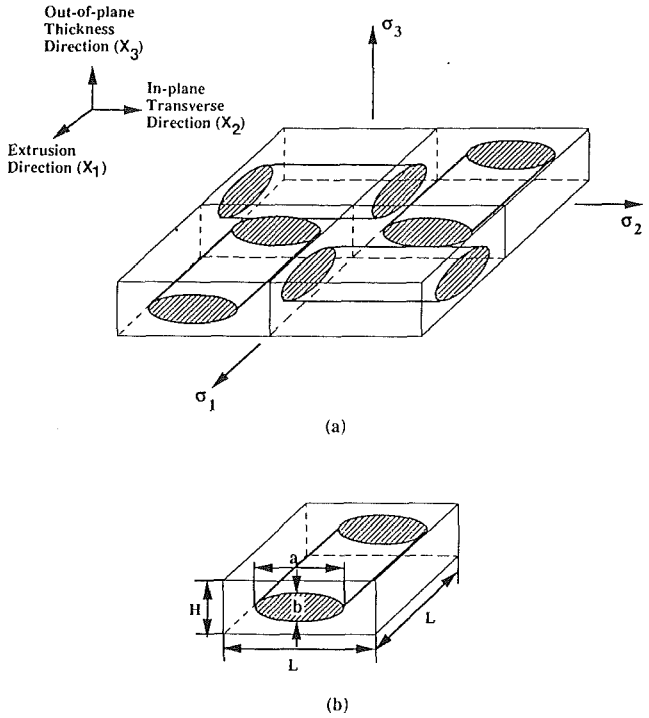

Fig. 9 *(a)* **Schematic of the two-phase model showing the assemblage of unit cells for the composite; *(b)* representative unit cell consisting of a right elliptical cylinder (SiC_p) in a rectangular box**

The goal of the present theoretical formulation is to develop a two-phase (SiC_p and Al) model for the prediction of the anisotropic effective conductivities of the extruded MMCs reinforced with particles oriented preferentially in the extrusion (x_1) and the in-plane transverse (x_1) directions (Figs. 1, 3, and 4). First, a representative unit cell is described based on the geometric characteristics of the composite available from the micrographs (Fig. 1). The unit cell is then analyzed to calculate the effective conductivities of the composite.

5.1.1 Unit Cell Construction. Based on the microstructural features observed in Fig. 1, an idealized model for the arrangement of SiC_p may be constructed, as presented in Fig. 8(*a*). In this arrangement, SiC_p is modeled as a right elliptical cylinder with its axes aligned alternately along the extrusion and in-plane transverse directions, so as to form a crisscross structure. Such an arrangement in Fig. 8(*b*) represents the extremes of the planar random orientation of SiC_p as observed on the extrusion (x_1-x_2) plane [Fig. 1(*b*)], while those in Figs. 8(*c*) and 8(*d*) reflect the preferentially aligned, elongated cross sections in the extrusion and the in-plane transverse directions [Figs. 1(*c*) and 1(*d*), respectively].

In Fig 9(*a*), the composite is modeled as being made up of unit cells. A representative unit cell for the idealized regular arrangement is shown in Fig. 9(*b*). The unit cell is composed of a rectangular box, in the center of which is placed a SiC_p, right elliptical and cylindrical in shape. The cross-sectional dimensions of a unit cell are defined as follows: "*a*" and "*b*" are the major and the minor axes of the elliptical cross section of SiC_p, respectively, and L is the length of the square base of the unit cell [Fig. 9(*b*)]. The crisscross arrangement in Fig. 8(*a*) can be generated by placing the unit cells in such a manner that the cylindrical axis of SiC_p in any unit cell is perpendicular to the axes of all its adjacent neighbors on the extrusion plane.

In the two-phase model, the shape of the rectangular unit cell can be related to the particle shape, and, thus, the box size in terms of the SiC_p size and volume fraction (percentage), v, can be determined. In order to accommodate the crisscross arrangement of SiC_p on the extrusion plane, the base of the rectangular box must be a square of side L. The square shape is actually a consequence of the fact that the SiC_p's are distributed and oriented uniformly and randomly on the extrusion plane [Figs. 1(*b*) and 3], which in the idealized model, is shown by the crisscross arrangement [Fig. 9(*a*)]. Furthermore, SiC_p (an elliptical cylinder in the model) is assumed to extend in length all along the base, L, of the unit cell, so as to represent the anisotropy of the arrangement as much as possible.

The height, H, of the box can be related to the base size, L, and the elliptical cross section of the reinforcement particle by making use of the fact that the SiC_p cross sections are distributed uniformly and randomly, but are oriented preferentially on the x_1-x_3 and x_2-x_3 planes. It may be argued that an equispaced array of ellipses on a two-dimensional plane best models a uniform-random arrangement. Any deviation from the equispaced arrangement will result in the cross sections being clustered along either their major or minor axes (so as to preserve the reinforcement volume fraction), thereby departing from the uniform-random configuration.

For an equispaced two-dimensional array of ellipses, the unit cell is a rectangle with the length-to-height ratio equal to the major axis to minor axis ratio of the ellipse. This trend indicates that the box base length-to-height ratio, L/H, must equal the SiC_p cross-sectional axes ratio, a/b, i.e.,

$$\frac{L}{H}=\frac{a}{b} \tag{1}$$

The box and the SiC_p sizes can now be interrelated in terms of the volume percentage (v) of SiC_p, which is simply the ratio of the right elliptical cylinder volume to the rectangular box volume. From the definition of the volume fraction, and using Eq. (1), the following equations can be derived:

$$v=\frac{\pi}{4}\left(\frac{b}{H}\right)^2 \text{ or } \frac{H}{b}=\frac{L}{a}=\sqrt{\frac{\pi}{4v}} \tag{2}$$

Equation (2) completely defines the unit cell. Given "*a*" and "*b*", and the SiC_p volume fraction, v, the unit cell dimensions can be determined.

It must be mentioned that the actual dimensions of the unit cell and the reinforcement particle are not necessary for the present analysis. The quantities of importance are the ratios of the box-to-particle dimensions, H/b and L/a, which are analogous to the "pitch-to-diameter" ratios used in connection with the unidirectional circular fiber-reinforced composites. In the present analysis, the two ratios, H/b and L/a, are equal, and are a function of the SiC_p volume fraction alone, by virtue of the assumption of the uniform-random distribution of SiC_p.

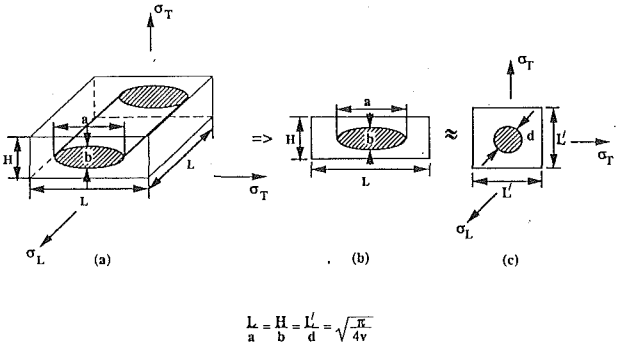

$$\frac{L}{a}=\frac{H}{b}=\frac{L'}{d}=\sqrt{\frac{\pi}{4v}}$$

Fig. 10 Transformation of the three-dimensional unit cell to a two-dimensional cell [(*a*) to (*b*)], and subsequently to a two-dimensional square cell with an enclosed circular reinforcement particle [(*b*) to (*c*)]

In the absence of any detailed information regarding the interparticle spacings, the present model is a reasonably accurate description of the reinforcement particle arrangement. Physically, this analysis means that the particle volume fraction is the main geometric parameter, which affects the analysis to the first order of accuracy. Additional microstructural features may be incorporated to improve the accuracy.

5.1.2 Conduction Analysis. In the two-phase model, the transverse and longitudinal conductivities (σ_T and σ_L, respectively) of the unit cell [Fig. 10(*a*)] will be first determined. The effective conductivities of the composite are then represented in terms of the unit cell conductivities, and finally the planar conductivities of the composite are predicted for comparison with the experimental results.

5.1.2.1 Unit cell conductivities. In the idealized model, Figs. 9(*b*) and 10(*a*), since SiC_p extends all along the length, L, of the unit cell, the problem of estimating the conductivities of the three-dimensional cell [Fig. 10(*a*)] is reduced to that of evaluating the conductivities of a two-dimensional cell shown in Fig. 10(*b*). Furthermore, by virtue of the fact that $L/H = a/b$ [Eq. (1)], the two-dimensional cell in Fig. 10(*b*), which is composed of an ellipse within a rectangle, under a geometric scaling with respect to the sides of the rectangle (i.e., scaling the x_2 coordinate with respect to L and the x_3 coordinate with respect to H), reduces to the two-dimensional arrangement of a circle within a unit square cell. This transformation is presented schematically in Figs. 10(*b*)-(*c*). This transformation was used to develop analytical expressions for the composite conductivities. It was shown in [29] that the conductivities of the elognated cell in Figs. 10(*b*) and the square cell in Fig. 10(*c*) are approximately equal for $a/b \leq 3$.

Figure 10(*c*) is also the unit cell for a continuous fiber-reinforced composite with a square packing of fibers. Several numerical and analytical results [30–34] are available in the literature on the conductivities of the square cell in Fig. 10(*c*). The analytical expression for the transverse conductivity [in the σ_T in Fig. 10(*c*)] derived by Behrens [34] was employed in the present analysis, which agrees very well with the numerical results for square fiber arrays, with volume fraction less than about 60 percent [33].

Behrens' formula [34] for the transverse conductivity can be written in a nondimensional form as:

$$\frac{\sigma_T}{\sigma_m}=\frac{(\beta+1)+(\beta-1)v}{(\beta+1)-(\beta-1)v} \tag{3}$$

where σ_T is the transverse conductivity of the square cell [Fig. 10(*c*)], σ_m represents the conductivity of the matrix (base alloy), β equals the reinforcement particle (fiber) to matrix conductivity ratio, and v is the particle (fiber) volume fraction of the reinforcement particle.

The longitudinal conductivity [σ_L in Fig. 10(*c*)] is determined by a volume average of the reinforcement particle and the matrix conductivities, and can be expressed in the following dimensionless form:

$$\frac{\sigma_L}{\sigma_m}=1+(\beta-1)v \tag{4}$$

Equations (3) and (4) are also the transverse and longitudinal conductivity ratios with respect to the matrix conductivity, respectively, of the three-dimensional rectangular unit cell (Fig. 10(*a*)] in the current analysis.

5.1.2.2 Effective composite conductivities. The effective conductivity of the particulate-reinforced composite can be determined using the unit cell conductivities, by considering an assemblage of unit cells, as presented in Fig. 9(*a*). It is of interest to estimate the conductivity of the assemblage along the extrusion (x_1), in-plane transverse (x_2), and out-of-plane thickness (x_3) directions.

The total resistance (electrical, thermal etc.) along the x_1 and the x_2 directions is a series combination of the transverse and the longitudinal resistances of the rectangular unit cell [Figs. 9(*b*) and 10(*a*)]. Thus, the effective conductivity in the extrusion or the in-plane transverse direction, σ_1 or σ_2, respectively [Fig. 9(*a*)], is a harmonic average of the transverse and longitudinal conductivities [Eqs. (3) and (4)]. In a dimensionless form, it may represented as:

$$\frac{\sigma_1}{\sigma_m}=\frac{\sigma_2}{\sigma_m}=\frac{2\left(\frac{\sigma_T}{\sigma_m}\right)\left(\frac{\sigma_L}{\sigma_m}\right)}{\left(\frac{\sigma_T}{\sigma_m}\right)+\left(\frac{\sigma_L}{\sigma_m}\right)} \tag{5}$$

where σ_T/σ_m and σ_L/σ_m are expressed by Eqs. (3) and (4), respectively.

In Fig. 9(*a*), the conductivity of the assemblage in the out-of-plane thickness direction (σ_3) equals the transverse conductivity of the unit cell [Eq. (3)], i.e.,

$$\frac{\sigma_3}{\sigma_m}=\frac{\sigma_T}{\sigma_m} \tag{6}$$

5.1.2.3 Planar conductivities. In the present investigation, a circular eddy current probe was employed in the measurements of conductivities. The measured values were, therefore, an average of the conductivities along several directions spanning the entire plane. Thus, in order to be able to compare the model predictions with the experimental values, it is necessary to calculate the planar conductivities for each of the three planes, x_1–x_2, x_1–x_3, and x_2–x_3 in Fig. 9(*a*). In the present two-phase model, the planar conductivity is determined by averaging the conductivities along two orthogonal directions defining the plane. For instance, the conductivity on the x_1–x_3 plane, σ_{1-3}, is the arithmetic mean of σ_1 and σ_3.

It is expected that the simplified average used in the present analysis will not vary grossly from a refined average, which considers several directions spanning the plane. A refined average will probably improve upon the present analysis at the expense of simplicity but, as will be found from the comparisons with the experimental results, is probably not warranted.

Using the simplified averaging technique, the three planar conductivities, σ_{1-2}, σ_{1-3}, and σ_{2-3}, scaled with respect to the matrix conductivity, σ_m, can be represented as follows:

$$\frac{\sigma_{1-2}}{\sigma_m}=\frac{1}{2}\left(\frac{\sigma_1}{\sigma_m}+\frac{\sigma_2}{\sigma_m}\right) \tag{7}$$

$$\frac{\sigma_{1-3}}{\sigma_m}=\frac{\sigma_{2-3}}{\sigma_m}=\frac{1}{2}\left(\frac{\sigma_1}{\sigma_m}+\frac{\sigma_3}{\sigma_m}\right) \tag{8}$$

Table 2 Conductivities of SiC_p and A1 matrix alloys, and values of β used in theoretical modeling

SiC_p (%IACS)	Al Matrix Alloys (%IACS)	β
1.82×10^{-6} - 0.086	33 - 50	3.64×10^{-8} - 0.0026

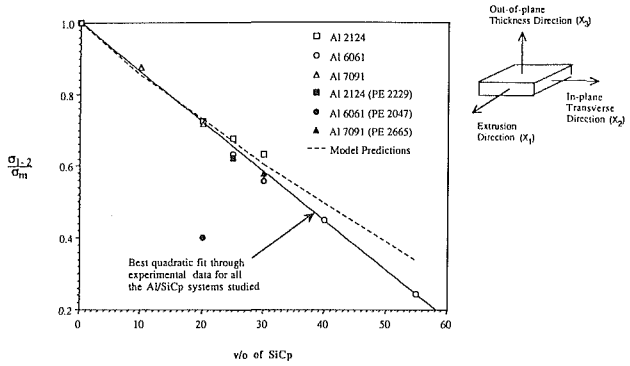

Fig. 11 Comparisons of measured and theoretically predicted (two-phase model) conductivity ratios on the x_1-x_2 plane

In Section 6, the theoretically predicted conductivity ratios using Eqs. (7) and (8) are compared with the experimental data.

5.2 Three-Phase (SiC_p, Intermetallics and A1) Model. The objective of the model is to quantify the influence of the three composite constituent phases (SiC_p, intermetallics, and A1) on the anisotropic conductivity behavior of composite extrusions. The theoretical treatment to include the effect of intermetallics is based on the two-phase (SiC_p and A1) model developed in the previous sections for predicting the anisotropic conductivity of extruded composites. The proposed scheme models the three-phase (SiC_p, intermetallics, and A1) composites as being composed of a "modified"-A1-matrix reinforced with SiC_p, where the "modified"-A1-matrix is, in turn, formed, if the A1-matrix is reinforced with intermetallics. In this model, the effective composite conductivity is calculated using a two-step procedure outlined below:

1 First, the conductivity of the "modified" matrix conductivity is evaluated by considering the "modified" matrix to be a two-phase composite with the intermetallics as the reinforcements. The "modified" matrix conductivity ratios along the extrusion (x_1), in-plane transverse (x_2), and out-of-plane thickness (x_3) directions (Fig. 1), σ'_{m1}/σ_m, σ'_{m2}/σ_m, and σ'_{m3}/σ_m, respectively, are obtained using Eqs. (9) and (10), with v and β replaced by the effective intermetallics volume fraction, v_{im}, in the "modified" matrix, and the intermetallics to matrix conductivity ratio, β_{im}, respectively. The resulting expressions may be written as follows:

$$\frac{\sigma'_{m1}}{\sigma_m}=\frac{\sigma'_{m2}}{\sigma_m}=\frac{2[(\beta_{im}+1)+(\beta_{im}-1)v_{im}][1+(\beta_{im}-1)v_{im}]}{(\beta_{im}+1)+(\beta_{im}-1)v_{im}+[1+(\beta_{im}-1)v_{im}][(\beta_{im}+1)-(\beta_{im}-1)v_{im}]} \quad (9)$$

$$\frac{\sigma'_{m3}}{\sigma_m}=\frac{(\beta_{im}+1)+(\beta_{im}-1)v_{im}}{(\beta_{im}+1)-(\beta_{im}-1)v_{im}} \quad (10)$$

2 The second step is to calculate the conductivity of the two-phase SiC_p – "modified" matrix composite, where the conductivities of the "modified" matrix are given by Eqs. (9) and (10). Once again, the conductivities along the three directions are evaluated using Eqs. (3)–(6), where β is replaced by the SiC_p to "modified" matrix conductivity ratios, β'_1, β'_2, and β'_3, along the three directions, respectively (where $\beta'_1 = \beta'_2 \neq \beta'_3$). The effective conductivities of the composites, expressed as a ratio with respect to the "modified" matrix conductivity, are, therefore, given by the following equations:

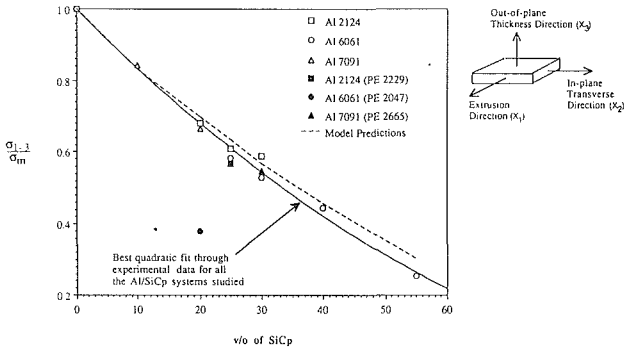

Fig. 12 Comparisons of measured and theoretically predicted (two-phase model) conductivity ratios on the x_1-x_3 plane

$$\frac{\sigma_1}{\sigma'_{m1}}=\frac{\sigma_2}{\sigma'_{m2}}=\frac{2[(\beta'_1+1)+(\beta'_1-1)v][1+(\beta'_1-1)v]}{(\beta'_1+1)+(\beta'_1-1)v+[1+(\beta'_1-1)v][(\beta'_1+1)-(\beta'_1-1)v]} \quad (11)$$

$$\frac{\sigma_3}{\sigma'_{m3}}=\frac{(\beta'_3+1)+(\beta'_3-1)v}{(\beta'_3+1)-(\beta'_3-1)v} \quad (12)$$

Note that v in Eqs. (11) and (12) is the SiC_p volume fraction.

In practice, however, it is useful to express the conductivities as a ratio with respect to the A1 matrix conductivities. These ratios may be obtained from Eqs. (9)–(12), using the relationships given below:

$$\frac{\sigma_1}{\sigma_m}=\left(\frac{\sigma_1}{\sigma'_{m1}}\right)\left(\frac{\sigma'_{m1}}{\sigma_m}\right);\quad \frac{\sigma_2}{\sigma_m}=\left(\frac{\sigma_2}{\sigma'_{m2}}\right)\left(\frac{\sigma'_{m2}}{\sigma_m}\right);\quad \frac{\sigma_3}{\sigma_m}=\left(\frac{\sigma_3}{\sigma'_{m3}}\right)\left(\frac{\sigma'_{m3}}{\sigma_m}\right) \quad (13)$$

The planar conductivity ratios, which will be used in the data comparisons presented in the next section, are given by Eqs. (7) and (8).

6 Evaluation of Theoretical Models and Discussion

6.1 Comparisons of Theoretical Predictions (Two-Phase Model) and Experimental Results. The range of the conductivity values of the constitutent SiC_p and A1 matrix alloys are listed in Table 2 along with the corresponding range of the reinforcement particle to matrix conductivity ratio, β. The conductivities for SiC_p were obtained using the resistivity data developed by Marshall et al. [36]. The conductivity values of the A1 base alloys were the presently measured data for the 2124/SiC/0p, 6061/SiC/0p, and 7091/SiC/0p materials. In Table 2, the values of both SiC_p conductivities and β cover a wide range. A study of the influence of varying β, in the range given in Table 2, was conducted, and the resulting theoretical

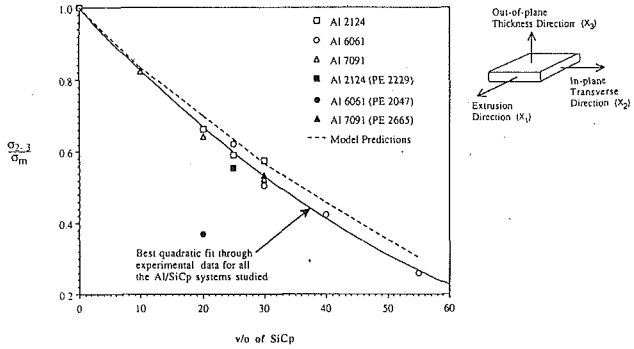

Fig. 13 Comparison of measured and theoretically predicted (two-phase model) conductivity ratios on the x_2-x_3 plane

Table 3 Composite extrusions studied and their compositions

Composite (Billet number)	Volume Percentage (v/o) of SiC_p (%)	Primary Inter-metallics	Volume Percentage (v/o) of Inter-metallics (%)	β_{im}
2124/SiC/25p (PE 2229)	25	$CuAl_2$	10	0.67
6061/SiC/20p (PE 2047)	20	Mg_2Si	15.5	10^{-4}
7091/SiC/30p (PE 2665)	30	$MgZn_2$	6.9	0.31

conductivity ratios were found to be fairly insensitive (less than 1 percent) to the change in β. Therefore, a value of $\beta = 0.0026$, which corresponds to the upper limit of the range, was chosen for the comparative examination shown as follows.

Figures 11–13 present the comparisons between the theoretical planar conductivity ratios [Eqs. (7) and (8)] predicted by the two-phase model and the experimental values, for all the composite systems included in Table 1. The experimental data on the planar conductivities were cast into a nondimensional form (σ_{1-2}/σ_m, σ_{1-3}/σ_m, and σ_{2-3}/σ_m) by normalizing with respect to the conductivity of the corresponding base alloy on the respective plane. In other words, the value of σ_m equals that of the corresponding 2124/SiC/0p, 6061/SiC/0p, or 7091/SiC/0p base alloy for the three composite systems examined. These normalized conductivities are employed in the comparisons. In the figures, the two-phase model predictions are represented by dashed lines, while the symbols are the experimental data for the three composite systems. The solid line shows the best-fit curve through the experimental results, and may be used as a reference for the comparisons. In Figs. 11–13, increasing the volume precentages of SiC_p generally decreases the conductivity ratios, σ_{1-2}/σ_m, σ_{1-3}/σ_m, and σ_{2-3}/σ_m, on the x_1-x_2, x_1-x_3, and x_2-x_3 planes, respectively. The symbols labeled A1 2124 (PE 2229), A1 6061 (PE 2047), and A1 7091 (PE 2665) will be discussed later in this section.

It is clear from Fig. 11 that on the x_1-x_2 plane, the theoretical predictions and the experimental data compare very well, to within about 8 percent, for the SiC_p volume fractions less than or equal to about 35 percent. For higher volume fractions, the present theoretical model is found to overpredict the conductivities. This behavior may result from the assumption of the planar arrangement in the theoretical model, which does not consider the resistance due to the presence of SiC_p's between planes. The influence is more distinguished for the higher volume fractions because, due to the closer packing, there may be more out-of-plane SiC_p's.

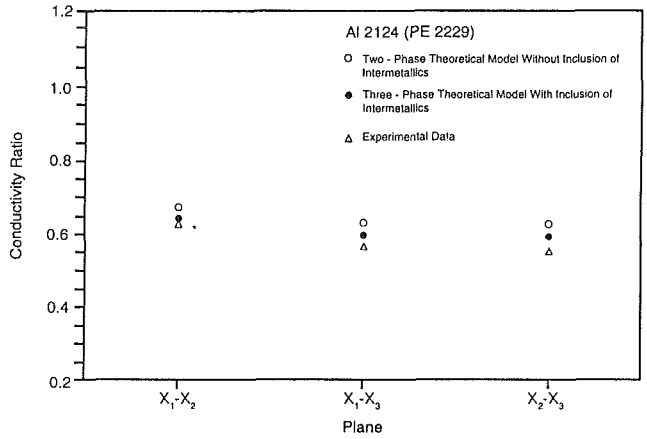

Fig. 14 Comparisons of measured and theoretically predicted (two-phase and three-phase models) conductivity ratios for the 2124/SiC/25p composite

On the x_1-x_3 and x_2-x_3 planes (Figs. 12 and 13, respectively), the conductivities predicted by the present model exhibit good agreement, to within 5 percent, with the experimental results over almost the entire range of SiC_p volume fractions from 0 to 55 percent.

The differences between the model predictions and the experimental results may be attributed to the following three factors: (*a*) the assumption of the uniform-random arrangement of SiC_p, (*b*) the approximation in calculating the planar conductivities, and (*c*) the contributions of intermetallics, which are neglected in the two-phase model. These three factors were discussed qualitatively in [29]. In the next section, the effects of intermetallics [factor (*c*) above] are examined using the three-phase model derived in Section 5.2.

6.2 Comparisons of Theoretical Predictions (Three-Phase Model) and Experimental Results. The three-phase model, presented in Section 5.2 for including the influence of the intermetallics on the conductivity behavior, was applied to the three different A1 matrix composite extrusions, which have a relatively large volume fraction of intermetallics: 2124/SiC/25p (PE 2229), 6061/SiC/20p (PE 2047), and 7091/SiC/30p (PE 2665).

Table 3 describes the composition of these three composites. It must be mentioned that in each of these composites, the intermetallic phases were not unique. The intermetallic given in Table 3 is the primary intermetallic phase that was identified in the present investigation. Also given in Table 3 are the conductivity ratios, β_{im}, between the intermetallics and the A1 matrix. The conductivities of the intermetallics were obtained from the data obtained by Touloukian [37] and Schroder [38], while the conductivity of SiC_p was calculated using the resistivity data gathered by Marshall et al. [36]. The A1 matrix conductivity was calculated using the experimental measurements of the base alloy, as mentioned before.

For each of the three composite extrusions, the theoretical effective conductivity ratios on the x_1-x_2, x_1-x_3, and x_2-x_3 planes were calculated using the procedure given previously. The conductivity ratios evaluated using the three-phase model including the effect of intermetallics are shown in Figs. 14–16, for the three samples: 2124/SiC/25p (PE 2229), 6061/SiC/20p (PE 2047), and 7091/SiC/30p (PE 2665), respectively, along with the experimental measurements using eddy current techniques. For the purpose of comparison, the conductivities predicted by the two-phase model, which neglects the effect of the intermetallics, are also included in Figs. 14–16.

In may be generally found from Figs. 14–16 that the three-phase model predictions improve considerably upon those of the two-phase model. The agreement between the three-phase

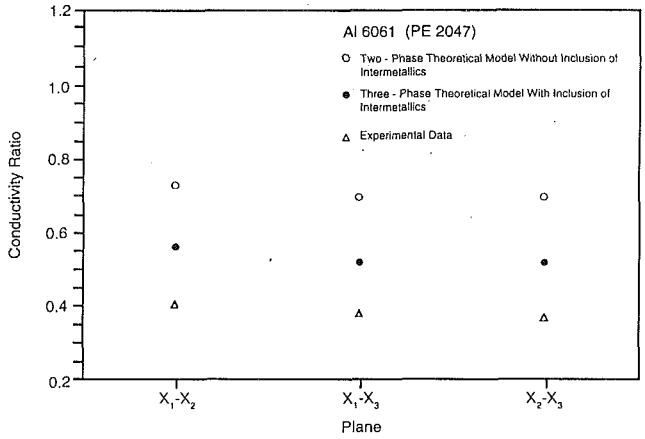

Fig. 15 Comparisons of measured and theoretically predicted (two-phase and three-phase models) conductivity ratios for the 6061/SiC/20p composite

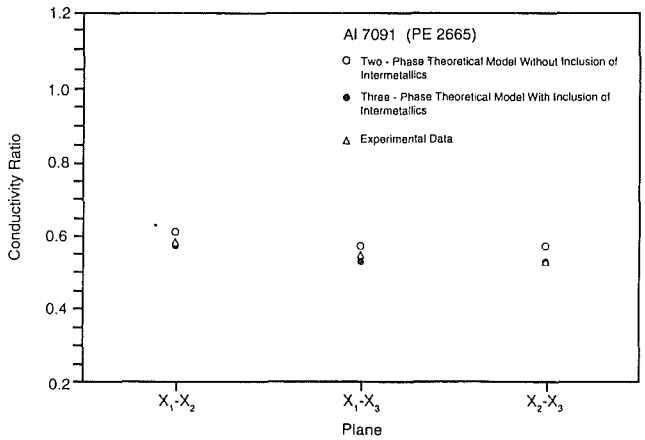

Fig. 16 Comparsions of measured and theoretically predicted (two-phase and three-phase models) conductivity ratios for the 7091/SiC/30p composite

model and the experimental data is within 5 percent in the case of the 2124/SiC/25p and 7091/SiC/30p composites. For the 6061/SiC/20p composite, despite the improvements due to the three-phase model, the discrepancy between the experimental data and the theoretical predictions is still nonnegligible. The anomalous behavior of the 6061/SiC/20p composite was also observed in the calculation of the elastic constants [25]. Further investigations are necessary before a conclusive explanation can be given.

It may be noted from Figs. 14–16 and Table 3 that, as expected, the effect of intermetallics is more pronounced, when the intermetallics to matrix conductivity ratio deviated from unity and/or when the intermetallics volume fraction is large. In conclusion, the results suggest that the three-phase analytical model is simple, yet very effective in accounting for extraneous phases, such as intermetallics. This model can be extended to quantify the effects of several (greater than three) composite constituents on the anisotropic conductivity behavior of particulate reinforced composite materials.

7 Conclusions

Eddy current methods have been used to assess the electrical conductivities of silicon-carbide particulate (SiC_p) reinforced aluminum (A1) metal-matrix composites (MMCs). The composites investigated were 2124, 6061, and 7091 A1-base alloys reinforced by SiC_p. The volume percentage of SiC_p covered a wide range from 0 to 55 percent. The composites demonstrated anisotropic conductivity with the maximum conductivity occurring along the extrusion plane. Microstructural analyses revealed that the observed anisotropic conductivity could be related to the preferred orientation distribution of SiC_p. A theoretical model including the effects of composite constituents (SiC_p, intermetallics and base alloy) was developed to estimate the anisotropic conductivities of the composites. The theoretical predictions of conductivities were found to be in good agreement with the experimental results.

Acknowledgments

The authors are grateful to Dr. G. Y. Baaklini for his kind help in reviewing this paper.

References

1 Liaw, P. K., "Commentary: The Nondestructive Evaluation of Materials Properties," *JOM*, Vol. 10, Oct. 1992, p. 10.

2 Liaw, P. K., Ijiri, Y., Taszarek, B. J., Frohlich, S., Gungor, M. N., and Logsdon, W. A., *Metallurgical Transactions A*, Vol. 21A, 1990, p. 529.

3 Ijiri, Y., Liaw, P. K., Taszarek, B. J., Frohlich, S., and Gungor, M. N., *Metallurgical Transactions A*, Vol. 19A, 1988, p. 2215.

4 Mott, G., and Liaw, P. K., *Metallurgical Transactions A*, Vol. 19A, 1988, p. 2233.

5 Clark, W. G., Jr., and Iyer, J. N., *Materials Evaluation*, Vol. 47, Apr. 1989, p. 460.

6 Champagne, B., and Piche, L., *Powder. Metall. Int.*, Vol. 18, No. 4, 1986, p. 261.

7 Hsu, D. K., Jeong, H., Shannon, R. E., and Liaw, P. K., *Review of Progress in Quantitative Nondestructive Evaluation 9*, D. O. Thompson and D. E. Chimenti, eds., Plenum Press, 1990, p. 1395.

8 Liaw, P. K., Shannon, R. E., Clark, W. G., Jr., and Harrigan, W. C., Jr., *Morris E. Fine Symposium*, TMS-AIME, P. K. Liaw, J. R. Weertmann, H. L. Marcus, and J. S. Santner, eds., 1991, p. 193.

9 Liaw, P. K., Shannon, R. E., Clark, W. G., Jr., and Harrigan, W. C., Jr., ASTM STP 1157, M. R. Mitchell and O. Buck, eds., 1992, p. 251.

10 Schramm, S. W., *Review of Progress in Quantitative Nondestructive Evaluation 4B*, D. O. Thompson and D. E. Chimenti, eds., Plenum Press, 1985, p. 1263.

11 Daniel, I. M., Wooh, S. C., and Lee, J. W., *Review of Progress in Quantitative Nondestructive Evaluation 6B*, D. O. Thompson and D. E. Chimenti, eds., Plenum Press, 1987, p. 1195.

12 Rogovsky, A. J., *Review of Progress in Quantitative Nondestructive Evaluation 3B*, D. O. Thompson and D. E. Chimenti, eds., 1984, p. 1063.

13 Rohatgi, P. K., Raman, S., Majumdar B. S., and Banerjee, A., *ASM Symposium on Cast Reinforced Metal Composites*, S. G. Fishman and A. K. Dhingra, eds., 1988, p. 341.

14 Shannon, R. E., Liaw, P. K., Clark, Jr., W. G., *Symposium on Fundamental Relationship Between Microstructure and Mechanical Properties of Metal Matrix Composites*, TMS-AIME, M. N. Gungor and P. K. Liaw, eds., 1990, p. 581.

15 Huber, S., *Review of Progress in Quantitative Nondestructive Evaluation 6B*, D. O. Thompson and D. E. Chimenti, eds., Plenum Press, 1987, p. 1065.

16 Busse, L. J., Lemon, D. K., Doctor, P. G., Melton, R. B., Hartmann, H. S., Johnson, G. H., and Lear, J. D., *Review of Progress in Quantitative Nondestrutive Evaluation 3B*, D. O. Thompson and D. E. Chimenti, eds., Plenum Press, 1984, p. 1035.

17 Simmons, J. A., Drescher-Krasicka, E., Wadley, H. N. G., Rosen, M., and Hsieh, T. M., *Review of Progress in Quantitative Nondestructive Evaluation 7A*, D. O. Thompson and D. E. Chimenti, eds., Plenum Press, 1987, p. 893.

18 Osman, T. M., Stiffler, R. C., and Hunt, Jr., W. C., *Symposium on Nondestructive Evaluation and Material Properties of Advanced Materials*, TMS-AIME, P. K. Liaw, O. Buck, and S. M. Wolf, eds., 1991, p. 51.

19 Shannon, R. E., Liaw, P. K., and Harrigan, Jr., W. C., *Metallurgical Transactions A*, Vol. 23A, 1992, p. 1541.

20 Jeong, H., Hsu, D. K., Shannon, R. E., and Liaw, P. K., *Morris E. Fine Symposium*, TMS-AIME, P. K. Liaw, J. R. Weertman, H. L. Marcus, and J. S. Santner, eds., 1991, p. 209.

21 Liaw, P. K., Shannon, R. E., and Harrigan, W. C., Jr., *Symposium on Nondestructive Evaluation and Material Properties of Advanced Materials*, TMS-AIME, P. K. Liaw, O. Buck, and S. M. Wolf, eds., 1991, p. 43.

22 Jeong, H., Hsu, D. K., Shannon, R. E., and Liaw, P. K., *Symposium on Nondestructive Evaluation and Material Properties of Advanced Materials*, TMS-AIME, P. K. Liaw, O. Buck, and S. M. Wolf, eds., 1991, p. 37.

23 Harrigan, W. C., unpublished results, DWA Composite Specialties, Inc., 1988.

24 Hilliard, J. E., and Cahn, J. W., *Transactions of the Metallurgical Society of AIME*, Vol. 221, 1961, p. 344.

25 Jeong, H., Ph.D Thesis, Iowa State University, 1990.

26 Junker, W. R., private communication, Westinghouse R&D Center, Pittsburgh, PA, 1988.

27 Libby, H. L., *Introduction to Electromagnetic Nondestructive Test Methods*, R. E. Krieger Publishing Company, Huntington, NY, 1979.

28 Rosen, M., *Metallurgical Transactions A*, Vol. 20A, 1989, p. 605.

29 Pitchumani, R., Yao, S. C., Liaw, P. K., Shannon, R. E., Hsu, D. K., and Foster, B., *Transport Phenomena in Materials Processing and Manufacturing*, ASME HTD-Vol. 196, 1992, p. 201.
30 Holman, J. P., *Heat Transfer*, 7th ed., McGraw-Hill Company, 1990, p. 76.
31 Hashin, Z., *Journal of Applied Mechanics*, Vol. 50, 1983, p. 481.
32 Pitchumani, R., and Yao, S. C., ASME *Journal of Heat Transfer*, Vol. 113, 1991, p. 788.
33 Han, L. S., and Cosner, A. A., ASME *Journal of Heat Transfer*, Vol. 103, 1981, p. 387.
34 Behrens, E., *Journal of Composite Materials*, Vol. 2, 1968, p. 2.
35 Hatta, H., and Taya, M., *Journal of Applied Physics*, Vol. 58, 1985, p. 2478.
36 Marshall, R. C., Faust, Jr., J. W., and Ryan, C. E., eds., *Silicon Carbide—1973*, University of South Carolina Press, Columbia, SC, 1974, p. 673.
37 Touloukian, Y. S., ed., 1967, *Thermophysical Properties of High Temperature Solid Materials, Vol. 6, Part I: Intermetallics*, The MacMillan Company, New York.
38 Schroder, K., ed., 1983, *CRC Handbook of Electrical Resistivities of Binary Metallic Alloys*, CRC Press, Inc., Boca Raton, FL.

P. Nava
Nuovo Pignone SpA,
Firenze, Italy

N. Paone

G. L. Rossi

E. P. Tomasini

Dipartimento di Meccanica,
Università di Ancona,
Ancona, Italy

Design and Experimental Characterization of a Nonintrusive Measurement System of Rotating Blade Vibration

A measurement system for nonintrusive monitoring of rotating blade vibration in turbomachines based on fiber optic sensors is presented. The design of the whole system is discussed; the development of special purpose sensors, their interfacing to the data acquisition system, and the signal processing are outlined. The processing algorithms are tested by software simulation for several possible blade vibrations. Experimental tests performed on different bladed rotors are presented. Results are compared to simultaneous strain gage measurements.

Introduction to the Measurement Technique

A great deal of interest has been devoted for many years to nonintrusive techniques suitable for the measurement of rotor blade vibrations by noncontact sensors mounted statically on the casing of the turbomachine (McCarty and Thompson, 1981; Roth, 1981; Kiraly, 1981). They are very appealing because of their potential reliability and their nonintrusivity, due to the absence of sensing elements mounted on the rotating blades (Watkins and Robinson, 1985; Paone et al., 1989; Stanoe, 1990).

These techniques are all based on the measurement of the transit time of the blade tip below a set of sensing heads; time of flight variations Δt are due to blade deflection forward or backward. The accurate measurement of blade tip velocity and of the variations of arrival time allows one to compute one or two blade tip deflection samples

$$s_i = v_b \Delta t_i \tag{1}$$

when the blade passes in front of each sensor (Paone et al., 1990; Simmons et al., 1990; Paone et al., 1991; Kawashima et al., 1992). Several sensing heads along the outer circumference of the casing allow one to measure different samples of the blade tip deflection. The angular displacement Θ between each sensor head and the angular velocity ω define the sampling frequency of the measurement system as:

$$f = \omega/\Theta \tag{2}$$

This means that the Shannon theorem, which states that sampling frequency f must be at least double the blade vibration frequency f_b, can be satisfied by proper positioning of the sensors for given f_b and ω. The number of samples depends on the employed number of sensors. The uncertainty associated with each sample of blade deflection s_i affects the uncertainty in the computation of the maximum blade tip deflection S and of the vibration frequency f_b (Paone et al., 1991). The previous statement is true for every kind of vibration, either synchronous or asynchronous with rotating speed. This is an important feature, in order to measure vibrations during transient operation of the machine, when asynchronous vibrations are most important. The angular displacement Θ can be different for each pair of sensing heads. In such a case, deflection samples s_i are nonuniformly spaced. This basic method is needed to measure deflections effectively over a wide range of frequencies.

These kinds of measurement technique are accurate if the characteristics of the vibration, i.e., its amplitude and frequency, remain constant during the measurement time; accuracy decreases if these characteristics vary in time. In most cases it is possible to estimate the vibration amplitude because the blade damping coefficient is so low that for many cycles it continues to vibrate; this allows one to detect vibrations induced by events occurring before the start of the time window that do not repeat themselves at each revolution. The characteristics of typical vibrations were experimentally investigated by the same authors in 1990 and 1991; it was observed that the synchronous vibrations show constant characteristics in time, while during transients of the machine they change in time.

If just one sensor is used at each measurement point, only bending vibrations can be detected, and the sensor should be placed at the center of the blade chord, where torsional deformation is minimum. If more than one sensor is used at each measuring point, torsional vibrations can be detected as well.

Measurement System

A measurement system has been designed on the basis of the principles above and it is suited for measuring synchronous

Contributed by the International Gas Turbine Institute and presented at the 38th International Gas Turbine and Aeroengine Congress and Exposition, Cincinnati, Ohio, May 24–27, 1993. Manuscript received at ASME Headquarters February 12, 1993. Paper No. 93-GT-16. Associate Technical Editor: H. Lukas.

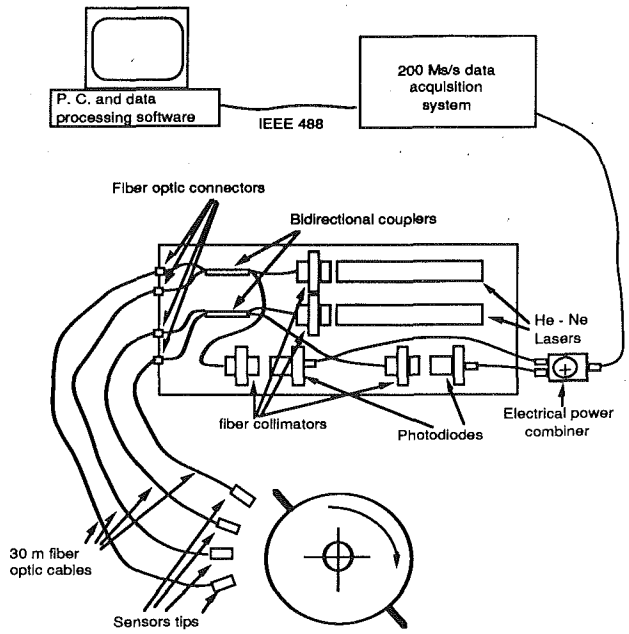

Fig. 1 Components of the measurement system

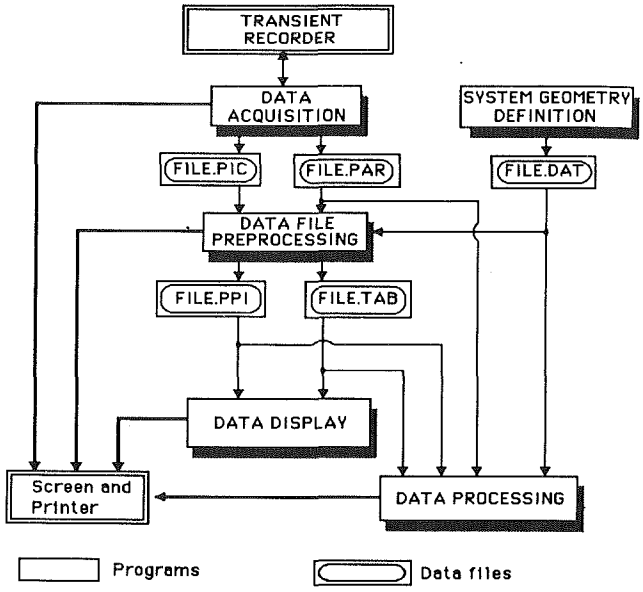

Fig. 2 Software block diagram

and asynchronous blade vibrations in the first stages of an industrial axial compressor, which operates on a 5 MW gas turbine power plant.

Figure 1 shows a schematic drawing of the layout of the measurement system.

The system is based on four optical sensing heads, which detect the passage of every blade, as described by Paone and Rossi (1992). Optical sensors have been chosen for two main reasons: their extremely high bandwidth and their intrinsic insensitivity to electromagnetic interference. The need for a large bandwidth is due to the necessity to measure very small variations of transit time of each blade, which is about 300 ns or less for a blade moving at a tangential velocity of 300 m/s and having a tip deflection $S = 0.1$ mm. The rise time of the pulse produced by the blade passage in front of the sensor should be significantly smaller than that; therefore these sensors have to be designed to have bandwidth on the order of 100 MHz, quite high for mechanical applications.

There are two sensing heads for each laser and photodiode. This is achieved by using a 50/50 fiber optic directional coupler. This device, which acts as a beam splitter for any optical wave traveling along the fiber link, either emitted from the laser and going towards the sensing head or reflected from the blade and returning backward to the photodetector, reduces the number of electro-optical elements, realizing a distributed fiber-optic sensor. In this case four sensing heads require only two lasers and two photodetectors. Therefore the system gains in economy and simplicity. As a drawback, this kind of optical multiplexing reduces the total power available per unit head and reduces the useful power that reaches the photodetector; two heads per sensor is a good trade-off.

The laser is a 10 mW He-Ne gas laser, operating in the visible range ($\lambda = 633$ nm), which allows easier tuning of the system, with respect to invisible laser diode radiation, which is often employed in fiber optic sensors.

The photodetector is an avalanche photodiode, with a bandwidth of more than 1 GHz. To improve its signal-to-noise performances, it is operated with a bias voltage close to the breakdown value; this means that very low levels of reflected light produce a very strong signal, although not linearly related to the input. Since the technique is based on a time measurement, the amplitude of the signal is important only in a binary sense, in order to indicate the presence or absence of the blade under the sensing head.

A multimode fiber is used in the system; since the overall length of the fibers is not longer than 30 m, a fiber with core diameter of 100 μm maintains a sufficiently high bandwidth and offers easy alignment. The sensing heads are connected to the 50/50 bidirectional fiber coupler by low loss connectors.

The criterion that must be used when positioning the sensing heads along the circumference of the case is that only one sensing head detects any blade at a certain instant; it must be impossible that two sensing heads are active simultanously. The signals from the photodetectors are combined and produce a sequence of individual pulses, thanks to the particular positioning of the sensing heads. This allows the use of only one A/D converter, i.e., a one-channel transient recorder for all the sensors. This considerably reduces the cost and the complexity of the acquisition system.

The acquisition system is based on a single channel transient recorder, operating at a maximum sampling rate of 200 MHz on a 2 Mbyte buffer with 8 bit vertical resolution. This is interfaced to a personal computer for data processing.

Nomenclature

f = vibration sampling frequency, Hz
f_b = vibration frequency of blade, Hz
f_T = transient recorder sampling frequency, Hz
n = revolutions per minute, rpm
s = blade tip deflection, mm
S = maximum blade tip deflection, mm
Δt = transit time, s
v = velocity, m/s
Θ = angular separation of sensors, rad
λ = laser wavelength, nm
Φ = phase of vibration, rad
ω = rotating speed, rad/s

Subscripts

b = blade tip
i = general sample
m = measured
R = reference
T = transient recorder

A special software has been developed to drive the transient recorder and subsequently, in a preprocessing phase, to identify each pulse and to reduce all the samples to a set of pulse parameters. A second step of the analysis is performed on these parameters in order to measure the time shift of each pulse and to compute blade tip deflection. The main output of the software is the time history of blade tip deflection. Figure 2 shows a block diagram of the software. It requires the geometric configuration of the rotor and of the sensing heads as input.

Simulation of the Measurement System

The processing software has been validated by using simulated signals. A proper simulator of the measurement system has been developed, which produces the series of pulses that would be generated by the four sensing heads on a real machine when a vibrating blade is running inside a machine. The program requires as input the characteristics of the machine, a model of blade vibration, and the configuration of the measurement system. In particular the following parameters can be varied: the dimensions of the rotor, its angular speed, the number of blades, the vibration amplitude, its frequency and phase, the number of the sensors and their position, the sampling frequency f_T, and memory depth of the transient recorder.

Figure 3 shows some results of the simulator, in which the working conditions that will be found experimentally on the test bench are simulated; in particular it simulates a measurement system with four sensors, not uniformly spaced. The figure shows the simulated vibration amplitude of the blade tip versus time; it is imposed on a sinusoidal vibration of frequency f and amplitude S_R. The samples obtained by the simulation of the measurement system are drawn on the same figure; four samples per rotor revolution are shown, because it simulates a measurement system with four sensors. In the figure below is represented the angle of rotation versus time.

Figures 3(*a*) and 3(*b*) represent the results obtained with the rotor running at 2400 rpm (40 Hz) and the blade vibrating at $f = 395$ Hz, i.e., asynchronous to the rotor, with amplitude $S_R = 0.11$ mm, with two different initial phases $\Phi = 0$ and $\Phi = \pi/2$. The sampling frequency of the simulated transient recorder is $f_T = 12.5$ MHz, its memory depth 2 Mbyte. The

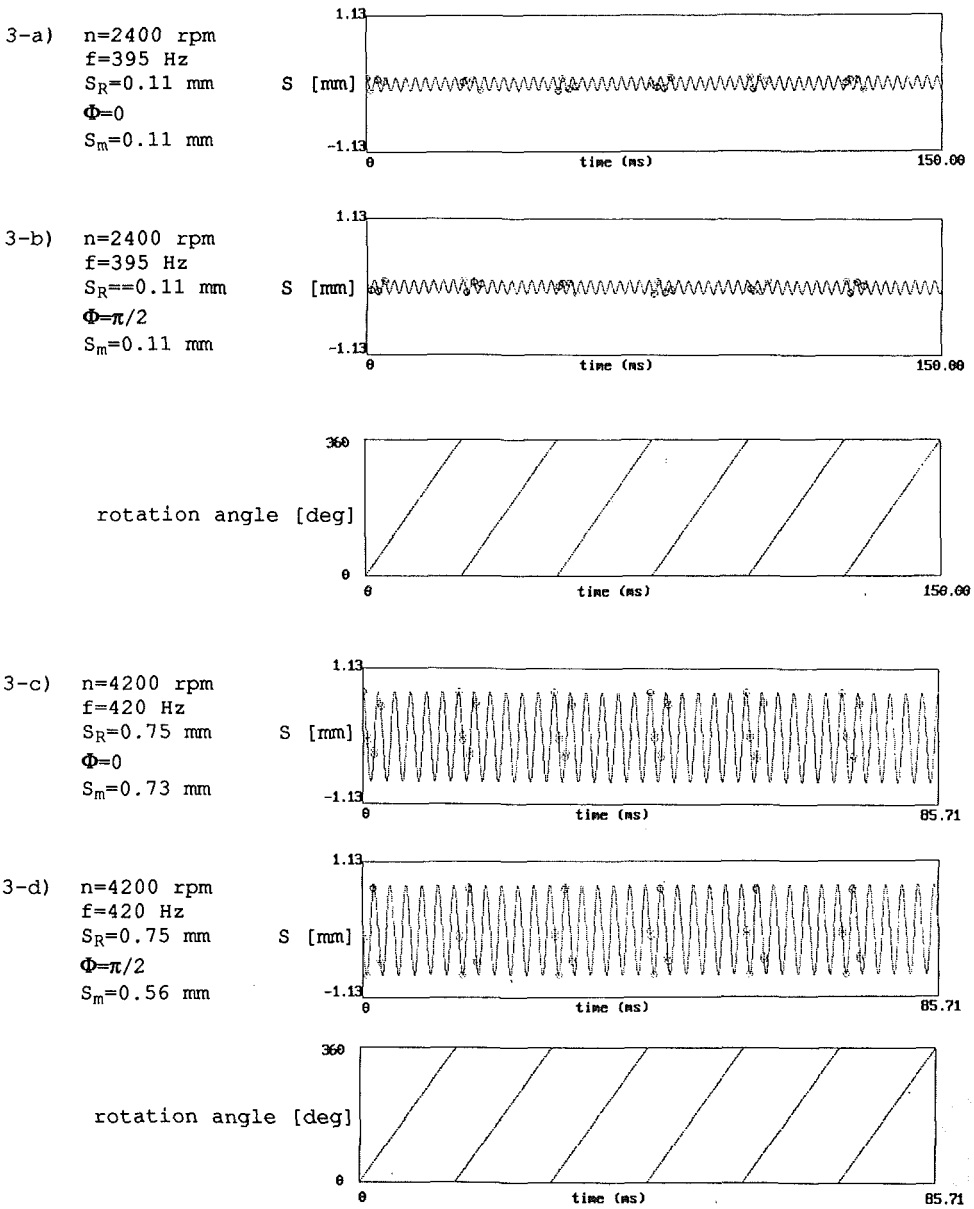

Fig. 3 Results from the simulator of the measurement system

samples clearly show that no synchronism exists between vibration and rotation, in fact at each revolution they occur at different positions along the sinusoid. Both the results in Figs. 3(*a*) and 3(*b*) allow one to estimate a vibration amplitude $S_m = 0.11$ mm.

Figures 3(*c*) and 3(*d*) represent the results obtained by the simulation of the rotor running at 4200 rpm (70 Hz) and the same blade vibrating at $f = 420$ Hz, which is synchronous to the rotor, with amplitude $S_R = 0.75$ mm, again with two different initial phases Φ. The sampling frequency of the simulated transient recorder is $f_T = 25$ MHz, its memory depth 2 Mbyte. The synchronism existing between vibration and rotation appears from the samples measured by the system, in fact at each revolution they occur at the same positions along the sinusoid; the different phase in Figs. 3(*c*) and 3(*d*) depends on the initial phase of the vibration at the beginning of the time window. The results in Fig. 3(*c*) allow one to estimate a vibration amplitude $S_m = 0.56$ mm, those of Fig. 3(*d*) give $S_m = 0.73$ mm. Both amplitude measurements are underestimated; this agrees with what is predicted by the simulator. The magnitude of the error is related to the phase of the vibration at the beginning of the acquisition time window, which is random. In the case of asynchronous vibrations this kind of error is smaller, because the phase of vibration changes at each revolution, therefore improving the statistics of the population of vibration amplitude samples.

The underestimation of the vibration amplitude is due to the statistics of the sampling, which is performed by the measurement system on the sinusoidal vibration. Due to the density of probability of the amplitude of the sinusoidal vibration it results that in most cases the measurement system will not measure samples in the maximum and minimum of the sinusoidal vibration, therefore it will underestimate the vibration amplitude. This fact depends on the phase of the vibration at the beginning of the acquisition time window, on the position of the sensors, on the vibration frequency and on the synchronism or asynchronism of the vibration with respect to the rotation. A larger number of samples provide a population statistically meaningful, but attention must be focused on the different behavior of synchronous and asynchronous vibrations. In case of asynchronous vibrations the position of the samples along the sinusoid is varying, depending on the noninteger ratio between vibration frequency and rotation speed. This means that a longer memory will provide the capability to sample a sufficient number of samples, which will be distributed over the whole span of the amplitude distribution function; therefore the vibration amplitude could be correctly measured. On the other hand, in case of synchronous vibrations, the expansion of the memory will not produce better samples, although their number will be larger; in fact, due to the integer ratio between vibration frequency and rotation speed, all the samples will be equal at each revolution and they will not be distributed along the whole amplitude, therefore underestimation will always occur, and its magnitude will be related to the initial phase of the vibration at the beginning of the acquisition window, to the position of the sensors, and to the frequency of vibration. The only way to measure the amplitude correctly in the case of synchronous vibrations is to start the acquisition system repeatedly in order to vary the initial phase of the vibration randomly, thus producing a large number of samples randomly distributed at different amplitudes. Of course this procedure will be valid for both kinds of vibration, so that it is the suggested one, for improving the accuracy of measurements made with the system developed.

All the discussion above is valid in case of vibrations whose characteristics do not change during the whole duration of acquisition or series of successive acquisitions. The stationarity of blade vibrations was confirmed to be sufficient for the operation of the measurement system by Paone et al. (1991).

These results describe the operation of the measurement system, which has been developed to confirm the good performance of the software and validate the processing algorithms that have been implemented. They also suggest the correct measurement procedure to be used and the statistics of the particular sampling that is performed when employing this measurement system.

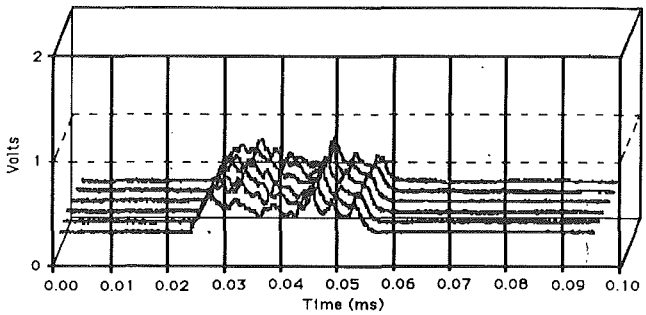

Fig. 4 Typical signals of the sensors produced by one particular blade passing in front of one sensing head at different successive revolutions

Experimental Tests of the Sensors

An experimental evaluation of the performance of the measurement system has been made on a test bench where interfering and modifying inputs and noise are actually present.

The first tests have been performed on a static blade. Their purpose was to investigate the sensor behavior as a proximity sensor. They have allowed us to observe that the sensor output is affected by the blade surface finishing. Roughness effects can be observed at the output as pulse amplitude distorsion, which can reach the order of 30 percent in the presence of rough surface. This implies a very careful triggering to measure the start and finish instants of each pulse. Also the focal spot diameter and the range of operating distance of the sensor for different focal lengths have been measured on the static bench. These measurements confirm that the sensor that has been developed is capable of detecting the blade presence for blades that are 2 to 6 mm distant from the front lens. These values make it suitable for most turbomachinery applications.

A second series of experimental tests has been performed on a small bladed rotor, which provides a maximum blade tip tangential velocity of 30 m/s. The blades are not vibrating in this configuration. These tests have allowed to verify the correlation of the shape of each signal produced by one blade with its surface roughness. Figure 4 represents the superposition of several pulses produced by one particular rotating blade. Each blade shows a characteristic signature in terms of shape of the pulses. This feature could be implemented in the software to enforce the signal processing; direct recognition of the pulses of each blade can be developed, further to the recognition by counting, which has already been implemented. Damages due to the accidental contact between blade tip and casing could also be detected.

Experimental Tests of the Measurement System

A high-speed test bench has been developed for further testing of the measurement system; its rotor can reach a maximum tangential speed larger than 300 m/s and it has vibrating blades. The two blades installed on the rotor are instrumented with conventional strain gages and slip rings for signal transmission, so that the actual vibration can be monitored and compared to the measurements performed by the proposed system. The two blades can be forced to vibrate by six air jets coming out from supersonic nozzles. Vibrations of smaller amplitude are induced by the rotor dynamic behavior. The natural first bending mode of vibration of the blades can be excited during the

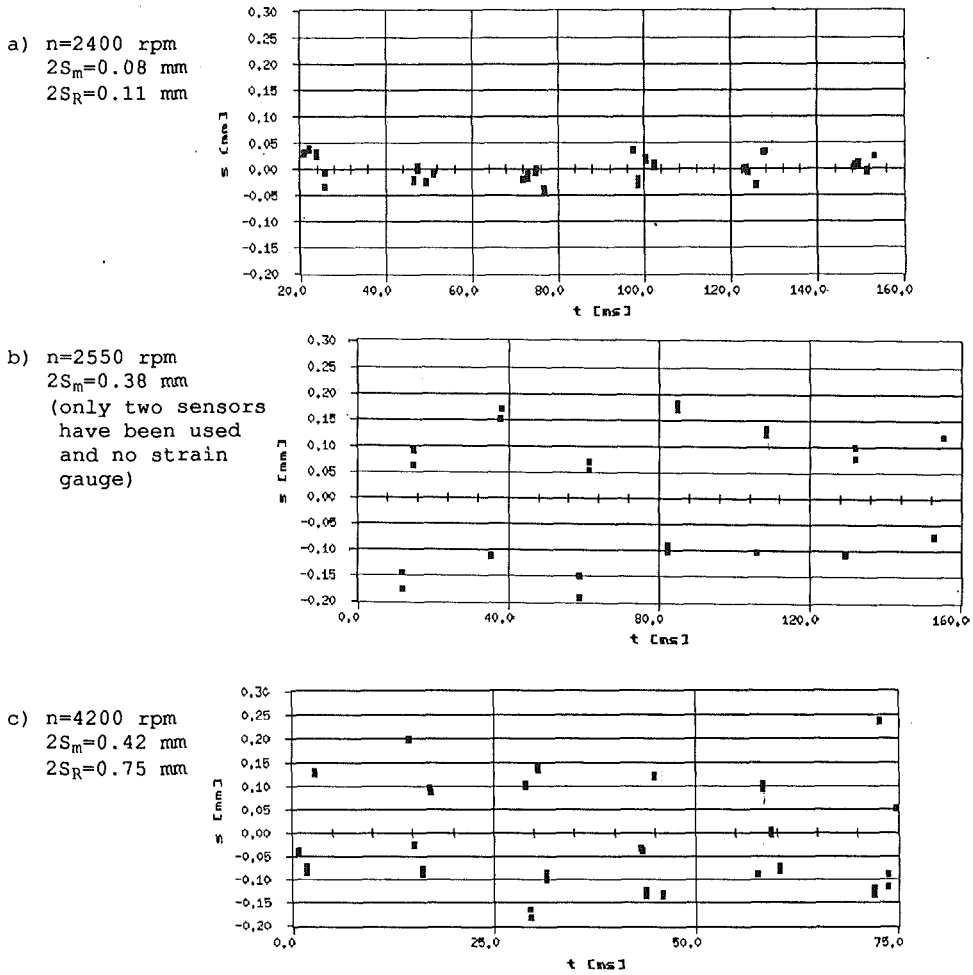

Fig. 5 Blade tip displacement samples measured by the system

revolution of the rotor at 4200 rpm with the 6 air jets (420 Hz). Resonance conditions give rise to maximum amplitudes of the deflection at blade tip. Amplitudes and frequencies are similar to those encountered in the first stages of industrial axial compressors. The simulation of the measurement system presented above is based on this test bench. It has been possible to determine a calibration factor that relates the strain gage output signal to the actual blade tip deflection, which was measured independently by eddy current probes on the steady bladed rotor. Therefore the strain gage output can be used to measure a reference value of blade tip deflection, when the blade vibrates according to its first bending mode.

Preliminary measurements have been performed in different conditions. Figures 5(*a*), 5(*b*), and 5(*c*) show the output of the measurement system at 2400 rpm, 2550 rpm, and 4200 rpm with air excitation. When the rotor runs at 2400 rpm and 2550 rpm the signals of the sensors are digitized at f_T = 12.5 MHz, while at 4300 rpm the transient recorder is operated at f_T = 25 MHz. With a memory depth equal to 2 Mbytes, it is sufficient to digitize six revolutions of the rotor in all cases. The three figures show the samples of blade tip deflection versus time; at each revolution eight samples are measured by four optical sensors so that 48 deflection samples are available in each case, with exception of case 5(*b*) where only two sensors were used. The sensors are not equally spaced along the circumference of the casing. The transient recorder is triggered by the signal of the sensors; no key phase sensor is used. Uncertainty in the measurement of each sample can be estimated, according to a methodology presented by the same authors in 1991, to be about 2 percent.

Figures 5(*b*) shows a series of samples, which repeat themselves quite similar from one revolution to the other: This is the experimental result that is obtained in case of synchronous vibrations, as explained above by the use of the simulator software. Figures 5(*a*) and 5(*c*) show instead two cases in which asynchronous vibrations are measured; the samples appear randomly distributed across the vertical scale. In these cases the angular velocity of the rotor was varying.

The measurements of Figs. 5(*a*) and 5(*c*) are made while the vibration was monitored also by strain gages. Alongside of each figure are reported the values of twice the vibration amplitude, measured independently by the strain gages and by the nonintrusive measurement system and indicated respectively as $2S_R$ and $2S_m$. S_R is measured by FFT analysis of the strain gage signals, while $2S_m$ is computed as the difference among maximum and minimum amplitude. The results confirm what is observed by using the simulator, i.e., the vibration amplitude is underestimated, due to the statistical reasons discussed previously. At 2400 rpm the fiber optic measurement system measures $2S_m$ = 0.08 mm against $2S_R$ = 0.11 mm measured by the strain gages, while at 4300 rpm it results in $2S_m$ = 0.42 mm against $2S_R$ = 0.75 mm. The difference is the same order of magnitude as the predictions of the simulator. As explained above, the increase in the number of samples leads to a population that is statistically meaningful and whose analysis allows a more accurate measurement of vibration amplitude.

Many hours of extensive testing in an industrial environment have proved the reliability of the sensing elements and of the whole measurement chain. In fact the dust and oil particles

present in the test rig did not significantly affect the signal-to-noise ratio of the sensor. Furthermore the intense electromagnetic fields, caused by the 500 hp electrical engine, which drives the rotor, did not affect the performance of the system. Air cooling of the fiber optic heads is under development; air is also used to clean the front lens. The sensors will then be suited for industrial applications on operating turbomachines.

Conclusions

A measurement system for detecting synchronous and asynchronous rotating blade vibrations based on static fiber optic sensors has been realized and tested. Its performance has been characterized by software simulation. Its different performance in case of synchronous and asynchronous vibrations is put in light; in all cases, if the number of samples of vibration is little, the vibration amplitude is underestimated. The means to increase the number of samples by expansion of the memory of the transient recorder and by acquisition of successive time windows have been proposed. The experiments performed on a test rig in conditions very close to those of an industrial axial compressor have confirmed the capabilities of the measurement system to detect blade vibrations. Comparison with strain gage measurements shows the underestimation of vibration amplitude that was investigated by the simulator. Therefore the conclusions derived by using the simulator can be implemented in the measurement system in order to improve its accuracy. The system has also proved to be reliable when operating in difficult environmental conditions. Further work is necessary to verify its performance on a real machine and to implement refined algorithms for data processing.

Acknowledgments

The authors wish to thank Mr. V. Ponzio for his technical support to the experimental part, Mr. O. Massi for the construction of the sensors, and Mr. A. Pasqualini for the development of part of the software.The collaboration with Mr. V. Quercioli of Nuovo Pignone is acknowledged.

References

Kawashima, T., et al., 1992, "Turbine Blade Vibration Monitoring Systems," ASME Paper No. 92-GT-159.

Kiraly, L. J., 1981, "Digital System for Dynamic Turbine Engine Blade Displacement Measurements," NASA TM-81382.

McCarty, P. E., and Thompson, W. Jr., 1981, "Development of Non Interference Technique for Measurement of Turbine Engine Compressor Blade Stress," Arnold Engineering Development Center Technical Report 79-78, US Air Force, TN.

Paone, N., Rossi, G. L., and, Tomasini, E. P., 1989, "Una Metodologia per la Misura delle Vibrazioni di Organii di Macchine in Moto Mediante Sensori Stazionari Senza Contatto (A Non Contact Measurement Technique to Measure Vibrations of Moving Components of Machines by Non-contact Stationary Sensors)," presented at the XVII Convegno AIAS, Ancona, Italy.

Paone, N., Rossi, G. L., and Tomasini, E. P., 1990, "La Misura Senza Contatto delle Vibrazioni di Pale di Turbomacchine: Caratteristiche del Misurando, del Modello e della Tecnica di Misura (Non Contact Measurement of Turbomachinery Blade Vibration: Characteristics of the Measurand, of the Model and of the Measurement Technique)," presented at the XVIII Convegno AIAS, Amalfi, Italy.

Paone, N., Rossi, G. L., and Tomasini, E. P., 1991, "Non-intrusive Measurement of Blade Tip Vibration in Turbomachines," ASME Paper No. 91-GT-301.

Paone, N., and Rossi, G. L., 1992, "Large-Bandwidth Reflection Fiber-Optic Sensors for Turbomachinery Rotor Blade Diagnostics," *Sensors and Actuators A*, Vol. 32, pp. 539–542.

Roth, H., 1981, "Vibration and Clearance Measurements on Rotating Blades Using Stationary Probes," Von Karman Institute Lecture Series 81-7, Rhode-St.-Genése, Belgium.

Simmons, H. R., et al., 1990, "Measuring Rotor and Blade Dynamics Using an Optical Blade Tip Sensor," ASME Paper No. 90-GT-91.

Stanoe, W. A., 1990, "Non-instrusive Sensing Techniques for Advanced Turbine Engine Structures," ASME Paper No. 90-GT-389.

Watkins, W. B., and Robinson, W. W., 1985, "Non-contact Engine Blade Vibration Measurements and Analysis," presented at the AIAA/SAE/ASME/ASEE 21st Joint Propulsion Conference, Monterey, CA.

Three-Dimensional Vibration Analysis of Rotating Laminated Composite Blades

O. G. McGee
School of Civil Engineering,
Georgia Institute of Technology,
Atlanta, GA 30332

H. R. Chu
Department of Civil Engineering,
Ohio State University,
Columbus, OH

This work offers the first known three-dimensional continuum vibration analysis for rotating, laminated composite blades. A cornerstone of this work is that the dynamic energies of the rotating blade are derived from a three-dimensional elasticity-based, truncated quadrangular pyramid model incorporating laminated orthotropicity, full geometric nonlinearity using an updated Lagrangian formulation and Coriolis acceleration terms. These analysis sophistications are included to accommodate the nonclassical directions of modern blade designs comprising thin, wide chord-lifting surfaces of laminated composite construction. The Ritz method is used to minimize the dynamic energies with displacements approximated by mathematically complete polynomials satisfying the vanishing displacement conditions at the blade root section exactly. Several tables and graphs are presented that describe numerical convergence studies showing the validity of the assumed displacement polynomials used herein. Nondimensional frequency data are presented for various rotating, truncated quadrangular pyramids, serving as first approximations of practical blades employed in aircraft engines and fans. A wide scope of results explain the influence of a number of parameters coined to rotating, laminated composite blade dynamics, namely aspect ratio (a/b), chord ratio (c/b), thickness ratio (b/h), variable thickness distribution (h_l/h_t), blade pretwist angle (ϕ_0), composite fiber orientation angle (θ), and angular velocity (Ω). Additional examples are given that elucidate the significance of the linear and nonlinear kinematics used in the present three-dimensional formulation along with the importance of the Coriolis acceleration terms included in the analysis.

Introduction

Chronicled in the published literature over the past decades are hundreds of references related to the rotating blade vibration problem (Rao, 1973, 1977, 1980; Leissa, 1980, 1981). Much of the previous work done on this problem employed one-dimensional beam models, while considering, oftentimes not collectively, various complicating topics, such as variable cross section, pretwist, skewness, precone (sweep), curved spanwise axis, centrifugal axial stiffening and lateral softening, Coriolis force, first-order shear deformation and rotary inertia terms, combined bending and torsion, large displacements, elastic support constraints, and attached shrouds. Some of these complicating effects were considered collectively in some recent dynamic studies of composite turboprops using beam models (Kosmatka and Friedmann, 1989; Subrahmanyam and Kaza, 1986).

It is well known that when the blade aspect ratio is small, generalized beam models for the rotating substructures in Fig. 1 are inadequate. Similar inadequacies are presented by classical plate models employing the Poisson hypothesis that normals to the midplane before deformation remain so after deformation. With such models, the flexural stresses are underpredicted, whereas the natural frequencies are overpredicted (Dokainish and Rawtani, 1971; MacBain, 1975; Shaw et al., 1988), especially in the higher modes. These results are due to the neglect of transverse shear stresses in the classical approach. It turns out that a number of investigators have exercised plate formulations that allow first-order transverse shear flexibilities to analyze the linear dynamics of rotating isotropic blades (Ramamurti and Kielb, 1984) and composite ones (Henry and Lalanne, 1974; Wang et al., 1987). More recently, Bhumbla et al. (1989, 1990) extended the analysis of shear deformable, composite rotating blades by including geometric nonlinearity in the form of von Kármon strains along with plane stress assumptions in the constitutive relations.

It turns out that the work of Bossak and Zienkiewicz (1973) provided the first known three-dimensional elasticity-based finite element formulation a propos to the natural vibration of centrifugally stressed solids such as those used in turbomachinery. In the dissertation of Jacob (1986), the vibration and buckling of twisted parallelepipeds were addressed using

Contributed by the International Gas Turbine Institute and presented at the 38th International Gas Turbine and Aeroengine Congress and Exposition, Cincinnati, Ohio, May 24–27, 1993. Manuscript received by the ASME Headquarters March 1, 1993. Paper No. 93-GT-133. Associate Technical Editor: H. Lukas.

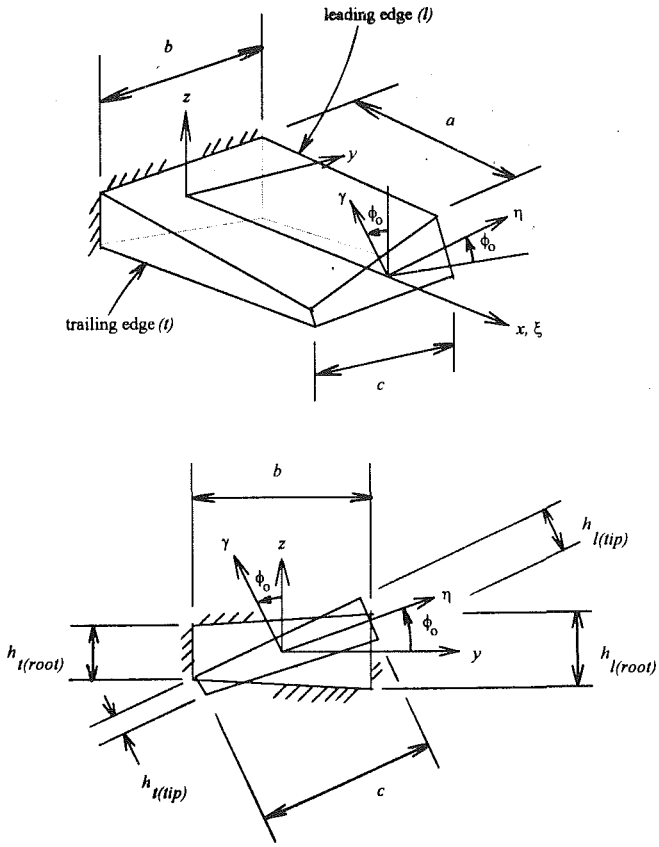

Fig. 1 Twisted cantilevered truncated quadrangular pyramid

three-dimensional elasticity theory including differential stiffness effects due to initial stress. However, Jacob's work did not include second-order strains due to geometric nonlinearity nor did it consider dynamic energies resulting from centrifugal accelerations. The latter accelerations (minus those due to Coriolis acceleration) were incorporated in the three-dimensional vibration analysis of Giaimo (1991) a propos to rotating, isotropic cantilevered blades.

We know of no previous or ongoing work offering a three-dimensional elasticity-based theory for vibrations of rotating laminated composite blades including full geometric nonlinearities and centrifugal accelerations in the blade kinematics. It is our purpose here to employ such theories in energy-based Ritz models of blades, so as to determine efficiently and accurately the steady-state displacement position and natural vibration of arbitrarily shaped, laminated composite blades prestressed by large displacement-dependent centrifugal loads.

The advantages of the present three-dimensional approach are twofold. First, no additional kinematic constraints (as in beam, plate, or shell theories) are imposed, except the vanishing displacement conditions at the root section of the blade. Imposition of the latter displacement constraints is required when selecting an assumed displacement model of the present Ritz approach. Second, the effects of transverse shear strains, rotary inertia, anticlastic flexure, and in-plane behaviors (such as thickness-shear and thickness-twist actions) are inherent. The impact of this work provides to structural dynamists and aeroelasticians a versatile nonlinear simulation model that emits cost-effective analysis experimentation of rotating blade dynamics over a wide range of geometric and material property parameters.

Consider the cantilevered, twisted, truncated quadrangular pyramid shown in Fig. 1, as a first approximation of typical blading used in aircraft engines and fans. A truncated quadrangular pyramid is a three-dimensional body, which is derived from a pyramid- or wedge-like configuration having a rectangular base and an arbitrarily oriented plane truncating the top portion of the pyramid. As shown in Fig. 1, the reference dimensions of the quadrangular pyramid are length a, root chord b, and tip chord c. A linear variation of pretwist is assumed along the length of the pyramid, such that $\phi = \phi_o(x/a)$, which results in the angle of pretwist being zero at the root and ϕ_o at the tip. The truncated quadrangular pyramid has a variable chordwise width along the spanwise (x) direction, given as $w = b - (1 - c/b)(bx/a)$, where c/b is the chord ratio. Besides this, variable thickness is assumed in the spanwise (x) and chordwise (y) directions. The variable thickness parameters are defined in terms of the leading and trailing edges (l and t, respectively) upon which they are located (see Fig. 1). For instance, the leading and trailing edge thicknesses at the root are denoted as $h_{l(\text{root})}$ and $h_{t(\text{root})}$, respectively, while like thicknesses at the tip are indicated as $h_{l(\text{tip})}$ and $h_{t(\text{tip})}$, respectively. Variable thickness in the chordwise (y) direction is defined as $h_c = h_t - (h_t - h_l)(y + b/2)/b$, where h_l and h_t are the leading and trailing edge thicknesses, respectively, at a typical section of the truncated quadrangular pyramid. Similar variable thickness distributions are assumed in the spanwise (x) direction, which are $h_t = h_{t(\text{root})} - (h_{t(\text{root})} - h_{t(\text{tip})})(x/a)$ and $h_l = h_{l(\text{root})} - (h_{l(\text{root})} - h_{l(\text{tip})})(x/a)$.

The present work offers the first known three-dimensional continuum vibration results for a rotating, laminated composite blade modeled as a cantilevered, truncated quadrangular pyramid. The dynamic energies are constructed using three-dimensional elasticity theory incorporating laminated orthotropicity and full geometric nonlinearity using an updated Lagrangian formulation and including all centrifugal acceleration effects. Displacements are assumed as simple polynomials, which are mathematically complete (Kantorovich and Krylov, 1958) and which satisfy the vanishing displacements at the blade root exactly. The Ritz method is used to minimize the dynamic energies to obtain upper bound approximate natural frequencies as close to the exact ones, as sufficient numbers of polynomial terms are retained. The accuracy of the present three-dimensional method is established by convergence studies explicitly showing the influence of solution determinant size. Nondimensional frequency results are studied showing the effect of several parameters coined to rotating, laminated composite blade vibrations, namely aspect ratio (a/b), chord ratio (c/b), thickness ratio (b/h), variable thickness distribution (h_l/h_t), blade pretwist angle (ϕ_o), composite fiber orientation angle (θ), and angular velocity (Ω). Additional examples are given that elucidate the significance of the linear and nonlinear kinematics used in the present three-dimensional formulation along with the importance of the Coriolis effects included in the analysis.

Theoretical Formulation

The strain vector $\{\epsilon\}$ is related to the displacements u, v, and w along the Cartesian coordinates (x, y, z) of the blade (or truncated quadrangular pyramid as shown in Fig. 1),

$$\{\epsilon\} = \{\epsilon_x, \epsilon_y, \epsilon_z, \gamma_{xy}, \gamma_{yz}, \gamma_{xz}\}^T = \{\epsilon^L + \epsilon^{NL}\} \tag{1}$$

where $\{\epsilon^L\}$ is the linear classical strain vector and $\{\epsilon^{NL}\}$ is the nonlinear geometric strain vector incorporating the usual squares and products of the displacement gradients. In Eq. (1),

$$\epsilon_x = \partial u/\partial x + 1/2[(\partial u/\partial x)^2 + (\partial v/\partial x)^2 + (\partial w/\partial x)^2]$$
$$\epsilon_y = \partial v/\partial y + 1/2[(\partial u/\partial y)^2 + (\partial v/\partial y)^2 + (\partial w/\partial y)^2]$$
$$\epsilon_z = \partial w/\partial z + 1/2[(\partial u/\partial z)^2 + (\partial v/\partial z)^2 + (\partial w/\partial z)^2]$$
$$\gamma_{xy} = \partial u/\partial y + \partial v/\partial x + \partial u/\partial x \cdot \partial u/\partial y + \partial v/\partial x \cdot \partial v/\partial y + \partial w/\partial x \cdot \partial w/\partial y$$
$$\gamma_{yz} = \partial v/\partial z + \partial w/\partial y + \partial u/\partial y \cdot \partial u/\partial z + \partial v/\partial y \cdot \partial v/\partial z + \partial w/\partial y \cdot \partial w/\partial z$$
$$\gamma_{xz} = \partial u/\partial z + \partial w/\partial x + \partial u/\partial x \cdot \partial u/\partial z + \partial v/\partial x \cdot \partial v/\partial z + \partial w/\partial x \cdot \partial w/\partial z \quad (2)$$

For laminated composite blades, the stress vector for the pth ply is

$$\{\sigma^{(p)}\} = [Q^{(p)}]\{\epsilon\} \quad (3)$$

where $\{\sigma^{(p)}\} = \{\sigma_x, \sigma_y, \sigma_z, \tau_{xy}, \tau_{yz}, \tau_{xz}\}^{(p)T}$ and $[Q^{(p)}]$ is a matrix of stiffness coefficients for laminated orthotropicity (see Appendix A). Equation (2) suggests that the strains are continuous, whereas the actual stresses are discontinuous across the layer interfaces as a result of the displacement "smear" approach (that is, continuous displacements assumed across layer interfaces) employed in this analysis.

Using Eqs. (1)–(3), the strain energy (U) of the rotating composite blade model (Fig. 1) is expressed by the volume integral

$$U = 1/2 \iiint \{\sigma^{(p)}\}^T\{\epsilon\}dV$$
$$= 1/2 \iiint \{\sigma^{(p)^L} + \sigma^{(p)^{NL}}\}^T\{\epsilon^L + \epsilon^{NL}\}\mathrm{d}V \quad (4)$$

where $\{\sigma^{(p)^L}\} = [Q^{(p)}]\{\epsilon^L\}$ and $\{\sigma^{(p)^{NL}}\} = [Q^{(p)}]\{\epsilon^{NL}\}$ are linear and nonlinear stresses in the pth lamina, and $dV = dx \cdot dy \cdot dz$. This energy is decomposed into

$$U = U_L + U_o + U_{NL} \quad (5)$$

where U_L is the usual linear elastic strain energy,

$$U_L = 1/2 \iiint \{\sigma^{(p)^L}\}^T\{\epsilon^L\}dV \quad (5a)$$

U_o is supplemental strain energy due to tension-flexure coupling,

$$U_o = 1/2 \iiint \{\sigma_o^{(p)^L}\}^T\{\epsilon^{NL}\}dV \quad (5b)$$

where $\{\sigma_o^{(p)^L}\}$ is the initial linear stress vector, and U_{NL} is higher order strain energy

$$U_{NL} = 1/2 \iiint \{\sigma^{(p)^{NL}}\}^T\{\epsilon^{NL}\}dV \quad (5c)$$

which is neglected in the present work.

The total kinetic energy (T) of the rotating composite blade model (Fig. 1) is

$$T = 1/2 \iiint \{\rho^{(p)}\mathbf{a_A}\}\cdot\Delta dV \quad (6)$$

where $\rho^{(p)}$ is the mass density of the pth lamina of the blade, $\Delta = \{u, v, w\}^T$ is the vector of displacements, and $\mathbf{a_A}$ is the acceleration vector of a typical mass point A of the blade with respect to the inertial axes ($\hat{x}$, $\hat{y}$, $\hat{z}$) (see Fig. 2):

$$\mathbf{a_A} = \mathbf{a_o} + \Omega \times [\Omega \times (\mathbf{r} + \Delta)] + \mathbf{a_c} + \mathbf{a_{rel}} \quad (7)$$

where $\mathbf{a_o}$ is the centripetal acceleration of the origin of the blade coordinates (x, y, z), given by

$$\mathbf{a_o} = \Omega \times (\Omega \times \mathbf{r_o}) \quad (8)$$

and $\mathbf{a_c}$ is the Coriolis acceleration, defined as

$$\mathbf{a_c} = 2\Omega \times \mathbf{v_{rel}} \quad (9)$$

In Eqs. (7)–(9), $\Omega = \Omega\{\Omega_x, \Omega_y, \Omega_z\}^T$ is the angular velocity vector, $\mathbf{r_o} = \{x_o, y_o, z_o\}^T$ is a vector of translational offsets of the blade coordinates from the inertial coordinates, $\mathbf{r} = \{x, y, z\}^T$ is the position vector of mass point A measured from the origin of the blade coordinates (x, y, z, see Fig. 2), and finally, $\mathbf{a_{rel}} = \{\ddot{u}, \ddot{v}, \ddot{w}\}^T$ and $v_{rel} = \{\dot{u}, \dot{v}, \dot{w}\}^T$ are the relative acceleration and velocity vectors, respectively, where the dots ($\dot{}$) indicate derivatives with respect to time (t). Besides this,

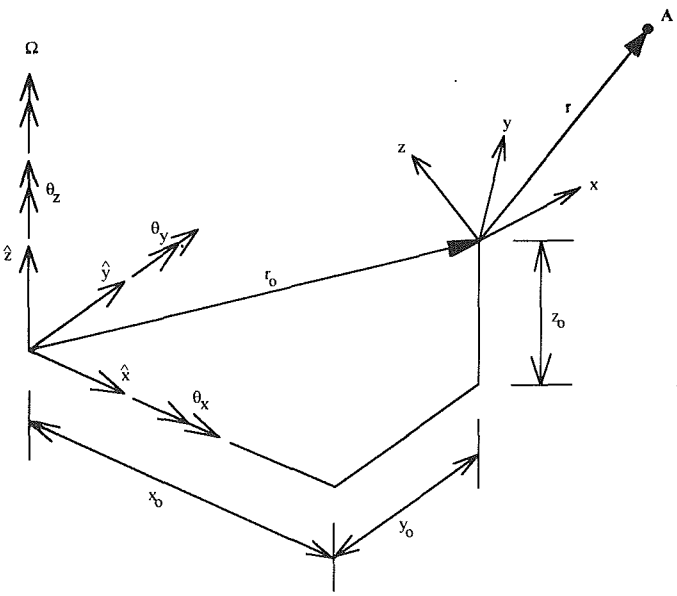

Fig. 2 Euler angles and translational offsets of rotating blade local (x, y, z) axes with respect to inertial ($\hat{x}$, $\hat{y}$, $\hat{z}$) axes

$$\{\Omega_x, \Omega_y, \Omega_z\}^T = \{0, 0, 1\}[T_{\theta_z}]^T[T_{\theta_y}]^T[T_{\theta_x}]^T \quad (10)$$

where the transformation between the blade coordinates (x, y, z) and the inertial coordinates ($\hat{x}$, $\hat{y}$, $\hat{z}$) is obtained by rotations through the Euler angles θ_x, θ_y, and θ_z about the inertial axes (see Fig. 2). Specifically, when $y_o = z_o = 0$, θ_x is the blade setting (or pitch) angle, and θ_y is the blade sweep (or precone). The order of rotations is θ_z, θ_y, and θ_x. In Eq. (10),

$$[T_{\theta_x}] = \begin{bmatrix} 1 & 0 & 0 \\ 0 & \cos(\theta_x) & \sin(\theta_x) \\ 0 & -\sin(\theta_x) & \cos(\theta_x) \end{bmatrix}$$

$$[T_{\theta_y}] = \begin{bmatrix} \cos(\theta_y) & 0 & -\sin(\theta_y) \\ 0 & 1 & 0 \\ \sin(\theta_y) & 0 & \cos(\theta_y) \end{bmatrix}$$

$$[T_{\theta_z}] = \begin{bmatrix} \cos(\theta_z) & \sin(\theta_z) & 0 \\ -\sin(\theta_z) & \cos(\theta_z) & 0 \\ 0 & 0 & 1 \end{bmatrix} \quad (11)$$

Using Eqs. (6)–(11), several dynamic energies are employed. First, the usual kinetic energy is

$$T_o = \iiint \rho^{(p)}\ddot{\Delta}^T\Delta dV \quad (12)$$

Additional kinetic energy due to centrifugal accelerations is

$$T_\Omega = \Omega^2/2 \iiint \rho^{(p)}\Delta^T[\Omega]\Delta dV \quad (13)$$

and supplemental energy due to Coriolis acceleration is

$$T_C = 2\Omega \iiint \rho^{(p)}\dot{\Delta}^T[R]\Delta dV \quad (14)$$

Finally, the work done by the centrifugal body forces is

$$(W_\Omega) = \{P_{CF}\}^T\Delta = \Omega^2 \iiint \rho^{(p)}(\mathbf{r} + \mathbf{r_o})^T[\Omega]\Delta dV \quad (15)$$

In Eqs. (13)–(15), $[\Omega] = [R]^T[R]$, where

$$[R] = \begin{bmatrix} 0 & -\Omega_z & \Omega_y \\ \Omega_z & 0 & -\Omega_x \\ -\Omega_y & \Omega_x & 0 \end{bmatrix} \quad (16)$$

In using the Ritz method, the total potential energy of the rotating blade given by

$$\pi = U_L + U_o + T_o - T_\Omega - T_C - W_\Omega \tag{17}$$

is minimized with respect to a set of generalized coefficients $\{q\}$ used in the Ritz trial space for u, v, and w. For free vibrations, the displacement components of the rotating blade are assumed simple harmonic, as follows:

$$u(x, y, z, t) = u_i(x, y, z)e^{j\omega t}$$

$$v(x, y, z, t) = v_i(x, y, z)e^{j\omega t}$$

$$w(x, y, z, t) = w_i(x, y, z)e^{j\omega t} \tag{18}$$

where ω is the circular frequency of vibration, e is the exponential function, t is time, and $j = (-1)^{1/2}$. The displacement functions (u_i, v_i, w_i) are expressed in terms of algebraic polynomials, as follows:

$$u_i(x, y, z) = \sum_{p=1}^{P}\sum_{q=0}^{Q}\sum_{r=0}^{R} A_{pqr}x^p y^q z^r$$

$$v_i(x, y, z) = \sum_{p=1}^{P}\sum_{q=0}^{Q}\sum_{r=0}^{R} B_{pqr}x^p y^q z^r$$

$$w_i(x, y, z) = \sum_{p=1}^{P}\sum_{q=0}^{Q}\sum_{r=0}^{R} C_{pqr}x^p y^q z^r \tag{19}$$

where from Eq. (19), we define $\{q\} = \{A_{pqr}, B_{pqr}, C_{pqr}\}$ as generalized coefficients to be determined. The summation index ($p = 1$) in Eqs. (19) indicates that each term of the series satisfies the vanishing displacement conditions at the blade root, that is $u_i(0, y, z) = v_i(0, y, z) = w_i(0, y, z) = 0$. Substituting Eqs. (18) and (19) into Eq. (17), and setting the exponential terms to unity, one obtains the maximum dynamic energies, which in turn are minimized with respect to the generalized coefficients $\{q\}$ of the trial functions [Eqs. (19)]. If no kinematic constraints other than the blade root conditions are imposed, and no other admissible terms up to P, Q, and R are omitted, then the set of polynomial terms in Eqs. (19) are mathematically complete (Kantorovich and Krylov, 1958). With a sufficient number of terms, the calculated frequencies should *in principle* converge from above to exact values.

The Ritz minimization result in $3 \times P \times (Q + 1) \times (R + 1)$ nonlinear equations, which are iteratively solved for $\{q\}$. The nonlinear equations of motion are expressed as

$$[K_L + K_{CF} + K_{NL}(q)]\{q\} + [C]\{\dot{q}\} + [M]\{\ddot{q}\} = \{P_{CF}\} \tag{20}$$

where $[K_L + K_{CF} + K_{NL}(q)]$ contains the linear, centrifugal, and geometrically nonlinear stiffness contributions, $[C]$ and $[M]$ are the gyroscopic and mass matrices, and $\{P_{CF}\}$ is the centrifugal force vector. Definitions of the structural matrices and vectors in Eq. (20) are given in Appendix B.

Equation (20) is solved in two steps: first, determine the nonlinear static equilibrated position $\{q_s\}$ due to the centrifugal force $\{P_{CF}\}$, and second, perform a free vibration analysis using the time-varying terms of Eq. (20) and $\{q_s\}$ as input. The geometrically nonlinear static analysis is performed by solving the following equation:

$$[K_L + K_{CF} + K_{NL}(q_s)]\{q_s\} = \{P_{CF}\} \tag{21}$$

using Newton–Raphson iterative solution procedures. In the second step, the rotating blade undergoes a linear time-dependent perturbation $\{q_p(t)\}$ about the static displaced position $\{q_s\}$, as follows:

$$[K_T]\{q_p\} + [C]\{\dot{q}_p\} + [M]\{\ddot{q}_p\} = \{0\} \tag{22}$$

where

$$[K_T] = [K_L + K_{CF} + K_{NL} + (\partial K_{NL}/\partial\{q\})\{q\}]_{\{q\}=\{q_s\}} \tag{23}$$

Table 1 Convergence of nondimensional frequencies $\omega a^2(\rho h/D)^{1/2}$ of a rotating isotropic blade with sweep ($a/b = c/b = 1$, $b/h = 10$, $x_o = 3a$, $y_o = z_o = 0$, $\Omega = \omega_o$, $\theta_x = 30$ deg, $\theta_y = 10$ deg, $\theta_z = \phi_o = 0$ deg, $\nu = 0.3$)

Size	3x3x3	4x4x3	4x4x4	5x5x4	5x6x4	6x5x4
d.o.f.	81	144	192	300	360	360
Mode 1	2.6420	2.6268	2.6255	2.6187	2.6187	2.6156
Mode 2	3.6478	3.5506	3.5415	3.5355	3.5224	3.5312
Mode 3	7.2629	7.0231	7.0230	6.9923	6.9824	6.9831
Mode 4	8.9382	8.2224	8.1954	7.9205	7.9062	7.9088
Mode 5	10.832	9.6063	9.5561	8.8845	8.8726	8.8768
Mode 6	12.835	10.660	10.600	10.557	10.512	10.531
Mode 7	16.493	16.391	16.390	16.173	16.114	16.122
Mode 8	19.037	17.606	17.463	16.347	16.345	16.328
Mode 9	20.156	18.430	18.430	18.405	18.373	18.403
Mode 10	31.495	24.807	24.566	19.692	18.437	19.334

Assuming $\{x\} = \{\dot{q}_p, q_p\}^T = \{c\}e^{\lambda t} = \{c\}e^{-\zeta t} \cdot e^{j\omega t}$, a first-order eigenvalue problem is applicable

$$([A] - \lambda[B])\{x\} = \{0\} \tag{24}$$

where $[A]$ is symmetric and $[B]$ is antisymmetric:

$$[A] = \begin{bmatrix} [M] & [0] \\ [0] & [K_T] \end{bmatrix} \quad [B] = \begin{bmatrix} [0] & [M] \\ -[M] & -[C] \end{bmatrix} \tag{25}$$

and λ is a complex eigenvalue; the real part representing exponential variations (of decay rate $= \zeta$) and the imaginary part as the harmonic component (at circular frequency ω).

Finally, the twisted coordinates (ξ, η, γ) shown in Fig. 1 are related to the Cartesian ones (x, y, z) through the orthogonal transformation

$$\xi = x; \quad \eta = y\cos\phi + z\sin\phi$$
$$\gamma = -y\sin\phi + z\cos\phi \tag{26}$$

or inversely

$$x = \xi; \quad y = \eta\cos\phi - \gamma\sin\phi$$
$$z = -\eta\sin\phi + \gamma\cos\phi \tag{27}$$

where $\phi = \phi_o(x/a) = \phi_o(\xi/a)$. Since the transformation Eqs. (26) and (27) are orthogonal, the Jacobian of the transformation between (x, y, z) and (ξ, η, γ) is unity (that is, $dV = dx \cdot dy \cdot dz = d\xi \cdot d\eta \cdot d\gamma$). For convenience of analysis, volumetric integral terms of the structural matrices and vectors (Appendix B) are first transformed to twisted coordinates, and then numerically integrated, since the change of variables yields integrands that are prohibitively complicated for exact integration.

Numerical Studies and Validation of Three-dimensional Results

Using the three-dimensional analysis outlined in the previous discussion, it is now appropriate to address how many terms of the assumed displacement polynomials [Eq. (19)] are required to yield reasonably accurate vibration solutions. Table 1 summarizes a convergence study of the first ten nondimensional frequencies $\omega a^2(\rho h/D)^{1/2}$ of a rotating cantilevered blade with sweep modeled as a moderately thick parallelepiped with sweep ($a/b = 1$, $c/b = 1$, $b/h = 10$, $x_o = 3a$, $y_o = z_o = 0$, $\Omega = \omega_o$, $\theta_x = 30$ deg, $\theta_y = 10$ deg, $\theta_z = 0$ deg), where $h = h_1 = h_t = h_c$, $D = Eh^3/12(1 - \nu^2)$, and ω_o is the natural frequency of the first mode of the stationary cantilevered parallelepiped. The blade model is assumed isotropic with the Poisson ratio (ν) set to 0.3 in the present three-dimensional formulation. Double precision arithmetic on an IBM 3090 machine has been used for all numerical calculations.

Convergence of frequency results is shown in Table 1 as the solution size is increased from a $3 \times 3 \times 3$ (81 degrees of

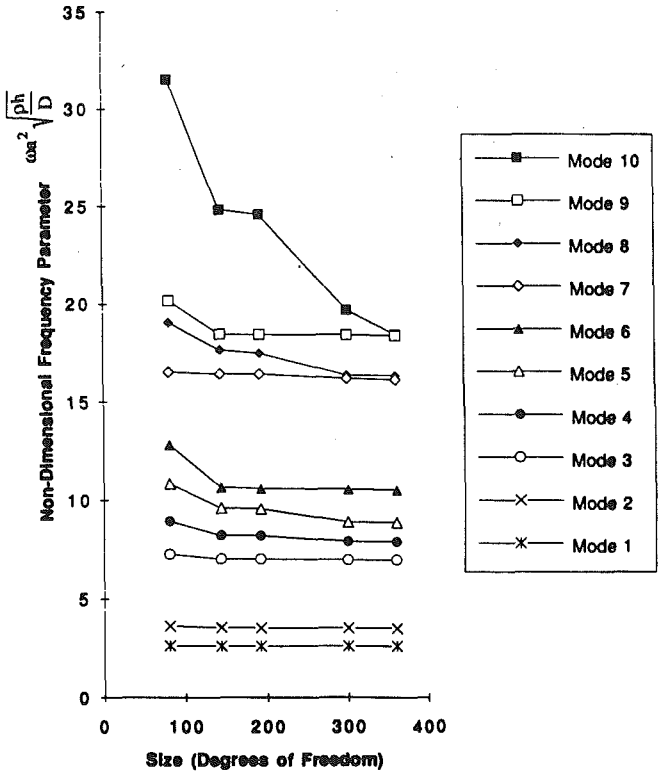

Fig. 3 Convergence of nondimensional frequencies of a rotating isotropic blade with sweep

freedom) solution to a 6 × 5 × 4 (360 degrees of freedom) solution. For instance, a 6 × 5 × 4 (360 degrees of freedom) solution indicates that six terms in the x direction, five terms in the y direction, and four terms in the z direction have been retained in the Ritz trial functions [Eqs. (19)] for a total of 360 degrees of freedom. A small sequential level of convergence is exhibited by the frequency solutions of Table 1, since large solution sizes contain all terms of certain of the previous smaller ones. For example, a 6 × 5 × 4 solution contains all terms of the 5 × 5 × 4 solution, which in turn contains all terms of the 4 × 4 × 4 solution, and so on.

One can see clearly from the variation of $\omega a^2(\rho h/D)^{1/2}$ with increasing degrees of freedom in Fig. 3 that a reasonably good monotonic convergence of solution for at least the first nine frequency modes is achieved using the present three-dimensional Ritz analysis. Indeed, the least upper bound frequency values are obtained by using either a 5 × 6 × 4 or a 6 × 5 × 4 (360 degrees of freedom) solution. The frequencies of the tenth mode do show some convergence difficulty, which is expected when using a Ritz approach. By retaining additional terms in the displacement polynomials [Eqs. (19)], one can, in principle, achieve better convergence of solution for mode 10; however, some matrix ill-conditioning in the mass operator prohibits further reduction of the eigensystem with excessively large determinant sizes (i.e., large degrees of freedom). This matrix ill-conditioning is due to the nonorthogonal nature of the algebraic polynomials assumed in Eqs. (19). Use of these polynomials, albeit simple, results in a mass operator characteristic of a Hilbert matrix, which can be notoriously ill-conditioned when inadequate computational precision is utilized. Such matrix ill-conditioning may be alleviated when quadruple (28 significant digit) rather than double (14 significant digit) arithmetic is employed in some supercomputers and powerserver machines.

Table 2 shows the convergence of the first ten nondimensional frequencies $[(\omega a^2/h)(\rho/E_{22})^{1/2}]$ of a rotating, cantilevered laminated composite blade modeled as a cantilevered

Table 2 Convergence of nondimensional frequencies $(\omega a^2/h)(\rho/E_{22})^{1/2}$ of a rotating graphite/epoxy laminated composite blade (a = 3 in., b = 3 in., $x_o = 2a$, $y_o = z_o = 0$, $\Omega = \omega_o$, θ_x = 45 deg, $\theta_y = \theta_z = \phi_o$ = 0 deg)

Size	3x3x3	4x4x3	4x4x4	5x5x4
d.o.f.	81	144	192	300
Mode 1	5.3796	5.3251	5.3245	5.3017
Mode 2	7.1235	6.7748	6.7703	6.7590
Mode 3	11.615	11.439	11.428	10.742
Mode 4	28.278	20.320	20.302	19.745
Mode 5	34.804	21.682	21.638	21.768
Mode 6	53.268	27.133	27.098	26.724
Mode 7	108.990	38.977	38.860	35.375
Mode 8	167.400	61.533	61.310	47.845
Mode 9	176.350	86.996	86.546	55.456
Mode 10	190.480	92.690	92.214	56.398

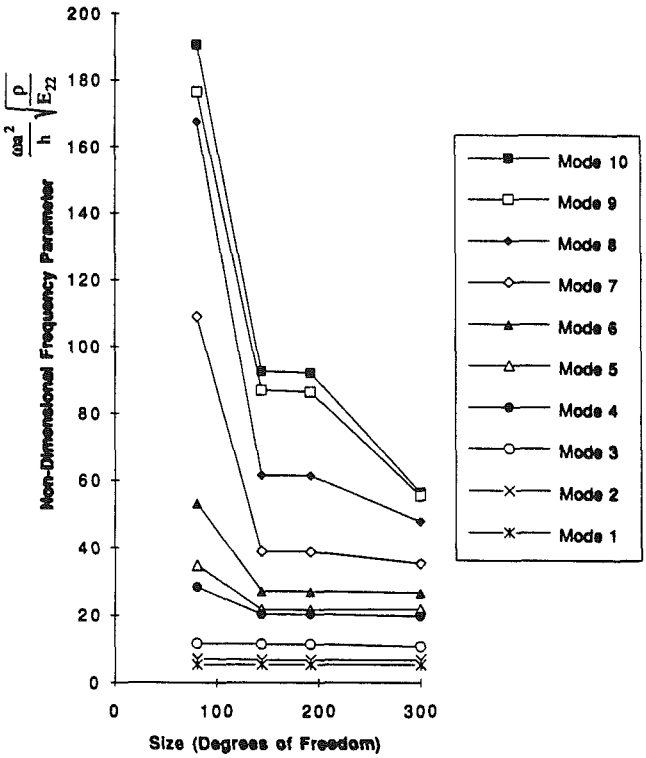

Fig. 4 Convergence of nondimensional frequencies of a rotating graphite/epoxy laminated composite blade

parallelepiped having a graphite/epoxy laminate material with $[\pm 30/\mp 30]_s$ symmetric stacking of eight layers with the thickness of each layer being 0.0052 in. Additional transversely isotropic lamina material properties and geometric parameters for this sample blade model are defined as follows (cf. Crawley, 1979; Baharlou and Leissa, 1987): ($E_L = E_{11} = 18.5 \times 10^6$ psi, $E_T = E_{22} = E_{33} = 1.6 \times 10^6$ psi, $G_{LT} = G_{12} = 0.65 \times 10^6$ psi, $G_{TT} = G_{13} = G_{23} = 0.222 \times 10^6$ psi, $\nu_{12} = \nu_{13} = \nu_{23} = \nu = 0.25$, $\rho = 0.055$ lb/in.^{3}, a = 3 in., $b = c$ = 3 in., $x_o = 2a$, $y_o = z_o = 0$, $\Omega = \omega_o$, θ_x = 45 deg, $\theta_y = \theta_z = \phi_c = 0$ deg).

In contrast to the convergence trends observed in Fig. 3, the variation of $[(\omega a^2/h)(\rho/E_{22})^{1/2}]$ with increasing degrees of freedom shown in Fig. 4 suggests that a reasonable level of convergence of frequency solutions for rotating laminated composite parallelepipeds is slightly more difficult to achieve by the present three-dimensional approach. In Table 2 the sequential level of convergence exhibited by the 3 × 3 × 3

Table 3 Comparison of nondimensional frequencies $\omega a^2(\rho h/D)^{1/2}$ of an isotropic cantilevered blade ($a/b = c/d = 1$, $b/h = 10$, $\Omega = 0$, $\nu = 0.3$)

	Mode Number				
	1	2	3	4	5
Present 3-D analysis[1]	3.4493	8.0958	20.213	25.578	28.408
Bhumbla, et al. (1989)[2]	3.4338	8.0833	20.752	26.055	28.953
Bhumbla, et al. (1989)[3]	3.4275	8.0545	20.144	25.576	28.307
Leissa (1969)[4]	3.4940	8.5470	21.440	27.460	31.170

[1]5x5x4 solution (300 d.o.f.). [2]8x8 mesh of four noded Mindlin plate finite elements. [3]4x4 mesh of eight noded Mindlin plate finite elements. [4]classical thin plate theory.

Table 4 Comparison of cyclic frequencies (Hz) of cantilevered graphite/epoxy blades ($\Omega = 0$)

	Mode Number				
	1	2	3	4	5
(a=3", b=c=3", $[0_2/\pm 30]_S$)					
Present 3-D analysis	261.78	363.04	759.12	1597.5	1628.0
Crawley (1979)[1]	234.2	362.	728.3	1449.	1503.
Crawley (1979)[2]	261.9	363.5	761.8	1662.	1709.
Baharlou & Leissa (1987)[3]	262.1	363.7	771.4	1642.	1653.
(a=6", b=c=3", $[0_2/\pm 30]_S$)					
Present 3-D analysis	65.377	137.49	407.80	524.81	582.69
Crawley (1979)[1]	53.8	148.	362.7	508.	546.
Crawley (1979)[2]	65.37	137.5	408.3	525.6	588.3
Baharlou & Leissa (1987)[3]	65.39	137.9	408.7	527.1	589.4
(a=3", b=c=3", $[0_2/\pm 45/90]_S$)					
Present 3-D analysis	223.95	420.03	1006.0	1399.8	1689.8
Crawley (1979)[1]	196.4	418.	960.	1215.	1550.
Crawley (1979)[2]	224.3	421.8	1012.	1426.	1722.
(a=6", b=c=3", $[0_2/\pm 45/90]_S$)					
Present 3-D analysis	55.580	174.78	344.83	590.23	810.95
Crawley (1979)[1]	48.6	169.	303.	554.	739.
Crawley (1979)[2]	55.58	175.4	345.3	591.8	820.1
(a=3", b=c=3", $[\pm 45/\mp 45]_S$)					
Present 3-D analysis	138.36	495.45	795.22	1307.9	1612.4
Crawley (1979)[1]	131.2	472.	790.5	1168.	1486.
Crawley (1979)[2]	138.9	499.5	805.	1326.	1648.
(a=6", b=c=3", $[\pm 45/\mp 45]_S$)					
Present 3-D analysis	65.377	137.49	407.80	524.81	582.69
Crawley (1979)[1]	53.8	148.	362.7	508.	546.
Crawley (1979)[2]	65.37	137.5	408.3	525.6	588.3

[1]experimental test results. [2]3x3 mesh of 8-noded moderately thick quadrilateral shallow shell finite elements. [3]Ritz method using classical thin plate theory.

(81 degrees of freedom) and $5 \times 5 \times 4$ (300 degrees of freedom) solutions is narrower in scope compared to the sequential convergence level shown in Table 1. Whereas, the strains in Eq. (2) are continuous, the stresses are indeed discontinuous across the layer interfaces as a result of the smear theory imposed in the present three-dimensional analysis. It is certainly plausible to deduce that these discontinuous stresses will somewhat degrade the rate of convergence of three-dimensional frequency data. We must underscore that the rapid upper bound convergence of frequencies for modes 8–10 is monotonically smoother, as more families of solution sizes are included (however, for the sake of brevity, a larger data base of frequencies is not shown in Table 2). Nonetheless, we have judged that the convergence of frequencies shown in Table 2 for this representative laminated composite parallelepiped is adequate enough for engineering accuracy to validate the correctness of the present three-dimensional formulation. Indeed, for the first seven modes, the average difference between the results calculated for the $4 \times 4 \times 4$ (192 degrees of freedom) and $5 \times 5 \times 4$ (300 degrees of freedom) solutions is less than 2 percent.

It is interesting now to compare the frequency results obtained from the present three-dimensional idealizations of composite blading with those acquired from select papers using classical thin plate and first-order shear deformable plate formulations (e.g., Leissa, 1969; Crawley, 1979; Baharlou and Leissa, 1987; Bhumbla et al., 1989, 1990) and experimental methods (e.g., Crawley, 1979). Like the present work, Baharlou and Leissa (1987) used the Ritz method to analyze the vibrations of stationary ($\Omega = 0$) isotropic and laminated composite blades. Here, the dynamic energies were constructed from classical thin plate theory with flexural displacements approximated as mathematically complete algebraic polynomials. Some useful experimental data for laminated composite blading was supplied by Crawley (1979) along with some analytical results for comparison using an assemblage of eight-noded moderately thick quadrilateral shallow shell finite elements. For stationary and rotating blades, Bhumbla et al. (1989, 1990) developed a finite element formulation based on Mindlin plate theory including geometric nonlinearity in the form of von Kármán strains along with plane stress assumptions in the constitutive relations.

The correctness of the present three-dimensional analysis is validated by the comparison of frequency data shown in Tables 3 and 4. Table 3 shows a comparison of nondimensional frequencies $\omega a^2(\rho h/D)^{1/2}$ of a stationary ($\Omega = 0$), moderately thick, low aspect ratio compressor blade ($a/b = c/b = 1$, $b/h = 10$, $h = h_1 = h_t = h_c$). Shown therein is a comparison of frequency results obtained from classical thin plate theory (CPT) (Leissa, 1969), first-order shear deformable plate theory (FOSDPT) (Bhumbla et al., 1989), and the present three-dimensional analysis. The latter analysis inherently possesses shear deformation and rotary inertia effects. As can be seen in Table 3, these effects tend to destiffen the frequencies obtained from CPT, more so in the higher modes than the lower ones. Moreover, the shear correction factor used in the FOSDPT tends to overcorrect the true effect of transverse shear flexibilities in the higher modes of thick blades. In Table 3, this trend is clearly seen as one compares the slightly higher frequency values obtained by the present three-dimensional analysis compared to those frequency values calculated by the higher level of approximation used in the eight-noded Mindlin plate finite element discretizations of Bhumbla et al. (1989).

Assumed displacement models based on classical plate theory (CPT) (Leissa, 1969; Baharlou and Leissa, 1987) assume that normals to the plate's undeformed midsurface remain normal after deformation. Of course, the CPT displacement models do not allow for shear deformable behavior, although rotary inertia effects are many times included by investigators. In contrast, Reissner-Mindlin plate deformation models (Bhumbla et al., 1989) assume that normals to the plate's undeformed midsurface remain straight but not necessarily normal to the midsurface after deformation. Assumed displacement models based on Mindlin's plate theory (MPT) limit their accuracy to the vibrations of moderately thick plates, mainly because the shear strain distribution of Mindlin plates is assumed independent of the (z) distance from the midsurface. However, the proper selection of a shear correction coefficient can to some extent alleviate errors resulting from this inadequate assumption, since the actual shear strain distribution of thick rhombic plates is indeed nonuniform.

In calculating the three-dimensional results in Tables 3 and 4, the in-plane and normal displacement fields are assumed as a cubic function in z to yield parabolic normal and transverse shear strain approximations of the actual nonuniform strain distributions through the plate thickness and some crossectional warping. Moreover, full geometric nonlinear strains were retained in conjunction with laminated orthotropicity in the three-dimensional constitutive laws. In contrast to the present three-

Table 5 Effects of nonlinear strains and Coriolis acceleration on nondimensional frequencies $\omega a^2(\rho h_{avg}/D_{avg})^{1/2}$ of a rotating twisted blade ($a/b = 1$, $c/b = 1$, $b/h_{l(root)} = 10$, $b/h_{l(tip)} = 50$, $h_l/h_t = 1.15$, $x_o = 2a$, $y_o = z_o = 0$, $\Omega = \omega_o$, $\theta_x = 45$ deg, $\theta_y = \theta_z = 0$ deg, $\phi_o = 60$ deg, $\nu = 0.3$)

Mode	A	B		C		D	
1	9.0284	8.9922	-(0.40%)	10.041	(11.22%)	10.013	(10.91%)
2	14.366	14.283	-(0.58%)	14.624	(1.80%)	14.536	(1.18%)
3	23.426	23.400	-(0.11%)	24.162	(3.14%)	24.004	(2.47%)
4	25.032	24.905	-(0.51%)	30.309	(21.08%)	30.258	(20.88%)
5	28.263	28.305	(0.15%)	35.164	(24.42%)	35.242	(24.69%)
6	45.183	45.106	-(0.17%)	43.448	-(3.84%)	43.376	-(4.00%)
7	47.050	47.043	-(0.01%)	49.782	(5.81%)	49.739	(5.72%)
8	57.542	57.560	(0.03%)	59.247	(2.96%)	59.338	(3.12%)
9	68.417	68.418	(0.00%)	69.495	(1.58%)	69.515	(1.60%)
10	71.151	71.276	(0.18%)	71.842	(0.97%)	71.891	(1.04%)

A = linear strain $\{\epsilon_L\}$ without Coriolis acceleration.
B = linear strain $\{\epsilon_L\}$ with Coriolis acceleration.
C = nonlinear strain $\{\epsilon_{NL}\}$ without Coriolis acceleration.
D = nonlinear strain $\{\epsilon_{NL}\}$ with Coriolis acceleration.
(Values in parentheses are percentage difference in frequencies with respect to those listed in column A).

Table 6 Effects of nonlinear strains and Coriolis acceleration on nondimensional frequencies $(\omega a^2/h)(\rho/E_{22})^{1/2}$ of a rotating $[\pm 30/\mp 30]_s$ graphite/epoxy laminated composite blade ($a/b = 1$, $c/b = 1.25$, $x_o = 2a$, $y_o = z_o = 0$, $\Omega = \omega_o$, $\theta_x = 45$ deg, $\theta_y = \theta_z = \phi_o = 0$ deg)

Mode	A	B		C		D	
1	5.2957	5.2963	(0.01%)	5.3005	(0.09%)	5.3017	(0.11%)
2	6.5771	6.7561	-(0.01%)	6.7616	(0.07%)	6.7590	(0.03%)
3	10.742	10.744	(0.02%)	10.741	-(0.01%)	10.742	(0.00%)
4	19.722	19.722	(0.00%)	19.745	(0.12%)	19.745	(0.12%)
5	21.738	21.740	(0.01%)	21.768	(0.14%)	21.768	(0.14%)
6	26.681	26.681	(0.00%)	26.724	(0.16%)	26.724	(0.16%)
7	35.336	35.331	-(0.01%)	35.377	(0.12%)	35.375	(0.11%)
8	47.756	47.757	(0.00%)	47.844	(0.18%)	47.845	(0.19%)
9	55.343	55.342	(0.00%)	55.457	(0.21%)	55.456	(0.20%)
10	56.289	56.289	(0.00%)	56.399	(0.20%)	56.398	(0.19%)

A = linear strain $\{\epsilon_L\}$ without Coriolis acceleration.
B = linear strain $\{\epsilon_L\}$ with Coriolis acceleration.
C = nonlinear strain $\{\epsilon_{NL}\}$ without Coriolis acceleration.
D = nonlinear strain $\{\epsilon_{NL}\}$ with Coriolis acceleration.
(Values in parentheses are percentage difference in frequencies with respect to those listed in column A).

dimensional analysis, Bhumbla et al. (1989) assumed normal displacements, which were independent of the plate's thickness coordinate, resulting in zero normal strain and allowing for the usual plane stress assumptions in the constitutive laws.

Shown in Table 4 is a comparison of analytically and experimentally determined cyclic frequencies of graphite/epoxy laminated composite blades having $a/b = 1$ and 2 and various ply stacking sequences. Generally speaking, the agreement between the analytical results is favorable in most of the frequency modes. In fact, the upper bound frequencies calculated by the present three-dimensional method are lower than the finite element frequencies reported by Crawley (1979) by about 2 percent in some of the higher modes, largely due to the inherent shear deformation and rotary inertia present. Across the board it does appear that the experimental data reported by Crawley (1979) are lower than the analytical results, albeit the present three-dimensional frequencies do agree more favorably with the experimental ones, particularly in the higher modes. Crawley offered that a 20 percent reduction in the transverse shear modulus used to calculate his finite element data resulted in less than 1 percent reduction in frequency values. This led to a conclusion that the transverse shear effect was not the cause of the difference between the analytical and experimental cyclic frequencies shown in Table 4. Given the close agreement between the analytical results in Table 4, it is difficult to make a clear conjecture about a primary cause of some of the destiffening present in the experimental frequencies.

From the data shown in Tables 5 and 6, one can fully ascertain the influence of the geometrically nonlinear strains and Coriolis acceleration terms retained in the present three-dimensional analysis on the natural vibration of typical blading used in practical disk assemblies. Table 5 lists nondimensional frequencies $\omega a^2(\rho h_{avg(root)}/D_{avg})^{1/2}$ of a rotating twisted blade modeled as a twisted, truncated quadrangular pyramid ($a/b = 1$, $c/b = 1$, $b/h_{l(root)} = 10$, $b/h_{l(tip)} = 50$, $h_l/h_t = 1.15$, $x_o = 2a$, $y_o = z_o = 0$, $\Omega = \omega_o$, $\theta_x = 45$ deg, $\theta_y = \theta_z = 0$ deg, $\phi_o = 60$ deg, $\nu = 0.3$). Table 6 shows nondimensional frequencies $[(\omega a^2/h)(\rho/E_{22})^{1/2}]$ of a typical rotating, laminated composite, wide chord, fan blade modeled as a cantilevered, truncated quadrangular pyramid ($a/b = 1$, $c/b = 1.25$, $x_o = 2a$, $y_o = z_o = 0$, $\Omega = \omega_o$, $\theta_x = 45$ deg, $\theta_y = \theta_z = \phi_o = 0$ deg) having a graphite/epoxy laminated material with $[\pm 30/\mp 30]_s$ symmetric stacking of eight layers with the thickness of each layer being 0.0052 in. Material properties are the same as those previously described for the example associated with Table 2.

Four sets of frequency data are given in Tables 5 and 6 identifying separately the influences of linear $\{\epsilon_L\}$ and nonlinear $\{\epsilon_{NL}\}$ strains with and without Coriolis acceleration terms [see Eqs. (1)-(2) and (9)]. Percentage differences in frequency values are shown in parentheses using those values obtained with the effects of linear strains $\{\epsilon_L\}$ only. It is clear that Coriolis acceleration has a minimal effect on the nondimensional frequencies shown in Tables 5 and 6, even as the angular velocity ($\Omega = \omega_o$) is well within the speeds of operation associated with practical blading. Of course, one could expect a larger influence of Coriolis acceleration on the natural vibration of blading operating at higher angular velocities and larger pitch angles (θ_x). A closer look at the percentage difference data does reveal that (1) the effect of Coriolis acceleration is slightly stronger in the presence of nonlinear strains $\{\epsilon_{NL}\}$ than without them, (2) the frequencies of the variable thickness, highly twisted, isotropic blade model (Table 5) show a larger influence of both the individual and net effects of Coriolis acceleration than those frequencies of the wide chord, laminated composite blade model (Table 6), and (3) the presence of nonlinear strains $\{\epsilon_{NL}\}$ further stiffens all modes, except the sixth mode in Table 5.

Table 7 shows a comparison of nondimensional frequencies $\omega a^2(\rho h/D)^{1/2}$ of rotating cantilevered blades modeled as moderately thick parallelepipeds ($a/b = c/b = 1$, $b/h = 10$, $h = h_l = h_t = h_c$, $x_o = 3a$, $y_o = z_o = 0$, $\Omega = \omega_o$, $\theta_x = 30$ deg, $\theta_y = 10$ deg, $\theta_z = \phi_o = 0$ deg, $\nu = 0.3$). As in Table 3, calculated frequency data obtained by the present three-dimensional method (including nonlinear strains $\{\epsilon_{NL}\}$ and Coriolis accelerations) are compared to data previously reported by Bhumbla et al. (1989) using a FOSDPT approach. Although the agreement between the frequency results is favorable, the shear correction factor used in the FOSDPT tends to overcorrect the true effect of transverse shear flexibilities of rotating thick blades, particularly in the higher modes. It appears that centrifugal stiffening does not significantly influence the transverse shear behavior of the blades. Interestingly, a supplemental fourth frequency mode is identified by the present three-dimensional analysis, which was predicted by the FOSDPT analysis.

Concluding Remarks

This work offers the first known three-dimensional continuum vibration solutions for rotating laminated composite blades. The Ritz method has been employed to determine ap-

Table 7 Comparison of nondimensional frequencies $\omega a^2(\rho h/D)^{1/2}$ of a rotating cantilevered blades ($a/b = c/b = 1$, $b/h = 10$, $x_o = 3a$, $y_o = z_o = 0$, $\Omega = \omega_o$, $\theta_x = 30$ deg, $\theta_y = 10$ deg, $\theta_z = \phi_o = 0$ deg, $\nu = 0.3$)

Theory	Ω_r	Mode Number 1	2	3	4	5	6
Present 3-D	1	3.6311	8.0982	20.440	21.875	25.890	28.803
FOSDPT[1]		3.5949	8.1779	20.287	--	25.651	28.481
Present 3-D	2	4.1043	8.5693	20.885	21.836	26.026	29.070
FOSDPT[1]		4.0491	8.5299	20.704	--	25.873	28.832
Present 3-D	3	4.7522	9.1090	21.575	21.761	26.489	29.711
FOSDPT[1]		4.6921	9.0653	22.054	--	26.238	29.478
Present 3-D	4	5.5542	9.8307	21.685	22.529	27.059	30.637
FOSDPT[1]		5.4414	9.7311	22.032	--	26.744	30.359
Present 3-D	5	6.4216	10.684	21.574	23.675	27.768	31.611
FOSDPT[1]		6.2456	10.842	22.369	--	27.407	31.446
Present 3-D	6	7.3263	11.673	21.442	24.985	28.628	32.814
FOSDPT[1]		7.0758	11.288	22.658	--	28.245	32.701

[1] 4x4 mesh of eight noded Mindlin plate finite elements [Bhumbla, et al. (1989)]

proximate nondimensional frequencies. The dynamic energies of the rotating blade have been derived from a three-dimensional elasticity-based, truncated quadrangular pyramid model incorporating laminated orthotropicity, full geometric nonlinearity using an updated Lagrangian formulation, and complete centrifugal and Coriolis acceleration terms. A set of algebraic polynomials, which are mathematically complete, have been utilized as trial functions. No additional kinematic constraints (as in beams, plates, or shells) have been imposed, except the vanishing displacements at the blade root, thereby guaranteeing monotonic convergence from above to the exact frequencies, as a sufficient number of polynomial terms are used.

To demonstrate the method, convergence studies of nondimensional frequencies of low aspect ratio, rotating laminated composite blades have been summarized to ascertain the number of polynomial terms required to achieve a reasonable degree of accuracy of solution. One focus has been to compare the correctness of frequency data obtained using a classical thin plate Ritz approach or a first-order shear deformable plate finite element approach with those obtained using a present three-dimensional Ritz method. A small scope of previously reported frequency data for rotating laminated composite blading has been corrected to some extent by the present method, since the effects of transverse shear strains, rotary inertia, anticlastic flexure, and in-plane behaviors (such as thickness-shear and thickness-twist actions) are inherent. Above all, the present three-dimensional method provides to structural dynamists and aeroelasticians a versatile nonlinear simulation model that permits cost-effective analysis experimentation of rotating blade dynamics over a wide range of geometric and material property parameters.

Acknowledgments

This research was supported by the National Science Foundation, Award No. MSS-9157972. The authors wish to express their sincere appreciation to Mr. Stephen C. Spry, an undergraduate research assistant in the School of Civil Engineering at Georgia Tech, for his helpful assistance with the final formating preparations of the manuscript.

References

Baharlou, B., and Leissa, A. W., 1987, "Vibration and Buckling of Generally Laminated Composite Plates With Arbitrary Edge Conditions," *International Journal Mechanical Sciences*, Vol. 29, No. 8, pp. 545–555.

Bhumbla, R., Reddy, J. N., and Kosmatka, J. B., 1989, "A Study of Vibrations in Rotating Laminated Composite Plates Accounting for Shear Deformation and Rotary Inertia," Virginia Polytechnic Institute and State University, Rept. CCMS-89-15.

Bhumbla, R., Kosmatka, J. B., and Reddy, J. N., 1990, "Free Vibration Behavior of Spinning Shear Deformable Plates Composed of Composite Materials," *AIAA Journal*, Vol. 28, No. 11, pp. 1962–1970.

Bossak, M. A. J., and Zienkiewicz, O. C., 1973, "Free Vibration of Initially Stressed Solids With Particular Reference to Centrifugal-Force Effects in Rotating Machinery," *Journal of Strain Analysis*, Vol. 8, No. 4, pp. 245–252.

Crawley, E. F., 1979, "The Natural Modes of Graphite/Epoxy Cantilever Plates and Shells," *Journal Composite Materials*, Vol. 13, pp. 195–205.

Dokainish, M. A., and Rawtani, S., 1971, "Vibration Analysis of Rotating Cantilever Plates," *International Journal for Numerical Methods in Engineering*, Vol. 3, No. 2, pp. 233–248.

Giaimo, G. T., 1991, "Three-Dimensional Vibrations of Rotating Cantilevered Truncated Pyramids," M.S. Thesis, Ohio State University.

Henry, R., and Lalanne, M., 1974, "Vibration Analysis of Rotating Compressor Blades," ASME *Journal of Engineering for Industry*, Vol. 96, No. 3, pp. 1028–1035.

Jacob, K. I., 1986, "Three-Dimensional Vibration and Buckling Analysis of Twisted Parallelepipeds," Ph.D. Dissertation, Ohio State University.

Kantorovich, L. V., and Krylov, V. I., 1958, *Approximate Methods of Higher Analysis*, P. Noordhoff, Ltd., Groningen, English Translation.

Kosmatka, J. B., and Friedmann, P. P., 1989, "Vibration Analysis of Composite Turbo-propellers Using a Nonlinear Beam-Type Finite Element Appraoch," *AIAA Journal*, Vol. 27, No. 11, pp. 1606–1614.

Leissa, A. W., 1969, "Vibrations of Plates," NASA SP-160.

Leissa, A. W., 1980, "Vibration of Turbine Engine Blades by Shell Analysis," *Shock and Vibration Digest*, Vol. 12, No. 11, pp. 3–10.

Leissa, A. W., 1981, "Vibrational Aspects of Rotating Turbomachinery Blades," *Applied Mechanics Reviews*, Vol. 34, No. 5, pp. 629–635.

MacBain, J. C., 1975, "Vibratory Behavior of Twisted Cantilevered Plates," *Journal of Aircraft*, Vol. 12, No. 4, pp. 343–349.

Ramamurti, V., and Kielb, R. E., 1984, "Natural Frequencies of Twisted Rotating Plates," *Journal of Sound and Vibration*, Vol. 97, No. 3, pp. 429–449.

Rao, J. S., 1973, "Natural Frequencies of Turbine Blading—a Survey," *Shock and Vibration Digest*, Vol. 5, No. 10, pp. 3–16.

Rao, J. S., 1977, "Turbine Blading Excitation and Vibration," *Shock and Vibration Digest*, Vol. 9, No. 3, pp. 15–22.

Rao, J. S., 1980, "Turbomachine Blade Vibration," *Shock and Vibration Digest*, Vol. 12, No. 2, pp. 19–26.

Shaw, D., Shen, K. Y., and Wang, J. T., 1988, "Flexural Vibration of Rotating Rectangular Plates of Variable Thickness," *Journal of Sound and Vibration*, Vol. 126, No. 3, pp. 373–385.

Subrahmanyam, K. B., and Kaza, K. R. V., 1986, "Vibration and Buckling of Rotating Pretwisted, Preconed Beams Including Coriolis Effects," ASME *Journal of Vibration, Acoustics, Stress, and Reliability in Design*, Vol. 108, pp. 140–149.

Wang, J. T., Shaw, D., and Mahrenholtz, O., 1987, "Vibration of Rotating Rectangular Plates," *Journal of Sound and Vibration*, Vol. 112, No. 3, pp. 455–468.

APPENDIX A

Constitutive Relations of Truncated Pyramid

For laminated orthotropicity, constitutive Eq. (3) is defined as

$$\begin{pmatrix}\sigma_{xx}\\ \sigma_{yy}\\ \sigma_{zz}\\ \tau_{yz}\\ \tau_{xz}\\ \tau_{xy}\end{pmatrix}^{(p)} = \begin{pmatrix}Q_{11} & Q_{12} & Q_{13} & 0 & 0 & Q_{16}\\ Q_{12} & Q_{22} & Q_{23} & 0 & 0 & Q_{26}\\ Q_{13} & Q_{23} & Q_{33} & 0 & 0 & Q_{36}\\ 0 & 0 & 0 & Q_{44} & Q_{45} & 0\\ 0 & 0 & 0 & Q_{45} & Q_{55} & 0\\ Q_{16} & Q_{26} & Q_{36} & 0 & 0 & Q_{66}\end{pmatrix}^{(p)} \begin{pmatrix}\epsilon_{xx}\\ \epsilon_{yy}\\ \epsilon_{zz}\\ \gamma_{yz}\\ \gamma_{xz}\\ \gamma_{xy}\end{pmatrix}$$

where Q_{ij} $(i, j = 1, 2, \ldots, 6)$ are defined as

$$Q_{11} = m^4\hat{Q}_{11} + n^4\hat{Q}_{22} + 2m^2n^2(\hat{Q}_{12} + 2\hat{Q}_{66})$$

$$Q_{12} = (m^4 + n^4)\hat{Q}_{12} + m^2n^2(\hat{Q}_{11} + \hat{Q}_{22} - 4\hat{Q}_{66})$$

$$Q_{22} = m^4\hat{Q}_{22} + n^4\hat{Q}_{11} + 2m^2n^2(\hat{Q}_{12} + 2\hat{Q}_{66})$$

$$Q_{16} = mn[m^2\hat{Q}_{11} - n^2\hat{Q}_{22} - (m^2 - n^2)(\hat{Q}_{12} + 2\hat{Q}_{66})]$$

$$Q_{26} = mn[-m^2\hat{Q}_{22} + n^2\hat{Q}_{11} + (m^2 - n^2)(\hat{Q}_{12} + 2\hat{Q}_{66})]$$

$$Q_{13} = m^2\hat{Q}_{13} + n^2\hat{Q}_{23}, \quad Q_{23} = m^2\hat{Q}_{23} + n^2\hat{Q}_{13}$$

$$Q_{33} = \hat{Q}_{33}, \quad Q_{36} = mn(\hat{Q}_{13} - \hat{Q}_{23})$$

$$Q_{44} = m^2\hat{Q}_{44} + n^2\hat{Q}_{55}, \quad Q_{55} = m^2\hat{Q}_{55} + n^2\hat{Q}_{44}$$

$$Q_{45} = mn(-\hat{Q}_{44} + \hat{Q}_{55})$$

$$Q_{66} = (m^2 - n^2)^2 \hat{Q}_{66} + m^2 n^2 (\hat{Q}_{11} + \hat{Q}_{22} - 2\hat{Q}_{12})$$

with $\hat{Q}_{ij}$ $(i, j = 1, 2, \ldots, 6)$ defined as

$$\hat{Q}_{11} = \frac{E_{11}}{\Delta}(1 - \nu_{23}\nu_{32}), \quad \hat{Q}_{12} = \frac{E_{11}}{\Delta}(\nu_{21} + \nu_{31}\nu_{23})$$

$$\hat{Q}_{22} = \frac{E_{22}}{\Delta}(1 - \nu_{13}\nu_{31}), \quad \hat{Q}_{13} = \frac{E_{11}}{\Delta}(\nu_{31} + \nu_{21}\nu_{32})$$

$$\hat{Q}_{33} = \frac{E_{33}}{\Delta}(1 - \nu_{12}\nu_{21}), \quad \hat{Q}_{23} = \frac{E_{22}}{\Delta}(\nu_{32} + \nu_{12}\nu_{31})$$

$$\hat{Q}_{44} = G_{23}, \quad \hat{Q}_{55} = G_{13}, \quad \hat{Q}_{66} = G_{12}$$

$$\Delta = 1 - \nu_{12}\nu_{21} - \nu_{23}\nu_{32} - \nu_{13}\nu_{31} - 2\nu_{21}\nu_{32}\nu_{13}$$

and $m = \cos(\theta)$ and $n = \sin(\theta)$ with θ as the fiber orientation angle for the pth layer.

APPENDIX B

Definition of Structural Matrices and Vectors

The following are definitions of the structural matrices and vectors used in Eq. (20).

Definition of Linear Stiffness Matrix $[K_L]$

$$[K_L] = \begin{pmatrix} K^{11} & K^{12} & K^{13} \\ & K^{22} & K^{23} \\ \text{sym.} & & K^{33} \end{pmatrix}, \text{ where}$$

$$(K^{11})_{ij} = \iiint \{Q_{11}^{(p)} u_{i,x} u_{j,x} + Q_{66}^{(p)} u_{i,y} u_{j,y} + Q_{16}^{(p)} u_{i,x} u_{j,y} + Q_{16}^{(p)} u_{i,y} u_{j,x} + Q_{55}^{(p)} u_{i,z} u_{j,z}\} dV$$

$$(K^{12})_{ij} = \iiint \{Q_{16}^{(p)} u_{i,x} v_{j,x} + Q_{26}^{(p)} u_{i,y} v_{j,y} + Q_{12}^{(p)} u_{i,x} v_{j,y} + Q_{66}^{(p)} u_{i,y} v_{j,x} + Q_{45}^{(p)} u_{i,z} v_{j,z}\} dV$$

$$(K^{13})_{ij} = \iiint \{Q_{13}^{(p)} u_{i,x} w_{j,z} + Q_{36}^{(p)} u_{i,y} w_{j,z} + Q_{55}^{(p)} u_{i,z} w_{j,x} + Q_{45}^{(p)} u_{i,z} w_{j,y}\} dV$$

$$(K^{22})_{ij} = \iiint \{Q_{66}^{(p)} v_{i,x} v_{j,x} + Q_{22}^{(p)} v_{i,y} v_{j,y} + Q_{26}^{(p)} v_{i,x} v_{j,y} + Q_{26}^{(p)} v_{i,y} v_{j,x} + Q_{44}^{(p)} v_{i,z} v_{j,z}\} dV$$

$$(K^{23})_{ij} = \iiint \{Q_{36}^{(p)} v_{i,x} w_{j,z} + Q_{23}^{(p)} v_{i,y} w_{j,z} + Q_{45}^{(p)} v_{i,z} w_{j,x} + Q_{44}^{(p)} v_{i,z} w_{j,y}\} dV$$

$$(K^{33})_{ij} = \iiint \{Q_{55}^{(p)} w_{i,x} w_{j,x} + Q_{44}^{(p)} w_{i,y} w_{j,y} + Q_{45}^{(p)} w_{i,x} w_{j,y} + Q_{45}^{(p)} w_{i,y} w_{j,x} + Q_{33}^{(p)} w_{i,z} w_{j,z}\} dV$$

Definition of Mass Matrix $[M]$

$$[M] = \begin{pmatrix} M^{11} & 0 & 0 \\ & M^{22} & 0 \\ \text{sym.} & & M^{33} \end{pmatrix}, \text{ where}$$

$$(M^{11})_{ij} = \iiint \rho^{(p)} u_i u_j dV, \quad (M^{33})_{ij} = \iiint \rho^{(p)} w_i w_j dV$$

$$(M^{22})_{ij} = \iiint \rho^{(p)} v_i v_j dV$$

Definition of Centrifugal Stiffness Matrix $[K_G]$

$$[K_\Omega] = \Omega^2 \begin{pmatrix} T^{11} & T^{12} & T^{13} \\ & T^{22} & T^{23} \\ \text{sym.} & & T^{33} \end{pmatrix}, \text{ where}$$

$$(T^{11})_{ij} = \iiint \rho^{(p)} \Omega_{11} u_i u_j dV, \quad (T^{22})_{ij} = \iiint \rho^{(p)} \Omega_{22} v_i v_j dV$$

$$(T^{12})_{ij} = \iiint \rho^{(p)} \Omega_{12} u_i v_j dV, \quad (T^{23})_{ij} = \int_V \rho^{(p)} \Omega_{23} v_i w_j dV$$

$$(T^{13})_{ij} = \iiint \rho^{(p)} \Omega_{13} u_i w_j dV, \quad (T^{33})_{ij} = \iiint \rho^{(p)} \Omega_{33} w_i w_j dV$$

Definition of Coriolis Matrix $[C]$

$$[C] = \begin{pmatrix} 0 & C^{12} & C^{13} \\ C^{21} & 0 & C^{23} \\ C^{31} & C^{32} & 0 \end{pmatrix}, \text{ where}$$

$$(C^{12})_{ij} = 2\Omega \iiint \rho^{(p)} \Omega_z u_i v_j dV, \quad (C^{21})_{ij} = -(C^{12})_{ji}$$

$$(C^{13})_{ij} = -2\Omega \iiint \rho^{(p)} \Omega_y u_i w_j dV, \quad (C^{31})_{ij} = -(C^{13})_{ji}$$

$$(C^{23})_{ij} = 2\Omega \iiint \rho^{(p)} \Omega_x y_i w_j dV, \quad (C^{32})_{ij} = -(C^{23})_{ji}$$

Definition of Centrifugal Force Vector $\{P_{CF}\}$

$\{P_{CF}\} = \{P^1, P^2, P^3\}^T$, where

$$(P^1)_i = \Omega^2 \iiint \rho^{(p)} \{(x + x_o)\Omega_{11} + (y + y_o)\Omega_{12} + (z + z_o)\Omega_{13}\} u_i dV$$

$$(P^2)_i = \Omega^2 \iiint \rho^{(p)} \{(x + x_o)\Omega_{12} + (y + y_o)\Omega_{22} + (z + z_o)\Omega_{23}\} v_i dV$$

$$(P^3)_i = \Omega^2 \iiint \rho^{(p)} \{(x + x_o)\Omega_{11} + (y + y_o)\Omega_{12} + (z + z_o)\Omega_{13}\} w_i dV$$

Definition of Nonlinear Stiffness Matrix $[K_{NL}]$

$$[K_{NL}] = \begin{pmatrix} S^{11} & 0 & 0 \\ & S^{22} & 0 \\ \text{sym.} & & S^{33} \end{pmatrix}, \text{ where}$$

$$(S^{11})_{ij} = \iiint \{[Q_{11}^{(p)} \hat{u}_{,x} + Q_{12}^{(p)} \hat{v}_{,y} + Q_{13}^{(p)} \hat{w}_{,z} + Q_{16}^{(p)} (\hat{u}_{,y} + \hat{v}_{,x})] u_{i,x} u_{j,x} + [Q_{12}^{(p)} \hat{u}_{,x} + Q_{22}^{(p)} \hat{v}_{,y} + Q_{23}^{(p)} \hat{w}_{,z} + Q_{26}^{(p)} (\hat{u}_{,y} + \hat{v}_{,x})] u_{i,y} u_{j,y} + [Q_{13}^{(p)} \hat{u}_{,x} + Q_{23}^{(p)} \hat{v}_{,y} + Q_{33}^{(p)} \hat{w}_{,z} + Q_{36}^{(p)} (\hat{u}_{,y} + \hat{v}_{,x})] u_{i,z} u_{j,z} + [Q_{44}^{(p)} (\hat{v}_{,z} + \hat{w}_{,y}) + Q_{45}^{(p)} (\hat{u}_{,z} + \hat{w}_{,x})] \times (u_{i,y} u_{j,z} + u_{i,z} u_{j,y}) + [Q_{45}^{(p)} (\hat{v}_{,z} + \hat{w}_{,y}) + Q_{55}^{(p)} (\hat{u}_{,z} + \hat{w}_{,x})] \times (u_{i,x} u_{j,z} + u_{i,z} u_{j,x}) + [Q_{16}^{(p)} \hat{u}_{,x} + Q_{26}^{(p)} \hat{v}_{,y} + Q_{36}^{(p)} \hat{w}_{,z} + Q_{66}^{(p)} (\hat{u}_{,y} + \hat{v}_{,x})] (u_{i,x} u_{j,y} + u_{i,y} u_{j,w})\} dV$$

$$(S^{22})_{ij} = \iiint \{[Q_{11}^{(p)} \hat{u}_{,x} + Q_{12}^{(p)} \hat{v}_{,y} + Q_{13}^{(p)} \hat{w}_{,z} + Q_{16}^{(p)} (\hat{u}_{,y} + \hat{v}_{,x})] v_{i,x} v_{j,x} + [Q_{12}^{(p)} \hat{u}_{,x} + Q_{22}^{(p)} \hat{v}_{,y} + Q_{23}^{(p)} \hat{w}_{,z} + Q_{26}^{(p)} (\hat{u}_{,y} + \hat{v}_{,x})] v_{i,y} v_{j,y} + [Q_{13}^{(p)} \hat{u}_{,x} + Q_{23}^{(p)} \hat{v}_{,y} + Q_{33}^{(p)} \hat{w}_{,z} + Q_{36}^{(p)} (\hat{u}_{,y} + \hat{v}_{,x})] v_{i,z} v_{j,z} + [Q_{44}^{(p)} (\hat{v}_{,z} + \hat{w}_{,y}) + Q_{45}^{(p)} (\hat{u}_{,z} + \hat{w}_{,x})] \times (v_{i,y} v_{j,z} + v_{i,z} v_{j,y}) + [Q_{45}^{(p)} (\hat{v}_{,z} + \hat{w}_{,y}) + Q_{55}^{(p)} (\hat{u}_{,z} + \hat{w}_{,x})] \times (v_{i,x} v_{j,z} + v_{i,z} v_{j,x}) + [Q_{16}^{(p)} \hat{u}_{,x} + Q_{26}^{(p)} \hat{v}_{,y} + Q_{36}^{(p)} \hat{w}_{,z} + Q_{66}^{(p)} (\hat{u}_{,y} + \hat{v}_{,x})] (v_{i,x} v_{j,y} + v_{i,y} v_{j,x})\} dV$$

$$(S^{33})_{ij} = \iiint \{[Q_{11}^{(p)} \hat{u}_{,x} + Q_{12}^{(p)} \hat{v}_{,y} + Q_{13}^{(p)} \hat{w}_{,z} + Q_{16}^{(p)} (\hat{u}_{,y} + \hat{v}_{,x})] w_{i,x} w_{j,x} + [Q_{12}^{(p)} \hat{u}_{,x} + Q_{22}^{(p)} \hat{v}_{,y} + Q_{23}^{(p)} \hat{w}_{,z} + Q_{26}^{(p)} (\hat{u}_{,y} + \hat{v}_{,x})] w_{i,y} w_{j,y} + [Q_{13}^{(p)} \hat{u}_{,x} + Q_{23}^{(p)} \hat{v}_{,y} + Q_{33}^{(p)} \hat{w}_{,z} + Q_{36}^{(p)} (\hat{u}_{,y} + \hat{v}_{,x})] w_{i,z} w_{j,z} + [Q_{44}^{(p)} (\hat{v}_{,z} + \hat{w}_{,y}) + Q_{45}^{(p)} (\hat{u}_{,z} + \hat{w}_{,x})] \times (w_{i,y} w_{j,z} + w_{i,z} w_{j,y}) + [Q_{45}^{(p)} (\hat{v}_{,z} + \hat{w}_{,y}) + Q_{55}^{(p)} (\hat{u}_{,z} + \hat{w}_{,x})] \times (w_{i,x} w_{j,z} + w_{i,z} w_{j,x}) + [Q_{16}^{(p)} \hat{u}_{,x} + Q_{26}^{(p)} \hat{v}_{,y} + Q_{36}^{(p)} \hat{w}_{,z} + Q_{66}^{(p)} (\hat{u}_{,y} + \hat{v}_{,x})] (w_{i,x} w_{j,y} + w_{i,y} w_{j,w})\} dV$$

The integration of each term in these equations is carried out by taking the following typical form:

$$J = \iiint Q_{ij}^{(p)} f(x, y, z) dV, \quad J = \iiint \rho^{(p)} f(x, y, z) dV$$

For laminated parallelepipeds, this integration can be rewritten as

$$J = \iint \sum_{p=1}^{m} \left(\int_{z_p}^{z_{p+1}} Q_{ij}^{(p)} f(x, y, z) dz \right) dA$$

$$J = \iint \sum_{p=1}^{m} \left(\int_{z_p}^{z_{p+1}} \rho^{(p)} f(x, y, z) dz \right) dA$$

where m is the total number of layers in a laminated configuration.

Y. C. Fan
Graduate Student.

M. S. Ju
Professor.

Y. G. Tsuei
Professor.

Structural Dynamics & Control Laboratory,
Department of Mechanical Engineering,
National Cheng Kung University,
Tainan, Taiwan 701

Experimental Study on Vibration of a Rotating Blade

The vibration of a rotating blade is investigated in this work. A rotor system is built and natural frequencies of the rotating blade are measured and compared with the numerical results from a finite element analysis. The experimental setup has a strain-gage-based telemetry system and a piezoelectric shaker that rotates with the rotor. The finite element model of the beam is derived based on the Timoshenko beam theory. The effects of varying rotating speeds and stagger angles on the blade natural frequencies are studied. The results indicate that the natural frequencies calculated from the finite element model and the experimental values are in good agreement. It is found that the blade natural frequencies increase with the rotating speed in a nonlinear way. The effects of the stagger angle on the measured natural frequencies are not clear.

Introduction

The vibration analysis of rotating blades is an important issue in turbomachinery research. In the past two decades, both analytical methods and experimental measurement techniques have been developed to analyze the vibration behavior of a rotating blade (Leissa, 1981). The stability of the blade vibration is affected by the centrifugal force due to the rotation, the stagger angle, the pretwist, and the taper of the blades (Mahrenholtz, 1984). In this work the effects of the rotating speed and blade stagger angle on the blade natural frequencies are studied. In general, the blade can be modeled as a cantilever beam mounted on the periphery of the rotor. Carnegie (1959) first derives the increment of strain energy of the blade and the hub due to centrifugal force and the Rayleigh's method is employed to solve the vibration problem. The relation between the shifting of fundamental frequency and the staggered angle is also explored. In another work, the finite difference method is employed to solve the blade vibration problem (Carnegie and Thomas, 1972a). The shear deformation and rotary inertia are considered and the selection of shear coefficients are also discussed (Carnegie et al., 1972b). The vibrations of pretwisted and tapered blades are also studied. Since the closed-form solution for the blade vibration problem is not obtainable, numerical analysis is employed. Thomas et al. (1973) suggest several finite element models based on Timoshenko beam theory. In this work only the geometric boundary conditions are considered. Latter, Thomas and Abbas (1975) develop a model that includes both geometric and a simple natural boundary condition.

Experimental measurement of the blade vibration is important for validating the analytical or numerical results. For noncontact measurement of blade vibration, Kulczyk and Davis (1973) develop a laser Doppler instrument. Stagardter (1977) uses mirrors that are mounted on the blade to measure the mode shapes from the deflection of a laser light. Frei (1977) uses strain gages and slip rings to measure the vibration of a rotating blade.

In this work, the experimental and finite element analysis of a rotating blade are performed. A strain-gage-based telemetry system and a piezo-electric shaker system are employed to measure the natural frequencies of a rotating blade. The results are compared with the finite element analysis. In the finite element model the blade is modeled as a Timoshenko beam and the following factors are considered, namely, the stiffness effect of the centrifugal field, the staggered angle, support elasticity, and the coupled vibrations of the disk and its blades.

Methods

Experimental Setup. The block diagram of the experimental setup is shown in Fig. 1. There are six subsystems, namely (*a*) piezo-electric shaker and slip ring to excite the blade, (*b*) telemetry system to transmit and receive strain gage signal, (*c*) servomotor system to drive the rotor to a constant speed, (*d*) velocity detector system to measure the rotating speed, (*e*) a spectrum analyzer to collect and calculate the frequency response function in real time. The steel shaft measures a diameter of 47 mm and the aluminum alloy rotor measures 229 mm in diameter and 101 mm in thickness. The blade is a flat aluminum beam measuring 253 mm in length, 25.4 mm in width, and 1.55 mm in thickness. The Young's modulus of the blade material is 70 GPa, 27 GPa for shear modulus and 2710 kg/m^3 for the density. The blade is bolted to a stand that can be indexed to different stagger angles (Fig. 2*a*). The stand is fastened to the rotor by four bolt screws. Two dynamic strain gages are attached on one side of the blade surface at 10 cm and 15 cm from the root surface, respectively. Since the telemetry system has only one channel, the strain signals are

Contributed by the International Gas Turbine Institute and presented at the 38th International Gas Turbine and Aeroengine Congress and Exposition, Cincinnati, Ohio, May 24–27, 1993. Manuscript received at ASME Headquarters March 1, 1993. Paper No. 93-GT-123. Associate Technical Editor: H. Lukas.

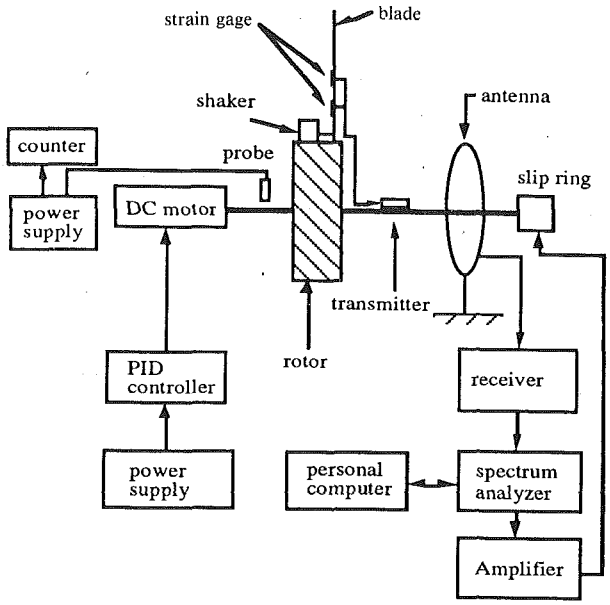

Fig. 1 Configuration of the experimental setup

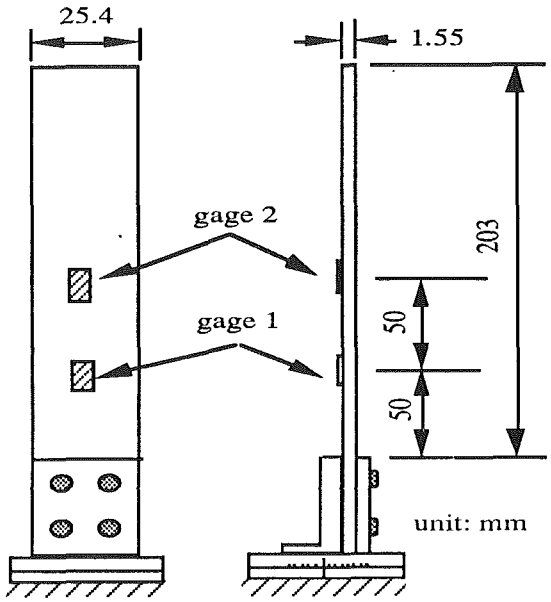

Fig. 2(*a*) Locations of strain gages and root support

measured one at a time. Attention should be paid to the connection between the shaker and the blade. Due to the lack of a slip ring channel for the load cell of the shaker, the shaking force cannot be measured directly. The exciting signal from the spectrum analyzer instead of the shaking force is used as the input for the blade system and the strain signal as the output. The shaking force is transmitted by the connector (or stinger) to the blade. The dynamic coupling between the shaker and the blade due to the stiffness of the connector may introduce errors in the measured frequency response functions. Straight and **U**-shaped connectors (Fig. 2*b*) are used in the tests when the rotor is still, the so-called static case. Random tests using the two connectors and an impulsive test with an accelerometer attached at the free end of the blade for the static case are performed to explore the dynamic coupling due to the connector. With the **U**-shaped connector and the strain gages, the first three modes of the blade in the static case are measured by using the swept sine tests with the exciting frequency around each resonant frequency found from the random test. The measured natural frequencies are compared with the analytical solutions based on Euler beam theory and the finite element results. These data are used as references for the dynamic (or rotating) cases.

In the dynamic cases, the continuous random signal is employed and two sets of experiments are performed, namely the speed-up and the slow-down tests. In the speed-up, the rotating speed is made to increase from zero rpm to 800 rpm with increments of 200 rpm. In the slow-down, the rotating speed is made to decrease from 800 rpm to zero rpm with decrements

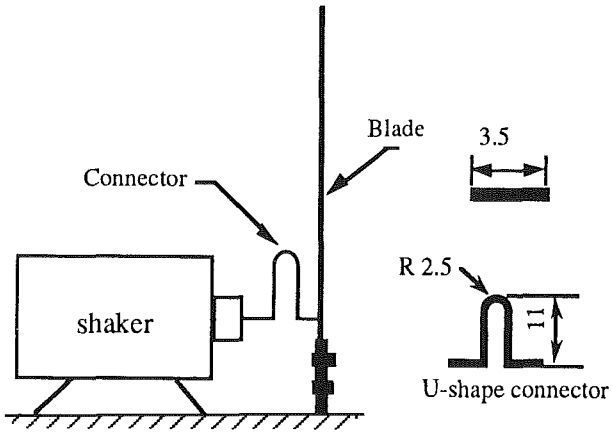

Fig. 2(*b*) Details of two connector designs

of 200 rpm. The servomotor is controlled by a PID controller to rotate at each desired speed. When the rotor speed reaches steady state, the analyzer sends a uniformly distributed signal to the shaker driver. After the transient response dies out, a total of 100 frequency response function (FRF) measurements are taken and averaged to yield an accurate estimate. The frequency band is from zero Hz to 800 Hz. The blade is tested with stagger angles ranged from zero deg to 70 deg. When the stagger angle is higher than 50 deg the highest rotor speed is limited to 600 rpm due to the aerodynamic resisting force.

Nomenclature

A = cross-sectional area of blade
b = width of the blade
E = Young's modulus
G = shear modulus
I_y, I_z = area moment of inertia of blade cross section about y and z axes
J = polar moment of inertia of the blade cross section
$\mathbf{K}(\Omega)$ = stiffness matrix of the assembled FEM model of the blade
$\mathbf{M}$ = mass matrix of the FEM model
$T(x)$ = centrifugal force field
u, v, w = elastic displacement components of a point of the blade at x, y, and z directions
θ, α, β = rotating angles of a point of the blade neutral axis about x, y, and z directions
κ = shear correction factor
ρ = density of blade material
ϕ = stagger angle
Ω = rotating speed
ω = natural frequency of blade
$(')$ = partial differentiation with respect to x
$(\dot{})$ = differentiation with respect to time t

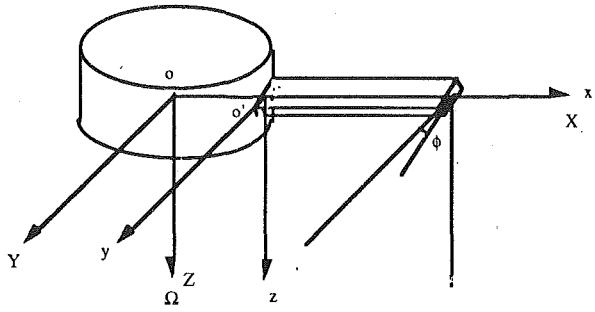

Fig. 3 Geometric model of a rotating blade

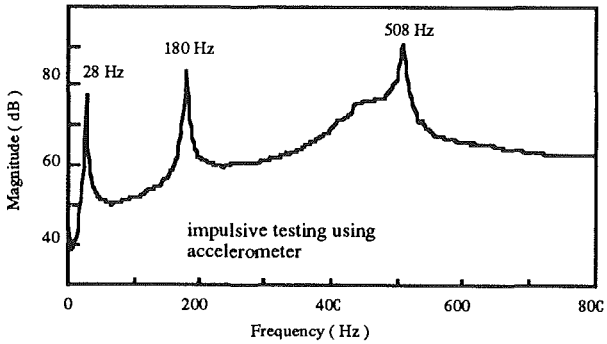

Fig. 4(*a*) Blade FRF measured by using an impulsive test with an accelerometer

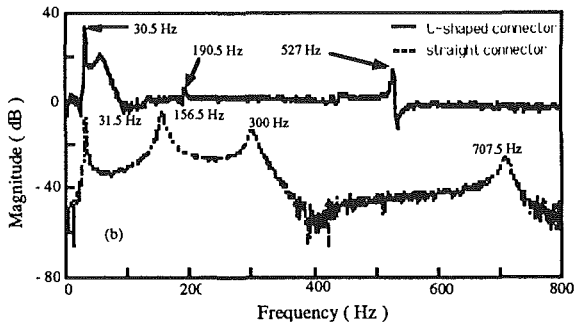

Fig. 4(*b*) Comparison of dynamic coupling effects of the two connectors

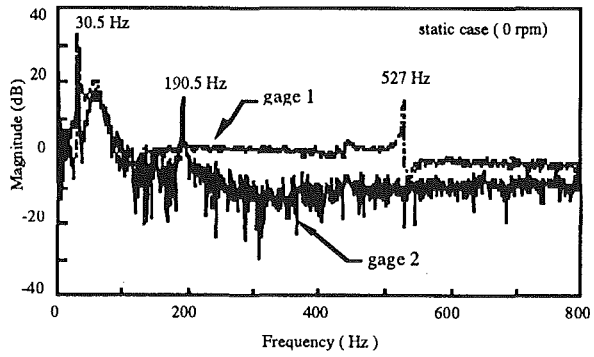

Fig. 5 FRF of the blade under static case

Modeling of the Rotating Blade. From the Timoshenko beam theory and the Hamiltonian principle the governing equations for the rotating blade can be written as (Fig. 3)

Table 1 Comparison of natural frequencies (Hz) for the static case

	first mode (error)	second mode (error)	third mode (error)
Experiment	30.71	190.10	527.16
Euler beam theory *	30.41 (0.98 %)	190.6 (0.26 %)	533.7 (1.24 %)
Euler beam theory+	30.48 (0.75 %)	191.02 (0.48 %)	534.92 (1.47 %)
Finite element method (Timoshenko beam)	30.40 (1.01 %)	190.50 (0.21 %)	533.40 (1.19 %)

* 2014 - T6 aluminum alloy + 1100 - T 14 aluminum alloy

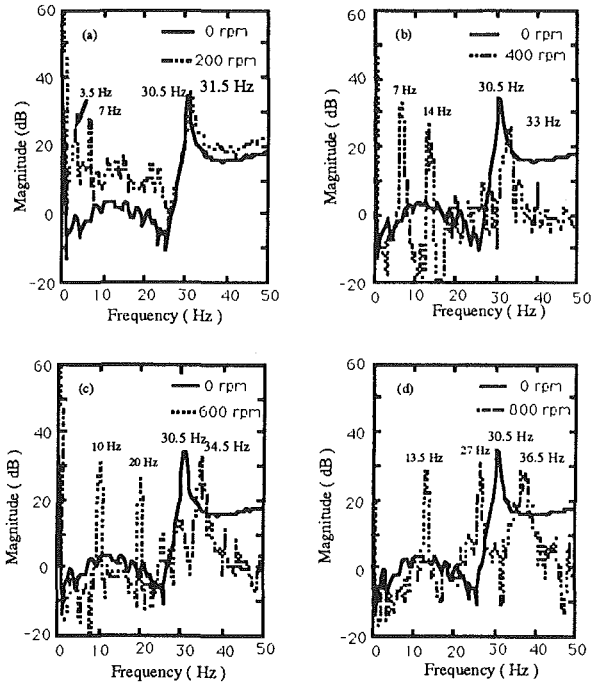

Fig. 6 Shifting of first-mode natural frequency at different rotating speeds

$$
\begin{aligned}
&EA\,u'' + \rho\Omega^2 A\,u = \rho A\,\ddot{u}\\
&\kappa GA\,(v'-\beta)' + \rho\Omega^2 Av + [T(x)v']' = \rho A\ddot{v}\\
&(w'+\alpha)' + [T(x)\,w']' = \rho A\ddot{w}\\
&EI_y\alpha'' - \kappa GA\,(\alpha + w') + \rho\Omega^2 I_y\alpha = \rho\, I_y\,\ddot{\alpha}\\
&EI_z\beta'' - \kappa GA\,\beta + \rho\Omega^2 I_z\,\beta = \rho\, I_z\,\ddot{\beta}\\
&\kappa GJ\theta'' + \rho\Omega^2 I_y\,\theta = \rho\, J\,\ddot{\theta}
\end{aligned}
\tag{1}
$$

with the following boundary conditions:

at the fixed end $x=0$

$u(0,t)=v(0,t)=w(0,t)=\alpha(0,t)=\beta(0,t)=\theta(0,t)=0,$

at the free end $x=L$

$u'(L,t)-\beta(L,t)=v'(L,t)-\alpha(L,t)=\alpha'(L,t)=0$

$\beta'(L,t)=\theta'(L,t)=0.$

where u, v, w are the displacements and θ, α, β are the rotation angles of a point on the neutral axis in the x, y, and z directions respectively. The prime denotes the partial differentiation with respect to x and the overdot denotes time derivative. Ω is the rotating speed, ρ is the density, E is the Young's modulus, A is the cross-sectional area, κ is the shear correction coefficient, G is the shear modulus, and $T(x)$ is the centrifugal force factor. Detailed derivation of the model can be found from (Fan, 1992; Chen and Chen, 1993). Since a closed-form solution for Eq. (1) does not exist, the Finite Element Method (FEM) is

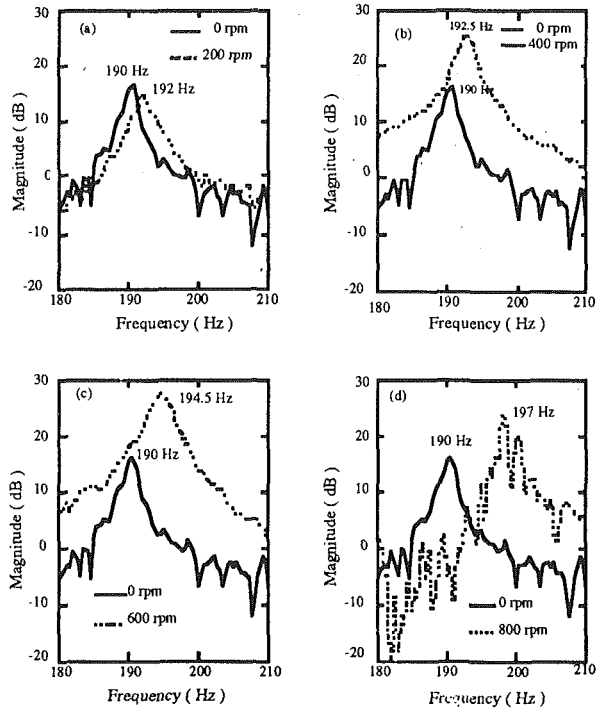

Fig. 7 Shifting of second-mode natural frequency at different rotating speeds

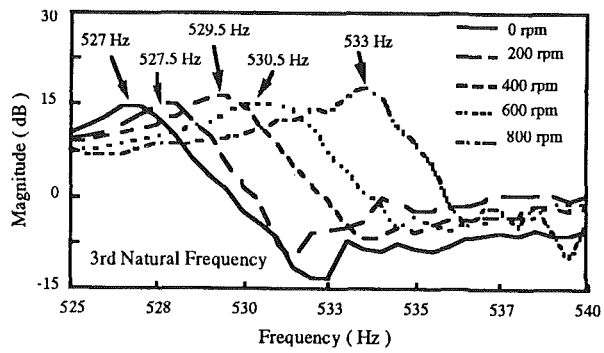

Fig. 8 Shifting of third-mode natural frequency at different rotating speeds

employed to obtain an approximate solution. The Galerkin method is employed to develop the discrete finite element model of the system. Beam elements are used and the discrete model can be written as

$$M\ddot{q}(t) + K(\Omega)q(t) = 0 \tag{2}$$

where q is the vector that consists of all the nodal variables of the system. At a constant rotating speed Ω let

$$q = \hat{q}\, e^{i\omega t} \tag{3}$$

and substituting Eq. (3) into Eq. (2) yields

$$-\omega^2 M\hat{q} + K(\Omega)\hat{q} = 0 \tag{4}$$

where ω is the natural frequency of the blade rotating at speed Ω.

Results

Static Case. The natural frequencies of the blade obtained from the impulsive testing are 28 Hz, 180 Hz, and 508 Hz (Fig. 4*a*). The FRFs measured with the two connectors show significant difference in both the number of modes and the natural

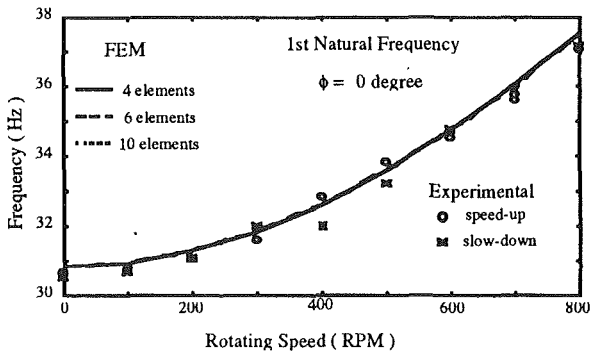

Fig. 9 Comparison of FEM and measured first-mode natural frequencies ($\phi = 0$ deg)

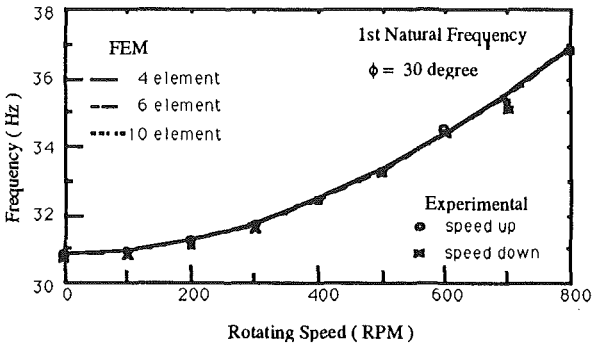

Fig. 10 Comparison of FEM and measured first-mode natural frequencies ($\phi = 30$ deg)

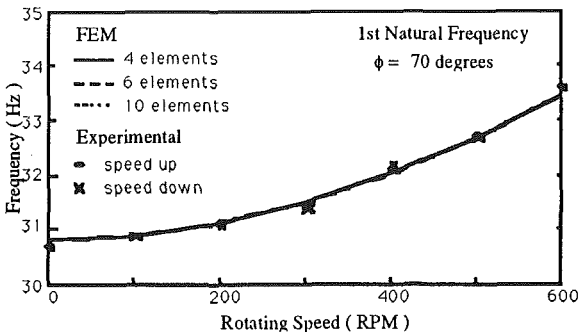

Fig. 11 Comparison of FEM and measured first-mode natural frequencies ($\phi = 70$ deg)

frequencies (Fig. 4*b*). By using the **U**-shaped connector, a set of natural frequencies close to that of the impulsive testing are obtained (30.5 Hz, 190.5 Hz, and 527 Hz). A swept-sine test reveals that the resonant peak at 60 Hz is a noise from the electronic devices. The dynamic coupling between the shaker and the blade is strong when the straight stinger is employed. Based on this finding, the **U**-shaped connector is adopted in all the dynamic cases. The FRFs measured with the two strain gages show that the natural frequencies are: 30.5 Hz for the first mode, 190.5 Hz for the second mode, and 527 Hz for the third mode (Fig. 5). Swept-sine tests around these frequencies yield resonant frequencies that agree well with the analytical and FEM results (Table 1). The relative errors are all below 1.5 percent.

Dynamic Cases. For zero stagger angle, the natural frequencies of the rotating blade increase with the rotating speed. Detailed shifts of the first three natural frequencies are shown in Figs. 6, 7, and 8. The first mode frequency is shifted by 1 Hz for the rotating speed of 200 rpm, by 2.5 Hz for 400 rpm,

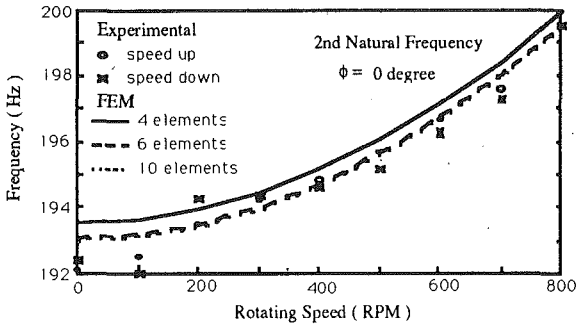

Fig. 12 Comparison of FEM and measured second-mode natural frequencies ($\phi = 0$ deg)

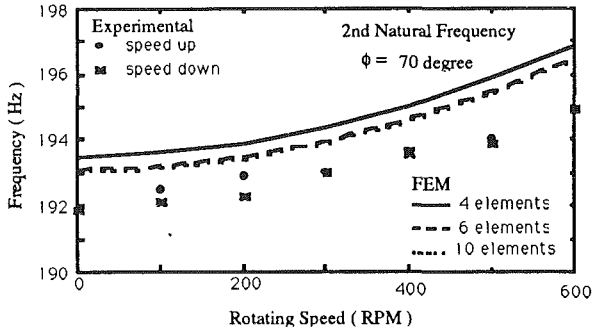

Fig. 14 Comparison of FEM and measured second-mode natural frequencies ($\phi = 70$ deg)

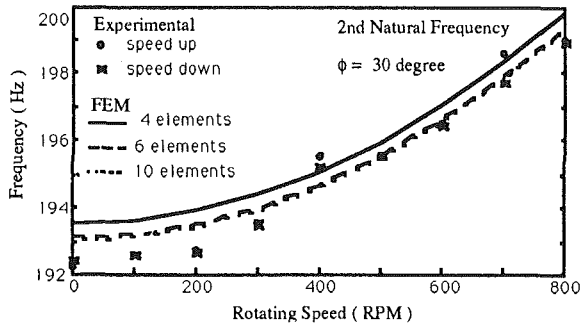

Fig. 13 Comparison of FEM and measured second-mode natural frequencies ($\phi = 30$ deg)

by 4 Hz for 600 rpm, and by 6 Hz for 800 rpm. The second mode frequency is shifted by 2 Hz for the rotating speed of 200 rpm, by 2.5 Hz for 400 rpm, by 4.5 Hz for 600 rpm, and by 7 Hz for 800 rpm. A similar trend can be observed for the third mode.

Effects of Stagger Angle. The measured and calculated natural frequencies of the first two modes for different stagger angles are compared. For zero stagger angle, the experimental results for the first mode follow the FEM results well (Fig. 9). For a stagger angle of 30 deg most of the first mode natural frequencies except at 700 rpm are higher than the FEM results (Fig. 10). For a higher stagger angle (70 deg) the deviations between the experimental and FEM results get significant (Fig. 11). The absolute errors are less than 0.6 Hz. The increase of natural frequency is a nonlinear function of the rotating speed. A similar trend can be observed for the second mode (Figs. 12, 13, and 14). The absolute errors between the measured and the calculated second mode frequencies are larger than those of the first mode. The largest absolute errors are 1.5 Hz, 1.5 Hz, and 1.8 Hz for stagger angles of 0, 30, and 70 deg, respectively. The relative errors are less than 1 percent. For the stagger angle of 70 deg most of the FEM results are underestimated.

Discussion and Conclusion

In the static test, the blade natural frequencies obtained from the impulsive testing are smaller than those obtained from the random excitations by means of the strain gage. This is due to the fact that the mass of the miniature accelerometer is comparable to that of the blade. The increase of mass reduces the natural frequencies. However, it indicates there are only three modes within the bandwidth and the dynamic coupling effect of the straight stringer is higher than the **U**-shaped connector. The good agreements of the measured natural frequencies and the analytical results by Euler beam theory and the FEM reveal that very accurate natural frequencies of the blade are obtained by the current setup. The **U**-shaped connector design can reduce the dynamic coupling between the shaker and the blade. The piezo-electric shaker has a load cell at the moving head, but due to the lack of a slip ring channel, only the exciting signal instead of the exciting force is available. By employing the **U**-shaped connector, the coupling effect is reduced and reliable FRFs of the rotating blade can be obtained. The gage numbered 2 is located near the nodal point of the third mode so no peak appears around 527 Hz.

In the dynamic tests, the increase of natural frequency for all the modes is a nonlinear function of the rotating speed. The increment of natural frequency is due to the fact that the centrifugal force field is proportional to the square of the rotating speed. Thus, the higher the rotating speed, the larger the frequency increment, although the rotor has a balance weight. Due to the facility limitation in this project it is not fully balanced. The forced vibration of the rotor does introduce forced vibration of the blade. In the band of 0-30 Hz peaks corresponding to the harmonics of the rotating speed can be observed. This reveals the importance of dynamically balancing the rotor bearing system, especially for turbomachineries with higher capacity. An unbalanced rotor may cause an excessive blade vibration. The attainable speed is limited by the stagger angle. For high stagger angle the highest rotating speed is 600 rpm. The reactive force from the air gives a limit on the rotating speed. The causes of the error between the experimental and the FEM results may be that in the FEM modeling aerodynamic force is neglected. However, in the real experiments the rotating blade is acted on by air resistance. For more accurate measurements, a vacuum chamber must be used to get rid of the aerodynamic effect, especially when much higher speed such as 4000 rpm is required. For rotating speed below 600 rpm the experimental results are in good agreement with the FEM predictions.

In summary, the natural frequencies of a rotating blade have been measured and the results are in good agreement with the FEM results. The **U**-shaped connector between the shaker and the blade has less dynamic coupling than the straight stringer. The increments of the natural frequencies vary nonlinearly to the rotating speeds. The effects of the stagger angle on the measured natural frequencies are not clear in our rotating speed range.

Acknowledgments

This research was partially supported by National Science Council and the Taiwan Power Company. The authors are grateful to Mr. H. K. Chen for helping us in the finite element analysis.

References

Carnegie, W., 1959, "Vibrations of Rotating Cantilever Blading: Theoretical Approaches to the Frequency Problem Based on Energy Method," *J. of Mechanical Engineering Science*, Vol. 1, No. 3, pp. 235–240.

Carnegie, W., and Thomas, J., 1972a, "The Coupled Bending-Bending Vi-

bration of Pre-twist Tapered Blading," ASME *Journal of Engineering for Industry*, Vol. 94, pp. 255–266.

Carnegie, W., and Thomas, J., 1972b, "The Effect of Shear Deformation and Rotary Inertia on the Lateral Frequencies of Cantilever Beams in Bending," ASME *Journal of Engineering for Industry*, Vol. 94, pp. 267–278.

Chen, L.-W., and Chen, H.-K., 1993, "The Vibrations of Pre-twisted Rotating Beams of General Orthotropy," *Journal of Sound and Vibration*, Vol. 164, No. 3.

Fan, Y. C., 1992, "Experimental Study on Vibration of Rotating Blade," M. S. Thesis, Dept. of Mechanical Engineering, National Cheng Kung University, Tainan, Taiwan.

Frei, O., 1977, "Design and Manufacturing of a Gas Turbine Rotor for Temperature and Vibration Measurement," ASME Paper No. 77-GT-54.

Kulczyk, W. K., and Davis, Q. V., 1973, "Laser Doppler Instrument for Measurement of Vibration of Moving Turbine Blades," *Proc. of IEEE, Control and Science*, Vol. 120, p. 1017.

Leissa, A. W., 1981, "Vibration Aspect of Rotating Turbomachinery Blade," *Applied Mechanics Reviews*, Vol. 34, No. 5, pp. 629–635.

Mahrenholtz, O., 1984, *Dynamic Aspect of Rotors: Stability and System Identification*, CISM, Udine, Italy.

Stagardter, H., 1977, "Optical Determination of Rotating Fan Blade Deflections," ASME *Journal of Engineering for Power*, Vol. 99, pp. 204–210.

Thomas, D. L., Wilson, J. M., and Wilson, R. R., 1973, "Timoshenko Beam Finite Elements," *Journal of Sound and Vibration*, Vol. 31, No. 3, pp. 315–330.

Thomas, D. L., and Abbas, B. A. H., 1975, "Finite Element Model for Dynamic Analysis of Timoshenko Beam," *Journal of Sound and Vibration*, Vol. 41, No. 3, pp. 291–299.

An Optimum Balance Weight Search Algorithm

J. C. Austrow
GE Aircraft Engines,
1 Neumann Way,
Cincinnati, OH 45215

A mathematical description for an optimum balance weight search algorithm for single-plane multipoint balance is presented. The algorithm uses influence coefficients, either measured or known beforehand, and measured complex vibration data to determine an optimum balance correction weight. The solution minimizes the maximum residual vibration. The algorithm allows user-defined balance weights to be analyzed and evaluated. A test case is presented showing actual results and comparison with a least-squares solution algorithm. An efficient multiplane influence coefficient calculation scheme is also presented.

Introduction

A typical balance operation for a gas turbine engine requires measurement of rotor synchronous vibration and phase for at least one sensor location and usually several speed points in the operating range. Each sensor and speed reading comprises one point (sensor-speed). This is often referred to as multi-speed-point or exact point-speed balancing [1]. The balance correction weight is usually the best compromise to reduce vibration at all sensor-speed points. The balance problem consists of finding the best correction weight with a minimum of trials. The optimization method described in this paper determines the correction weight, which minimizes the maximum residual vibration for all points.

The method relies upon influence coefficients, which relate the change in vibration vector of each sensor-speed point to a vector change in balance weight. It is assumed that these coefficients remain constant and linear throughout the balance process. This optimization method is used for single-plane balance problems.

Briefly described, the algorithm sequentially calculates the optimum balance between a pair of sensor-speed points. Then the residual vibration for each of the other sensor-speed points is determined. The maximum residual vibration is retained. This is repeated until the optimum between all pairs of points has been evaluated. The weight that provides the smallest maximum residual vibration is selected for the overall optimum.

This technique will determine the lowest maximum vibration to which the engine can be balanced. An advantage of this method is that the sensor-speed points that are the most important for the balance are identified. In combination with a graphic display, this information can provide better understanding of the problem and the best way to bias the balance. The technique is more instructive than the black box approach of least squares [2].

Contributed by the International Gas Turbine Institute and presented at the 38th International Gas Turbine and Aeroengine Congress and Exposition, Cincinnati, Ohio, May 24-27,1993. Manuscript received at ASME Headquarters March 1, 1993. Paper No. 93-GT-126. Associate Technical Editor: H. Lukas.

Mathematical Development

The general balance equation is [2, 3]:

$$V_{Rm} = V_{0m} + [\alpha]_{m \times n} W_n \tag{1}$$

where all the quantities are vectors and:

V_{Rm} is the residual synchronous vibration at sensor i and speed j. There are $i \times j = m$ sensor-speed points.

V_{0m} is the initial vibration at sensor i and speed j (without balance weights).

$[\alpha]$ is the matrix of influence coefficients, with $i \times j = m$ rows and n columns. Each coefficient relates weight at plane n to vibration at sensor i and speed j.

W_n is the balance weight applied at plane n.

For the single-plane balance problem Eq. (1) becomes:

$$V_{Rm} = V_{0m} + \alpha_m W_m \tag{2}$$

The balance weight for each sensor-speed point can be solved directly from Eq. (2) by setting V_{Rm} to zero,which is the theoretical result when the balance weight is applied. Solving for the required theoretical balance weight yields:

$$W_m = S_m V_{0m} \text{ where } S_m = \frac{-1}{\alpha_m} \tag{3}$$

In expression (3), V_{0m} is measured and S_m is calculated from measured data (see appendix). Since there are $i \times j = m$ sensor-speed points, m balance solutions of Eq. (3) are obtained. The subscript on W refers to the particular sensor-speed point for which it will theoretically produce zero residual vibration. Each of the m solution weights will balance that particular point (i.e., reduce vibration); however, it may be detrimental to the other points (i.e., increase vibration).

Optimum Solution. The following describes how the appropriate optimum balance weight can be selected from the m choices. Referring to Fig. 1, consider the best balance solution if there are only two weights to choose from, W_1 and W_2. For example, W_1 is the solution for sensor 1 at speed 1 and W_2 is the solution for sensor 2 at speed 1. Both weights are plotted in polar form. If weight W_1 is chosen, what will be the residual vibration for point 2 (sensor 2, speed 1) and vice versa? This

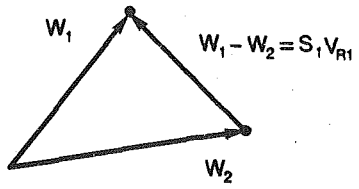

Fig. 1

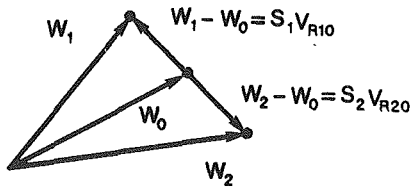

Fig. 2

can be determined by evaluating expression (2). Suppose W_2 is selected, then the residual vibration for point 1 will be

$$V_{R1} = V_{01} - W_2/S_1$$

However, $V_{01} = W_1/S_1$ so that

$$\boxed{V_{R1} = (W_1 - W_2)/S_1} \tag{4}$$

and

$$V_{R1}S_1 = W_1 - W_2 \tag{4a}$$

This result shows that when a weight other than the theoretical balance weight is applied, the residual vibration for a point is the difference between the applied weight and the theoretical weight divided by the sensitivity for the point.

We also observe that the magnitude of the residual vibration for point 1 is the distance between W_1 and W_2 divided by the sensitivity for point 1:

$$|V_{R1}| = |W_1 - W_2|/|S_1| \tag{4b}$$

Similarly for point 2

$$|V_{R2}| = |W_1 - W_2|/|S_2| \tag{4c}$$

The optimum between two weights is now defined as the weight, W_0, which produces equal and minimum magnitudes of residual vibration for both points.

It can be seen from Eq. (4) that the optimum weight will produce a residual vibration for point 1 equal to:

$$V_{R10} = (W_1 - W_0)/S_1 \tag{5a}$$

and for point 2

$$V_{R20} = (W_2 - W_0)/S_2 \tag{5b}$$

The residual vibrations V_{R10} and V_{R20} will be minimum when $W_1 - W_0$ and $W_2 - W_0$ are minimum, since S_1 and S_2 are constant.

From Fig. 2, it can be seen that $W_1 - W_0$ and $W_2 - W_0$ are minimum when they lie colinear with $W_1 - W_2$. Therefore, V_{R10} and V_{R20} are minimum when

$$|W_1 - W_2| = |W_1 - W_0| + |W_2 - W_0| \tag{6}$$

Graphically, the end point of W_0 must lie on the vector $W_1 - W_2$.

The magnitude for the residual vibration can be found. From Eqs. (5*a*) and (5*b*) we have

$$|W_1 - W_0| = |V_{R10}|\,|S_1| \tag{5c}$$

and

$$|W_2 - W_0| = |V_{R20}|\,|S_2| \tag{5d}$$

and by definition

$$|V_{R20}| = |V_{R10}| = |V_{R0}| \tag{7}$$

From substitution of Eqs.(5*c*), (5*d*), and (7) into Eq. (6), we have that the magnitude of the optimum residual is

$$|V_{R0}| = |W_1 - W_2| \frac{1}{|S_1| + |S_2|} \tag{8}$$

From Eq. (8), we obtain

$$|V_{R0}|\,|S_1| = |W_1 - W_2| \frac{|S_1|}{|S_1| + |S_2|} \tag{9}$$

from which we obtain

$$|W_1 - W_0| = |W_1 - W_2| \frac{|S_1|}{|S_1| + |S_2|} \tag{10}$$

Since $W_1 - W_0$ and $W_1 - W_2$ are colinear, Eq. (10) provides

$$W_1 - W_0 = (W_1 - W_2) \frac{|S_1|}{|S_1| + |S_2|} \tag{11}$$

This allows us to find W_0 as follows:

$$\boxed{W_0 = W_1 - (W_1 - W_2) \frac{|S_1|}{|S_1| + |S_2|}} \tag{12a}$$

or

$$\boxed{W_0 = W_2 - (W_1 - W_2) \frac{|S_2|}{|S_1| + |S_2|}} \tag{12b}$$

This result is used to calculate W_0 (the optimum weight) between every pair of theoretical weights. Then the corresponding residual vibrations are calculated using Eq. (4). The maximum residual vibration for each W_0 is retained and compared after all pairs of weights have been evaluated. Then the

Nomenclature

α_{mn} = influence coefficient vector for point m with weight at plane n
V_{Rm} = vector of residual vibration for point m
V_{0m} = vector of initial vibration for point m
W_m = balance correction weight vector for point m
W_n = balance correction weight vector for plane n
W_0 = optimum balance weight vector
W_1 = balance correction weight vector for point 1
W_2 = balance correction weight vector for point 2
S_m = sensitivity coefficient vector for point m
V_{R10} = residual vibration vector for point 1 with optimum weight installed
V_{R20} = residual vibration vector for point 2 with optimum weight installed
$|V|$ = magnitude of vector V
$|V_{R0}|$ = magnitude of residual vibration with optimum weight installed
Σ = summation sign
ΔW = weight vector difference
W' = weight installed for run 2
W'' = weight installed for run 3
ΔW_{real} = real part of weight vector difference
ΔW_{Imag} = imaginary part of weight vector difference

$$\begin{matrix} \Delta w_{11} & \Delta w_{12} & \Delta w_{13} & \cdots & \Delta w_{1m} \\ & \Delta w_{22} & \cdots & & \Delta w_{2m} \\ & & \Delta w_{33} & \cdots & \Delta w_{3m} \\ & & & & \\ \Delta w_{m1} & \Delta w_{m2} & \Delta w_{m3} & \cdots & \Delta w_{mm} \end{matrix}$$

Fig. 3(*a*) Matrix of all solution pairs

$$\begin{matrix} \Delta w_{12} & \Delta w_{13} & \cdots & \Delta w_{1m} \\ & \Delta w_{23} & & \Delta w_{2m} \\ & & \Delta w_{34} & \Delta w_{3m} \\ & & & \\ & & & \Delta w_{m-1,m} \end{matrix}$$

Fig. 3(*b*) Reduced matrix of pairs to search

W_0 that produced the lowest (minimum) maximum residual is selected as the overall optimum.

For a problem with i sensors and j speeds, $i \times j = m$ solution weights will be generated. The search for the optimum is facilitated by arranging the weight pairs in a matrix where the row and column subscripts denote the combination of solutions. For example, row 1 contains the combinations associated with the first theoretical solution weight (Fig. 3*a*).

The search process can be significantly reduced because none of the diagonal elements are evaluated (these are the individual solutions) and the combinations above and below the diagonal are identical. Therefore, only the combinations on one side of the diagonal need to be evaluated. This is shown in Fig. 3(*b*). For m solutions, the required number of W_0 calculations will be

$$\sum_{k=1}^{m-1} m-k \tag{13}$$

For example $m = 10$ ($i = 2, j = 5$) will require $+ 9 + 8 + 7 + 6 + 5 + 4 + 3 + 2 + 1 = 45$ W_0 calculations.

After all pairs have been evaluated, the pair that produces the lowest maximum residual vibration is selected as the overall optimum. The corresponding sensor-speed points are also identified. These are the "controlling" points for the balance. When the overall optimum weight is installed, the vibration response will not be higher than the maximum residual, assuming the influence coefficients are accurate.

This routine can also be used for "first-shot" calculations when the influence coefficients are known beforehand. In addition, Eq. (4) can be used to calculate the response for an arbitrary weight at the choice of the balancer. A flow diagram for the algorithm is shown in Fig. 4.

Field Test. The optimization search algorithm described here provides the basis for a computer balance program. A comparison of the results of balancing using this algorithm versus a least square algorithm is shown in Fig. 5. The data for the figure are shown in Table 1. Figure 5 compares the baseline (before balance) vibration amplitudes with the theoretical residual vibrations calculated by each of the two methods. Also shown are the actual and predicted vibration amplitudes with the installed balance weight. The data show that both solutions lead to nearly identical optimum balance solutions and results. The installed weight is slightly different because of the limitations in the weights and locations practically available, and to bias the balance more for the high speed points.

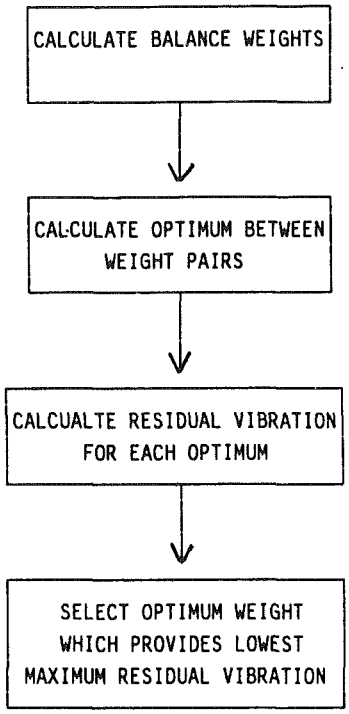

Fig. 4 Algorithm flow diagram

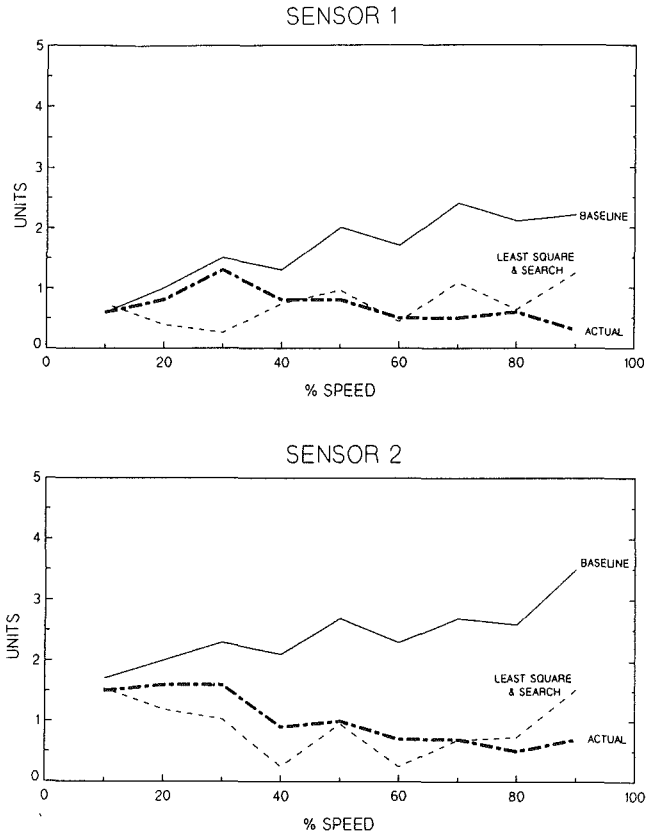

Fig. 5 1/rev vibration versus speed

Discussion/Summary

In the selection process, expression (4) shows that points that have small values of sensitivity (S_m) have greater influence on the balance than points with large sensitivity values. Points with small values are said to be "more sensitive." These points

Table 1 Comparison of vibration level (units) for baseline, least square, optimization search, and actual balance

SPEED %	SENSOR #	BASELINE 0 GM-IN 0°	LEAST SQUARES 154.3 GM-IN 270.1°	OPTIMIZATION SEARCH 154.4 GM-IN 269.5°	ACTUAL WEIGHT INSTALLED 173.4 GM-IN 269°	PREDICTED VIBRATION 173.4 GM-IN 269°
10	1	.6	.74	.75	.6	.83
20		1.0	.39	.4	.8	.47
30		1.5	.26	.25	1.3	.45
40		1.3	.74	.74	.8	.99
50		2.0	.96	.95	.8	.82
60		1.7	.44	.42	.5	.57
70		2.4	1.09	1.07	.5	1.10
80		2.1	.64	.62	.6	.50
90		2.2	1.24	1.23	.3	1.12
10	2	1.7	1.54	1.55	1.5	1.63
20		2.0	1.19	1.20	1.6	1.21
30		2.3	1.03	1.04	1.6	.97
40		2.1	.25	.25	.9	.12
50		2.7	.95	.96	1.0	.80
60		2.3	.25	.23	.7	.13
70		2.7	.69	.67	.7	.53
80		2.6	.73	.72	.5	.50
90		3.5	1.52	1.51	.7	1.28

cannot tolerate large deviations from their theoretical balance point because the effect on vibration will be large. Points with large sensitivity values are "less sensitive." These points can tolerate large differences from their theoretical balance position without large increases in vibration; therefore, they have less influence on the selection process.

This optimization process identifies the most influential points. The sensitivities of all balance points then determine the response signature. The difference between the theoretical and the applied weight can be used to evaluate the expected response and determine the acceptability and benefit of continuing the balance operation. Further balance runs may refine the sensitivity values and provide adjustment for the optimum weight.

Acknowledgment

The author wishes to thank Mr. A. Beck of SNECMA. This procedure is based upon his original insight and method.

References

1 Tessarzik, J. M., Badgley, R. H., and Anderson, W. J., "Flexible Rotor Balancing by the Exact Point-Speed Influence Coefficient Method," ASME *Journal of Engineering for Industry*, Vol. 94, 1972, p. 148.

2 Goodman, T. P., "A Least-Square Method for Computing Balance Corrections," ASME *Journal of Engineering for Industry*, Vol. 86, No. 3, 1964, p. 273.

3 Lund, J. W., and Tonnesen, J., "Analysis and Experiments on Multi-plane Balancing of a Flexible Rotor," ASME *Journal of Engineering for Industry*, Vol. 94, 1972, p. 233.

4 Wilson, D. S., Gunther, E. J., Palazzolo, A. B., Barrett, L. E., and Allaire, P. E., "Rotor-Bearing Dynamics Technology Design Guide. Part VII. Balancing," Interim Report Apr. 1976-June 1979, Report No. AFAPL-TR-78-6 Part VII, Air Force Aero Propulsion Laboratory/SPL, Air Force Systems Command, Wright-Patterson AFB, OH 45433.

APPENDIX

Influence Coefficient Calculation

The influence coefficient (sensitivity coefficient) can be calculated for a single-plane balance procedure using test data and Eq. (14)

$$\alpha_m = \Delta V_m / \Delta W = (V_m' - V_m)/(W' - W) \tag{14}$$

where α_m is the complex balance influence coefficient for sensor-speed point m.

W, W' are the weights installed for runs 1 and 2, respectively.

V_m, V_m' are the corresponding measured vibration vectors for run 1 and run 2.

To make this calculation, two "runs" are required with the balance weight changed after the first run. The weight change occurs in the same plane. The weight change must be large enough to produce a substantial vibration change.

In multiplane balancing, weights are changed in each plane, one plane at a time. Before proceeding to the next plane, the previous plane is returned to its original balance configuration. However, by utilizing a matrix solution approach, this need not be the case. Considering a two-plane problem, Eq. (1) gives for a single sensor-speed point:

$$V_{R1} = V_{01} + \alpha_{11} W_1 + \alpha_{12} W_2 \tag{15}$$

Using superscripts to denote two additional runs with different weights in each plane, we have

$$V_{R1}' = V_{01} + \alpha_{11} W_1' + \alpha_{12} W_2' \tag{16a}$$

$$V_{R1}'' = V_{01} + \alpha_{11} W_1'' + \alpha_{12} W_2'' \tag{16b}$$

Subtracting Eq. (15) from Eqs. (16a) and (16b) yields

$$V_{R1}' - V_{R1} = \alpha_{11}(W_1' - W_1) + \alpha_{12}(W_2' - W_2) \tag{17a}$$

$$V_{R1}'' - V_{R1} = \alpha_{11}(W_1'' - W_1) + \alpha_{12}(W_2'' - W_2) \tag{17b}$$

Putting this set of equations in matrix form, we have

$$\{\Delta V\} = [\Delta W] \quad \{\alpha\} \tag{18}$$

Since $\{\Delta V\}$ are measured and $[\Delta W]$ are known, the influence coefficients can be evaluated for each sensor-speed point, using standard equation solvers and noting that the quantities are complex.

Expanding Eq. (18) into real and imaginary form, we have

$$\begin{Bmatrix} \Delta V_{\text{real}} \\ \hline \Delta V_{\text{Imag}} \end{Bmatrix} = \left| \begin{array}{c|c} \Delta W_{\text{real}} & -\Delta W_{\text{Imag}} \\ \hline \Delta W_{\text{Imag}} & \Delta W_{\text{real}} \end{array} \right| \begin{Bmatrix} \alpha_{\text{real}} \\ \hline \alpha_{\text{Imag}} \end{Bmatrix} \tag{19}$$

For an n-plane balance, at least $n + 1$ runs are required. A weight change can be made in each plane for all runs. If only one plane is changed for each run, then the proceeding weight need not be changed back before the next plane is changed.

Dynamic Analysis of Squeeze Film Damper Supported Rotors Using Equivalent Linearization

A. El-Shafei
Department of Mechanical Design and Production, Cairo University, Giza, Egypt

R. V. Eranki
Alumax Mill Products, Inc., Morris, IL 60450

The technique of equivalent linearization is presented in this paper as a powerful technique to perform nonlinear dynamic analysis of squeeze film damper (SFD) supported rotors using linear rotor-dynamic methods. Historically, it is customary to design SFDs for rotor-dynamic analysis by assuming circular-centered orbits, which is convenient in making the nonlinear damper coefficients time independent and thus can be used in an iterative approach to determine the rotor-dynamic characteristics. However, the general synchronous orbit is elliptic in nature due to possible asymmetry in the rotor support. This renders the nonlinear damper coefficients time dependent, which would require extensive numerical computation using numerical integration to determine the rotor dynamic characteristics. Alternatively, it is shown that the equivalent linearization, which is based on a least-squares approach, can be used to obtain time-independent damper coefficients for SFDs executing eccentric elliptic orbits, which are nonlinear in the orbit parameters. The resulting equivalent linear forces are then used in an iterative procedure to obtain the unbalance response of a rigid rotor–SFD system. Huge savings over numerical integration are reported for this simple rotor. The technique can be extended to be used in conjunction with currently available linear rotor-dynamic programs to determine the rotor-dynamic characteristics through iteration. It is expected that for multirotor multibearing systems this technique will result in even more economical computation.

Introduction

In the design and analysis of high-performance rotor systems, usually linear techniques are employed both to gain insight into the behavior of the rotor system and to use the power of these well-developed linear techniques. This is done although it is well recognized that nonlinear devices, such as squeeze film dampers (SFDs) that are an integral part of the rotor system, can significantly alter the behavior of the rotor system from that predicted by linear techniques. To compensate for this, usually a nonlinear simulation is performed at the end of the design stage to check the predictions of linear theory.

In an effort to use the well-developed, powerful, available, and designer-friendly linear rotor-dynamics programs to perform nonlinear analysis, it is proposed in this paper to use the technique to equivalent linearization for SFD supported rotors. The purpose of using equivalent linearization is to overcome the difficulty in studying the dynamics of SFD supported rotors posed by the nonlinearity of SFDs. Historically, two alternative approaches have been used in the literature to handle the nonlinearity. One approach is to use numerical integration of the nonlinear equations of motion. This approach was taken, among others, by Gunter et al. (1977) and Taylor and Kumar (1980). In fact, Taylor and Kumar (1980) investigated the numerical integration techniques used to determine the response of a rigid rotor in SFDs. They were able to demonstrate the following drawbacks for numerical integration: (*a*) Only stable solutions could be found, (*b*) false convergence, (*c*) in regions of multivalued response, finding all possible solutions involves tedious trial and error, and (*d*) the particular algorithm and convergence criteria used in the iterative approach determine the accuracy and credibility of the results. Also if these algorithms are used for multirotor multibearing systems, they will become very time consuming.

The other approach to determine the nonlinear effects of SFDs is to assume a circular-centered orbit, for symmetric rotors, which is convenient in making the nonlinear damping coefficients time independent. Mohan and Hahn (1974) used this assumption to reduce the nonliner differential equations of motion of a simple Jeffcott rotor to nonlinear algebraic equations. Several of the analyses of SFDs (e.g., Taylor and Kumar, 1983; El-Shafei, 1990, 1991) relied on the assumption of circular-centered orbit. For multirotor, multibearing systems, such a technique would result in an inhibitively large number of nonlinear algebraic equations. A modification of this technique proposed by Greenhill and Nelson (1982) is to assume a circular-centered orbit and use an iterative scheme to determine the eccentricity of the journal in the damper. This allows linear rotor-dynamic analysis techniques to be used in conjunction with the iterative scheme to determine the non-

Contributed by the International Gas Turbine Institute and presented at the 38th International Gas Turbine and Aeroengine Congress and Exposition, Cincinnati, Ohio, May 24–27, 1993. Manuscript received at ASME headquarters February 12, 1993. Paper No. 93-GT-30. Associate Technical Editor: H. Lukas.

linear response of multirotor, multibearing systems with a huge saving in computer time. However, this technique is still limited to symmetric rotor systems.

For rotors mounted on unsymmetric supports, the general synchronous orbit of the journal in the SFD is elliptic in nature. This renders the nonlinear damping coefficients time dependent, which would require extensive numerical computation, using numerical integration, to determine the rotor-dynamic characteristics. Also, the same problem appears for eccentric orbits, where the nonlinear damping coefficients are also time dependent. Moreover, subharmonic motion may be possible, particularly with SFDs executing eccentric orbits.

An alternate approach for the analysis of SFDs was proposed by Hahn (1985), which uses an equivalent linearization technique based on energy considerations. Burrows et al. (1986) suggested a method using least-square-estimation, but this requires numerical integration. Chen and Liu (1986) showed that the equivalent linearization technique performed by either a Fourier expansion approach or the least-squares approach would result in the same equivalent linear forces. Crandall and Yeh (1986) indicated that the equivalent linearization technique can be used to determine the steady-state response of multirotor systems incorporating squeeze film dampers. El-Shafei and Eranki (1992) obtained equivalent linear dynamic force coefficients for SFDs executing centered elliptic orbits using an algorithm based on a least-squares approach.

In this paper, the equivalent linearization technique is presented as a general and powerful technique to be used to obtain the nonlinear response of SFD supported rotors, using linear rotor-dynamic techniques. Although it is possible to use this technique for any general orbit, we limit ourselves, as a first step, to study the most general synchronous orbits. Thus the equivalent linearization technique is used to determine time-independent damping coefficients for squeeze film dampers executing synchronous eccentric elliptic orbits, which are nonlinear in the orbit parameters (Eranki, 1990). The equivalent linearization is based on the minimization of the square of the error between the actual and equivalent linear forces in the damper. The resulting equivalent linear forces are then used in an iterative approach, similar to that used with the circular orbit, to determine the unbalance response of a simple rotor system. Thus equivalent linearization allows the nonlinear nature of the problem to be retained, while maintaining the luxury of using the currently available linear techniques of rotor dynamics, and with still a huge saving in computer time.

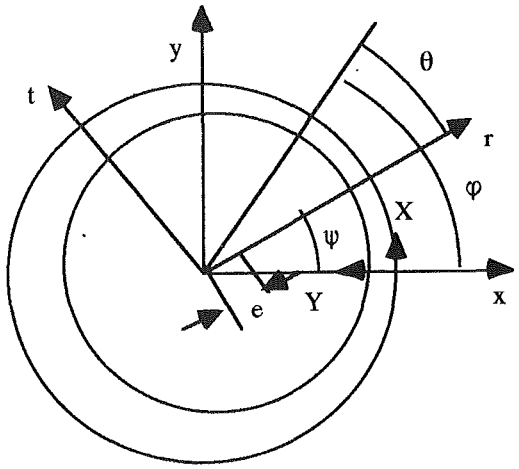

Fig. 1 Coordinate frames

Damping Forces in SFDs

Figure 1 shows a SFD, and the coordinate systems used. The film thickness h at any location is given by

$$h = c - e\cos\theta \tag{1}$$

Nomenclature

B = nondimensional bearing parameter $= \mu RL^3/c^3 m\omega_n$ (for short damper); $\mu R^3 L/c^3 m\omega_n$ (for long damper)

B_{xx}, B_{yy} = equivalent linear damping coefficients, Ns/m

B^*_{xx}, B^*_{yy} = nondimensional equivalent linear damping coefficients

c = radial clearance in the damper, m

C_{ij} = damping coefficients in SFDs, Ns/m

C^*_{ij} = nondimensional damping coefficients in SFDs

e = eccentricity of the journal, m

F_r = radial damping force in the damper, N

F_t = tangential damping force in the damper, N

F_x = damping force in the x direction, N

F_y = damping force in the y direction, N

F_{xe} = eqiuvalent damper forces in the x direction, N

F_{ye} = equivalent damper forces in the y direction, N

g = acceleration due to gravity, m/s^2

h = film thickness, m

K_x = stiffness of the retainer spring in x direction, N/m

K_y = stiffness of the retainer spring in y direction, N/m

K^*_x = nondimensional retainer spring stiffness $= K_x/m\omega_n^2$

K^*_y = nondimensional retainer spring stiffness $= k_y/m\omega_n^2$

K_{xx}, K_{yy} = equivalent linear stiffness coefficients, N/m

K^*_{xx}, K^*_{yy} = nondimensional equivalent linear stiffness coefficients

L = length of the damper, m

m = half the rotor disk mass, kg

m_{xx}, m_{yy} = equivalent linear mass coefficients, kg

m^*_{xx}, m^*_{yy} = nondimensional equivalent linear mass coefficients

p = pressure of the fluid in the damper, N/m^2

R = radius of the damper, m

t = time, s

u = rotor unbalance, m

U = nondimensional unbalance $= u/c$

W = nondimensional rotor disk weight $= g/c\omega_n^2$

X = nondimensional response in the x direction $= x/c$

Y = nondimensional response in the y direction $= y/c$

ϵ = eccentricity ratio $= e/c$

θ_1, θ_2 = extent of the fluid film in the damper, rad

μ = dynamic viscosity of the fluid, Ns/m^2

τ = nondimensional time $= \omega_n t$

ω_n = characteristic frequency, rad/s

Ω = rotor spin speed, rad/s

Ω^* = nondimensional rotor spin speed $= \Omega/\omega_n$

$( )'$ = denotes differentiation with respect to t

$( )'$ = denotes differentiation with respect to τ

Reference frames

(x, y, z) = stationary frame

(r, t, z) = whirling frame

Table 1 Damping coefficients

	Short Dampers	Long Dampers
C_{rr}^*	I_3^{02}	$\frac{6}{\varepsilon}\left(I_2^{01} - \int_{\theta_1}^{\theta_2} \frac{\cos\theta}{(1+\varepsilon)^2}\, d\theta\right)$
C_{rt}^*	I_3^{11}	$\frac{12}{(2+\varepsilon^2)}\left[2 I_2^{11} - \varepsilon I_2^{12}\right]$
C_{tr}^*	I_3^{11}	$\frac{6}{\varepsilon}\left(I_2^{10} - \int_{\theta_1}^{\theta_2} \frac{\sin\theta}{(1+\varepsilon)^2}\, d\theta\right)$
C_{tt}^*	I_3^{20}	$\frac{12}{(2+\varepsilon^2)}\left[2 I_2^{20} - \varepsilon I_2^{21}\right]$

where c is the clearance, e is the eccentricity of the journal, and θ is measured from the positive r axis of the whirling coordinate system (r, t, z). The z axis is perpendicular to the plane of the paper. Also shown in Fig. 1 are the stationary coordinate system (x, y, z) and the angle φ, which is measured from the positive x axis, and $\theta = \varphi - \psi$.

The damping forces in SFDs are obtained by the solution of Reynolds' equation, which for a SFD, reduces to

$$\frac{1}{R}\frac{\partial}{\partial\varphi}\left(\frac{h^3}{\mu R}\frac{\partial p}{\partial\varphi}\right) + \frac{\partial}{\partial z}\left(\frac{h^3}{\mu}\frac{\partial p}{\partial z}\right) = -12\,(e\dot{\psi}\sin\theta + \dot{e}\cos\theta) \quad (2)$$

wehre μ is the viscosity of the oil, R is the radius of the damper, p is the pressure, and $\dot{e}$ and $e\dot{\psi}$ are the radial and tangential velocities of the journal in the damper, respectively.

For dampers that are short in the axial direction, the short bearing approximation to Reynolds' equation applies, such that for a short damper $\partial p/\partial z >> \partial p/\partial\varphi$ and Reynolds' equation can be solved using the boundary conditions $p = 0$ at $z = \pm L/2$ where L is the length of the damper, to get for the pressure

$$p = \frac{6\mu}{h^3}\left(\frac{L^2}{4} - z^2\right)(e\dot{\psi}\sin\theta + \dot{e}\cos\theta) \quad (3)$$

On the other hand for a long damper $\partial p/\partial\varphi >> \partial p/\partial z$ and Reynolds' equation can be solved using the boundary conditions $p = 0$ at $\theta = \pm\pi$, to get for the pressure

$$p = \left(\frac{6\mu R^2}{c^3}\right)\left(\left[\frac{1}{\epsilon(1-\epsilon\cos\theta)^2} - \frac{1}{\epsilon(1+\epsilon)^2}\right]\dot{e} + \left[\frac{2\sin\theta(2-\epsilon\cos\theta)}{(2+\epsilon^2)(1-\epsilon\cos\theta)^2}\right]e\dot{\psi}\right) \quad (4)$$

Integrating the pressure obtained by the solution of Reynolds' equation, the damping forces in SFDs are obtained, which take the form

$$\begin{bmatrix} F_r \\ F_t \end{bmatrix} = \begin{bmatrix} -C_{rr} & C_{rf} \\ -C_{tr} & C_{tt} \end{bmatrix}\begin{bmatrix} \dot{e} \\ e\dot{\psi} \end{bmatrix} \quad (5)$$

where F_r and F_t are the radial and tangential damping forces, respectively. The damping coefficients C_{rr}, C_{tt}, C_{tr} and C_{rt} are in general nonlinear functions of the position and velocity of the journal in the damper, and can be written as functions of the journal-bearing integral

$$I_n^{lm} = \int_{\theta_1}^{\theta_2} \frac{\sin^l\theta\cos^m\theta}{(1-\epsilon\cos\theta)^n}\, d\theta \quad (6)$$

A table of the journal-bearing integral is given by Booker (1965). Table 1 lists the damping coefficients for both the short and long dampers as a function of the journal bearing integral. Note that for the short damper $C_{ij} = \mu R L^3/c^3 C_{ij}^*$, while for the long damper $C_{ij} = \mu R^3 L/c^3 C_{ij}^*$, where the indices i and j take the values r and t. For an uncavitated damper, the film extends for 2π rad, and the limits of the integral (6) are $\theta_1 = 0$ and $\theta_2 = 2\pi$. However, if cavitation occurs, then, using the Gumbel conditions, the integration (6) is only performed in the region of positive pressure, since the fluid cannot sustain tensile stresses. Thus, the limits of integration are obtained from Eqs. (3) and (4), for the short and long dampers, respectively. For a nearly circular-centered orbit $\theta_1 = 0$ and $\theta_2 = \pi$ for a counterclockwise whirl. Figure 2 shows a plot of the damping coefficients C_{rr}, C_{tt}, C_{tr}, and C_{rt} versus the eccentricity ratio ϵ for a cavitated damper executing a nearly circular-centered whirl. It can be seen from Fig. 2 that the damping coefficients for the short and long bearing approximations are nonlinear functions of the position of the journal in the damper.

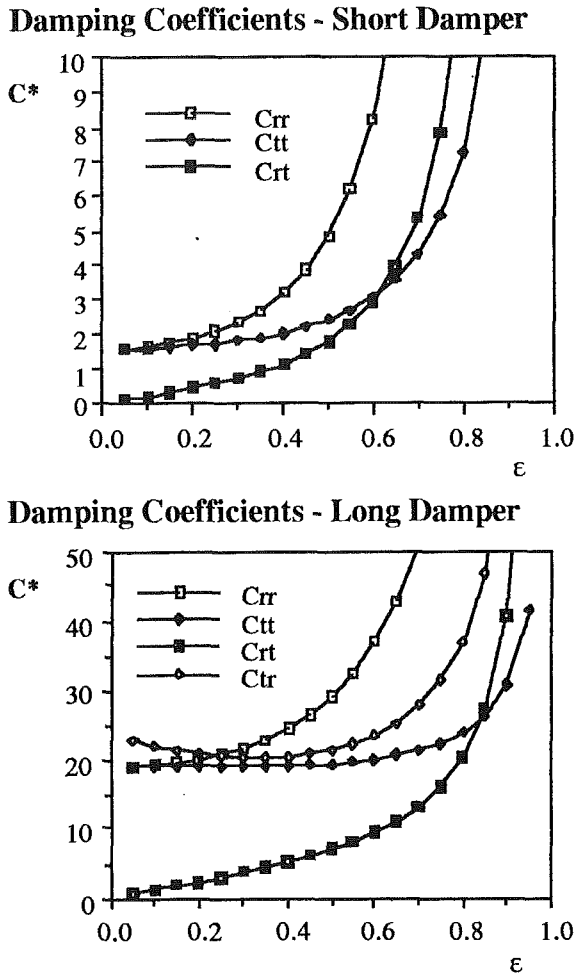

Fig. 2 Nondimensional damping coefficients versus ϵ

Transforming to the stationary coordinate system, the damping forces (5) become

$$\begin{bmatrix} F_x \\ F_y \end{bmatrix} = \begin{bmatrix} -C_{xx} & -C_{xy} \\ -C_{yx} & -C_{yy} \end{bmatrix}\begin{bmatrix} \dot{x} \\ \dot{y} \end{bmatrix} \quad (7)$$

where

$$-C_{xx} = [-C_{rr}\cos^2\psi + C_{rt}\sin\psi\cos\psi + c_{tr}\sin\psi\cos\psi - C_{tt}\sin^2\psi] \quad (8)$$

$$-C_{xy} = [-C_{rr}\sin\psi\cos\psi - C_{rt}\cos^2\psi + C_{tr}\sin^2\psi + C_{tt}\sin\psi\cos\psi] \quad (9)$$

$$-C_{yx} = [-C_{rr}\sin\psi\cos\psi + C_{rt}\sin^2\psi - C_{tr}\cos^2\psi + C_{tt}\sin\psi\cos\psi] \quad (10)$$

$$-C_{yy} = [-C_{rr}\sin^2\psi - C_{rt}\sin\psi\cos\psi - C_{tr}\sin\psi\cos\psi - C_{tt}\cos^2\psi] \quad (11)$$

Equivalent Linearization

The purpose of the equivalent linearization is to represent the nonlinear time-dependent damping coefficients by equivalent linear coefficients that are nonlinearly dependent on the parameters of the assumed motion. In general, the motion is assumed to be

$$x_j = x_{oj} + \sum_k x_{kj}\cos(\Omega_k t + \delta_k) \quad (12)$$

where x_j are the independent coordinates ($j=1, 2$), x_{oj} represents the static component of the assumed motion, x_{kj} represents the amplitude of the kth harmonic in the assumed motion, and δ_k represents the phase of the kth harmonic.

In the equivalent linearization, one seeks to represent the forces in the damper by

$$F_i = F_{oi} + \sum_j K_{ij}x_j + \sum_j B_{ij}\dot{x}_j + \sum_j m_{ij}\ddot{x}_j \quad (13)$$

where F_i are the forces in the damper ($i=1, 2$), F_{oi} is the equivalent linear static force and K_{ij}, B_{ij}, and m_{ij} are the equivalent linear stiffness, damping, and inertia coefficients, respectively.These equivalent linear coefficients are dependent on the parameters of the assumed motion x_{oj}, x_{kj}, and δ_k. It can be shown (Chen and Liu, 1986; Eranki, 1990) that the number of independent equivalent linear coefficients is not arbitrary. Actually, the number of stiffness, damping, and inertia coefficients (the dynamic coefficients) is equal to twice the number of harmonics in the assumed motion, for each degree of freedom, otherwise the coefficient matrix used to determine the equivalent linear coefficients will be of reduced rank and thus uninvertible (Chen and Liu, 1986; Eranki, 1990). This can be interpreted that each harmonic assumed in the motion has two motion parameters: amplitude x_{kj} and phase δ_k and thus to these two motion parameters there can be defined two equivalent linear dynamic coefficients. Moreover, it can be shown, that if a static motion parameter x_{oj} is assumed and exists, then there has to be a corresponding static force component F_{oi} (Eranki, 1990).

The equivalent linear coefficients can be determined by several methods. Hahn (1985) used an energy method to determine the equivalent linear coefficients, but the extension of his technique is not straightforward. The harmonic balance method and the least-squares approach were shown to give exactly the same results by Chen and Liu (1986). In this paper we adopt the least-squares approach, for convenience, to determine the equivalent linear coefficient of a SFD. However, the analysis presented herein, as a first step, is limited only to synchronous motion, since it is the most important motion in a SFD.

To apply the least-squares approach to determine the SFD equivalent linear coefficients, synchronous motion is first assumed. Thus the motions in the x and y directions are assumed to be

$$x = x_o + x_c\cos(\Omega t - \delta_1) \quad (14)$$

$$y = y_o + y_s\sin(\Omega t + \delta_2) \quad (15)$$

According to the previous discussion, there must be two static equivalent linear force components (one in the x direction and one in the y direction) and four dynamic equivalent linear coefficients. However, to illustrate the points made, we will assume redundant dynamic coefficients, for example six coefficients. The question that poses itself then is how can one choose these six equivalent linear coefficients from the possible twelve linear stiffness, damping, and inertia coefficients? At this point, one notes that nonsymmetric stiffness, damping, or inertia matrices unnecessarily complicate the dynamic analysis of the rotor, and thus to guarantee symmetry diagonal matrices are assumed. Thus we seek to model the equivalent linear forces to be

$$F_{xe} = (-m_{xx}\ddot{x} - B_{xx}\dot{x} - K_{xx}x - F_{ox}) \quad (16)$$

$$F_{ye} = (-m_{yy}\ddot{y} - B_{yy}\dot{y} - K_{yy}y - F_{oy}) \quad (17)$$

In order to obtain the equivalent linear coefficients using the least-squares error approach, the squares of the error integrals I_x and I_y are first formulated, such that

$$I_x = \int_0^{2\pi} (F_x - F_{xe})^2 d\Omega t \quad (18)$$

$$I_y = \int_0^{2\pi} (F_y - F_{ye})^2 d\Omega t \quad (19)$$

Simply stated, the square of the error integrals represents the square of the difference between the actual and equivalent linear forces during one complete orbit of the journal in the damper. It is then required that the square of the error integrals be minimized by the choice of the equivalent linear coefficients. Thus it is required that

$$\frac{\partial I_x}{\partial m_{xx}} = 0; \quad \frac{\partial I_x}{\partial B_{xx}} = 0; \quad \frac{\partial I_x}{\partial K_{xx}} = 0; \quad \frac{\partial I_x}{\partial F_{ox}} = 0$$

$$\frac{\partial I_y}{\partial m_{yy}} = 0; \quad \frac{\partial I_y}{\partial B_{yy}} = 0; \quad \frac{\partial I_y}{\partial K_{yy}} = 0; \quad \frac{\partial I_y}{\partial F_{oy}} = 0 \quad (20)$$

These eight conditions can be used to determine the eight (six dynamic plus two static) equivalent linear coefficients. These coefficients, when arranged in matrix form, using the assumed motion (14) and (15), become

$$\begin{bmatrix} \pi\Omega^4 x_c^2 & 0 & -\pi\Omega^2 x_c^2 & 0 \\ 0 & \pi\Omega^2 x_c^2 & 0 & 0 \\ -\pi\Omega^2 x_c^2 & 0 & \pi(2x_o^2 + x_c^2) & 2\pi x_o \\ 0 & 0 & 2\pi x_o & 2\pi \end{bmatrix} \begin{bmatrix} m_{xx} \\ B_{xx} \\ K_{xx} \\ F_{ox} \end{bmatrix} = \begin{bmatrix} F_{1x} \\ F_{2x} \\ F_{3x} \\ F_{4x}s \end{bmatrix} \quad (21)$$

where

$$F_{1x} = \int_0^{2\pi} (-F_x)\ddot{x}d\Omega t; \quad F_{2x} = \int_0^{2\pi} (-F_x)\dot{x}d\Omega t$$

$$F_{3x} = \int_0^{2\pi} (-F_x)x d\Omega t; \quad F_{4x} = \int_0^{2\pi} (-F_x)d\Omega t$$

and similarly in the y direction. However, because the determinant of the coefficient matrix in Eq. (21) is zero, the coefficient matrix for the x-equivalent linear coefficients is not invertible, and similarly for the y-equivalent linear coefficients. This implies that the system of equations is not solvable. Hence, as discussed earlier, one cannot have eight equivalent linear coefficients for a synchronous motion.

The question that still remains is whether the possible choices of the dynamic equivalent linear coefficients make a difference in the use of the equivalent linearization algorithm. Actually, at this point, there are two possible choices of equivalent linear coefficients; either to use damping and stiffness coefficients in addition to the static force (Model I), or to use inertia and damping coefficients in addition to the static force (Model II).

Model I. This model describes the system with the six equivalent linear coefficients B_{xx}, K_{xx}, F_{ox}, B_{yy}, K_{yy}, and F_{oy}.

Using this choice of equivalent linear coefficients, the matrix Eq. (21) can be solved to obtain the equivalent linear coefficients as

$$B_{xx}=\frac{F_{2x}}{\pi\Omega^2 x_c^2};\quad K_{xx}=\frac{(F_{3x}-x_oF_{4x})}{\pi x_c^2};\quad F_{ox}=\left(\frac{F_{4x}}{2\pi}-x_oK_{xx}\right)$$

and (22)

$$B_{yy}=\frac{F_{2y}}{\pi\Omega^2 y_s^2};\quad K_{yy}=\frac{(F_{3y}-y_oF_{4y})}{\pi y_s^2};\quad F_{oy}=\left(\frac{F_{4y}}{2\pi}-y_oK_{yy}\right)$$

Model II. This model describes the system with the six equivalent linear coefficients m_{xx}, B_{xx}, F_{ox}, m_{yy}, B_{yy}, and F_{oy}. Using this choice of equivalent linear coefficients, the matrix Eq. (21) can be solved to obtain the equivalent linear coefficients as

$$m_{xx}=\frac{F_{1x}}{\pi\Omega^4 x_c^2};\quad B_{xx}=\frac{F_{2x}}{\pi\Omega^2 x_c^2};\quad F_{ox}=\frac{F_{4x}}{2\pi}$$

and (23)

$$m_{yy}=\frac{F_{1y}}{\pi\Omega^4 y_s^2};\quad B_{yy}=\frac{F_{2y}}{\pi\Omega^2 y_s^2};\quad F_{oy}=\frac{F_{4y}}{2\pi}$$

In the following section, these two possible models of equivalent linearization will be used to obtain the unbalance response of a rigid rotor supported on SFDs. One of the main concerns will be to find the differences between these two possible equivalent linear models.

Rigid Rotor Incorporating SFDs

Figure 3 shows a rigid rotor of mass $2m$ mounted on two identical ball bearings, each of which is surrounded by an oil film constituting two identical squeeze film dampers. The outer race of each ball bearing, which is assumed rigid and massless, is constrained from rotating by a retainer spring of stiffnesses K_x and K_y in the x and y directions. This artificial introduction of asymmetry in the retainer spring allows the introduction of synchronous elliptic orbits in the rotor unbalance response.

The differential equations governing the rotor of Fig. 3, under unbalance excitation and gravity loading, are given by

$$\begin{bmatrix} m & 0 \\ 0 & m \end{bmatrix}\begin{bmatrix} \ddot{x} \\ \ddot{y} \end{bmatrix}+\begin{bmatrix} C_{xx} & C_{xy} \\ C_{yx} & C_{yy} \end{bmatrix}\begin{bmatrix} \dot{x} \\ \dot{y} \end{bmatrix}+\begin{bmatrix} K_x & 0 \\ 0 & K_y \end{bmatrix}\begin{bmatrix} x \\ y \end{bmatrix}=\begin{bmatrix} mu\Omega^2\cos\Omega t \\ mu\Omega^2\sin\Omega t-mg \end{bmatrix} \quad (24)$$

where C_{xx}, C_{xy}, C_{yx}, and C_{yy} are the SFD damping coefficients, u is the rotor unbalance, g is the acceleration due to gravity, and Ω is the angular speed of the shaft. Equation (24) in nondimensional form becomes

$$\begin{bmatrix} 1 & 0 \\ 0 & 1 \end{bmatrix}\begin{bmatrix} X'' \\ Y'' \end{bmatrix}+\begin{bmatrix} C_{xx}^n & C_{xy}^n \\ C_{yx}^n & C_{yy}^n \end{bmatrix}\begin{bmatrix} X' \\ Y' \end{bmatrix}+\begin{bmatrix} K_x^* & 0 \\ 0 & K_y^* \end{bmatrix}\begin{bmatrix} X \\ Y \end{bmatrix}=\begin{bmatrix} U\Omega^{*2}\cos\Omega^*t \\ U\Omega^{*2}\sin\Omega^*t-W \end{bmatrix} \quad (25)$$

In this differential equation, the damping coefficients are nonlinear functions of the eccentricity of the journal in the damper. In order to get the steady-state unbalance response we must use numerical integration, which is very time consuming. Thus in order to avoid this time-consuming procedure, we replace these nonlinear damping coefficients with the equivalent linear coefficients. To this end, one can use either Model I or Model II presented earlier.

Model I. Using this model described in the previous section, with damping and stiffness coefficients in addition to the static force, we can write the nondimensional differential equations of motion as

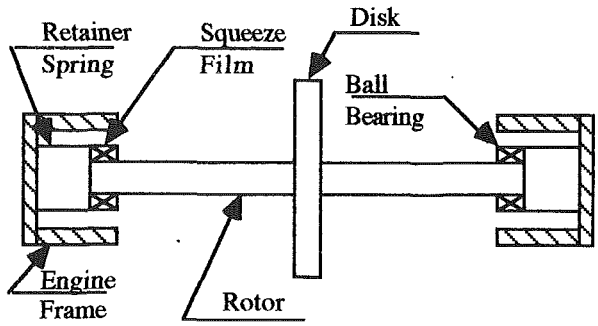

Fig. 3 Rigid rotor on squeeze film dampers

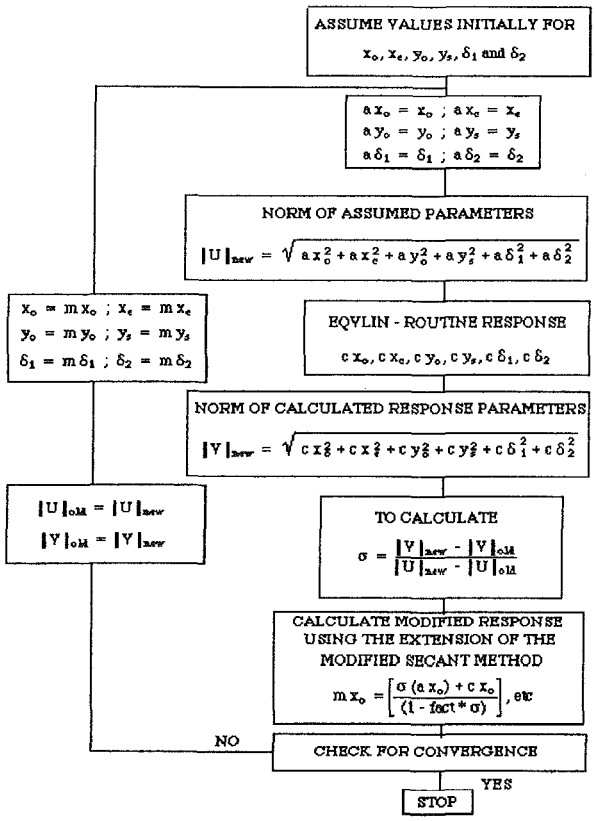

Fig. 4 Flow chart of the equivalent linearization algorithm

$$\begin{bmatrix} 1 & 0 \\ 0 & 1 \end{bmatrix}\begin{bmatrix} X'' \\ Y'' \end{bmatrix}+\begin{bmatrix} B_{xx}^* & 0 \\ 0 & B_{yy}^* \end{bmatrix}\begin{bmatrix} X' \\ Y' \end{bmatrix}+\begin{bmatrix} K_x^*+K_{xx}^* & 0 \\ 0 & K_y^*+K_{yy}^* \end{bmatrix}\times\begin{bmatrix} X \\ y \end{bmatrix}=\begin{bmatrix} U\Omega^{*2}\cos\Omega^*\tau \\ U\Omega^{*2}\sin\Omega^*\tau-W \end{bmatrix}-\begin{bmatrix} F_{ox}^* \\ F_{oy}^* \end{bmatrix} \quad (26)$$

Equations (14) and (15) in nondimensional form can be represented as

$$X=X_o+X_c\cos(\Omega^*\tau-\delta_1) \quad (27)$$

$$Y=Y_o+Y_s\sin(\Omega^*\tau+\delta_2) \quad (28)$$

which can be rewritten in the following form:

$$X=X_o+X_1\cos(\Omega^*\tau)+X_2\sin(\Omega^*t) \quad (29)$$

$$Y=Y_o+Y_1\cos(\Omega^*\tau)+Y_2\sin(\Omega^*t) \quad (30)$$

where

$$X_c=\sqrt{X_1^2+X_2^2};\quad Y_s=\sqrt{Y_1^2+Y_2^2}$$

$$\tan\delta_1=\frac{X_2}{X_1};\quad \tan\delta_2=\frac{Y_1}{Y_2}$$

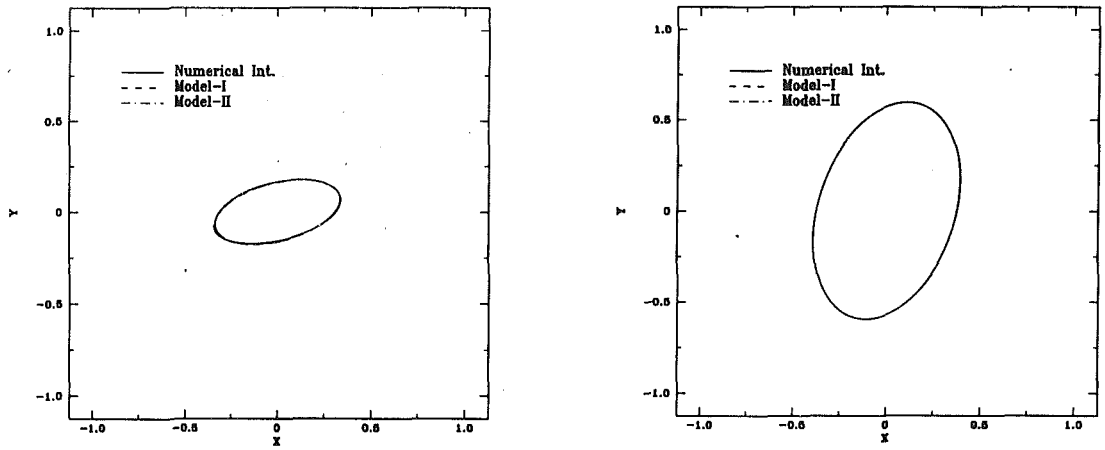

(i) $\Omega^* = 0.68$ (ii) $\Omega^* = 1.36$

Fig. 5*(a)* Centered rotor orbits for short damper: $K_x^* = 0.6$, $K_y^* = 1.0$, $U = 0.25$, $B = 0.2$, $W = 0.0$

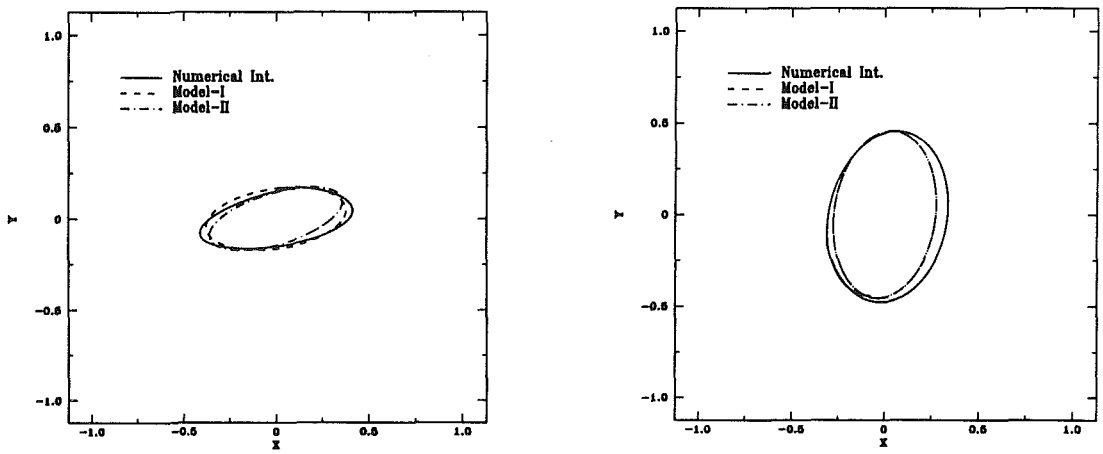

(i) $\Omega^* = 0.68$ (ii) $\Omega^* = 1.36$

Fig. 5*(b)* Centered rotor orbits for long damper: $K_x^* = 0.6$, $K_y^* = 1.0$, $U = 0.2$, $B = 0.01$, $W = 0.0$

Substituting Eqs. (29) and (30) into the differential Eqs. (26), then one obtains for the response in the X direction

$$X_o = \frac{-F_{ox}^*}{[K_{xx}^* + K_x^*]} \tag{31}$$

$$X_1 = \frac{U\Omega^{*2}[K_{xx}^* + K_x^* - \Omega^{*2}]}{[K_{xx}^* + K_x^* - \Omega^{*2}]^2 + [B_{xx}^*\Omega^*]^2} \tag{32}$$

$$X_2 = \frac{U\Omega^{*3}B_{xx}^*}{[K_{xx}^* + K_x^* - \Omega^{*2}]^2 + [B_{xx}^*\Omega^*]^2} \tag{33}$$

and in the Y direction

$$Y_o = \frac{[-F_{oy}^* - W]}{[K_{yy}^* + K_y^*]} \tag{34}$$

$$Y_1 = \frac{-U\Omega^{*3}B_{yy}^*}{[K_{yy}^* + K_y^* - \Omega^{*2}]^2 + [B_{yy}^*\Omega^*]^2} \tag{35}$$

$$Y_2 = \frac{U\Omega^{*2}[K_{yy}^* + K_y^* - \Omega^{*2}]}{[K_{yy}^* + K_y^* - \Omega^{*2}]^2 + [B_{yy}^*\Omega^*]^2} \tag{36}$$

Model II. Using this model described in the previous section, with inertia and damping coefficients in addition to the static force, we can write the nondimensional differential equations of motion as

$$\begin{bmatrix} 1+m_{xx}^* & 0 \\ 0 & 1+m_{yy}^* \end{bmatrix}\begin{bmatrix} X'' \\ Y'' \end{bmatrix} + \begin{bmatrix} B_{xx}^* & 0 \\ 0 & B_{yy}^* \end{bmatrix}\begin{bmatrix} X' \\ Y' \end{bmatrix} + \begin{bmatrix} K_x^* & 0 \\ 0 & K_y^* \end{bmatrix}\begin{bmatrix} X \\ Y \end{bmatrix} = \begin{bmatrix} U\Omega^{*2}\cos\Omega^*\tau \\ U\Omega^{*2}\sin\Omega^*\tau - W \end{bmatrix} - \begin{bmatrix} F_{ox}^* \\ F_{oy}^* \end{bmatrix} \tag{37}$$

Substituting Eqs. (29) and (30) into the differential Eqs. (37), then one obtains for the response in the X direction

$$X_o = \frac{-F_{ox}^*}{K_x^*} \tag{38}$$

$$X_1 = \frac{-U\Omega^{*2}[-(1+m_{xx}^*)\Omega^{*2} + K_x^*]}{[-(1+m_{xx}^*)\Omega^{*2} + K_x^*]^2 + [B_{xx}^*\Omega^*]^2} \tag{39}$$

$$X_2 = \frac{U\Omega^{*3}B_{xx}^*}{[-(1+m_{xx}^*)\Omega^{*2} + K_x^*]^2 + [B_{xx}^*\Omega^*]^2} \tag{40}$$

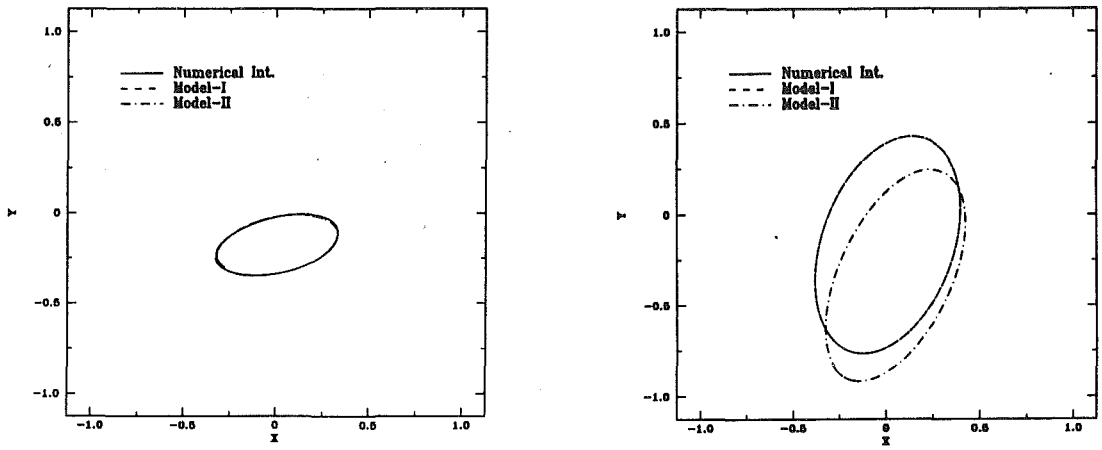

(i) $\Omega^* = 0.68$ (ii) $\Omega^* = 1.36$

Fig. 6(a) Eccentric rotor orbits for short damper: $K_x^* = 0.6$, $K_y^* = 1.0$, $U = 0.25$, $B = 0.2$, $W = 0.2$

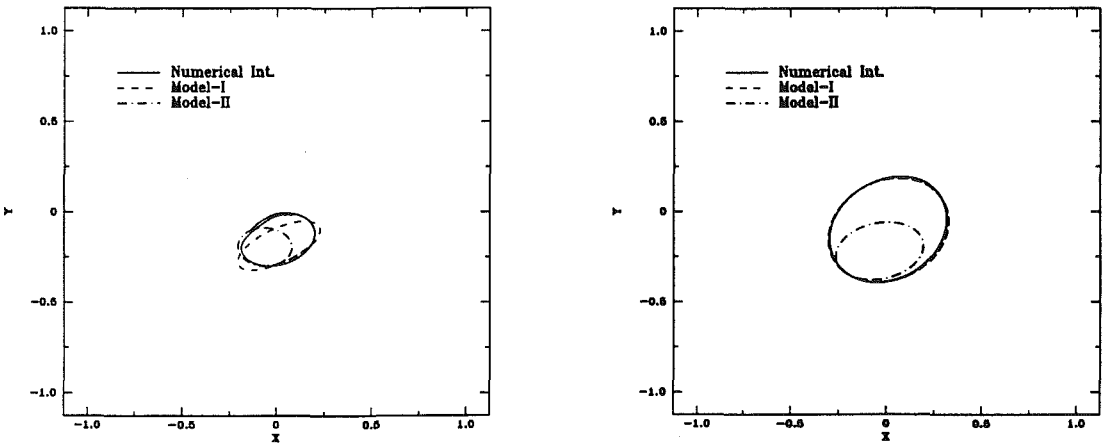

(i) $\Omega^* = 0.68$ (ii) $\Omega^* = 1.36$

Fig. 6(b) Eccentric rotor orbits for long damper: $K_x^* = 0.6$, $K_y^* = 1.0$, $U = 0.25$, $B = 0.05$, $W = 0.2$

and in the Y direction

$$Y_o = \frac{[-F_{oy}^* - W]}{K_y^*} \tag{41}$$

$$Y_1 = \frac{-U\Omega^{*3}B_{yy}^*}{[-(1+m_{yy}^*)\Omega^{*2}+K_y^*]^2+[B_{yy}^*\Omega^*]^2} \tag{42}$$

$$Y_2 = \frac{U\Omega^{*2}[-(1+m_{yy}^*)\Omega^{*2}+K_y^*]}{[-(1+m_{yy}^*)\Omega^{*2}+K_y^*]^2+[B_{yy}^*\Omega^*]^2} \tag{43}$$

Algorithm Development

Equations (31)–(36) for Model I and (38)–(43) for Model II represent the response of the rotor of Fig. 3 to the unbalance excitation and gravity loading, by using the equivalent linear coefficients. Thus in order to obtain the response of the rotor of Fig. 3, we need to know the equivalent liner coefficients beforehand. However, the equivalent linear coefficients depend on the response parameters. This obstacle can be overcome by iteration as illustrated in Fig. 4.

The iteration procedure starts by assuming values for the response parameters (i.e., by assuming a particular rotor orbit). Using the assumed response parameters the equivalent linear coefficients are obtained by using Eq. (22) for Model I, or Eqs. (23) for Model II. The integrals are computed using the Gauss Quadrature Six Point formula. The response of the rotor can then be obtained from Eqs. (31)–(36) for Model I and (38–(43) for Model II. If the calculated orbit parameters thus obtained are the same, within a specified tolerance, as the initially assumed values, then the iteration has converged to the response of the rotor. If not, then a new set of assumed values for the response parameters are employed and the iteration is repeated until convergence is achieved.

To ensure convergence particularly near the critical speeds, where it is very difficult to achieve convergence by direct iteration, the modified secant method developed by Greenhill and Nelson (1982) was extended and employed in this algorithm. To do so, the convergence parameter σ was calculated using the norms of the vectors of the assumed and the calculated parameters, such that

$$\sigma = \frac{\|V\|_{\text{new}} - \|V\|_{\text{old}}}{\|U\|_{\text{new}} - \|U\|_{\text{old}}} \tag{44}$$

where V is the vector of the calculated parameters and U is the vector of the assumed parameters. Then each of the calculated parameters was modified, for example X_o, according to the following formula:

$$mX_o = \frac{\sigma(aX_o) + cX_o}{1 - \text{fact} * \sigma} \tag{45}$$

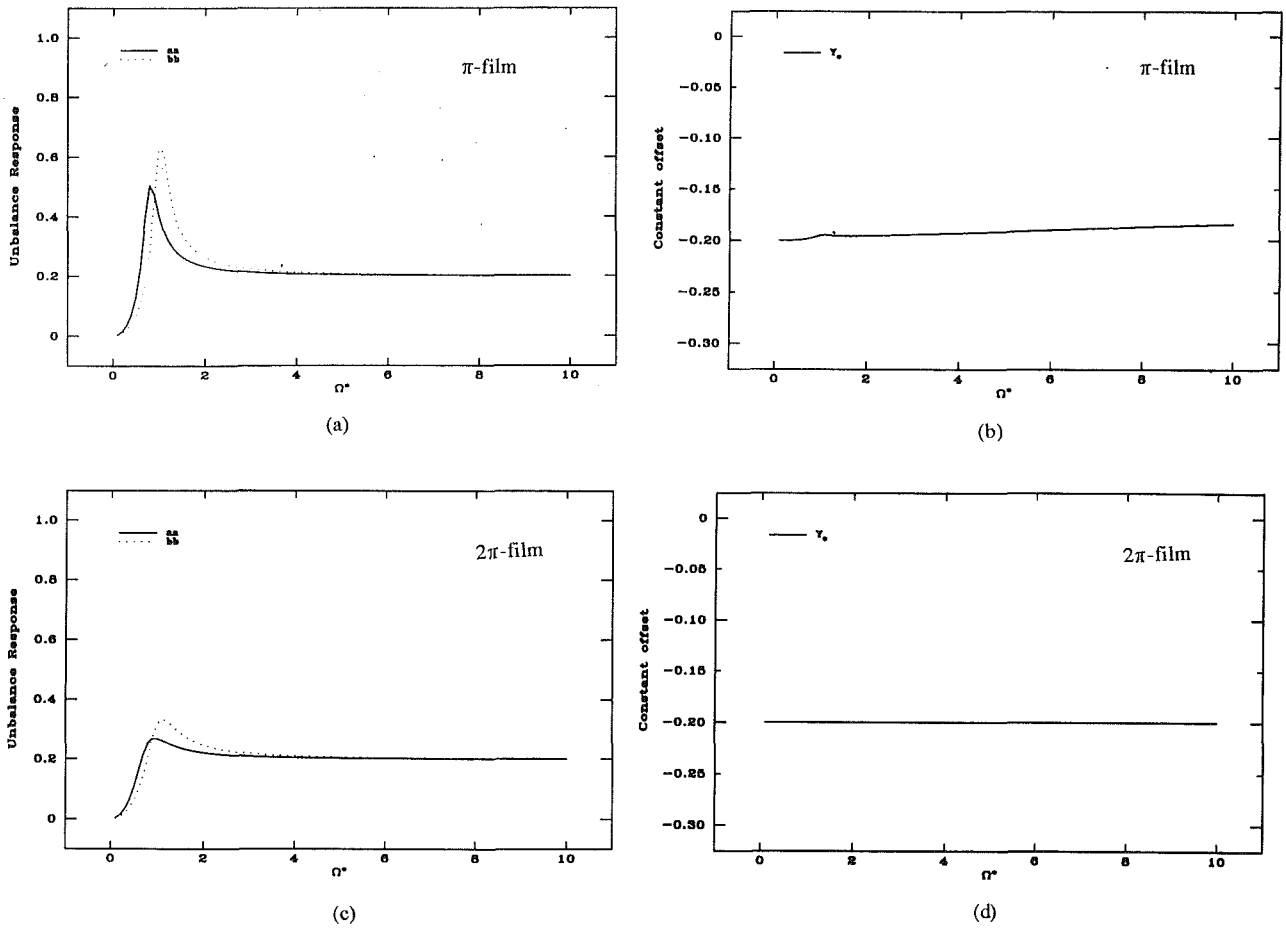

Fig. 7 Unbalance response of cavitated and uncavitated short dampers

where mX_o, aX_o, cX_o are the modified, assumed, and calculated values of X_o, respectively. Similar formulas were applied to all other response parameters. The convergence factor (fact) generally required a value of 1.5 to achieve convergence. Generally three to four iterations were enough to get the required convergence.

This algorithm was extremely efficient and robust. The CPU time taken to get a single steady-state unbalance response on a Sun 3/280 workstation was 3 seconds for the equivalent linearization algorithm, while it took over 5 minutes CPU time for numerical integration by the fourth-order Runge–Kutta method (Eranki, 1990). That is nearly two orders of magnitude savings in computational time.

Model Comparisons

The equivalent linearization algorithm was applied using both Model I and Model II, for both short and long SFDs. Figure 5 illustrates the unbalance response of the rigid rotor for centered orbits. It can be seen from Fig. 5 that both Model I and Model II obtained the same orbit as numerical integration for short dampers, while Model I was superior to Model II with long dampers, since it converged to an orbit much closer to that predicted by numerical integration.

Figure 6 illustrates the unbalance response of the rigid rotor of Fig. 3, when a static load is considered. It can be seen that, with the eccentric orbits of Fig. 6, the orbits predicted by Model II deviate even more from those predicted by numerical integration, than the case with centered orbits. With eccentric orbits, there are generally more harmonics predicted in the unbalance response obtained by numerical integration. This behavior has been observed earlier in the literature (Pan and Tonnesen, 1978). In this case, with the synchronous assumption adopted here, the equivalent linearization algorithm tries to fit the best ellipse to the rotor orbit. However, to predict the response accurately, more harmonics have to be included in the assumed motion within the equivalent linearization algorithm.

It can be concluded from Figs. 5 and 6 that Model I generally predicts the rotor orbits better than Model II. It is thus Model I that is used to obtain the complete unbalance response of the next section. However, it should be noted that Eranki (1990) compared the use of Model I and Model II, using a SFD model that incorporates both damping and fluid inertia forces (El-Shafei and Crandall, 1991). Eranki found that incorporating fluid inertia in the SFD model resulted in Model II being better than Model I in predicting the rotor orbits.

Earlier in the algorithm development it was noted that there was no particular reason to choose Model I (damping plus stiffness equivalent linear coefficients) or Model II (inertia plus damping equivalent linear coefficients). However, the simulations have shown that if there is no physical inertia effect present in the SFD, then an equivalent linear model should not incorporate equivalent linear mass coefficients. On the other hand, if inertia forces are present in the physical model of SFDs, then equivalent linear mass coefficients are desirable. Thus it should be concluded that the choice of the equivalent linear coefficients should rely on the physics of the problem at hand, to achieve the proper choice for the particular application of the equivalent linearization algorithm.

Unbalance Response

To illustrate the strengths of the equivalent linearization

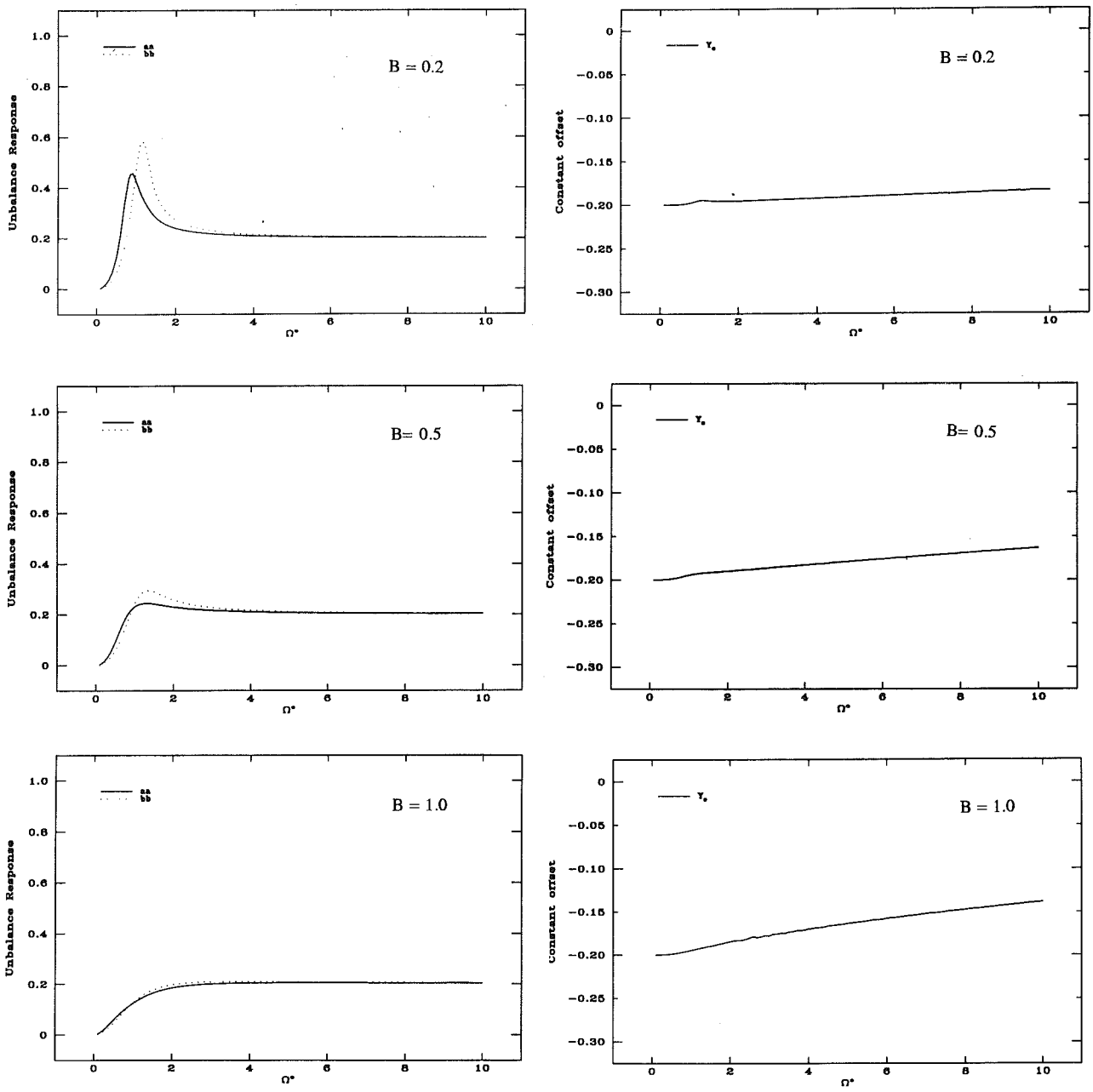

Fig. 8 Effect of bearing parameter on unbalance response

algorithm, Model I is used to obtain the complete unbalance response of the rotor shown in Fig. 3. The rotor-damper parameters were taken to be $K_x^* = 0.6$, $K_y^* = 1.0$, $U = 0.2$, $B = 0.2$, and $W = 0.2$. Figure 7 illustrates the unbalance response for cavitated and uncavitated short dampers. It can be seen from Fig. 7 that the equivalent linearization algorithm predicts the frequency splitting due to the asymmetry in the support stiffness: The critical speed due to K_x (aa in Fig. 7) is less than that due to K_y (*bb* in Fig. 7). Moreover, it can be seen that the equivalent linearization routine predicts that the orbit will tend to be circular at higher frequencies.

Comparing the response of cavitated and uncavitated dampers, it can be seen from Fig. 7 that the equivalent linearization algorithm correctly predicts the superior attenuation of the critical speeds by the uncavitated damper. Moreover, it can be seen from Fig. 7 that the orbit eccentricity decreases with frequency for the cavitated damper and is constant for the uncavitated damper. This "self-centering" phenomenon in cavitated dampers has been predicted earlier in the literature (Pan and Tonnesen, 1978), and is due to the lift force generated within the cavitated damper. The uncavitated damper, on the other hand, cannot provide this lift force (Van Eetvelt and Holmes, 1992) and thus the static load is completely carried by the retainer springs.

Figure 8 illustrates the effect of the bearing parameter B on the unbalance response of the rigid rotor of Fig. 3, supported on short SFDs, as predicted by the equivalent linearization algorithm. It can be seen from Fig. 8 that increasing the bearing parameter improves the attenuation of the critical speeds and decreases the eccentricity of the rotor orbit, both of which are desirable effects.

Conclusion

In this paper it was shown that the equivalent linearization algorithm is an efficient and fast technique for finding the nonlinear unbalance response of SFD supported rotors. It has been shown to give accurate results by comparison with nu-

merical integration with two orders of magnitude computational time savings. The main advantage of using the equivalent linearization technique is the ability to use the widely available linear rotor-dynamic programs in performing nonlinear analysis of rotors incorporating SFDs.

In developing the equivalent linearization algorithm, it was shown that if an eccentric orbit exists, then the equivalent linear model must include two static force components. Moreover, for each frequency component in the assumed motion, only four equivalent liner dynamic coefficients can be used. The choice of the appropriate four equivalent liner dynamic coefficients, out of the possible twelve coefficients, has to rely on the physical model of the SFD for proper convergence of the algorithm.

The equivalent linearization algorithm was shown to be able to predict some of the well-known behavior of SFD supported rotors, such as the self-centering effect at high frequencies for cavitated dampers, the frequency-splitting phenomenon for asymmetric supports, and the fact that large bearing parameter values result in better attenuation of the amplitude response.

References

Booker, J. F., 1965, "A Table of the Journal-Bearing Integral," ASME *Journal of Basic Engineering*, pp. 533–535.

Burrows, C. R., Sahinkaya, M. N., and Kucuk, N. C., 1986, "Modelling of Oil-Film Forces in Squeeze Film Bearings," ASME *Journal of Tribology*, Vol. 108, pp. 262–269.

Chen, S., and Liu, S., 1986, "Equivalent Linearization of a Squeeze Film Damper," ASME *Journal of Vibrations, Acoustics, Stress, and Reliability in Design*, Vol. 108.

Crandall, S. H., and Yeh, N. A., 1986, "Component Mode Synthesis of Multi-rotor Systems," *Proceedings of Euromech 219, Refined Dynamical Theories of Beams, Plates and Shells and Their Applications*, Kassel, West Germany.

El-Shafei, A., 1990, "Unbalance Response of a Jeffcott Rotor Incorporating Short Squeeze Film Dampers," ASME JOURNAL OF ENGINEERING FOR GAS TURBINES AND POWER, Vol. 112, pp. 445–453.

El-Shafei, A., 1991, "Unbalance Response of a Jeffcott Rotor Incorporating Long Squeeze Film Dampers," ASME *Journal of Vibration and Acoustics*, Vol. 113, pp. 85–94.

El-Shafei, A., and Crandall, S. H., 1991, "Fluid Inertia Forces in Squeeze Film Dampers," *Rotating Machinery and Vehicle Dynamics*, T. C. Huang et al., eds., ASME DE-Vol. 35, pp. 219–228.

El-Shafei, A., and Eranki, R. V., 1992, "Dynamic Force Coefficients of Short and Long Squeeze Film Dampers Executing Elliptic Orbits," *Proc. I. Mech. E., Vibrations in Rotating Machinery*, Paper No. C432/127, pp. 597–604.

Eranki, R. V., 1990, "Equivalent Linearization of Squeeze Film Dampers," M.Sc. thesis, University of South Florida, Tampa, FL.

Greenhill, L. M., and Nelson, H. D., 1982, "Iterative Determination of Squeeze Film Damper Eccentricity for Flexible Rotor Systems," ASME *Journal of Mechanical Design*, Vol. 104, pp. 334–338.

Gunter, E. J., Barrett, L. E., and Allaire, P. E., 1977, "Design of Nonlinear Squeeze Film Dampers for Aircraft Engines," ASME *Journal of Lubrication Technology*, Vol. 99, pp. 57–64.

Hahn, E. J., 1985, "An Energy Approach to Linearizing Squeeze Film Damper Forces," *Proc. I Mech E*, Vol. 199, pp. 57–63.

Mohan, S., and Hahn, E. J., 1974, "Design of Squeeze Film Damper Supports for Rigid Rotors," ASME *Journal of Engineering for Industry*, Vol. 96, pp. 976–982.

Pan, C. H., T., and Tonnesen, J., 1978, "Eccentric Operation of the Squeeze-Film Damper," ASME *Journal of Lubrication Technology*, Vol. 100, pp. 369–377.

Taylor, D. L., and Kumar, B. R. K., 1980, "Nonlinear Response of Short Squeeze Film Dampers," ASME *Journal of Lubrication Technology*, Vol. 102, pp. 51–58.

Taylor, D. L., and Kumar, B. R. K., 1983, "Closed Form Steady State Solution for the Unbalance Response of a Rigid Rotor in Squeeze Film Damper," ASME *Journal of Engineering for Power*, Vol. 105, pp. 551–559.

Van Eetvelt, P., and Holmes, R., 1992, "Analytical Investigation of the Load Capacity of the Full Squeeze-Film Bearing," *Proc. I Mech E, Journal of Mechanical Engineering Science*, Vol. 206, No. C3, pp. 215–217.

Chaotic Behavior of Rotor/Stator Systems With Rubs

P. Goldman

A. Muszynska

Bently Rotor Dynamics Research Corp., Minden, NV 89423

This paper outlines the dynamic behavior of externally excited rotor/stator systems with occasional, partial rubbing conditions. The observed phenomena have one major source of a strong nonlinearity: transition from no contact to contact state between mechanical elements, one of which is rotating, resulting in variable stiffness and damping, impacting, and intermittent involvement of friction. A new model for such a transition (impact) is developed. In case of the contact between rotating and stationary elements, it correlates the local radial and tangential ("super ball") effects with global behavior of the system. The results of numerical simulations of a simple rotor/stator system based on that model are presented in the form of bifurcation diagrams, rotor lateral vibration time-base waves, and orbits. The vibrational behavior of the system considered is characterized by orderly harmonic and subharmonic responses, as well as by chaotic vibrations. A new result is obtained in case of heavy rub of an anisotropically supported rotor. The system exhibits an additional subharmonic regime of vibration due to the stiffness asymmetry. The correspondence between numerical simulation of that effect and previously obtained experimental data supports the adequacy of the new model of impact.

Introduction

During the last 30 years researchers have documented irregular and unpredictable dynamic behavior of various physical systems under external excitation. Nonlinear phenomena occurring in these systems are responsible for these irregular and unpredictable effects that lead to chaos.

One of the mechanical systems that exhibits chaotic behavior is the rotating shaft with its stator and supporting structure. The normal conditions of rotor operation are determined by appropriate clearances at the joints and boundaries. There are possible divergences from the normal operational conditions, such as:

(*i*) Looseness in the stationary joints; for example, between the rotor supporting pedestal and foundation.

(*ii*) Oversize, poorly lubricated bearing: a looseness between the stationary and rotating elements. (The bearing clearance may increase from "normal" to "oversize" due to wear.)

(*iii*) Rubbing rotor: occasional physical contact between the rotating and stationary elements, which, during normal operational conditions, should not take place.

In these cases the dynamic phenomena revealed in the rotor motion occur as secondary effects of the primary cause. The latter is most often a trade-off, between the imbalance-related rotating exciting force, and the unilateral, radial force applied to the rotor. For instance, the looseness in the pedestal joint, or oversize bearing, would not be discovered until the lifting imbalance-related centrifugal force would exceed the gravity force that presses the joints into close contact. In the rotor-to-stator rub case the unwelcome rotor/stator contact occurs when the rotor is moved to the side due to the radial force, and/or amplitudes of its lateral precessional motion, such as excited by imbalance, exceed allowable clearances.

There are several physical phenomena that take place in the cases discussed:

- Occasional, time-variable increase/decrease of the system stiffness. In the case of looseness, the average stiffness level decreases; in the case of rubs, it increases. Similarly to stiffness, the system damping varies.
- Impacts. The sudden physical contact between elements is accompanied by characteristic local phenomena, followed by global motion changes of the system.
- Friction. In cases of the oversize bearing and rub malfunctions, the rotating shaft enters into contact with a stationary part. This contact is accompanied by friction, as an effect of relative motion of the rotating and stationary parts.

All these phenomena introduce nonlinearities into the system, and individually or interactively, they can contribute to chaotic behavior of the system.

Even though the chaotic phenomena in similar rotor/stator mechanical systems were investigated by several researchers (Thompson and Ghaffari, 1982; Evan-Iwanowski and Lu, 1991; Szczygielski, 1987; Ehrich, 1991; Gonsalves et al., 1992), their results have mostly qualitative character, since they employ oversimplified impact models. This paper presents a new, more

Contributed by the International Gas Turbine Institute and presented at the 38th International Gas Turbine and Aeroengine Congress and Exposition, Cincinnati, Ohio, May 24-27, 1993. Manuscript received at ASME Headquarters March 17, 1993. Paper No. 93-GT-387. Associate Technical Editor: H. Lukas.

adequate model of the impact. This model is further employed in numerical simulation of rotor/stator systems with various rubbing conditions. The results exhibit the orderly and chaotic behavior patterns of rotors.

Model of Elastic Impact at Rotor Mass Location

Accuracy in the description of the looseness and/or rub-related phenomena in mechanical structures with intermittent interelement contacts depends mainly on the adequacy of the impact model. The local/global effect of the impact introduces a nonlinearity to the system, and generates specific vibrational responses of the system.

There are three approaches employed in the description of impacts between rotational and stationary parts of the mechanical system. The first is based on the classical restitution coefficient model in which an impact is considered instantaneous and elastic (Szczygielski, 1987). The second approach considers nonelastic impact with a zero restitution coefficient; the impact is followed by a sliding stage (Muszynska, 1989). In this model, changes of the rotor precessional speed during the impact also occur instantaneously. In both these models, the other forces applied to the rotor do not practically affect the result of the impact, because they are relatively small. Neither model takes into account changes in the rotor displacement, which may occur during the impact. The third approach considers the mechanical system as having discontinuous piecewise characteristics with additional stiffness and damping of the stator at the contact period (Ehrich, 1988). This model seems more accurate, but it creates certain numerical problems, since two different time scales should be considered: one during the free motion of the shaft when there is no contact (global motion), and the other during the contact period characterized by much higher stiffness (local motion). This causes some difficulties in the description of the behavior of the system.

The analytical model of the impact presented in this paper is based on the third approach—analysis of the piecewise system with an assumption that the local stiffness of the stator or bearing at the intermittent contact location is much higher than the stiffness of the rotor. A similar approach was used in the description of "normal-loose" phenomena occurring due to an untightened rotor pedestal (Goldman and Muszynska, 1991).

The impact model will be derived with the assumption that the impact occurs at the rotor modal mass location. The first lateral mode of the rotor is taken into consideration. This approach can be easily modified for other cases.

A simple isotropic rotor with an anisotropic support is considered. During its lateral motion, the rotor occasionally rubs against the stator (Fig. 1). The mathematical model of the rotor lateral motion $x(t)$, $y(t)$ at the mode uncoupled from the stator is as follows:

$$M\ddot{x}+D\dot{x}+K_x x=mr\omega^2\cos(\omega t+\alpha)+S\cos\gamma$$

$$M\ddot{y}+D\dot{y}+K_y\dot{y}=mr\omega^2\sin(\omega t+\alpha)+S\sin\gamma,\ \bullet=\frac{d}{dt} \quad (1)$$

which can be transformed using polar coordinates $R(t)$ and $\psi(t)$: $x=R\cos\psi$, $y=R\sin\psi$ as follows:

$$M\ddot{R}=-RK-\Delta KR\cos 2\psi-D\dot{R}+MR\dot{\psi}^2+mr\omega^2\cos(\varphi-\psi)+S\cos(\gamma-\psi)$$

$$MR\ddot{\psi}=-D\dot{\psi}R-2M\dot{\psi}\dot{R}+\Delta KR\sin 2\psi+mr\omega^2\sin(\varphi-\psi)+S\sin(\gamma-\psi) \quad (2)$$

Nomenclature

a = radius of the shaft at the rotor/stator contact location
c = radial clearance between the shaft and the stator, respectively
D, K, M = modal damping, stiffness, and mass of the rotor, respectively
D_f, K_f = local damping and stiffness of the stator
D_{cont} = contact tangential viscous damping coefficient
f = dry friction coefficient
F_1, Φ_1 = defined in expressions (20)
$\overline{F_\tau}$ = friction force between the shaft and the stator when contact occurs
i, l = indices (integer numbers)
K_x, K_y = rotor/support stiffnesses in two stationary orthogonal directions
m, r, α = mass, radius, and angular orientation of shaft unbalance
N = normal force at the rotor/stator contact
$p=\omega/\nu$ = rotative speed-to-natural frequency ratio
R, ψ = radial and angular coordinates of the rotor
$R^{(i)}, \psi^{(i)}$ = ith approximations to the radial and angular coordinates
S, γ = radial force amplitude and its angular orientation
t = time
t_{dw}, τ_{dw} = time and nondimensional time of rotor/stator contact
x, y = horizontal and vertical displacements of the shaft at the modal mass location
z, z_i = radial displacement of the shaft and its ith approximation
$\beta=\dot{\psi}/\omega, \beta_i$ = ratio of the shaft precessional velocity to the rotative speed and its ith approximation
$\epsilon=\omega/\Omega$ = small parameter, a ratio of the rotative speed to the stator local natural frequency
$\zeta, \zeta_f, \zeta_{\text{cont}}$ = damping factors of the shaft, stator, and local contact damping, correspondingly
$\kappa_{0n}, \kappa_{0\tau}$ = zero approximations to the normal and tangential restitution coefficients, correspondingly
$\Delta K=(K_x-K_y)/2$ = stiffness asymmetry of the rotor/stator system
$\nu=\sqrt{K/M}$ = natural frequency of the rotor
$\sigma=\text{sign}(\dot{\psi}_-+\omega(a/c))$ = sign of the velocity of sliding at the instant of contact between the shaft and the stator
$\tau=\Omega t$ = nondimensional time
τ_0, τ_1 = duration of the rotor/stator contact (zeroth and first approximation)
$\varphi=\omega t+\alpha$ = phase of the unbalance force
ω = rotative speed of the shaft
$\Omega=\sqrt{K_f/M}$ = stator local natural frequency
"$-$", "$+$" = subscripts meaning that the corresponding variable is calculated at the instant of entering or leaving the contact (or the stage of contact), respectively

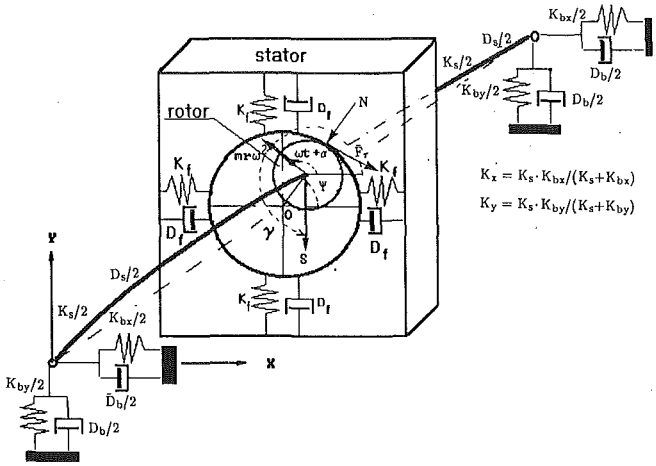

Fig. 1 *Model of the rotor entering occasionally into contact with the stator*

In Eqs. (1) and (2) M, D, K_x, K_y are modal mass, damping, and anisotropic stiffnesses of the rotor system, $K=(K_x+K_y)/2$, $\Delta K=(K_x-K_y)/2$; $\varphi=\omega t+\alpha$ is the total phase of the unbalance, ω is rotative speed of the shaft, S is radial force, γ is angle between this force and horizontal direction, m, r, α are the mass, radius, and angular orientation of the unbalance respectively. The rotor/stator contact occurs when $R \geq c$ where c is a radial clearance between the rotor and the stator. It is assumed that, during the contact, the stator acts as a spring with stiffness K_f and damping D_f in the radial direction, and creates a tangential friction force $\bar{F}_\tau$. Therefore, the system equations of motion at the rotor/stator contact stage written in polar coordinates are as follows:

$$M\ddot{R} = -(K+K_f)(R-c) - Kc - \Delta KR\cos 2\psi - (D+D_f)\dot{R} + MR\dot{\psi}^2 + mr\omega^2\cos(\varphi-\psi) + S\cos(\gamma-\psi)$$

$$MR\ddot{\psi} = -(D+D_f)\dot{\psi}R - 2M\dot{\psi}\dot{R} + \Delta KR\sin 2\psi + mr\omega^2\sin(\varphi-\psi) + S\sin(\varphi-\psi) + \bar{F}_\tau(1+a/R) \quad (3)$$

where a is a radius of the shaft at the contact cross section. The friction force $\bar{F}_\tau$ is attached to the shaft at the point of contact (Fig. 1). It is assumed that it has a mixed viscous/dry pattern, thus the following relation holds true:

$$\bar{F}_\tau = -D_{\text{cont}}(\dot{\psi}R+\omega a) - f[D_f\dot{R} + K_f(R-c)][\text{sign}(\dot{\psi}R+\omega a)] \quad (4)$$

where $(\dot{\psi}R+\omega a)$ is the relative velocity of the rotor at the stator rubbing surface. D_{cont} and f are the local contact viscous and dry friction coefficients, respectively.

Equation (4) is true only until $\dot{\psi}R+\omega a \neq 0$. If the sliding velocity becomes zero, the friction force creates a moment equal to the absolute value of the sum of all the other moments, M_Σ applied to the rotor, and has an opposite direction to it. It means that in the absence of sliding, there is $\ddot{\psi}=0$, $\dot{\psi}=-\omega a/R$. The sliding can start again if M_Σ satisfies the following inequality: $|M_\Sigma| \geq f[D_f\dot{R}+K_f(R-c)](a+R)$. In this case, the friction force at the sliding period can be expressed as follows:

$$\bar{F}_\tau = -f[D_f\dot{R}+K_f(R-c)]\text{sign}(M_\Sigma) \quad (5)$$

It is further assumed that if the sliding stopped, it would not start again during that particular contact period. This assumption means that the direction of sliding cannot be changed.

For further analytical considerations a small parameter, ϵ, is introduced. An assumption has been made that $\epsilon = \omega\sqrt{M/K_f}$ is small ($\epsilon \ll 1$). It means that considered range of rotative speeds is limited, and that the stator local stiffness is comparably high; therefore, the radial displacement of the stator is small. It is also assumed that, during the rotor/stator contact stage, the rotor radial motion is performed close to the stator surface, so that $R-c=\epsilon z$ where ϵ is again the small parameter, and z is a new variable.

In all practical cases, the shaft radius a is much larger than the clearance c. This means that the arm of the friction force can be approximated by a. Using these assumptions, and neglecting the terms of higher powers of the small parameter ϵ, Eqs. (3) can be transformed to the following:

$$z'' + 2\zeta_f z' + z = \epsilon\left[\dot{\Phi} + c\left(\beta^2 - \frac{1}{p^2}\right) - 2\zeta z'\right] + \epsilon^2[\ldots]$$

$$\beta' + \zeta_{\text{cont}}\left(\beta+\frac{a}{c}\right) + f\frac{a}{c^2}\text{sign}\left(\beta+\frac{a}{c}\right)(2\zeta_f z' + z) = \epsilon\left[F + \zeta_{\text{cont}}\left(\beta+\frac{2a}{c}\right)\frac{z}{c} - 2\beta\left(\zeta+\frac{z'}{c}\right) + 2f\frac{az}{c^3}(2\zeta_f z' + z)\text{sign}\left(\beta+\frac{a}{c}\right)\right] + \epsilon^2[\ldots] \quad (6)$$

where the following notation was introduced (the rest of the notations are in the Nomenclature):

$$' = \frac{d}{d\tau}, \quad \zeta_{\text{cont}} = \frac{a}{c}\frac{D_{\text{cont}}}{\Omega M}, \quad \zeta = \frac{D}{2\omega M}, \quad \zeta_f = \frac{D_f}{2M\Omega}$$

$$\Phi = \frac{S}{M\omega^2}\cos(\gamma-\psi) + \frac{mr}{M}\cos(\varphi-\psi) - \frac{\Delta Kc}{M\omega^2}\cos 2\psi$$

$$F = \frac{mr}{Mc}\sin(\varphi-\psi) + \frac{S}{Mc\omega^2}\sin(\gamma-\psi) + \frac{\Delta K}{M\omega^2}\sin 2\psi$$

The solution of Eqs. (6) is sought in the form of a power series of the small parameter ϵ:

$$z = z_0 + \epsilon z_1 + \epsilon^2 \ldots, \quad \beta = \beta_0 + \epsilon\beta_1 + \epsilon^2 \ldots,$$
$$\psi = \psi_- + \epsilon\int_0^\tau \beta_0(\tau)d\tau + \epsilon^2\int_0^\tau \beta_1(\tau)d\tau + \ldots \quad (7)$$

with the following initial conditions:

$$z(0)=0, \quad z'(0)=z'_-, \quad \beta(0)=\beta_- \quad (8)$$

where the subscript "$-$" means the value of the corresponding variable just before rotor/stator contact.

From Eqs. (6) and (7), the equations for zero approximation (all terms standing in front of ϵ^0) are as follows:

$$z_0'' + 2\zeta_f z_0' + z_0 = 0$$
$$\beta_0' + \zeta_{\text{cont}}\left(\beta_0+\frac{a}{c}\right) + f\frac{a}{c}\left(2\zeta_f\frac{z_0'}{c} + \frac{z_0}{c}\right)\text{sign}\left(\beta_0+\frac{a}{c}\right) = 0 \quad (9)$$

where z_0 and β_0 represent the zero approximation of the corresponding variables. Equations (8) are considered as initial conditions for Eqs. (9). All higher approximations would have then zero initial conditions.

The integration of the first Eq. (9) yields the following solution:

$$z_0(\tau) = \begin{cases} \dfrac{(z'_-)e^{-\zeta_f\tau}}{\sqrt{1-\zeta_f^2}}\sin[\sqrt{1-\zeta_f^2}\tau] & \text{if } \zeta_f \leq 1 \\ \dfrac{(z'_-)e^{-\zeta_f\tau}}{\sqrt{\zeta_f^2-1}}\sinh[\sqrt{\zeta_f^2-1}\tau] & \text{if } \zeta_f > 1 \end{cases} \quad (10)$$

As it was noted earlier, the condition for the beginning of the contact stage is geometric equality $z=0$, that is, $R=c$. Once occurred, the contact is maintained if the rotor/stator normal force is positive. The zero approximation for the normal force is equal to $2\zeta_f z_0' + z_0$, or according to the first Eq. (9), is equal to $(-z_0'')$. Therefore, the contact lasts until the radial acceleration is negative.

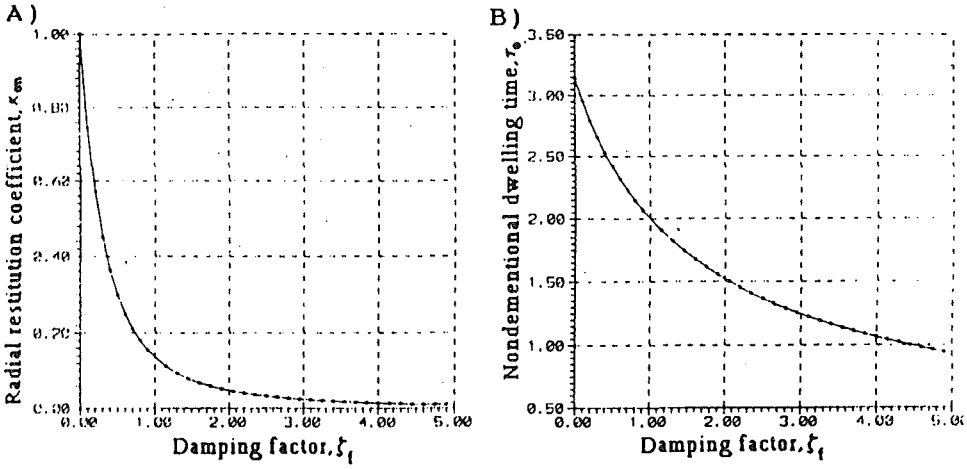

Fig. 2 Zero approximation to the (*a*) radial restitution coefficient, (*b*) nondimensional dwelling time versus local damping factor of the stator

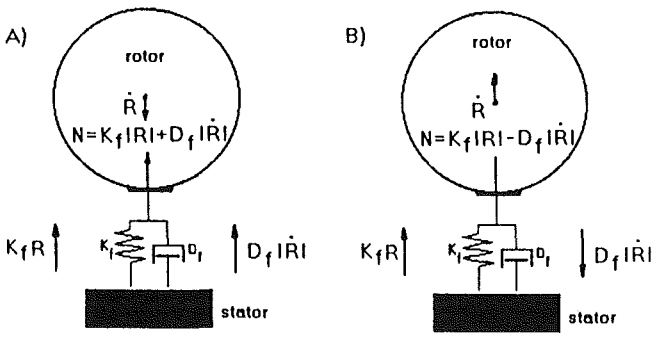

Fig. 3 Forces in the radial direction during the impact (*a*) when radial velocity is positive, (*b*) when radial velocity is negative. Note that in case (*b*), damping causes a decrease of the normal force.

The zero approximation τ_0 for the contact stage duration is the first root of the equation $z_0''(\tau_0)=0$, at which the radial acceleration has a positive derivative. This yields:

$$\tau_0=\begin{cases}\dfrac{\arccos(2\zeta_f^2-1)}{\sqrt{1-\zeta_f^2}} & \text{if } \zeta_f\le 1\\[2ex] \dfrac{2\ln(\zeta_f+\sqrt{\zeta_f^2-1})}{\sqrt{\zeta_f^2-1}} & \text{if } \zeta_f>1\end{cases} \tag{11}$$

The zero approximation z'_{0+} for the radial velocity z'_+ at the moment of the shaft departure from the contact is easily calculated using Eqs. (10) and (11):

$$z'_{0+}\equiv z'_0(\tau_0)=-\kappa_{0n}z'_- \tag{12}$$

with

$$\kappa_{0n}=\begin{cases}\exp\left[-\dfrac{\zeta_f}{\sqrt{1-\zeta_f^2}}\arccos(2\zeta_f^2-1)\right] & \text{if } \zeta_f\le 1\\[2ex] \exp\left[-\dfrac{2\zeta_f}{\sqrt{\zeta_f^2-1}}\ln[\zeta_f+\sqrt{\zeta_f^2-1}]\right] & \text{if } \zeta_f>1\end{cases} \tag{13}$$

where the subscript "+" means the value of the variable at the instant of separation, κ_{0n} is defined as a zero approximation for the *radial restitution coefficient*. Equations (11) and (13) determine the zero approximation for the rotor/stator coupling duration, and the radial restitution coefficient in the entire range of ζ_f. A graphic representation of these functions is shown in Fig. 2. It can be seen that the dwelling time decreases with an increase of the stator damping factor. The physical explanation of it is based on the change of the rotor radial velocity sign from positive to negative (Fig. 3). With the negative sign, the damping force opposes the normal force direction. Therefore, a higher stator damping leads to an earlier nullification of the normal force.

Looking at the graph of κ_{0n} versus ζ_f (Fig. 2A), it is clear that if $\zeta_f>8$, then $\kappa_{0n}<10^{-3}$, and κ_{0n} can be considered small, even in comparison with the terms of the first order of the small parameter. This case needs a separate consideration, and further it is referred to as the case of *nonelastic impact* (Muszynska and Goldman, 1993).

The integration of the second Eq. (9) yields the following expression:

$$\beta_0(\tau)=\left(\beta_-+\frac{a}{c}\right)e^{-\zeta_{\text{cont}}\tau}-\frac{a}{c}+\sigma\frac{fa}{c^2}\left[z'_0(\tau)-\zeta_{\text{cont}}z_0(\tau)-z'_-e^{-\zeta_{\text{cont}}\tau}+\zeta_{\text{cont}}^2e^{-\zeta_{\text{cont}}\tau}\int_0^\tau z_0(\tau)e^{\zeta_{\text{cont}}\tau}d\tau\right] \tag{14}$$

where $\sigma=\text{sign}(\beta_-+(a/c))=\pm 1$.

Assuming that the contact tangential damping D_{cont} is relatively small so that the last term of Eq. (14) can be neglected, calculate now β_0 at the moment of departure τ_0:

$$\beta_0(\tau_0)\equiv\beta_{0+}=\left(\beta_-+\frac{a}{c}\right)\kappa_{0\tau}-\frac{a}{c}-\sigma\frac{fa}{c^2}\left[(z'_-)(\kappa_{0n}+\kappa_{0\tau})+\zeta_{\text{cont}}z_0(\tau_0)\right] \tag{15}$$

where Eq. (12) was used, and, by definition, the zero approximation to the *tangential restitution coefficient* $\kappa_{0\tau}=e^{-\zeta_{\text{cont}}\tau_0}$ was introduced. Note that, based on Eqs. (10) to (13), $z_0(\tau_0)=2\zeta_f\kappa_{0n}z'_-$, thus the last term of Eq. (15) containing the product $(\zeta_f\zeta_{\text{cont}})$ also becomes relatively small, and can be further neglected.

Equation (15) holds true only if, during the contact, the rotor slides on the stator surface. This means that the rotor velocity $\omega(\beta c+a)$ does not change sign, and implies from Eq. (15) the following condition:

$$\left|\beta_-+\frac{a}{c}\right|\kappa_{0\tau}>\frac{fa}{c^2}(z'_-)(\kappa_{0n}+\kappa_{0\tau}) \tag{16}$$

If the inequality (16) is not satisfied, the sliding stops. At this moment, the viscous friction component of the tangential force $\bar{F}_\tau$ turns to zero, and the dry friction component increases.

The rotor velocity cannot change direction, thus $\beta_- = -a/c$. In summary, there is, therefore,

$$\beta_{0+} = \begin{cases} (\beta_-)\kappa_{0\tau} - \dfrac{a}{c}(1-\kappa_{0\tau}) - \dfrac{\sigma f a}{c^2}(z_-')(\kappa_{0n}+\kappa_{0\tau}), & \text{if } \left|\beta_- + \dfrac{a}{c}\right| > f\dfrac{a(z_-')}{c^2}\left(1+\dfrac{\kappa_{0n}}{\kappa_{0\tau}}\right) \\ -\dfrac{a}{c}, & \text{if } \left|\beta_- + \dfrac{a}{c}\right| < f\dfrac{a(z_-')}{c^2}\left(1+\dfrac{\kappa_{0n}}{\kappa_{0\tau}}\right) \end{cases} \tag{17}$$

Using Eqs. (10), (11), and (14) with introduced simplifications, the zero approximation for the rotor original polar coordinates ψ, R at the end of the contact period can be calculated:

$$R_+^{(0)} = c + \epsilon z_0(\tau_0) = c + \frac{2\kappa_{0n}\zeta_f}{\Omega}\dot{R}_-$$

$$\psi_+^{(0)} = \psi_- + \frac{\omega}{\Omega}\int_0^{\tau_0}\beta_0(\tau)d\tau = \psi_- + \frac{1-\kappa_{0\tau}}{\zeta_{\text{cont}}\Omega}\left(\dot{\psi}_- + \frac{a\omega}{c}\right) - \frac{a\omega}{c}\frac{\tau_0}{\Omega} - \frac{\sigma f a}{c^2\Omega}(\dot{R}_-)\left[\frac{1-\kappa_{0\tau}}{\zeta_{\text{cont}}} - 2\kappa_{0n}\zeta_f\right] \tag{18}$$

where ψ_- is the rotor angular coordinate at the instant when the contact with the stator occurs, $R_+^{(0)}$, $\psi_+^{(0)}$ are zero approximations to both polar coordinates at the moment of the rotor departure from the contact.

As it follows from Eqs. (12) and (15), the zero approximation describes the impact in terms of the stator properties, as well as the normal and tangential velocities of the rotor during the contact period. In order to analyze the influence of the shaft unbalance and radial forces on the impact, it is necessary to calculate the first approximation of the solution (7). The balance of terms associated with the first power of the small parameter ϵ in Eqs. (6) yields the following equations for the first approximation:

$$z_1'' + 2\zeta_f z_1' + z_1 = \Phi_1 + c\left(\beta_0^2 - \frac{1}{p^2}\right) - 2\zeta z_0'$$

$$\beta_1' + \zeta_{\text{cont}}\beta_1 + \frac{fa}{c^2}\sigma(2\zeta_f z_1' + z_1) = F_1 - 2\beta_0\left(\frac{z_0'}{c} + \zeta\right) + \zeta_{\text{cont}}\frac{z_0}{c}\left(\beta_0 + 2\frac{a}{c}\right) - 2\frac{fa}{c^3}\sigma z_0'' z_0 \tag{19}$$

where

$$\Phi_1 = \frac{S}{M\omega^2}\cos(\gamma - \psi_-) + \frac{mr}{M}\cos[(\varphi_-) - (\psi_-)] - \frac{\Delta K c}{M\omega^2}\cos 2\psi_-,$$

$$F_1 = \frac{mr}{Mc}\sin[(\varphi_-) - (\psi_-)] + \frac{S}{Mc\omega^2}\sin(\gamma - \psi_-) - \frac{\Delta K}{M\omega^2}\sin 2\psi_- \tag{20}$$

φ_- is the unbalance force phase at the instant of entering the contact. The integration of Eqs. (19) with zero initial conditions, taking into account Eq. (14) and neglecting small terms, yields:

$$z_1 = \left[\Phi_1 + c\left(\beta_-^2 - \frac{1}{p^2}\right)\right][1 - e^{-\zeta_f\tau}X_1(\zeta_f, \tau)]$$

$$\beta_1 = F_1\tau - \frac{2\beta_-}{c}(z_-')e^{-\zeta_f\tau}X_2(\zeta_f, \tau) \tag{21}$$

where

$$X_1(\zeta_f, \tau) = \begin{cases} \cos\sqrt{1-\zeta_f^2}\tau + \dfrac{\zeta_f}{\sqrt{1-\zeta_f^2}}\sin\sqrt{1-\zeta_f^2}\tau & \text{if } \zeta_f \le 1 \\ \cosh\sqrt{\zeta_f^2-1}\tau + \dfrac{\zeta_f}{\sqrt{\zeta_f^2-1}}\sinh\sqrt{\zeta_f^2-1}\tau & \text{if } \zeta_f > 1 \end{cases}$$

$$X_2(\zeta_f, \tau) = \begin{cases} \dfrac{\sin\sqrt{1-\zeta_f^2}\tau}{\sqrt{1-\zeta_f^2}} & \text{if } \zeta_f \le 1 \\ \dfrac{\sinh\sqrt{\zeta_f^2-1}\tau}{\sqrt{\zeta_f^2-1}} & \text{if } \zeta_f > 1 \end{cases} \tag{22}$$

The first approximation of the rotor-to-stator contact stage duration τ_{dw} can be calculated based on Eqs. (7), (10), and (21) if τ in the expression $[2\zeta_f z'(\tau) + z(\tau)]$ is substituted by the series $\tau_{dw} = \tau_0 + \epsilon\tau_1 + \ldots$. The balance of the first power terms gives the following equation for τ_1:

$$\tau_1 = \left[\Phi_1 + c\left(\beta_-^2 - \frac{1}{p^2}\right)\right]\frac{1+\kappa_{0n}}{\kappa_{0n}z_-'} \tag{23}$$

The first approximations of the radial z_{1+}' and angular β_{1+} velocities at the moment of rotor departure from the contact can be calculated using Eqs. (10), (12), (14), and (21) with accuracy up to the second power of the small parameter ϵ:

$$z_+' = -\kappa_{0n}\left\{z_-' - 2\epsilon\left[\Phi_1 + c\left(\beta_-^2 - \frac{1}{p^2}\right)\right]\zeta_f\right\}$$

$$\beta_+ = \kappa_{0\tau}\beta_- - \frac{a}{c}(1-\kappa_{0\tau}) - \frac{fa\sigma}{c^2}(z_-')(\kappa_{0n}+\kappa_{0\tau}) - 4\epsilon\kappa_{0n}\frac{(\beta_-)(z_-')}{c}\zeta_f + \epsilon F_1\tau_0 \tag{24}$$

The first approximation of the rotor polar coordinates $R_+^{(1)}$, $\psi_+^{(1)}$ at the moment of departure from the contact are the sums of two components, respectively. The first component reflects the influence of the first approximation τ_1 of the dwelling duration on the zero approximation of the coordinates. The second one represents the result of the integration of the first approximation of the angular and radial velocities on the zero approximation to the dwelling duration. Using Eqs. (23) and (24), the resulting expressions for $R_+^{(1)}$, $\psi_+^{(1)}$ are as follows:

$$R_+^{(1)} = \left.\frac{dz_0}{d\tau}\right|_{\tau=\tau_0}\tau_1 + z_1(\tau_0) = -4\kappa_{0n}\frac{\zeta_f^2}{\omega^2}[\Phi_1\omega^2 + c(\dot{\psi}_-^2 - \nu^2)]$$

$$\psi_+^{(1)} = \frac{\omega}{\Omega}\left[(\beta_-)\tau_1 + \int_0^{\tau}\beta_1(\tau)d\tau\right] = \frac{\omega}{\Omega}\left\{[\Phi_1\omega^2 + c(\dot{\psi}_-^2 - \nu^2)]\frac{(1+\kappa_{0n})\dot{\psi}_-}{\kappa_{0n}\omega^2\dot{R}_-} + \frac{F_1\tau_0^2}{2} - 2(\dot{\psi}_-)(\dot{R}_-)[1-\kappa_{0n}(4\zeta_f^2-1)]\right\} \tag{25}$$

Summary of Analytical Results: Rub Impact Model

Since the shaft motions in both radial and tangential directions at the contact stage are relatively small, this entire stage can be considered as a transformation mapping of the starting point to the ending point of the contact:

$$t_- \to t_+, \quad t_+ = t_- + t_{dw}$$
$$\dot{R}_- \to \dot{R}_+, \quad \dot{\psi}_- \to \dot{\psi}_+, \quad R_- \to R_+, \quad \psi_- \to \psi_+ \tag{26}$$

When using relationships obtained in the previous section, and returning to the original polar variables, the final results for the first order approximation of the rotor rub-related responses are as follows:

$$t_{dw}=\sqrt{\frac{M}{K_f}}\tau_0+\frac{M}{K_f}\frac{1+\kappa_{0n}}{\kappa_{0n}\dot{R}_-}\left[\omega^2\Phi_1+c\left(\dot{\psi}_-^2-\frac{K}{M}\right)\right]; \quad (27)$$

$$\dot{R}_+=\kappa_{0n}\left\{\dot{R}_- -2\sqrt{\frac{K}{K_f}}\left[\omega^2\Phi_1+c\left(\dot{\psi}_-^2-\frac{K}{M}\right)\right]\right\}; \quad (28)$$

Table 1 Rotor-to-stator rub: parameters used in numeric simulation

Case No.		R.1	R.2	R.3
$\frac{K_x}{K_y}$	—	1	1	0.65
$\sqrt{\frac{K_x}{K_f}}$	—	0.0816	0.0816	0.073
$\sqrt{\frac{K_f}{M}}$	1/s	3000	3000	3000
$\frac{D}{2\sqrt{K_fM}}$	—	0.015	0.015	0.015
$\frac{D_f}{2\sqrt{K_fM}}$	—	0.25	0.25	0.25
$\frac{mr}{MC}$	—	0.0857	0.0857	0.0857
$\frac{S}{K_yC}$	—	6.76×10^{-4}	8.69×10^{-4}	8.69×10^{-4}
$f\frac{a}{C}$	—	0.2	0.2	0.2
D_{cont}	kg/s	0	0	0
γ	deg	270	270	270

$$\dot{\psi}_+=\kappa_{0\tau}\dot{\psi}_- -\frac{a\omega}{c}(1-\kappa_{0\tau})-\frac{fa}{c^2}(\dot{R}_-)(\kappa_{0n}+\kappa_{0\tau})\text{sign}\left(\dot{\psi}_-+\frac{a\omega}{c}\right)$$
$$-2\frac{K_f}{D_f}\kappa_{0n}\frac{(\dot{\psi}_-)(\dot{R}_-)}{c}+\sqrt{\frac{M}{K_f}}\tau_0\omega^2F_1$$
$$\text{if sign}\left(\dot{\psi}_++\frac{a\omega}{c}\right)=\text{sign}\left(\dot{\psi}_-+\frac{a\omega}{c}\right); \quad (29)$$

$$\dot{\psi}_+=-\frac{a\omega}{c} \quad \text{if sign}\left(\dot{\psi}_++\frac{a\omega}{c}\right)\neq\text{sign}\left(\dot{\psi}_-+\frac{a\omega}{c}\right); \quad (30)$$

$$R_+=c+\kappa_{0n}\frac{D_f}{\omega\sqrt{K_fM}}\left[\dot{R}_- -\frac{D_f}{\omega\sqrt{K_fM}}\left(\omega^2\Phi_1+c\left(\dot{\psi}_-^2-\frac{K}{M}\right)\right)\right]; \quad (31)$$

$$\psi_+=\psi_-+\left(\dot{\psi}_- -\frac{\sigma fa}{\Omega c^2}\dot{R}_-\right)\tau_0+\frac{\sigma fa}{c^2}\frac{K_f}{D_f}\kappa_{0n}\dot{R}_-$$
$$+\frac{M}{K_f}\left\{\frac{(1+\kappa_{0n}}{\kappa_{0n}\dot{R}_-}\dot{\psi}_-\left[\omega^2\Phi_1+c\left(\dot{\psi}_-^2-\frac{K}{M}\right)\right]+\frac{\tau_0^2}{2}\omega^2F_1\right.$$
$$\left.-2(\dot{\psi}_-)(\dot{R}_-)[1+\kappa_{0n}(1-(D_f/K_f)^2)]\right\}. \quad (32)$$

The rotor system presented in Fig. 1 has two stages of motion: free uncoupled stage without contact described by Eq. (2), and impacting stage, when the contact is maintained between rotor and stator. The last stage is described by Eqs. (26) to (32). The switch from the free stage to the impact occurs when $R=c$, $\dot{R}>0$.

Expression (32), which describes the impact angular position with the accuracy up to the second power of the small parameter defined as $\epsilon=\omega/\Omega=\omega\sqrt{\frac{M}{K_f}}$, depends on the angles between the normal line at the point of contact and the radial load force $(\gamma-\psi_-)$, as well as between the normal line and the unbalance force $[(\varphi_-)-(\psi_-)]$. For example, Eq. (27) yields

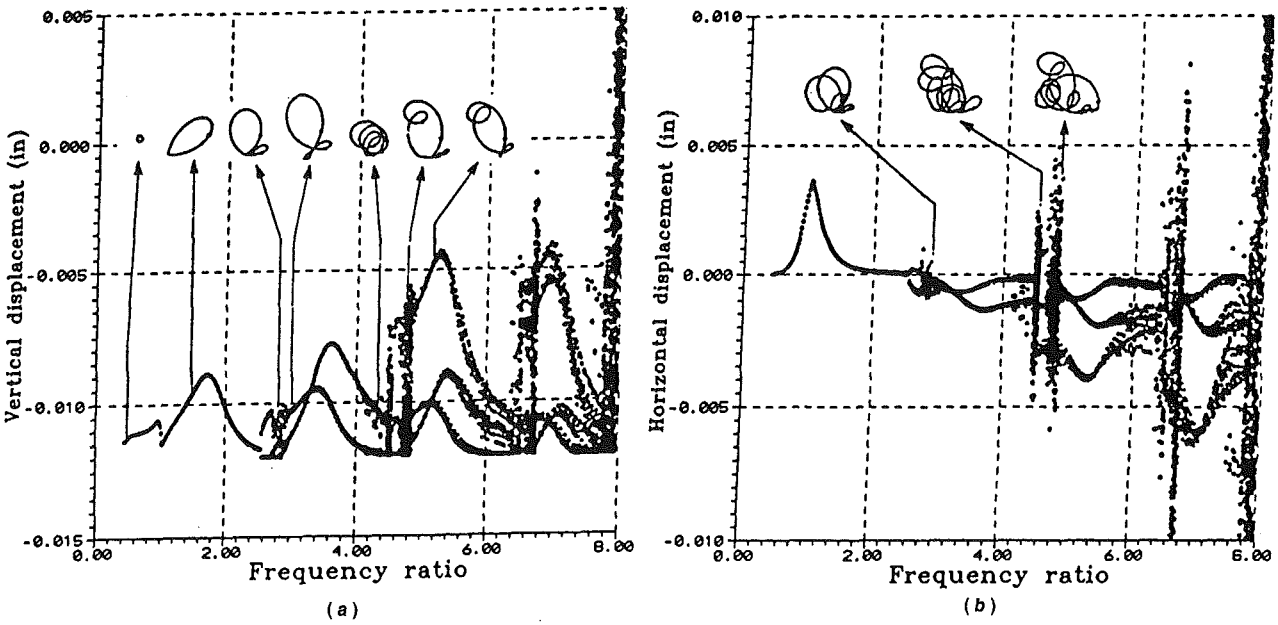

Fig. 4 Bifurcation diagrams: rotor vertical (*a*) and horizontal (*b*) displacements versus rotative frequency-to-natural frequency $\sqrt{K/M}$ ratio with a sequence of orderly regime orbits (*a*), and chaotic regime orbits (*b*). For case R.1 (Table 1) of isotropic lightly radially loaded rotor. Semi-elastic impact, $\kappa_{0n}=0.5$ (Eq. (13)).

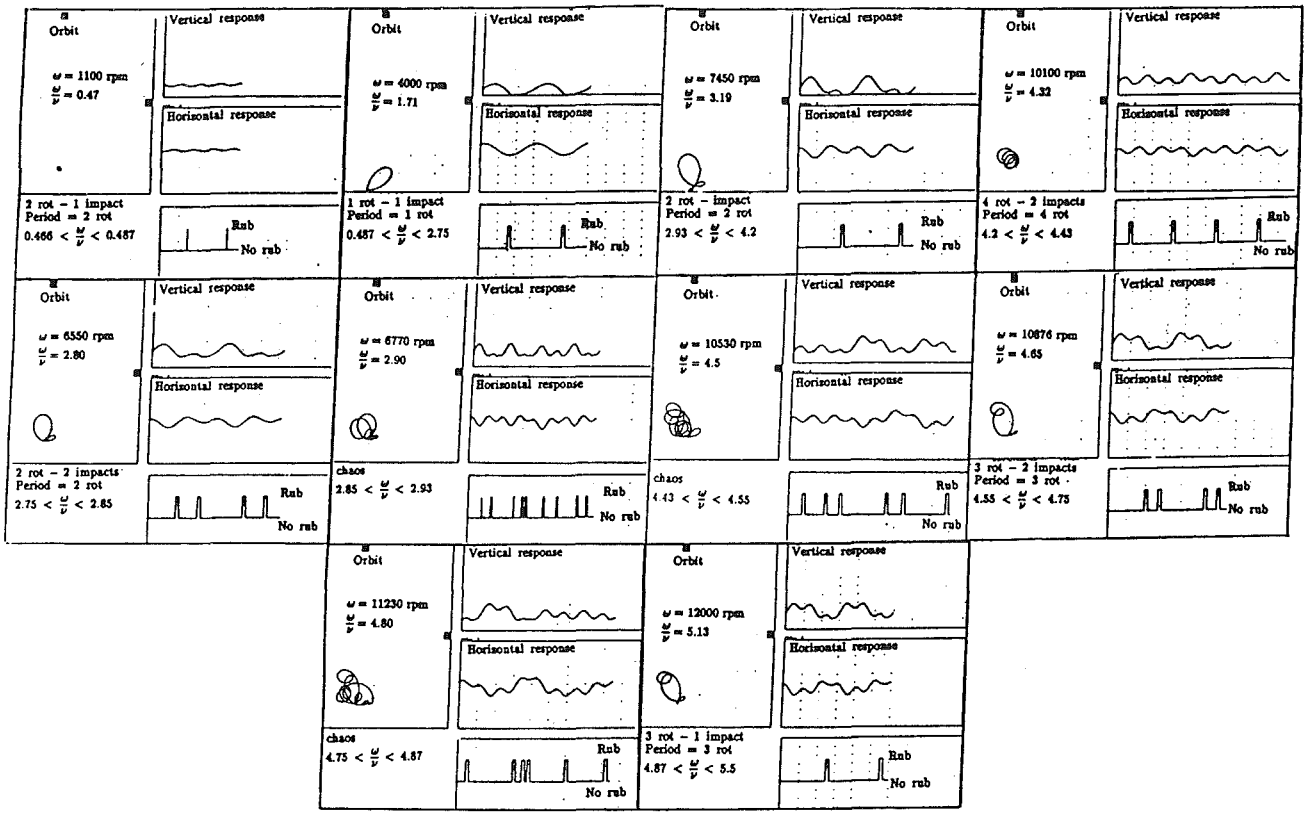

Fig. 5 Sequence of rotor time-base waveforms and orbits for the case R.1 of isotropic lightly radially loaded rotor (Table 1). Amplitude scale = 3.2 mil/div. The orbits presented are typical in the indicated bands of the frequency ratio.

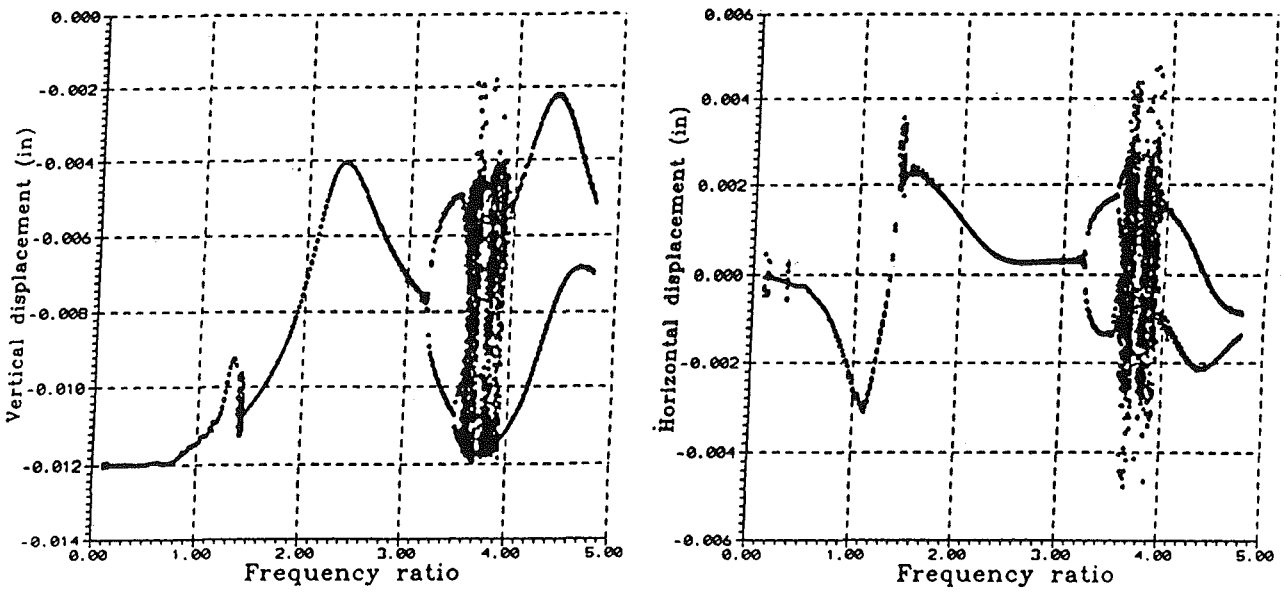

Fig. 6 Bifurcation diagrams: rotor vertical and horizontal displacements versus rotative frequency-to-rotor natural frequency ratio for the case of isotropic highly radially loaded rotor, case R.2 (Table 1). Semi-elastic impact, $\kappa_{0n} = 0.5$.

that the maximum dwelling time occurs when $\psi_- = \gamma + 2\pi i$, $\varphi_- = \gamma + 2\pi l$ (l, i are integers). It means that, in that case, unbalance and radial forces have the direction opposite to the direction of the normal line. Therefore, the radial motion of the rotor at the moment of departure from the contact is opposed by the unbalance and radial forces. This case corresponds to the minimum absolute value of the radial velocity R_+ of the rotor departing from the contact. The angular velocity of precession $\dot{\psi}_+$, in this case, does not depend on the external forces since they have perpendicular direction to the tangential component of velocity.

Results of the Numerical Simulations

The model of rotor-to-stator contact impact developed in previous section is used for numerical simulation of the rotor

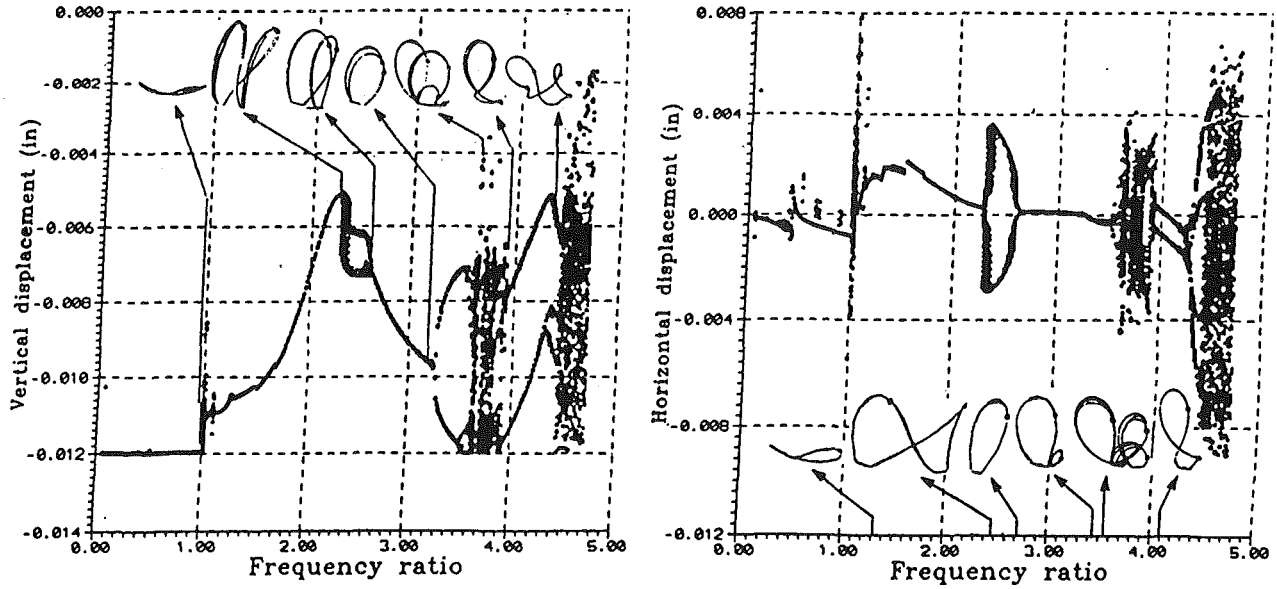

Fig. 7 Bifurcation diagrams: rotor vertical and horizontal displacements versus rotative frequency-to-rotor natural frequency $\sqrt{K_x/M}$ ratio for the case of anisotropic, highly radially loaded rotor, case R.3 (Table 1) accompanied by some orbits. Note different orbit scales specified in Fig. 8. Semi-elastic impact, $\kappa_{0n}=0.5$.

response. The numerical values of the parameters chosen for the numerical simulation are shown in Table 1, and the results are illustrated in Figs. 4 to 8. Case R.1 represents lightly radially loaded isotropic, one-lateral-mode rotor with isotropic supports; Cases R.2 and R.3 show the behavior of heavily radially loaded rotors with isotropic and anisotropic supports, respectively. In all cases the parameters were chosen so that partial rub was maintained in the entire range of relative speeds. For the chosen parameters, the integration of the differential equations describing the system was performed in a wide range of the rotative speed. The latter was incremented with 30 rpm. At every rotative speed, the data started to be sampled after 200 rotations in order to eliminate transient regimes. When the steady-state regime was established, 100 consecutive once-per-rotative speed marks (Keyphasor marks), which appear on the vibration response waveforms, were recorded. If the vibrational regime (response) was periodic, the Keyphasor marks appeared at constant positions for any number of rotations. For a steady synchronous ($1\times$) regime, there will be one constant position, that is one mark. For a steady subsynchronous regime of 1/2, there will be two constant Keyphasor positions, etc. Chaotic regimes result in multiple positions, sampled through consecutive 100 rotations. These results are presented in the form of bifurcation diagrams versus frequency ratio, where the observed variables are vertical y and horizontal x displacements (Figs. 4, 6, 7). The bifurcation diagrams obtained by the described technique are known as brute-force bifurcation diagrams (Parker and Chua, 1989). Some bifurcation diagrams are accompanied by sequences of typical orbits of the rotor precessional motion. The rotor orbits represent the actual path of the rotor centerline in the x–y plane. As it follows from observation of the rotor waveforms and contact data (Figs. 5, 8), the change from one regime to the other occurs when inside one oscillation period the number of contact occurrences changes.

In all considered cases there exist frequency ratio ranges exhibiting orderly harmonic ($1\times$) and subharmonic ($1/2\times$, $1/3\times$ . . .), as well as chaotic patterns of responses. The latter not only occur as transitions from one to another harmonic regime, such as $1\times$, $1/2\times$ (Figs. 4, 6, 7).

The case R.3 differs from R.2 (Table 1) by taking into account the rotor support stiffness anisotropy. Lower overall stiffness of the system in case R.3 causes slightly lower response amplitude level. The anisotropy results in an additional $1/2\times$ regime (named "butterfly rub," associated with the specific orbit patterns (Bently et al., 1992)) occurring in the range between frequency ratio 2.3 and 2.6. The orbits obtained by numerical simulation for that case correspond very well to those obtained experimentally on the rubbing rotor rig (Fig. 9). The details of the experiment can be found in the report by Bently et al. (1992).

Final Remarks

This paper presented the analytical and numerical simulation of unbalanced rotor rubbing against the stator. The rotor vibrational behavior is characterized by orderly harmonic and subharmonic responses, as well as by a chaotic pattern of vibrations. The most important result presented in this paper is the development of a more adequate impact model. The impact dynamic effects in similar systems discussed in the available references were usually modeled in very simplified forms. The model developed here takes into account the local stator stiffness and radial/tangential damping parameters, and correlates them with the globally considered impacting body, that is, with rotor parameters. During the impact of a rotating shaft against a stationary element, not only the radial (straight impact) effects are taken into consideration, but also, due to shaft rotation, the tangential effects. The latter are sometimes called "super ball" effects (Szczygielski, 1987). The correlation of the local contact conditions, and global dynamic behavior of the rotor presented in this paper, throws a new light on the problem of adequate modeling of the mechanical systems with intermittent, partial rubbing. In the wide frequency range, the numerical results showed the sequence of subharmonic and chaotic regimes strongly correlated with the number of impacts per oscillation. The obtained orbits are typical for the real rubbing rotor responses (Muszynska et al., 1990; Ehrich, 1991). For the lower orders of harmonic and subharmonic vibrations ($1\times$ and $1/2\times$), the dominant, with the widest frequency ranges, are one-impact-per-oscillation periodic regimes. All other regimes represent bifurcation and transition between the latter. The same is true for $1/3\times$ oscillation, but the tendency of the multi-impacting and chaotic regimes to increase their

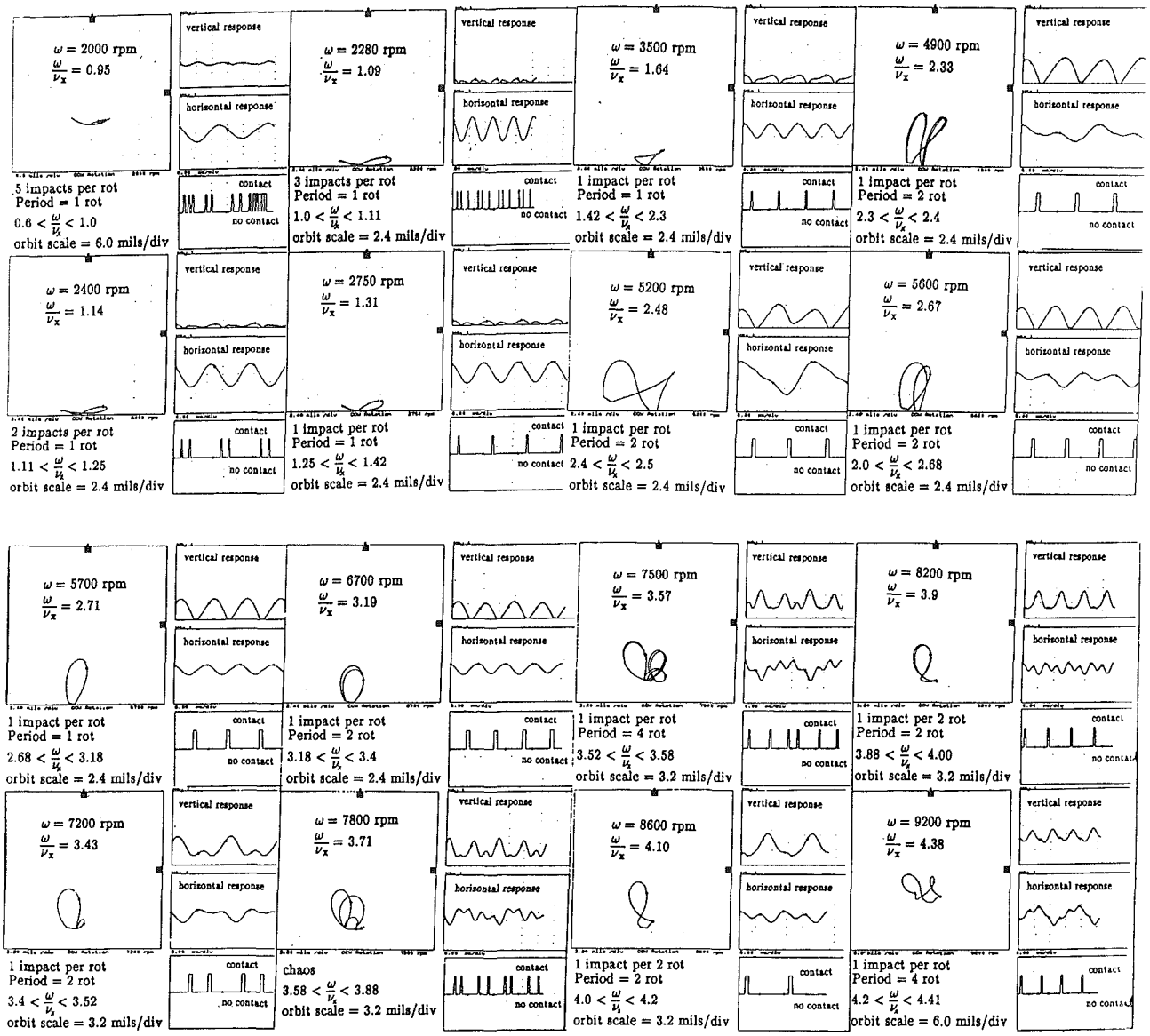

Fig. 8 Sequence of rotor time-base waveforms and orbits for the case R.3 of anisotropic highly radially loaded rotor (Table 1). The orbits presented are typical in the indicated bands of the frequency ratio.

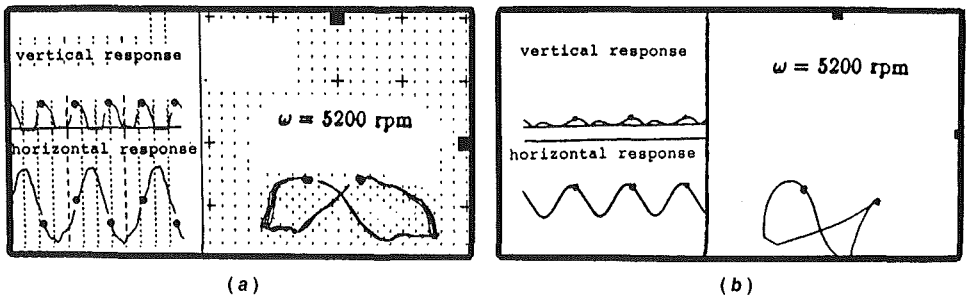

(*a*) (*b*)

Fig. 9 Time-base waveforms of the rubbing anisotropic rotor response at 5200 rpm: (*a*) experimental results (Bently et al., 1992), (*b*) analytical results (see Fig. 8). Rotor rotation is counterclockwise.

frequency band was noted. This indicates an increasing intensity of the chaotic motion generation at higher rotative frequency.

Another result worth mentioning is an insight into the influence of mixed viscous/dry friction forces, as well as rotor anisotropy on the rub-related responses.

References

Bently, D. E., Grant, J. W., and Goldman, P., 1992, "A 'Butterfly' Rub Response," *Bently Rotor Dynamics Research Corporation*, BRDRC Report 3.

Ehrich, F. F., 1988, "High Order Subharmonic Response of High Speed Rotors in Bearing Clearance," ASME *Journal of Vibration, Acoustics, Stress, and Reliability in Design*, Vol. 110, pp. 9–16.

Ehrich, F. F., 1991, "Observations of Subcritical Superharmonic and Chaotic

Response in Rotordynamics," *Rotating Machinery and Vehicle Dynamics*, ASME DE-Vol. 35, pp. 1–9.

Evan-Iwanowski, R. M., and Chu-Ho Lu, 1991, "Transitions Through Period Doubling Route to Chaos," *Vibration Analysis—Analytical and Computational*, ASME DE-Vol. 37, pp. 135–146.

Goldman, P., and Muszynska, A., 1991, "Analytical and Experimental Simulation of Loose Pedestal Dynamic Effects on a Rotating Machine Vibrational Response," *Rotating Machinery and Vehicle Dynamics*, ASME DE-Vol. 35, pp. 11–17.

Gonsalves, D., Neilson, R. D., and Barr, A. D. S., 1992, "Response of a Discontinuously Nonlinear Rotor System," *Proc. of "Rotordynamic 92,"* Venice, Italy, pp. 182–189.

Muszynska, A., 1989, "Rotor-to-Stationary Element Rub-Related Vibration Phenomena in Rotating Machinery," Literature Survey, *The Shock and Vibration Digest*, Vol. 21, No. 3, pp. 3–11.

Muszynska, A., Franklin, W. D., and Hayashida, R. D., 1990, "Rotor-to-Stator Partial Rubbing and Its Effects on Rotor Dynamic Response," NASA CP 3122, College Station, TX, pp. 345–362.

Muszynska, A., and Goldman, P., 1993, "Chaotic Vibrations of Rotor/Bearing/Stator Systems With Looseness or Rub," presented at the ASME Vibration Conference, Albuquerque, NM.

Parker, T. S., and Chua, L. O., 1989, *Practical Numerical Algorithms for Chaotic Systems*, Springer-Verlag, New York.

Szczygielski, W. M., 1987, "Application of Chaos Theory to the Contacting Dynamics of High-Speed Rotors," *Rotating Machinery Dynamics*, Proc. of ASME 11th Biennial Conference of Vibration and Noise, Boston, MA, pp. 319–326.

Thompson, J. M. T., and Ghaffari, R., 1982, "Chaos After Period Doubling Bifurcation in the Resonance of an Impact Oscillator," *Physics Letters*, Vol. 91A, No. 1.

On Curve Veering and Flutter of Rotating Blades

D. Afolabi[1]
Department of Mechanical Engineering,
Purdue University,
Indianapolis, IN 46202
and
Institute for Computational Mechanics
in Propulsion,
NASA Lewis Research Center,
Cleveland,OH 44135

O. Mehmed
NASA Lewis Research Center,
Cleveland, OH 44135

The eigenvalues of rotating blades usually change with rotation speed according to the Stodola-Southwell criterion. Under certain circumstances, the loci of eigenvalues belonging to two distinct modes of vibration approach each other very closely, and it may appear as if the loci cross each other. However, our study indicates that the observable frequency loci of an undamped rotating blade do not cross, but must either repel each other (leading to "curve veering"), or attract each other (leading to "frequency coalescence"). Our results are reached by using standard arguments from algebraic geometry—the theory of algebraic curves and catastrophe theory. We conclude that it is important to resolve an apparent crossing of eigenvalue loci into either a frequency coalescence or a curve veering, because frequency coalescence is dangerous since it leads to flutter, whereas curve veering does not precipitate flutter and is, therefore, harmless with respect to elastic stability.

1 Introduction

Rotating blades are commonly encountered in a variety of mechanical and aeronautical structures such as turbines, compressors, propfans, and helicopters. It is well known that such blades may flutter when a sufficiently high critical speed is reached or exceeded. There are basically two types of flutter—"single mode flutter" and "coalescence flutter." This study is mainly about coalescence flutter.

The problem of flutter in general is of vital importance not only in the case of rotating blades, but also with respect to various engineering structures and components in aeronautics and space applications. At the Lewis Research Center of the National Aeronautics and Space Administration, a variety of theoretical and experimental investigations of flutter is currently in progress. In this paper, we present a summary of a theoretical investigation of the flutter of rotating blades using mathematical techniques from algebraic geometry, i.e., catastrophe theory (Arnol'd, 1983), and the theory of real algebraic curves (Brieskorn, 1986).

An important conclusion from our investigation is the following. Frequency loci belonging to two distinct modes of vibration will intersect each other only when the *coupling* between the two modes is assumed to be completely absent. On the other hand, the presence of a small but nonvanishing amount of coupling will cause the two loci either to repel each other (leading to curve veering), or to attract each other (leading to frequency coalescence). Frequency crossing is illustrated in Fig. 1(*a*), while curve veering and frequency coalescence are depicted, respectively, in Figs. 1(*b*) and 1(*c*). Curve veering is commonly called "avoided crossing," especially in the physics literature. The term "curve veering" seems to have been introduced to the engineering literature by Leissa (1974) in his study of the eigenvalues of rectangular plates, while frequency coalescence is well known in aeroelasticity as "coupled mode flutter" (Bisplinghoff and Ashley, 1962).

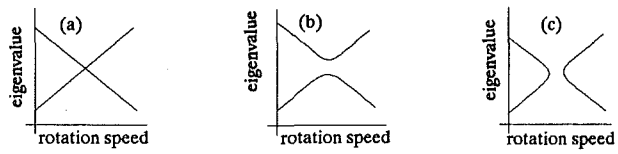

Fig. 1 (*a*) Frequency crossing; (*b*) curve veering; and (*c*) frequency coalescence

The procedure used in arriving at our main result originates from the *qualitative method* of mathematical models. The qualitative method was initiated by Poincaré (1892) for the study of differential equations. It was developed further by Andronov and his co-workers (1966), who introduced the concept of "structural stability." The structural stability idea was further developed by Thom (1972) into *catastrophe theory*—"a general theory of models" for applications in the physical, social, and biological sciences.

There exist several studies in the literature on rotating blades where a crossing of eigenvalue loci, as in Fig. 2(*a*), has been reported. For examples, one may cite the studies of MacBain (1975, his Fig. 10), Chen and Dugundji (1984, Fig. 5), Ramamurti and Kielb (1984, Figs. 4 and 10), among others. It is also remarkable that, in two different theoretical studies of the same system of SR-5 blades recently carried out for NASA Lewis Research Center by two independent contractors, one study reports a crossing of eigenvalue loci whereas the other study does not. The principal reason why crossings of eigenvalue loci have been published by many investigators is that the small but inevitable amount of coupling between two interacting modes (such as bending and torsion) is usually ignored by such investigators.

[1]On leave. Temporary address: Room 3-360, Department of Mechanical Engineering, MIT, Cambridge, MA 02139.

Contributed by the International Gas Turbine Institute and presented at the 38th International Gas Turbine and Aeroengine Congress and Exposition, Cincinnati, Ohio, May 24-27,1993. Manuscript received at ASME Headquarters March 1, 1993. Paper No. 93-GT-148. Associate Technical Editor: H. Lukas.

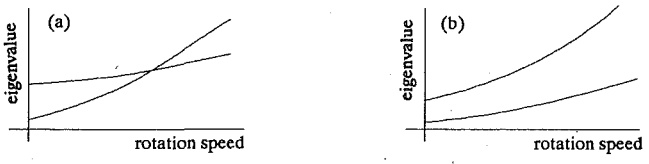

Fig. 2 Variation of resonance frequencies with rotation speed showing (*a*) intersecting loci; (*b*) diverging loci

In practice, as distinct from theory, a small amount of coupling is unavoidable when two eigenvalue loci approach each other very closely; see Section 2.3. This *coupling* could be "conservative" or "nonconservative" in the terminology of Crandall and Mroszczyk (1988).Conservative coupling leads to curve veering, whereas nonconservative coupling leads to frequency coalescence. The role of coupling on curve veering has been discussed by Perkins and Mote (1988). However, the influence of coupling on the topology of eigenvalue loci is, in general, usually overlooked or considered to be inconsequential by most investigators, in their theoretical models of flutter of rotating blades. Consequently, the prediction from a large number of theoretical studies is that two or more eigenvalue loci do intersect one another. Such a prediction is, however, in serious qualitative error, and it has particular significance in propulsion systems in which the blading has a low mass ratio.

2 Eigenloci Crossing, Veering, or Coalescence

In this section, we carry out a background discussion on the phenomena of frequency crossing, curve veering, and eigenvalue coalescence. Our prototype element in this discussion is the locus of an eigenvalue of a rotating blade as a function of the rotation speed.

2.1 Variation of Eigenvalues With Rotation Speed. It is now well known, due to the works of Stodola (1914), Lamb and Southwell (1921), and Southwell (1922), that the natural frequencies of a rotating blade or uniform disk vary approximately as quadratic functions of the rotation speed, i.e.,

$$\omega_m^2(\Omega) = \omega_m^2(0) \pm s_m \Omega^2, \tag{1}$$

where m denotes a mode of vibration, Ω is the rotation speed, $\omega_m(\Omega)$ is the natural frequency at that speed, $\omega_m(0)$ is the bench natural frequency, measured when the rotation speed is zero, and $s_m > 0$ is a Stodola–Southwell coefficient for the mth mode of vibration. Formua (1) is widely attributed to Southwell but, according to Campbell (1924, p. 53), the formula was independently derived earlier by Stodola (1914). The formula derived by Southwell relates to uniform circular *disks*, while that of Stodola was derived for turbine *blades*. In any case, experience has shown that Eq. (1) yields acceptable results not only for turbine blades and uniform circular disks, but also for other types of rotating structures such as helicopter blades, propellers, bladed disk assemblies, cylinders, etc.

2.2 Intersection of Projected Eigenvalue Loci. Consider a rotating blade modeled as a vibrating system having two degrees of freedom, such that there is no coupling between the two modes of vibration. The two uncoupled natural frequencies of the system will individually vary as functions of the rotation speed. For example, the second bending and first torsional frequencies of a rotating blade generally exhibit a variation with rotation speed. Let the natural frequencies at the nonrotating condition of the bending and torsion modes for such a blade be written as $\omega_B^2(0)$ and $\omega_T^2(0)$, respectively. The frequency loci of the bending mode $\omega_B(\Omega)$ and the torsion mode $\omega_T(\Omega)$ may appear as if they cross each other eventually at the rotation speed Ω^*, as illustrated in Fig. 2(*a*). Alternatively, the frequencies may diverge from each other, as illustrated in Fig. 2(*b*). This follows from the fact that the Stodola–Southwell coefficients are not likely to be exactly equal for the two modes, so that the two frequency loci would not be curvilinearly "parallel."

As indicated earlier, there exist many studies in the literature on rotating blades where crossings of eigenvalue loci as in Fig. 2(*a*) have been reported. However, although eigenvalue loci may *apparently* intersect, further analysis leads one to the conclusion that, in fact, such loci do *not* cross. The loci may approach each other arbitrarily closely, but they do not cross.

2.3 Eigenvalue Loci of Rotating Blades Do Not Cross. Observable frequency loci of rotating blades do not cross as a rule. There are at least two reasons why frequency loci cannot cross each other in a realistic model of rotating blades. The first follows from mathematical reasoning, and the other from physical or engineering considerations.

The mathematical reason why a crossing does not occur in the frequency loci of realistic models of rotating blades is due to the fact that such a crossing signifies *degenerate* eigenvalues, and degenerate mathematical objects are "structurally unstable," according to a corollary of the weak transversality theorem (Thom and Levin, 1959). As a result of the structural instability of degenerate objects, they are unobservable. Under the smallest perturbation, such degenerate and unobservable objects undergo a bifurcation and split into two or more structurally stable "generic" objects, which then become observable. This idea, called an "unfolding" by Thom, is very inportant in catastrophe theory (Thom, 1972), the theory of singularities of differentiable mappings, (Arnol'd et al., 1985), and the theory of algebraic curves (Brieskorn, 1986).

The physical or engineering reason why a crossing of loci cannot be observed is due to the inevitable existence of a *coupling* between two or more modes in a vibrating system when such modes approach each other arbitrarily closely. This is called modal "interference," mode "coupling," or modal "interaction" in vibration analysis; see, for instance, Afolabi (1991). It is convenient to illustrate the foregoing with a two degree of freedom undamped system. If the two eigenvalues of such a system are equal (at the critical rotation speed at which the loci purportedly intersect), it would imply that the system has degenerate eigenvalues at that critical speed. However, the only way a coupled two degree of freedom system can have degenerate eigenvalues is when the system disintegrates into two identical, *uncoupled* subsystems, so that $\omega_1 = \omega_2$. But this would violate the assumption that the two degree of freedom system constitutes a *coupled* system, leading to a contradiction.

Although crossings of the eigenvalue loci of rotating blades do not occur in practice, such crossings are frequently reported in various publications in structural dynamics. In those theoretical studies where crossings have been reported, one finds that simplifying assumptions have usually been made (implicitly or otherwise) leading to a loss of modal coupling. In the case of experimental studies, what seems to be frequency crossings have been reported because, typically, it is very difficult or expensive to record the large number of data points that are required in the neighborhood of an assumed crossing, so that the experimenter is unable to resolve whether a crossing has actually taken place or not. If a special effort is made to gather sufficient data points in the neighborhood of the assumed crossing, then one may be able to resolve the presumed crossing into either an avoided crossing or a frequency coalescence.

2.4 Coalescence of Eigenvalue Loci Induces Flutter. In general, the quantitative difference between the eigenvalues in

systems exhibiting a crossing, an avoided crossing, or a frequency coalescence, is usually very small, except in the neighborhood of a crossing. Yet, for qualitative reasons, it is important to resolve an apparent crossing into a coalescence or veering. The importance of this lies in the fact that a frequency coalescence is a dangerous event, since it leads to flutter, whereas a curve veering does not usually lead to flutter and is, thus, relatively harmless.

If, in a flutter analysis, one mistakenly predicts a frequency coalescence condition as a frequency crossing or a curve veering, then evidently one has erroneously downgraded an unsafe flutter condition to a safe condition, with potential catastrophic consequences. Because there is a considerable qualitative difference between the dynamics of a system exhibiting frequency coalescence on the one hand, and a system characterized by curve veering or avoided crossing on the other hand, it is absolutely important to resolve an apparent crossing into either a frequency coalescence or a curve veering.

3 Mode Coupling

The existence or otherwise of *mode coupling* lies at the heart of a resolution of the question as to whether a frequency crossing does or does not occur in a realistic model of rotating blades. This question cannot be resolved by using many of the theoretical models currently employed in engineering analysis in which the small but nonzero coupling that takes place when two modes approach each other arbitrarily closely in real systems is assumed to be completely nonexistent. In what follows, we give three causes of mode coupling in rotating blades to support the view point that mode coupling should not be assumed to be completely absent.

3.1 Mode Coupling Induced by Imperfection. In theoretical analyses of an assembly of rotating blades, it is frequently assumed that all the blades (on a turbine disk, or in a helicopter rotor, for example) are completely identical. Such a model is called a "tuned" system. A theoretical model in which the effects of small amounts of imperfection or asymmetry are accounted for is called a "mistuned" model. However, it is impossible to manufacture all the blades in an assembly in such a way that they are all identical. Furthermore, small amounts of imperfection are also introduced into the system when the blades are mounted on the disk or hub. Moreover, wear and tear during normal operating conditions are inevitable, and these further introduce another level of imperfection. The probability that all these imperfections will somehow cancel one another out so that all the blades end up being exactly identical, is almost zero. Therefore, one must conclude that perfect geometric symmetry does not exist in a system of rotating blades. This lack of perfect geometric symmetry has serious physical consequences—it induces mode coupling.

It is easy to verify that curve veering is induced by imperfection or "mistuning." First, one sets up a theoretical model accounting for mistuning (i.e., imperfection or geometric asymmetry). Then the mistuning parameter is set to zero in one study, and to a nonzero value in another study, and the results of the two studies are compared.

For example, consider a simple lumped parameter model of a centrifugally loaded vibrating system with three degrees of freedom in which gyroscopic forces are ignored. Let k_c be a nominal coupling stiffness, k_g a "grounding" stiffness, and ϵ a mistuning or imperfection parameter. The following quasi-circulant matrix form of the equations of motion of the mistuned cyclic system may be written:

$$\ddot{\mathbf{x}} + \mathbf{K}\mathbf{x} = 0, \tag{2a}$$

$$\mathbf{x}^T = \{x_1, x_2, x_3\}, \tag{2b}$$

and

$$\mathbf{K} = \begin{bmatrix} (k_g + 2k_c - \Omega^2) & -k_c & -k_c \\ -k_c & (k_g + 2k_c - \Omega^2) \pm \epsilon & -k_c \\ -k_c & -k_c & (k_g + 2k_c - \Omega^2) \end{bmatrix}. \tag{2c}$$

When the eigenvalues of system (2) are plotted against the rotation speed, two loci belonging to two distinct modes of vibration would cross at $\Omega = 0$ when $\epsilon = 0$. However, when the mistuning parameter is set to $\epsilon \neq 0$, the loci do not cross at $\Omega = 0$ but veer away from each other. The occurrence of curve veering is an evidence that a coupling of modes has taken place. This is analogous to what Poincaré calls the principle of "exchange of stabilities," and which may be called the principle of "exchange of modes" in our context.

A more detailed consideration of the influence of imperfection on the flutter of rotating blades has been carried out in a recent study by Wang and Chopra (1992) in connection with helicopter blades.

3.2 Mode Coupling Induced by Asymmetry. In addition to imperfection, mode coupling is also induced by geometric asymmetry. In theoretical models of a rotating blade, for example, it is frequently assumed that the *cross section* of the blade is perfectly symmetric, so that the elastic and geometric axes coincide. In such an idealized case, there is no coupling whatsoever between the bending and torsional motions of the blade. Thus, a crossing of the bending and torsion eigenvalue loci may be reported from a study made using such a model.

However, in practical cases, an arbitrarily small amount of asymmetry of the cross section is unavoidable during the manufacturing process. Thus, there always exists a *small* but nonvanishing offset between the geometric and elastic axes, and this leads to a coupling of modes. Consequently, asymmetry in the geometric section or profile of a rotating blade is another source of mode coupling.

3.3 Mode Coupling Induced by Gyroscopic or Circulatory Forces. Even if a single rotating blade had perfectly symmetric geometric properties, or all traces of imperfections were somehow made to vanish completely in an assembly of blades, there exists yet another source of coupling one has to contend with, and that is from *rotation* and the *aerodynamic* environment.

Some coupling is introduced by gyroscopic forces, or other skew-symmetric forces induced by rotational velocity, or angular momentum. These are also called "Coriolis forces." Some coupling is also introduced by skew-symmetric forces induced by displacement, and these are sometimes called "circulatory forces." Whereas gyroscopic coupling arises mainly from rotation, circulatory coupling originates mainly from aerodynamics. In some systems, both gyroscopic and circulatory coupling may be present at the same time.

4 Conservative and Nonconservative Coupling

A mathematical analysis of the vibration of a multi-degree of freedom system may be made in physical coordinates or in modal coordinates. The equations of motion are usually coupled in physical coordinates, and generally uncoupled in modal coordinates (for systems without damping, or with proportional damping). This is the case when the modes are not subject to parametrically dependent coupling.

If the modal characteristics of a vibrating system depend on a parameter such as rotation speed, then although the equations of motion in modal coordinates may be uncoupled at a given rotation speed where the modes are well separated, there nevertheless will be a coupling of modes at another rotation speed when the modes become so close that they interact.

If, for example, one makes a two-mode approximation of a rotating blade, one may *assume* that there is no parametric coupling whatsoever between the two modes. In that case, one may write the following equations of motion for vibrations, in the modal coordinates of bending and torsion for example, as

$$\begin{bmatrix} 1 & 0 \\ 0 & 1 \end{bmatrix} \begin{Bmatrix} \ddot{\phi}_B \\ \ddot{\phi}_T \end{Bmatrix} + \begin{bmatrix} \omega_B^2(0) + s_B\Omega^2 & 0 \\ 0 & \omega_T^2(0) + s_T\Omega^2 \end{bmatrix} \begin{Bmatrix} \phi_B \\ \phi_T \end{Bmatrix} = 0. \quad (3)$$

Without loss of generalization, unit modal mass has been assumed in the above. The eigenvalue matrix, **A**, as in $\mathbf{Au} = \lambda\mathbf{u}$, of system (3) may be written as

$$\mathbf{A} = \begin{bmatrix} \omega_B^2(0) + s_B\Omega^2 - \lambda & 0 \\ 0 & \omega_T^2(0) + s_T\Omega^2 - \lambda \end{bmatrix} \quad (4)$$

where $\lambda = \omega^2(\Omega)$.

Because of the assumption that there is no modal coupling in Eqs. (3) or (4), the frequency loci are given by the equations

$$\lambda_1 = \omega_1^2(\Omega) = \omega_B^2(0) + s_B\Omega^2; \; \lambda_2 = \omega_2^2(\Omega) = \omega_T^2(0) + s_T\Omega^2. \quad (5)$$

These loci will either intersect or diverge, as in Figs. 2(*a*) or 2(*b*), respectively.

However, one may also assume that a parametric coupling does indeed exist between the bending and torsion modes. In that case, this coupling could be enforced in modal coordinates either as a *conservative coupling*, or as a *nonconservative coupling*; see, for instance, Crandall and Mroszczyk (1988).

4.1 Conservative Coupling in Modal Coordinates. If we consider a system without damping, then a coupling could take place between two modal coordinates, either in the modal mass matrix, or the modal stiffness matrix.

Assuming unit mass modal mass matrix, as before, and if we let $\beta \equiv \beta(\Omega)$ represent the coupling strength in the modal mass matrix while the modal stiffness matrix is uncoupled, one gets the following equations of motion in modal coordinates:

$$\begin{bmatrix} 1 & -\beta \\ -\beta & 1 \end{bmatrix} \begin{Bmatrix} \ddot{\phi}_B \\ \ddot{\phi}_T \end{Bmatrix} + \begin{bmatrix} \omega_B^2(0) + s_B\Omega^2 & 0 \\ 0 & \omega_T^2(0) + s_T\Omega^2 \end{bmatrix} \begin{Bmatrix} \phi_B \\ \phi_T \end{Bmatrix} = 0. \quad (6)$$

Alternatively, one may assume that the conservative coupling exists in the modal stiffness matrix but not in the modal mass matrix. In that case, the modal equations of motion may be written as

$$\begin{bmatrix} 1 & 0 \\ 0 & 1 \end{bmatrix} \begin{Bmatrix} \ddot{\phi}_B \\ \ddot{\phi}_T \end{Bmatrix} + \begin{bmatrix} \omega_B^2(0) + s_B\Omega^2 & -\beta \\ -\beta & \omega_T^2(0) + s_T\Omega^2 \end{bmatrix} \begin{Bmatrix} \phi_B \\ \phi_T \end{Bmatrix} = 0. \quad (7)$$

In either case, one gets a linear algebraic eigenvalue problem, the eigenmatrix **A** of which is similarity invariant with the following matrix:

$$\mathbf{A} = \begin{bmatrix} \omega_B^2(0) + s_B\Omega^2 - \lambda & -\alpha \\ -\alpha & \omega_T^2(0) + s_T\Omega^2 - \lambda \end{bmatrix}, \quad (8)$$

where $\alpha \equiv \alpha(\Omega)$, $\beta \equiv \beta(\Omega)$. The eigenvalues of **A** in Eq. (8) are

$$\lambda_1 = \omega_1^2(\Omega) = \frac{1}{2}[\omega_B^2(0) + \omega_T^2(0) + (s_B + s_T)\Omega^2] - \sqrt{\alpha^2 + \frac{1}{4}[\omega_B^2(0) - \omega_T^2(0) + \Omega^2(s_B - s_T)]^2}; \quad (9)$$

$$\lambda_2 = \omega_2^2(\Omega) = \frac{1}{2}[\omega_B^2(0) + \omega_T^2(0) + (s_B + s_T)\Omega^2] + \sqrt{\alpha^2 + \frac{1}{4}[\omega_B^2(0) - \omega_T^2(0) + \Omega^2(s_B - s_T)]^2}; \quad (10)$$

It may be noted that each of the two eigenvalues λ_1, λ_2 above, of the system (6) or (7) with conservative coupling, is a function of both the bending ω_B and torsion ω_T nonrotating frequencies, as well as the corresponding Stodola-Southwell coefficients for the bending and torsion modes, s_B and s_T.

If the conservative coupling vanishes completely, i.e., $\alpha = 0$, then Eqs. (9) and (10) become, respectively,

$$\lambda_1 = \omega_1^2(\Omega) = \omega_B^2(0) + s_B\Omega^2; \; \lambda_2 = \omega_2^2(\Omega) = \omega_T^2(0) + s_T\Omega^2, \quad (11)$$

which are the results previously obtained as Eq. (5) for the system without coupling.

4.2 Nonconservative Coupling in Modal Coordinates. If the modal equations have nonconservative coupling in the modal mass matrix, one gets an equation of motion of the form

$$\begin{bmatrix} 1 & \beta \\ -\beta & 1 \end{bmatrix} \begin{Bmatrix} \ddot{\phi}_B \\ \ddot{\phi}_T \end{Bmatrix} + \begin{bmatrix} \omega_B^2(0) + s_B\Omega^2 & 0 \\ 0 & \omega_T^2(0) + s_T\Omega^2 \end{bmatrix} \begin{Bmatrix} \phi_B \\ \phi_T \end{Bmatrix} = 0. \quad (12)$$

If, in the alternative, the nonconservative coupling exists in the modal stiffness matrix only, then the modal equations of motion may be written as

$$\begin{bmatrix} 1 & 0 \\ 0 & 1 \end{bmatrix} \begin{Bmatrix} \ddot{\phi}_B \\ \ddot{\phi}_T \end{Bmatrix} + \begin{bmatrix} \omega_B^2(0) + s_B\Omega^2 & \beta \\ -\beta & \omega_T^2(0) + s_T\Omega^2 \end{bmatrix} \begin{Bmatrix} \phi_B \\ \phi_T \end{Bmatrix} = 0. \quad (13)$$

The eigenvalue problem of Eqs. (12) or (13) has an eigenmatrix **A**, which is similar to the following matrix:

$$\mathbf{A} = \begin{bmatrix} \omega_B^2(0) + s_B\Omega^2 - \lambda & \alpha \\ -\alpha & \omega_T^2(0) + s_B\Omega^2 - \lambda \end{bmatrix}. \quad (14)$$

The eigenvalues of the above are

$$\lambda_1 = \omega_1^2(\Omega) = \frac{1}{2}[\omega_B^2(0) + \omega_T^2(0) + (s_B + s_T)\Omega^2] - \sqrt{-\alpha^2 + \frac{1}{4}[\omega_B^2(0) - \omega_T^2(0) + \Omega^2(s_B - s_T)]^2}; \quad (15)$$

$$\lambda_2 = \omega_2^2(\Omega) = \frac{1}{2}[\omega_B^2(0) + \omega_T^2(0) + (s_B + s_T)\Omega^2] + \sqrt{-\alpha^2 + \frac{1}{4}[\omega_B^2(0) - \omega_T^2(0) + \Omega^2(s_B - s_T)]^2}; \quad (16)$$

5 Composition of Plane Algebraic Curves

Most of the mathematical ideas and techniques that are currently used in engineering analysis date back to three or more centuries. Newer results arising from recent research in mathematics (from the 1950s to the present, for instance), are hardly utilized in engineering analysis at present, mainly due to the inaccessible language utilized by mathematicians. According to V. I. Arnol'd (1989, p. ix),

> "The new discoveries . . . have potentially extremely wide applications, but since these results were discovered rather recently, they are discussed only in specialized [mathematical journals], and applications are impeded by the difficulty of the mathematical exposition for the nonmathematicians."

In the course of our discussion in this paper, we shall find

it useful to apply some relatively new results and ideas from algebraic geometry: the weak transversality theorem from catastrophe theory (Thom and Levin, 1959; Thom, 1972), and the effect of small perturbations on the composition of real algebraic curves (Brieskorn, 1986).

The transversality theorems (the weak transversality theorem and Thom's transversality theorem) are very useful in studying the qualitative behavior of mathematical objects in the neighborhood of a degeneracy. In recent years, these theorems have been used directly, or indirectly through catastrophe theoretic formalisms, by Afolabi (1989, 1991, 1993, 1994), to furnish insight into the qualitative behavior and "structural stability" of linear vibrating systems.

The effect of small perturbations on the composition of real algebraic curves has been discussed by Arnol'd (1983) and Brieskorn (1986), among others. In demonstrating that the observable eigenvalue loci belonging to two distinct modes do not intersect, we shall find it useful to study the local topology of real algebraic curves in the plane, in the neighborhood of a presumed "intersection."

5.1 Linear Characteristics of Smooth Functions. Thom's classification theorem of catastrophe theory is based on the differentiable topology of smooth functions in one or two variables, and their (uni)versal unfoldings. By a "smooth function" is meant an infinitely differentiable function, also called a C^∞ function. The locus of a given eigenvalue of a rotating blade as a function of the rotation speed is a C^∞ function. It follows from the Implicit Function Theorem that any C^∞ function may be linearized everywhere, except in the neighborhood of its critical points. In general, the eigenvalue loci of a rotating blade, or a system of rotating blades, do not have critical points (except, possibly, at the nonrotating frequency). Therefore, the eigenvalue loci may be approximated as linear functions at almost all rotation speeds.

Consider the neighborhood of a point where two eigenvalue loci are presumed to intersect. We now propose to show that given an arbitrarily small amount of perturbation (or, a coupling of the two curves), the "intersection" will disappear, leaving either an avoided crossing or a frequency coalescence.

5.2 Effect of Coupling on the Composition of Plane Algebraic Curves. Suppose, in the neighborhood of a "crossing," that the two curves that are presumed to intersect have linear representations, as a consequence of the Implicit Function Theorem. Then, using the illustration in Fig. 1(*a*) as an example, the two curves may be described as polynomials of the first degree. Consequently, they are real algebraic curves in the plane. Thus, we may write

$$p_1 \equiv y = m_1 x + c_1,\ p_2 \equiv y = m_2 x + c_2 \tag{17}$$

where m_i is the slope of the ith curve, and c_i its intercept with the y axis.

From the local algebra of plane algebraic curves (Arnol'd, 1983, p. 78; or Brieskorn, 1986) the composite curve may be written as

$$p \equiv p_1 \circ p_2 = 0. \tag{18}$$

The formula above corresponds to an ordinary multiplication of the two polynomials of the first degree, i.e.,

$$(y - m_1 x - c_1) \cdot (y - m_2 x - c_2) = 0. \tag{19}$$

However, the procedure of composition of algebraic curves is a mathematical "surgery," in which the neighborhood of the intersection is deleted and the resulting pieces "glued" together. All this is done mathematically, using standard techniques of algebraic topology; see, for instance, the review article by Atiyah (1976). As a result of this "surgery," the right-hand side of Eq. (19) is not completely zero, but a small, nonvanishing real number, here denoted by ϵ. Thus, although Eq. (19) is theoretically imaginable, it is not practically realizable, and Eq. (19) therefore becomes

$$(y - m_1 x - c_1) \cdot (y - m_2 x - c_2) = \epsilon. \tag{20}$$

Expanding the equation above yields

$$y^2 - [(m_1 + m_2)x + (c_1 + c_2)]y + [(c_1 c_2 - \epsilon) + (m_1 c_2 + m_2 c_1)x + m_1 m_2 x^2], \tag{21}$$

which may be solved as a quadratic in y to get

$$y(x;\ \epsilon) = \frac{(m_1 + m_2)x + (c_1 + c_2) \pm \sqrt{[(m_1 - m_2)x + (c_1 - c_2)]^2 + 4\epsilon}}{2}. \tag{22}$$

Equation (22) is a general form from which one could generate composite curves having qualitatively different differentiable topological characteristics. For example, one could generate the three qualitatively different curves or "loci" in Figs. 1 by using the parameters, $m_1 = 1$, $m_2 = -1$, $c_1 = 1$, $c_2 = 2$, to get the parametric equation

$$(y - x - 1)(y + x - 2) - \epsilon = 0 \Rightarrow y^2 - 3y - (x^2 - x - 2 + \epsilon) = 0, \tag{23}$$

which, when solved, yields

$$y(x;\ \epsilon) = 1.5 \pm \sqrt{(x - 0.5)^2 + \epsilon}. \tag{24}$$

The degenerate case of Eq. (19) is obtained when the parameter $\epsilon = 0$, yielding the intersecting loci in Fig. 1(*a*). In this case, the effect of "perturbation" on the surgical procedure involved in the composition of the two curves is *assumed* to have vanished completely. If, however, we set $\epsilon > 0$, i.e., to any arbitrary *positive* real number, then the curves in Fig. 1(*b*) result. This is similar to the case of "curve veering" well known in structural dynamics. Larger values of ϵ give rise to stronger coupling, while smaller values correspond to weaker coupling. As $\epsilon \to 0$, the two curves develop very sharp local curvatures. They approach each other arbitrarily closely, and may *appear* to cross each other when ϵ is almost zero. However, provided ϵ does not *exactly* vanish, the two composing curves do not cross each other. If, on the other hand, we set $\epsilon < 0$, i.e., to any arbitrary *negative* real number, then we get the curves shown in Fig. 1(*c*). This is similar to the case of "frequency coalescence" characteristic of coupled mode flutter, which is well known in aeroelasticity. The separation between the two segments of the now surgically coupled curves indicate a *flutter zone*. At any rotation speed within this zone, the rotating blade flutters, and becomes unstable. As in the preceding case of curve veering, smaller values of ϵ imply weaker coupling, while large values imply strong coupling. The stronger the coupling, the larger the flutter zone.

Similar results to Figs. 1 may be obtained by using different values of m_i, c_i, and ϵ in Eq. (20). For example, one may set $m_1 = 1$, $m_2 = 0$, $c_1 = 1$, $c_2 = 2$, and $\epsilon = 0$, $\epsilon > 0$, $\epsilon < 0$ for the (*a*), (*b*), and (*c*) versions of Figs. 3. Globally, the eigenvalue loci as functions of rotation speed may be illustrated as in Figs. 4.

From what has been said above, we come to the conclusion that a composition of two plane curves yields a crossing if and only if $\epsilon = 0$. Such an intersection is, however, not in "general position," and an infinitesimally small amount of perturbation, signified by $\epsilon \neq 0$, will induce a topological surgery, which is manifested either as "curve veering" or "frequency coalescence."

6 Physical Significance of Curve Veering and Frequency Coalescence

Figure 3(*a*) shows two eigenvalue loci which intersect; the two loci in Fig. 3(*b*) repel each other, exhibiting the curve

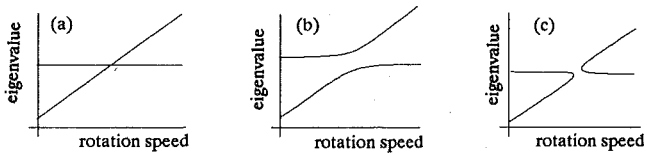

Fig. 3 Two loci, one showing linear variation of resonance frequency with rotation speed, the other invariant with speed; (*a*) frequency crossing; (*b*) curve veering; (*c*) frequency coalescence

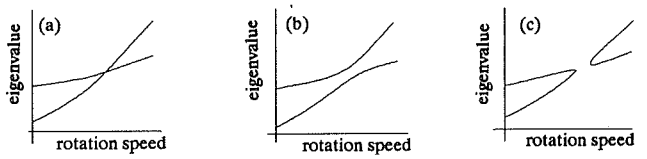

Fig. 4 Nonlinear variation of resonance frequencies with rotation speed showing (*a*) frequency crossing; (*b*) curve veering; (*c*) frequency coalescence

veering phenomenon; while Fig. 3(*c*) is characterized by the coalescence of the two loci.

If we superimpose the curves in Figs. 3(*a*), 3(*b*), and 3(*c*), the quantitative difference between the eigenvalue loci in a given diagram and the corresponding loci in the other two diagrams is very small. The largest difference occurs near the point where the uncoupled curves intersect in Fig. 3(*a*). Yet, the dynamics represented by the three diagrams are significantly different from one another in a qualitative sense. In this section, we discuss the importance of frequency coalescence on the one hand, and curve veering on the other, with regard to the flutter and stability of a rotating blade or a rotating system of blades.

6.1 Frequency Crossing Implies Eigenvalue Degeneracy. Two loci can cross each other if and only if there is *zero* coupling between the vibration modes represented by each eigenvalue locus. For example, the eigenlocus of the torsion branch will cross that of the bending branch only if there is no coupling whatsoever between the bending and torsion modes. If such a crossing of eigenloci were to occur in an actual engineering system, then the system's eigenvalues must be degenerate at the point where the two loci meet.

However, the occurrence of degenerate eigenvalues in a coupled two degree of freedom vibrating system is impossible, from physical or engineering considerations, as discussed in Sect. 2.3. Thus, the type of eigenvalue loci shown in Fig. 3(*a*) cannot occur in a coupled system with two degrees of freedom (e.g., bending and torsion degrees of freedom).

Theoretically, one could always *assume*, of course, that a coupled two degree of freedom with degenerate eigenvalues existed, in which case the loci would intersect. The degenerate eigenvalues at each intersection point could also be assumed to have a linearly independent set of eigenvectors, so that the eigenvalue and eigenvector matrices may be written, respectively, as

$$\Lambda = \begin{bmatrix} \lambda & 0 \\ 0 & \lambda \end{bmatrix}, \quad \mathbf{U} = \begin{bmatrix} 1 & 0 \\ 0 & 1 \end{bmatrix}, \tag{25}$$

at the intersection point.

In such a case, the physically unrealizable system having this eigensolution would have "elastic stability" (since the eigenvectors are linearly independent), but not "structural stability" in the topological sense (because the eigenvalues are degenerate).

6.2 Frequency Coalescence Implies Eigenvector Degeneracy and, Consequently, Flutter. Consider now the case depicted in Fig. 3(*c*). Each of the two points at which the loci belonging to two distinct modes coalesce constitutes a *flutter boundary*. To see this, one observes that the eigenvalue matrix of the system may be written in a canonical form due to Crandall and Mroszczyk (1988) as

$$\mathbf{A} = \begin{bmatrix} 1-\alpha & -\beta \\ \beta & 1+\alpha \end{bmatrix}. \tag{26}$$

The eigenvalues, as well as the *eigenvectors*, of Eq. (26) are degenerate when $\alpha = \pm\beta$, which are the two flutter boundaries. The implication of eigenvector degeneracy in this case is very different from that of eigenvalue degeneracy considered in Sect. 6.1. An important fact for system dynamics in this case is this: at the flutter boundaries, because the *eigenvectors are also degenerate*, the system matrix *cannot be diagonalized*; it is only reducible to the Jordan normal form. Thus, the eigensolution at the flutter boundaries may be written in the Jordon canonical form

$$\Lambda = \begin{bmatrix} \lambda & 0 \\ 1 & \lambda \end{bmatrix}, \quad \mathbf{U} = \begin{bmatrix} 1 & 1 \\ 0 & 0 \end{bmatrix}, \quad \mathbf{V} = \begin{bmatrix} 1 & -1 \\ 0 & -1/\alpha \end{bmatrix}, \tag{27}$$

where **U** is a matrix of ordinary eigenvectors, while **V** is a matrix of generalized eigenvectors of the system matrix. From the foregoing, one observes that the eigenvalue matrix is not diagonal, and the matrix of ordinary eigenvectors is singular. Due to the singularity, or noninvertibility, of the ordinary eigenvector matrix, **U**, a matrix of generalized eigenvectors, **V**, must be computed. By means of these generalized eigenvectors a nonsingular linear change of coordinates may be found so that the system matrix may be reduced to the Jordan normal form. It is easy to show that the existence of a Jordan matrix in a linear vibrating system necessarily implies the occurrence of flutter in that system.

6.3 Curve Veering Does Not Lead to Flutter. In order for flutter to occur in an *undamped* vibrating system with two degrees of freedom, the two eigenvalues of the system must coalesce, leading to eigenvalue degeneracy. More significantly, the corresponding eigenvectors must also be degenerate, so that the system matrix becomes nondiagonalizable *at the flutter boundary*. Such a situation cannot arise in an undamped system that exhibits curve veering, for the simple reason that the two eigenvalues repel each other when they get arbitrarily close, thereby preventing a degeneracy or mode coalescence. The system exhibiting curve veering may, nevertheless, lose elastic stability if net negative damping is later added, and it may lose elastic stability by "divergence," when one of its eigenvalues becomes zero.

7 Effect of Damping on Flutter Boundaries

The discussion in the preceding sections of this paper has been based on a model without damping. In this section, we briefly discuss the role of damping on the systems exhibiting curve veering on the one hand, and frequency coalescence on the other.

As discussed earlier, systems that give rise to curve veering only cannot flutter when there is no damping. Introducing positive damping to the system is generally beneficial, and does not usually destabilize the system.

Undamped systems giving rise to frequency coalescence can behave in very interesting ways when *positive* damping is added to the system. In the cases where mode coalescence is due to circulatory forces (i.e., skew-symmetric coupling via the stiffness or mass matrices), the introduction of positive damping to the system has a beneficial effect—the flutter zone is reduced. On the other hand, where the coalescence is due to gyroscopic forces (i.e., skew-symmetric coupling via the damping matrix), the addition of positive damping worsens the situation, and further destabilizes the system. Thus, the flutter

zone is widened by damping, so that flutter occurs at a lower rotational speed relative to the corresponding undamped system. In either case (of circulatory or gyroscopic coupling), damping may prevent the two vibration frequencies from coalescing. Therefore, a major difference between a damped and an undamped model of a fluttering system is that the eigenvalue loci actually coalesce at the flutter boundary when there is no damping, but they do *not* necessarily coalesce at the flutter boundary when damping is added to the system.

8 Conclusions

In this paper, some standard results from the theory of plane algebraic curves and from catastrophe theory have been used to show that the loci of two or more eigenvalues depending on a common parameter (such as rotation speed, Ω) almost always do *not* cross. Cases where such eigenvalue loci are reported to have crossed exist only in unrealistic theoretical models where it is assumed that no coupling exists between the two different modes of vibration. If, in an experimental work insufficient data are recorded due to a variety of practical factors, it is quite possible to interpolate the experimental data erroneously in such a way as to imply that the loci cross each other. In reality, however, frequency loci of undamped rotating blades do not cross, but must either repel each other leading to curve veering, or attract each other leading to frequency coalescence.

From the mathematical point of view, a crossing of eigenvalue loci implies the existence of degenerate eigenvalues. Degenerate objects of a category are not in "general position," and are necessarily "structurally unstable." Therefore, they are unobservable. The existence of degenerate eigenvalues also indicates a nontransversal condition. By the weak transversality theorem, an arbitrarily small shift will lead to a bifurcation of a nontransversal intersection leading to algebraic curves exhibiting veering or coalescence which will then be in general position and are thus "structurally stable."

From the engineering point of view, a crossing of eigenvalue loci implies the existence of degenerate eigenvalues, such that the eigenvectors are independent at the degeneracy. Two or more eigenvalue loci of a rotating blade intersect only in theoretical studies where it is *presumed* that some form of *perfect* symmetry exists, and there is *zero* coupling of modes. Minute asymmetry or imperfections are inevitable in practice, and these lead to a coupling of neighboring modes. If the coupling is conservative, then the eigenvalue loci would exhibit avoided crossings or curve veering. On the other hand, if there is nonconservative coupling, the eigenvalue loci exhibit frequency coalescence.

Frequency coalescence in an undamped rotating blade, or system of blades, is very dangerous since it leads to flutter. On the contrary, curve veering in an undamped rotating blade or system of rotating blades is benign with respect to flutter.

Acknowledgments

Part of the work of the first author was supported by a grant at ICOMP, NASA Lewis Research Center, Cleveland, Ohio. The support is gratefully acknowledged.

References

1 Afolabi, D., 1989, "Effects of Mistuning and Matrix Structure on the Topology of Frequency Response Curves," NASA TM 102290.

2 Afolabi, D., 1991, "Modal Interaction in Linear Dynamic Systems Near Degenerate Modes," NASA TM 105315.

3 Afolabi, D., 1993, "The Cusp Catastrophe and the Stability Problem of Helicopter Ground Resonance," *Proc. R. Soc. Lond.*, Series A, Vol. A441, pp. 399-401.

4 Afolabi, D., 1994, "Flutter Analysis Using Transversality Theory," *Acta Mechanica*, Vol. 103, pp. 1-15.

5 Andronov, A. A., and Vitt, A. A., 1966, *Theory of Oscillators*, Pergamon, London; republished Dover, New York, 1987.

6 Arnol'd, V. I., 1983, *Catastrophe Theory*, Springer-Verlag, New York.

7 Arnol'd, V. I., Gusein-Zade, S. M., and Varchenko, A. N., 1985, *Singularities of Differentiable Maps*, Vol. 1, Birkhauser, Boston, MA.

8 Arnol'd, V. I., 1989, *Mathematical Methods of Classical Mechanics*, 2nd ed., Springer-Verlag, New York.

9 Atiyah, M. F., 1976, "Bakerian Lecture, 1975—Global Geometry," *Proc. R. Soc. Lond.*, Vol. A347, pp. 291-299.

10 Bisplinghoff, R. L., and Ashley, H., 1962, *Principles of Aeroelasticity*, Dover Publications, New York.

11 Brieskorn, E., 1986, *Plane Algebraic Curves*, Birkhauser, Boston.

12 Campbell, W., 1924, "The Protection of Steam Turbine Disk Wheels From Axial Vibration," *Trans. ASME*, Vol. 46, pp. 31-160.

13 Chen, L.-T., and Dugundji, J., 1984, "Investigation of the Vibration Characteristics of Shrouded Bladed Disk Rotor Stages," *J. Aircraft*, Vol. 17, pp. 479-486.

14 Crandall, S. H., and Mroszczyk, J. W., 1988, "Conservative and Nonconservative Coupling in Dynamic Systems," *Proc. Intl. Conf. Vib. Rotating Mach.*, IMechE, Cambridge, pp. 567-572.

15 Lamb, H., and Southwell, R. V., 1921, "The Vibrations of a Spinning Disc," *Proc. R. Soc. Lond.*, Vol. A99, pp. 272-280.

16 Leissa, A. W., 1974, "On a Curve Veering Aberration," *ZAMP* (*J. Appl. Math. Phys.*), Vol. 25, pp. 99-111.

17 MacBain, J., 1975, "Vibratory Behavior of Twisted Cantilevered Plates," *J. Aircraft*, Vol. 12, pp. 343-349.

18 Perkins, N. C., and Mote, C. D., 1988, "Comments on Curve Veering in Eigenvalue Problems," *J. Sound Vib.*, Vol. 106, pp. 451-463.

19 Poincaré, H., 1892, "New Methods of Celestial Mechanics," NASA TT-F-450, 451, 452. National Technical Information Service, Springfield, VA (in French: "Les Méthodes Nouvelle de la Mécanique Céleste," Dover, New York, 1957; Guthier-Villas, Paris, 1892, 1893, 1899).

20 Ramamurti, V., and Kielb, R. E., 1984, "Natural Frequencies of Twisted Rotating Plates," *J. Sound Vib.*, Vol. 97, pp. 429-449.

21 Southwell, R V., 1922, "On the Free Transverse Vibrations of a Uniform Circular Disc Clamped at its Centre and on the Effect of Rotation," *Proc. R. Soc. Lond.*, Vol. A101, pp. 133-153.

22 Stodola, A., 1914, *Schweitzerische Bauzeitung*, May.

23 Thom, R., and Levin, H. I., 1959, "Singularities of Differentiable Mappings," *Bonn Math. Schri.*, (reprinted in *Lecture Notes in Math.*, #192, Springer, New York; 1971).

24 Thom, R., 1972, *Structural Stability and Morphogenesis*, Benjamin, Reading, MA, (republished by Addison Wesley, Reading, MA, 1989).

25 Wang, J. M., and Chopra, I., 1992, "Dynamics of Helicopters in Ground Resonance With and Without Blade Dissimilarities," AIAA Paper.

Fluid-Thermoacoustic Vibration of a Gas Turbine Recuperator Tubular Heat Exchanger System

F. L. Eisinger
Foster Wheeler Energy Corporation,
Perryville Corporate Park,
Clinton, NJ 08809-4000
Mem. ASME

Low-frequency acoustic vibration of a vertical gas turbine recuperator during cold start-up is described. The vibration was identified as fluid-thermoacoustic instability driven by a modified Sondhauss tube-like thermoacoustic phenomenon. The problem and its underlying theoretical basis are described. A design guideline for prevention of instability and alternative solutions for the elimination of the vibration are given.

Introduction and Brief Review of Published Work

The phenomenon of acoustic vibration or pressure oscillation in a gas caused by a constant heat source may occur in one of two ways named after their discoverers: Sondhauss oscillations and Rijke oscillations. The Sondhauss pressure oscillation occurs when heat is added (either externally or internally) to a gas-filled tube having at least one end closed and no net flow of gas through the tube (Sondhauss, 1850). The Rijke oscillation occurs when heat is added to an internal grid located in the lower half of a vertical tube having both ends open, with flow of gas upward through the tube (Rijke, 1859). An earlier literature review on both the Sondhauss and Rijke oscillations was published by Feldman (Feldman, 1968a,b).

Thermoacoustic oscillations are known to occur in various industrial installations but they are generally difficult to diagnose. They occur either in their pure Sondhauss or Rijke form and also in a modified form such as in the case described in this paper. These oscillations have been described in combustion processes as an unwanted phenomenon (Putman and Dennis, 1953), or as a desired phenomenon in pulsed combustion (see for example *Proceedings*, 1991). Acoustic oscillations in rocket engines have been studied extensively over the last 20–30 years by many researchers. In this connection, the Rijke phenomenon was thought to be dominant in many cases, attributed to a velocity-coupling mechanism (Culick, 1970). Research in refrigeration and cryogenics turned to the Sondhauss tube phenomenon as the basis for what is known as pulse-tube refrigeration (Gifford and Longworth, 1963; Wheatley et al., 1985; Radebaugh, 1990).

Both the Sondhauss and Rijke phenomenon are governed by the Rayleigh criterion, which states that "If heat be given to the air at the moment of greatest condensation or be taken from it at the moment of greatest rarefaction, the vibration is encouraged" (Rayleigh, 1945).

Several publications deal specifically with the Sondhauss oscillation phenomenon. Chu described a pressure wave theory and analyzed the wave stability (Chu, 1955, 1956). Feldman did extensive experimental work and contributed significantly to the theoretical explanation of the phenomenon (Feldman, 1966; Feldman and Carter, 1970). Kramers is known for his stability analysis (Kramers, 1949). Utilizing Kramers' work, Rott presented a theoretical basis of thermoacoustic oscillation and stability with particular emphasis on the Sondhauss phenomenon and applications in cryogenic engineering (Rott, 1969, 1980; Rott and Zouzoulas, 1976).

In this paper, we will concentrate on the Sondhauss acoustic oscillation, as a modified version of this phenomenon with net axial flow through the tube has turned out to be the cause of a strong acoustic oscillation in a gas turbine discharge duct/recuperator system.

Description of Turbine/Recuperator System

The gas turbine recuperator under consideration is a vertical tubular heat exchanger consisting of 6084 31.8 mm (1.25 in.) O.D., 1.07 mm (0.042 in.) thick carbon steel tubes arranged in a triangular pitch pattern with a pitch of 39.7 mm (1.5625 in.). The tubes are parallel to each other and are supported in two tubesheets at their lower and upper ends, and by support baffles at intermediate points. The tube length is 13,330 mm (525 in.). The tube bundle is located within a cylindrical shell with an inside diameter of 3962 mm (13 ft) and wall thickness of 12.7 mm (0.5 in.). At the bottom the shell extension forms a gas inlet chamber (plenum), which receives exhaust gases from the gas turbine via a duct system. The recuperator is supported at the top from a steel structure with thermal expansion allowed in the downward direction.

The recuperator is of a counterflow type with gas flow from the turbine on the tube side and air on the shell side. The hot turbine exhaust gas enters the tube bundle at the bottom and the cooled gas exits to the atmosphere at the top. The air enters the shell at the top and the heated air leaves the recuperator at the bottom. Figure 1 shows the general arrangement. The design conditions of the recuperator are given in Table 1.

The gas turbine drives an air compressor and both operate at a variable speed with a maximum speed of 5500 rpm. Both the gas flow and the air flow are functions of the speed of the gas turbine.

Contributed by the Nuclear Engineering Division and presented at the ASME Winter Annual Meeting, Anaheim, California, November 8–13, 1992. Manuscript received by the Nuclear Engineering Division June 26, 1992. Associate Technical Editor: S. M. Cho.

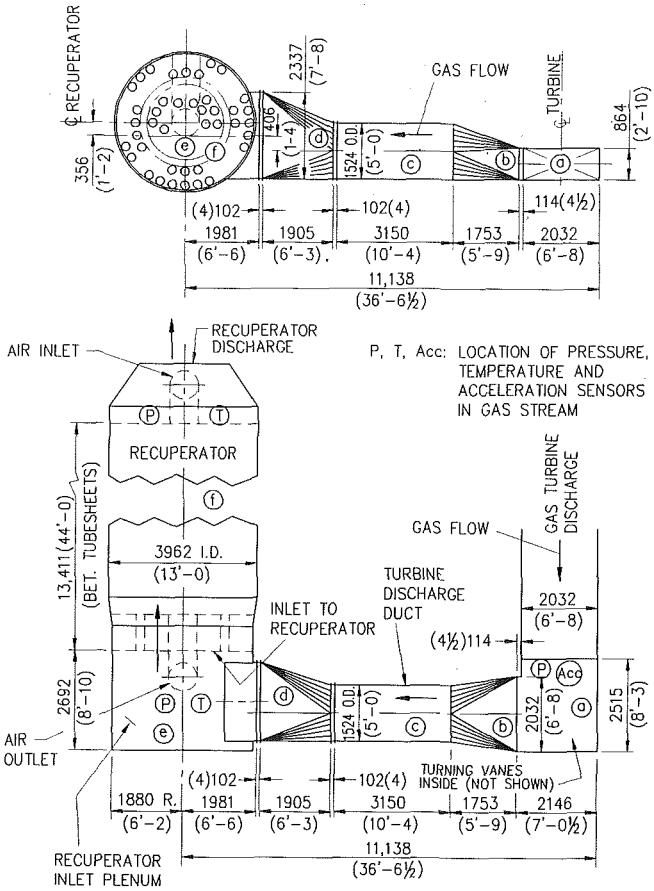

Fig. 1 General arrangement of recuperator/duct system (dimensions shown are in mm)

The turbine operating conditions are:

- Cold start-up, during which both the recuperator and the duct system leading to it are in a cold condition at ambient temperature.
- Warm start-up, during which the system is in a warm or hot condition from previous operation.
- Normal operation with load and turbine speed changes as required with recuperator/duct system in a hot condition.

The cold start-up typically consists of:

Table 1 Design parameters of recuperator

Condition	Gas		Air	
Maximum flow, kg/hr (lb/hr):	162,800	(358,000)	162,800	(358,000)
Inlet temperature, °C (°F)	477	(890)	199	(390)
Outlet temperature, °C (°F)	252	(486)	438	(820)
Inlet pressure (absolute), KPa (psi)	98	(14.2)	515	(74.6)
Pressure drop KPa (psi)	1.34	(0.194)	6.5	(0.95)

- Turbine roll with no fire in turbine.
- Warm-up or turbine roll after fire.
- Turbine operation following warm-up.

Vibration Problem

Description. A severe vibration problem was experienced during the cold start-up of the gas turbine. A build-up of the vibration was noticeable with increase in turbine speed. At turbine speed of about 4000 rpm the vibration became so strong that the unit had to be tripped to preclude damage to the equipment. Large pressure pulsations occurred in the discharge duct/recuperator system causing severe structural vibration of the ducting from the turbine to the recuperator, and vibration of the surrounding structures, including the turbine itself. (There was no audible sound associated with this pulsation, except for the metallic noise effects caused by the structural motion.) After warm-up, during a number of starts and trips the vibration disappeared and the turbine could operate freely within the entire speed and load range. Thus, the vibration occurred only during the cold start-up condition.

Vibration Test Results. Vibration testing was performed in order to gain a better insight into the problem. Temperatures and acoustic pressures on the gas side and on the air side were measured using thermocouples, pressure transducers, and accelerometers mounted at several locations throughout the system. See Fig. 1 for locations of sensors on gas side. Performance calculations based on combustion analysis were used to calculate gas flows.

Instrumentation Used. For temperature measurements, type K (chromel/alumel) thermocouples were used. These were inserted approximately 460 mm (18 in.) into the gas stream. Strain gage type differential pressure transducers type PM 8052 with a pressure range of up to ±34.5kPa (±5 psi) made by Statham Instruments were used for pressure pulsation meas-

Nomenclature

c = speed of sound
D = diameter
f = frequency
F = area
g = acceleration of gravity
k = c_p/c_v = ratio of specific heats
l = length
L = resonator length
p = acoustic pressure
Q = heat energy
r = radius
T = gas temperature
u = acoustic particle velocity
v = flow velocity or specific volume
V = volume
$\dot{w}$ = rate of heat release
x = coordinate
α = temperature ratio
β = exponent for viscosity-temperature power law
ζ = variable
ξ = geometry parameter for Sondhauss tube
ρ = density
σ = Prandtl number

Subscripts

AMB = ambient
c = cold
cr = critical
exp = experimental
f = flow
h = hot
i, j = denominates section of tube
max = maximum
min = minimum
N = neck of resonator
o = steady-state undisturbed condition
r = reference value
s = sensible
v = volume effect in form factor l_v

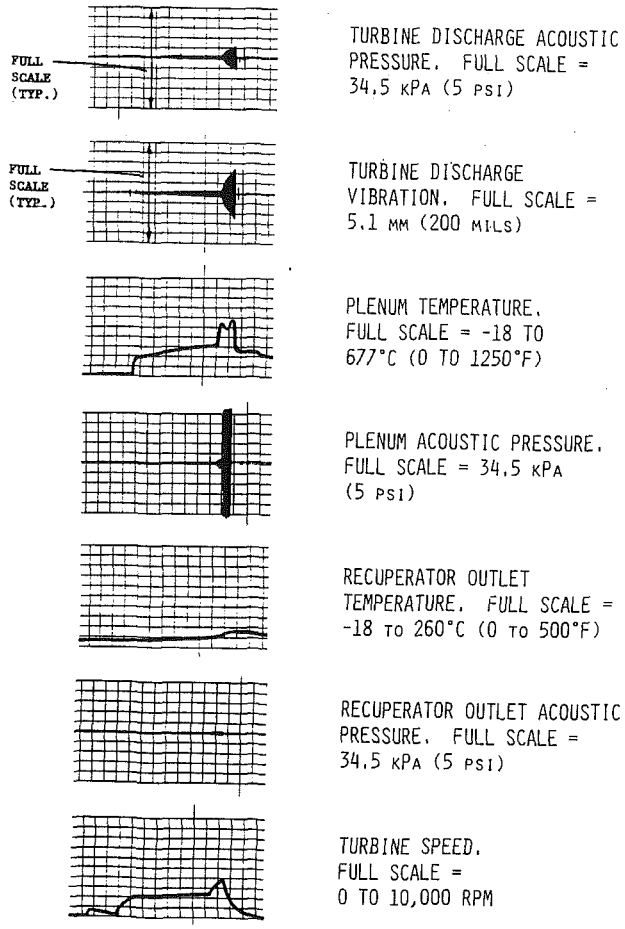

Fig. 2 Test results of recuperator/duct system during cold start-up (Test 1) (horizontal scale: 0.32 min/division)

urements. These were attached to taps penetrating the duct or recuperator casing. Columbia Research Laboratories' Force Balance Accelerometer, Model SA-107 with a range of ±1.0 g, specially suited for low-frequency measurements, was used for structural vibration measurements at the turbine discharge duct. A Nicolet Scientific Corporation Model 444A FFT spectrum analyzer and a Lockheed Store 70 type instrumentation recorder were used for acquisition and processing of the data.

During the diagnostic testing, it was determined that provision of an opening in the wall of the recuperator inlet plenum stopped the vibration. This was accomplished by using two 254 mm (10 in.) diameter pipes with flap covers attached to a manhole opening.

The testing was performed at three conditions:

Test 1: Cold start-up (flap covers closed)
Test 2: Cold start-up (flap covers open)
Test 3: Warm start-up (flap covers closed)

Figure 2 shows selected on-line data taken from Test 1. Figure 3 gives more detailed results for the period of the vibration build-up in Test 1. (Detailed test results for the non-vibratory conditions of Tests 2 and 3 are not included in this paper.)

To get a better understanding on the distribution of the vibration levels throughout the system, test data collected from a second test series at different operating conditions were plotted along the developed length of the recuperator/duct system. Figure 4 provides a graphical representation of the vibration levels obtained at a turbine speed of about 3000 rpm, just below the initiation of the large vibration, and at about 4000 rpm with the large vibration present.

From the test data (Figs. 2–4) we can make the following observations:

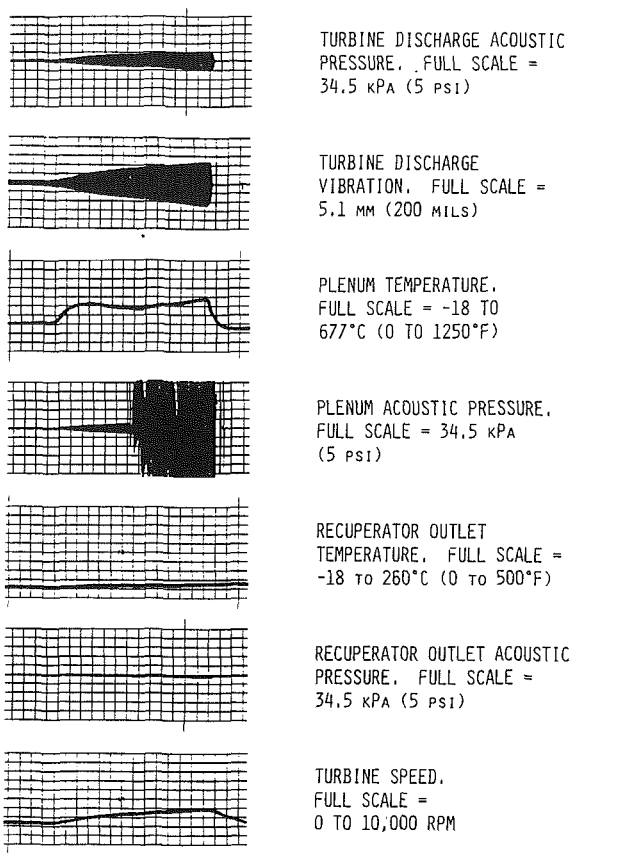

Fig. 3 Details of data of Test 1 (horizontal scale: 1.6 s/division)

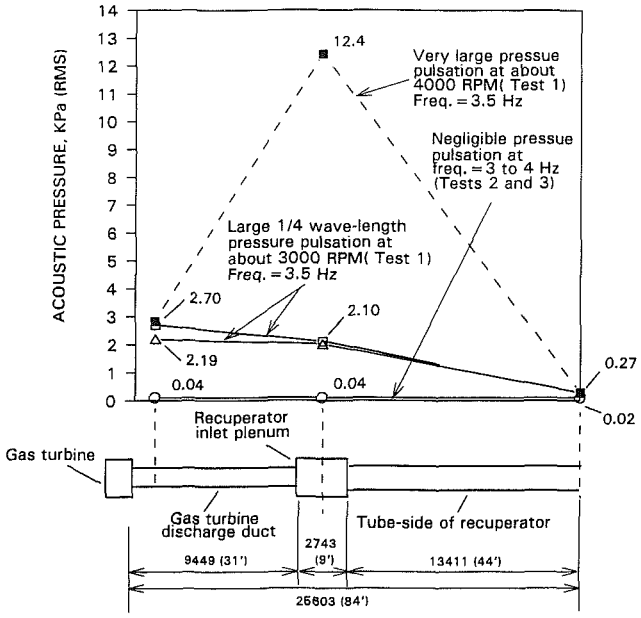

Fig. 4 Acoustic pressure distribution along recuperator/duct system at turbine speeds of approximately 3000 and 4000 rpm

1 The pressure pulsation is characterized by a frequency of 3–3.5 Hz during a recuperator cold condition, increasing to about 4 Hz when the recuperator is hot.
2 The vibration starts building up at a turbine speed of about 2000 rpm, and at about 3000 rpm abruptly increases, forcing a unit shut-down, which typically occurred at 4000 rpm.
3 The distribution of acoustic pressures along the dis-

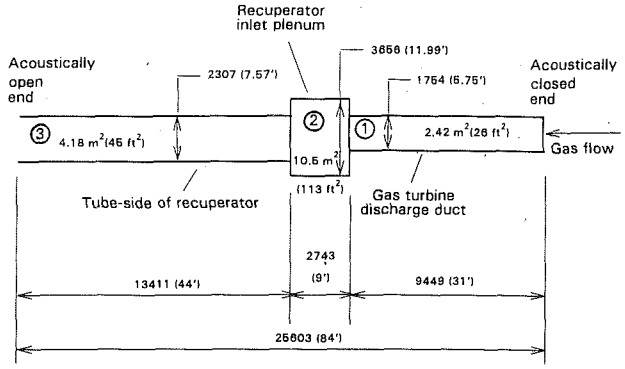

Fig. 5 Simplified Helmholtz resonator model of gas side of recuperator/duct system

charge duct recuperator system up to the 3000 rpm speed is of the quarter wavelength type, with a minimum at the top of the recuperator and a maximum in the duct at the turbine discharge. It can be seen that the gas-filled combined spaces of the discharge duct and of the tube side of the recuperator act like a quarter-wave or Helmholtz resonator. This resonator vibrated at 3–3.5 Hz and 4 Hz in the cold and hot recuperator conditions, respectively.

4 At a turbine speed of about 4,000 rpm, very large pressure pulsation occurred in the recuperator inlet plenum, causing a local distortion of the quarter wave behavior.

5 With the flap covers open during the cold start-up, or during a warm start-up with the flaps closed, no vibration problem occurred.

The data on the air side, not reported here, showed no significant magnifications in acoustic pressures. It was thus determined that the problem was confined to the gas side of the system and that it was related to the temperature of the recuperator. Typically, after the gas temperature at the recuperator discharge reached about 82°C (180°F), the vibration did not materialize.

Theoretical Analysis

Quarter Wave (Helmholtz Resonator) Model of Recuperator-Duct System. The lengths, cross-sectional areas, and volume associated with the individual sections of the duct (*a–d*), inlet plenum of the recuperator (*e*), and the tube-side of the recuperator (*f*), Fig. 1, were combined into an equivalent simplified Helmholtz resonator model (Fig. 5) representing the system. The three cylindrical sections 1, 2, and 3 of this model represent the duct, the inlet plenum, and the tube-side of the recuperator, respectively.

Frequency of Helmholtz Resonator. The frequency of the Helmholtz resonator filled with a gas of constant temperature and density is given by (Alster, 1972)

$$f=\frac{c}{2\pi}\times\sqrt{\frac{F_N}{1.21(V+V_N)\left\{\dfrac{V}{V+V_N+V_{01}}\dfrac{L}{L+l_N+l_{01}}\left[l_v+(l_N+l_{01})\left(1+\frac{1}{2}\left[\dfrac{V_N+V_{01}}{V}+\dfrac{l_N+l_{01}}{L}\right]+\frac{1}{3}\dfrac{V_N+V_{01}}{V}\dfrac{l_N+l_{01}}{L}\right)\right]+l_{02}\right\}}} \tag{1}$$

where f is the resonant frequency, c is the speed of sound, F_N is the area of the neck at the open end, l_N is the length of the neck, V_N is the volume of the neck, V is the volume of the resonator without the neck, L is the length of the resonator, and l_v is a form factor.

The form factor is defined as:

$$l_v=\frac{F_N}{VL}=\int_0^L\frac{xV(x)}{F(x)}\,dx \tag{2}$$

where $F(x)$ is the area of the resonator cross section at distance x from the closed end, and

$$V(x)=\int_0^x \xi d\xi \tag{3}$$

Further: l_{01}, l_{02} are correction lengths, usually $l_{01}=l_{02}=0.245\,r$, where r is the radius of the neck of the resonator opening and V_{01} is the volume of the neck elongated due to the motion of gas particles outside of resonator ($V_{01}=F_N\,l_{01}$).

The temperature variation along the resonator affects the speed of sound and the density of the gas. A numerical procedure was used to account for these effects, as follows:

For two adjacent sections of lengths, li, lj, densities ρ_i, ρ_j and absolute temperature T_i, T_j, the form factor can be expressed by

$$l_v=\frac{1}{\rho_j}\frac{F_N}{Vl}\left[\rho_i\int_{li}\frac{xV(x)}{F(x)}\,dx+\rho_j\int_{l_j}\frac{xV(x)}{F(x)}\,dx\right] \tag{4}$$

and the speed of sound by

$$c=\frac{c_r}{\sqrt{T_r}}\frac{(l_i+l_j)\sqrt{TiTj}}{l_i\sqrt{T_j}+l_j\sqrt{T_i}} \tag{5}$$

where c_r and T_r are reference values of sound speed and corresponding absolute temperature, respectively.

Figure 6 gives the computed Helmholtz resonator frequencies for four thermal conditions of the recuperator. It can be seen that the computed frequencies agree with those obtained during testing. This result further confirms the observation made earlier that the vibration experienced is of the acoustic type and is governed by the Helmholtz resonator characteristics. As this vibration involves both the tube-side of the recuperator and the discharge duct, it can be classified as a system problem.

Flow Velocities Through Duct/Recuperator System. Representative gas flows following start-up and at normal operation were determined, based on test data taken at turbine speeds of 4000 rpm and 5500 rpm. The calculated values were: 49,300 kg/h (108,400 lb/hr) at 4000 rpm, and 94,550 kg/h (208,000 lb/hr) at 5500 rpm. These flows are a function of load. However, the lower value at 4000 rpm following a turbine start-up can be considered a representative flow in the critical vibratory range.

The average gas flow velocities through the individual cross sections of the duct/recuperator system for the two conditions described above are shown graphically in Fig. 6. In order to obtain the flow velocities at the inlet to the recuperator tube bundle a finite length penetration into the cold section was assumed at the location of the sharp temperature change.

Velocities at Entrance to Tube Bundle at Critical Vibratory Conditions. The flow velocities entering the recuperator tubes at the critical conditions during the cold start-up are important.

From the test data (Figs. 2 and 3) we can see that:

- At about 2000 rpm acoustic vibration was initiated and started to increase gradually.

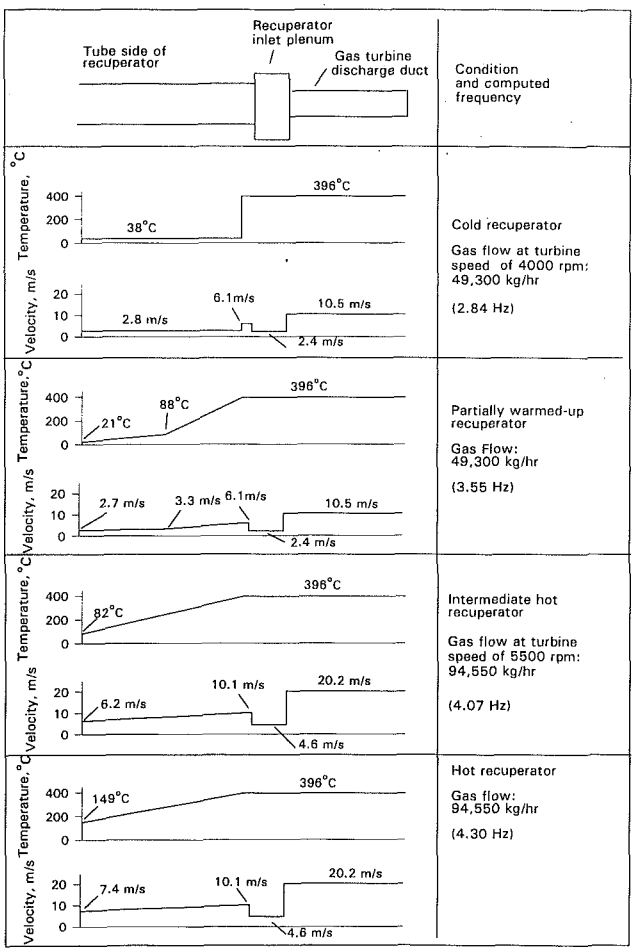

Fig. 6 Gas temperatures and frequencies of Helmholtz resonator representing recuperator/duct system at four thermal conditions; flow velocities through the system are also shown

- At about 3000 rpm a sudden increase (jump) occurred.
- At about 4000 rpm, very large vibration occurred followed by unit shutdown.

The estimated gas velocities at the entrance to the tube bundle (in the recuperator inlet plenum) are given in Table 2.

It can be seen that due to the sharp temperature gradient from 396°C (744°F) to 38°C (100°F) during cold start-up, the hot gas velocity entering the tube bundle is abruptly reduced by more than a factor of 2 when changing to the cold condition. The entrance velocities are thought to be relatively small—too small to disrupt the Helmholtz resonator effect but large enough to cause disturbances that will initiate the vibration.

Acoustic Pressures and Acoustic Velocities During Cold Start-up. At a turbine speed of about 2000 rpm at vibration initiation, the acoustic pressures in the system were small. With increase in turbine speed, the pressures increased steadily up to about 3000 rpm; above this speed a sharp increase (jump) in vibration levels occurred (Figs. 2 and 3). The frequency of the vibration was 3 Hz–3.5 Hz.

Based on the measured acoustic pressures at 3000 rpm of about 2.7 kPa (0.4 psi) at the turbine discharge and 2.1 kPa (0.3 psi) in the recuperator plenum (Fig. 4), acoustic particle motions using the theoretical quarter-wave distribution at a frequency of 3 Hz were calculated. The effect of a local distortion of this wave due to lower temperatures in the recuperator was included. Table 3 gives the results.

At 4000 rpm the vibration reached very large levels in the recuperator inlet plenum, where pressure pulsations of up to about 35 kPa (5 psi) peak-to-peak (Fig. 3) were recorded. While

Table 2 Average gas flow velocities at entrance to recuperator tube bundle

Gas Flow Velocity	2,000 rpm	3,000 rpm	4,000 rpm
Velocity of hot gas: m/s (ft/sec)	3 (10)	4.5 (15)	6.1 (19.9)
Velocity of "cold" gas: m/s (ft/sec)	1.5 (5)	2.1 (6.9)	2.8 (9.3)

Table 3 Acoustic pressures and acoustic particle motions during cold start-up at 3000 rpm turbine speed (before onset of large vibration)

Location	Acoustic Pressure kPa (psi) RMS	Acoustic Particle Velocity m/s (in/sec) RMS	Acoustic Particle Displacement Amplitude m (in) RMS
At top of recuperator	0	4.2 (165)	0.22 (8.8)
At inlet to tube bundle	2.1 (0.3)	3.5 (137)	0.19 (7.2)
At turbine discharge	2.7 (0.4)	0	0

the acoustic pressure was very high in the inlet plenum, the acoustic pressure at the turbine discharge or recuperator discharge was not proportionately higher as would be expected, based on the pressure wave distribution. Thus a local concentration of pressure occurred (see also Fig. 4).

Possible Velocity Coupling Mechanism. A comparison of the gas flow velocities in Table 2 with the acoustic particle velocities in Table 3 indicates a remarkable match at about the 3000 rpm speed. Figure 7 shows the mean values of these velocities plotted as a function of turbine speed. It can be seen that the match of these velocities coincides with the onset of the large acoustic vibration experienced. It seems that a velocity-coupling mechanism might be at work at the inlet to the recuperator tube bundle. This might explain the large local distortion of the acoustic wave, which resulted in a very high pressure pulsation of up to 12.4 kPa (1.8 psi), rms in the inlet plenum (Fig. 3 and 4).

Discussion of the Sondhauss Tube Phenomenon as a Probable Explanation of the Vibration

A Sondhauss tube is a tube closed at one end and open at the other. If such a tube is filled with air or gas and heated internally or externally at a section adjacent to the closed end, or cooled internally or externally at a section adjacent to the open end, acoustic oscillation of the gas in the tube may be initiated. The initiation of oscillation requires a sufficient heat input/output corresponding to a minimum temperature ratio α between the hot (T_h) and cold (T_c) sections (Fig. 8). For a detailed description of the phenomenon, see Feldman (1966), Feldman and Carter (1970), and Rott (1980).

Characteristics of Sondhauss Tube Vibration. We summarize here the most important aspects affecting the proper functioning of a Sondhauss tube:

1 Some minimum heat input (or heat withdrawal), leading to a threshold (critical) temperature ratio $\alpha_{cr} = T_h/T_c$ between the hot and cold sections is required to initiate the vibration. If the temperature is reduced below this critical ratio, the vibration stops.

2 The heat source can be steady, it need not be a fluctuating one.

3 The length-to-diameter ratio of a Sondhauss tube is typically in the range of $L/D = 8$–50. An L/D ratio around 12 has been found to give rise to the strongest vibration.

4 The location of the heat source or the position of the temperature ratio α most favorable for inducing Sondhauss vibration is where both acoustic particle velocity and acoustic pressure are large, and where both are positive or negative, but not exactly in phase. This is necessary because the heat transfer during the oscillation is proportional to the acoustic particle velocity. As the heat transport lags the acoustic particle velocity somewhat, the heat input can be in phase with the

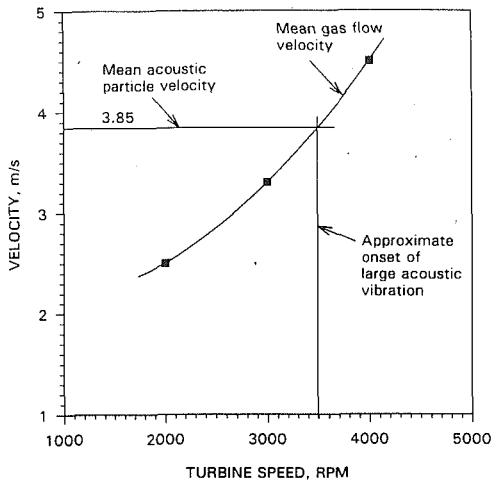

Fig. 7 Coincidence of mean gas flow velocity with mean acoustic particle velocity at entrance to recuperator tube bundle at the onset of large acoustic vibration

acoustic pressure, which 1/4 cycle out-of-phase and thus driving the pressure. The optimum location where the critical temperature ratio is a minimum is in the center of the tube at $\xi = (L = 1)/l = 1$ (Fig. 8).

5 The acoustic wave generated is nearly a perfect plane wave.

6 Based on experimental evidence, the frequency of vibration occurs primarily in the first mode, with maximum acoustic pressure at the closed end and minimum at the open end.

7 The most pronounced vibratory results are obtained when the heated and cooled sections are adjacent to each other and "touching."

8 At the critical heat input/output, Q_{cr}, or at the critical temperature ratio α_{cr}, a small disturbance (external or internal) is usually sufficient to start the oscillation. For the oscillation to be sustained, the total energy of the system per cycle of vibration must be maintained.

9 The basic driving mechanism is simple thermal expansion and compression occuring periodically, combined with mixing of the hot and cold gases (Feldman and Carter, 1970; Feingold, 1964).

10 An engine analogy can be used for the description of the Sondhauss phenomenon: Heat input and heat rejection cause a time varying output, as they drive an acoustic pressure wave. The work as in an engine may be described by a specific thermodynamic cycle characterized by a pressure-specific volume diagram.

11 The Sondhauss tube phenomenon is governed by the Rayleigh principle, which states that heat must be added at the moment of greatest expansion to "encourage" a vibration.

Tube Bundle at the Boundary of Hot and Cold Tube Sections. As shown by Feldman and Carter (1970), the Sondhauss tube will become more efficient, i.e., will produce higher acoustic pressures, when a tube bundle of a certain size is placed between the hot and the cold tube sections. The explanation is that:

- The tube bundle acts as a *regenerator*—it absorbs heat during the expansion or cooling strokes, and gives up heat during the return compression or heating strokes, like a Stirling engine.
- The tube bundle also acts as a porous low friction *thermal insulator*, i.e., it thermally insulates the heated region from the cooled region while allowing the gas to move freely from one region to the other.
- Finally the tube bundle acts as an *acoustic impedance*; this causes a phase shift between the pressure variation and the specific volume variation, which is necessary for the production of net work in a cycle.

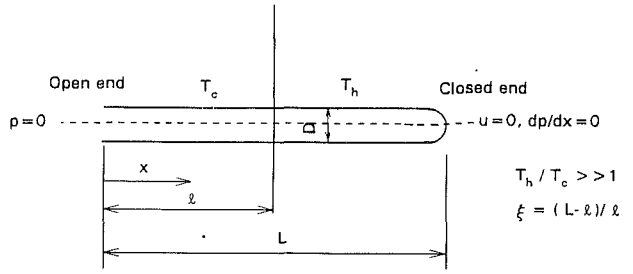

Fig. 8 Line diagram of Sondhauss tube

Prediction of Acoustic Pressures Based on Wave Theory. Based on the heat-generated one-dimensional wave theory, Chu (1955) defined the pressure wave ratio for a moderate compressive wave, given by the expression:

$$\left(\frac{\Delta p}{p_o}\right)_1 = \frac{k-1}{2}\frac{\dot{w}}{c_o\, p_o} \tag{6}$$

where $\dot{w}$ is the rate of heat release per unit area [energy/(area × time)], Δp is the pressure jump across the wave to the undisturbed steady state pressure p_o, c_o is the speed of sound, and k is the ratio of specific heats.

The moderate amount of heat release was defined by Chu by the nondimensional heat release parameter:

$$\frac{\dot{w}}{c_o\, p_o} \ll 1 \tag{7}$$

(The subscript o indicates the steady-state undisturbed conditions ahead of the pressure wave.)

For a very high rate of heat release in a shock wave, the pressure ratio is given by:

$$\left(\frac{\Delta p}{p_o}\right)_2 = 1.625\,\frac{k-1}{2}\left(\frac{\dot{w}}{c_o\, p_o}\right)^{2/3} \tag{8}$$

According to Feldman (1966), Eq. (6) accurately predicts the acoustic pressures at the mouth of a Sondhauss tube, and Eq. (8) predicts the maximum acoustic pressures in the tube.

Prediction of Sonhauss Tube Frequency. The frequency of a constant diameter Sondhauss tube with a uniform temperature distribution in the hot and cold sections with one end closed and the other end open can be evaluated reasonably accurately by the formula:

$$f = \frac{c}{4L} \tag{9}$$

where c is the speed of sound in the cold tube section and L is the total tube length. A numerical value of $f = 3.5$ Hz can be calculated for a temperature of 37.8°C in the cold section and a total length of 25.6 m. This frequency is within the range of the frequencies computed from the formulas of the Helmholtz resonator (Fig. 6).

Numerical Evaluation of Acoustic Pressures. The rate of heat release per unit area can be expressed by:

$$\dot{w} = v_f\, \rho\, Q_s \tag{10}$$

where v_f is the gas flow velocity entering the recuperator, ρ is the gas density, and Q_s is the sensible heat content (energy/mass). (Sensible heat at temperature T is the energy needed to raise the temperature of 1 kg of gas from a reference temperature of 26.7°C to temperature T.)

At a gas temperature $T = 396$°C (744°F) entering the recuperator tube bundle at a gas flow rate of $W = 49{,}300$ kg/h

Table 4 Comparison of theoretical and experimental values of acoustic pressures at open and closed ends of the Sondhauss tube

Location	Acoustic Pressure, Pa (dB, re: 2×10^{-5} Pa), RMS	
	Theory (Equ. 6 & 8)	Experiment (Fig. 4)
Open End At Top of Recuperator Equation (6)	480 (150)	270 (143)
Closed End At Turbine Discharge Equation (8)	2,719 (164)	2,100 (161) 2,700 (162.8)

(108,400 lb/hr) at the high vibratory condition during cold start-up (Fig. 6), the numerical values are:

$v_f = 6.1$ m/s (19.9 ft/sec) (Fig. 6)

$\rho = 0.538$ kg/m^3 (0.0335 lb/ft^3)

$Q_s = 382 \frac{\text{kJ}}{\text{kg}} \left(164 \frac{\text{Btu}}{\text{lb}}\right)$, for gas with zero moisture content.

From Eq. (10), we have the value of the rate of heat release per unit area:

$$\dot{w} = 1249 \frac{\text{kJ}}{m^2 s} \left(109.3 \frac{\text{Btu}}{\text{ft}^2\text{sec}}\right)$$

Since the value of Q_s increases with moisture content, the rate of heat release for gases with higher moisture content would also increase.

The numerical values for the acoustic pressures from Eqs. (6) and (8) (using $k = 1.375$ and $p_o = 1.0135 \times 10^5$Pa), and their comparison with experimental data are given in Table 4. It can be seen that the experimental results are in reasonably good agreement with theory.

The agreement of experimental data with the theoretical predictions appears to confirm the correct evaluation of the rate of heat release from the flowing gas and more importantly that the Sondhauss acoustic pressures are indeed generated by a heat-generated pressure wave, initiated at the interface between the hot and the cold sections.

Prediction of Stability Limits for Onset of Vibration. Based on boundary layer theory, Rott derived stability limits for a Sondhauss tube of a constant diameter, and also for one with a step change in diameters between the heated and unheated sections (Rott, 1973, 1980; Rott and Zouzoulas, 1976). In his analysis of constant-diameter Sondhauss tubes, Rott derived the threshold critical temperature ratio α_{cr} at the interface between the heated and unheated sections of the tube as a function of $\xi = (L - l)/l$, where ξ indicates the position of the temperature change. The α_{cr} versus ξ stability diagrams for a tube filled with helium gas and tube filled with nitrogen gas are practically parallel to each other, both having a minimum α_{cr} almost exactly at $\xi = 1$. The governing parameters for a particular gas in Rott's theory are the ratio of specific heats k, the Prandtl number σ, and the exponent β for the viscosity-temperature power law. As the numerical values of these parameters for nitrogen and air are very close to each other, the nitrogen-based stability diagrams can be used for a Sondhauss tube filled with air, and can also be used for the turbine exhaust gas whose representative parameters are very close to those of nitrogen gas.

Rott also derived the stability limits for Sondhauss tubes with a step change in diameters D_h/D_c between the hot tube section adjacent to the closed end and the cold tube section adjacent to the open end (Rott and Zouzoulas, 1976). Theoretical relationships are given for $D_h/D_c = 1, 2, 5, \ldots, \infty$. Excellent agreement is shown between theoretical predictions and experimental results for nitrogen gas-filled vibrating tubes with a diameter ratio of $D_h/D_c = 2$ ($D_h = 4$ mm, $D_c = 2$ mm) at $\xi = 1$ for tubes with various lengths. The value of $D_h/D_c = 2$ is reasonably close to that of the Sondhauss tube of $D_h/D_c = 1.55$ representing the recuperator/duct system and will be used for comparison.

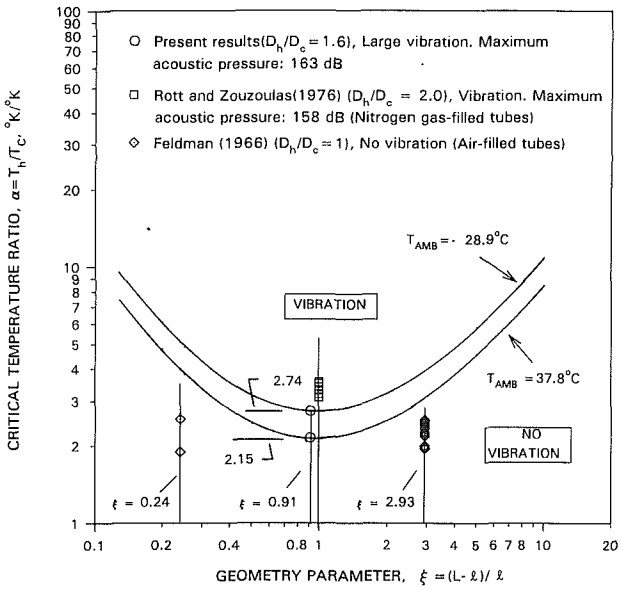

Fig. 9 Stability diagram showing curves defining onset of large acoustic vibration of recuperator/duct system for two ambient temperatures; shape of curves after Rott (1980)

Stability Diagram for the Sondhauss Tube Representing the Recuperator/Duct System. The Helmholtz resonator or the Sondhauss tube is characterized by the following dimensions (Fig. 5):

- Total length: $L = 25.603$ m (84 ft)
- Length of hot section: $L - l = 12.192$ m (40 ft)
- Length of cold section: $l = 13.411$ m (44 ft)
- Diameter of hot section: $D_h = 3.656$ m (12 ft)
- Diameter of cold section: $D_c = 2.3$ m (7.57 ft)
- Diameter ratio: $D_h/D_c = 1.55$

The position of the temperature gradient is:

$$\xi = \frac{L - l}{l} = \frac{12.192}{13.411} = 0.91$$

Based on experimental measurements, the onset of large acoustic vibrations in the recuperator/duct system occurred at a gas temperature entering the recuperator of $T_h = 395.6$°C (744°F) = 668.7 K.

This gas temperature was almost always the same at the onset of the large acoustic vibration. What varied was the temperature of the recuperator comprising the cold section. As the recuperator was located outdoors, its temperature varied. For evaluation purposes we will consider two temperature conditions: (1) $Tc = -28.9$°C (−20°F) = 244.3K and (2) $T_c = 37.8$°C (100°F) = 311 K. The critical temperature ratios that initiated the large oscillations thus were:

Condition (1): $\alpha_{cr} = 668.7/244.3 = 2.74$

Condition (2): $\alpha_{cr} = 668.7/311.0 = 2.15$

The stability diagrams, i.e., the curves defining the onset of large acoustic vibration for a Sondhauss tube representing the recuperator system based on the stability curves of Rott (1980) are shown in Fig. 9. (These curves were constructed using the shape derived by Rott with α and ξ values determined for the recuperator.) Also shown are experimental results reported by Rott and Zouzoulas (1976) for nitrogen-gas-filled tubes for $D_h/D_c = 2$ and $\xi = 1$, and by Feldman (1966) for air-filled constant-diameter Sondhauss tubes 102 mm (4 in.) in diameter and 1500 mm (59 in.) long at $\xi = 0.24$ and 2.93. Feldman reported no vibration for the points shown; however, at values of ξ greater than 0.24 or smaller than 2.93 the tubes did vibrate at the same heat input. As can be seen from Fig. 9, the stability diagram represents the vibratory characteristics of the recuperator/duct system over the entire range of ξ. We can also

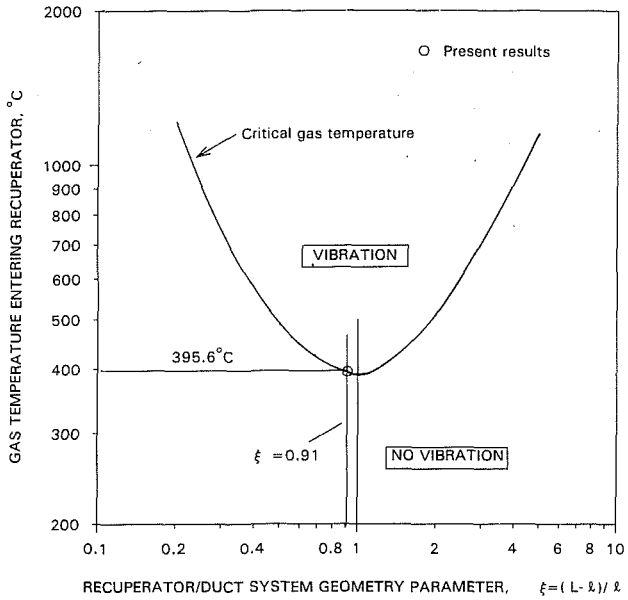

Fig. 10 *Critical turbine exhaust gas temperature entering recuperator tube bank at initiation of large acoustic vibration*

see that the geometric arrangement of the recuperator/duct system at $\xi = 0.91$ leads to critical temperature ratios of $\alpha_{cr} = 2.74$ and $\alpha_{cr} = 2.15$ for the cold ($-28.9°C$) and average ($37.8°C$) ambient temperatures, respectively, which are close to the minimum values of α. From the shape of the stability curve it is clear that for increased resistance to vibration the system should be designed with values of ξ greatly different from 1, either $\xi > 1$ or $\xi < 1$.

The stability curves in Fig. 9 can be represented by a parabola:

$$(\log \xi)^2 = 1.52\ (\log \alpha - \log \alpha_{\min}) \qquad (11)$$

where $\alpha_{\min}$ is the value of α at the vertex of the parabola at $\xi = 1$. The accuracy of the numerical values is approximately ± 3 percent within range of $0.2 \le \xi \le 5.0$.

It is advantageous to represent the stability of the system based on the temperature of the hot gas only. Figure 10 shows the relationship between the critical temperatures of the gas $T_{cr}°(C)$ entering the recuperator (temperatures initiating the large vibration), and the geometry parameter ξ. For practical purposes the two stability curves from Fig. 9 merge into one, thus virtually eliminating the effect of the ambient temperature variation.

The critical gas temperatures shown in Fig. 10 can be described by the formula:

$$\log T = 2.824 + (\log \xi)^2/1.52 \qquad (12)$$

where T is the absolute temperature in degrees Kelvin. The accuracy of Eq. (12) is similar to that of Eq. (11) within the same range of ξ.

Based on the diagram in Fig. 10, the system can be designed to be vibration free if a value of ξ is selected to give a critical temperature T_{cr} adequately above the maximum gas temperature $T_{\max}$. The critical temperature T_{cr} is selected either from the left $\xi < 1$, or from the right $\xi > 1$ branch of the stability curve, depending upon the design layout requirements. When determining T_{cr} an appropriate safety factor $s = T_{cr}/T_{\max} > 1$ is needed for a vibration-free design.

Review and Discussion

The recuperator/duct system vibrated during cold start-up as a quarter wave-length Helmholtz resonator as shown by the experimentally measured mode shape of acoustic pressures and by the experimentally and theoretically determined acoustic frequencies. During this start-up, turbine speed, gas flow velocity, and gas temperature are increasing. At first, a small-amplitude 3 Hz vibration occurred, perhaps in response to turbulent excitation. This amplitude grew steadily with turbine speed up to about 3000 rpm. When the turbine exhaust temperature reached about 396°C (744°F), large vibration began leading to large acoustic pressure oscillations of 161 dB at a frequency of 3.5 Hz.

During the above-described large acoustic oscillation, the turbine speed was increased to about 4000 rpm. At this point the mean gas flow velocity entering the recuperator tube bundle became about the same as the vibratory acoustic particle velocity. Indications are that the matching of the velocities activated a velocity-coupling mechanism generating extremely high acoustic pressures in the inlet plenum at the inlet to the recuperator tube bundle. This pressure, which reached 12.42 kPa (1.8 psi) or 176 dB (re: 2×10^{-5} Pa), led to a strongly distorted pressure wave, and forced a shut-down of the unit to preclude structural damage.

The vibration was driven by a modified Sondhauss tube phenomenon with the exhaust gas system acting as the hot portion of the Sondhauss tube, and the tube side of the recuperator acting as the cold side of the tube. The sharp temperature gradient at the inlet of the recuperator is the source of the Sondhauss oscillation. While by definition a Sondhauss oscillation occurs in a tube with one end closed and the other end open, with no net flow through the tube the reported oscillation did occur under net flow conditions. There is no evidence that the flow suppressed the Sondhauss oscillation or affected the frequency. On the contrary, there is supportive evidence that the flow strongly increased the pressure pulsation due to the velocity coupling effect, and may have initiated the vibratory process.

Good agreement between theoretical predictions of acoustic pressures based on wave theory by Chu (1955) and experimental values gives credence to the heat-generated wave theory as one of the major driving components of the Sondhauss tube oscillation. Excellent agreement of the stability analysis of Rott and Zouzoulas (1976), and Rott (1980) with experiments shows that disturbances in the boundary layer in the region of the interface between the hot and the cold sections are the underlying physical causes of the instability.

As shown above, the arrangement of the recuperator/duct system in which the hot/cold interface at the inlet to the recuperator is located close to the center of the total developed length of the system (at $\xi = 0.91$), made the system particularly sensitive to vibration by lowering the critical temperatures needed for vibration initiation. With the gas temperatures being at or very close to the critical temperatures of the system, the system was on the verge of instability. The system can be made strongly resistant to the vibration by arranging it more asymmetrically, i.e., by making the duct system shorter or longer and thereby changing the Sondhauss tube geometry parameter ξ to a value below or above one. The geometry parameter ξ must be selected such that the critical gas temperatures from the stability diagram are sufficiently higher than the temperatures of the exhaust gas.

Features Eliminating or Reducing the Sondhauss Tube Phenomenon

Prevention of Problem by Design. The vibration problem can be prevented in the design stage by selecting the right length of hot duct in relation to the length of the recuperator. In this way the system critical temperatures can be made high enough so that the exhaust gas temperatures never reach them.

Alternative (Remedial) Solutions. Alternative solutions, some of which were experimentally verified, can also be used. A partial list follows:

1 Opening in the Turbine Exhaust Gas Discharge Duct. We have shown that a sufficiently large opening in the recuperator inlet plenum (Test 2) eliminated the vibration during cold start-up by destroying the Helmholtz resonator effect. A portion of the gases was released to the atmosphere for a period of time until the recuperator warmed up sufficiently. After the warm-up, the opening can be closed and turbine load increased. For this purpose an automatic valve system can be used, which opens during cold start-up, and closes after the unit is warm, thereby eliminating the loss of a portion of the waste gases. Although closing the valve restores the Helmholtz resonator phenomenon, this does no harm to the system when it is hot.

2 Partial Blockage of the Recuperator Discharge. By partially obstructing the exit from the recuperator or placing a silencer at the discharge it is possible to affect the level of the oscillation, as was suggested by Kosten (1982). Increased pressure drop might become a problem, however.

3 Increase Acoustic Impedance and Damping in Discharge Duct. Increasing acoustic impedance and damping to the longitudinal waves in the duct by using screens, acoustic panels, baffles, etc. may reduce or eliminate the vibration. Here again, increased pressure drop may become a problem and this can be aggravated by the fact that at increased pressures, increased acoustic pressure waves may be detrimental (Chu, 1955). However, it may be possible to achieve a beneficial trade-off among the factors affecting the vibration.

4 Preheat System Externally Prior to Start-up. This solution requires the availability of an external heat source such as an operating similar system, which would be temporarily connected prior to start-up for the heating purposes (Kosten, 1982).

Some of the alternative solutions have been used or are used in existing installations. To obtain a successful solution, in-situ experimental verification is often necessary.

Summary and Conclusions

The large acoustic vibration that occurred in a full-size gas turbine exhaust gas recuperator system was caused by a Sondhauss tube thermoacoustic phenomenon in possible combination with a fluid-acoustic (flow velocity/acoustic particle velocity coupling) mechanism. The Sondhauss phenomenon materialized despite the presence of a net axial flow through the system.

The recuperator/duct system design described was such that the exhaust gas temperature was at or very close to the critical gas temperature needed to initiate the vibration. The location of the sharp temperature gradient at the junction between the hot and cold sections of the system (at the inlet to the recuperator), which drives the vibration, was very close to the midpoint of the developed length of the system, minimizing the system's resistance to heat-driven oscillations. The system could be designed to be fully resistant to vibration by placing the inlet of the recuperator sufficiently off-center of the combined length of the recuperator/duct system. This asymmetric arrangement increases the critical gas temperatures needed to excite the vibration. The critical temperatures must be sufficiently greater than the anticipated temperatures of the exhaust gas to prevent the oscillation. The information included in this paper may be of use to designers of such systems (or systems similar to these) in selecting a vibration-resistant configuration.

Acknowledgments

The author would like to thank J. R. Presley for his help during the testing and engineering evaluation of the problem, and to R. E. Sullivan and J. T. Francis for their help in the preparation of this paper.

The author is indebted to his colleague M. D. Bernstein who reviewed the manuscript and offered many valuable suggestions.

The author gratefully acknowledges the permission of Foster Wheeler Energy Corporation to publish the results contained in this paper.

References

Alster, M., 1972, "Improved Calculation of Resonant Frequencies of Helmholtz Resonators," *Journal of Sound and Vibration*, Vol. 24 (1), pp. 63–85.

Chu, B. T., 1955, "Pressure Waves Generated by Addition of Heat in a Gaseous Medium," National Advisory Committee for Aeronautics, Technical Note 3411, pp. 1–47.

Chu, B. T., 1956, "Stability of Systems Containing a Heat Source—The Rayleigh Criterion," National Advisory Committee for Aeronautics, Research Memorandum 56D27.

Culick, F. E. C., 1970, "Stability of Longitudinal Oscillations With Pressure and Velocity Coupling in a Solid Propellant Rocket," Combustion Science and Technology, Gordon and Breach Science Publishers, Vol. 2, pp. 179–201.

Feingold, A., 1964, "Mixing of Gases at the Same Original Pressure but Different Original Temperatures," presented at the Missouri Academy of Sciences, University of Missouri, Columbia, MO, Apr.

Feldman, K. T., 1966, "A Study of Heat Generated Pressure Oscillations in a Closed End Pipe," Ph.D. Dissertation, Mechanical Engineering, University of Missouri, Columbia, MO.

Feldman, K. T., 1968a, "Review of the Literature on Sondhauss Thermoacoustic Phenomena," *Journal of Sound and Vibration*, Vol. 7, No. 1, pp. 71–82.

Feldman, K. T., 1968b, "Review of the Literature on Rijke Thermoacoustic Phenomena," *Journal of Sound and Vibration*, Vol. 7, No. 1, pp. 83–89.

Feldman, K. T., and Carter, R. L., 1970, "A Study of Heat Driven Pressure Oscillations in a Gas," ASME *Journal of Heat Transfer*, Vol. 92, pp. 536–541.

Gifford, W. E., and Longworth, R. C., 1963, "Pulse-Tube Refrigeration," ASME Paper No. 63-WA-290.

Kosten, G. J., 1982, "Vibration of a Regenerative Gas Turbine Exhaust System," presented at the American Gas Association Transmission Conference, May 17, pp. 1–16.

Kramers, H. A., 1949, "A Vibration of a Gas Column," *Physica* (Utrecht), Vol. 15, pp. 971–984.

Proceedings of the International Symposium on Pulsating Combustion, 1991, Sandia National Laboratory and the Gas Research Institute, Aug.

Putnam, A. A., and Dennis, W. R., 1953, "A Study of Burner Oscillations of the Organ-Pipe Type," *Transactions of the ASME*, Vol. 75, pp. 15–28.

Radebaugh, Ray, 1990, "A Review of Pulse Tube Refrigeration," *Advances in Cryogenic Engineering*, Vol 35, pp. 1191–1205.

Rayleigh, Lord, 1945, *Theory of Sound*, Dover Publications, New York, Vol. II, pp. 224–234.

Rijke, P. L., 1859, "Notiz uber eine neue Art, die an einer an beiden Enden offenen Rohre enthaltene Luft in Schwingungen zu versetzen," *Poggendorff Annalen der Physik und Chemie*, Vol. 107, May, pp. 339–345.

Rott, N., 1969, "Damped and Thermally Driven Acoustic Oscillations in Wide and Narrow Tubes," *Journal of Applied Mathematics and Physics* (*ZAMP*), Vol. 20, pp. 230–243.

Rott, N., and Zouzoulas, G., 1976, "Thermally Driven Acoustic Oscillations, Part IV: Tubes With Variable Cross-Section," *Journal of Applied Mathematics and Physics* (*ZAMP*), Vol. 27, pp. 197–224.

Rott, N., 1980, "Thermoacoustics," *Advances in Applied Mechanics*, Vol. 20, Academic Press.

Sondhauss, C., 1850, "Uber die Schallschwingungen der Luft in erhitzten Glasrohren und in gedeckten Pfeifen von ungleicher Weite," *Poggendorff Annalen der Physik und Chemie*, Vol. 79, Feb., pp. 1–34.

Wheatley, J., Hofler, T., Swift, G. W., and Migliori, A., 1985, "Understanding Some Simple Phenomena in Thermoacoustics With Applications to Acoustical Heat Engines," *American Journal of Physics*, Vol. 53, No. 2, American Association of Physics Teachers, pp. 147–162.

A. Turpin
Mechanical Design Engineer,
Engineering Department,
Newfoundland and Labrador Hydro,
St. John's, Newfoundland, Canada

A. M. Sharan
Professor,
Faculty of Engineering,
Memorial University of Newfoundland,
St. John's, Newfoundland, Canada,
A1B 3X5

Balancing of Rotors Supported on Bearings Having Nonlinear Stiffness Characteristics

In real-life applications, multi-disk-rotor systems are supported on bearings with nonlinear flexibility. The balancing of such systems at high speeds is a challenging task. This work presents a method of balancing such systems. The dynamic equations of motion for a nonlinear system are derived first using the influence coefficient method and then Lagrangian equations. An equivalent linear system is found using the optimization principles. Finally, the correct balance weights for the nonlinear system are obtained based on the equivalent linear system. The results thus obtained establish the utility of such a method of balancing nonlinear systems.

1 Introduction

The major cause of rotor vibrations in rotating shafts is residual unbalance. These unbalances in the rotor can be due to material inhomogeneities, manufacturing processes, keyways, slots, etc. Also, during the operating of the rotor, there is a deterioration in the balance of the rotor due to component wear, thermal bending, and process contamination, all of which cause an increase in the vibratory response of a rotor. In addition to causing vibration in the rotor shafts, the unbalance forces are transmitted to the rotor bearings and support structure. The object of a rotor balancing procedure is to reduce these unbalance forces to obtain acceptable levels of vibration for reliable operation of rotating equipment.

The rotor model used for the response computations usually incoporates linear bearing support characteristics. However, many rotors experience nonlinear forces at the rotor interactive devices such as bearings and seals. For example, rolling element bearings are commonly used in the various kinds of turbomachinery, such as compressors and gas turbine engines. The spring characteristic of the rolling element bearing is nonlinear and the vibration response of the rotor has to be calculated taking this nonlinearity into account. The nonlinear problem has to be solved numerically as a function of time, to obtain the steady-state response. In addition, the current balancing techniques of modal balancing and influence coefficient balancing are based on the assumption of linear superposition of rotor response. If the rotor nonlinearities are considered, it would be difficult to balance the rotor since linear superposition would not be valid.

Flexible rotor balancing theory was first developed by Meldahl in 1954. He showed the orthogonality conditions between any two modes, and that it was possible to balance a flexible rotor mode by mode. Beginning in 1959 this method was further developed by Bishop and his co-workers. These papers greatly advanced the theory and application of the modal balancing method and resulted in the development of practical techniques for flexible rotor balancing. Further developments in this area can be found in the works of several other researchers (Bishop and Gladwell, 1959; Gladwell and Bishop, 1959; Bishop and Parkinson, 1972; Kellenberger, 1972).

The influence coefficient method of flexible rotor balancing utilizes the rotor-bearing sensitivity for the calculation of balance correction weights. At first, the unbalance of the rotor measuring planes is determined at the given speed without any correction weights. A trial weight is applied in one of the balancing planes and the rotor response is obtained for all of the measuring planes. This process is repeated for all of the balancing planes and from these data the influence coefficient matrix is obtained. The required correction weights can be calculated by multiplying the inverse of the influence coefficient matrix with the original unbalance response vector (Rao, 1983). Developments in this method of flexible rotor balancing can be found in the work of various researchers (Goodman, 1964; Rieger, 1967; Lund and Tonneson, 1972; Tonneson, 1974; Tessarzik et al., 1972; Tessarzik and Badgley, 1974; Little and Pilkey, 1976).

In view of the discussions above, the objectives of this work can be summarized as follows:

1 To develop a mathematical model of a multimass rotor supported on nonlinear roller bearings, and then find an equivalent linear model for the nonlinear rotor.
2 To balance the nonlinear rotor using the equivalent linear system.

The assumptions are that the rotary inertia and the effect of gyroscopy are negligible in the present analysis.

Contributed by the Power Division for publication in the JOURNAL OF ENGINEERING FOR GAS TURBINES AND POWER. Manuscript received by the Power Division November 18, 1981. Associate Technical Editor: R. W. Porter.

2 Mathematical Formulation

2.1 Equivalent Linearization of Multi-Degree-of-Freedom Systems Using Optimization Principles. Before going through the details about the balancing of a nonlinear bearing-rotor system, it is worthwhile to mention briefly the equivalent linearization method using the optimization principle (Sharan and Turpin, 1989).

For a multi-degree-of-freedom system, one can write the error between the actual nonlinear response obtained using the Runge–Kutta method, $x_{jk}(t)_R$, and the equivalent linear response $x_{jk}(t)_{\text{Eq}}$ as

$$e_{jk} = x_{jk}(t)_R - x_{jk}\ (t)_{\text{Eq}} \tag{1}$$

Now if we define an objective function U such that

$$U = \sum_{k=1}^{n^*} \sum_{j=1}^{N_1} e_{jk}^2 \tag{2}$$

then if $U \to 0$, the equivalent linear system will accurately represent the nonlinear system. Here the indices j and k stand for the number of points selected in the time period τ and the degrees of freedom in the system, respectively. For the equivalent system we can define a vector $\{V\}$ as

$$\{V\} = \begin{Bmatrix} K_1 \\ C_1 \\ \dot{K}_n \\ C_n \end{Bmatrix} \tag{3}$$

where K_k and C_k are the stiffness and damping parameters, respectively. To obtain $x_{jk}(t)_R$, one can use the Runge–Kutta method applicable to system of nonlinear equations, whereas $x_{jk}(t)_{\text{Eq}}$ is obtained from the modal analysis of the equivalent system of linear differential equations given by

$$[M]\{\ddot{x}(t)\} + [C]\{\dot{x}(t)\} + [K]\{x(t)\} = \{F(t)\} \tag{4}$$

Thus the steps involved in this method for the n^* degrees-of-freedom system are:

1 Assume a vector $\{V\}$, given by Eq. (3), within the upper and lower limits for the damping and stiffness parameters.
2 Obtain the time history of each of the degrees of freedom within a time period using modal analysis of Eq. (4).
3 Calculate U given by Eq. (2).
4 Follows steps *a–f* in the minimization algorithm given below:

The Steps

(*a*) With the assumed vector $\{V\}$, assume a $(b \times b)$ positive symmetric matrix $[H]$. If the number of elements in the vector $\{V\}$ were n, then $[H]$ would be of the size $b \times b$.

(*b*) Calculate the gradient of the objective function, $\{\nabla U\}$ at the point $\{V\}_i$ and evaluate $\{G\}_i$ using

$$\{G\}_i = -[H]_i\ \{\nabla U\}_i \tag{5}$$

(*c*) Obtain the optimal step length λ^* in the direction $\{G\}_i$ and set

$$\{V\}_{i+1} = \{V\}_i + \lambda_i^* \{G\}_i \tag{6}$$

(*d*) Compute the objective function corresponding to $\{V\}_{i+1}$ and test for optimality. If it is achieved within the required tolerance then stop, otherwise go to the next step.

(*e*) Update the matrix $[H]_{i+1}$ for the next iteration using the relation

$$[H]_{i+1} = [H]_i + [L]_i + [N]_i \tag{7}$$

where

$$[L]_i = \frac{\lambda_i^* \{G\}_i \{G\}_i^T}{\{G\}_i^T \{P\}_i} \tag{8}$$

$$[N]_i = \frac{-\{[H]_i\{P\}_i\}\{[H]_i\{P\}_i\}^T}{\{P\}_i^T [H]_i\ \{P\}_i} \tag{9}$$

$$\{P\}_i = \nabla U_{i+1} - \nabla U_i \tag{10}$$

(*f*) Go to step (*b*).

In this way the equivalent linear parameters of K_k and C_k can be found.

2.2 Balancing of Rotors Supported on Nonlinear Bearings. The Optimization Method of Linearization discussed just above shall now be used in the balancing of a rotor supported on nonlinear bearings. The procedure is outlined on Fig. 1. This section is divided into the following subsections:

1 Formulation of the equations of motion for the unbalanced response of a rotor supported on nonlinear bearings.
2 Development of a numerical procedure to solve the nonlinear equations.
3 Solution of a linear system of equations using the impedance method.
4 Equivalent linearization of the nonlinear system using the optimization method.
5 Balancing of a rotor with nonlinear bearings.

Nomenclature

a_{ij} = elements of the matrix $[A]$
$[A]$ = matrix of influence coefficients
C_i = damping coefficient for the ith damper
$[C]$ = damping matrix
e_{jk} = error at $t = t_j$ for the kth degree of freedom
F_i = force acting on the ith mass
$F(t)$ = forcing function
F_z, F_y = bearing forces
$\{F\}$ = force vector
$\{\bar{F}\}$ = complex phasor of $\{F\}$
K, K^* = spring stiffness coefficients
K_i = stiffness coefficient for the ith degree of freedom
$[K_s]$ = matrix of shaft stiffness coefficients
$K_{zz}^{1B}, K_{yy}^{1B}, K_{zz}^{2B}, K_{yy}^{2B}$ = bearing linear stiffness coefficients
$[K]$ = nonlinear stiffness matrix
L^* = the Lagrangian
L, l_i = shaft lengths
m_i = ith disk mass
$\{m_c\}$ = vector of correction masses
$[M]$ = mass matrix
n^* = degrees of freedom
n = number of rotor disks
N_1 = number of data points
N = number of iterations
q_i = generalized displacement coordinate for the ith degree of freedom
$\{q\}$ = vector of generalized coordinates
$\{q\}_0$ = vector of the value of the generalized coordinates at $t = 0$
$\{Q\}$ = harmonic response vector
$\{\bar{Q}\}$ = complex phasor of $\{Q\}$
r_i = eccentricity of the ith rotor disk
t = time

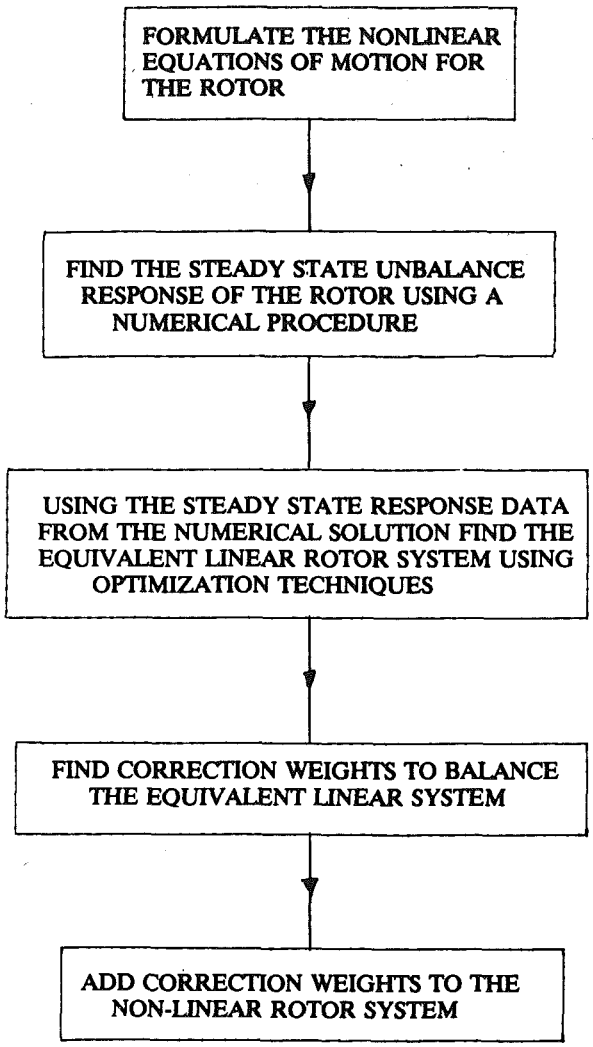

Fig. 1 Flow chart of balancing procedure for rotors supported on nonlinear bearings

2.2.1 Derivation of Equations of Motion for a Rotor Supported on Nonlinear Bearings. A multimass rotor mounted on nonlinear ball bearings, one on each end of the shaft, is shown in Fig. 2. The equations of motion for this multi-degree-of-freedom system are formulated using flexibility influence coefficients and Lagrange equations (Tse et al., 1978). Using the Lagrange approach the system of equations is derived from two scalar functions; the kinetic energy T, and the potential energy V. The equations apply to nonlinear as well as linear systems.

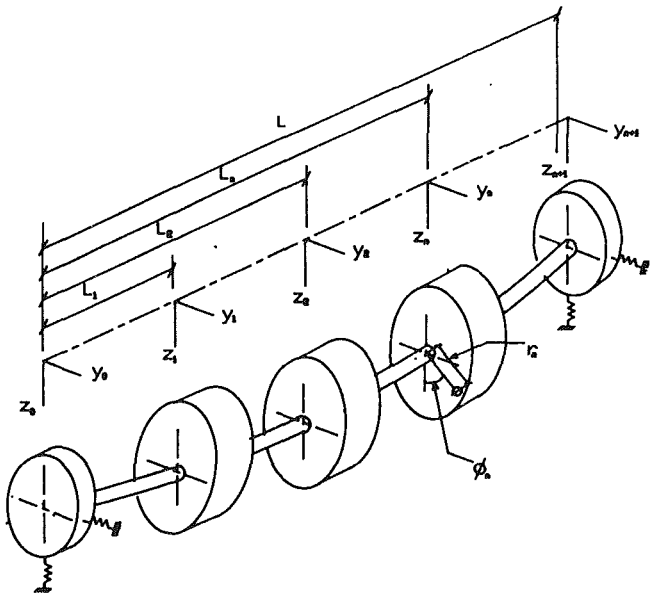

Fig. 2 Multimass rotor supported on nonlinear bearings

Referring to Fig. 2, the displacements of the rotor disks due to the bearing displacements are given by z_i^* and y_i^* while the elastic deformations along the z and y axes represented by vectors $\{u\}_z$ and $\{u\}_y$ are given by

$$\{u\}_z = \begin{Bmatrix} z_1 - z_1^* \\ z_2 - z_2^* \\ \cdot \\ z_n - z_n^* \end{Bmatrix} \quad \{u\}_y = \begin{Bmatrix} y_1 - y_1^* \\ y_2 - y_2^* \\ \cdot \\ z_n - y_n^* \end{Bmatrix} \tag{11}$$

The potential energy of the rotor comprises of the strain energy from both bearing deflections and rotor elastic deformations. The nonlinear bearings are modeled as ball bearings, such that they have a cubic nonlinear term (Genta and Repaci,

Nomenclature (cont.)

T = kinetic energy
T_j = trial mass in the jth balancing plane
U = objective function
V = potential energy
V_B = potential energy of bearings
V_s = potential energy of shaft
V_T = potential energy of rotor system
$x(t)$ = displacement at time t
$x_{jk}(t)$ = value of x at $t = t_j$ for the kth degree of freedom
z_i, y_i = deflections of the ith rotor disk
z_i^*, y_i^* = deflections of the ith rotor disk due to bearing deflections only
$[Z]$ = impedance matrix
z_{ij} = ith vibration reading with trial mass installed in jth balancing plane
z_{i0} = ith vibration reading with no trial mass
$\{z_0\}$ = response vector due to original rotor unbalance
α = constant
β = constant
$\epsilon^{1B}, \epsilon^{2B}$ = constants
θ_z, θ_y = constant, angular displacement
λ^* = optimal step length
τ = time period
ϕ_i = phase angle of the ith rotor disk
ψ = Rayleigh's dissipation function
ω = angular frequency
$\{\ \}$ = vector
$[\ ]$ = matrix
$(\cdot)$ = $d(\ )/dt$
$(\cdot\cdot)$ = $d^2(\ )/dt^2$
$\{\nabla U\}_i$ = gradient of the objective function U at the ith iteration stage
Δt = time step

1988), where the force and displacement expressions are given by

$$F_{z_0} = K_{zz}^{1B}\, z_0 + \epsilon^{1B}\, z_0^3$$
$$F_{z_{n+1}} = K_{zz}^{2B}\, z_{n+1} + \epsilon^{2B}\, z_{n+1}^3$$
$$F_{y_0} = K_{yy}^{1B}\, y_0 + \epsilon^{1B}\, y_0^3$$
$$F_{y_{n+1}} = K_{yy}^{2B}\, y_{n+1} + \epsilon^{2B}\, y_{n+1}^3 \quad (12)$$

The potential energy for the bearings is given by

$$V_B = \int_0^{z_0} (K_{zz}^{1B}\, z + \epsilon^{1B}\, z^3)\, dz + \int_0^{y_0} (K_{yy}^{1B}\, y + \epsilon^{1B}\, y^3)\, dy + \int_0^{z_{n+1}} (K_{zz}^{2B}\, z + \epsilon^{2B}\, z^3)\, dz + \int_0^{y_{n+1}} (K_{yy}^{2B}\, y + \epsilon^{2B}\, y^3)\, dy \quad (13)$$

The potential energy of rotor due to the elastic deformations is given by

$$V_s = \frac{1}{2}\{u\}_z^T [K_s] \{u\}_z + \frac{1}{2}\{u\}_y^T [K_s] \{u\}_y \quad (14)$$

where $[K_s]$ is the matrix of stiffness influence coefficients for the shaft. The matrix $[K_s]$ can be found by taking the inverse of the flexibility influence coefficients (Sharan and Rao, 1985). The total potential energy V_T is the sum of V_B and V_s such that

$$V_T = V_B + V_s \quad (15)$$

The expression for the system kinetic energy is given by

$$T = \sum_{i=1}^{n} \frac{1}{2} m_i \left[\frac{d}{dt}\{z_i + r_i \cos(\omega t + \phi_i)\}\right]^2 + \sum_{i=1}^{n} \frac{1}{2} m_i \left[\frac{d}{dt}\{y_i + r_i \sin(\omega t + \phi_i)\}\right]^2 \quad (16)$$

Having found the kinetic and potential energy expressions, we can introduce the Lagrangian, defined by

$$L^* = T - V_T \quad (17)$$

The Lagrange equations of motion (Tse et al., 1978) can be written as

$$\frac{d}{dt}\left(\frac{\partial L^*}{\partial \dot{q}_i}\right) - \frac{\partial L^*}{\partial q_i} + \frac{\partial \Psi}{\partial \dot{q}_i} = F_i \quad i = 1, \ldots, n \quad (18)$$

In Eq. (18), F_i represents the nonconservative forces, q_i the generalized coordinate, and ψ represents the Rayleigh dissipation function. In this rotor example, there is no viscous damping and therefore $d\psi/d\dot{q}_i = 0$. The rigid body mode displacements z_i^* and y_i^* can be eliminated from Eq. (14) using the following relationships:

$$z_i^* = z_0 + l_i \tan\theta_z = z_0\left(1 - \frac{l_i}{L}\right) + \left(\frac{l_i}{L}\right) z_{n+1}$$
$$y_i^* = y_0 + l_i \tan\theta_y = y_0\left(1 - \frac{l_i}{L}\right) + \left(\frac{l_i}{L}\right) y_{n+1} \quad (19)$$

Substituting Eqs. (15), (16), and (19) into Eq. (18), one obtains the dynamic equations of motion of the system as:

$$[M]\begin{Bmatrix} \ddot{z}_0 \\ \ddot{y}_0 \\ \vdots \\ \ddot{z}_{n+1} \\ \ddot{y}_{n+1} \end{Bmatrix} + [K]\begin{Bmatrix} z_0 \\ y_0 \\ \vdots \\ z_{n+1} \\ y_{n+1} \end{Bmatrix} = \{F\} \quad (20)$$

where $\{F\}$ is the unbalanced force vector. For example, for the system shown in Fig. 2 with four rotor disks this force vector will be

$$\{F\} = \begin{Bmatrix} 0 \\ 0 \\ m_2 r_2 \omega^2 \cos(\omega t + \phi_2) \\ m_2 r_2 \omega^2 \sin(\omega t + \phi_2) \\ \vdots \\ m_5 r_5 \omega^2 \cos(\omega t + \phi_5) \\ m_5 r_5 \omega^2 \sin(\omega t + \phi_5) \\ 0 \\ 0 \end{Bmatrix} \quad (21)$$

Introducing a modal equivalent viscous damping matrix $[C]$ based on the modal values and using the generalized coordinate q_i, the final set of equations becomes

$$[M]\{\ddot{q}\} + [C]\{\dot{q}\} + [K]\{q\} = \{F\} \quad (22)$$

where

$$\{q\} = \begin{Bmatrix} z_0 \\ y_0 \\ z_1 \\ y_1 \\ \vdots \\ z_{n+1} \\ y_{n+2} \end{Bmatrix} \quad (23)$$

The overall system stiffness matrix $[K]$ contains the bearing nonlinear stiffness terms expressed in Eq. (12) as

$$K_{zz}^{1B} + \epsilon^{1B} z_0^2$$
$$K_{yy}^{1B} + \epsilon^{1B} y_0^2$$
$$K_{zz}^{2B} + \epsilon^{2B} z_{n+1}^2$$
$$K_{yy}^{2B} + \epsilon^{2B} y_{n+1}^2 \quad (24)$$

2.2.2 Numerical Solution of the Nonlinear System—Iterative Solution. The numerical time response solution for the nonlinear system of equations is calculated using the Newmark integration method (Rao, 1986; Subbiah and Reiger, 1988) in conjunction with an iteration procedure. From the Newmark method the resulting equations for the velocity and displacement vectors can be expressed as

$$\{\dot{q}\}_{k+1} = \{\dot{q}\}_k + [(1-\beta)\{\ddot{q}\}_k + \beta\{\ddot{q}\}_{k+1}]\Delta t, \text{ and} \quad (25)$$
$$\{q\}_{k+1} = \{q\}_k + \Delta t[\dot{q}\}_k + [(0.5-\alpha)\{\ddot{q}\}_k + \alpha\{\ddot{q}\}_{k+1}]\Delta t^2 \quad (26)$$

where k is the iteration step in time, and the parameters α and β indicate how much acceleration, at the end of interval Δt, enters into the velocity and displacement equations. To find the value of $\{\ddot{q}\}_{k+1}$, the equation of motion (Eq. (22)) for $t = t_{k+1}$ is given by

$$[M]\{\ddot{q}\}_{k+1} + [C]\{\dot{q}\}_{k+1} + [K]\{q\}_{k+1} = \{F\}_{k+1} \quad (27)$$

If we substitute $\{\ddot{q}\}_{k+1}$ and $\{\dot{q}\}_{k+1}$ in terms of $\{q\}_{k+1}$ in

Eq. (27), all the vectors at the time instant k in Eq. (25) and Eq. (26) will be known from the initial conditions. One can express $\{\ddot{q}\}_{k+1}$ in terms of $\{q\}_{k+1}$ in Eq. (26) and substituting $\{\ddot{q}\}_{k+1}$ in terms of $\{q\}_{k+1}$ in Eq. (25) one can find out $\{\ddot{q}\}_{k+1}$ in terms of $\{q\}_{k+1}$. In this way we can rewrite Eq. (27) with $\{q\}_{k+1}$ as the unknown, which is written as

$$\{q\}_{k+1} = \left[\left(\frac{1}{\alpha(\Delta t)^2}\right)[M] + \left(\frac{\beta}{\alpha\Delta t}\right)[C] + [K]_{k+1}\right]^{-1} \times \{\{F\}_{k+1} + [M]\left(\frac{1}{\alpha(\Delta t)^2}\{q\}_k + \frac{1}{\alpha\Delta t}\{\dot{q}\}_k + \left(\frac{1}{2\alpha} - 1\right)\{\ddot{q}\}_k\right) + \left([C]\left\{\frac{\beta}{\alpha\Delta t}\{q\}_k + \left(\frac{\beta}{\alpha} - 1\right)\{\dot{q}\}_k + \left(\frac{\beta}{\alpha} - 2\right)\frac{\Delta t}{2}\{\ddot{q}\}_k\right\}\right) \quad (28)$$

In the nonlinear rotor's case, the stiffness matrix $[K]_{k+1}$ in Eq. (28) has nonlinear terms that depend on the values of the elements in vector $\{q\}_{k+1}$. Equation (28) is a set of nonlinear algebraic equations now. Therefore an iteration procedure is utilized in conjunction with the Newmark method to find $\{q\}_{k+1}$. The following steps describe the numerical procedure:

1 Specify initial conditions at $t=0$, $\{q\}_0$, and $\{\dot{q}\}_0$.
2 Using the known initial conditions from Step (1) and Eq. (22), $\{\ddot{q}\}_0$ is calculated as

$$\{\ddot{q}\}_0 = [M]^{-1}[\{F_{t=0}\} - [C]\{\dot{q}\}_0 - [K]\{q\}_0 \quad (29)$$

where some of the terms of $[K]$ are a function of $\{q\}_0$.
3 Select the time step Δt, and parameters α and β.
4 Starting with $k=0$, assume a displacement vector $(\{q\}_{k+1})_A$.
5 Calculate the nonlinear terms of the stiffness matrix $[K]$, using values from the assumed displacement vector $(\{q\}_{k+1})_A$ in Eq. (24). Assemble the stiffness matrix $[K]$.
6 Calculate displacement vector $\{q\}_{k+1}$ using Eq. (28) and the stiffness matrix $[K]$ from Step (5).
7 Compare $\{q\}_{k+1}$ with assumed displacement vector. If the difference is not within specified tolerances, use an average value of the assumed displacement vector from Step (4) and the calculated displacement vector from Step (6) for the new assumed vector, and return to Step (5). If the difference is within tolerance then proceed to Step (8).
8 Calculate the acceleration and velocity at t_{k+1} from the following expressions, which are slightly modified forms of Eqs. (27) and (26):

$$\{\ddot{q}\}_{k+1} = \frac{1}{\alpha\Delta t^2}\{\{q\}_{k+1} - \{q\}_k\} - \frac{1}{\alpha\Delta t}\{\dot{q}\}_k - \left(\frac{1}{2\alpha} - 1\right)\{\ddot{q}\}_k \quad (30)$$

$$\{\dot{q}\}_{k+1} = \{\dot{q}\}_k + (1-\beta)\Delta t\{\ddot{q}\}_k + \beta\Delta t\{\ddot{q}\}_{k+1} \quad (31)$$

9 Update the assumed vector for t_{k+2} and go to Step (5). Continue for $k=N$ iterations to obtain the steady-state solution.

2.2.3 Solution of Linear Systems Using the Impedance Method. In Section 2.2.2 we obtained the numerical solution of the nonlinear system. As was discussed in Section 2.1, we will find an equivalent linear system using the optimization principles and then balance the equivalent linear system with a set of weights. Before we find the equivalent system it is worth briefly going over the impedance method (Tse et al., 1978) for finding the response of the linear system. Moreover, even to find the equivalent linear system one needs to know the linear response equations. The equations of motion for a linearized system are given by

$$[M]\{\ddot{q}\} + [C]\{\dot{q}\} + [K_{Eq}]\{q\} = \{F\} \quad (32)$$

where the matrix $[K_{\text{Eq}}]$ is the equivalent linear stiffness matrix, and $[M]$, $[C]$, and $\{F\}$ matrices are unchanged from the original nonlinear equations (Eq. (22)).

In the case of the rotor, the excitation force vector from the inherent unbalance is harmonic and all the elements in $\{F\}$ are of the same frequency. Therefore $\{F\}$ is expressed as

$$\{F\} = \{\bar{F}e^{j\omega t}\} = \{\bar{F}\}e^{j\omega t} \quad (33)$$

where $\{\bar{F}\}$ is the complex phasor of $\{F\}$. If we let the harmonic response be $\{Q\}$ where

$$\{Q\} = \{\bar{Q}e^{j\omega t}\} = \{\bar{Q}\}\ e^{j\omega t} \quad (34)$$

and $\{\bar{Q}\}$ is the complex phasor of $\{Q\}$; applying the impedance method and factoring out $e^{j\omega t}$, Eq. (32) becomes

$$-\omega^2[M]\{\bar{Q}\} + j\omega[C]\{\bar{Q}\} + [K_{Eq}]\{\bar{Q}\} = \{\bar{F}\} \quad (35)$$

or

$$[[K_{Eq}] - \omega^2[M] + j\omega[C]]\{\bar{Q}\} = \{\bar{F}\} \quad (36)$$

$$[Z]\{\bar{Q}\} = \{\bar{F}\} \qquad \{\bar{Q}\} = [Z]^{-1}\{\bar{F}\} \quad (37)$$

where $[Z]$ is the impedance matrix, and $\{\bar{Q}\}$ is the solution vector, which gives the amplitude and phase angle of the response. From the harmonic unbalance force vector $\{F\}$, the elements of the complex force vector $\{\bar{F}\}$ corresponding to the two-bearing four-rotor disks in Eq. (37) are given by

$$\begin{aligned}
\bar{F}(1) &= 0\\
\bar{F}(2) &= 0\\
\bar{F}(3) &= (m_2r_2\omega^2\cos\phi_2) + (m_2r_2\omega^2\sin\phi_2)j\\
\bar{F}(4) &= \left(m_2r_2\omega^2\cos\left(\phi_2+\frac{3\pi}{2}\right)\right) + \left(m_2r_2\omega^2\sin\left(\phi_2+\frac{3\pi}{2}\right)\right)j\\
\bar{F}(5) &= (m_3r_3\omega^2\cos\phi_3) + (m_3r_3\omega^2\sin\phi_3)j\\
\bar{F}(6) &= \left(m_3r_3\omega^2\cos\left(\phi_3+\frac{3\pi}{2}\right)\right) + \left(m_3r_3\omega^2\sin\left(\phi_3+\frac{3\pi}{2}\right)\right)j\\
\bar{F}(7) &= \left(m_4r_4\omega^2\cos\phi_4\right) + (m_4r_4\omega^2\sin\phi_4)j\\
\bar{F}(8) &= \left(m_4r_4\omega^2\cos\left(\phi_4+\frac{3\pi}{2}\right)\right) + \left(m_4r_4\omega^2\sin\left(\phi_4+\frac{3\pi}{2}\right)\right)j\\
\bar{F}(9) &= (m_5r_5\omega^2\cos\phi_5) + (m_5r_5\omega^2\sin\phi_5)j\\
\bar{F}(10) &= \left(m_5r_5\omega^2\cos\left(\phi_5+\frac{3\pi}{2}\right)\right) + \left(m_5r_5\omega^2\sin\left(\phi_5+\frac{3\pi}{2}\right)\right)j\\
\bar{F}(11) &= 0\\
\bar{F}(12) &= 0
\end{aligned} \quad (38)$$

2.2.4 Equivalent Linearization of the Rotor-Bearing System Using the Optimization Principle. Once the nonlinear steady-state solution is found, we can find the equivalent linear system using the optimization method outlined in Section 2.1. An equivalent linear stiffness matrix $[K_{\text{Eq}}]$ can be found to replace the nonlinear stiffness matrix $[K]$ such that the error in the rotor amplitudes between the numerical solution and the equivalent linear system solution is minimized. The following steps are used to obtain the values of the $[K_{\text{Eq}}]$ matrix:

1 Select a period of the steady-state solution from the numerical solution, and obtain vector $\{q(t)\}_{\text{NUM}}$.
2 Assume a vector whose components are the bearing equivalent linear stiffness values within specified upper and lower ranges:

$$\{V\} = \begin{Bmatrix} K^{1B}_{zz\text{Eq}} \\ K^{1B}_{yy\text{Eq}} \\ K^{2B}_{zz\text{Eq}} \\ K^{2B}_{yy\text{Eq}} \end{Bmatrix} \quad (39)$$

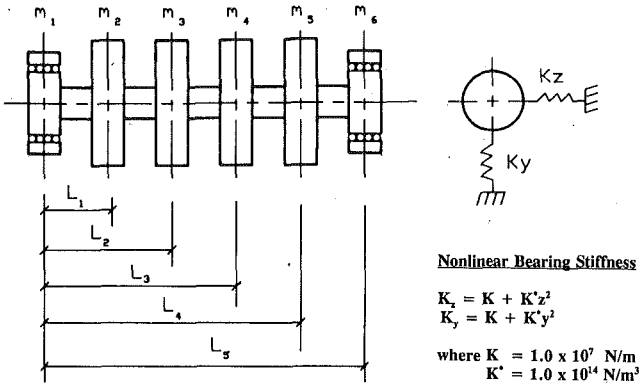

Fig. 3 Rotor system

Table 1 Rotor parameters

Rotor Parameters	Rotor No. 1	Rotor No. 2	Rotor No. 3
Shaft Diameter	0.050 m	0.076 m	0.089 m
M1	0.10 kg	0.05 kg	0.05 kg
M2	30.0 kg	20.0 kg	20.0 kg
M3	30.0 kg	20.0 kg	20.0 kg
M4	30.0 kg	20.0 kg	20.0 kg
M5	30.0 kg	20.0 kg	20.0 kg
M6	0.10 kg	0.05 kg	0.05 kg
L1	0.127 m	0.20 m	0.30 m
L2	0.254 m	0.45 m	0.55 m
L3	0.508 m	0.75 m	0.75 m
L4	0.635 m	1.00 m	1.10 m
L5	0.760 m	1.20 m	1.40 m
	L/D = 15.2	L/D = 15.79	L/D = 15.73

3 Replace the nonlinear stiffness terms shown in Eq. (24) with the assumed values from vector $\{V\}$ and calculate the equivalent linear stiffness matrix $[K_{Eq}]$. Obtain the steady-state response for each degree of freedom for the equivalent liner system using the impedance method, i.e., using Eq. (37), given earlier. Using $\{\overline{Q}\}$, the response vector for the equivalent linear system $\{q(t)\}_{Eq}$ can be found using Eq. (34).

4 Calculate the value of the objective function by defining the error as

$$e_j = \{q(t)\}_{NUM} - \{q(t)\}_{Eq} \tag{40}$$

The objective function becomes

$$U = \sum_{j=1}^{N_1} e_j^2 \text{ where } j = 1, N_1 \tag{41}$$

5 Follow the steps in the minimization algorithm outlined in Section 2.1 to find the equivalent linear stiffness values in vector $\{V\}$.

2.2.5 Balancing of a Linear System Using the Least-Squares Influence Coefficient Method. As discussed earlier, the influence coefficient method utilizes the rotor-bearing sensitivity for the calculation of balance correction weights (Rao, 1983). For linear systems this sensitivity can be expressed in matrix form, where the complex elements are terms as influence coefficients. The influence coefficients can be mathematically expressed as

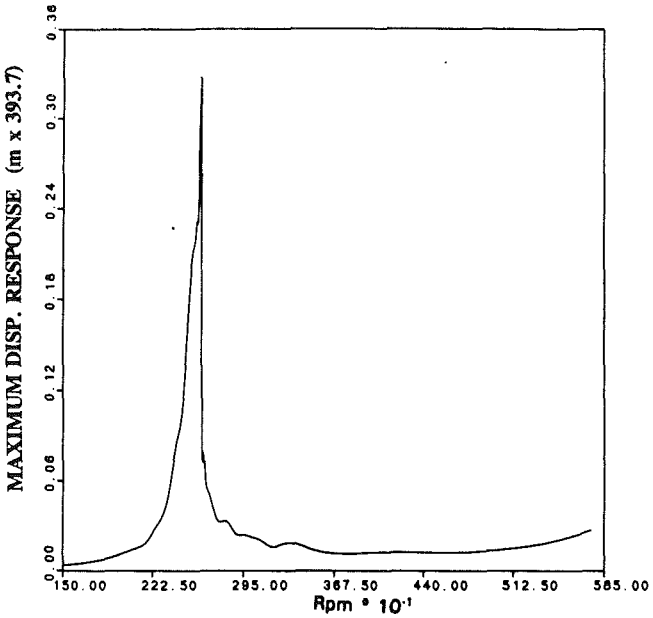

Fig. 4 Rotor unbalance response—typical

$$a_{ij} = \frac{(z_{ij} - z_{i0})}{T_j} \tag{42}$$

where a_{ij} is the complex influence coefficient, which is also an element of the matrix $[A]$ discussed subsequently; z_{io} is the ith vibration reading (the displacement amplitude and phase) with no trial masses installed in the jth balancing plane, z_{ij} is the ith vibration reading with the trial mass installed in the jth balancing plane; and T_j is the trial mass installed, expressed as a complex value representing its magnitude and angular location on the balancing jth plane. In addition to the initial uncorrected rotor data, for b balancing planes, b runs are necessary to collect all the data to calculate the influence coefficient matrix. Here we will assume that there are p vibration measurement planes taken along the rotor for each run.

If the number of measurements p is greater than the number of balancing planes, then we cannot, in general, reduce all residual vibrations to zero, but we can minimize the sum of their squares (squares of the displacement amplitudes).

In such cases, one can obtain (Goodman, 1964)

$$\{m_c\} = -([\overline{A}]^T [A])^{-1} [\overline{A}]^T \{z_0\} \tag{43}$$

where $[\overline{A}]$ is the complex conjugate of $[A]$. This is the set of correction masses that minimizes the residual vibration of the linear rotor system.

2.2.6 Balancing of a Rotor Supported on Nonlinear Bearings. The balancing procedure discussed in the previous section applies to linear systems. To use rotor response programs in precise balancing work for rotors with nonlinearities, i.e., with nonlinear supports, the nonlinearities have to be considered. This can be accomplished by using equivalent linearization. Once the nonlinear equations of motion are formulated, an equivalent linear system is obtained for the balancing speed of interest for use in the balancing program. The equivalent linear system is found by using the optimization techniques discussed in Section 2.1. This linear system is used to calculate the rotor response to the unbalance forces near its critical speed. The least-squares influence coefficient method of balancing is then used to find the correction weights to reduce the equivalent linear rotor's response to acceptable levels. These correction weights are used to balance the original nonlinear rotor.

3 Results and Discussion

3.1 Rotor Model. To illustrate the balancing procedure a rotor-bearing system with four disks was chosen. A negligible bearing mass was included in the model. Figure 3 shows the rotor configuration while Table 1 gives the parameters of the three different rotors considered. Rotor No. 1 consists of a shaft, 0.050 m in diameter, 0.760 m in length, with four 30 kg masses corresponding to the disks, and two 0.10 kg masses corresponding to the bearings. The shaft diameter and length was increased on Rotor No. 2, and the disk masses decreased to 20 kg. Rotor No. 3 has the same disk masses as Rotor No. 2, but the rotor length and shaft diameter were increased. For all three rotors the slenderness ratio was approximately constant.

The material density of 7832 kg/m^3 and an elastic modulus of 200 $\times$ 10^9 N/m^2 were used to model the rotor shaft. The bearing linear stiffness coefficient was chosen as 1.0 $\times$ 10^7 N/m while the nonlinear bearing stiffness coefficient was selected as 1.0 $\times$ 10^{14} N/m.

The unbalance condition assumed for each of the four disks was an eccentricity of 0.00002 m, with m_2 and m_3 in phase with a phase angle of 0.785 rad, and m_4 and m_5 in phase angle of 2.355 rad.

3.2 Numerical Solution. The solution technique used for the numerical solution of the equations of motion was the Newmark-β method in conjunction with an iteration procedure as described earlier in this chapter. The time step chosen was 0.0001 seconds. The constants α and β mentioned in Eq. (28) were chosen to give a numerically stable response (Rao, 1986). The total number of iterations was chosen such that the plotted results represented acceptable steady-state conditions.

This method consumed large amounts of computer time, since the steady-state amplitudes for a large number of speeds were required to generate a speed versus amplitude curve as shown in Fig 4. This figure shows the speed versus amplitude curve for z_2 of Rotor No. 1. Sufficient computer time must be allowed at each speed for the initial transients to die out. In order to minimize this time the damping coefficient in the structural damping matrix was increased to 0.05. Despite this high assumed damping a typical calculation for the steady-state rotor response at one speed took just under 2 hours CPU time on a VAX 785 digital computer, with a total elapsed time of approximately 4 hours.

This time increased when the speed selected approached the critical speed. The steady-state amplitudes with the balance weights added were calculated for the selected balancing speeds only.

3.3 Equivalent Linearization. In the optimization method of linearization, one cycle of the steady-state response of each degree of freedom of the rotor disks was selected, at a speed near the critical speed. This datum became the "exact solution." There were 501 data points (amplitude versus t) for each of the degrees of freedom.

The optimization problem parameters were chosen. The maximum and minimum values of the equivalent linear bearing stiffness were chosen as 5.0$\times$10^7 N/m and 1.0 $\times$ 10^7 N/m, respectively. Starting values for the four stiffness values were each selected within these limits. If the solution failed to converge after 50 runs, then the procedure was stopped. The convergence was sensitive to the selected starting values. Table 2 shows the equivalent linear stiffness values calculated for each of the rotors.

3.4 Balancing. Once the rotor system's equivalent linear bearing stiffness values were determined, the least-squares influence coefficient balancing procedure was used to determine the correction weights. These weights were then added to the nonlinear rotor system to reduce the rotor response.

The number of rotor balancing planes was chosen as 3, while the number of measuring planes was selected as 6. The vertical rotor displacements only were used in the balancing data. The rotor displacements were calculated using the impedance method discussed earlier. They were calculated at the first natural frequency for the equivalent linear system, which differed from the critical speeds observed from the rotor amplitude curves for the nonlinear rotors. From the impedance solution, the complex rotor amplitudes at the selected measuring planes were obtained for the original unbalanced condition. Then with a trial weight added to a balancing plane, three additional sets of rotor amplitudes were found. From these data, the matrix of influence coefficients were calculated as per Eq. (42). As an example, Table 3 shows the balancing data obtained for Rotor No. 2. The details about this process

Table 2 Equivalent linear bearing stiffness

	Rotor No. 1	Rotor No. 2	Rotor No. 3
$(K_{z1})_{Eq}$	1.0000 X 10^7	1.2121 X 10^7	1.0400 X 10^7
$(K_{y1})_{Eq}$	1.0272 X 10^7	1.2109 X 10^7	1.0478 X 10^7
$(K_{z2})_{Eq}$	1.5106 X 10^7	1.0650 X 10^7	1.3171 X 10^7
$(K_{y2})_{Eq}$	1.4181 X 10^7	1.0650 X 10^7	1.2975 X 10^7
SPEED	2550	3270	3250

Table 3 Balancing data—rotor No. 2

BALANCING DATA - ROTOR NO. 2											
ORIGINAL UNBALANCE			TRIAL WT. NO. 1			TRIAL WT. NO. 2			TRIAL WT. NO. 3		
Plane	Kg*m	Radians	Plane	Kg*m	Radians	Plane	Kg*m	Radians	Plane	Kg*m	Radians
2 & 3	.0004	0.785	2	.0009	0.785	3	.0009	4.713	5	.0009	2.356
4 & 5	.0004	2.355									
COMPLEX AMPLITUDES (m)			COMPLEX AMPLITUDES (m)			COMPLEX AMPLITUDES (m)			COMPLEX AMPLITUDES (m)		
z_{10}	6.29X10^{-4}	3.09x10^{-7}	z_{11}	9.19X10^{-4}	-2.90X10^{-4}	z_{12}	4.53X10^{-5}	6.99X10^{-6}	z_{13}	9.41X10^{-4}	2.99X10^{-4}
z_{20}	1.27X10^{-3}	-1.32X10^{-6}	z_{21}	1.85X10^{-3}	-5.92X10^{-4}	z_{22}	8.81X10^{-5}	1.43X10^{-5}	z_{23}	1.89X10^{-3}	6.02X10^{-4}
z_{30}	1.81X10^{-3}	-3.25X10^{-6}	z_{31}	2.63X10^{-3}	-8.50X10^{-4}	z_{32}	1.23X10^{-4}	2.08X10^{-5}	z_{33}	2.70X10^{-3}	8.60X10^{-4}
z_{40}	1.83X10^{-3}	-4.45X10^{-6}	z_{41}	2.66X10^{-3}	-8.66X10^{-4}	z_{42}	1.22X10^{-4}	2.29X10^{-5}	z_{43}	2.74X10^{-3}	8.72X10^{-4}
z_{50}	7.33X10^{-3}	-3.91X10^{-6}	z_{51}	1.93X10^{-3}	-6.32X10^{-4}	z_{52}	8.70X10^{-5}	1.82X10^{-5}	z_{53}	1.99X10^{-3}	6.35X10^{-4}
z_{60}	7.21X10^{-4}	-2.72X10^{-6}	z_{61}	1.05X10^{-3}	-3.45X10^{-4}	z_{62}	4.55X10^{-5}	1.13X10^{-5}	z_{63}	1.08X10^{-3}	3.47X10^{-4}

Note:Speed = 350.3 Rad/s

Table 4 Rotor response—rotor No. 1

RPM	Mass Station	Unbalanced Response (m x 39.37)	After First Balancing Run (m x 39.37)	% Reduction
2300	2	0.002576	0.000139	94.6
	3	0.003518	0.000153	95.6
	4	0.003515	0.000070	98.0
	5	0.002571	0.000033	98.7
2610	2	0.02237	0.000086	99.6
	3	0.03200	0.000167	99.5
	4	0.03163	0.000279	99.1
	5	0.02173	0.000247	98.9
5500	2	0.002716	0.001471	45.8
	3	0.002065	0.000955	53.7
	4	0.001686	0.000997	40.9
	5	0.002422	0.001533	36.7

Table 5 Rotor response—rotor No. 2

RPM	Mass Station	Unbalanced Response (m x 39.37)	After First Balancing Run (m x 39.37)	% Reduction
3000	2	0.002535	0.000018	99.3
	3	0.003482	0.000037	98.9
	4	0.003485	0.000105	96.9
	5	0.002539	0.000120	95.3
3300	2	0.011510	0.000205	98.2
	3	0.016260	0.000203	98.7
	4	0.016232	0.000117	99.3
	5	0.011445	0.000034	99.7
5000	2	0.000964	0.000272	71.8
	3	0.001205	0.000149	87.6
	4	0.001164	0.000106	90.9
	5	0.000890	0.000243	72.7

can be found from Turpin (1991). The balancing process can be understood from this table as well as referring to Fig. 3. The original unbalance information in planes 2 and 5 is given in the first three columns of this table. The displacement amplitude and phase information expressed in complex numbers are shown in the lower portion of these columns when no trial weights are added. Next, similar information with trial weights added, one at a time, is shown in three different sets, each set consisting of three columns. The locations of all the planes are shown in the Fig. 3. To enhance the clarity, it should be mentioned here that the trial weights required use of additional terms in the force vector expressed as Eq. (38) and the corresponding response values were obtained from Eq. (37). Using Eq. (43), a set of correction weights that minimized the unbalance responses were obtained. These correction weights were then added to the nonlinear rotors and the rotor response was calculated. Tables 4–6 show the reduction in the unbalance response near the first critical speed and one other higher operating speed for each of the nonlinear rotors. These results clearly show that one can balance the nonlinear system, by first finding an equivalent linear system, and then balancing weights for this linear system.

4.0 Conclusions

In this work, the equations of motion were derived using the Lagrange equations and the influence coefficient method.

Table 6 Rotor response—rotor No. 3

RPM	Mass Station	Unbalanced Response (m x 39.37)	After First Bal.Run (m x 39.37)	% Red.	After Second Bal. Run (m x 39.37)	% Red.
3250	2	0.011150	0.001732	84.5	0.000444	96.0
	3	0.014063	0.002096	85.1	0.000519	96.3
	4	0.014400	0.002110	85.3	0.000508	96.5
	5	0.010828	0.001581	85.4	0.000361	96.7
3400	2	0.009638	0.000324	96.7	0.000117	96.6
	3	0.012455	0.000349	97.2	0.000110	99.1
	4	0.012793	0.000319	97.5	0.000085	99.3
	5	0.009472	0.000208	97.8	0.000032	99.7
5000	2	0.000924	0.000191	99.3	0.000116	87.4
	3	0.001272	0.000107	91.6	0.000056	95.6
	4	0.001285	0.000022	98.3	0.000018	98.6
	5	0.000981	0.000095	90.3	0.000100	90.3

The nonlinear set of equations was solved using the Newmark-Beta time-marching scheme in conjunction with an iteration procedure. The equivalent linear system was obtained using the optimization principle. The balancing weights for this linear system were obtained using the least-squares influence coefficient matrix. The peak response values of the linear system were at different frequencies from the nonlinear system. The balancing had to be done at the frequency that corresponded to the peak of the equivalent linear system. These weights were then used on the nonlinear system and the results obtained were quite good.

References

Bishop, R. E. D., 1959, "The Vibrations of Rotating Shafts," *Journal of Mechanical Engineering Science*, Vol. 1, No. 1, pp. 50–64.

Bishop, R. E. D., and Gladwell, G. M. L., 1959, "The Vibration and Balancing of an Unbalanced Flexible Rotor," *Journal of Engineering Science*, Vol. 1, No. 1, pp. 66–77.

Bishop, R. E. D., and Parkinson, A. G., 1972, "On the Use of Balancing Machines for Flexible Rotors," ASME *Journal of Engineering for Industry*, Vol. 94, pp. 561–576.

Genta, G., and Repaci, A., 1988, "Circular Whirling and Unbalance Response of Non-linear Rotors," *Rotating Machinery Dynamics*, Vol.–Bentley Rotor Dynamics Research Corporation, pp. 441–448.

Gladwell, G. M. L., and Bishop, R. E. D., 1959, "The Vibration and Balancing of Rotating Shafts Supported in Flexible Bearings," *Journal of Mechanical Engineering Science*, Vol. 1, No. 3, p. 195.

Goodman, T. P., 1964, "A Least Square Method for Computing Balance Corrections," ASME *Journal of Engineering for Industry*, Vol. 86, pp. 273–279.

Kellenberger, W., 1972, "Should a Flexible Rotor Be Balanced in N or $(N+2)$ Planes," ASME *Journal of Engineering for Industry*, Vol. 94, pp. 548–560.

Little, R. M., and Pilkey, W. D., 1976, "A Linear Programming Approach for Balancing Flexible Rotors," ASME *Journal of Engineering for Industry*, Vol. 98, pp. 1030–1035.

Lund, J. W., and Tonneson, J., 1972, "Analysis and Experiments in Multiplane Balancing of Flexible Rotors," ASME *Journal of Engineering for Industry*, Vol. 94, pp. 233–242.

Meldahl, A., 1954, "Auswuchten Elastischer Rotoren," *Z. angew. Math. und Mech.*, Vol. 34.

Rao, J. S., 1983, *Rotor Dynamics*, Wiley Eastern Ltd., New Delhi, India, pp. 207–214.

Rao, S. S., 1986, *Mechanical Vibrations*, Addison-Wesley Publishing Company, Inc., MA, pp. 489–491.

Rieger, N. F., 1967, "Computer Program for Balancing of Flexible Rotors," Mechanical Technology Incorporated Report No. 67TR68, Sept.

Sharan, A. M., and Rao, J. S., 1985, "Imbalance Response of Rotor Disks Supported by Fluid Film Bearings With a Negative Cross Coupled Stiffness Using Influence Coefficient Method," *Mechanics and Machine Theory*, Vol. 20, No. 5, pp. 414–426.

Sharan, A. M., and Turpin, A. E., 1989, "Solution of Non-linear Vibration

Problems Using Optimzation Principles," *ASME 12th Biennial Conference on Mechanics Vibration and Noise*, Montreal, Quebec, Canada, Vol. 18-5.

Subbiah, R., and Reiger, N. F., 1988, "On the Transient Analysis of Rotor-Bearing System," ASME *Journal of Vibration, Acoustics, Stress, and Reliability in Design*, Vol. 110, pp. 515–520.

Tessarzik, J. M., Badgley, R. H., and Anderson, W. J., 1972, "Flexible Rotor Balancing by the Exact Point-Speed Influence Coefficient Method," ASME *Journal of Engineering for Industry*, Vol. 94, pp. 148–158.

Tessarzik, J. M., and Badgley, R. H., 1974, "Experimental Evaluation of the Exact Point-Speed and Least Squares Procedures for Flexible Rotor Balancing by the Influence Coefficient Method," ASME *Journal of Engineering for Industry*, Vol. 96, No., pp. 633–643.

Tonneson, J., 1974, "Further Experiments on Balancing of a High Speed Flexible Rotor," *Journal of Engineering for Industry*, Vol. 96, pp. 431–440.

Tse, F. S., Morse, I. E., and Hinkle, R. T., 1978, *Mechanical Vibrations, Theory and Applications*, Allyn and Bacon, Inc., Boston, MA, pp. 356–360; 406–407.

Turpin, A., 1991, "Balancing of Flexible Rotors Supported on Bearings Having Non-linear Flexibility," M. Eng. Thesis, Memorial University of Newfoundland, St. John's, Newfoundland, Canada.